NASA Conference Publication 2335

Research in Structures and Dynamics—1984

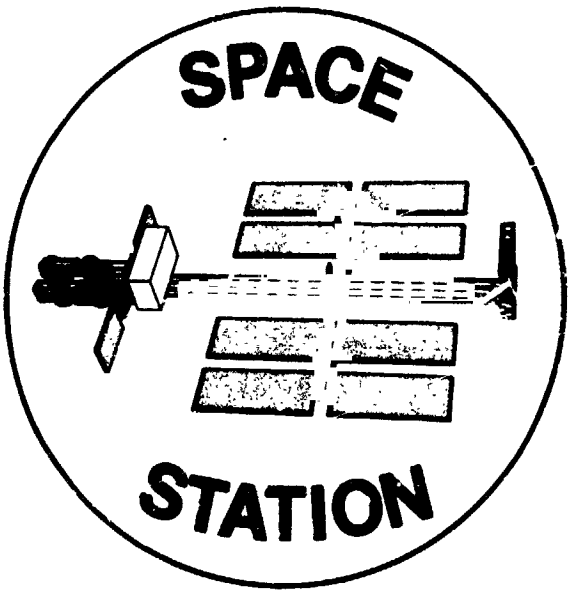

Research-in-progress papers presented at a symposium held at Washington, D.C. October 22-25, 1984

NASA

NASA Conference Publication 2335

Research in Structures and Dynamics—1984

Compiled by
Robert J. Hayduk
NASA Langley Research Center

Ahmed K. Noor
The George Washington University
Joint Institute for Advancement of Flight Sciences
Hampton, Virginia

Research-in-progress papers presented at a symposium sponsored by NASA Langley Research Center, Hampton, Virginia, and The George Washington University, Washington, D.C., in cooperation with the National Science Foundation, the Air Force Office of Scientific Research, the American Institute of Aeronautics and Astronautics, the American Society of Mechanical Engineers, and the American Society of Civil Engineers, and held at Washington, D.C. October 22–25, 1984

NASA
National Aeronautics and Space Administration

Scientific and Technical Information Branch

1984

FOREWORD

Notable advancements have been made in the structures and dynamics disciplines in recent years. These advances have been, and continue to be, strongly impacted both by the new developments in computer technology and by the growing interaction with other disciplines such as applied mathematics, applied mechanics, numerical analysis, computer science, and controls technology.

The growing importance of discipline interaction and computational technology recently led the Directorate for Structures at NASA Langley Research Center to institute the new Interdisciplinary Research Office (IRO) and to start a new initiative on Computational Structural Mechanics (CSM). The Interdisciplinary Research Office will enable multidisciplinary and cross-disciplinary research on the most advanced computer systems available in a research laboratory environment. The Computational Structural Mechanics initiative will encourage collaboration by individuals across organizational lines of management and from government laboratories, universities, and industry. Other organizations besides NASA are encouraging collaboration between researchers of interacting disciplines. For example, the National Science Foundation has initiated a new program to support engineering research centers to meet a need for providing cross-disciplinary research opportunities for faculty and students at academic institutions. The annual operating cost for each center is expected to range between $2.5 million and $5.0 million.

As a step toward stronger interaction among experts in the fields that are likely to impact developments in the structures and dynamics disciplines, a symposium entitled "Advances and Trends in Structures and Dynamics" was held in Washington, D.C., on October 22-25, 1984. The symposium was jointly sponsored by NASA Langley Research Center and George Washington University. Cooperating organizations were the National Science Foundation, Air Force Office of Scientific Research, American Institute of Aeronautics and Astronautics, American Society of Mechanical Engineers, and American Society of Civil Engineers.

The symposium brought together the researchers and their peers from industry, academia, and government laboratories who are advancing the state-of-the-art in structures and dynamics and setting the trends for the future.

This NASA Conference Publication contains 19 research-in-progress papers plus 8 full-length papers presented at the symposium. The present publication is a companion to the Pergamon Press conference proceedings,* which contains 68 full-length papers presented at the symposium.

The papers in this document are divided into the following seven topics:

1. Multiprocessors, parallel computation, and database management systems
2. Advances in finite element technology
3. Interactive computing and optimization
4. Mechanics of materials

---

*Noor, A. K.; and Hayduk, R. J. (eds.): Advances and Trends in Structures and Dynamics. Pergamon Press, Ltd., 1985.

5. Structural stability

6. Dynamic response of structures

7. Advanced computer applications

The fields covered by the symposium are rapidly changing, and if new results and anticipated future directions are to have maximum impact and use, it is imperative that they reach workers in the field as soon as possible. This consideration led to the decision to publish these proceedings prior to the symposium. Special thanks go to the Research Information and Applications Division at NASA Langley Research Center for their cooperation in publishing this volume.

The use of trademarks or manufacturers' names does not constitute endorsement, either expressed or implied, by the National Aeronautics and Space Administration.

R. J. Hayduk
A. K. Noor
Compilers

CONTENTS

MECHANICS OF MATERIALS

STRUCTURAL STABILITY

DYNAMIC RESPONSE OF STRUCTURES

ADVANCED COMPUTER APPLICATIONS

THE FLEX/32 MULTICOMPUTING ENVIRONMENT

Nicholas Matelan
Flexible Computer Corporation
Dallas, TX

SUMMARY

The FLEX/32 MultiComputer is a generic environment for cooperating multiple processors. The FLEX/32 can support a number of different processors, making it heterogeneous in terms of the instruction sets it can support, and homogeneous in its ability to provide consistent storage and input/output facilities to its differing processors. These facilities are accessed through standard 32-bit VMEbus connections.

The FLEX/32 supports the full UNIX* System V Operating System and languages associated with it, plus the extended ConCurrent C† and ConCurrent FORTRAN† 77 languages that allow programming of concurrent software at a high level. Direct programming support at all levels is provided by the environment hardware for concurrent software execution and optimization, including hardware support for shared-resource access arbitration, conditional critical-region arbitration, and interprocessor messages.

INTRODUCTION

The past thirty years have seen dramatic improvements in the performance of computers. In general, these improvements have been due to improvements in components. Today, as we approach physical limits in the performance of components, the architectures of computers become more and more important. While we still see a great deal of improvement to be made in the application of faster component technologies, the effects of these components on conventional architectures using a single central processing unit begin to show diminishing returns. Architectures based on multiple central processing units show promise of providing not only increased power, but also increased flexibility in meeting the varying demands of future computation. The FLEX/32 is such a system.

*UNIX is a trademark of AT&T Bell Laboratories

†ConCurrent C and ConCurrent FORTRAN are trademarks of Flexible Computer Corporation

The FLEX/32 is a MultiComputing Environment, that is, it is an environment that supports multiple computers working on one or more tasks together or independently under coordinated software. These computers need not be the same. Therefore, the environment is heterogeneous in nature. The computers supported in this environment can differ in power, in the amount of memory supported, and in their basic orientations. Some of these computers could contain processors dedicated to control, while others might be used for array processing and floating-point operations, for example.

The addition of a new computer, with its new processor and instruction set, requires only adaptation to the environment. This means that once the adaptation has been made, the generic software and input/output capabilities of the environment are fully available to the new processor. Such software includes the UNIX System V Operating System, and other special tools needed for developing concurrent programs.

Input/output is performed via a set of standard VMEbuses. These buses support interfaces to peripheral equipment that may be purchased from any of the 80 to 100 current providers of VMEbus interfaces or from Flexible Computer Corporation, giving a truly open architecture.

A final, but no less significant, feature of the environment is its SelfTest System. Built into the environment and distributed throughout its modules (computers, memory and peripheral interfaces) are test circuits dedicated to determining the health and performance of the environment as a whole. This system allows not only such features as automatic shutdown and restart in response to power failures, but also fault isolation and repair verification, and performance analysis based on information collected during the run-time execution of programs.

LEVELS OF DESCRIPTION

In describing a computer, it is important to distinguish between its architecture and its implementation. An architecture is a description of the fundamental attributes and functionality of a device or program without regard to its detail. An implementation is a description of the collection of details needed to construct a product. It is the product that provides certain levels of performance and power. It is the architecture that provides product line consistency throughout its history.

Both hardware and software have an architecture. A major thrust of the FLEX/32, in addition to its great flexibility of configuration, is to provide an environment for programmers to produce software more cost effectively. The dichotomy of the architecture and implementation is maintained primarily to guarantee that software interfaces to the FLEX/32 MultiComputing Environment will not change throughout the life of the product line. We all know that as time passes there

will be better ways to produce hardware that is faster, more reliable, and cheaper. However, it is the intention of the Flexible Computer Corporation that changes in FLEX/32 hardware, as they must come, will not involve changes in existing application software. The architecture defines a set of invariant interfaces for the users and builders of software intended for the FLEX/32 product line, even as its hardware is adapted over the years to the use of newer and better techniques. Its software, at every level, can remain invariant [illegible] its interface to the hardware remains invariant.

THE FLEX ARCHITECTURE

The FLEX/32 is a MIMD (Multiple Instruction Stream/Multiple Data Stream) Multiprocessor System. Its architecture (generically represented in figure 1) is composed of devices, buses, processes, and topologies.

Devices are either computational or peripheral. Computational devices include processors, memories, bus interfaces, interprocessor signaling mechanisms, and common locks. Peripheral devices are those devices that control and sense the outside environment. These include tapes, disks, printers, terminals, and their controllers.

Devices are connected one to another by buses. There are four separate buses defined in the FLEX/32 architecture. These are the Common Bus, the Local Bus, the Peripheral Bus, and the SelfTest Bus. Common buses are those that are intended to allow the sharing of resources, such as shared memory or shared devices. Local buses are intended to provide paths between a processor and its attached local devices, such as local memory. Since each local bus is defined as multi-master, more than one processor can be attached to it.

Peripheral buses are those buses that allow attachment between devices on local buses to the controllers of peripheral devices and actuators in the outside environment. The SelfTest Bus runs throughout the MultiComputing Environment and is that transfer path that allows information about the state of the machine to be received and control of the machine to be sent.

Of course, all this hardware would be useless without a method for applying algorithms to control and direct operations toward a useful result. The FLEX/32 supports multiple, truly concurrent processes. True concurrency is the execution of processes on different processors at exactly the same time. This is often called multiprocessing. Apparent concurrency is the execution of processes in a shared fashion on a single processor at a rate fast enough to lead an observer to believe that they execute at the same time. This is

usually called multitasking or multiprogramming. The FLEX/32 is a parallel processing system and, therefore, allows both true concurrency and apparent concurrency depending on the needs of the programmer.

Each of the devices, processes, and buses outlined above may be connected in a number of possible configurations. Figure 1 shows the physical topology of the FLEX/32 MultiComputing Environment. Any number of local buses may be attached through ports to several common buses. Common buses are fully arbitrated and will allow only one access at a time from each local bus in a fair arbitration scheme. Each local bus is attached to its own common lock device. This device can be programmed to allow the processes mutually exclusive access to shared resources for an arbitrarily complex use of shared data. In general, interprocessor communication is maintained through shared memories residing on the common bus. Notice that this topology does not allow processors to reside on the common bus, only resources. Processors are always attached to local buses. Peripheral devices are attached to local buses through bus interfaces.

There is no limit to the number of local buses or the number of processors that may be attached to local buses in the architecture. Implementations, however, must put a bound on the number of buses and processors that can be contained in any particular unit, such as a cabinet. The architecture, however, fully allows multiple cabinets; therefore, even in the implementation there is no inherent bound on the number of processors that can placed together in a FLEX/32 configuration.

The SelfTest Bus connects all devices in the architecture together. Processes that actually perform selftest functions reside within one of the processors in the system.

THE FLEX/32 HARDWARE IMPLEMENTATION

The FLEX architecture is an abstract representation of the allowable interconnections of devices. As such it makes no demands for execution speed, word sizes, and so forth. The FLEX/32 product line is a 32-bit implementation of the FLEX architecture. It specifies the technology from which the FLEX/32 is built, its packaging, and physical parameters. The FLEX/32 hardware implementation is the environment used to carry out the commands of the FLEX software described below.

The philosophy of the FLEX/32 implementation is the provision of a flexible, universal hardware and software environment for a number of different instruction sets. Just as software environments have become a way of supporting programs written in different languages, the FLEX/32 hardware is an environment for different processors. These processors are supplied with generic memory, input/output sup-

port, and multicomputer and network interprocess communication mechanisms. This environment is the same for each processor type, but the instruction sets supported are different. This allows not only software written in different languages, but also different machine instruction sets, to execute together.

The components of the FLEX/32 hardware are divided into the Card Level, the Backplane Level, and the Unit Level. Circuit cards define the replaceable module level of the FLEX/32. There are three classes of cards in a FLEX/32 System. These are Universal Cards, Common Communication Cards, and Peripheral Cards.

Universal Cards support local bus activities such as computation, memory storage, array processing, and other such activities. Common Communication Cards allow access to, arbitration of, and control over the common buses and their shared resources, such as the common memory. Peripheral Interface Cards are standard single, dual, or triple Eurocard interfaces available from commercial manufacturers. There are currently 80 to 100 commercial manufacturers producing cards to control standard peripheral equipment based on the VMEbus Eurocard format. These cards are interconnected via a backplane supporting the Local Bus, Common Bus, and SelfTest Buses.

The Local Bus is a standard, asynchronous 160 megabit per second VMEbus with extensions for control internal to one FLEX/32 cabinet. The Common Bus is a synchronous version of the Local Bus. The Common Communication Cards house a high-speed shared memory. The SelfTest Bus is a RS422 bus supporting the HDLC protocol. All external communications are through bus interfaces on Universal Cards to standard VMEbuses (no extensions). Peripheral buses are attached to standard VMEbus Interface Cards.

The cards connected to the backplanes are supported by card cages, and divided into two types of units. One unit is the MultiComputer Unit, or MU. It is the MU that houses both Universal Cards and Common Communication Cards. All Interface Cards to peripheral equipment are housed in a second type of unit called a Peripheral Control Unit or PCU. Cables between the two units allow computers attached to local buses to control their various I/O devices.

The MultiComputer Unit can house up to ten local buses and two common buses. There can be twenty universal cards in a MultiComputer Unit, two per local bus. The MultiComputer Unit supports up to ten communication cards, one for each local bus, allowing any processor attached to any local bus to communicate with any other processor, either through a shared memory associated with a common communication card or through the direct interprocessor messaging capability. Furthermore, a common lock capability allows a processor to define a critical region in the shared memory and to own that region for operations without affecting traffic on the Common Bus.

The initial Universal Cards offered by Flexible Computer Corporation are the Computer1 Card and the Mass Memory Card. The

Computer1 Card includes a 1 MIP (million instructions per second) processor with attached floating-point coprocessor and 128K bytes of ROM, a full megabyte of memory protected by error correction and detection logic, and a VMEbus port that can be configured to either 32 or 16-bits of data. The processor can access its bus interfaces and its memory on this card without affecting the operation of its local bus. This is important when both slots associated with local buses are used for computer cards.

The Mass Memory Card supports from 1 to 8 megabytes of random access memory protected by error correction and detection logic. It also contains a VMEbus interface.

The MultiComputer Unit can be configured in a number of ways. For example, a unit can be configured with twenty computer cards giving a machine with twenty 1-MIP processors, twenty megabytes of memory, and twenty VMEbus interfaces. This system could also be configured to support up to 2 megabytes of fast common memory. Another system could be configured with one computer card, and the remainder of the MU filled with memory. This would give a system with one processor and twenty VMEbus interfaces plus 153 megabytes of memory. A more usual card complement would be four or five computer cards with an extra mass memory card giving processors with 9 megabvtes of memory each, and perhaps a few single processing cards without extra memory. Future computer card types will include floating-point capability in the 4 to 6 megaflops (millions of floating-point operations per second) range. It should be noted that all FLEX/32 processor types can be mixed and matched in each FLEX/32 MultiComputer Unit.

VMEbus interfaces can be simply jumpered together giving extra shared paths than those associated with the common buses. Interprocess communications over these paths can be made using read/modify/write interprocess communication instructions between Local Memories. The same jumpers can be used to connect multiple MultiComputer Units together forming much larger systems. Four of these VMEbuses, for example, could be used to connect to neighbors north and south, and east and west. Such a method could be used to define a plane of MultiComputer Units. Similarly, six interconnections could be used to define hypercubes of MultiComputer Units yielding a large number of computers (dozens to hundreds) that could be applied to the same tasks. The possibility of such large multiple processor systems makes the selection of the algorithms very important in determining the usefulness of any configuration. As is the case with any computer, infinitely expandable may not mean infinitely useful, except for a narrow range of algorithms. It is fortunate, however, that some of these algorithms are very useful indeed.

FLEX/32 SOFTWARE IMPLEMENTATION

For system development, Flexible Computer provides the full UNIX System V Operating System supported on each computer within the MultiComputing Environment.

Flexible Computer has also extended the C and FORTRAN languages to produce the new languages ConCurrent C and ConCurrent FORTRAN. These languages are standard C and FORTRAN with an extra set of statements that allows direct specification of concurrent programs for execution in the FLEX/32 environment.

The FLEX/32 can execute programs directly under ConCurrent C or FORTRAN program control instead of under UNIX. Flexible supplies a set of MultiComputing Multitasking Support Utilities to facilitate such dedicated operation.

UNIX SYSTEM V

UNIX System V is a true industry standard for software development. It includes support software such as SCCS (Source Code Control System) and its associated editors and language processors, such as FORTRAN 77, which Flexible has extended with the ISA real-time extensions (Std.1), RATFOR, SNOBOL, and Assembly Language. It provides development and debugging tools and file management capabilities within the most portable operating system presently available. In addition, concurrent execution of processes can be simulated using the "shared memory" software capability of UNIX System V, or truly executed simultaneously.

THE CONCURRENT C PROGRAMMING LANGUAGE

The C Programming Language has proven to be an excellent tool for programming in a sequential processing environment. The ConCurrent C Language (ref. 1) is designed to further increase the capabilities of the C language by facilitating direct concurrent and real-time processing for advanced parallel multiprocessor systems, while maintaining the original C style and philosophy. The C is upward compatible to ConCurrent C which preserves all of C's definitions and features.

The design objectives of the ConCurrent C Programming Language were

- to extend C Language capabilities to support, directly and as language constructs, real-time event supervision and concurrent processing on parallel multiprocessor systems, as well as in the usual sequential environments

- to provide simple, structured, and C-like syntax with a minimal number of new key words. Additional features are obtained by combining explicitly provided features with programming techniques and styles

- to supply generic capabilities that can be used to implement various programming concepts. This makes the language more adaptable to different hardware structures and applications; ConCurrent C provides mechanisms without dictating techniques

- to provide constructs to allow procedural and non-procedural event supervision. Consequently, machine-level operations (interrupts, timers, traps, etc.) can be specified and controlled by a high-level language

- to avoid redefining, extending, or modifying any C Language features or definitions. This objective was included to make the ConCurrent C and C languages compatible

- to directly support multiprocessor configurations reflected in new statement types

These objectives were realized by including in ConCurrent C capabilities to directly support

- protected shared data access, to prevent a process from using data that is still being operated on by another process

- interprocess communications and synchronization, regardless of the process physical location

- creation and concurrent execution of processes

- event definition and event supervision at a level that allows events to be used as efficient inter- and intraprocess synchronization tools, as well as response to real-time incidents (universally required in real-time applications)

ConCurrent C constructs are categorized in two classes: new variable definitions (event variables and shared variables) and new control-flow statements (process interaction, process control, concurrent execution, and event supervision). The following discussion is an informal description of some of the constructs supported by ConCurrent C. Note that a variety of techniques can be implemented using ConCurrent C capabilities, and that only some of those are shown in the examples of figure 2.

ConCurrent C introduces a new type, event variables, to support real-time event handling. All real-time events are either timers or exceptions. The key words timer and exception are used to declare and define event variables. An exception can cause incidents that affect either its defining process (internal exceptions or traps), or a separate process (external exceptions or interrupts).

The WHEN statement is used to suspend its enclosing process until a specified event is satisfied, at which time its associated statement list is executed. The WHEN-ELSE, however, evaluates the condition; if the condition is satisfied, it also executes the statement(s) immediately following the when; otherwise the else statement list is executed. The syntax of the WHEN-ELSE is similar to IF-ELSE statement.

The WHENEVER statement is provided to support non-procedural event supervision. This statement, for a specific scope of the program, specifies an event to be observed as a parallel task while the program is being executed. It also defines an event handler to be executed whenever the event occurs. If the specified event occurs, normal execution will be interrupted and the event handler executed. Upon completion of the event handler, control will return to the point at which the program was interrupted.

The WHEN statement is also used, in addition to procedural event response, to synchronize access to shared data between processes. The WHEN statement synchronizes shared access based on conditions that are evaluated at the time the access is to be made. A condition is an expression that always evaluates to true or false; it is this result that controls whether the statement block associated with the WHEN is executed. The WHEN statement can thus be used to directly implement the Conditional Critical Region technique of sharing data. Note that any combination of condition testing and synchronization by event is allowed.

The process concept is the basis of true concurrent execution. A process in ConCurrent C is defined and started by a process statement. Each process statement includes

- a unique identifier for subsequent control of process instantiations
- the code that it uses for execution
- the processor that executes it (optional)
- and the system dependent attributes that define its environment, such as priority, stack size, and so forth (optional)

System dependent attributes, if required, are placed in a predefined structure and passed to the system support environment. This structure can be customized for different implementations, or totally omitted.

Proper combinations of these statements and other existing C Language statements can define and cause to be executed every known multiple process intercommunication technique, including semaphores, monitors and messages.

Each of the capabilities of ConCurrent C listed here are also available in ConCurrent FORTRAN 77.

MULTICOMPUTING MULTITASKING SUPPORT UTILITIES

The FLEX/32's MultiComputing Multitasking Support (MMS) Utilities provide support for real-time, run-time embedded applications.

The MMS Utilities are resident in the System Library and are included by the loader to resolve all external calls generated by the ConCurrent C preprocessor. The capabilities of the MMS Utilities include the following:

a. Priority-Oriented Task Management and Multiprogramming

b. MultiComputing, by providing interprocessor communication, synchronization, and data protection for concurrent or sequential processing

c. Interprocess Communication and Signaling

d. Event Management to supervise conventional interrupts, interprocessor messages, user-defined exceptions, system-defined exceptions, and timers

e. Memory Pool Management

A METHODOLOGY FOR CONCURRENT PROGRAM DEVELOPMENT

Of major importance in producing commercial quality (that is, useful) concurrent programs is the availability of a development methodology fully supported by software tools.

Figure 3 provides a block diagram of the flow of program compilation, loading, and execution within the FLEX/32 MultiComputing Environment. The steps from sequential code development through final concurrent program integration constitute the FLEX/32 development methodology.

At the top of figure 3, a ConCurrent C program source file is shown. It is first processed via the ConCurrent C Preprocessor, resulting in the output of a C Language Source File containing unresolved MMS system calls. The Preprocessed ConCurrent C Source is next compiled under UNIX System V by the C compiler, resulting in an object code file. The object code file can then run through the system loader having all system calls resolved by the MMS Utilities contained in the System Library, resulting in an executable image file.

The right side of figure 3 depicts the several execution options provided by the FLEX/32 MultiComputing Environment. Three different environments are provided with the FLEX/32 MultiComputer. The first allows execution under a Concurrent Executive and provides for a true

parallel computer, concurrent operating environment. The second is execution in a simulation of a concurrent environment under the UNIX System V environment. This program is called the FLEX/32 Concurrency Simulator. The third environment is UNIX System V which allows either non-concurrent (sequential) operation, or distributed operation.

The FLEX/32 methodology for concurrent program development is a phased migration of processes from one environment to another. Separate compilation and test of sequential programs under UNIX and its tools allow a number of programmers to contribute to the development of large software systems. As these programs are developed and known to be functionally correct, they can be collected under a ConCurrent C program as processes. This concurrent program can be fully debugged using the Concurrency Simulator, still under UNIX and its many support tools. If appropriate, this program can be forever executed in multiple processors under UNIX. If, however, the program was intended to execute directly on the MultiComputer, processes can be moved one at a time, or all at once, into the intended processors under MMS. This allows incremental use of true concurrency from the shelter of apparent concurrency and UNIX support afforded by the Concurrency Simulator.

The diagram also depicts a number of source processes written in some of the languages that can be compiled via their individual language compilers and combined by the system loader. Again, their system calls are resolved and images are produced that allow them to execute together in different computers under any of the concurrent, simulated concurrent, and non-concurrent environments provided.

CONCLUSION

Concurrent processing utilizing multiple processors is an advanced technique for achieving more processing power, faster computation and flexible application of computing hardware to changing requirements.

ConCurrent C and FORTRAN were developed to provide high-level software development tools for the concurrent programming of true Multiple Instruction Stream/Multiple Data Stream (MIMD) computing environments such as the FLEX/32 MultiComputer.

REFERENCE

1. Naeini, Ray: A few statement types adapt C language to parallel processing. Electronics, vol. 57, no. 13, June 28, 1984.

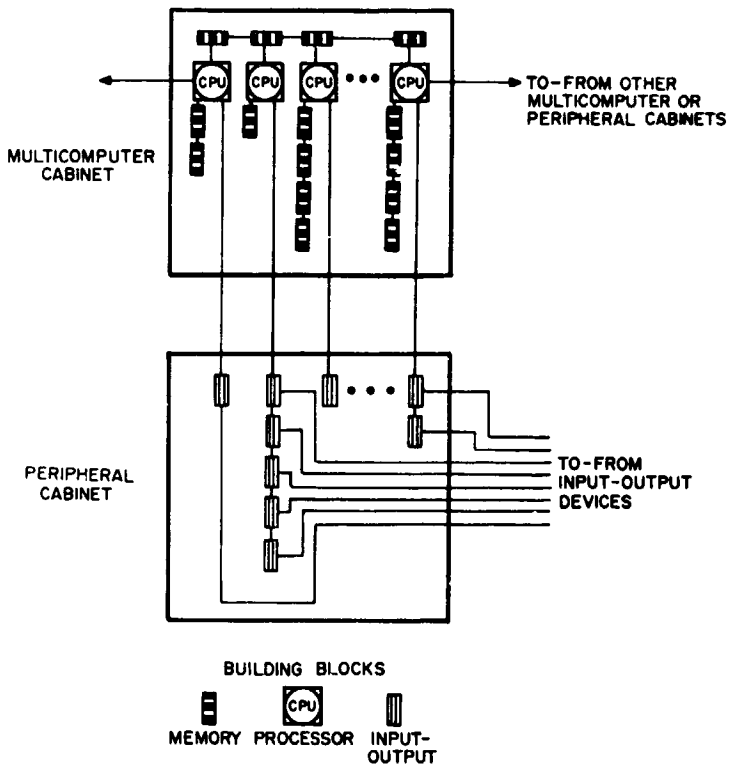

Figure 1.- Generic FLEX architecture.

```
Synchronization Using "Exceptions", "When"
And "whenever" :

        exception msg_ready  sender   --> receiver ;
        exception msg_rcved  receiver --> sender   ;
        exception msg_end    sender   --> receiver ;

 sender process :                 receiver process :

...                               ...
...                               whenever (msg_end) recv_exit() ;
...                               ...
do {                              for (;;)  {
  put_msg() ;                       when (msg_ready) get_msg() ;
  activate (msg_ready) ;            activate (msg_rcved) ;
  when (msg_rcved) ;              }
} while (more_msg) ;              ...
activate (msg_end) ;              ...
...                               ...

Conditional Critical-Region Implementation
Using "When" :

  In process p1 :
...
when (buffer_status == EMPTY) {
  write_buffer() ;
  buffer_status = FULL ;
}
...

  and in process p2 :
...
when (buffer_status == FULL) {
  read_buffer() ;
  buffer_status = EMPTY ;
}
...

"Process" Statements :

/* start processes p1 and p2 :  */
process (p1, func1(), processor1) ;
process (p2, func2(arg1), processor2) ;
/* multiprogramming : */
process (p3, func3(), processor2) ;
/* default processor, when not specified */
process (p4, func1()) ;
```

Figure 2.- ConCurrent C examples.

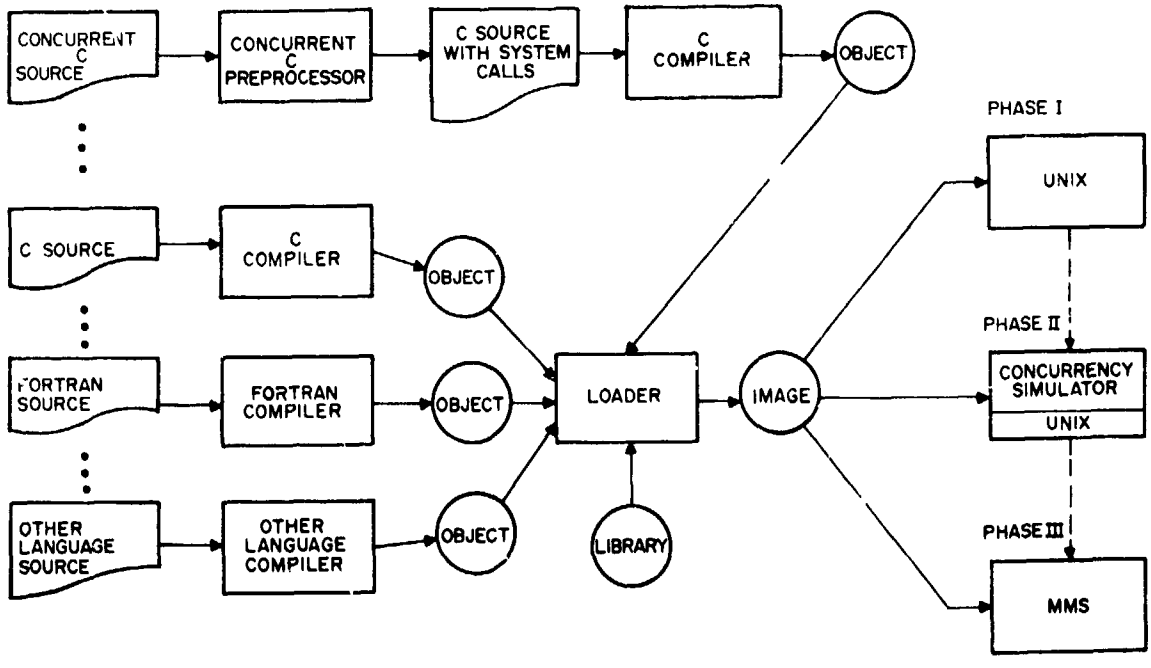

Figure 3.- Software development methodology.

N85 10379

FINITE ELEMENT COMPUTATION ON NEAREST NEIGHBOR CONNECTED MACHINES

Alastair D. McAulay
Texas Instruments, Central Research Laboratories
Dallas, Texas

SUMMARY

We describe research aimed at faster, more cost effective parallel machines and algorithms for improving designer productivity with finite element computations. A set of 8 boards, containing 4 nearest neighbor connected arrays of commercially available floating point chips and substantial memory, are inserted into a commercially available machine. One-tenth Mflop (64 bit operation) processors provide an 89% efficiency when solving the equations arising in a finite element problem for a single-variable regular grid of size 40 by 40 by 40. This is approximately 15 to 20 times faster than a much more expensive machine such as a VAX 11/780 used in double precision. The efficiency falls off as faster or more processors are envisaged because communication times become dominant. Consequently, we propose, for the first time, a novel SOR algorithm which uses cyclic reduction in order to permit data transfer and computation to overlap in time. For a future 0.63 Mflop single chip processor, this new algorithm raises the efficiency from 56% to 98% for a 40 by 40 by 40 3-D mesh, and from 92% to 99% for a 285 by 285 2-D mesh.

INTRODUCTION

We discuss research aimed at cost effective finite element machines which are expandable to utilize high levels of parallelism. Our approach is to hypothesize a group of arrays of nearest neighbor connected parallel processors with substantial distributed memory operating in a commercially available machine, the NuMachine, as shown in Figure 1. The distributed memory overcomes the memory bandwidth problem of most machines and the NuMachine provides us with economic computing amenities, such as a parallel Unix operating system, a high speed bus, high quality graphics, an interactive mouse, ethernet interconnections, a diagnostic processor, a multibus for peripheral interconnections and a symbolic processor.

We plan to reduce the overall design time and cost for finite element computations by three means. First, we make extensive and efficient use of parallelism to reduce computation time and cost. We plan to determine the efficiency of many alternative finite element algorithms and will modify the algorithms and processor board configuration so as to be most efficient for the most widely used algorithms. We show in this paper, for the first time, the use of cyclic reduction with an SOR algorithm in order to overlap data transfers and computations. This provides impressive gains in efficiency for our machine. Second, an expert system is used to provide an improved probability of achieving the desired results in order to substantially reduce the number of repeat runs. The symbolic processor may also be useful for computing derivatives used in

reanalysis (ref. 1,2) and nonlinear computations. Thirdly, we are engaged in parameter optimization research which will reduce the guesswork and hence the number of repeat runs involved in design optimization (ref. 3).

Finite element computations have been performed on many existing and prototype parallel machines (ref. 4). The research finite element machine at NASA Langley Research Center (ref. 5), is unique in that it was configured specifically with this type of computation in mind. Results of parallel computations on this machine have been published (ref. 6,7). A general discussion of finite element algorithms on parallel machines is contained in reference 8. A parallel microprocessor system used for finite element experiments is discussed in ref. 9 and an idea for optical implementation in ref. 10. Other researchers at NASA and in academia are addressing the more difficult task of determining an optimum overall software and hardware design for finite element machines from the ground up (ref. 11).

ARCHITECTURE

Details of the NuMachine are available (ref. 12,13), and will not be discussed here, except to mention that the bus speed of 37.5 Mbytes/sec is unusually high for a machine in its price range. The NuMachine rack unit version has 21 slots and we plan to have approximately 8 multiprocessor boards. Each board has 4 or more processing units connected in a nearest neighbor manner, figure 2.

We plan to use commercial arithmetic units such as the National Semiconductor 32081 or the Motorola 68881 Coprocessor. We expect such devices to multiply a 64 bit word in double precision in approximately 10 microseconds (0.1 Mflop rate). Higher performance pipelined multiple chip processors from Weitek, AMD and TRW are at least an order of magnitude faster, but are not desirable because of complexity and because they require more board space and thus limit the number of processors on a board. Single chip higher performance processors are planned; for example, the AMD 29325 will be approximately 30 times faster than the NS 32801 but dissipates several times more power and is several times more costly. The power dissipation will require special attention if several processors like this are used on a board. The arithmetic unit does not require all the capability of a general purpose microprocessor and we expect to eventually place many more than 4 processors on a single board, as well as having much faster processors. We anticipate the eventual use of special VLSI designs to take advantage of small size, high speed, low cost and minimal power. The repetitive nature of the arrays considered simplifies the VLSI design process. Consequently, in evaluating performance we restrict ourselves to processors between the 0.1 Mflop and 10 Mflop range for a 64 bit multiply. The lower end of the performance range is available in convenient form today.

Each processing unit is assumed to have 32,000 words of 64 bit memory. The nearest neighbor connection on the board utilises the least number of pin connections, thus maximising reliability and minimizing power and space requirements. An arithmetic unit with asscciated control and miscellaneous chips is estimated to occupy approximately three times the area of the 32,000 words of memory. Later studies will optimize the trade offs between more processors, speed of processors and more memory chips while satisfying the real estate constraint and the requirement to achieve high performance with commonly used algorithms.

FINITE ELEMENT COMPUTATION STAGES

The problem formulation stage is assisted by an expert system in the symbolic processor. This advises the user whether variational, Galerkins, least square or other approaches are preferred. It provides consulting regarding the input information he must supply and the results he may expect.

The modeling stage involves partitioning or mapping the selected formulation on to the specific machine configuration. At this stage, the user may direct the partitioning or allow the machine to handle it. Substructuring is a commonly used technique for subdividing the problem into reasonable parts, generally with minimum interconnections or to maximize the number of similar sub-parts, (ref. 7,14). Much computation and design time is saved by intelligent partitioning. For example, we need to reduce the number of degrees of freedom only once for a part which is used several times in a scaled form. If the original problem had not been partitioned in this manner, this computation would have been repeated for each of those similar parts. Subdivision into parts with few interconnections permits high computation efficiency on a parallel machine because the computation associated with connecting the regions is small relative to that for each region, which may be computed in parallel. The expert system contains a numerical model of the computation process similar to that used in evaluating performance in order to predict the efficiency of computation for alternative partitioning selections.

The mesh generation stage utilises the mouse and high resolution graphics. It must be possible to interactively add or remove points and to specify regions in which grids must be more or less dense. The user must be informed of the computational impact of selecting more or less points. He must also be advised when denser or less dense points would be desirable. For example, in field scattering problems, high resolution is required at sharp corners. The numbering of the nodes is a critical factor affecting computation and is addressed extensively in reference 15. It would appear that existing schemes, used with sequential machines, could be modified to provide good partitioning for a parallel machine.

The element integrations for matrix element formulation can be a computationally demanding phase. However, considerable reduction in computation for this stage results if, during problem modeling, we

make use of similar or similar shaped elements. The machine must allocate the element computations to the processors in some balanced manner. In some cases, scheduling the next element to the next available processor may be adequate. The matrix must then be set up for all elements. In other cases, where every element has a different value, the mesh might best be subdivided evenly among processors. In this case, it may be preferable to compute the matrix elements in the processors where they will be required for equation solution. Element formulation is expected to run fairly efficiently on a parallel machine (ref. 6), especially when the grid is regular or a distortion of a regular grid.

The equation solution stage is normally the most computationally demanding. This is addressed in more detail in the remainder of this paper. Several basic algorithms are listed, together with some of their principal differences.

1. Successive overrelaxation is a simple iterative technique which avoids explicitly forming matrices. Consequently, little and distributed storage is used, which makes large regular or distorted from regular grids easy to partition. Fast convergence requires good selection of the overrelaxation parameter, which is accomplished readily only for matrices having certain optimal properties such as property A and consistent ordering. These properties apply to a 5 point finite difference method but do not generally apply to finite elements. Iterative techniques may be superior to direct methods when an approximate initial solution is known (ref. 16).

2. Gauss Elimination and LU Decomposition are widely used for finite elements because irregular grids are frequently used and solutions are obtained in a fixed number of operations for well conditioned matrices. Computation of displacement for many loads is frequently required in structures, and the LU decomposition enables the most computationally demanding part to be performed only once for many loads. The computation is speeded by renumbering for bandwidth reduction or to maintain sparsity in the decomposition (ref. 15).

3. Preconditioned conjugate gradients is a popular iterative technique involving systematic error reduction using the finite element matrices. It is preferred to SOR because it avoids determination of optimum convergence parameters and requires fewer restrictions on the matrix A for good behavior. For example, it will handle ill conditioned matrices. Approximate knowledge of the solution enables even faster computation. Many people are working on efficient parallel implementations (ref. 6).

4. Alternating Direction Implicit Method enhances speed by partitioning the finite element matrix into a sum of matrices. The method lends itself to parallel computation because much of the computation is performed on these partitioned parts. However, in our preliminary experiments it became clear that more theory was required in order to maintain nice properties in the

submatrices while balancing load for a parallel machine.

5. Q-R algorithm is a popular method for solving for eigenvalues. It is used widely to determine resonances in finite elements. Parallel versions have been investigated (ref. 17,18)

After solving the equations, it is frequently necessary to compute other parameters on each mesh point. The same computation is performed independently across the grid so that high parallel efficiency is readily achievable. Sophisticated graphics software is required to display sections through mutiparameter 3-D displays and for contour and interpolated image views of the structure and the field.

PERFORMANCE PREDICTIONS FOR SOR EQUATION SOLVING

Three color SOR algorithm

The successive overrelaxation algorithm, SOR, is selected for evaluation first because of its simplicity, having only one computation step repeated many times. The SOR algorithm applied to a regular 2-D grid of triangular elements requires repeated solution at each node or mesh point of

$$u_{\ell,m}^{(i+1)} = \omega\left[\alpha_1 u_{\ell+1,m}^{(i+1)} + \alpha_2 u_{\ell-1,m}^{(i+1)} + \alpha_3 u_{\ell,m+1}^{(i+1)} + \alpha_4 u_{\ell,m-1}^{(i+1)} + \alpha_5 u_{\ell+1,m+1}^{(i+1)} + \alpha_6 u_{\ell-1,m-1}^{(i+1)} + \alpha_0 k_{\ell,m}^{(i+1)}\right] - (\omega-1)u_{\ell,m}^{(i)} \qquad (1)$$

The mesh is subdivided evenly among the processors and the matrix coefficients (α) and overrelaxation factors ω, $(\omega-1)$ are loaded into the appropriate processor memories. Colors are assigned to the nodes in the sequence Red, Black and Green from left to right. Succesive rows are shifted one place to the right and wrapped around, to correspond with triangular elements arranged such that nodes are connected to the NE and SW (ref. 16). All processors compute their assigned color first and then cycle synchronously through the other colors in the order Red, Black and Green. After a predetermined number of iterations, checks are made to determine whether adequate convergence has occured. This involves computing the sum of the squares of the node values at a processor and the sum of the squares of the node value changes since the last iteration. This information is assembled by the host in order to compute whether convergence is adequate and may be computed while the array boards continue with the next iteration. A 3-D SOR algorithm may be developed similarly for an element shape selected.

SOR performance equations without overlapping transfer and computation

We assume triangular elements in the 2-D case and tetrahedral elements in the 3-D case. An approximate performance estimate (on the worst case side) is derived using the definitions:

$N_b = 8$ the number of boards

$N_p = 4$ the number of processors per board

$M_p = 28{,}000$ the number of storage words/processor (4000 extra words are reserved for control and buffers)

$S_b = 4.69 \times 10^{6}$ the bus speed in words/second (64 bit words)

S_c the time in seconds for the processor to perform a 64 bit floating point multiply

$S_n = 0.4 \times 10^{-6}$ the time in seconds for a 64 bit word to travel between neighboring processors

A the number of multiplications (with additions) per iteration of equation (1), including 2 convergence related multiplications not shown in equation (1); A = 11 for the 2-D case and A = 17 for the 3-D case

M_a the number of words stored for each node, including 2 convergence related check words which are not shown in equation (1). Note that in the 2-D case, M_a=11, because 6 coefficients are shared with their neighbors and need be stored only once. In the 3-D case there are 12 such coefficients and M_a=14.

The number of nodes handled directly is the total memory divided by the storage per node

$$N_n = N_p N_b M_p / M_a \tag{2}$$

One iteration of equation (1), for these nodes, may be computed in parallel with the N_p processors in time

$$T_c = N_n A S_c / (N_p N_b) \tag{3}$$

For a 2-D mesh, the amount of data that must be transferred from one board to another for one of the 3 colors during computation of one iteration of equation (1) is the perimeter of the data stored on the board for that color. Consequently, the time taken for communicating from every board to every other for one iteration of equation (1) and 3 colors is

$$T_t = 12\, N_b (M_p N_p / 3)^{1/2} / S_b \tag{4}$$

For a 3-D mesh, the number of colors required also depends on the element shape; 6 colors are required for tetrahedral elements because 6 lines pass through every point and 13 colors are required for cubic elements. We will use 6 colors as this is more efficient for our machine. However, we assume the mesh of elements is fitted inside a cube for simplicity of calculations. The approximate time required for bus communication between boards in a 3-D problem is

$$T_{t(3\text{-}D)} = 3\tau_b (M_p N_p/6)^{2/3}/S_b \tag{5}$$

For a 2-D triangular mesh and a 2-D configuration of processors on a board, the only data transfer required on a board is between neighbors and occurs concurrently for all processors. The time for on board transfers for 3 colors is

$$T_n = 3(M_p/3)^{1/2} S_n \tag{6}$$

For a 3-D mesh and a 2-D configuration of processors we consider a simple though not necessarily efficient arrangement in which the board handles a part of one horizontal plane of the 3-D mesh. In this case, information involving the upper and lower faces of a cube is transferred to the board edge from every processor via others during one iteration. A third cube face is included for the nearest neighbor horizontal path. The average number of processor outputs is $(N_p-1)^{1/2}/2$, as data accumulates on the path to the board edge. The distance from the array center to the board edge is $(N_p-1)^{1/2}$. The resulting time for 6 colors is approximately

$$T_{n(3\text{-}D)} = 18(M_p/6)^{1/2}(N_p-1)/2\ S_n \tag{7}$$

The efficiency of computation relative to a sequential machine, assuming no overlap between data transfer and computation, is then

$$\eta = T_c/(T_c + T_t + T_n) \tag{8}$$

The overall computation time includes the time to check for convergence (the last term in the brackets) and the loading and unloading time (last term)

$$T_T = N_I(T_c + T_t + T_n + 2N_n S_c/(N_p N_b)) + 2N_b N_p M_p/S_b \tag{9}$$

where, based on a colored SOR algorithm, the number of iterations to reduce the error to $1/(N^{1/2}+1)^2$ is

$$N_I = 0.72\ N_n^{1/2} \log_{10} N_n^{1/2} \tag{10}$$

SOR performance equations with data transfer and computation overlap

We propose a new algorithm which improves performance by permitting overlap between data transfer and computation. This can be used to reduce the effect of bus and nearest neighbor communications. We describe the method in terms of a 2-D mesh and in terms of reducing bus effects because these are more significant in our configuration.

Six color labeling is introduced by odd-even cyclic reduction of the three color grid. The red nodes are renumbered sequentially; odd nodes are called R_0 and even nodes R_1. Black and green nodes are similarly labeled (figure 5). At each of the 6 time steps shown in the figure, the boxed nodes are updated according to equation (1). Updating a node requires the use of values from North, South, East, West, NE and SW for a triangular finite element grid. Six steps are required to update all nodes in a six color system.

The line shown at each step in figure 5 marks the interface separating those mesh values in one processor from those stored in a processor on another board. Only nodes immediately adjacent to this interface are shown in figure 5. At each time step, in addition to updating node values, the values updated on the previous step are transmitted across the bus to be available at the new processor when desired. The transfers are marked with arrows in figure 5. Examination of nodes below the line in figure 5 show that when they are updated, the North and NE values required from the upper board will have been transmitted on the immediate two previous steps. Similarly, for nodes above the line, the South and SW values required will have been transmitted on two previous stages. This arrangement permits all data transfers across the interface between boards, that take less time than the time spent in computation for that step, to occur overlapped in time with the computations.

In the 2-D case, the data transfer time between boards T_t modified for the 6 color algorithm in place of the 3 color one becomes

$$T_t' = 24\, N_b (M_p N_p/6)^{1/2}/S_b \tag{11}$$

A similar cyclic reduction for a 3-D mesh increases the 6 colors to 12 colors, producing

$$T_{t(3\text{-}D)}' = 72\, N_b (M_p N_p/12)^{2/3}/S_b \tag{12}$$

The data transfer time on a board is also modified for the new approacn for the 2-D and 3-D cases,

$$T_n' = 6(M_p/6)^{1/2}\, S_n \tag{13}$$

and

$$T_{n(3\text{-}D)}' = 36(M_p/12)^{1/2}\, (N_p-1)/2\, S_n \tag{14}$$

Consequently, for $T_t' < T_c$, the efficiency in equation (8) is modified

to

$$\eta_0 = T_c/(T_c + T_n') \tag{15}$$

and the total computation time, equation (9) is modified to

$$T_T = N_I(T_c + T_n' + 2N_nS_c/(N_pN_b)) + 2N_bN_pM_p/S_b \tag{16}$$

For $T_t' > T_c$, the efficiency is

$$\eta_1 = T_c/(T_c + T_n' + (T_t' - T_c)) \tag{17}$$

and the computation time

$$T_T = N_I(T_c + (T_t' - T_c) + T_n' + 2N_nS_c/(N_pN_b)) + 2N_bN_pM_p/S_b \tag{18}$$

We observe that the above approach is equally applicable to a finite difference algorithm. In this case the red-black algorithm would be extended to a four color algorithm in order to overlap data transfer and computation.

SOR performance results

Figure 3 shows the performance for solving the equations for a 285 by 285 2-D mesh problem as a function of log processor speed. The slowest processor, 0.1 Mflops, is available today. The fastest is slightly faster than single chip processors anticipated by 1986. The efficiency is shown in figure 3(a) for the conventional 3 color algorithm (equation (8)) and the new 6 color algorithm (equation (17)). The dashed curve (equation 15) shows the efficiency if the bus is assumed perfect, requiring zero delay to communicate data. For the 3 color algorithm, the efficiency for a 0.1 Mflop processor is 98% and falls off for hypothesized future processors because the bus communication time increases relative to the computation time. The introduction of the new algorithm permits overlap of bus communication and computation. Processors of speed less than 5 Mflops now no longer have to wait for the bus. We observe that for a 0.63 Mflop processor, the efficiency is improved from 92% to 99% by the new algorithm.

Figure 3(b) shows the estimated time to solve the equations for the 2-D mesh for the conventional algorithm (equation (9)) and the new algorithm (equation (18)). The time decreases even when the efficiency is falling off. For a 5 Mflop processor the new algorithm is approximatley 40% faster.

Figure 4(a) shows the estimated performance for solving the equations for a 40 by 40 by 40 3-D mesh as a function of processor speed for a conventional 6 color algorithm and a new 12 color algorithm. The efficiency of 89% for the conventional algorithm and a 0.1 Mflop processor is lower than for the 2-D mesh because more data has to be transferred on the bus relative to computation. The efficiency drops off rapidly. The use of the new algorithm provides an impressive improvement up to 0.63 Mflops. Above this, the bus is

essentially saturated for the algorithm chosen.

The dashed curve shows the situation with no bus delays. This shows that with the small number of processors per board, the communication delays on the board, although worse than for the 2-D case, are not significant until closer to 10 Mflops. This suggests that the balance between bus and board communication delay could be improved by having more processors on a board and fewer boards. This is entirely feasible with future VLSI. The impact on board communication may be further reduced by applying cyclic reduction in a similar manner as was used to permit computation and bus transfer. The interfaces in figure 5 are now considered to be between processors on a board rather than between boards.

Figure 4(b) shows the computation time for the conventional 3-D 6 color algorithm and the new 12 color algorithm. There is a 40% reduction in computation time for a 0.63 Mflop processor. At this point bus transfer equals computation time. Consequently, the use of faster processors will not improve speed with the algorithm selected.

Significantly faster performance may also be achieved by using the more complex multigrid method, which on a serial machine can reduce the number of operations from $O(N_n N_I)$ to $O(N_n)$, (ref. 19,20). Multigrid loses some of its efficiency on a parallel machine (ref. 21), but for the machine discussed, there are many nodes relative to the number of processors and multigrid techniques should still be efficient. Multigrid is not included in the evaluation here as it may also be used with a sequential machine.

CONCLUSION

We discussed improvements to the design time involving finite element computations by using parallelism, expert systems and optimization techniques. We considered a commercially available computer into which we inserted 8 identical processor boards. Each board has 4 processing units and each unit consists of 4 commercially available processors and 32000 words of memory. We showed that this configuration is highly efficient for solving the equations for single-variable regular grids up to 285 by 285 for 2-D and up to 40 by 40 by 40 for 3-D. Efficiency with a 0.1 Mflop processor is estimated to be 89%, providing an improvement of 15 to 20 times relative to a more costly VAX 11/780 used in double precision. The next most demanding part of the computation, setting up the equations, is also expected to be similarly efficient for regular grids. At least an order of magnitude faster processors are anticipated within a couple of years. For these processors the efficiency would fall off dramatically. We proposed a new SOR algorithm which enables overlapping in time for data transfer and computation. For a 0.63 Mflop processor, this algorithm improves efficiency from 56% to 98% for a 40 by 40 by 40 3-D mesh and from 92% to 99% for a 285 by 285 2-D mesh. Non-regular grids are common in structural finite element computations. Consequently, we plan to investigate the efficiency of our machine for direct decomposition methods such as Gauss Elimination and Nested Dissection.

ACKNOWLEDGEMENTS

I would like to thank Harvey Cragon, Senior Fellow at Texas Instruments, for his contributions and interest in this paper.

REFERENCES

1. Noor, A.K. and Lowder, H.E.: Approximate Reanalysis Techniques With Substructuring. Journal of the Structural Division, ASCE, Vol. 101, No. ST8, Paper 11523, Aug. 1975, pp. 1687-1698.

2. Noor, A.K. and Lowder, H.E.: Approximate Techniques of Structural Reanalysis. Computers and Structures, Vol. 4, 1974, pp. 801-812.

3. McAulay, A.D.: Least Square Inversion: A Novel Approach. Expanded Abstract SEG Publn. ISBN: 0-931830-28-1, 53 Annual International Meeting of the Society of Exploration Geophysicists, Las Vegas, Sept. 11-15, 1983, pp. 501-504.

4. McAulay, A.D.: Parallel Arrays or Vector Machines, Which Direction in VLSI? IEEE Publn. 83CH1879-6, IEEE International Workshop on Computer Systems Organization, IEEE Computer Society, New Orleans, March 1983, pp. 179-184.

5. Storaasli, O. et al.: The Finite Element Machine: A Experiment in Parallel Processing. Research in Structures and Solid Mechanics, NASA CP-2245, Oct. 1982, pp. 201-217.

6. Adams, L.M.: Iterative Algorithms for Large Sparse Linear Systems on Parallel Computers. NASA CR-166027, Nov. 1982. (Also Ph.D. thesis, Univ. of Virginia, Charlottesville, 1983.)

7. Adams, L.M. and Voigt, R.G.: A Methodology for Exploiting Parallelism in the Finite Element Process. NASA CR-172219, Sept. 1983. (Also NATO Advanced Research Workshop on High Speed Computing, Springer-Verlag, 1983.)

8. Salama, M., Utku, S. and Melhosh, R.: Parallel Solution of Finite Element Equations. Proc. 8th ASCE Conf. on Electronic Computation, Houston, Feb. 1983, pp. 526-538.

9. McGregor, J. and Salama, M.: Finite Element Computation With Parallel VLSI. Proc. 8th ASCE Conf. on Electronic Computation, Houston, Feb. 1983, pp. 540-553.

10. McAulay, A.D.: Nearest Neighbor Hybrid Deformable Mirror Optical Computer. Proceedings of SPIE - The International Society for Optical Engineering, Vol. 431, Real Time Signal Processing VI, 1983, pp. 215-220.

11. Pratt, T.W. et al.: The FEM-2 Design Method. Proceedings 1982 Int. Conf. on Parallel Processing, IEEE Comp. Soc. Press, Los Angeles, 1983, pp. 132-134.

12. Nu Machine Technical Summary. Texas Instruments, Irving, CA, 1982.

13. NuBus Specification. Texas Instruments, Irving, CA, 1983.

14. Utku, S. et al.: On Nonlinear Finite Element Analysis in Single-, Multi- and Parallel-Processors. Computers and Structures, Vol. 15, No. 1, 1982, pp. 39-47.

15. George, A. and Liu, J.W.: Computer Solution of Large Sparse Positive Definite Systems. Prentice-Hall, Series in Computational Mathematics, 1981.

16. Adams, L.M. and Ortega, J.M.: A Multicolor SOR Method for Parallel Computation. ICASE Rept. No. 82-9, April 1982.

17. Sameh, A.H. and Kuck, D.J.: A Parallel QR Algorithm for Symmetric Tridiagonal Matrices. IEEE Trans. on Computers, Vol. C-26, No. 2, Feb. 1977, pp. 147-153.

18. Brent, R.P. and Luck, F.T.: A Systolic Architecture for Almost Linear Time Solution of the Symmetric Eigenvalue Problem. TR-82-525, Cornell Univ., Aug. 1982.

19. Brandt, A.: Multi-Level Adaptive Solutions to Boundary Value Problems. Math. of Comp., Vol. 31, Apr. 1977, pp. 333-390.

20. Nicolaides, R.A.: On the l^2 Convergence of an Algorithm for Solving Finite Element Equations. Math. of Comp., Vol. 31, No. 140, Oct. 1977, pp. 892-906.

21. Grosch, C.E.: Poisson Solvers on a Large Array Computer. Proc. 1978 LASL Workshop on Vector and Parallel Processors, Los Alamos Scientific Lab., Sept. 20-22, 1978, p. 93. (Also TR 78-4, Old Dominion Univ., Norfolk, VA, 1978.)

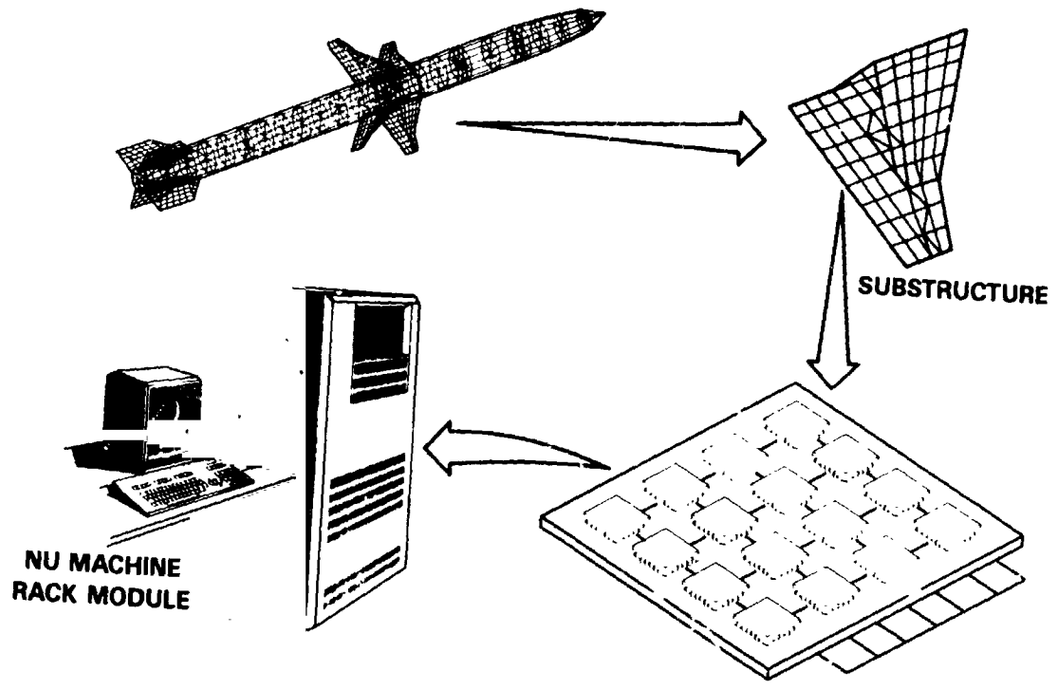

Figure 1. Parallel finite element computation.

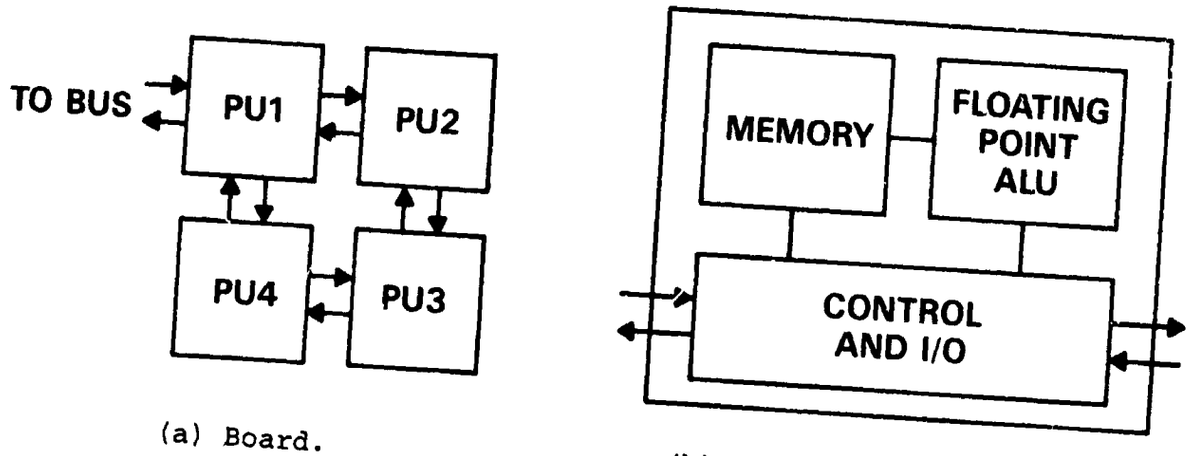

(a) Board.

(b) Processing unit (PU).

Figure 2. Computer architecture.

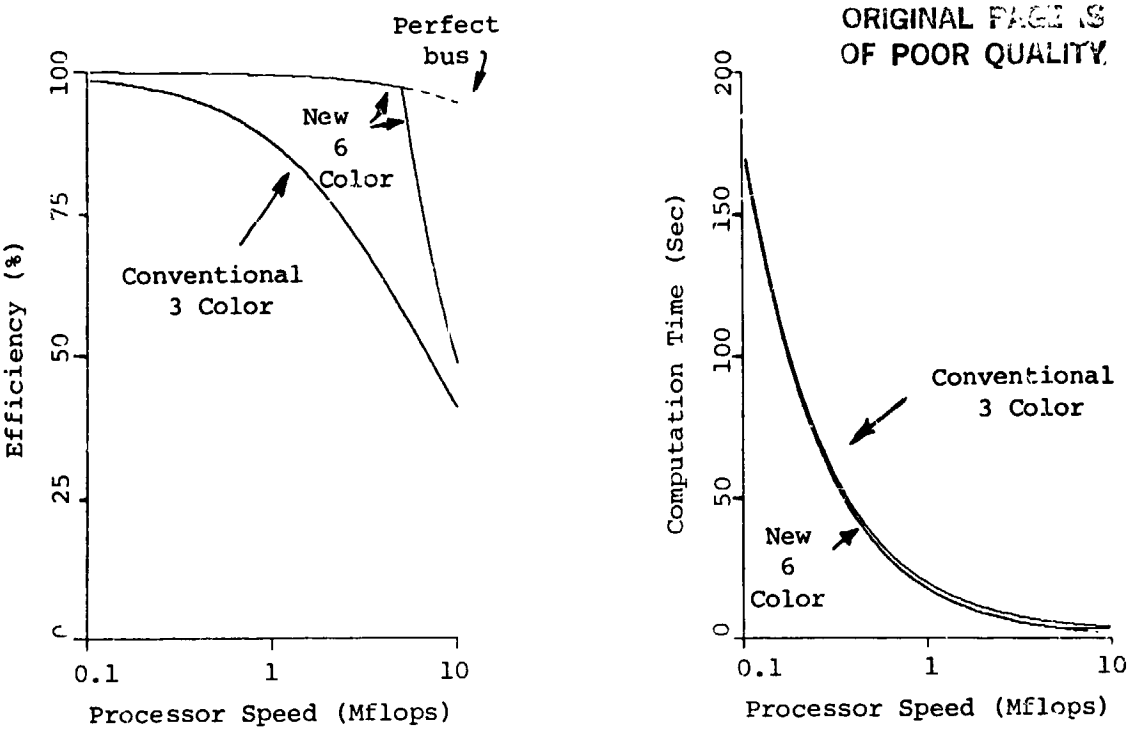

(a) Efficiency. (b) Computation time.

Figure 3. Performance estimates for 285 x 285 2-D mesh.

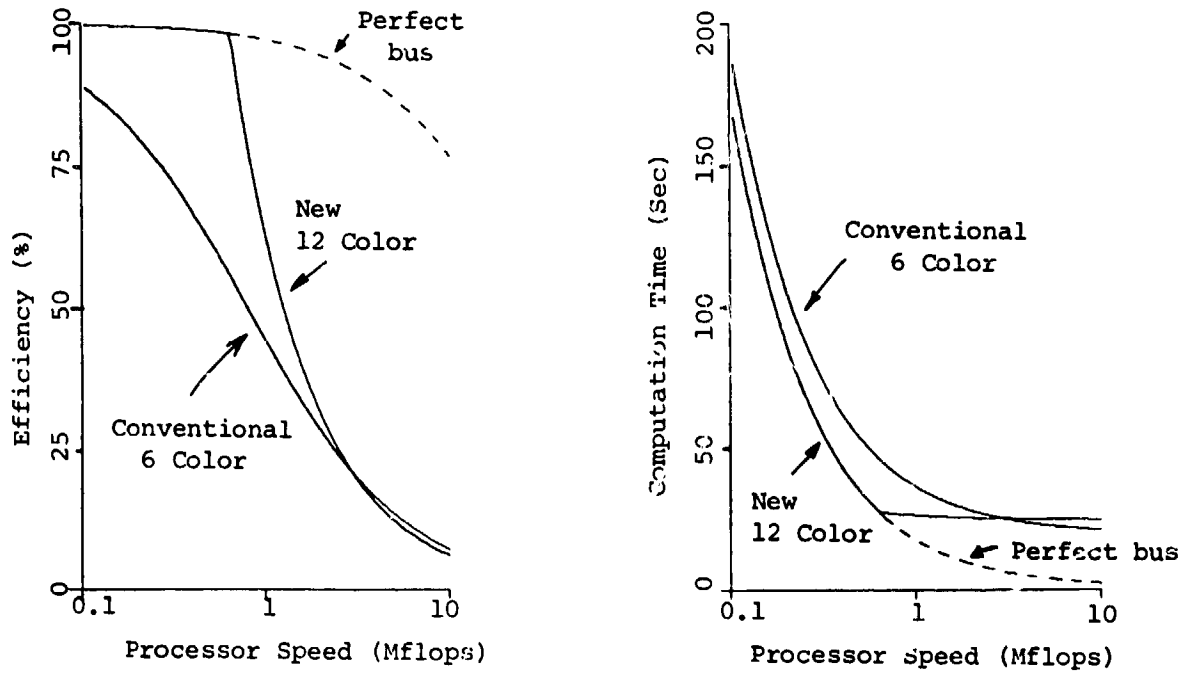

(a) Efficiency. (b) Computation time.

Figure 4. Performance estimates for 40 x 40 x 40 3-D mesh.

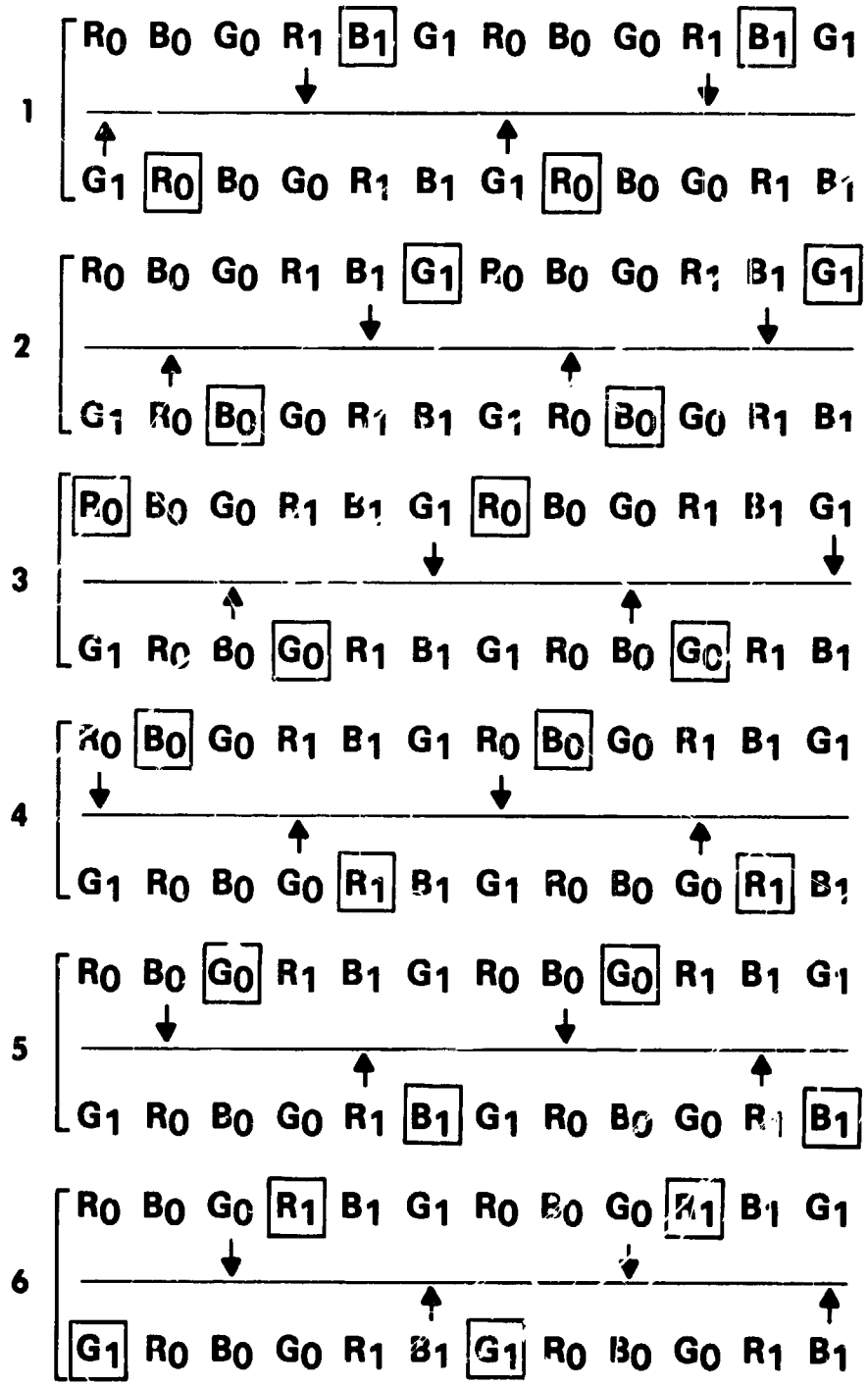

Figure 5. Six color grid for overlapping data transfer and computation.

N85 10380

APPLICATION OF CONCURRENT PROCESSING TO STRUCTURAL DYNAMIC RESPONSE COMPUTATIONS

Jonathan Ransom, Olaf Storaasli and Robert Fulton
NASA Langley Research Center
Hampton VA 23665

SUMMARY

Equations of large order structural problems are often difficult to solve on current sequential computers due to memory and time constraints. The introduction of a new generation of computers based on concurrent processing offers an alternative that promises to alleviate these constraints. The trend of future computers (based on new products under developement) is toward new generation computers referred to as multiple instruction multiple data (MIMD) computers. These MIMD computers provide an opportunity for significant gains in computing speed which makes the solution of large-scale structural problems tractable. This paper describes the experiences gained from solving for the dynamic response of two simple structures on an experimental MIMD computer called the Finite Element Machine. The paper introduces MIMD computing concepts, describes how the concurrent algorithmic techniques were implemented and gives results for the two example problems. The results show computational speedups of up to 7.83 using eight of the Finite Element Machine processors and indicate that significant computational speedups are possible for large order structural computations.

INTRODUCTION

A typical method of solving structural dynamic response problems is to discretize the structure using finite element or finite difference techniques and to solve the resulting system of equations (often a large number of equations) on a sequential computer. The solution of the resulting equations on sequential computers for large-order problems is often very demanding on both memory and time. The introduction of a new generation of computers based on concurrent processing offers an alternative that promises to alleviate these constraints. A concurrent processing computer contains many processors which may operate simultaneously to share the computational load, thereby reducing the computation time for applications where concurrent algorithms can be developed.

A crude model used to analyze the crash dynamics of a typical transport aircraft is shown in figure 1. The model contains a relatively small number of elements and equations, but, even so, it takes more than an hour of computer time to calculate displacements for only a fraction of a second of real (crash) time. Analysts would prefer using a more complex (more accurate) model in order to predict the failure modes of the structure. However, the analysis of such a complex model would be so demanding on a sequential computer that it is currently not done.

The chronological growth in speed of scientific computers as measured in MFLOPS (millions of floating point operations per second) is shown in figure 2. Current estimates are that the peak performance achievable for a single-processor computer is approximately 1000 MFLOPS (shown by the horizontal hatched marks) in the figure. Also shown in the figure is the estimated speed of up to a million MFLOPS required for routine large-order nonlinear dynamic response calculations. The figure shows that the near-term introduction of a new series of multiprocessor computers (termed multiple instruction multiple data or MIMD) promises to provide a significant advance in high-speed scientific computing capability. The development of suitable algorithms on concurrent computers in the future may lead to breakthroughs in the solution of large-order nonlinear dynamic response problems. The key to utilizing this opportunity is the effective selection and implementation of appropriate algorithms which exploit concurrent processing concepts.

This paper describes results for several applications on a research concurrent processor machine (Finite Element Machine, FEM) at NASA Langley Research Center and updates results shown in previous work of the authors (ref. 1).

DESCRIPTION OF APPLICATIONS

This study describes the solution of two dynamic response problems: (1) the finite difference analysis of a simply supported arch under a uniform step load; and (2) the finite element analysis of a two-dimensional beam grillage under a uniform step load at its nodal points. The objective in both problems is to solve for the displacements as functions of the time and the loading.

The simply supported arch shown in figure 3 contains both displacement, w, and time, t, as variables. Finite difference approximations were used to discretize the structure. The response of the center point for 5 milliseconds after application of the uniform step load is also shown.

The beam grillage shown in figure 4 is also simply supported and discretized using a finite element method. The response at nodes 1, 2, and 3 in terms of transverse displacement as a function of time is also shown in the figure.

CONCURRENT SOLUTION ALGORITHM

In general, for a lumped mass formulation, the acceleration for each degree of freedom for each node of a structural model is a function of all the displacements, the velocities, and time. In this concurrent approach, m equations of motion can be distributed over n processors. A typical distribution of m equations of motion is as follows

$$\begin{aligned} \ddot{w}_1 &= f_1(w_1, w_2, \ldots, w_m, \dot{w}_1, \dot{w}_2, \ldots, \dot{w}_m, t) \\ \ddot{w}_2 &= f_2(w_1, w_2, \ldots, w_m, \dot{w}_1, \dot{w}_2, \ldots, \dot{w}_m, t) \end{aligned} \qquad \text{Processor 1}$$

$$\begin{aligned} \ddot{w}_3 &= f_3(w_1, w_2, \ldots, w_m, \dot{w}_1, \dot{w}_2, \ldots, \dot{w}_m, t) \\ \ddot{w}_4 &= f_4(w_1, w_2, \ldots, w_m, \dot{w}_1, \dot{w}_2, \ldots, \dot{w}_m, t) \end{aligned} \qquad \text{Processor 2} \qquad (1)$$

$$\vdots$$

$$\ddot{w}_1 = f(w_1, w_2, \ldots, w_m, \dot{w}_1, \dot{w}_2, \ldots, \dot{w}_m, t)$$
$$\ddot{w}_m = f_m(w_1, w_2, \ldots, w_m, \dot{w}_1, \dot{w}_2, \ldots, \dot{w}_m, t) \qquad \text{Processor n}$$

where w_i is the displacement of the ith degree of freedom and a dot denotes differentiation with respect to time. If m is a multiple of n, there is an equal distribution of the computational load. Otherwise, the work load should be judiciously balanced to minimize processor idle time and increased overhead.

A common procedure for integrating dynamic equations is the Newmark-Beta method (ref. 2). The original formulation does not use matrix inversion but calculates new accelerations iteratively. This formulation was chosen for this study to maximize parallelism of the algorithm. The m equations of motion are distributed and solved on n processors (i.e., m=n) as indicated in figure 5. All processors perform identical functions (same software) and act as "integration engines". Moving from t to t+Δt, each processor begins with an assumed acceleration for each assigned degree of freedom. The corresponding first derivatives and displacements are calculated using the following equations

$$\dot{w}_i(t+\Delta t) = \dot{w}_i(t) + (\ddot{w}_i(t) + \ddot{w}_i(t+\Delta t))\, t/2 \qquad (2)$$

$$w_i(t+\Delta t) = w_i(t) + \Delta t \dot{w}_i(t) + \Delta t^2 (\ddot{w}_i(t+\Delta t)b + \ddot{w}_i(t)(0.5-b)) \qquad (3)$$

where b=1/4 (trapezoidal integration).

The computation is then interrupted so that each processor can communicate results for its assigned degrees of freedom to its neighboring processors. The accelerations are then computed and compared with the assumed accelerations. If a given convergence criterion for the assigned degrees of freedom is met, then "local convergence" is achieved. The computations are interrupted again to check for convergence of all processors (i.e., global convergence) by using a flag network that sets a flag on each converged processor and sends its status to other processors. If either the local or the global convergence test fails, each processor uses the current calculated value as the assumed acceleration and repeats the computations. When global convergence is met, all processors simultaneously proceed to the next time step.

CONCURRENT PROCESSING SOLUTION METHOD

On conventional sequential computers, a sequential time-consuming process of repeatedly iterating over both time steps and spacial variables is required to determine the response. However, on a parallel computer (refs. 3-5), one may distribute specific geometric locations (nodes) or masses to be solved over different processors. Iteration then occurs simultaneously over all processors. Communication between the processors is accomplished by the interprocessor communications capability of the parallel computer. The user can invoke either direct nearest-neighbor communications or (for distant processors) global bus communications.

In addition, on concurrent processors (refs. 3-6), one must take into account such things as which computations can be performed concurrently, how many processors can be used, how to distribute the computations, and the amount of communication required between processors. At some point communication between processors may become too

time consuming. Then a trade-off must be made between sequential and concurrent processing.

Software

The user interface to the Finite Element Machine is accomplished by using a typical minicomputer referred to as the "controller". The software on the controller for the Finite Element Machine is an extended version of the menu-driven minicomputer operating system. In addition, software (termed PASLIB) was written to support a set of companion commands residing on each processor in the array. Thus, a user constructs a concurrent algorithm using the text editor and other features of the controller. When the algorithm and data have been prepared, a command is given to transfer the program and associated data from the controller to each element in the array. Next, the processor connectivity is transferred to each processor to store the location of its neighbors. This neighbor assignment process is currently automated, requiring no user input for most cases. However, the user must include in the concurrent algorithm the appropriate code (SENDs and RECEIVEs) to communicate with neighboring processors. For concurrent processing, processor connectivity permits greater flexibility in the creation of algorithms to solve structures problems than is possible by conventional sequential computing.

Concurrent Processing Hardware

The concurrent processing research hardware used in this study is the NASA Langley Finite Element Machine shown schematically in figure 6. It consists of an array of processors (figure 7a) with three boards per processor, such as the typical board shown in figure 7b. The processors can communicate with each other over two paths (local or global) and with the controller using one path (global bus) as indicated in figure 6. For a broad class of structures problems the finite element matrix is sparse. Consequently, the design of the hardware took this sparcity into account by providing up to twelve nearest-neighbor links of which eight are shown in figure 6. A global communications bus allows communications from one processor to any or all other processors. The hardware contains a global flag network that can be used to signal when a processor has completed its computations.

SPEEDUP AND EFFICIENCY OF METHOD

The concurrent solution algorithm described in the previous section was applied to two example dynamic response problems. The typical responses are shown on the lower right of figures 3 and 4. The primary computational results of interest are the times to calculate the structural response on a varied number of processors. The computational speedup derived from the concurrent processing approach compared to the sequential approach can then be computed. The computational speedup is defined as the computation time to calculate results on one processor divided by the computation time to calculate the same results on n processors.

The computational speedups versus the number of processors for the shallow arch problem and the beam grillage problem are shown in figures 8 and 9, respectively. The theoretical maximum speedups would be the speedups if there were no overhead for concurrent processing. Thus, the theoretical computational speedups are equal to the number of processors used. The computational speedups for solving the arch problem using 64 and 128 equations are shown in figure 8. There is a speedup of up to 7.83

for 128 equations using eight processors. The computational speedups for solving the beam grillage problem using 24 and 48 equations are shown in figure 9. For this example, there is a speedup of up to 7.36 using eight processors. The computational speedups using eight processors approaches the theoretical maximum with fewer equations because the matrix multiplication used in the finite element method requires more computational effort.

The efficiency of concurrent computations for an increasing number of processors for the beam grillage problem using 48 equations is shown in figure 10. The efficiency is defined as the computational speedup divided by the number of processors. The figure shows a typical composition of the overhead using eight processors. Since the transferral and receipt of data are not instantaneous, communication is one of the factors that contributes to the overhead. For iterative methods, it is necessary to synchronize the processors before making convergence checks, which creates another source of overhead. In addition, there is overhead from establishing looping parameters and indices identifying processors uniquely and from nonparallel coding.

ESTIMATION OF COMPUTATIONAL SPEEDUP

The computation or execution time of an algorithm for a concurrent processing computer is measured from the first processor initiation to the last processor completion. For predicting the computational speedup, the execution time E can be thought of as a composition of arithmetic time A, communication time C, synchronization time S and idle time or wait time D as given by the equation

$$E = A + C + S + D \qquad (4)$$

The value for A is the time taken for all floating point operations. The integer arithmetic, loop overhead and array indexing have been neglected for simplicity. The value for C is the time to communicate values from one processor to another. For the Finite Element Machine, the processors communicate directly with each other over the communication links instead of shared memory. Therefore, this time is the time to send and receive information to and from processors. The value for S is the time the processor spends synchronizing with other processors and participating in global decision making. The value for D is the idle time the processor spends waiting on other processors to finish computations (ref. 7).

Equation (4) can be used to estimate the potential computational speedup by using a concurrent processing technique for the shallow arch problem. Because the solution procedure for this problem makes use of an iterative method and the equations are evenly distributed over the processors, the same amount of floating point operations, communication, and synchronization occurs during each iteration. Because there is no wait time ($D = 0$), equation (4)can be written as

$$E = (a + c + s)I \qquad (5)$$

where a, c, and s represent the arithmetic, communication, and synchronization time per iteration and I is the number of iterations. For this example problem, the computational speedup for p processors may be expressed as

$$SPEEDUP(p) = E(1)/E(p) = (a(1)+c(1)+s(1))/(a(p)+c(p)+s(p)) \quad (6)$$

This equation is independent of the number of iterations.

For the shallow arch problem, the solution algorithm required the following number of floating point operations per iteration:

(7)

multiply	: 24n/p
divide	: 9n/p
add,subtract	: 18n/p

where n is the number of degrees of freedom and p is the number of processors.

Since the standard central difference approximation for the fourth derivative is used in the solution procedure, the ith degree of freedom computation must use the i-2, i-1, i+1, i+2 values of the displacement. The maximum number of communications, c, to compute the fourth derivative for all the degrees of freedom assigned to a processor is either four, two, or one for the assumed even distribution. If the number of the degrees of freedom is equal to the number of processors, data is communicated to the ith processor from four neighboring processors (i.e., the i-2, i-1, i+1, and i+2 processors). If the number of degrees of freedom is greater than the number of processors, data is communicated to the ith processor twice, once from each of its immediate neighboring processors. With two processors, data is communicated once to the ith processor from its neighbor.

The processors must be synchronized and a global convergence test must be made once for each iteration.

The estimation parameters used for the Finite Element Machine speedup calculations are listed in Table 1. The times in the table were obtained by one of two techniques: either by adding the instruction times required for the operation, or by performing timing experiments on the actual hardware. Because equation (4) for the execution time neglects some operations (e.g., decision time, indexing, etc), the resulting estimates are not absolute. However, the estimation does predict the execution time ratio (speedup) very accurately because the neglected execution time factor cancels in the ratio. The observed and predicted computational speedups as the number of processors increases for 128 equations are shown in figure 11. The figure shows that the computational speedup continues to increase as the number of processors is increased because the maximum amount of communication remains constant for this problem. The maximum communication time is for the case of one equation per processor (128 processors). However, the prediction shows that the speedup of 92.8 (72.6% efficiency) is still near the theoretical limit.

CONCLUDING REMARKS

Two transient response problems (a one-dimensional problem and a two-dimensional problem) have been solved on both single and multiprocessor computer systems and the performance compared. A description of the method to achieve concurrent solutions of these structural problems is discussed, and results for computation time are given. The results show computational speedups of up to 7.83 using eight processors (98%

efficiency). These results are encouraging and they hold the promise for significant reductions in computation time for both linear and nonlinear statics and dynamics problems. An equation that estimates the computational speedup has been formulated and tested on the research hardware for a varied number of processors. Results from this computational speedup estimation are encouraging and indicate that speedups for large order dynamic analysis can be achieved by continuously increasing the number of processors. It is expected that computers for future large-scale engineering computations will be multiple instruction multiple data (MIMD) systems. It is evident from the algorithm used in this study that much algorithm research is required by engineers to make such computers function efficiently in the solution of structural problems. The significant performance gains possible will make such algorithm research worthwhile.

REFERENCES

1. Storaasli,O.;Ransom,J.; and Fulton,R.:Structural Dynamic Analysis On A Parallel Computer:The Finite Element Machine, AIAA Publication 84-0966, May 1984.

2. Newmark,N.: A Method of Computation for Structural Dynamics. ASCE, Proceedings, Vol. 85, No. EM-3, July 1959, pp. 67-94.

3. Storaasli,O.;Peebles,S.;Crockett,T.;Knott,J.; and Adams,L.: The Finite Element Machine: An Experiment in Parallel Processing. NASA TM-84514, July 1982. (Also in Research in Structural and Solid Mechanics - 1982, NASA CP-2245, pp. 201-217.)

4. Hoshino,T. et al: PACS: A Parallel Microprocessor Array for Scientific Calculations. ACM Transactions on Computer Systems, Vol 1,No. 3, August 1983, pp195-221.

5. Hoshino,T. et al: Highly Parallel Processor Array "PAX" for Wide Scientific Applications. Proceedings of the 1983 International Conference on Parallel Processing, IEEE Computer Society Press, 1983, pp. 95-105.

6. Noor,A.;Storaasli O.; and Fulton R.: Impact of New Computing Systems on Finite Element Computations. Impact of New Computing Systems on Computational Mechanics, Proceedings of the Symposium, ASME, 1983, pp. 1-32.

7. Adams,L.; and Crockett,T.: Modelling Algorithm Execution Time on Processor Arrays. NASA CR-172289, January 1984.

TABLE 1 - ESTIMATION PARAMETERS

Cost Parameters	Time(milliseconds)
Multiplication	0.518
Division	0.533
Addition, Subtraction	0.475
Send	1.870
Receive	1.870
Synchronize	0.129
Global Flag Check	0.278

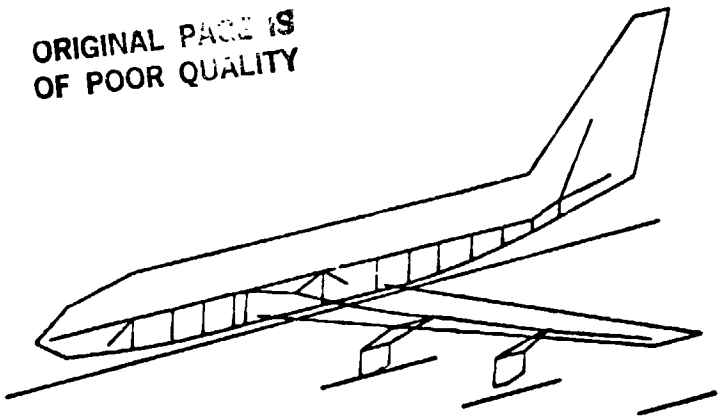

ELEMENTS	221	COMPUTER CORE	303 300 WORDS MAX FIELD
EQUATIONS	232		CYBER 175
REAL TIME	0.4 sec	COMPUTER TIME	1.4 hr

Figure 1 State of the Art Aircraft Crash Model

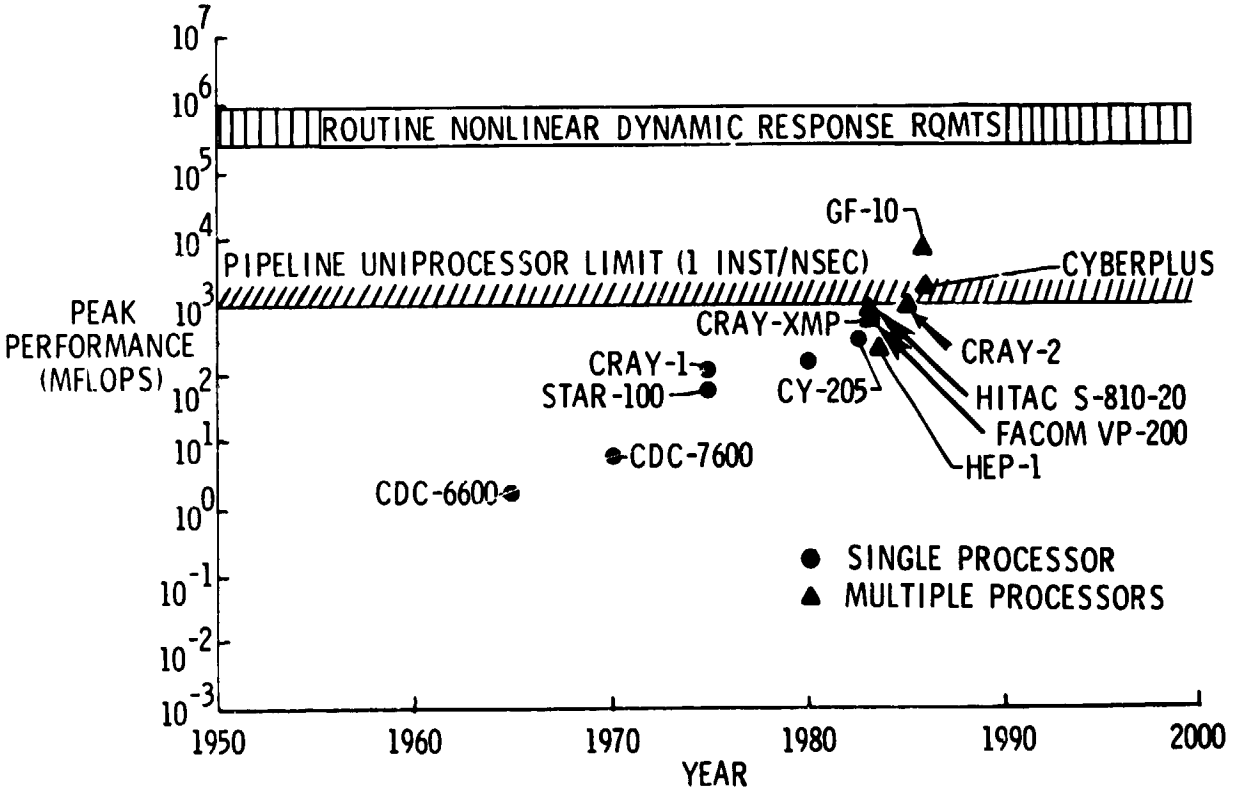

Figure 2 Historical and Projected Growth in Computer Speed

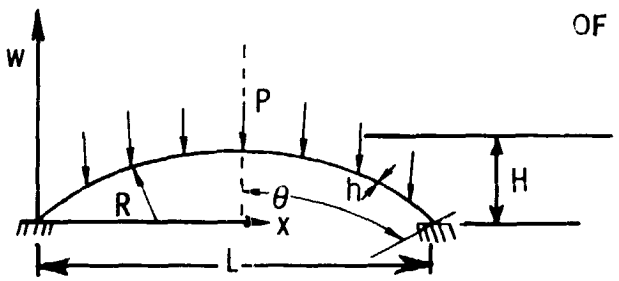

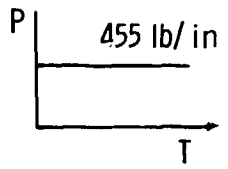

$R = 67.115$ in.
$h = 1$ in.
$A = 1$ in.^{2}
$I = 1/12$ in.^{4}
$E = 10^7$ psi
$G = 4.167 \times 10^6$ psi
$\rho = .000244$ lb $-$ sec^2/in.^{4}
$\theta = 15^0$
$M = .000244$ lb-sec.^{2}/in.^{2}

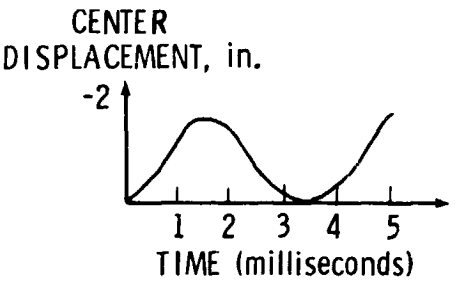

$w_0 = H \sin \pi x/L$ (INITIAL DISPLACEMENT)

$$E I w^{IV} - N(w_0^{II} + w^{II}) + M \ddot{w} = P(x,t)$$

GOVERNING EQUATION

Figure 3 Simply Supported Shallow Arch

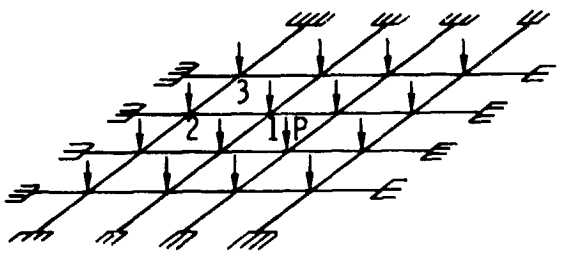

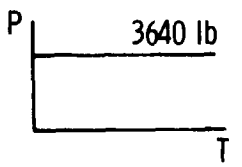

BEAM PROPERTIES

$E = 10 \times 10^6$ psi
$I = 1/12$ in^4
$A = 1$ in^2
LUMPED MASS = 0.003904 lb-sec^2/in^2
(AT EACH NODE)

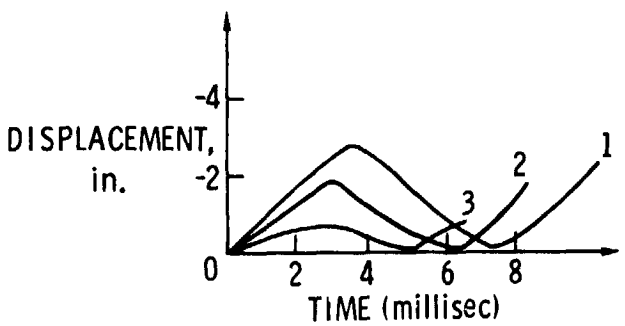

Figure 4 Simply Supported Beam Grillage

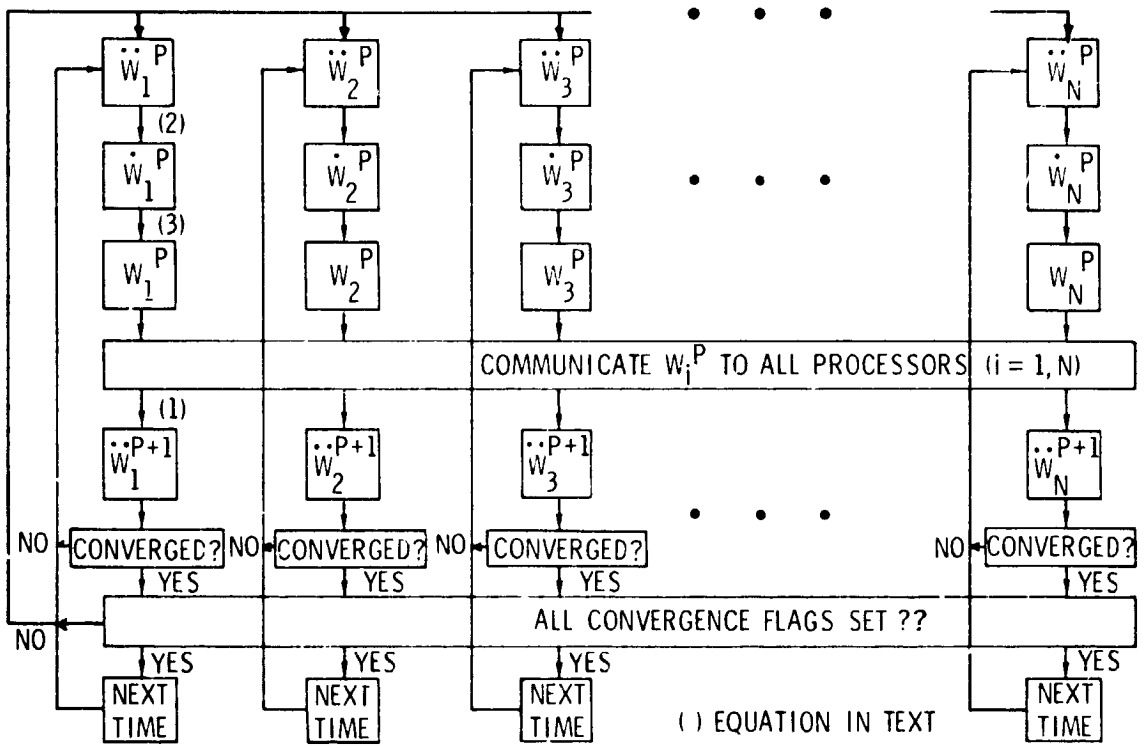

Figure 5 Concurrent Integration Method

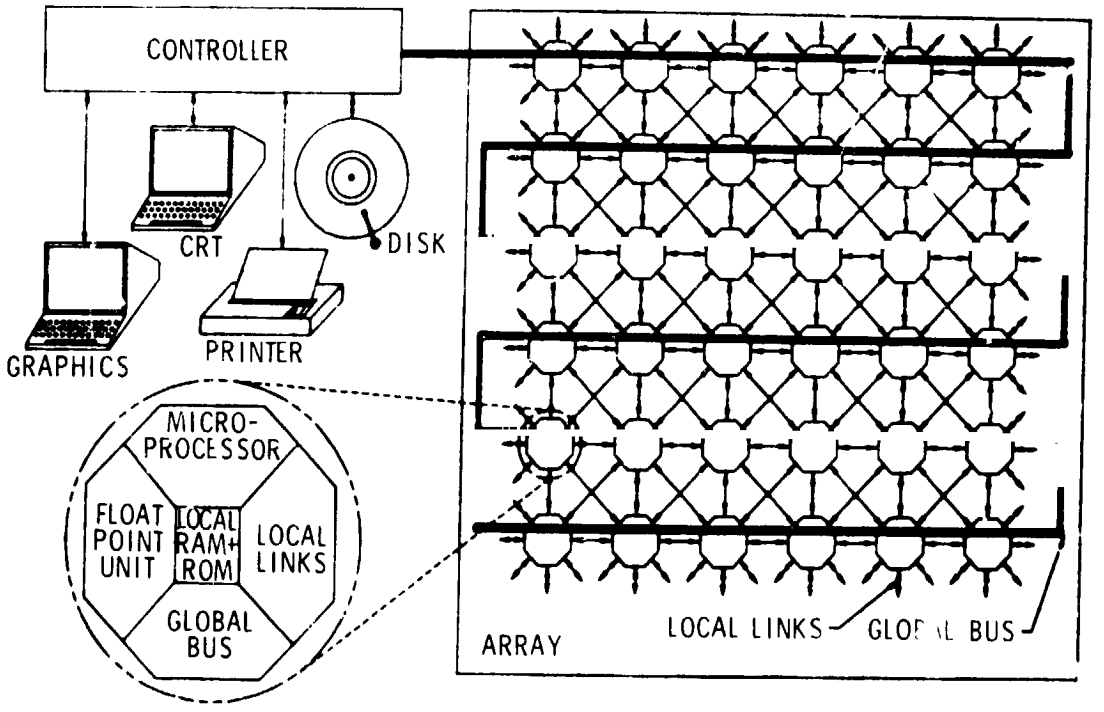

Figure 6 Finite Element Machine and Software

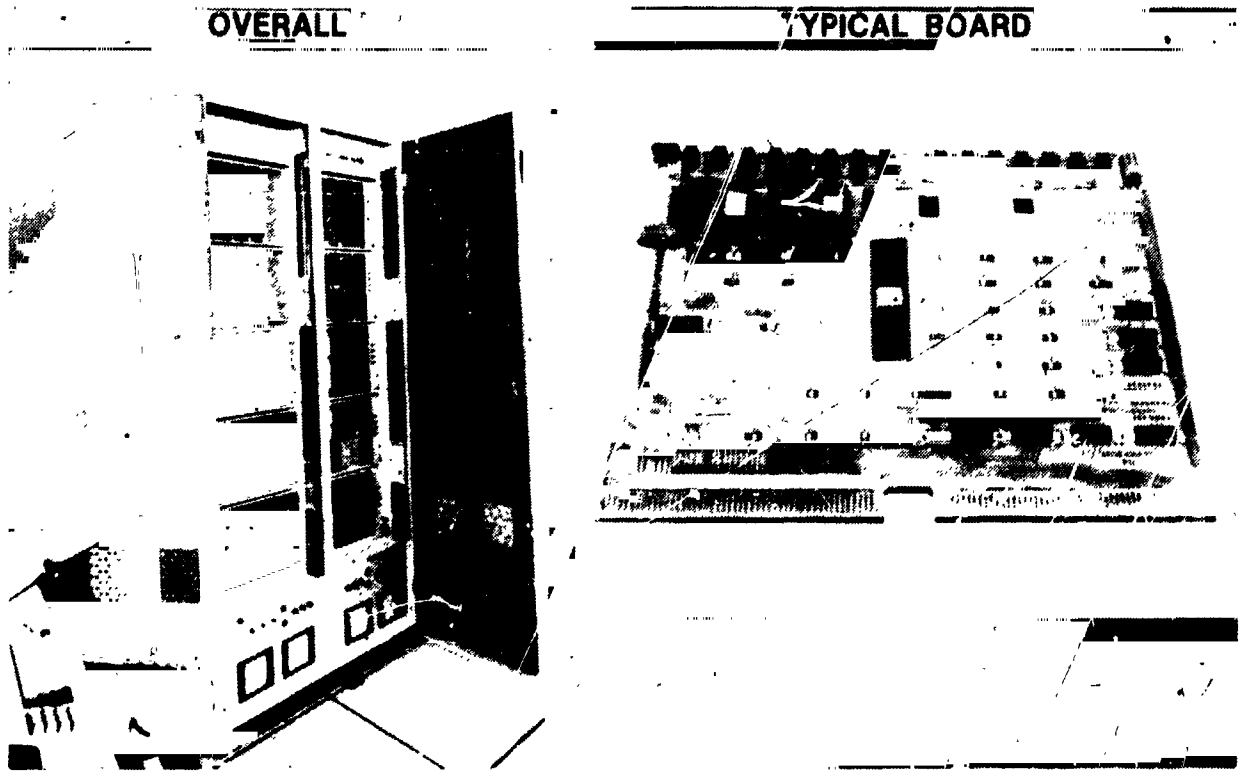

Figure 7a F nite Element Machine System

Figure 7b Typical Board

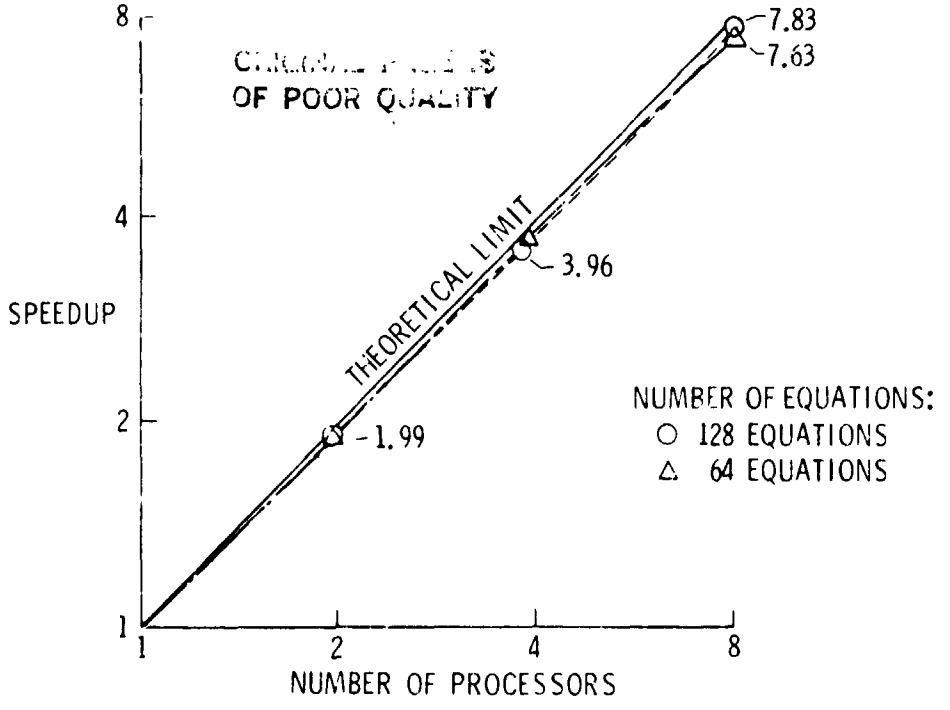

Figure 8 Computational Speedup Versus Number of Processors for Shallow Arch Problem

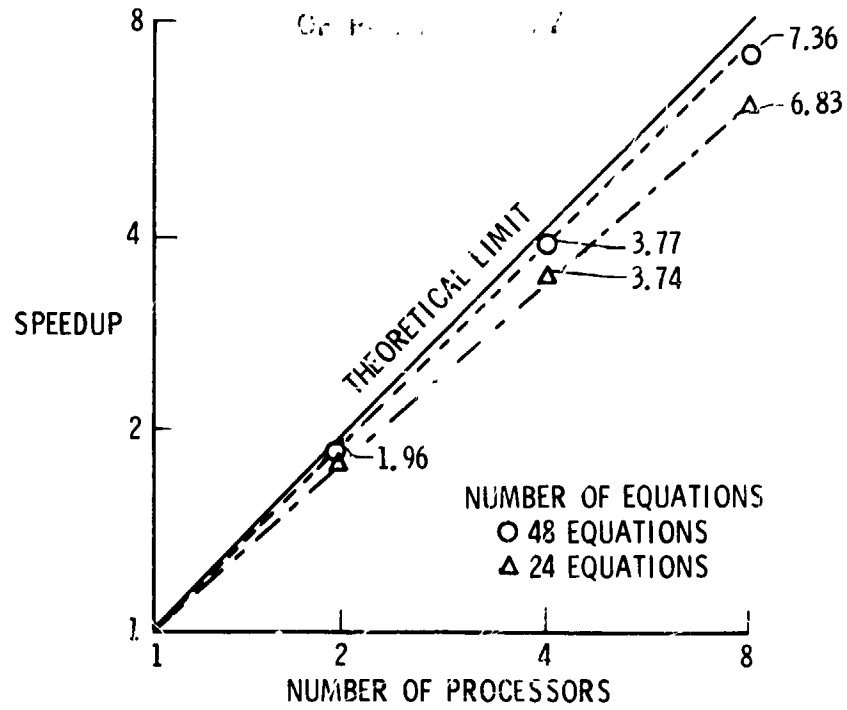

Figure 9 Computational Speedup Versus Number of Processors for Beam Grillage Problem

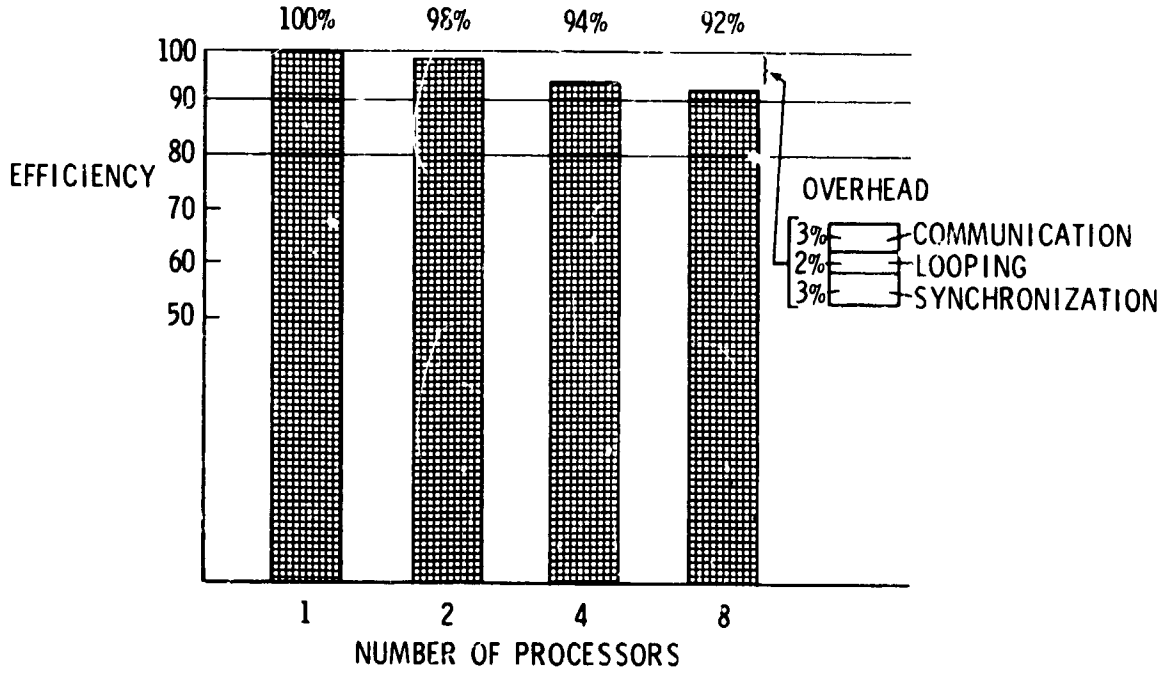

Figure 10 Computational Efficiency Versus Number of Processors for 48 Equation Beam Grillage Problem

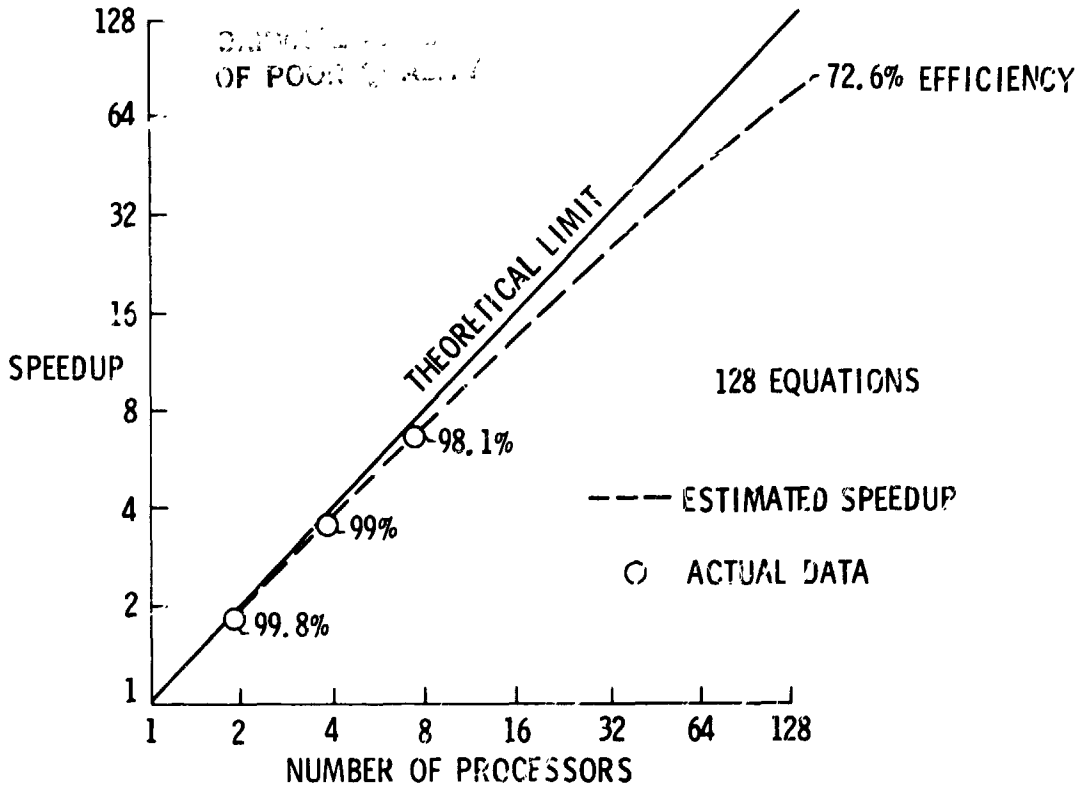

Figure 11 Estimated Speedup Versus Number of Processors for 128 Equation Shallow Arch Problem

INITIAL EXPERIENCES WITH DISTRIBUTING STRUCTURAL CALCULATIONS AMONG COMPUTERS OPERATING IN PARALLEL

James L. Rogers, Jr. and Jaroslaw Sobieszczanski-Sobieski
NASA Langley Research Center
Hampton, Virginia

INTRODUCTION

As the speed of a single-processor computer approaches a physical limit, computer technology is beginning to advance toward parallel processing to provide even faster speeds. Network computing and multiprocessor computers are two discernible trends in this advancement. Given the two extremes, a few powerful processors or many relatively simple processors, it is not yet clear how engineering applications can best take advantage of parallel architecture. Neither is it clear at this time the extent to which engineering analysis programs will have to be recoded to take advantage of these new hardware opportunities. It is clear, however, that these questions can be examined immediately by exploiting the physical parallelism of selected problems and the modular organization of existing programs to solve these problems.

To gain experience in exploiting parallel computer architecture, an existing program is currently being adapted to perform finite-element analysis by distributing substructures over a network of four Apple IIe microcomputers connected to a shared disk. This network of microcomputers is regarded merely as a simulator of a parallel computer because it should be obvious that substructure analysis of a practical problem of significant size should be performed on a computer with much more power than this particular microcomputer. In this network, one microcomputer controls the entire process while the others perform the analysis on each substructure in parallel. This substructure analysis is used in an iterative, fully stressed, structural resizing procedure. This procedure allows experimentation with resizing in which all analyses are not completed during a single iteration. Methods to handle the resulting mixture of old and new analysis data, referred to as asynchronous parallelism, need to be developed for parallel computing applications. Although the present work involves only structural analysis, it is hoped that this research will give some insight on how to configure multidisciplinary analysis and optimization procedures for decomposable engineering systems using either high-performance engineering workstations or a parallel processor supercomputer. In addition, the operational experience gained will facilitate the implementation of analysis programs on these new computers when they become available in an engineering environment.

BACKGROUND

In 1975 a feasibility study (ref. 1) was performed to determine the effort required to convert NASTRAN (ref. 2) to execute on the ILLIAC IV computer, and to assess the advantages that would be gained from such a conversion. The projected advantages in speed improvement were significant. For example, the decomposition

of a 10,000 degree-of-freedom matrix on the ILLIAC IV was estimated to be 40-100% faster than on a CDC 6600 computer when the matrix could not be contained in central memory. The problem that the study pointed out was that the code conversion effort would require 110-140 man months over a period of 36-50 months. If funds had been supplied and the project begun in 1976, it would probably not have been completed until 1980. About 2 years later, in 1982, the ILLIAC IV was taken off line. This historical example illustrates the difficulties that could be encountered in future wholesale conversions of engineering analysis codes to parallel processor computers which appear to be the wave of the future (refs. 3, 4).

While such wholesale conversion efforts will eventually be pursued, it is obviously important to find ways to benefit from the speed improvements offered by parallel computing without the cost, manpower, and time involved in the conversion of major analysis codes. One purpose of this research is to demonstrate this for structural analysis and to show that the current investment in sequential, modular structural analysis programs can be salvaged in the process.

APPROACH

The approach taken for this project was to establish reference results using the Engineering Analysis Language (EAL, ref. 5) to analyze a finite-element model that was not substructured. An existing small finite-element analysis code was then modified to handle substructures and applied to the same model on a CYBER mainframe computer. Next, this program was implemented on a microcomputer to test the substructure method sequentially. The program was then distributed over a network of these microcomputers with little change to the analysis code to test the substructure method in parallel. A Fully Stressed Design (FSD) capability was added to test the behavior of substructure analysis in an iterative process in which some of the analyses were completed before others.

The Model

The finite-element model used for testing is shown in figure 1. This model contains 16 joints, 21 beam elements, and 42 degrees of freedom (the size of the model was limited by the memory of the microcomputer). The framework has three substructures with each substructure composed of seven beams. The cross sections and material properties are identical for all beams. A load is applied at one of the boundary nodes as shown in figure 1.

The Small Finite-Element Program

Input for the model was written for a small, undocumented finite-element program developed in the past for a CYBER computer without any intent to ever use it for parallel processing. It did not even have an explicit substructuring capability. In this study, this program represented an "investment in existing software" that was to be salvaged. The results from the unchanged program were verified against the reference run. New code for substructuring based on equations from reference 6 was then added to the program. The model was divided into three substructures with the new code used to compute the boundary stiffness matrix for each substructure using equation 1:

$$K_b = K_{bb} - K_{bi} K_{ii}^{-1} K_{bi}^T \quad (1)$$

Each of the three 18 x 18 substructure stiffness matrices was reduced to 6 x 6 equivalent beam stiffness matrices (figure 2). These three stiffness matrices were input to the program, assembled to represent a stiffness-equivalent framework composed of three beams, each beam representing one substructure. The forces and displacements at the boundary nodes were computed for each such beam. Modifications were made to the program for reading these forces from a file and applying them to the corresponding substructures. By applying support conditions to the substructures, solutions were obtained for the interior node displacements, internal forces, and elemental stresses. These results were also verified against the reference run. It should be noted that the substructure analysis was simplified because the external loads were applied only to the boundary nodes. Should any loads be applied to the interior substructure nodes, it would have been necessary to add code to transfer these loads to the boundary nodes.

Conversion to the Microcomputer

At this point, the program for sequentially performing substructure analysis existed on a CYBER mainframe computer. The next step was to convert the program to the microcomputer. Since the entire program was written in FORTRAN-77, the move was quite simple and the program was contained in the microcomputer's 64K-byte memory without overlay. Although the program itself was entirely core resident, the test case shown in figure 1 was too large for analysis without substructuring. Therefore, the first step on the microcomputer was to run the substructuring sequentially. The problem took 57 minutes to execute. The results checked out against the reference run with little loss in precision (less than 1%).

Distributing the System

The approach selected for distributing the system was to use one microcomputer to execute a controller program and three microcomputers to analyze each of the substructures. All of the microcomputers were connected to a 20-MB Corvus hard disk which was used for data communication between the computers. The operations assigned to each computer are shown in figure 3. The controller program started the system (operation 0), assembled the substructure stiffness matrices and solved for the forces on each substructure at the boundary nodes (operation 2), and output the data (operation 4). The substructure programs computed the substructure stiffness matrices (operation 1), and used the forces from the controller program to solve for internal forces, node displacements, and elemental stresses for each substructure (operation 3). Note that parallelism only exists in operations 1 and 3. The output of the data (operation 4) also could have been distributed, but it was found to be easier to keep it centrally located.

When distributing the system to four microcomputers, the purpose was to minimize changing the original analysis code. Only procedures involved in operations 0, 2, and 4 were retained in the controller program while only those procedures involved in operations 1 and 3 were retained in the substructure program.

A subroutine was added to both the controller program and the substructure program to schedule their execution. This scheduling was accomplished by using three files on the shared disk, one file for each substructure program. When it was time for the controller program to execute, each of the three files contained a zero, and when it was time for a substructure program to execute, its respective file contained a nonzero number. Each program queried its file and if it was not its turn for execution it was put in a "holding pattern" by performing a simple multiplication loop before querying again. The system could have been implemented on only three processors with one processor doubling for executing the controller and substructure programs.

The ideal is to reduce the time required to solve the same problem sequentially on a single processor to (time/n) where n is the number of processors used to solve the problem. However, it is seen in figure 3 that not all of the calculations can be executed in parallel. In addition, some time was lost in an inevitable overhead such as checking and looping while waiting for a substructure or controller program to finish executing. Thus, the parallel system with substructures took about 27 minutes to complete execution, which is short of the ideal but still more than twice as fast as the sequential system.

The particular division of the structure from figure 1 into substructures is, of course, not the only one possible. If a larger number of smaller substructures were used, larger numbers of parallel computers could have been employed. However, the larger the number of substructures the larger the dimensionality of the assembled structure stiffness matrix (ultimately, if each substructure represents a single-beam component, the assembled stiffness matrix would return to the size it would have had if no substructuring was used). Consequently, to minimize the overall computer time, an attempt should be made to balance the size of the assembled structure stiffness matrix against the size and number of the substructure stiffness matrices. The degree of the time reduction depends also on the number of substructuring levels (ref. 7). Thus, tailoring the analysis process for a particular application to take advantage of multiprocessor efficiency is an important issue that faces an analyst using a multiprocessor system.

Resizing

An FSD algorithm was added to examine the behavior of parallel substructure analysis in an iterative process. A loop counter was added to the controller and substructure programs to make sure certain actions, such as initializations, were only done on the first pass through the system.

The FSD was performed by resizing all the beams in a given substructure according to the ratio of the maximum absolute normal stress occurring in the substructure to a specified allowable stress. The stress ratio was used as a scale factor to modify the beam cross-sectional moment of inertia. Consistently, the cross-sectional area was multiplied by the square root of the scale factor, and the cross-section linear dimensions were all multiplied by the scale factor to power 1/4. An iteration history of the changes in the design variable (plotted as the factor on cross-section linear dimension) for each substructure is shown in figure 4.

Asynchronous Resizing

Since most of the engineering calculations performed in support of design are iterative in nature, the computational behavior of an iterative distributed process in which some subtasks are completed later than others because of unequal computational requirements for various subtasks is of significant interest (refs. 8, 9). If such an imbalance of computational requirements occurs, a choice can be made to let the iterative process continue, temporarily using old data for those processes which are late. The process then becomes asynchronous as it mixes new and old data (a synchronous process, in contrast, would always wait for new data before proceeding). The effect of this mixing on the convergence and efficiency can easily be tested in a parallel system such as described above. The tests are conducted by bypassing analysis of selected substructures in some iterations. Obviously during the first loop through the system, all of the substructures will be analyzed to provide a starting point.

There are a large number of different ways in which an asynchronous iterative process can proceed. Using the framework structure from figure 1 as an example, it is conceivable to have at least these variants.

1. Referring to figure 3, consider being at the outset of iteration "i." Operations 1.1, 1.2, and 1.3 are expected to yield the boundary stiffness matrices for substructures 1, 2, and 3, all of which having been resized as a result of an FSD operation at the end of the previous iteration "i-1." Assume that operation 1.1 is late but the process moves on anyway using the old boundary stiffness matrix from iteration "i-1," that does not reflect the "i-1" resizing. That means that operation 2 combines the updated matrices for substructures 2 and 3 with an outdated matrix for substructure 1. In operations 3.1, 3.2, and 3.3, consistently, an old stiffness matrix that does not reflect the "i-1" resizing is used, while the updated stiffness matrices are used in operations 3.2 and 3.3.

After this analysis based on the partially incorrect data, all substructures, including substructure 1, are subject to the FSD resizing.

2. Proceed as above, but do not resize that particular substructure for which the old stiffness matrix was used in the analysis (substructure 1 in this example).

3. Complicate variants 1 and 2 by changing: the number of substructures that are assumed to be "late," the number of iterations over which the old data are being used for each substructure, etc. Obviously, a very large number of possibilities can be considered.

To make a beginning, variants 1 and 2 have been tested. The results shown in figures 5 and 6, respectively, indicate that the asynchronous operation, shown as connected lines, had only a slight influence on the convergence as manifested in small discrepancies that can be seen between the lines and symbols from the synchronous sizing. For instance, asynchronous results for substructures 2 and 3 (figure 6) are above the synchronous ones but both results converge after about eight iterations. This behavior is to be expected because the FSD process is known to converge to the same result (for a nonpathological structure) regardless of the starting point, and, in fact, the asynchronous operation in this case may be regarded as a continuation of the FSD process from an artificially injected new starting point. One may speculate that a different behavior will be observed in cases where nonlinear programming is used instead of FSD for nonconvex cases. Then,

there will be a potential for such an asynchronous operation to trigger a switch to another path through the design space that could end up at a different local minimum.

PLANS

Following initial experiments with the FSD synchronous and asynchronous iteration, it is planned to make the iterative computation more complex by replacing the FSD method with nonlinear mathematical programming including applications to nonconvex cases. One possibility includes reducing CONMIN (ref. 10) to a size that will fit on a microcomputer. CONMIN contains nine subroutines and a driver program. Some of the subroutines would be deleted and the code may have to be overlayed to fit onto the microcomputer. With this capability, distributed analysis with centralized optimization can be performed. Another possibility includes adding an optimization feature to each of the substructure programs. Although this feature probably will not be as general purpose as CONMIN, it will allow the investigation of distributed analysis and distributed optimizaton.

At this point, research on the microcomputers for this experiment will conclude. Plans call for having several large engineering workstations installed by that time. When a network of these computers is available, this investigation will continue on a much greater scale using large, general-purpose, state-of-the-art analysis and optimization programs and building on the experience gained from the microcomputer network. The plan is to use these workstations to investigate analysis and optimization in a multidisciplinary environment where three workstations would be used for the analysis of different disciplines and a fourth workstation for the optimization. The process could be controlled by a network-wide operating system - a novel feature which is interesting from a computer science viewpoint. Compared to the currently prevailing mode of operation in which most analysis and optimization operations are being done in a sequential mode, a workstation environment will allow each discipline to process in parallel, feed all of the constraints to the optimizer at one time, and then iterate through the process. This should result in a more optimum design in less time.

CONCLUDING REMARKS

An experiment is currently underway to see if advantage can be taken of parallel processing without making major changes to an analysis code. This experiment uses a network of four microcomputers to simulate a parallel processing computer. A small finite-element analysis computer program with a substructuring capability is applied to a framework of beams. One microcomputer controls the system while the other three analyze the substructures. The results verified that the computer time when compared to a single computer was indeed reduced, as expected, by a factor proportional to the number of computers minus corrections for data communication and incomplete parallelism of the problem. The reduction was achieved with almost no change to the analysis portion of the code. The experiment also includes resizing of the design variables using a Fully Stressed Design algorithm to simulate an iterative optimization to obtain an indication of the effect of asynchronous parallel computing on the convergence of an iterative process. The preliminary result showed only a very minor effect. Further testing

will be done with asynchronous resizing procedures, subsequently implementing them using large state-of-the-art analysis and optimization programs on engineering workstations.

REFERENCES

1. Field, E. I., "Feasibility Study for the Implementation of NASTRAN on the ILLIAC 4 Parallel Processor." NASA CR-132702, 1975.

2. "The NASTRAN User's Manual." NASA SP-222 (06), September 1983.

3. Noor, A. K.; Storaasli, O. O.; and Fulton, R. E., "Impact of New Computing Systems on Finite Element Computations." Impact of New Computing Systems on Computational Mechanics," (ed., A. Noor). ASME Publication H00275, 1983, pp. 1-32.

4. Siewiorek, D.; Bell, C.; and Newell, A., Computer Structures: Principles and Examples, McGraw-Hill Book Co., 1982, pp. 33-48.

5. Whetstone, W., "EISI-EAL: Engineering Analysis Language." Proceedings of the Second Conference on Computing in Civil Engineering, ASCE, 1980, pp. 276-285.

6. Przemieniecki, J. S., "Theory of Matrix Structural Analysis." Ch. 9, McGraw-Hill Book Co., 1968.

7. Sobieszczanski-Sobieski, Jaroslaw; James, Benjamin; and Dovi, Augustine, "Structural Optimization by Multilevel Decomposition." AIAA Paper No. 83-0832, AIAA/ASME/ASCE/AHS 24th Structures, Structural Dynamics and Materials Conference, Lake Tahoe, Nevada, May 2-4, 1983.

8. Baudet, G. M., "The Design and Analysis of Algorithms for Asynchronous Multiprocessors." Ph.D. Thesis, Department of Computer Science, Carnegie-Mellon University, 1978.

9. Sobieszczanski-Sobieski, Jaroslaw, "A Linear Decomposition Method for Large Optimization Problems. Blueprint for Development." NASA TM-83248, February 1982.

10. Vanderplaats, G. N., CONMIN - A FORTRAN Program for Constrained Function Minimization. Users Manual, NASA TMX-62282, August 1973.

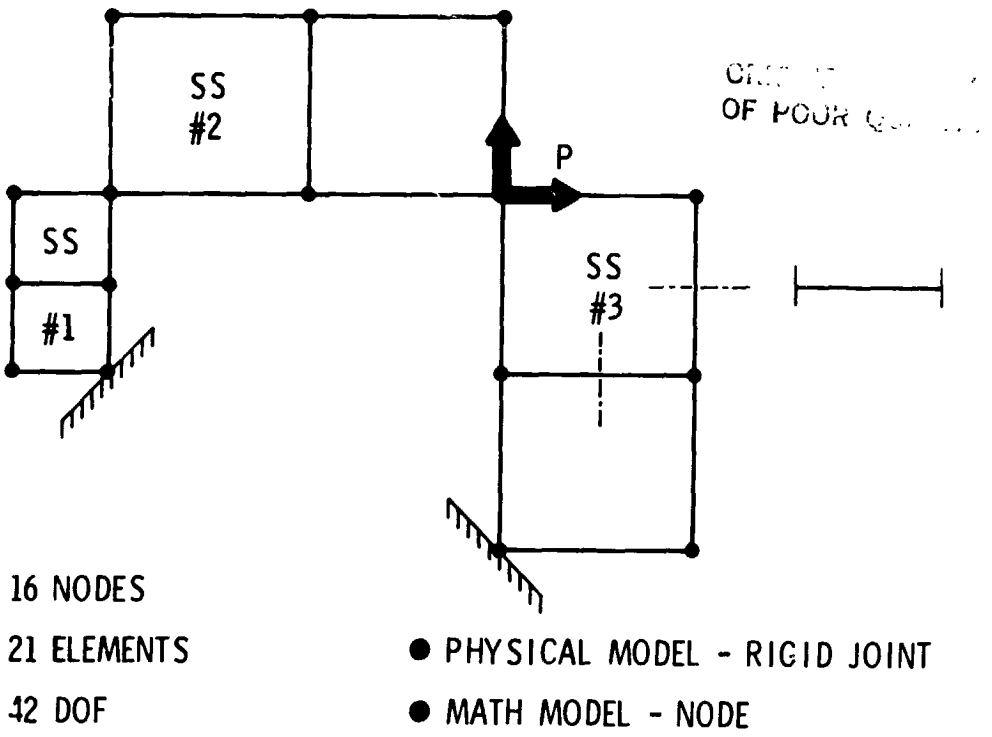

Figure 1.- Framework used for testing.

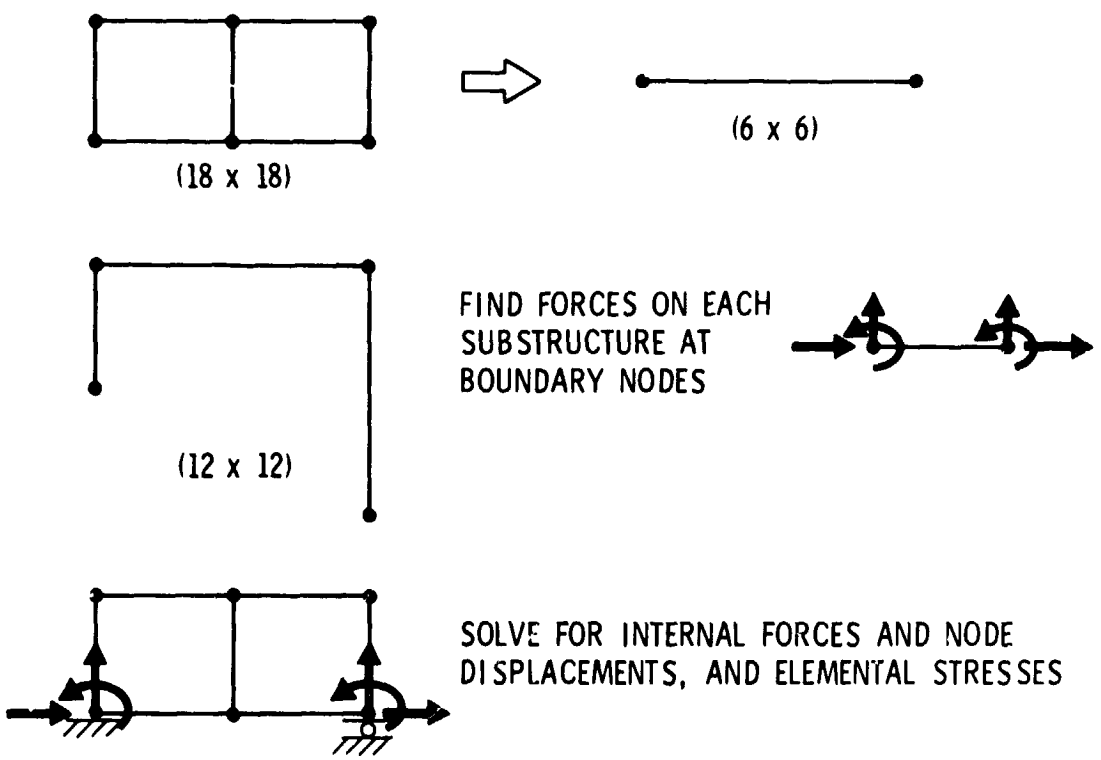

Figure 2.- Actions being taken at each step.

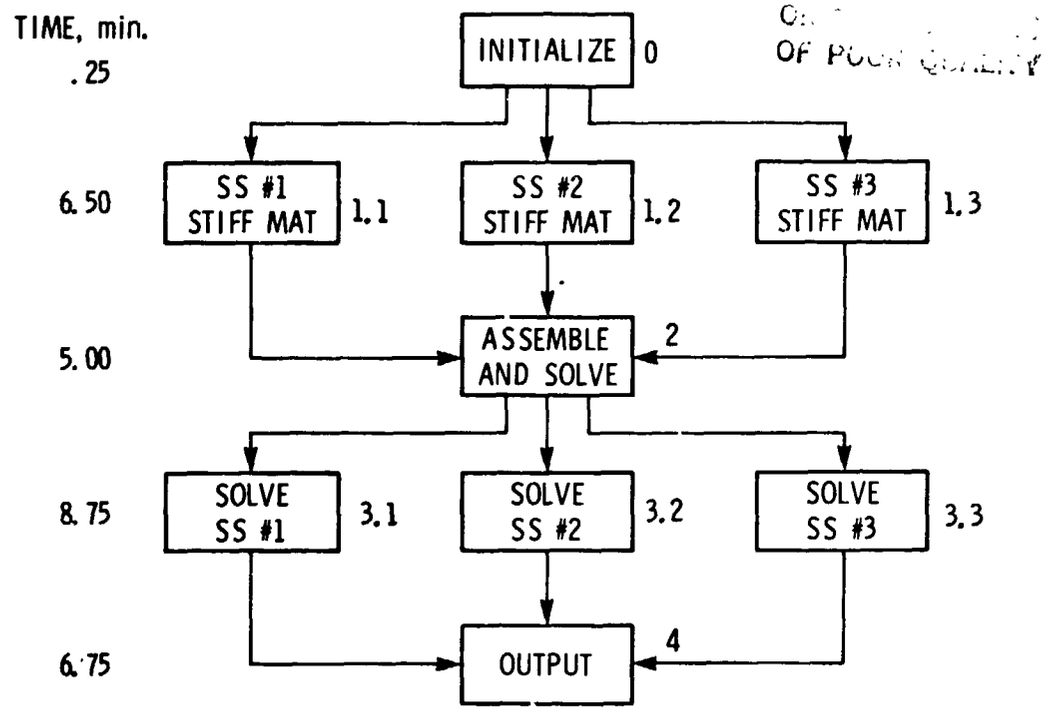

Figure 3.- Flowchart of substructure analysis.

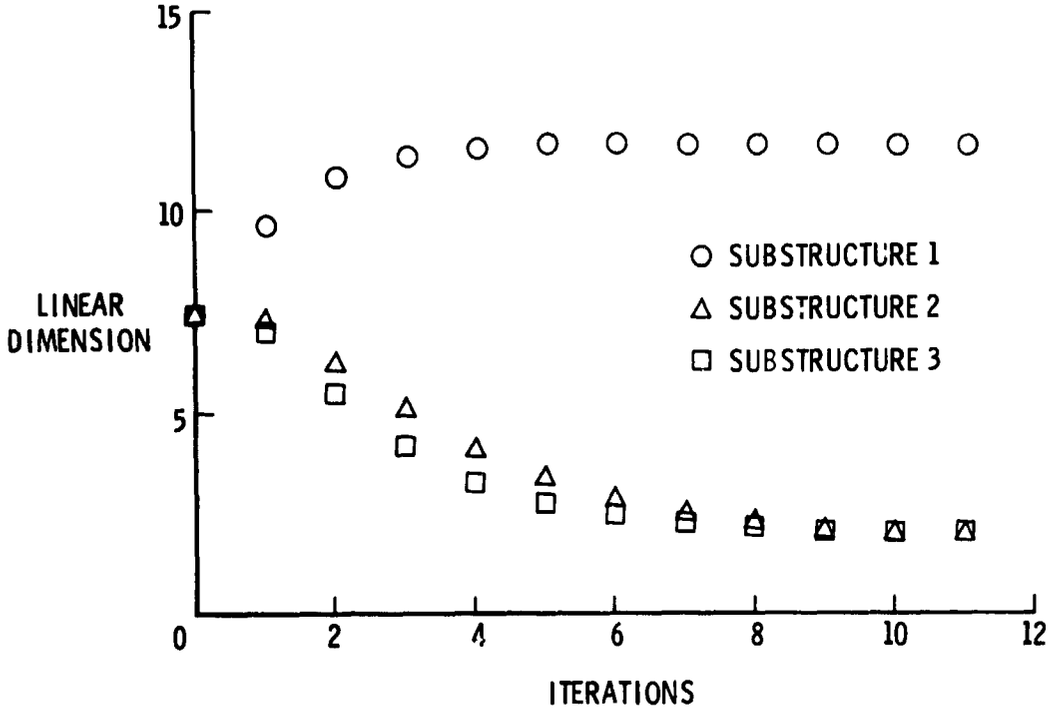

Figure 4.- Synchronous resizing.

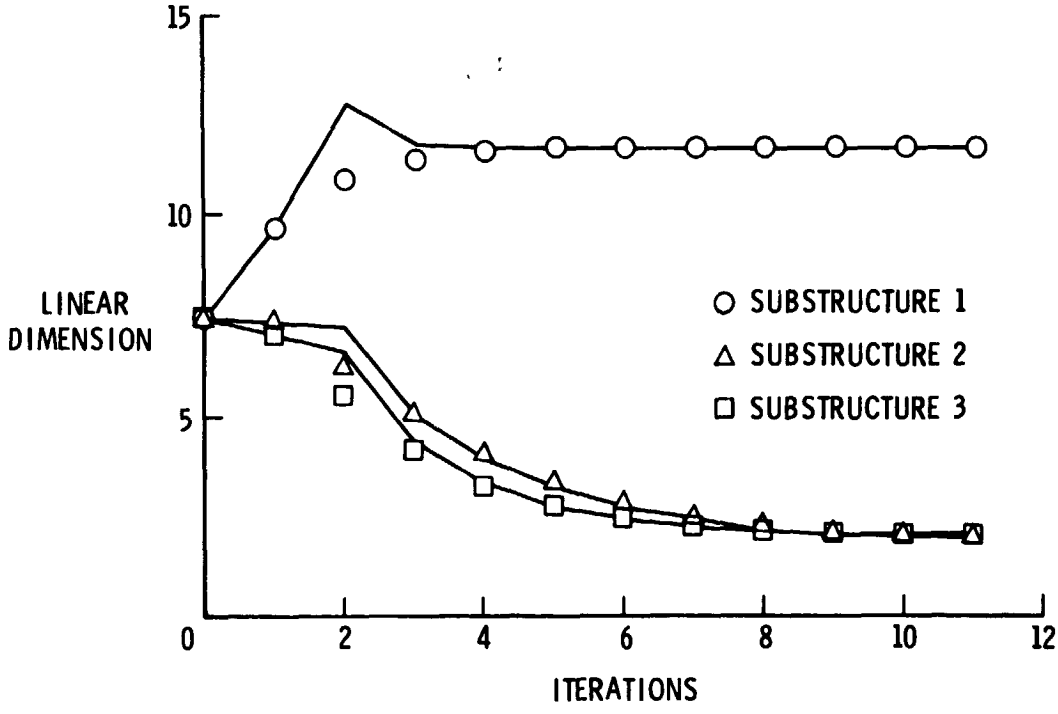

Figure 5.- Asychronous resizing (resize with old data).

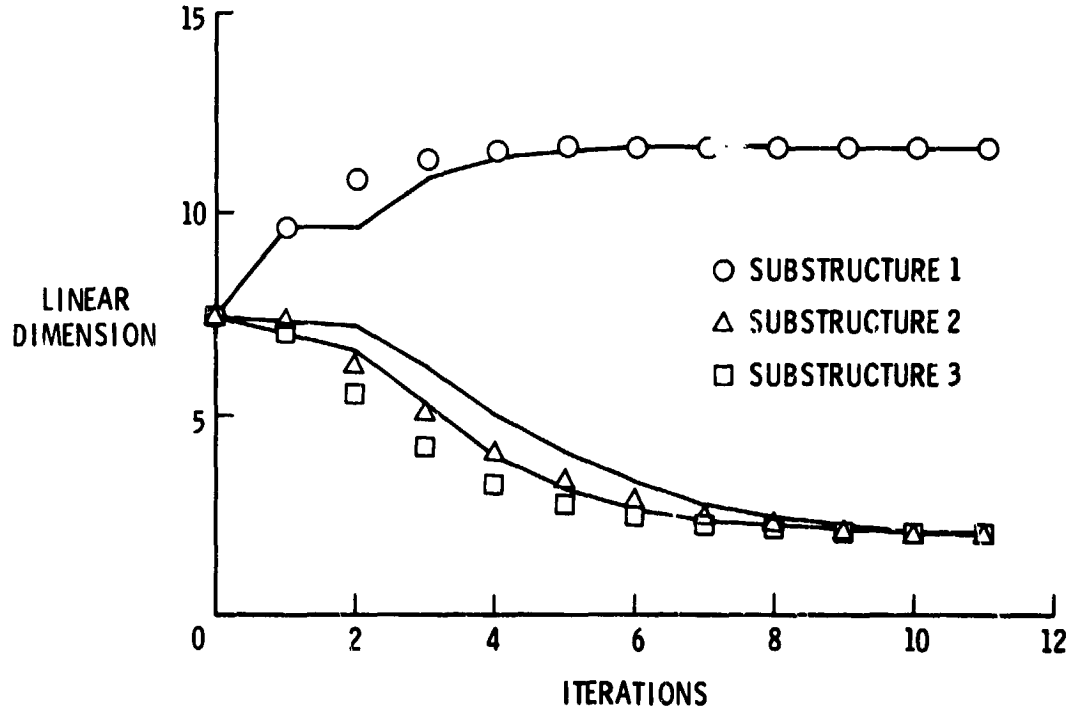

Figure 6.- Asychronous resizing (delay resizing one iteration).

TEQUEL : THE QUERY LANGUAGE OF SADDLE

S. D. Rajan
Department of Civil Engineering
Arizona State University
Tempe, Arizona 85287

SUMMARY

An relational database management system is presented that is tailored for engineering applications. A wide variety of engineering data types is supported and the data definition language (DDL) and data manipulation language (DML) are extended to handle matrices. The system can be used either in the standalone mode or through a FORTRAN or PASCAL application program. The query language is of the relational calculus type and allows the user to store, retrieve, update and delete tuples from relations. The relational operations including union, intersect and differ facilitate creation of temporary relations that can be used for manipulating information in a powerful manner. Sample applications are shown to illustrate the creation of data through a FORTRAN program and data manipulation using the TEQUEL DML.

INTRODUCTORY REMARKS

The use of database management techniques for engineering applications is quite widespread (refs. 1-3). Design of structural, mechanical and other systems through the use of computer graphics, finite element and optimizations techniques requires a sophisticated software system whose needs tax both the computer system and the software developer. The design system must be user-oriented, catering to the needs of users of different proficiencies. It also must be efficient, providing reasonable throughput; must be amenable to controlled future growth, able to incorporate changes in all multi-disciplines that constitute the design system; and must be intelligent enough to detect some forms of syntax and semantic errors. The system should give the designer freedom to specify the requirements peculiar to current needs and in essence control the flow of computations toward the final design.

While data base management systems (DBMS) have provided techniques to satisfy most of the needs of such general-purpose software development, the user perception of data bases is still an area of intense research. The user is expected to specify the requirements and carry out the data manipulations within the scope and in the language of the DBMS. TEQUEL is the first step in enhancing the capabilities of the SADDLE system (ref. 4) that has been used for the optimal design of various structures.

The topic of relational databases is discussed in this paper. The relative merits and demerits of this data model versus the other well-known data models are not presented and it is assumed that the relational model is appropriate for the task at hand. The first part of the paper reviews two relational, engineering DBMS. This review is followed by an outline of the procedural steps required to use a DBMS. The first step is the formulation of the database scheme which is discussed in some

detail. The second part of the paper presents the subsequent steps involving the implementation of the database scheme through the data definition language and the use of the database through the data manipulation language. Details of TEQUEL DDL and DML are presented. Later a few applications of the query language are shown with emphasis on the usage in a computer-aided design (CAD) environment. The paper concludes with some thought on future developments.

ENGINEERING DBMS

Commercial (business-oriented) DBMS cannot be used for engineering applications for a variety of reasons. First, they do not support engineering data types, which precludes their interaction with almost all technical programs. Second, engineering data exist in several forms and are used by technical and non-technical personnel for both administrative and technical purposes. Such a situation implies integration problems, access and control conflicts and multiple views of the database that would tax most business-oriented DBMS. Last, most engineering application programs work on local databases that are small in comparison to business databases but an enormous amount of computations take place involving the entire database.

Some Engineering DBMS

One of the most widely used engineering DBMS is the RIM subsystem of the IPAD design software system (ref. 5). The University of Washington Relational Information Management System (UWRIM) (ref. 6) is the result of substantial enhancements and improvements to the RIM program. It is based upon the relational algebra model for data management and has been used for a wide variety of applications ranging from engineering to accounting. The UWRIM user can use the system one of several ways - through the menu mode, through the command mode or through a high-level language program that can call FORTRAN subroutines contained in the UWRIM library. The standalone mode makes it possible for a user with little or no programming experience to define the database, enter data and manipulate the information with a set of relational commands. The database can also be protected using passwords and access lists. In defining the database, constraints on relations between attributes may be specified using boolean operators. The relational operations that are supported include intersect, union, project, subtract and join operators, and database modifications can be carried out using rename, remove, change, delete and reload commands. These same features are available through a high-level language program. While the standalone mode is suitable for a technical information system, the interaction through an application program makes possible the development of a wide variety of technical and non-technical programs. Using the standalone mode, relevant data can be extracted from the technical database and reformatted for use by administrative/non-technical personnel, allowing for data dissemination.

The SPIRE (Space Payload Integration and Rocket Experiment) DBM (ref. 7) is also based on a relational model of database. It provides a query language called Query-by-Example (QBE) to the user through which the user is able to define the model, retrieve and manipulate data. Through the QBE language, the user interacts with the SPIRE DBMS as though examining and manipulating a set of tables. QBE allows each and every user to have a different view of a common set of data. This facility makes it possible for users of different proficiencies to interact with the same global database. The next section discusses in some generality the procedural steps for using any DBMS.

Procedural Steps in the Use of a DBMS

There are essentially two steps in the use of a relational DBMS. During the first step, entity sets and their attributes are identified and the interrelationships between these attributes are established. Formally, the relationships are expressed in terms of data dependency; that is, a constraint on the possible relations that can be the current value for a relation scheme (ref. 8). In fig. 1, several lines are shown. The entity set, LINES, can be described by the attributes (line_identifier (LID), line_type (LTYP), number_of_internal_points (NIP), list_of_point_identifiers (LIP)). The entity set, POINTS, can be described by the attributes (point_identifier (PID), x-coordinate (X), y-coordinate (Y), z-coordinate (Z)). In the set POINTS, the attribute PID uniquely determines X. In other words, there is a functional dependency of X on PID and is denoted PID ->X (in fact, PID -> XYZ). Similarly, in LINES, LID -> LTYP, LTYP -> NIP, (LID, NIP) -> LIP. While these dependencies cannot be proved mathematically, the user must ensure that these functional dependencies (FDs) represent the real world.

The study of functional dependencies leads to identification of relation schemes. The number of relation schemes and the key for each scheme, given a set of FDs, are determined by following a set of guidelines that try to achieve some desirable properties which ensure that update, insertion and deletion anomalies do not arise and that redundancy of data is as minimal as possible. The relation schemes that have these properties are in the normal form. With FDs, the objective is to cast the relation scheme in the third normal form (3NF). The concept of 3NF is restricted by the fact that X -> Y implies that X determines Y uniquely. There are instances where, given a value of attributes of X, there is a set of zero or more associated values for the attributes of Y. This situation is denoted by X ->-> Y, that is, there is a multivalued dependency (MVD) of Y on X. With MVDs, the objective is to cast the relation scheme into the fourth normal form (4NF). The database theory that is used to decompose a scheme into better relation schemes is by no means complete. Perhaps the biggest problem is to represent the real world through FDs and MVDs, and hence caution should be excercised not only in specifying the dependencies but also in interpreting the results derived from decomposition algorithms.

As a part of the next step, the relation schemes forming the database can now be specified to the DBMS as a data model using the DDL. Using the DDL, the user specifies the relation schemes, the attributes and their data types, the keys for the relation and the constraints between the attributes. The DBMS prepares for its bookkeeping chores based on the supplied information. The DBMS is now ready to accept DML commands that would allow transactions such as creation, insertion, deletion or updating of information.

The query language forms the most important subset of the DML (nonquery aspects deal with the transactions mentioned before). Query languages for the relational model break down into two broad classes (ref. 9):

(a) Algebraic languages, where queries are expressed by applying specialized operators to relations

(b) Predicate calculus languages, where queries describe a desired set of tuples by specifying a predicate the tuples must satisfy

These relational operations provide an elegant approach to manipulation of information. Using a non-procedural language, it is possible for the user to express queries without knowing anything about the physical database. In a relational

calculus language, the result of a query is a relation obtained by the general formula

New relation = {tuple definition | conditions}

This formula is quite simple and complicated queries involving several relations can be easily formulated. The following sections show how the TEQUEL system can be used in an engineering database environment.

TEQUEL DATA DEFINITION LANGUAGE

The data model is created using three terminologies - domain, attribute and relation. A TEQUEL domain is the set of values that an attribute may assume. The domain is defined in terms of a variable and its data type. There are 9 data types that are supported - character, fixed point (integer), floating point (real) involving single and double precision, logical, packed logical, and floating and fixed point submatrices. An attribute is defined in terms of an already defined domain. Finally, relation schemes are defined in terms of attributes (domains), one or more of which is identified as keys of the relation. The keys ensure that each tuple is unique.

An example of a relation describing material properties is given below.

```
DOMAIN    : name*15      char;
            Y_modulus    double;
            density      real;

ATTRIBUTE : R_modulus, B_modulus   Y_modulus;
            Poissonratio, cost     density;

RELATION  : Mat_Table (name*, Y_modulus, R_modulus, B_modulus, density,
                       Poissonratio, cost);
```

Note that the elastic modulus attributes are of double precision type, and the density, Poisson ratio and cost are single precision. The attribute name (character of length 15) is the key to the relation scheme implying that no two material types have the same name. To the user, the relation scheme will appear as a table, Mat_Table (Table 1). In addition the user can open the data base directory containing one or more relation schemes with the command

OPEN databasename password;

The user automatically becomes the database administrator (DBA) when this command is issued for a particular database the first time. The DBA can assign user identification, password and level of access to different users of the database.

TEQUEL DATA MANIPULATION LANGUAGE

Once the data model is created using the DDL, the user can use the DML commands to store, retrieve, update and delete data. The commands operate on one or more relations and create a set of tuples involving the specified attributes that satisfy the given condition.

DML in a Standalone Mode

In this mode, the user is able to carry out the database transactions without having to write an application program.

Store: Information is loaded into the database by using the STORE command.

Example: The relation MAT_TABLE is stored as -

```
STORE MAT-TABLE:
Aluminum  7.1 2.5 7.7 2.7 0.343 0.45;
Copper    11.7 4.5 13.5 8.96 0.35 0.63;
Lead      1.8 0.76 4.3 11.34 0.45 0.50;
Zinc      8.0 3.5 6.0 7.14 0.33 0.80;
*
```

The rest of the transactions are carried out using the Select-From-Where (SFW) command -

```
SELECT    attribute name(s)
FROM      relation name(s)
WHERE     condition(s);
```

A temporary 'relation' is created as a result of this command. This relation may then be used to carry out other database operations.

Retrieve: Information is retrieved for viewing, deletion or modification of information using the SFW command. The attribute names in the SELECT clause can be differentiated from one another if more than one relation is used in the FROM clause. This is done by qualifying the attributes with their relation name - relation_name.attribute_name. In the WHERE clause, one or several conditions can be specified involving attributes, arithmetic operations and boolean operations.

Example: If from the relation MAT_TABLE, it is necessary to identify all materials whose square root of the sum of Young's modulus and Rigidity modulus is greater than 3.0 and the cost is less than or equal to 0.70, the following query can be used -

```
SELECT ?
FROM  mat_table
WHERE (sqrt (y_modulus+r_modulus) > 3.0) & (cost <= 0.70);
```

The ? in the SELECT clause specifies that all attribute values are to be selected.

Delete: To delete certain tuples, the SFW clause may be used to identify the tuples and then the DELETE command can be issued.

Example: Delete all material having Poisson ratio less than 0.34.

```
SELECT ?
FROM  mat_table
WHERE Poisson ratio < 0.34;
DELETE;
```

Update: To update specific attributes, the SFW command may be used to identify the tuples and then the UPDATE command can be issued with new values.

Example: Inflation has caused the cost of all materials to increase by 10 percent.

```
SELECT cost
FROM mat_table;
UPDATE 1.1*cost;
```

DML Through an Application Program

These same functions can be carried out from either a FORTRAN or a PASCAL program. The application program calls routines/procedures in the TEQUEL library through the TQL interface much the same as commands are issued in the standalone mode. Appendix A illustrates a graphics pre-processor program developed using the TEQUEL DBMS. Routines in the TQL interface are recognized by the prefix TQL that precedes all routine names.

The program generates a hexahedron as specified by the user who inputs the minimum amount of information to specify the solid and the program automatically generates the rest of the nodal and solid information. The key to the information transfer between the application program and the TQL interface is the COMMON blocks (TRNODE, TRBCK, and TRSLD8). They contain the attributes in the relation ordered by decreasing lengths (as determined by their data types). In order to store, update or retrieve information, the application program specifies the values of the keys and then calls are made to TQL_PUTDAT (to store) and TQL_GETDAT (to retrieve). The TQL interface determines the location of the specified tuple by converting the values of the keys to a unique address. This task is handled by the File Management System (FMS) of the TEQUEL DBMS.

The program looks somewhat different from conventional programs that are often bogged down by the tasks that the DBMS performs. The programmer is freed from such mundane tasks and is allowed to concentrate on the intricacies of application development.

DDL/DML EXTENSIONS TO OPERATE ON MATRICES

Studies of dynamic behavior of programs operating in paged memories have indicated clearly the poor performance exhibited by programs designed originally for conventional systems (ref. 10). Two important results were obtained from the study.

(i) Order of magnitude improvement can be made in the number of page faults and page residence times for several common matrix operations by suitably sequencing the individual computations.

(ii) Storage by submatrices is superior to storage by rows with the possible exception of forward elimination involved in equation solving in which partial pivoting is required. However the difference becomes significant only for large matrices, and therefore whether the savings obtained by submatrix storage are worth the price paid in increase in addressing complexity is a question that is best answered for specific cases.

There are two questions that are unanswered in ref. 10. First, how easy is it to develop general purpose programs with general size matrices if external storage is not used? Second, if external storage is used, should 'complex' addressing be carried out by the application program or is it possible for a DBMS to handle the data transfer efficiently and easily? Experience has shown that the use of submatrices (refs. 11,12) is most efficient for general-purpose program development whenever such use is possible under a DBMS. The matrix support under TEQUEL is intended for applications where submatrix storage is likely to be superior to convertional storage.

TEQUDL DDL allows the user to define matrices of three data types -

```
DOMAIN:  X(5)          realarray    (10);
         Y(20,20)      doublearray  (5,15);
         CODE (8,2)    intlarray    (10,9);
```

where X is a vector of single precision numbers partioned into 10 subvectors each having 5 elements; Y is a matrix of double precision numbers partioned into 75 submatrices of 5 superrows and 15 supercolumns with each submatrix having 20 rows and 20 columns. Similarly, CODE is a matrix of integer numbers. Typical relations involving submatrices are defined as-

```
RELATION:    XVECTOR (XROW*, X);
             YARRAY  (YROW*, YCOL*, Y);
             CODE_MAT (CROW*, CCOL*, CODE);
```

where XROW, YROW, YCOL, CROW and CCOL denote the superrow and supercolumn numbers and hence act as the keys for the relations. It is also possible to store sparse matrices under this scheme by indicating that the number of superrows and supercolumns is zero. The TEQUEL DBMS automatically creates a sparse matrix directory for the relation in question.

EXAMPLES IN A CAD ENVIRONMENT

Appendix A shows a program that generates nodal and solid information for a hexahedron with parallel and identical front and back sides (fig. 2). The user specifies the dimensions of the hexahedron and the number of subdivisions that the hexahedron must be divided into. The rest of the information is automatically calculated by the program.

The relation schemes are defined using the TEQUEL DDL as follows -

```
DOMAIN:  NODENO, POINT(8)      intl;
         X, LENGTH             real;
         BRICK_NAME*10         char;
         NAME*15               char;
```

```
ATTRIBUTE:  SOLIDNO          NODENO:
            Y,Z              X;
            WIDTH,HEIGHT     LENGTH;

RELATION:   NODES   (NODENO*, X, Y, Z);
            SLD8    (SOLIDNO*, POINT);
            BRICKS (BRICK_NAME*, FIRSTNODE, LASTNODE, FIRSTSLD, LASTSLD, NAME,
                LENGTH, WIDTH, HEIGHT);
```

Each hexahedron is created in a local coordinate system and is identified in the relation BRICKS by BRICK_NAME. The nodes and the 8-node bricks are created with consecutive node numbers (NODENO) and solid numbers (SOLIDNO) and of material NAME. The solids are identified by the key, SOLIDNO, and described by the 8 nodes contained in the vector, POINT. The nodes in turn are identified by the key, NODENO, and described by their location in space, X,Y and Z coordinates.

Example 1: Creation of the solid model in Fig. 3.
The FLANGE and RIB are created using the program with dimensions 100 x 20 x 10. The local coordinate system (LCS) of FLANGE coincides with the global coordinate system (GCS). In order to position RIB in the GCS, the TEQUEL DML is used as follows -

(a) Translation of the origin from (0,0,0) to (60,20,0).

```
SELECT  nodes.x nodes.y
FROM    nodes bricks
WHERE   (bricks.brickname = 'RIB') & (nodes.nodeno >=
        bricks.firstnode) & (nodes.nodeno <= bricks.lastnode);

UPDATE  (x+60); (y+20);
```

(b) Rotation about z-axis by 90 degrees (counterclockwise).

```
UPDATE  (x*cos(90) + y*sin(90));
        (-x*sin(90) + y*cos(90));
```

Example 2: Statistics on the solid model.

(a) Model limits in the X, Y, Z directions.

Two macros could be created as MINIMUM.TQL -

```
MIN { SELECT %1%
      FROM NODES; };
```

and MAXIMUM.TQL -

```
MAX { SELECT %1%
      FROM NODES; };
```

These macros can be invoked as -

```
MINIMUM x;
MAXIMUM x;
```

to find the minimum and maximum coordinates in the x-direction (and similarly for y and z directions).

(b) Cost of aluminum used in the model.
The query can be posed as follows to generate a temporary relation

```
SELECT ?
FROM bricks
WHERE name = 'Aluminum':
```

and the cost evaluated as volume times the unit cost -

```
SUM { EVALUATE length*width*height*0.45 };
```

(c) Nodal coordinates of nodes that belong to both FLANGE and RIB.
A set operation is involved in formulating the query. First two sets must be created that contain the nodal coordinates of the nodes that form FLANGE and RIB. Then the intersection of the two sets would yield the required information.

Define a macro COMMON.TQL -

```
SELECT  nodes.x nodes.y nodes.z
FROM    nodes bricks
WHERE   (bricks.brick_name = %1%) & (nodes.nodeno >=
        bricks.firstnode) & (nodes.nodeno <= bricks.lastnode);
```

The query can be then posed as -

```
INTER { COMMON FLANGE; COMMON RIB };
```

These examples illustrate some of the different types of queries that can be used in order to accomplish a wide variety of engineering tasks. There are three clear advantages to this approach.

(i) The user need not write an application program for small and new queries.
(ii) The application program does not contain any elaborate bookkeeping logic pertaining to information manipulation. The DBMS handles these chores in a transparent manner.
(iii) The relational operations again are handled by the DBMS in a manner that is transparent to the application program.

CONCLUDING REMARKS

An engineering DBMS is presented that has been used for a limited number of applications. However, its usage is likely to increase in the future. The DMBS supports several data types that have widespread engineering use including special storage and retrieval schemes for matrices stored as submatrices. The DML is easy yet powerful to use either in the standalone mode or through an application program. Currently research is being conducted in the following areas to improve the efficiency and enhance the features of the system.

(i) Key-to-Address (KAT) Transformations: The efficiency of a DBMS depends largely on the FMS. In order to locate a tuple, the FMS must use a scheme to convert the information contained in the keys to an address. In the example discussed in the appendix, the keys for NODES and SLD8 are integers, perhaps the simplest form of a relation key. With character keys or multi-attribute keys, in general, it is not possible to locate

the tuple with one access. Several 'hashing' algorithms are available each having its merits and demerits. In addition, the FMS must also be capable of memory management since the information is likely to exist on primary and secondary storages. The Memory Management Scheme (MMS) should be able to achieve maximum efficiency on a particular computer system, a tall order.

(ii) Automated Database Design: Quite often, the database administrator is face with a dilemma - How many relation schemes are required to describe the database scheme and what attributes should be the keys for the relations? The study of automated database design is necessary in order to preserve the relations in the normal forms especially as the interrelationships become complex between attributes. It will be desirable to have the user specify the FDs and MVDs and have the DBMS formulate the relation schemes and other required information.

(iii) Multiple-User Environment: Engineering DBMS are inherently complex since any project is manned by several groups and multi-disciplines. In addition, the information in the database is required at several locations in several forms. This form of distributed database in a multi-user environment will make the DBMS more complex and consequently less responsive.

It is hoped that the issues will be resolved without sacrificing integrity of the database, turnaround time, security and other similar requirements.

REFFRENCES

1. Giles, G. L. and M. Vallas: "Use of an Engineering Data Management System in the Analysis of Space Shuttle Orbiter Tiles." AIAA Computers in Aerospace 3rd Conference, San Diego, AIAP paper no. 81-2192 (1981)

2. Rogers, V. A., T. R. Sutter, C. L. Blackburn, and S. H. Choi, "Application of Data Management to Thermal/Structural Analysis of Space Trusses." Proceedings Structures, Structural Dynamics and Materials 24th Conference, Lake Tahoe, AIAA paper no. 83-1020 (1983).

3. Blackburn, C. L., O. O. Storaasli and R. E. Fulton, "The Role and Applications of Database Management in Integrated Computer-Aided Design," 23rd Structures, Structural Dynamics and Materials Conference, AIAA, New Orleans (1982). Also, J. Aircraft, vol. 3, pp. 717-725 (1983).

4. Rajan, S. D.: "SADDLE: A computer-aided Structural Analysis and Dynamic Design Language." Ph.D. Thesis, Division of Materials Engineering, University of Iowa, Iowa City (1983).

5. Dube, R. P.: "IPAD Software Workbook." IPAD Integration Prototype Software, Boeing Aircraft Company (1979).

6. UWRIM Primer and Reference Manual, Academic Computer Center, Univeristy of Washington, (1980).

7. SPIRE Data Base User's Guide. Cosmic Program #GSC-12684, Computer Software Management and Information Center, Athens, GA (1980).

8. Tsichritzis, D. C. and F. H. Lochovsky: Data Models. Prentice-Hall, New Jersey (1982).

9. Ullman, J. D.: Principles of Database Systems. Computer Science Press, Second ed., Maryland (1982).

10. McKellar, A. C. and E. G. Coffman: "Organizing Matrices and Matrix Operations for Paged Memory Systems." Comm. ACM, 12, pp. 153-165 (1969).

11. Kamel, H. A., M. W. McCabe and W. W. Spector: GIFTS 5 Systems Manual. Interactive Graphics Engineering Laboratory, University of Arizona, Tucson (1979), ONR Contract No. N00014-75-C-0837, USCG Contract No. DOT-CG-43565-A.

12. Schrem, E.: "Computer Implementation of the Finite Element Procedure." Numerical and Computer Methods in Structural Mechanics (Edited by S. J. Fenves et al.). Academic Press, New York (1973).

Table I. - A Sample Material Table

MAT_TABLE

Name	Y_modulus	R_modulus	B_modulus	Density	Poisson ratio	Cost
Aluminum	7.1	2.5	7.7	2.7	0.343	0.45
Copper	11.7	4.5	13.5	8.96	0.35	0.63
Lead	1.8	0.76	4.3	11.34	0.45	0.50
Zinc	8.0	3.5	6.0	7.14	0.33	0.80

APPENDIX A

```
C *** PROGRAM TO GENERATE A SOLID MODEL USING 'TEQUEL' DBMS
C
C     THE PROGRAM DEVELOPES A HEXAHEDRON AS DEFINED BY THE USER.
C     PROGRAM RESTRICTIONS -
C       (1) THE HEX IS A BRICK
C       (2) ALL NODAL INFORMATION IS GENERATED IN A LOCAL
C           COORDINATE SYSTEM
C
C *** TYPE DECLARATION BLOCK
      INTEGER NODENO, SOLIDNO, POINT, ERRCODE, PANEL
      INTEGER XDIV, YDIV, ZDIV, PANEL, BOTLEFT, BOTRIGHT, BASENO
      REAL LENGTH, WIDTH, HEIGHT, X, Y, Z
      CHARACTER*15 DBNAME, DBPASS, USERNAME, USERPASS
      CHARACTER*15 NODES, SLD8, BRICKS, ACCESS
C
      INTEGER FIRSTNODE, LASTNODE, FIRSTSLD, LASTSLD
      CHARACTER*15 NAME, BRICK_NAME, BLANK
C
C *** ARRAY DEFINITION BLOCK
      DIMENSION POINT(8)
C
C *** GLOBAL VARIABLES BLOCK
      COMMON /UNITS / LUIN, LUOUT
      COMMON /TRNODE/ X, Y, Z, NODENO
      COMMON /TRPANL/ SOLIDNO, POINT
      COMMON /TRBCK / BRICK_NAME, NAME, LENGTH, WIDTH, HEIGHT,
     $                FIRSTNODE, LASTNODE, FIRSTSLD, LASTSLD
C
C *** DATA INITIALIZATION BLOCK
      DATA X, Y, Z /3*0.0/
      DATA DBNAME  /'HEX            '/, DBPASS  /'GRAPHMAN       '/,
     $     USERNAME/'SYSTEM         '/, USERPASS/'TEQUEL         '/,
     $     NODES   /'NODES          '/, SLD8    /'SLD8           '/,
     $     BRICKS  /'BRICKS         '/, ACCESS  /'RS             '/,
     $     BLANK   /'               '/
C
C --- INITIALIZE EXECUTION
      CALL TQL_INIT
C
C --- SET USER IDENTIFICATION
      CALL TQL_USERID (USERNAME, USERPASS, ERRCODE)
      IF (ERRCODE .NE. 0) CALL TQL_MESSAGE (ERRCODE)
C
C --- OPEN THE DATABASE
      CALL TQL_DBOPEN (DBNAME, DBPASS, ERRCODE)
      IF (ERRCODE .NE. 0) CALL TQL_MESSAGE (ERRCODE)
C
C --- SET SCOPE FOR RELATIONS 'NODES', 'BRICKS' & 'SLD8'
      CALL TQL_SETSCOPE (NODES, ACCESS, ERRCODE)
      IF (ERRCODE .NE. 0) CALL TQL_MESSAGE (ERRCODE)
      CALL TQL_SETSCOPE (BRICKS, ACCESS, ERRCODE)
      IF (ERRCODE .NE. 0) CALL TQL_MESSAGE (ERRCODE)
      CALL TQL_SETSCOPE (SLD8, ACCESS, ERRCODE)
      IF (ERRCODE .NE. 0) CALL TQL_MESSAGE (ERRCODE)
```

```
C
C --- INITIALIZE VARIABLES
      LASTNODE=0
      LASTSLD=0
C
C === GET INFORMATION ON USER-DESCRIBED BRICK
    1 WRITE (LUOUT, 2)
    2 FORMAT (1X,'Name of solid : ',$)
      READ (LUIN, *) BRICK_NAME
      IF (BRICK_NAME .EQ. BLANK) GO TO 999
      WRITE (LUOUT, 20)
   20 FORMAT (1X,'Material name : ',$)
      READ (LUIN, *) NAME
      WRITE (LUOUT, 21)
   21 FORMAT (1X,'Length, width and height ? ',$)
      READ (LUIN, *) LENGTH, WIDTH, HEIGHT
C
C === GET NUMBER OF SUBDIVISIONS IN THE X, Y & Z DIRECTIONS
  101 WRITE (LUOUT, 100)
  100 FORMAT (1X,'Subdivisions along the x-direction : ',$)
      READ (LUIN, *, ERR=101) XDIV
  102 WRITE (LUOUT, 103)
  103 FORMAT (1X,'Subdivisions along the y-direction : ',$)
      READ (LUIN, *, ERR=102) YDIV
  104 WRITE (LUOUT, 105)
  105 FORMAT (1X,'Subdivisions along the z-direction : ',$)
      READ (LUIN, *, ERR=104) ZDIV
C
C --- CALCULATE INCREMENTS IN X, Y, Z-DIRECTIONS
      XINC=LENGTH/FLOAT(XDIV)
      YINC=WIDTH/FLOAT(YDIV)
      ZINC=HEIGHT/FLOAT(ZDIV)
C
C --- GENERATE NODES IN PLANES PARALLEL TO X-Z PLANE
      NODENO=LASTNODE+1
      FIRSTNODE=NODENO
      DO 106 I=1,YDIV+1
      Y=FLOAT(I-1)*YINC
      DO 107 J=1,XDIV+1
      X=FLOAT(J-1)*XINC
      DO 108 K=1,ZDIV+1
      Z=FLOAT(K-1)*ZINC
      NODENO=NODENO+1
      CALL TQL_PUTDAT (NODES, X, ERRCODE)
      IF (ERRCODE .NE. 0) CALL TQL_MESSAGE (ERRCODE)
  108 CONTINUE
  107 CONTINUE
  106 CONTINUE
      LASTNODE=NODENO
C
C --- STORE THE SOLID INFORMATION
      SOLIDNO=LASTSLD+1
      FIRSTSLD=SOLIDNO
      DO 400 I=1,YDIV
      DO 401 J=1,XDIV
      DO 402 K=1,ZDIV
```

```
C
C >>> FRONT AND BACK PANEL INFORMATION
      DO 403 PANEL=1,2
      BASENO=(I-1+PANEL-1)*(ZDIV+1)*(XDIV+1)+1
      BOTLEFT=BASENO+(J-1)*(ZDIV+1)+(K-1)
      BOTRIGHT=BASENO+J*(ZDIV+1)+(K-1)
      INC=(PANEL-1)*4
      POINT(1+INC)=BOTLEFT
      POINT(2+INC)=BOTRIGHT
      POINT(3+INC)=BOTRIGHT+1
      POINT(4+INC)=BOTLEFT+1
  403 CONTINUE
C
C --- OUTPUT THE INFORMATION
      SOLIDNO=SOLIDNO+1
      CALL TQL_PUTDAT (SLD8, SOLIDNO, ERRCODE)
      IF (ERRCODE .NE. 0) CALL TQL_MESSAGE (ERRCODE)
  402 CONTINUE
  401 CONTINUE
  400 CONTINUE
C
C --- UPDATE RELATION 'BRICKS'
      LASTSLD=SOLIDNO
      CALL TQL_PUTDAT (BRICKS, BRICK_NAME, ERRCODE)
      IF (ERRCODE .NE. 0) CALL TQL_MESSAGE (ERRCODE)
      GO TO 1
C
C --- CANCEL THE SCOPES IN EFFECT
  999 CALL TQL_CANCELSCOPE (NODES, ERRCODE)
      IF (ERRCODE .NE. 0) CALL TQL_MESSAGE (ERRCODE)
      CALL TQL_CANCELSCOPE (SLD8, ERRCODE)
      IF (ERRCODE .NE. 0) CALL TQL_MESSAGE (ERRCODE)
C
C --- CLOSE THE DATABASE
      CALL TQL_DBCLOSE (DBNAME, DBPASS, ERRCODE)
      IF (ERRCODE .NE. 0) CALL TQL_MESSAGE (ERRCODE)
C
C --- TERMINATE EXECUTION
      CALL EXIT
      END
```

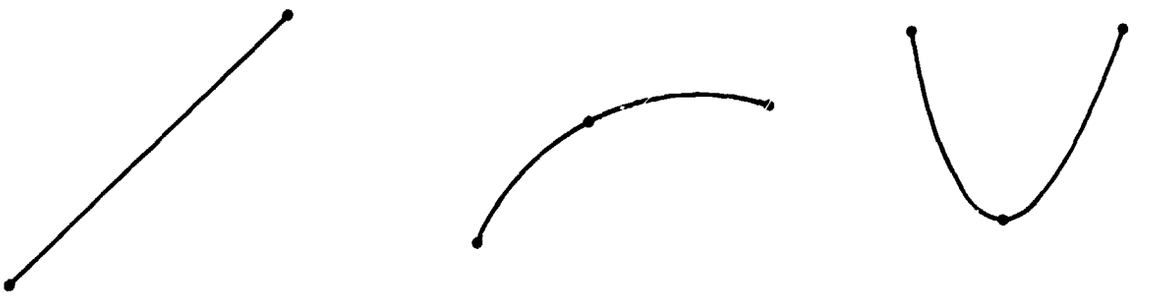

(a) Straight line. (b) Circular arc. (c) Parabolic arc.

Figure 1. Components of entity set LINES.

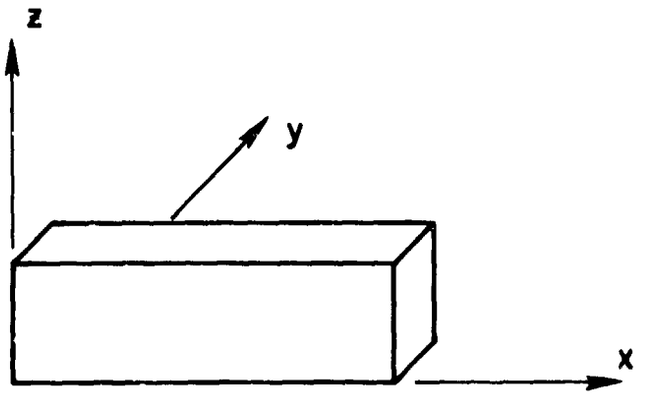

Figure 2. 'Brick' in the local coordinate system.

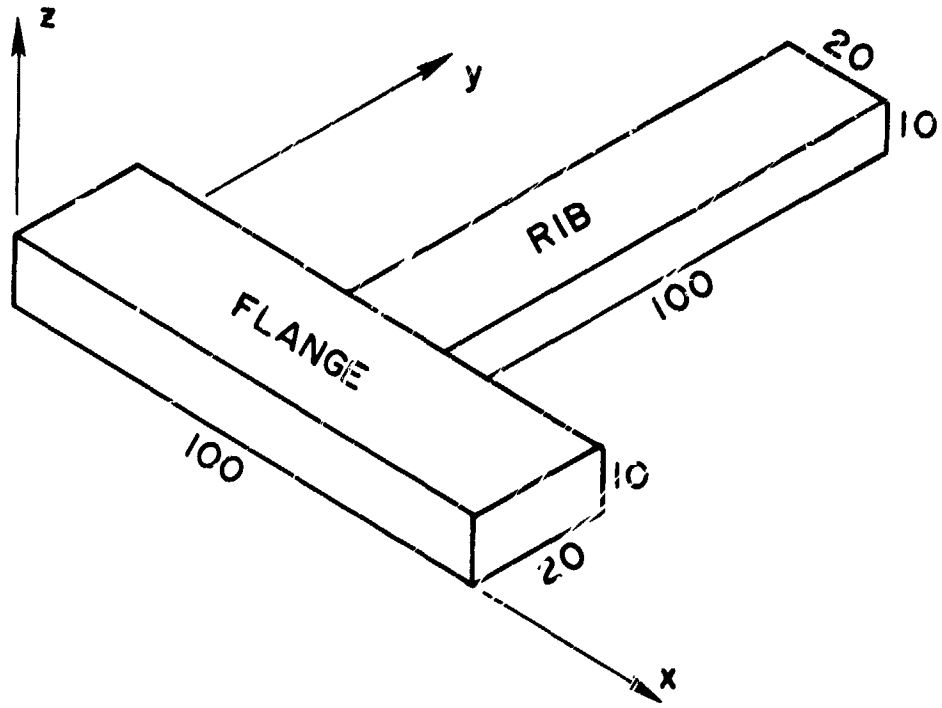

Figure 3. Solid model in examples 1 and 2.

PERFORMANCE OF THE h, p and h-p VERSIONS OF THE FINITE ELEMENT METHOD

I. Babuška[1] and W. Gui[2]
Institute for Physical Science and Technology
University of Maryland
College Park, MD

B. Szabo[3]
Washington University
St. Louis, MO

1. INTRODUCTION

There are three basic versions of the finite element method, called the h, p and h-p versions. They are essentially characterized by the way in which the finite element meshes and polynomial degree of elements are chosen. They differ in computer implementation (program architecture) and mathematical analysis. This paper is concerned mainly with the question of how the meshes and polynomial degree of the elements affect the accuracy of finite element solutions. Our approach is to fix certain parameters or their relation and increase the number of degrees of freedom so that the finite element solutions converge to the exact solution. Such a systematic increase of the number of degrees of freedom is called extension because it can be interpreted as a systematic extension of finite element spaces.

When emphasis is on analysis of accuracy and not aspects of implementation, then we speak about the h, p and h-p extensions rather than versions. Understanding the various extension processes and their numerical performance is essential for resolving certain basic questions of implementation.

The h-extension is the most commonly used approach to error reduction. The polynomial degree (p) of the elements is fixed and the errors of approximation are reduced through mesh refinement. The size of the elements is usually denoted by h, hence the name: h-extension. Typically, the polynomial degree of elements is low, usually $p = 1$ or $p = 2$.

In the p-extension the mesh is fixed and convergence is achieved by increasing the polynomial degree of elements either uniformly or selectively.

The h-p extension combines the h- and p-versions, i.e., reduction of error is achieved by mesh refinement and concurrent choices in the polynomial degree of elements.

The parameters that characterize extension processes can be chosen either a

---

[1]Partially supported by ONR Contract No. 0014-77-C-9623.

[2]Partially supported by NSF Grant DMS-8315216.

[3]Partially supported by ONR Contract No. N0014-81-K0625.

priori, on the basis of certain characteristics of the exact solution, known a priori, or a posteriori, through utilization of some feedback procedure, in which case the parameters of the extension process depend on previously computed data.

The analysis and especially optimization or extension processes (selection of optimal meshes, polynomial degree distributions, etc.) presented herein indicate the potential of alternative approaches and provide a basis for decisions concerning implementation.

In order to keep the essential points in focus, we consider only two simple model problems based on the displacement formulation and two measures of error, the error measured in energy norm and the error of stress components computed at specific points.

Specifically, we denote the exact and finite element solutions respectively by u_0 and $\tilde{u}$. The error is then $e = u_0 - \tilde{u}$. The energy norm of e is denoted by $\|e\|_E$ and is defined as the square root of the energy of the error:

$$\|e\|_E = (W(e))^{1/2}$$

The relative error in energy norm is denoted by $\|e\|_{ER}$ and is defined as:

$$\|e\|_{ER} = \frac{\|e\|_E}{\|u_0\|_E}$$

The error in stress components at some point x_0 is defined as

$$e_{ij}(x_0) = |\sigma^0_{ij}(x_0) - \tilde{\sigma}_{ij}(x_0)|$$

where $\sigma^0_{ij}(x_0)$ and $\tilde{\sigma}_{ij}(x_0)$ respectively denote the exact and computed components of the stress tensor at point x_0. The relative error in stresses is defined by:

$$e^R_{ij}(x_0) = \frac{|e_{ij}(x_0)|}{|\sigma^0_{ij}(x_0)|}$$

The one dimensional problem can be analyzed theoretically and experimentally in great detail. One dimensional problems can also serve as models for higher dimensional problems which are vastly more complicated and less well understood. Presentation of details and derivation of formulas quoted herein is beyond the scope of this paper. For application in two dimensions we refer to references 1 to 4.

2. MODEL PROBLEMS

2.1. Model Problems

We consider the following simple model problems:

$$-u''(x) = f(x), \qquad x \in I = (0,1) \tag{2.1}$$

$$u(0) = u(1) = 0 \tag{2.2}$$

and exact solutions of the form:

$$u_0(x) = (x+\xi)^\alpha - \xi^\alpha - x\left[(1+\xi)^\alpha - \xi^\alpha\right] \tag{2.3}$$

with $\alpha > 1/2$ and $\xi > 0$. The solutions minimize the potential energy defined as:

$$\pi(u) = W(u) - 2\int_0^1 fu\, dx$$

where $W(u) = \int_0^1 (u')^2\, dx$.

The finite element solutions are characterized by the mesh and p-distributions. Specifically we denote the mesh by the partition:

$$\Delta =: 0 = x_0^\Delta < x_1^\Delta < \cdots < x_{M(\Delta)}^\Delta = 1$$

where $x_0^\Delta, x_1^\Delta, \cdots, x_{M(\Delta)}^\Delta$ are the mesh (or nodal) points. The j^{th} finite element is denoted by $I_{j+1} = (x_j^\Delta, x_{j+1}^\Delta)$. The size of the j^{th} element is defined by $h_j = x_j^\Delta - x_{j-1}^\Delta$. The size of the largest element is denoted $h(\Delta)$. The set of all functions w defined on I that satisfy the following conditions:

(a) $W(w) < \infty$,

(b) the boundary conditions (2.2),

(c) on I_j^Δ w is a polynomial of degree p_j^Δ,

is denoted by $S^{\underline{p}(\Delta)}(\Delta)$ where $\underline{p}(\Delta) = (p_1^\Delta, p_2^\Delta, \cdots, p_{M(\Delta)}^\Delta)$ is the vector of p-distribution. Here, $S^{\underline{p}(\Delta)}(\Delta)$ is called the finite element space. The number of degrees of freedom is denoted by $N(\Delta)$.

$$N(\Delta) = \dim S^{\underline{p}(\Delta)}(\Delta) = \sum_{j=1}^{M(\Delta)} p_j^\Delta - 1$$

The finite element method consists of finding $\tilde{u} \in S^{\underline{p}(\Delta)}$ which minimizes $\pi(u)$ over $S^{\underline{p}(\Delta)}(\Delta)$. The extension processes are characterized by the selection of sequences of Δ and $\underline{p}(\Delta)$.

2.2. The Two-Dimensional Model Problem

We shall consider the model problem of Fig. 1 assuming plane strain conditions and using the elastic parameters $E = 1$, $\nu = 0.3$. The tractions on the boundary are chosen so that the exact solution is known and the singularity at the crack tip is characterized by the stress intensity factors $K_I = K_{II} = 1$.

The solution of Model Problem 1 has certain similarities with the solution of Model Problem 2 from the point of view of numerical performance when $\xi = 0$ and $0.5 < \alpha < 1$.

3. THE PERFORMANCE OF THE FINITE ELEMENT METHOD IN ONE DIMENSION WITH RESPECT TO THE ENERGY NORM MEASURE

We now demonstrate how the performance of the various extension processes depends on the mesh and the polynomial degree of elements. The principal mathematical tool is asymptotic analysis which provides information on how the error depends on the number of degress of freedom when only one parameter is being varied, and on certain essential characteristics of the exact solution provided that the number of degrees of freedom is large. We shall consider Model Problem 1 and choose the parameters ξ and α so as to represent problems with solutions of various smoothness ($\xi = 0$, $\alpha > 1/2$) and $\xi > 0$.

3.1. H-Extensions Based on Uniform Mesh Refinement ($\xi = 0$)

In this case $M(\Delta) = \frac{1}{h(\Delta)}$, p is fixed. The number of elements fully characterizes the mesh and the error in energy norm for $\xi = 0$ is estimated as follows:

$$\|e\|_{ER} \cong \frac{C(\alpha)}{M^{\mu} p^{\rho}} \tag{3.1}$$

where the symbol $\cong$ means "asymptotically equal", $C(\alpha)$ is a constant independent of the mesh and the polynomial degree of elements:

$$\mu = \min(\alpha - 1/2, p) \tag{3.2}$$

$$\rho = 2\alpha - 1 \tag{3.3}$$

and the number of degrees of freedom is given by:

$$N = Mp - 1 \tag{3.4}$$

Although (3.1) is an asymptotic estimate, it holds even for reasonably low values of N. In order to demonstrate this, we have computed the value

$$D = \|e\|_{ER} M^{\mu} p^{\rho} \tag{3.5}$$

Here D is called the numerical value of $C(\alpha)$. The results for $\alpha = 0.7$ (and therefore $\mu = 0.2$, $\rho = 0.4$) are shown in Table 1. Here $\|e\|_{ER}$ is shown as "percent relative error". It is seem that (3.1) holds well also when $M(\Delta)$ is small

and the error is large. In view of the fact that ρ is twice the value of μ, for the same number of degrees of freedom the higher order elements perform better.

3.2. h-Extensions Based on Nearly Optimal Mesh Refinement ($\xi = 0$)

We once again consider the case $\xi = 0$. In this case the optimal mesh (for fixed p) is asymptotically:

$$x_j^{\Delta} = \left(\frac{j}{M}\right)^{\beta_0} \tag{3.6}$$

where

$$\beta_0 = \frac{p + 1/2}{\alpha - 1/2} \tag{3.7}$$

The estimate of error measured in energy norm is given by:

$$\|e\|_{ER} \cong C(\alpha) \frac{\sqrt{\beta}}{p^{\alpha}} \left(\frac{\beta}{4M}\right)^{p} \sqrt{\frac{1-M^{-[(2\alpha-1)\beta-2p]}}{(2\alpha-1)\beta-2p}} = \hat{C}\, N^{-p} \tag{3.8a}$$

provided that

$$\beta > \bar{\beta} = \frac{p}{\alpha - 1/2} \tag{3.8b}$$

When $\beta < \bar{\beta}$ then the rate of convergence with respect to M decreases. The reliability of estimate (3.8) for $\beta = \beta_0$ is shown in Tables 2a and 2b.

With reference to Tables 2a and 2b, we note the following observations:

(a) The asymptotic estimate (3.8) is of good quality when $M \geq 2p$. For $M < 2p$ the formula is pessimistic. The reason for this is that (3.8) is based on the assumption that $M \to \infty$. Therefore it cannot be expected to give close estimates for low values of M. In the case $M < 2p$, analysis based on p-extension rather than h-extension should be used.

Table 3 shows the error for optimal distribution of the nodal points for $M = 2$ and $\alpha = 1.1$. It is seen that for small values of p ($p = 1,2$) the asymptotically optimal mesh performs very nearly as well as the optimal mesh.

(b) When α is small (strong stress singularity occurs) the optimal refinement is so strong that roundoff limitations are encountered even when the computations are performed in double precision. Table 4 shows the values of β_0, $\bar{\beta}$, the coordinate of the first nodal point for the optimal mesh, x_1^{Δ} (opt), and for the mesh at which the rate of convergence begins to decrease, x_1^{Δ} (min), for $\alpha = 0.7$, $M = 32$.

(c) Overrefinement is more advantageous than underrefinement. If α is not known precisely, then the refinement should be designed for lower bound estimates of α. Overrefinement increases the value of $\hat{C}$ in (3.8a) but does not alter the rate of convergence (N^{-p}). The penalty, in terms of increased values of C and increased values of N for achieving comparable levels of accuracy, is shown in

Table 5. The mesh refinement is optimal for $\alpha = 0.7$, and the penalty values are shown for $\alpha = 1.1,\ 1.6,\ 2.1$.

It is seen that the penalty for overrefinement is not small. Underrefinement also reduces the rate of convergence. Therefore the penalty for underrefinement is still larger. This shows the importance of correct selection of mesh refinement.

3.3. P-Extensions Based on Uniform Meshes ($\xi = 0$)

In this case $M(\Delta) << p$ and the estimate (3.1) holds. The results of computational experiments are shown in Table 6.

On comparing the results on the basis of the number of degrees of freedom ($N = Mp-1$), it is seen that the best choice is $M = 1$. Comparing Tables 6 and 2a it is evident that h-extensions based on optimal meshes yield better results than p-extensions based on uniform meshes. The performance of p-extensions cannot be improved substantially through optimizing the p-distribution. Table 7 shows the effect of optimal p-distributions for $M = 2$ and $\alpha = 0.7$ and 1.1.

3.4. H-p Extensions ($\xi = 0$)

In this case the meshes and p distributions are optimized concurrently. The asymptotically optimal mesh is characterized by the following geometric progression of nodal points:

$$x_j^{\Delta} = \kappa_0^{M(\Delta)-j} \qquad j = 1,2,\ldots,M(\Delta) \tag{3.9}$$

where

$$\kappa_0 = \left(\sqrt{2} - 1\right)^2. \tag{3.10}$$

The polynomial degrees of elements are assigned as follows:

$$p_j = [s(\alpha)j] \tag{3.11}$$

where

$$s(\alpha) = 2(\alpha - 1/2) \tag{3.12}$$

and $[\cdot]$ means the integral part.

The error estimate is:

$$\|e\|_{ER} = C(\alpha)\left[\left(\sqrt{2} + 1\right)^2\right]^{-\sqrt{(\alpha - 1/2)N}}$$

$$= C(\alpha)e^{-\gamma_0\sqrt{(\alpha - 1/2)N}}, \qquad \gamma_0 = 1.574 \tag{3.13}$$

The numerical performance of h-p extensions is illustrated in Table 8. On comparing the results with those in Table 2a, it is seen that the rate of convergence of the h-p extension is much greater than the rate of convergence of the h-extension based on asymptotically optimal meshes.

3.5. The h-p Extension with Uniform p and Optimal Mesh ($\xi = 0$)

The mesh is the same as in Section 3.4, i.e., with the nodal points defined by (3.9), (3.10), and we assume that the p-distribution is uniform. In this case the estimate for $\frac{1}{2} < \alpha < 1$ is

$$\|e\|_{ER} = C(\alpha) \frac{1}{p^{2\alpha-1}} e^{\frac{-\gamma_0}{\sqrt{2}}\sqrt{(\alpha-1/2)N}} \tag{3.14}$$

where, as in (3.13), $\gamma_0 = 1.574$ and

$$p = [s(\alpha)]M(\Delta) \tag{3.15}$$

$$s(\alpha) = 2(\alpha - 1/2) \tag{3.16}$$

The numerical performance of the h-p extension with uniform p is shown in Table 9. On comparing Table 9 with Table 8, it is seen that the performance of the h-p extension with uniform p is not substantially different from that of the h-p extension with optimal p-distribution. The performance can be analyzed also for p-distributions other than that given in (3.15). When p increases more rapidly than (3.15), then the rate of convergence diminishes until it reaches the algebraic rate characteristic of p-extensions. When p increases less than (3.15), then the rate of convergence diminishes because $h(\Delta)$ does not change.

3.6. H-Extensions that Utilize Feedback ($\xi = 0$)

In Section 3.2 it was pointed out that the quality of performance of h-extensions depends on the mesh design. Proper mesh design depends on the exact solution which generally is not known. It is possible to devise feedback procedures, however, that construct meshes which asymptotically perform as well as the optimal meshes. Such feedback procedures are called adaptive (refs. 5 to 8).

Tables 10a and 10b show the results of numerical experiments. The numerical value D is based on a formula for optimal meshes that utilize only nodal points which can be constructed by successive bisection of elements, not all meshes, as considered before, because the feedback procedure uses only such meshes.

3.7. H-p Extensions that Utilize Feedback

It is possible to devise feedback procedures that perform nearly as well as the optimal h-p extension. Results obtained with such a procedure are shown in Table

11 ($\alpha = 0.7$). The meshes were generated by bisection; therefore, D is based on an estimate developed for such meshes only.

3.8. p-Extension Based on Properly Designed Meshes and Feedback ($\xi = 0$)

In this case the mesh is strongly graded toward singular points, on the basis of (3.9), with $\kappa_0 = (\sqrt{2} - 1)^2 = 0.1715$ or slightly smaller (say, $\kappa_0 = 0.15$) and $M(\Delta)$ is fixed. The polynomial degree of elements is uniformly increased. The error decreases first exponentially and then, if p is too large, algebraically, as explained in Section 3.5. Feedback is utilized to ensure (through proper selection of $M(\Delta)$) that the desired accuracy is reached in the range where the convergence is exponential.

3.9. Smooth Solutions ($\xi > 0$)

We have considered various extension processes when the solution has singular character. When the solution is smooth, then p-extensions perform especially well for small M. The error estimates for $\xi > 0$ in (2.3) are as follows:

(a) for $\xi = 0$

$$\|e\|_{ER} = \frac{C(\alpha)}{p^{2\alpha-1}} \tag{3.17}$$

(b) for $\xi > 0$

$$\|e\|_{E} = C(\alpha)\left(\frac{1-q^2}{2q}\right)\frac{q^p}{p^\alpha} \tag{3.18}$$

where

$$q = \frac{\sqrt{1+\xi} - \sqrt{\xi}}{\sqrt{1+\xi} + \sqrt{\xi}} \tag{3.19}$$

In Table 12 results are presented for $\alpha = 0.7$ and $\xi = 0$, $\xi = 0.01$, and $\xi = 0.1$. These results demonstrate that the performance of p-extensions very rapidly improves with increasing smoothness of the solution.

4. ACCURACY OF STRESS APPROXIMATIONS IN ONE DIMENSION

In one dimension the stress is simply $u'(x_0)$. In contrast to the two dimensional case, the behavior of the finite element solution in our example is entirely local; therefore, we need to consider only the case with one element. The results of numerical experiments for $\alpha = 0.7$ and various ξ values are shown in Table 13. It is seen that the element that contains the singularity ($\xi = 0$) yields very poor stress approximations.

When quantities other than the energy are of interest (for example, stresses), then the mesh and p-distribution should be optimal or nearly optimal with respect to

the purpose of computation. Optimal meshes and p-distributions depend not only on the purpose of computation but also on the method used for computing the quantities of interest. See, for example, references 6 and 9.

5. PERFORMANCE OF THE FINITE ELEMENT METHOD IN TWO DIMENSIONS WITH RESPECT TO THE ENERGY NORM

The theory of two dimensional problems presents more difficulties and is therefore less well understood than the theory of one dimensional problems. Nevertheless there are important similarities which make it possible to gain valuable insight from the analysis of one dimensional problems. There are important differences also; for example, errors in stresses in two dimensions behave quite differently from the errors in stresses in one dimension. Stress computations are discussed in the next section. Here we discuss the properties of various versions and present numerical results for our two dimensional model problem. The results were obtained by means of the h-version program FEARS with feedback capabilities (ref. 10) and the p-version program FIESTA-2D (ref. 11). FEARS has elements of polynomial degree 1 only. The polynomial degree of elements in FIESTA-2D ranges from 1 to 8.

5.1. H-Extension Based on Uniform Meshes

The estimate for our model problem, defined in Section 2.2, is:

$$\|e\|_{ER} = C(p)N^{-1/4} \tag{5.1}$$

Detailed theoretical analysis, comparable to the one dimensional case, is not available. The results of computations are shown in Table 14, where D represents the numerical value of C(p). The results indicate that the asymptotic estimate (5.1) is of good quality.

5.2. H-Extension with Feedback

As in the one dimensional case, the sequence of optimally designed meshes leads to a rate of convergence independent of the singularity. The estimate for optimally designed meshes is:

$$\|e\|_{ER} = C(p)N^{-p/2} \tag{5.2}$$

Note that the exponent of N is p/2, not p as in the one dimensional case.

H-extension with properly utilized feedback (adaptive approach) should lead to the same asymptotic rate of convergence as the optimally designed sequence of meshes. Table 15 shows the results obtained with FEARS.

5.3. P-Extension on Uniform Mesh

In this case the estimate is (refs. 1 and 2):

$$\|e\|_{ER} = C(\varepsilon)N^{-1/2+\varepsilon} \tag{5.3}$$

where $\varepsilon > 0$ arbitrarily. It is not known whether the term ε can be removed.

Table 16 shows the results obtained with FIESTA-2D using four square elements.

5.4 H-p Extension

The estimate for h-p extensions based optimal mesh and on either optimally or uniformly distributed p is

$$\|e\|_{ER} \leq C\, e^{-\gamma\sqrt[3]{N}}, \qquad \gamma > 0 \tag{5.4}$$

In the two dimensional case the optimal value of γ is not known nor is it known whether the term $\sqrt[3]{N}$ can be improved. The value of γ depends on the distribution of p.

5.5. p-Extension Based on Properly Designed Mesh and Feedback Information

As in the one dimensional case, the p-extension performs in much the same way as the h-p extension when p in not too large and the mesh is properly designed. For large p the p-version performs as if the mesh were uniform. An example is presented in Table 17. The fact that the rate of convergence slows for high p is an indication that the mesh should be refined. Slowing of the rate of convergence can be detected. This is the feedback information needed for increasing the number of finite elements.

5.6. Smooth Solutions

When the solution is smooth, the p-version is very effective and, as in the one dimensional case, the convergence is exponential.

6. STRESS COMPUTATIONS IN TWO DIMENSIONS

Stress approximations behave quite differently in two dimensions than in one dimension. In one dimension in our example the error depended only on the behavior of the solution in the particular element in question, i.e., the error was completely localized. In two dimensions on the other hand, the error is comprised of two parts: the local error and the error associated with all other elements. This second part is called pollution error.

The error in stresses depends to a large extent on how the stresses are computed. Indirect techniques are available which substantially reduce both the local and pollution error, as compared with the conventional (direct) methods of stress computations (refs. 6, 9, and 12).

6.1. Performance of h-Extensions Based on Nearly Optimal Meshes

Let us examine the stresses at point $x_1 = x_2 = 0.25$ in the model problem. Solutions were obtained by means of the computer program FEARS. The point under consideration is the vertex of four elements. Therefore, four different values can be computed, using the derivatives of the four elements and the appropriate stress-strain low. The relative errors are shown in Table 18 for the three stress components σ_{11}, σ_{22}, σ_{12} for the four adjacent elements. The error of the average value (A) is also shown. It is seen that the error of the average value is smaller than the error in most elements. This is a well known fact which is generally utilized in stress computations.

The relative error in the same stress components computed by means of an indirect (postprocessing) technique (ref. 9) is shown in Table 19.

The improvement is very substantial. The postprocessing technique yields stress values which are not sensitive to the meshes and the error is of the magnitude $\|e\|^2_{ER}$.

6.2. Performance of the p-Version

When the solution is smooth, the p-version performs well. When the solution is not smooth and the elements are large, then the pollution error is generally large. Satisfactory theoretical analysis is not available. It is known, however, that the pollution error can be reduced very substantially by surrounding points of stress singularity with one or more layers of elements.

The relative errors at point $x_1 = 0.1$, $x_2 = 0.2$ (which is located at element boundaries) are shown in Tables 20a and 20b. The results presented in Table 20a are strongly affected by pollution because the vertex of the neighboring element was on the singular point. The results presented in Table 20b are much less affected by pollution because an extra layer of elements was added so that the neighboring element no longer had a vertex on the singular point. The local error is, of course, the same in both cases. Tables 20a and 20b illustrate the importance of proper mesh design when the stresses are computed from the finite element solution directly. The postprocessing method removes sensitivity to mesh design.

REFERENCES

1. Babuška, I.; Szabo, B.; Katz, N.: The p-Version of the Finite Element Method. SIAM J. Numer. Anal. 18, pp. 515-545, 1981.

2. Babuska, I.; and Szabo, B.: On the Rate of Convergence of the Finite Element Method. Internat. J. Numer. Methods Engrg. 18, 1982, pp. 323-341.

3. Dorr, M. R.: The Approximation Theory for the p-Version of the Finite Element Method I, II. SIAM J. Numer. Anal., Submitted, 1984.

4. Babuška, I.; and Dorr, M. R.: Error Estimates for the Combined h and p Versions of the Finite Element Method. Numer. Math. 37, 1981, pp. 257-.

5. Babuška, I.; Vogelius, M.: Feedback and Adaptive Finite Element Solution of One-Dimensional Boundary Value Problem. Numer. Math. 44, 1984, 75-102.

6. Babuška, I.; Miller, A.; and Vogelius, M.: Adaptive Methods and Error Estimation for Elliptic Problems of Structural Mechanics. Adaptive Computational Methods for Partial Differential Equations. Eds. I. Babuška, J. Chandra, and J. E. Flaherty. SIAM, 1983, pp. 57-73.

7. Babuška, I.; and Rheinboldt, W. C.: Adaptive Finite Element Processes in Structural Mechanics. Elliptic Problem Solvers II. Eds. G. Birkhoff and A. Schoenstadt. Academic Press, 1983, pp. 345-378.

8. Rheinboldt, W. C.: Feedback Systems and Adaptivity for Numerical Computations, Adaptive Computational Methods for Partial Differential Equations. Eds. I. Babuška, J. Chandra, J. E. Flaherty. SIAM, 1983, pp. 3-19.

9. Babuška, I.; Miller, A,: The Post-Processing Approach in Finite Element Method. Part I. Calculation of Displacements Stresses and Other Higher Derivatives of the Displacements. Part II. The Caculation of Stress Intensity Factors. Part III. A-Posteriori Error Estimates and Adaptive Mesh Selection. Internat. J. Numer. Methods Engrg., in press, 1984.

10. Mesztenyi, C.; and Sztmczak, W.: FEARS User's Manual for UNIVAC 1100. University of Maryland Oct. 1982. (Avail. from NTIS as AD-A125047 bN-991.)

11. Szabo, B. A.; and Myers, K. W.: FIESTA-2D: User's Manual for Release 1.1, Washington University Technology Associates, St. Louis, 1984.

12. Izadpanah, K.: Computation of Stress Components in the P-Version of the Finite Element Method. Ph.D. Dissertation, Washington University, St. Louis, 1984.

TABLE 1.- H-EXTENSION WITH UNIFORM MESH REFINEMENT, $\alpha = .7$

M	p = 1		p = 2		p = 3		p = 4	
	$\|e\|_{ER}^{\%}$	D	$\|e\|_{ER}^{\%}$	D	$\|e\|_{ER}^{\%}$	D	$\|e\|_{ER}^{\%}$	D
2	87.31	1.00	66.57	1.01	56.70	1.01	50.58	1.01
4	76.11	1.00	57.96	1.01	49.37	1.01	44.03	1.01
8	66.26	1.00	50.44	1.01	42.98	1.01	38.33	1.01
16	57.70	1.00	43.91	1.01	37.40	1.01	33.36	1.01
32	50.23	1.00	38.24	1.01	32.57	1.00	29.05	1.01
64	43.72	1.00	33.29	1.01	28.35	1.00	25.29	1.01
128	38.08	1.00	28.98	1.00	24.68	1.01	22.01	1.01
256	33.13	1.01	25.22	1.01	21.48	1.00	19.16	1.01

TABLE 2a.- H-EXTENSION WITH ASYMPTOTICALLY OPTIMAL MESH, $\alpha = 0.7$

M	p = 1 (β = 7.50)		p = 2 (β = 12.50)	
	$\|e\|_{ER}^{\%}$	D	$\|e\|_{ER}^{\%}$	D
2	80.71	.314	70.65	.133
4	57.59	.402	39.94	.300
8	29.14	.454	14.77	.445
16	15.46	.482	4.365	.526
32	7.966	.496	1.168	.562

TABLE 2b.- H-EXTENSION WITH ASYMPTOTICALLY OPTIMAL MESH, $\alpha = 1.1$

M	p = 1 (β =2.50)		p = 2 (β=3.17)		p = 3 (β=5.83)		p = 4 (β=7.50)	
	$\|e\|_{ER}^{\%}$	D	$\|e\|_{ER}^{\%}$	D	$\|e\|_{ER}^{\%}$	D	$\|e\|_{ER}^{\%}$	D
2	58.91	1.19	21.99	.851	15.10	.540	12.66	.275
4	31.88	1.29	7.128	1.20	3.162	.905	1.982	.688
8	16.55	1.34	2.042	1.23	.4953	1.13	.1812	1.01
16	8.434	1.37	.5387	1.33	.688(-1)	1.26	.134(-1)	1.19
32	4.257	1.41	.1361	1.34	.904(-1)	1.32	.908(-3)	1.29
64	2.138	1.39	.345(-1)	1.36	.115(-2)	1.35	.586(-4)	1.33
128	1.071	1.38	.868(-2)	1.38	.146(-3)	1.38	.376(-5)	1.37
256	.5364	1.38	.217(-2)	1.38	.184(-4)	1.38	.240(-6)	1.38

TABLE 3.- PERFORMANCE OF AN OPTIMAL MESH (M = 2, α = 1.1)

p = 1	p = 2	p = 3	p = 4
$\|e\|_{ER}^{\%}$	$\|e\|_{ER}^{\%}$	$\|e\|_{ER}^{\%}$	$\|e\|_{ER}^{\%}$
57.42	17.31	8.213	4.762

TABLE 4.- MESH PARAMETERS (α = 0.7)

p	β_0	$\bar{\beta}$	x_1^{Δ}(opt)	x_1^{Δ}(min)
1	7.5	5	5.14(-12)	2.99(-8)
2	12.50	10	1.53(-19)	8.38(-16)
3	17.50	15	4.56(-27)	2.64(-23)
4	22.50	20	1.36(-36)	7.8 (-31)
5	27.50	25	4.05(-42)	2.35(-38)

TABLE 5.- PENALTY FOR USING OVERREFINED MESH IN TERMS OF INCREASED VALUES OF C (FIRST ROW) AND N (SECOND ROW)

p \ α	.7	1.1	1.6	2.1
1	1.00 1.00	1.97 1.97	3.40 3.40	4.81 4.81
2	1.00 1.00	4.69 2.17	14.73 3.84	29.97 5.47
3	1.00 1.00	12.08 2.29	69.09 4.19	292.90 5.88
4	1.00 1.00	32.19 2.30	337.15 4.29	1430.90 6.15

TABLE 6.- P-EXTENSIONS ON UNIFORM MESHES (α = .7)

p	M = 1		M = 2		M = 3		M = 4	
	$\|e\|_{ER}$%	D	$\|e\|_{ER}$%	D	$\|e\|_{ER}$%	D	$\|e\|_{ER}$%	D
1			87.31	1.00	80.59	1.00	76.11	1.00
2	76.47	1.01	66.57	1.01	61.39	1.01	57.96	1.01
3	65.14	1.01	56.70	1.01	52.29	1.01	49.37	1.01
4	58.10	1.01	50.58	1.01	46.64	1.01	44.03	1.01
5	53.15	1.01	46.27	1.01	42.67	1.01	40.27	1.01
6	49.42	1.01	43.02	1.01	39.66	1.01	37.45	1.01
7	46.48	1.01	40.46	1.01	37.31	1.01	35.21	1.01
8	44.05	1.01	38.36	1.01	35.37	1.01	33.39	1.01
9	42.02	1.01	36.58	1.01	33.74	1.01	31.85	1.01
10	40.29	1.01	35.09	1.01	32.34	1.01	30.54	1.01
11	38.80	1.01	33.76	1.01	31.15	1.01	29.40	1.01

TABLE 7.- PERFORMANCE OF p-EXTENSION BASED ON OPTIMAL p-DISTRIBUTION AND UNIFORM MESH (M = 2)

α	p_1	p_2	$\|e\|_{ER}$%
.7	41	1	5.05
1.1	3	1	23.79
1.1	26	2	1.834

TABLE 8.- PERFORMANCE OF h-p EXTENSION (α= 0.7, s = 0.4), ASYMPTOTICALLY OPTIMAL MESH AND p-DISTRIBUTION

M	N	$\|e\|_{ER}$%	D	M	N	$\|e\|_{ER}$%	D
2	3	54.18	2.62	8	21	7.031	2.82
3	5	38.68	2.66	9	25	4.998	2.77
4	7	28.02	2.61	10	30	3.523	2.82
5	10	19.82	2.70	11	35	2.492	2.80
6	13	14.10	2.69	12	41	1.754	2.89
7	17	9.942	2.82	20	100	.1071	2.94

C-2

TABLE 9.- PERFORMANCE OF THE h-p EXTENSION, ASYMPTOTICALLY OPTIMAL MESH AND UNIFORM p (α= .7)

M	N	p	$\|e\|_{ER}$%	D
2	1	1	74.36	1.50
3	5	2	38.68	1.70
4	7	2	28.02	1.50
5	14	3	16.17	1.57
8	31	4	5.037	1.46
10	49	5	2.262	1.43
15	104	7	.3376	1.25

TABLE 10a.- H-EXTENSION UTILIZING FEEDBACK, α = 0.7

p = 1			p = 2		
N	$\|e\|_{ER}$%	D	N	$\|e\|_{ER}$%	D
4	58.54	.570	9	43.93	.516
9	31.66	.617	19	22.01	1.03
20	14.48	.592	29	11.09	1.17
39	7.326	.571	39	5.719	1.07
85	3.327	.557	81	1.121	.886
101	2.788	.553	101	.3689	.802

TABLE 10b.- H-EXTENSION UTILIZING FEEDBACK, α = 1.1

p = 1			p = 2			p = 3		
N	$\|e\|_{ER}$%	D	N	$\|e\|_{ER}$%	D	N	$\|e\|_{ER}$%	D
4	28.21	1.44	9	8.295	2.01	14	4.979	2.78
11	12.06	1.46	21	1.567	1.83	29	.6506	2.91
19	7.255	1.46	41	.4123	1.76	44	.1736	2.62
28	5.011	1.47	51	.2710	1.77	62	.05706	2.36
37	3.837	1.47	79	.1111	1.72	77	.02979	2.34
63	2.266	1.45	99	.07155	1.73	95	.01617	2.37
137	1.052	1.46	125	.04411	1.69	137	.005006	2.17
255	.5673	1.46	251	.01093	1.68	227	.001095	2.15

TABLE 11.- H-p EXTENSION UTILIZING FEEDBACK, $\alpha = 0.7$

N	$\|e\|_{ER}\%$	D
4	58.54	2.795
9	31.66	2.88
25	10.47	3.69
39	4.235	3.52
60	1.548	3.64
120	.2933	3.51

TABLE 12.- PERFORMANCE OF THE p-EXTENSION WITH $M = 1$, $\alpha = 0.7$ and $\xi = 0, 0.1, 0.1$

	$\xi = 0$		$\xi = .01$		$\xi = .1$	
p	$\|e\|_{ER}\%$	D	$\|e\|_{ER}\%$	D	$\|e\|_{ER}\%$	D
2	76.47	1.01	57.75	.391	36.61	.443
3	65.14	1.01	37.90	.416	15.42	.462
4	58.10	1.01	26.37	.432	6.922	.473
5	53.15	1.01	18.57	.443	3.224	.481
6	49.42	1.01	13.91	.451	1.541	.486
7	46.47	1.01	10.38	.458	.7578	.490
8	44.05	1.01	7.831	.463	.3677	.494
9	42.01	1.01	5.961	.468	.1825	.495
10	40.29	1.01	4.571	.471	.09136	.496
11	38.80	1.01	3.525	.475	.04603	.498

TABLE 13.- ERROR IN STRESSES IN DEPENDENCE ON POLYNOMIAL DEGREE AND SMOOTHNESS

ξ	x_0 \ p	2	3	4	5	6	7	8	9	10	11	EXACT
0	0	/	/	/	/	/	/	/	/	/	/	∞
	.25	.2910	.2151	- .0159	-.1538	-.1143	.0186	.1052	.0780	.0165	-.0803	.0871
	.50	.1974	- .1060	- .1060	-.0728	-.0728	-.0554	-.0557	.0452	.0452	-.0382	-.1974
	.75	- .0397	- .1156	- .1155	-.0223	-.0618	.0710	-.0156	-.0427	.0518	-.0120	-.3384
	1.0	- .3277	.2792	- .2490	.2278	-.2118	.1992	-.1888	.1801	-.1727	.1663	-.4286
.01	0	-1.960	-1.519	-1.193	-.9440	-.7511	-.5999	-.4805	-.3858	-.3103	-.2500	.2599
	.25	.2036	.1485	.0057	-.0661	-.0488	.0001	.0267	.0198	-.0005	-.0118	.1163
	.50	.1578	- .0625	- .0625	-.0307	-.0307	-.0165	-.0165	.0094	.0094	.0055	-.1578
	.75	- .0240	- .0791	- 0.636	-.0083	-.0256	.0232	-.0034	-.0104	.0098	-.0015	-.2959
	1.0	- .2551	.1857	- .1404	.1083	-.0846	.0666	-.0528	.0419	-.0335	.0268	-.3827
.1	0	- .3641	- .1809	- .0922	-.0476	-.0246	-.0129	-.0067	-.0035	-.0019	-.0010	.7532
	.25	- .0678	- .0452	.0064	-.0065	-.0044	-.0006	.0007	.0005	.0001	.0001	.1281
	.50	- .0765	- .0138	.0138	-.0030	-.0030	-.0007	-.0007	.0002	.0002	.0000	-.0765
	.75	- .0037	- .0263	.0125	-.0005	-.0025	.0013	-.0001	-.0003	.0002	.0000	-.1921
	1.0	- .1215	.0590	- .0296	.0151	-.0078	.0040	-.0021	.0011	-.0006	.0003	-.2703

TABLE 14.- H-EXTENSION BASED ON UNIFORM MESHES (p = 1)

N	$\|e\|_{ER}$%	D
51	36.02	.96
167	27.07	.97
591	19.81	.97

TABLE 15.- H-EXTENSION WITH FEEDBACK (p = 1)

N	$\|e\|_{ER}$%	D
67	32.91	2.03
101	26.38	2.66
143	21.35	2.56
221	16.79	2.50
301	13.61	2.36
617	9.63	2.40

TABLE 16.- PERFORMANCE OF THE p-EXTENSION (UNIFORM MESH, 4 ELEMENTS)

p	$\|e\|_{ER}$%	D
1	32.61	2.01
2	18.35	1.82
3	15.89	1.99
4	13.24	2.06
5	11.06	2.06
6	9.47	2.07
7	8.27	2.08
8	7.37	2.08

TABLE 17.- P-EXTENSION BASED ON PROPERLY DESIGNED MESH

p	$\|e\|_{ER}\%$
1	31.96
2	12.36
3	6.197
4	3.277
5	2.131
6	1.436
7	1.128
8	.8839

TABLE 18.- RELATIVE ERROR IN STRESS COMPONENTS AT POINT (0.25, 0.25) DIRECT COMPUTATION

N		$e_{11}^R\%$	$e_{22}^R\%$	$e_{12}^R\%$
221	A	10.99	7.57	11.16
	1	4.79	2.32	35.86
	2	12.21	2.01	.093
	3	17.27	17.42	106.43
	4	9.71	13.01	71.49
617	A	4.09	5.47	13.42
	1	1.46	2.68	22.96
	2	4.41	.099	55.69
	3	4.41	13.43	3.88
	4	6.07	11.74	28.85

TABLE 19.- RELATIVE ERROR IN THE STRESS COMPONENTS AT POINT (0.25, 0.25) INDIRECT COMPUTATION

N	$e_{11}^R\%$	$e_{22}^R\%$	$e_{12}^R\%$
221	1.69	2.63	1.94
617	.56	.866	.81

TABLE 20a.- RELATIVE ERROR IN STRESSES. A VERTEX OF THE ADJACENT ELEMENT LIES ON THE CRACK TIP

p	$e_{11}^{R}\%$	$e_{22}^{R}\%$	$e_{12}^{R}\%$
1	7.903	34.17	18.18
2	6.222	14.09	11.20
3	1.014	10.53	3.254
4	5.249	9.652	4.844
5	2.864	5.411	.1114
6	.6259	3.848	.8387
7	.6893	3.119	.9926
8	1.438	2.233	1.316

TABLE 20b.- RELATIVE ERROR IN STRESSES. THE ADJACENT ELEMENT IS SEPARATED FROM THE CRACK TIP BY ONE LAYER OF ELEMENTS

p	$e_{11}^{R}\%$	$e_{22}^{R}\%$	$e_{12}^{R}\%$
1	13.57	33.108	17.39
2	2.124	6.976	.6688
3	1.091	3.843	3.620
4	.9997	1.923	1.852
5	.2653	.7836	.7166
6	.1702	.3928	.3503
7	.0784	.2123	.1529
8	.04005	.1256	.07431

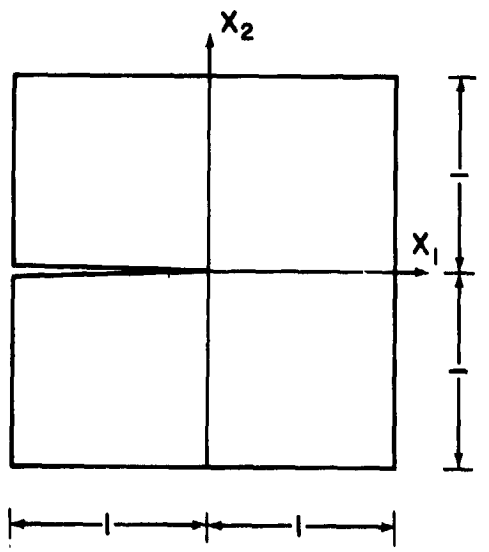

Figure 1. Scheme of the cracked panel.

AUGMENTED WEAK FORMS AND ELEMENT-BY-ELEMENT PRECONDITIONERS: EFFICIENT ITERATIVE STRATEGIES FOR STRUCTURAL FINITE ELEMENTS - A PRELIMINARY STUDY†

Arthur Muller
Graduate Research Assistant, Stanford University

Thomas J. R. Hughes
Professor of Mechanical Engineering, Stanford University

SUMMARY

This paper presents a weak formulation in structural analysis that provides well-conditioned matrices suitable for iterative solutions. A mixed formulation ensures the proper representation of the problem and, for the sake of good conditioning, the constitutive relations are added in a penalized form. The problem is then solved by means of a double conjugate gradient algorithm combined with an element-by-element approximate factorization procedure.

The double conjugate gradient strategy resembles Uzawa's variable-length type algorithms (ref. 1), the main difference being the presence of quadratic terms in the mixed variables. In the case of shear-deformable beams these terms ensure that the proper finite thickness solution is obtained.

INTRODUCTION

Element-by-element approximate factorizations have been successfully employed as a preconditioner for various problems (ref. 2 and 3). In the structural field, however, little progress has been made heretofore, mainly due to the highly ill-conditioned matrices resulting from finite element discretizations. The presence of deformation modes whose stiffnesses are orders of magnitude apart -- bending and shear are a good example -- requires an excessive number of iterations. The need to present the preconditioned conjugate gradient driver with a "better" problem was evident. For the thin limits, Uzawa's algorithm (ref. 1) appears to be an excellent approach. However, when

† Work supported by NASA Lewis Research Center under Grant No. NAG 3-319

dealing with Timoshenko beams where the solution accounts for shear deformation as well as bending, Uzawa's algorithm is no longer applicable.

Just as in Uzawa's algorithm, a "mixed" formulation is presented, and the problem is then solved for the mixed variables. At the same time, the displacements are updated and convergence in the mixed variables can be checked as the algorithm progresses. A conjugate gradient accelerated version of Uzawa's algorithm is used.

CONJUGATE GRADIENT(CG) METHODS

The CG method is an iterative procedure used to solve the system of linear equations $\mathbf{Ax} = \mathbf{b}$ resulting from the finite element discretization of the problem under consideration. In its preconditioned version, the method can be best summarized by the flowchart that follows.

Step 1. Initialization:

$$m = 0 \tag{1}$$

$$\mathbf{x}_0 = 0 \tag{2}$$

$$\mathbf{r}_0 = \mathbf{b} \tag{3}$$

$$\mathbf{p}_0 = \mathbf{z}_0 = \mathbf{B}^{-1}\mathbf{r}_0 \tag{4}$$

Step 2. Update of Solution and Residual:

$$\alpha_m = \frac{\mathbf{r}_m \cdot \mathbf{z}_m}{\mathbf{p}_m \cdot \mathbf{A}\mathbf{p}_m} \tag{5}$$

$$\mathbf{x}_{m+1} = \mathbf{x}_m + \alpha_m \mathbf{p}_m \tag{6}$$

$$\mathbf{r}_{m+1} = \mathbf{r}_m - \alpha_m \mathbf{A}\mathbf{p}_m \tag{7}$$

Step 3. Convergence check:

$$\text{If } \|\mathbf{r}_{m+1}\| < \delta\|\mathbf{r}_0\| \text{ , return.} \tag{8}$$

Step 4. Update conjugate direction:

$$\mathbf{z}_{m+1} = \mathbf{B}^{-1}\mathbf{r}_{m+1} \tag{9}$$

$$\beta_m = \frac{\mathbf{r}_{m+1} \cdot \mathbf{z}_{m+1}}{\mathbf{r}_m \cdot \mathbf{z}_m} \tag{10}$$

$$\mathbf{p}_{m+1} = \mathbf{z}_{m+1} + \beta_m \mathbf{p}_m \tag{11}$$

$$m = m + 1 \tag{12}$$

Go to Step 2 (13)

In the above, a dot between two vectors indicates the dot product, $\|\cdot\|$ is the usual Euclidean norm, and δ is a pre-specificed tolerance. In the basic CG algorithm, $\mathbf{B}$ is replaced by the identity and consequently $\mathbf{z}_m = \mathbf{r}_m$.

As will be seen below, we will simultaneously employ two conjugate gradient drivers. While the outer loop is concerned with the mixed variables, the inner loop involves a standard finite element solution. Preconditioning will only be applied to the inner loop, where an element-by-element preconditioner will be used.

A Crout approximate factorization is preferred for the preconditioner; its expression is specified below and a more thorough discussion can be found in reference 2. We have

$$\mathbf{B} = \mathbf{W}^{1/2} \times \prod_{e=1}^{N_{el}} L_p\left[\overline{\mathbf{A}}^e\right] \times \prod_{e=1}^{N_{el}} D_p\left[\overline{\mathbf{A}}^e\right] \times \prod_{e=N_{el}}^{1} U_p\left[\overline{\mathbf{A}}^e\right] \times \mathbf{W}^{1/2} \tag{14}$$

where

$$\overline{\mathbf{A}}^e = \mathbf{I} + \mathbf{W}^{-1/2}[\mathbf{A}^e - \mathbf{W}^e]\mathbf{W}^{-1/2} \tag{15}$$

$$\mathbf{W} = diag(\mathbf{A}), \tag{16}$$

$$\mathbf{W}^e = diag(\mathbf{A}^e), \tag{17}$$

and $\mathbf{A}^e$ is the e^{th} element matrix, $\mathbf{I}$ is the identity matrix and $L_p[\cdot]$, $D_p[\cdot]$ and $U_p[\cdot]$ are the lower, diagonal and upper factors in the Crout factorization.

AUGMENTED WEAK FORMS

Weak formulations of boundary value problems have been used as the main tool in deriving finite element methods for quite a long time. Most formulations used so far in structural analysis may be derived from the Hu-Washizu principle (ref. 4), either in its most general form or, as is more common, in a displacement variational form. In its general form, the weak formulations are widely known as mixed formulations, since stresses and/or strains are primary variables along with displacements. However, in these cases, the resulting matrix is indefinite and iterative drivers such as conjugate gradients cannot be directly applied.

The displacement formulation, on the other hand, results in a positive-definite matrix. However, for thin beams and plates the condition number is very large and even with sophisticated preconditioning the number of iterations for convergence is excessive.

Uzawa's algorithm for constrained minimization presents the iterative driver with a series of well conditioned problems, the solution of each being done in a relatively small number of iterations. The basic idea behind the algorithm is the introduction of Lagrange multipliers and penalization terms. Satisfaction of the constraints is then guaranteed even with a small penalty parameter due to the presence of the Lagrange multipliers. An iterative scheme is then devised to update the multipliers. Given the multipliers, the solution is also updated and the process is repeated until convergence.

We consider the strong form of a boundary value problem for the Timoshenko beam: Given the vertical force $f : [0, L] \to \mathcal{R}$, and the distributed moment $c : [0, L] \to \mathcal{R}$, find the vertical displacement w, the rotation θ, the moment M and the shear force q satisfying

$$\left.\begin{aligned} M_{,x} - q + c &= 0 \\ q_{,x} + f &= 0 \end{aligned}\right\} \text{(equilibrium)} \tag{18}$$

$$\left.\begin{aligned} M &= -\left(Et^3/12\right)\theta_{,x} \\ q &= Gt(w_{,x} - \theta) \end{aligned}\right\} \text{(constitution)} \tag{19}$$

where E, G and t stand for the Young's modulus, shear modulus and thickness, respectively, subject to the following boundary conditions

$$M(0) = M_0 \tag{20}$$

$$w(0) = w_0 \tag{21}$$

$$\theta(L) = \theta_L \tag{22}$$

$$q(L) = q_L \tag{23}$$

Although particularized, the boundary conditions for the above problem possess the main ingredients that make them easily extendable to more general situations.

For the construction of the augmented weak form, we introduce the spaces

$$S_w = \{ w \in H^1[0,L] | w(0) = w_0 \} \tag{24}$$

$$S_\theta = \{ \theta \in H^1[0,L] | \theta(L) = \theta_L \} \tag{25}$$

$$\mathcal{V}_w = \{ w \in H^1[0,L] | w(0) = 0 \} \tag{26}$$

$$\mathcal{V}_\theta = \{ \theta \in H^1[0,L] | \theta(L) = 0 \} \tag{27}$$

$$\mathcal{V}_q = H^0[0,L] \tag{28}$$

where $H^0[0,L]$ is the set of square integrable functions defined over $[0,L]$ and $H^1[0,L] = \left\{ f \in H^0 | f_{,x} \in H^0 \right\}$.

Let $w \in S_w$, $\bar{w} \in \mathcal{V}_w$, $\theta \in S_\theta$, $\bar{\theta} \in \mathcal{V}_\theta$ and $q, \bar{q} \in \mathcal{V}_q$. Assume that the moment constitutive equation holds. Then, the following weak form is equivalent to the equilibrium equations, shear constitutive equation, and moment and shear boundary conditions:

$$0 = \int_0^L \left[\frac{Et^3}{12}\bar{\theta}_{,x}\theta_{,x} + \epsilon_s Gt\left(\overline{w}_{,x} - \bar{\theta}\right)\left(w_{,x} - \theta\right)\right]dx +$$

$$+ \int_0^L (1-\epsilon_s)\left[\overline{q}(w_x - \theta) + q\left(\overline{w}_{,x} - \bar{\vartheta}\right)\right]dx - \int_0^L (1-\epsilon_s)\frac{\overline{q}q}{Gt}dx +$$

$$+ \int_0^L \left(\bar{\theta}c - \overline{w}f\right)dx - \overline{w}(L)q_L - \bar{\theta}(0)M_0$$

$$= \int_0^L \left[\bar{\theta}(M_{,x} - q + c) - \overline{w}(q_{,x} + f)\right]dx + \int_0^L \overline{q}\left(w_{,x} - \theta - \frac{q}{Gt}\right)dx +$$

$$+ \int_0^L \epsilon_s Gt\left(\overline{w}_{,x} - \bar{\theta} - \frac{\overline{q}}{Gt}\right)\left(w_{,x} - \vartheta - \frac{q}{Gt}\right)dx +$$

$$+ \bar{\theta}(0)[M(0) - M_0] + \overline{w}(L)[q(L) - q_L] \qquad (29)$$

The second line follows after an integration-by-parts and use of the moment constitutive relation. The non-dimensional scalar ϵ_s is introduced in order to ensure that a certain sub-matrix resulting from the partition of the discrete system into displacement and transverse shear variables is positive definite. This is described more fully below. It should be emphasized that the moment constitutive equation is exactly satisfied whereas the mixed treatment is only applied to the shear.

The finite element discretization of the above weak form is standard and leads to a matrix system of the form

$$\begin{pmatrix} \mathbf{A} & \mathbf{C}^T \\ \mathbf{C} & -\tilde{\mathbf{A}} \end{pmatrix}\begin{pmatrix} \mathbf{u} \\ \tilde{\mathbf{u}} \end{pmatrix} = \begin{pmatrix} \mathbf{b} \\ \tilde{\mathbf{b}} \end{pmatrix}. \qquad (30)$$

where $\mathbf{A} = \mathbf{A}_b + \mathbf{A}_s$, in which $\mathbf{A}_b$ is a bending contribution, $\mathbf{A}_s$ is a shear contribution, the vector $\mathbf{u}$ contains nodal values of displacements and $\tilde{\mathbf{u}}$ contains transverse shear forces.

In our calculations, we employ piecewise linear interpolations for w, θ, $\overline{w}$ and $\bar{\theta}$, and piecewise constant interpolations for q and $\overline{q}$. Shear locking is avoided by using a one-point reduced integration rule for the shear contribution $\int_0^L \epsilon_s Gt(w_{,x} - \theta)\left(\overline{w}_{,x} - \bar{\theta}\right)dx$.

The element counterparts of the above arrays are given as follows:

$$\mathbf{A}_b^e = \frac{Et^3}{12h}\begin{bmatrix} 0 & 0 & 0 & 0 \\ 0 & 1 & 0 & -1 \\ 0 & 0 & 0 & 0 \\ 0 & -1 & 0 & 1 \end{bmatrix} \tag{31}$$

$$\mathbf{A}_s^e = \frac{\epsilon_s G t}{h}\begin{bmatrix} 1 & h/2 & -1 & h/2 \\ h/2 & h^2/4 & -h/2 & h^2/4 \\ -1 & -h/2 & 1 & -h/2 \\ h/2 & h^2/4 & h/2 & h^2/4 \end{bmatrix} \tag{32}$$

$$\mathbf{C}^e = (1-\epsilon_s)[-1 \quad -h/2 \quad 1 \quad -h/2] \tag{33}$$

$$\tilde{\mathbf{A}}^e = \frac{h(1-\epsilon_s)}{Gt} \tag{34}$$

$$\mathbf{b}^e = [fh/2 \quad -ch/2 \quad fh/2 \quad -ch/2]^T + \text{boundary condition terms} \tag{35}$$

$$\tilde{\mathbf{b}}^e = \text{boundary condition terms} \tag{36}$$

where h stands for the element length and all functions (e.g. E, G, t etc.) are evaluated at the element center.

In the above expression the matrices $\mathbf{A}$ and $\tilde{\mathbf{A}}$ are positive definite, the former due to the non-vanishing positive scalar ϵ_s. We can then solve the above system for u and substitute the result in the equation for $\tilde{u}$, getting

$$\left(\mathbf{C}\mathbf{A}^{-1}\mathbf{C}^T + \tilde{\mathbf{A}}\right)\tilde{\mathbf{u}} = \mathbf{C}\mathbf{A}^{-1}\mathbf{b} - \tilde{\mathbf{b}} \tag{37}$$

We propose to solve (37) by a basic (i.e. unpreconditioned) conjugate gradient scheme We shall refer to the iterations for the above system as the outer iterations while those associated with "inverting" the matrix A will be denoted as inner iterations.

We now particularize the basic conjugate gradient algorithm to the above problem, getting

Step 1. Initialization:

$$m = 0 \tag{38}$$

$$\tilde{\mathbf{u}}_0 = 0 \tag{39}$$

$$\mathbf{b}_0 = \mathbf{b} \tag{40}$$

$$\mathbf{u}_0 = \mathbf{A}^{-1}\mathbf{b}_0 \tag{41}$$

$$\tilde{\mathbf{r}}_0 = \mathbf{C}\mathbf{u}_0 - \tilde{\mathbf{b}} \tag{42}$$

$$\tilde{\mathbf{p}}_0 = \tilde{\mathbf{r}}_0 \tag{43}$$

Step 2. Update of solution and residual

$$\tilde{\mathbf{z}}_m = \tilde{\mathbf{A}}\tilde{\mathbf{p}}_n \tag{44}$$

$$\mathbf{b}_{m+1} = \mathbf{C}^T\tilde{\mathbf{p}}_m \tag{45}$$

$$\mathbf{x}_m = \mathbf{A}^{-1}\mathbf{b}_{m+1} \tag{46}$$

$$\tilde{\mathbf{z}}_m \leftarrow \tilde{\mathbf{z}}_m + \mathbf{C}\mathbf{x}_m \tag{47}$$

$$\tilde{\alpha}_m = \frac{\tilde{\mathbf{r}}_m \cdot \tilde{\mathbf{r}}_m}{\tilde{\mathbf{z}}_m \cdot \tilde{\mathbf{p}}_m} \tag{48}$$

$$\tilde{\mathbf{u}}_{m+1} = \tilde{\mathbf{u}}_m + \tilde{\alpha}_m\tilde{\mathbf{p}}_m \tag{49}$$

$$\mathbf{u}_{m+1} = \mathbf{u}_m - \tilde{\alpha}_m\mathbf{x}_m \tag{50}$$

$$\tilde{\mathbf{r}}_{m+1} = \tilde{\mathbf{r}}_m - \tilde{\alpha}_m\tilde{\mathbf{s}}_m \tag{51}$$

Step 3. Convergence check:

$$\text{If } \|\tilde{\mathbf{r}}_{m+1}\| < \delta\|\tilde{\mathbf{r}}_0\| \text{ , return.} \tag{52}$$

Step 4. Update conjugate direction

$$\tilde{\beta}_m = \frac{\tilde{\mathbf{r}}_{m+1} \cdot \tilde{\mathbf{r}}_{m+1}}{\tilde{\mathbf{r}}_m \cdot \tilde{\mathbf{r}}_m} \tag{53}$$

$$\tilde{\mathbf{p}}_{m+1} = \tilde{\mathbf{r}}_{m+1} + \tilde{\beta}_m \tilde{\mathbf{p}}_m \tag{54}$$

$$m = m + 1 \tag{55}$$

Go to Step 2 (56)

The variation of the scalar parameter ϵ_s from 0 to 1 gives us a family of weak forms that range between the classical mixed formulation and the displacement formulation. As will be seen later, the optimal choice for ϵ_s minimizes the condition number of the preconditioned matrix $\mathbf{B}^{-1}\mathbf{A}$.

In the present paper, the inner loop solution, $\mathbf{A}^{-1}\mathbf{b}_m$, is obtained with a preconditioned conjugate gradient algorithm. Since the matrix $\mathbf{A}$ is constructed from a standard finite element assemblage, the element-by-element preconditioner described is used.

In order to distinguish the values of δ associated with the inner and outer loops, we will use the notation δ^i and δ^o, respectively.

Accounting for axial effects is straightforward. For this purpose, one needs to add the equations

$$T_{,x} + s = 0 \tag{57}$$

$$T = Etu_{,x}, \tag{58}$$

where $s : [0, L] \to \mathcal{R}$ is the prescribed axial body force and T is the axial stress resultant. Suitable boundary conditions need also to be added in the usual way.

We now append to the weak form above the additional terms

$$= \cdots \int_0^L (1-\epsilon_a)\left(\overline{T}u_{,x} + T\overline{u}_{,x}\right)dx - \int_0^L \overline{u}s\,dx$$

$$- \int_0^L (1-\epsilon_a)\frac{\overline{T}T}{Et}dx + \int_0^L \epsilon_a Et\overline{u}_{,x}\,u_{,x}\,dx$$

$$+ \text{boundary condition terms}$$

$$= \cdots - \int_0^L \left[\overline{u}(T_{,x}+s) - \overline{T}\left(u_{,x} - \frac{T}{Et}\right)\right]dx$$

$$+ \int_0^L \epsilon_a Et\left(\overline{u}_{,x} - \frac{\overline{T}}{Et}\right)\left(u_{,x} - \frac{T}{Et}\right)dx$$

$$+ \text{boundary condition terms} \qquad (59)$$

The introduction of axial stresses has a much wider implication: other structural elements with entirely different stiffnesses can also be combined. We do so by inputting their stiffnesses in augmented mixed form and choosing appropriate ϵ-parameters. Then, although their stiffnesses may vary substantially, the ϵ-parameters can present the inner conjugate gradient driver with a reasonably conditioned system.

RESULTS

Beam with Bending and Shear

The results to be presented all refer to an end-loaded cantilever beam discretized with 64 elements, with geometric and material parameters given by

$$E = 1 \qquad (60)$$

$$G = 0.5 \qquad (61)$$

$$L = 1 \qquad (62)$$

The bending contribution to the stiffness matrix is $O(Et^3/12L)$ while the shear and axial contributions are $O(GtL)$ and $O(EtL)$, respectively. The parameters

$$\gamma_{s/b} = \frac{GtL}{Et^3/12L} = 12\left(\frac{G}{E}\right)\left(\frac{L}{t}\right)^2 \tag{63}$$

$$\gamma_{a/b} = \frac{EtL}{Et^3/12L} = 12\left(\frac{L}{t}\right)^2 \tag{64}$$

are the ratios of shear to bending and axial to bending, respectively. The larger of these parameters is a measure of the condition number of $\mathbf{A}|_{\epsilon=1}$, which is but the stiffness matrix resulting from the displacement formulation. We now see that when the ϵ's are close to *one* the condition number of $\mathbf{A}$ depends upon the ratio $(L/t)^2$, usually a large number. The introduction of smaller values of ϵ brings the condition number of $\mathbf{A}$ to reasonable values, independent of this ratio.

Table 1 presents the total number of inner loop iterations(n_i) required for convergence. This number is taken to be a measure of the total amount of work expended in obtaining the solution. The quantity $\epsilon_s\gamma_{s/b}$ is also presented. The tolerances δ^i and δ^o varied from problem to problem such that the tip displacement was correct to 1%. As may be seen, the total number of outer iterations (i.e., n_o) is *two* in all cases.

The most striking observation is that the number of iterations for convergence does <u>not</u> depend on the beam thickness. Rather, it is the parameter $\epsilon_s\gamma_{s/b}$ that seems to determine the number of iterations. It is interesting to note that the associated ϵ_s's are indeed very small, showing that the augmented stiffness tends more towards a mixed than a displacement formulation.

For the sake of comparison, the same problems were run with the displacement formulation and solved by an element-by-element preconditioned conjugate gradient driver. Table 2 presents the number of iterations for the various thicknesses analyzed. The number of iterations required for thin beams reveals the great advantage one can take of the formulation presented in this paper.

From Tables 1 and 2 we note that, for thin beams, the present formulation shows a great improvement as compared to the element-by-element solution with the displacement formulation. It should be pointed out that for the thick beam ($t = 0.1$) the number of iterations for the present formulation involves <u>two</u> solutions(i.e. $\mathbf{A}^{-1}\mathbf{b}_0$ and $\mathbf{A}^{-1}\mathbf{b}_1$), the minimum required.

Beam with Bending, Shear and Axial Effects

The same cantilever beam was used for the introduction of axial stresses. It should be pointed out that for a straight beam, the axial problem is uncoupled from the bending and shear problem. Despite the

fact that the problems are uncoupled, the present strategy cannot take advantage of this fact because the scalars α and β combine information from the entire solution vector.

The same geometric and material properties were used. A unit axial load was applied at the free end. Tables 3 and 4 show the total number of inner iterations for convergence as well as the number of iterations required in the displacement formulation. The differences are seen to be considerable.

Due to the enormous difference in the magnitude of displacements resulting from axial and bending solutions, a convergence criterion as specified in the conjugate gradient algorithm would not ensure convergence of the former unless δ^i was set to a very small value. In order to avoid this, the residual vector was divided into *three* independent vectors: one associated with the vertical displacements, one with the axial displacements and one with the rotations. The smallest non-zero of these initial residual norms was then used as r_0; δ^i was then set to 0.01.

The outer convergence criterion is more subtle. It should be observed that the initial residual is proportional to the displacement solution of the "soft" problem(i.e. $\epsilon < 1$). As can be seen in equation (30) the soft problem stiffness becomes singular as the ϵ's go to zero. This creates the problem that the initial residual grows indefinitely and the proper solution of the problem requires a large reduction in the residual. That is, the outer convergence tolerance δ^o is highly dependent on the ϵ's chosen. This still seems to be a problematic area since no explicit expression is available that allows us to precisely delineate the outer convergence tolerance. A possible solution being investigated is the utilization of a preconditioner for the outer loop. Since the number of outer loop iterations is already very small (< 7 in all cases) it seems that a preconditioner would allow us to establish convergence by limiting the number of outer iterations, irrespective of the initial residual.

Another important fact is that the proper evaluation of the ϵ's is still not precise. However, it seems that a preconditioner as mentioned above would ensure that a low condition number in the inner loop stiffness would be a good way of obtaining the ϵ's. With the number of outer loops reduced to an almost constant small number, the solution cost would depend solely on the inner loop cost.

CONCLUSIONS

The iterative solution of thin structural finite element models is not yet a viable alternative to direct solution. The combination of augmented mixed weak forms and iterative strategies such as element-by-element preconditioned conjugate gradients enables a desensitizing of the matrix equations. A significant reduction of iterations is achieved thereby when the structure is very thin. Further development of this concept should enhance the performance of iterative strategies for thin structural elements. The one-dimensional models

used in this paper to demonstrate ideas can of course be solved more effectively with direct solution methods. However, in the future it may be possible to solve large-scale three dimensional shell models more efficiently by employing iterative techniques. An indication of possibilities has been shown herein. Much research clearly remains to be done.

ACKNOWLEDGEMENTS

The authors would like to thank the Brazilian National Commission for Nuclear Energy (Comissão Nacional de Energia Nuclear - *CNEN*) for support of Arthur Muller through a graduate fellowship. Helpful conversation with Dr. Shohei Nakazawa of MARC Analysis is gratefully acknowledged.

REFERENCES

1. Fortin M. and Glowiniski, R., *Augmented Lagrangian Methods: Applications to the Numerical Solution of Boundary-Value Problems,* Studies in Mathematics and its Applications, vol.15, North-Holland, 1983.

2. Hughes, T.J.R., Winget, J., Levit, I. and Tezduyar, T. , "New Alternating Direction Procedures in Finite Element Analysis Based Upon EBE Approximate Factorizations", *Computer Methods for Nonlinear Solid and Structural Mechanics,* ASME, 1983.

3. Hughes, T.J.R., Raefsky, A., Muller, A., Winget, J. and Levit, I., "A Progress Report on EBE Solution Procedures in Solid Mechanics", *Numerical Methods for Nonlinear Problems,* Pineridge Press, Swansea, UK, 1984.

4. Washizu, K., *Variational Methods in Elasticity and Plasticity,* Pergamon Press, 1968.

Table 1. **Bending and shear effects: present formulation**

t	$\epsilon_s\gamma_{s/b}$	ϵ_s	n_i	n_o
0.1	1.0	1.67×10^{-3}	80	2
0.1	10.0	1.67×10^{-2}	69	2
0.1	100.0	1.67×10^{-1}	87	2
0.01	1.0	1.67×10^{-5}	80	2
0.01	10.0	1.67×10^{-4}	69	2
0.01	100.0	1.67×10^{-3}	87	2
0.001	1.0	1.67×10^{-7}	80	2
0.001	10.0	1.67×10^{-6}	71	2
0.001	100.0	1.67×10^{-5}	87	2
0.0001	1.0	1.67×10^{-9}	80	2
0.0001	10.0	1.67×10^{-8}	71	2
0.0001	100.0	1.67×10^{-7}	88	2

Table 2. **Bending and shear effects: displacement formulation**

Thickness	n*
0.1	47
0.01	146
0.001	473
0.0001	830

***This number should be compared with n_i in Table 1**

Table 3. **Bending, shear and axial effects: present formulation**

t	$\epsilon_s\gamma_{s/b}$	ϵ_s	$\epsilon_a\gamma_{a/b}$	ϵ_a	n_i	n_o
0.1	1.0	1.67×10^{-3}	4.0	3.33×10^{-3}	191	3
0.1	10.0	1.67×10^{-2}	40.0	3.33×10^{-2}	176	3
0.1	100.0	1.67×10^{-1}	400.0	3.33×10^{-1}	204	3
0.01	1.0	1.67×10^{-5}	4.0	3.33×10^{-5}	233	4
0.01	10.0	1.67×10^{-4}	40.0	3.33×10^{-4}	176	3
0.01	100.0	1.67×10^{-3}	400.0	3.33×10^{-3}	204	3
0.001	100.0	1.67×10^{-5}	400.0	3.33×10^{-5}	301	5
0.001	1000.0	1.67×10^{-4}	4000.0	3.33×10^{-4}	216	3
0.001	10000.0	1.67×10^{-3}	40000.0	3.33×10^{-3}	481	3
0.0001	100.0	1.67×10^{-7}	400.0	3.33×10^{-7}	406	6
0.0001	1000.0	1.67×10^{-6}	4000.0	3.33×10^{-6}	279	4
0.0001	10000.0	1.67×10^{-5}	40000.0	3.33×10^{-5}	387	4

Table 4. **Bending, shear and axial effects: displacement formulation**

Thickness	n*
0.1	69
0.01	179
0.001	863
0.0001	2431

*This number should be compared with n_i in Table 3

STRESS-DERIVATIVE CONTROL OF KEYSTONING DEFORMATION IN FINITE ELEMENT CODES

J. C. Schulz and O. E. R. Heimdahl

Naval Weapons Center
China Lake, California 93555

SUMMARY

The stress-derivative technique for control of keystoning deformation in underintegrated finite elements is based on expansion of the stress in a Taylor series about the element center and retention of additional terms beyond the constant stress term. It has the advantage over other control techniques that keystoning resistance is provided by actual rather than artificial material properties. Application of this technique to the quadrilateral ring elements used for modelling solids of revolution subjected to axisymmetric loads is described. In a cylindrical coordinate system additional terms appear in the formulation which must be dealt with in arriving at a workable keystoning control scheme.

INTRODUCTION

Isoparametric quadrilateral or hexahedral elements employed in finite element codes for analysis of nonlinear, dynamic structural response are usually underintegrated. One-point Gaussian quadrature (which is essentially the same as the assumption of constant stress throughout the element) is used for evaluation of element area or volume integrals. Compared to full integration (which can be obtained using four- or eight-point quadrature for quadrilateral or hexahedral elements, respectively), one-point quadrature significantly reduces the amount of time required for element calculations.

There is, however, a price associated with the use of underintegrated elements. Due to the assumption of constant stress within an element, some modes of deformation are not sensed and, hence, are not resisted in the underintegrated formulation. These are the well-known keystoning modes (also referred to as hourglassing, zero-energy or kinematic modes in the literature). Under certain conditions these modes can grow without limit, thus obscuring the actual solution. A method for adequate control of keystoning deformation is essential if meaningful solutions are to be obtained.

Early attempts at keystoning control involved the use of artificial viscosity (References 1 and 2). In this approach nodal forces proportional to and opposing a measure of the keystoning deformation rate are introduced. No additional storage and only a relatively small increase in computational effort are required. However, because the keystoning rate rather than the keystoning itself is opposed, there is no attempt to remove any keystoning deformation that might creep in. Consequently, artificial viscosity control is often ineffective unless a large viscous constant is used, which can result in reduction of the stable time step and distortion of the solution.

More recently, a procedure utilizing artificial stiffness for keystoning control has been developed (References 3 and 4). In this case forces proportional to and opposing the keystoning deformation are introduced. Some additional storage and about the same increase in computational effort as for artificial viscosity are required. Because the keystoning itself is opposed, artificial stiffness is much more effective than artificial viscosity. With this increased effectiveness, however, comes an increased risk of solution distortion.

A different technique for keystoning control, termed "stress-derivative" control, is described in Reference 5. This technique is based on expansion of the stress in a Taylor series about the element centroid. Additional terms beyond the constant stress term are retained to provide keystoning control. In its complete form stress-derivative control is intermediate between higher-order quadrature and artificial viscosity and stiffness in terms of storage and computation requirements. Through the introduction of additional approximations simplified stress-derivative procedures are obtained which are competitive with artificial stiffness procedures.

Derivation of stress-derivative control procedures for quadrilateral and hexahedral elements is given in Reference 5. In the present paper the application of this technique to quadrilateral ring elements used for modelling solids of revolution subjected to axisymmetric loads is considered. This is a situation of considerable practical interest. In the cylindrical coordinate system employed, additional terms appear in the governing equations which are not present for cartesian systems. Both a complete control procedure and a simplified procedure with reduced storage and computation requirements are described. These procedures are applied to a test problem.

COMPLETE CONTROL

Cylindrical coordinates r, θ, z are used. A ring element is generated by inscribing a quadrilateral in a radial plane and rotating this plane about the axis. This ring element is specified by the nodal coordinates r_I, z_I of the quadrilateral in the generating plane. Element geometry is shown in Figure 1.

Local material coordinates ξ_1, ξ_2 are defined by the transformation

$$r = r_I N_I (\xi_1, \xi_2) \quad ; \quad z = z_I N_I (\xi_1, \xi_2) \qquad (1a,b)$$

where N_I are the usual bilinear isoparametric shape functions.

NOTE: Indicial notation with implied summation of repeated indices is used. Lower case subscripts refer to the material coordinates and range from 1 to 2. Upper case subscripts refer to the nodes and range from 1 to 4. Subscripts r, θ, z are exempt from the above conventions. Although a more compact notation could have been adopted, it is hoped the one used will make the derivations clearer.

Displacements u, v in the r, z directions, respectively, are approximated as

$$u = u_I N_I \quad ; \quad v = v_I N_I \tag{2a,b}$$

where u_I, v_I are the displacements at the nodes.

Application of the principle of virtual displacements yields

$$f_{rI} = \int_A \left(\sigma_{rr} \frac{\partial N_I}{\partial r} + \sigma_{rz} \frac{\partial N_I}{\partial z} \right) r dA + \int_A \sigma_{\theta\theta} N_I \, dA$$

$$f_{zI} = \int_A \left(\sigma_{rz} \frac{\partial N_I}{\partial r} + \sigma_{zz} \frac{\partial N_I}{\partial z} \right) r dA \tag{3a,b}$$

where f_{rI}, f_{zI} are the nodal forces per radian in the r, z directions, respectively, and A is the area of the generating quadrilateral.

The stress can be expanded in a Taylor series as

$$\sigma_{rr} = \overline{\sigma}_{rr} + \frac{\overline{\partial \sigma_{rr}}}{\partial \xi_k} \xi_k + \ldots$$

$$\sigma_{zz} = \overline{\sigma}_{zz} + \frac{\overline{\partial \sigma_{zz}}}{\partial \xi_k} \xi_k + \ldots \tag{4a,b,c,d}$$

$$\sigma_{rz} = \overline{\sigma}_{rz} + \frac{\overline{\partial \sigma_{rz}}}{\partial \xi_k} \xi_k + \ldots$$

$$\sigma_{\theta\theta} = \overline{\sigma}_{\theta\theta} + \ldots$$

where the bars denote evaluation at the element center. It would appear that the contribution of the circumferential component $\sigma_{\theta\theta}$ to keystoning control in this axisymmetric situation is secondary to that of the other components. Consequently, this component was not expanded beyond the constant term.

Substitution of Equation 4 into Equation 3 yields

$$\frac{f_{rI}}{\bar{r}} = \bar{\sigma}_{rr}\left(B_{rI} + \frac{\Delta r_k}{\bar{r}} B_{rkI}\right) + \bar{\sigma}_{rz}\left(B_{zI} + \frac{\Delta r_k}{\bar{r}} B_{zkI}\right)$$

$$+ \frac{\bar{\sigma}_{\theta\theta}}{4\bar{r}}\left(A + \frac{\Delta\Delta r A_{rI} + \Delta\Delta z A_{zI}}{6}\right) + \frac{\partial\bar{\sigma}_{rr}}{\partial\xi_k}\left(B_{rkI} + \frac{\Delta r_k B_{rI} + \Delta\Delta r B_{rk'I}}{12\bar{r}}\right)$$

$$+ \frac{\partial\bar{\sigma}_{rz}}{\partial\xi_k}\left(B_{zkI} + \frac{\Delta r_k B_{zI} + \Delta\Delta r B_{zk'I}}{12\bar{r}}\right) \qquad (5a,b)$$

$$\frac{f_{zI}}{\bar{r}} = \bar{\sigma}_{rz}\left(B_{rI} + \frac{\Delta r_k}{\bar{r}} B_{rkI}\right) + \bar{\sigma}_{zz}\left(B_{zI} + \frac{\Delta r_k}{\bar{r}} B_{zkI}\right)$$

$$+ \frac{\partial\bar{\sigma}_{rz}}{\partial\xi_k}\left(B_{rkI} + \frac{\Delta r_k B_{rI} + \Delta\Delta r B_{rk'I}}{12\bar{r}}\right) + \frac{\partial\bar{\sigma}_{zz}}{\partial\xi_k}\left(B_{zkI} + \frac{\Delta r_k B_{zI} + \Delta\Delta r B_{zk'I}}{12\bar{r}}\right)$$

where $k' = k(\text{mod } 2) + 1$ and expressions for the geometric quantities $\bar{r}$, Δr_k, $\Delta\Delta r$, $\Delta\Delta z$, B_{rI}, B_{zI}, B_{rkI}, B_{zkI}, A, A_{rI}, A_{zI} are given as functions of the nodal coordinates in the appendix.

Equation 5 contains a number of additional terms compared to the corresponding equations for planar quadrilaterals given in Reference 5. However, for elements very far from the axis (where the radius at the element center $\bar{r}$ is large and plane strain conditions are approached) the ring equations simplify to the planar equations.

Hypoelastic material behavior will be assumed (although other material representations are possible). The hypoelastic stress rate can be written as

$$\dot{\sigma}_{rr} = \lambda d_V + 2\mu d_{rr} + 2w_{rz}\sigma_{rz}$$

$$\dot{\sigma}_{zz} = \lambda d_V + 2\mu d_{zz} - 2w_{rz}\sigma_{rz}$$

$$\dot{\sigma}_{rz} = 2\mu d_{rz} + w_{rz}(\sigma_{zz} - \sigma_{rr}) \qquad (6a,b,c,d)$$

$$\dot{\sigma}_{\theta\theta} = \lambda d_V + 2\mu d_{\theta\theta}$$

where d_{rr}, d_{zz}, d_{rz}, $d_{\theta\theta}$, w_{rz} are the deformation rate components and spin, λ and μ are the Lame parameters and $d_V = d_{rr} + d_{zz} + d_{\theta\theta}$.

The Lame parameters are taken as constant within an element (but not necessarily throughout the entire body). The derivatives of the stress rate with respect to the local coordinates then become

$$\frac{\partial \dot{\sigma}_{rr}}{\partial \xi_k} = \lambda \frac{\partial d_V}{\partial \xi_k} + 2\mu \frac{\partial d_{rr}}{\partial \xi_k} + 2\sigma_{rz} \frac{\partial w_{rz}}{\partial \xi_k} + 2w_{rz} \frac{\partial \sigma_{rz}}{\partial \xi_k}$$

$$\frac{\partial \dot{\sigma}_{zz}}{\partial \xi_k} = \lambda \frac{\partial d_V}{\partial \xi_k} + 2\mu \frac{\partial d_{zz}}{\partial \xi_k} - 2\sigma_{rz} \frac{\partial w_{rz}}{\partial \xi_k} - 2w_{rz} \frac{\partial \sigma_{rz}}{\partial \xi_k} \qquad (7a,b,c)$$

$$\frac{\partial \dot{\sigma}_{rz}}{\partial \xi_k} = 2\mu \frac{\partial d_{rz}}{\partial \xi_k} + \frac{\partial w_{rz}}{\partial \xi_k} (\sigma_{zz} - \sigma_{rr}) + w_{rz} \left(\frac{\partial \sigma_{zz}}{\partial \xi_k} - \frac{\partial \sigma_{rr}}{\partial \xi_k} \right)$$

Expressions for the deformation rate components, spin and derivatives of these quantities all evaluated at the element center are given as functions of the nodal coordinates and velocities in the appendix.

A complete finite element procedure including stress-derivative keystoning control has thus been formulated. At any given time the geometric quantities in Equation 5 and the deformation rate and spin quantities in Equations 6 and 7 can be determined. The stress and its derivatives can then be updated and used to calculate the nodal forces. The nodal velocities and displacements can then be updated by means of an appropriate explicit integration scheme, and the whole process repeated.

Compared to the usual constant stress procedure, this complete stress-derivative procedure requires six additional storage locations per element (for the stress derivatives) and a sizeable increase in computation time. Additional approximations can be made to obtain a simplified procedure competitive with artifical viscosity and stiffness procedures.

PARALLELOGRAMMATIC CONTROL

In many practical finite element meshes the generating quadrilaterals for ring elements are very close to being parallelograms. Moreover, mesh refinement usually makes these quadrilaterals more parallelogrammatic. For a parallelogram

$$\Delta\Delta r = 0 \quad ; \quad \Delta\Delta z = 0 \qquad (8a,b)$$

As shown in Reference 3 the vector quantities $\Delta r_k B_{rI}$ and $\Delta r_k B_{zI}$ in Equation 5 are orthogonal to the keystoning modes for parallelogrammatic elements. Hence, the stress-derivative terms associated with these quantities do not oppose the keystoning deformation. It is reasonable, therefore, to neglect them. The nodal forces then become

$$\frac{f_{rI}}{\bar{r}} = \bar{\sigma}_{rr}\left(B_{rI} + \frac{\Delta r_k D_{rk}}{\bar{r}}\Gamma_I\right) + \bar{\sigma}_{rz}\left(B_{zI} + \frac{\Delta r_k D_{zk}}{\bar{r}}\Gamma_I\right) + \frac{\bar{\sigma}_{\theta\theta}A}{4\bar{r}} + Q_r\Gamma_I$$

$$\frac{f_{zI}}{\bar{r}} = \bar{\sigma}_{rz}\left(B_{rI} + \frac{\Delta r_k D_{rk}}{\bar{r}}\Gamma_I\right) + \bar{\sigma}_{zz}\left(B_{zI} + \frac{\Delta r_k D_{zk}}{\bar{r}}\Gamma_I\right) + Q_z\Gamma_I \qquad (9a,b)$$

where $\Gamma_I = (1, -1, 1, -1)$ and the generalized forces are given by

$$Q_r = \frac{\overline{\partial\sigma_{rr}}}{\partial\xi_k} D_{rk} + \frac{\overline{\partial\sigma_{rz}}}{\partial\xi_k} D_{zk}, \quad Q_z = \frac{\overline{\partial\sigma_{rz}}}{\partial\xi_k} D_{rk} + \frac{\overline{\partial\sigma_{zz}}}{\partial\xi_k} D_{zk} \qquad (10a,b)$$

(Expressions for the geometric quantities D_{rk}, D_{zk} are given in the appendix.)

If the deformation rate is assumed to be small compared to the spin, the generalized force rates are

$$\dot{Q}_r = \left(\lambda\frac{\overline{\partial d_V}}{\partial\xi_k} + 2\mu\frac{\overline{\partial d_{rr}}}{\partial\xi_k}\right) D_{rk} + 2\mu\frac{\overline{\partial d_{rz}}}{\partial\xi_k} D_{zk} + Q_z w_{rz}$$

$$\dot{Q}_z = 2\mu\frac{\overline{\partial d_{rz}}}{\partial\xi_k} D_{rk} + \left(\lambda\frac{\overline{\partial d_V}}{\partial\xi_k} + 2\mu\frac{\overline{\partial d_{zz}}}{\partial\xi_k}\right) D_{zk} - Q_r w_{rz} \qquad (11a,b)$$

A simplified stress-derivative procedure has thus been obtained. The generalized forces are updated using Equation 11 and substituted into Equation 9 to determine the nodal forces. Only two additional storage locations are required (for the generalized forces) and the computation time is considerably less than for the complete procedure.

It should be noted that the additional assumptions introduced for parallelogrammatic control apply primarily to the stress-derivative terms in Equation 5. These terms are in the nature of relatively small modifications to the constant stress terms for keystoning control. Hence, some inaccuracy in these terms due to violation of the assumptions can be tolerated without deterioration of the physical solution.

TEST PROBLEM

The stress-derivative keystoning control techniques presented here were applied to the problem of a simply supported circular plate subjected to a uniform step pressure loading. This test problem is analogous to the beam problem suggested in Reference 3 and provides a severe test of element behavior since no deflection is possible without excitation of keystoning modes. Geometry of the circular plate is shown in Figure 2. Dimensions and property values are:

Radius, 0.4

Thickness, 0.1

Young's modulus, 1×10^9

Poisson's ratio, 0.3

Density, 1,000

Pressure, 2.5×10^6

Deformed shapes of the beam with increasing time for no control and complete stress-derivative control are compared in Figure 3. It is obvious that with no control the solution deteriorates rapidly, while with complete stress-derivative control keystoning is eliminated entirely. Parallelogrammatic control likewise eliminates keystoning and leads to deformed shapes almost indistinguishable from those for complete control. The peak deflections of the plate are 0.0719 and 0.0711 for complete and parallelogrammatic control, respectively.

CONCLUSION

Application of the stress-derivative keystoning control technique to quadrilateral ring elements has been described. Both a complete procedure and a simplified procedure for elements that are nearly parallelograms in the generating plane were presented. The simplified procedure has roughly the same storage and computation requirements as artificial viscosity or stiffness methods and has the advantage that keystoning resistance is provided by actual rather than artificial properties.

A second form of simplified stress-derivative control, termed "pressure" control, is described in Reference 5. Pressure control can also be applied to ring elements. In this technique the stress is separated into hydrostatic and deviatoric parts and only the hydrostatic part is expanded in a Taylor series. Pressure control is not limited to parallelogrammatic elements. Because only a portion of the anti-keystoning term is applied, pressure control cannot be expected to provide adequate resistance in all cases. However, it appears to do a satisfactory job in most situations.

As shown in Reference 4, elements with parallelogrammatic control do not satisfy the patch test unless they are exactly parallelograms. However, as long as the departure from "parallelogramness" is not great, these elements will come close to satisfying the patch test and should not exhibit convergence difficulties. Elements with either complete or pressure control will always meet the patch test.

REFERENCES

1. G. Maenchen and S. Sack. "The TENSOR Code," in *Methods in Computational Physics, Advances in Research and Applications*, Vol. 3, Fundamental Methods in Hydrodynamics (Ed. B. Alder, et al.). Academic Press, 1964, pp. 181-210.

2. M. L. Wilkins, R. E. Blum, E. Cronshagen and P. Grantham. "Method for Computer Simulation of Problems in Solid Mechanics and Gas Dynamics in Three Dimensions and Time." Lawrence Livermore Laboratory, Report UCRL-51574, Revision 1, May 1975.

3. D. P. Flanagan and T. Belytschko. "A Uniform Strain Hexahedron and Quadrilateral with Orthogonal Hourglass Control." *International Journal for Numerical Methods in Engineering*, Vol. 17, 1981, pp. 679-706.

4. T. Belytschko, W. K. Liu and J. M. Kennedy. "Hourglass Control in Linear and Nonlinear Problems," in *Recent Developments in Computer Methods for Linear and Nonlinear Analysis*, edited by S. Atluri and N. Perrone. ASME Symposium Volume, CONF-830615-3, 1983.

5. J. C. Schulz "Finite Element Hourglassing Control," *International Journal for Numerical Methods in Engineering*, accepted for publication, 1984.

APPENDIX

In this appendix expressions for the various geometric quantities and also the deformation rate components, spin and their derivatives are given as functions of the nodal positions and velocities.

$$\bar{r} = (r_1 + r_2 + r_3 + r_4)/4$$

$$\Delta r_1 = (-r_1 + r_2 + r_3 - r_4)/2$$

$$\Delta r_2 = (-r_1 - r_2 + r_3 + r_4)/2$$

$$\Delta z_1 = (-z_1 + z_2 + z_3 - z_4)/2$$

$$\Delta z_2 = (-z_1 - z_2 + z_3 + z_4)/2$$

$$\Delta\Delta r = r_1 - r_2 + r_3 - r_4$$

$$\Delta\Delta z = z_1 - z_2 + z_3 - z_4$$

$$B_{rI} = \frac{1}{2}\left[(z_2 - z_4),\ (z_3 - z_1),\ (z_4 - z_2),\ (z_1 - z_3)\right]$$

$$B_{zI} = \frac{1}{2}\left[(r_4 - r_2),\ (r_1 - r_3),\ (r_2 - r_4),\ (r_3 - r_1)\right]$$

$$B_{rkI} = \frac{1}{12}\begin{bmatrix}(z_4 - z_3),\ (z_3 - z_4),\ (z_1 - z_2),\ (z_2 - z_1)\\ (z_3 - z_2),\ (z_1 - z_4),\ (z_4 - z_1),\ (z_2 - z_3)\end{bmatrix}$$

$$B_{zkI} = \frac{1}{12}\begin{bmatrix}(r_3 - r_4),\ (r_4 - r_3),\ (r_2 - r_1),\ (r_1 - r_2)\\ (r_2 - r_3),\ (r_4 - r_1),\ (r_1 - r_4),\ (r_3 - r_2)\end{bmatrix}$$

$$A = \Delta r_1 \Delta z_2 - \Delta r_2 \Delta z_1$$

$$A_1 = \Delta r_1 \Delta\Delta z - \Delta z_1 \Delta\Delta r$$

$$A_2 = \Delta z_2 \Delta\Delta r - \Delta r_2 \Delta\Delta z$$

$$A_{rI} = \left[(z_2 - z_4),\ (z_1 - z_3),\ (z_4 - z_2),\ (z_3 - z_1)\right]$$

$$A_{zI} = \left[(r_4 - r_2),\ (r_3 - r_1),\ (r_2 - r_4),\ (r_1 - r_3)\right]$$

$$D_{rk} = \frac{1}{12}\left(-\Delta z_1,\ \Delta z_2\right)$$

$$D_{zk} = \frac{1}{12}\left(\Delta r_1,\ -\Delta r_2\right)$$

$$\bar{d}_{rr} = \frac{\dot{u}_I B_{rI}}{A}$$

$$\bar{d}_{zz} = \frac{\dot{v}_I B_{zI}}{A}$$

$$\bar{d}_{rz} = \frac{1}{2A}\left(\dot{u}_I B_{zI} + \dot{v}_I B_{rI}\right)$$

$$\bar{d}_{\theta\theta} = \frac{(\dot{u}_1 + \dot{u}_2 + \dot{u}_3 + \dot{u}_4)}{4\bar{r}}$$

$$\bar{w}_{rz} = \frac{1}{2A}\left(\dot{u}_I B_{zI} - \dot{v}_I B_{rI}\right)$$

$$\frac{\partial \overline{d_{rr}}}{\partial \xi_k} = \frac{12\ \dot{u}_I B_{rkI}}{A} - \frac{A_k \overline{d_{rr}}}{A}$$

$$\frac{\partial \overline{d_{zz}}}{\partial \xi_k} = \frac{12\ \dot{v}_I B_{zkI}}{A} - \frac{A_k \overline{d_{zz}}}{A}$$

$$\frac{\partial \overline{d_{rz}}}{\partial \xi_k} = \frac{6}{A}\left(\dot{u}_I B_{zkI} + \dot{v}_I B_{rkI}\right) - \frac{A_k \overline{d_{rz}}}{A}$$

$$\frac{\partial \overline{w_{rz}}}{\partial \xi_k} = \frac{6}{A}\left(\dot{u}_I B_{zkI} - \dot{v}_I B_{rkI}\right) - \frac{A_k \overline{d_{rz}}}{A}$$

$$\frac{\partial \overline{d_{\theta\theta}}}{\partial \xi_1} = \frac{(-\dot{u}_1 + \dot{u}_2 + \dot{u}_3 - \dot{u}_4)}{2\bar{r}} - \frac{\Delta r_1 \overline{d_{\theta\theta}}}{\bar{r}}$$

$$\frac{\partial \overline{d_{\theta\theta}}}{\partial \xi_2} = \frac{(-\dot{u}_1 - \dot{u}_2 + \dot{u}_3 + \dot{u}_4)}{2\bar{r}} - \frac{\Delta r_2 \overline{d_{\theta\theta}}}{\bar{r}}$$

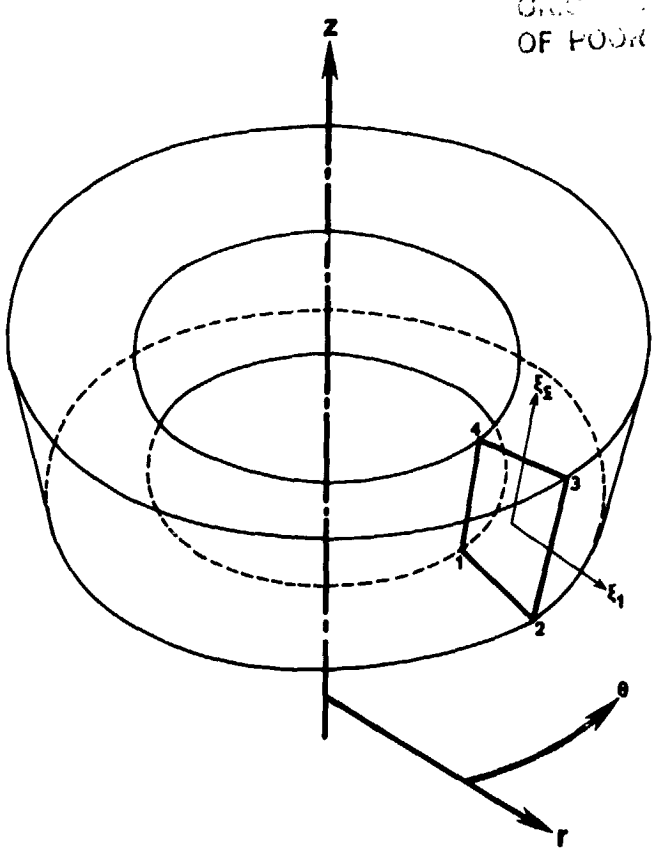

Figure 1. Ring element geometry.

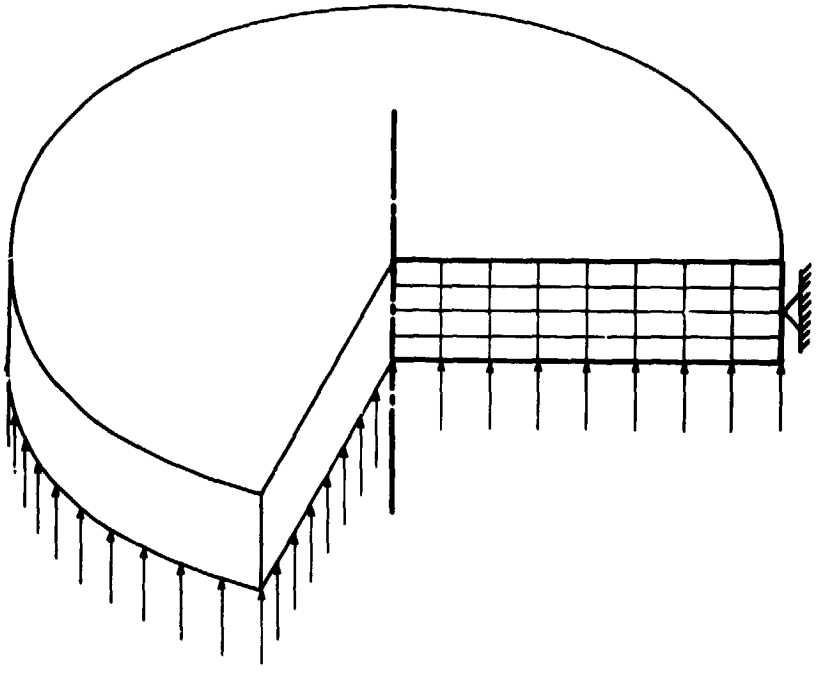

Figure 2. Circular plate test problem geometry.

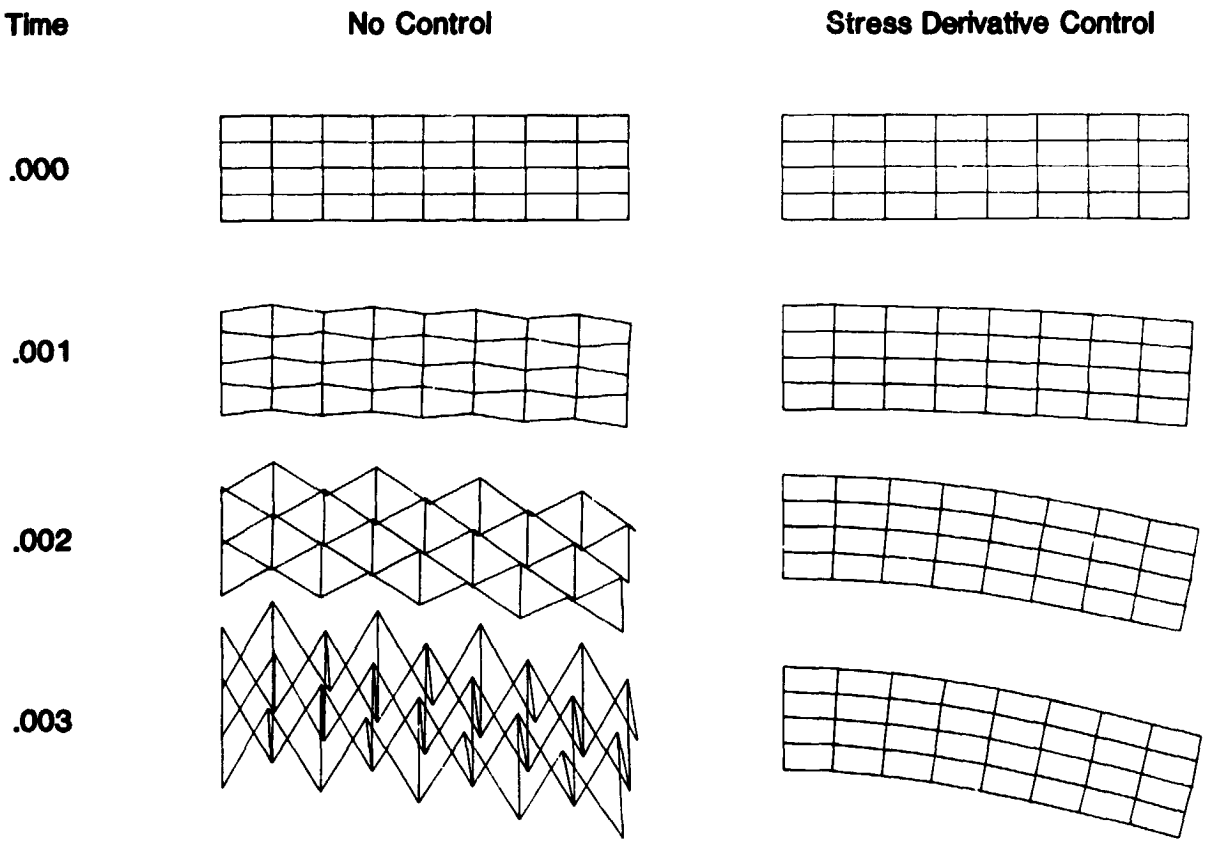

Figure 3. Deformed shapes of circular plate.

A TRIANGULAR FINITE ELEMENT FOR THIN PLATES AND SHELLS

S. W. Lee* and C. C. Dai**
Department of Aerospace Engineering
University of Maryland
College Park, Maryland

SUMMARY

A finite-element modeling technique which utilizes a triangular element called TSHEL with 45 degrees of freedom and seven-point integration has been tested for analysis of thin-plate and shell structures. The element formulation is based on the degenerate solid-shell concept and the mixed formulation with assumed independent inplane and transverse shear strains. Numerical results indicate effectiveness of the present modeling technique which features combined use of elements with kinematic modes and those without kinematic modes in order to eliminate both locking and spurious kinematic modes at the global structural level.

INTRODUCTION

The concept of the degenerate solid shell is very attractive because it can easily describe curved geometry and kinematics of deformation of arbitrary shell structures without invoking complicated shell theories [1]. However, the undesirable locking effect associated with zero inplane strain and zero transverse shear strain has been the major obstacle to a successful application of the degenerate solid-shell concept for finite-element modeling of thin-shell structures. The most popular scheme to alleviate locking effect has been either reduced or selective integration. However, an alternative and perhaps more general approach is to use mixed formulation based on either the Hellinger-Reissner principle or a modified Hellinger-Reissner principle [2]. Following this approach, studies have been made on various plate-bending elements [3,4]. In particular, in reference 4, Lee and Zhang studied a six-node mixed formulation plate-bending element in which elements with spurious kinematic modes were used to eliminate locking and then these modes were suppressed by adjacent elements without kinematic modes, thus resulting in a finite-element model which is less sensitive to locking and also kinematically stable at the global structural level.

The work presented in this paper represents a logical extension of the concept in reference 4 to finite-element modeling of thin-shell structures. A ten-node shell element, designated as TSHEL, is developed by following the degenerate solid-shell concept and the mixed formulation based on a modified Hellinger-Reissner principle with independent inplane strain and transverse shear strain.

A description of formulation for the triangular-shell element is given in the next section. In the subsequent section, effectiveness of the present modeling technique is demonstrated by solving several simple example problems.

---

*Associate Professor
**Graduate Research Assistant

FINITE-ELEMENT FORMULATION

The ten-node triangular shell element, designated as TSHEL, follows the concept of degenerate solid shell for the description of shell geometry and the kinematics of deformation, and finite-element formulation is based on a modified Hellinger-Reissner principle with independent inplane and transverse shear strains in addition to inplane displacement variables and rotational angles.

The concept of degenerate solid shell was introduced by Ahmad et al [1], and a good description if also found in references 5 and 6. Here we will describe this concept in a very concise manner for the sake of completeness and also to help facilitate subsequent discussion.

(a) Degenerate Solid Shell

Figure 1 shows the midsurface of a ten-node degenerate solid-shell element which is capable of modeling curved geometry. A degenerate solid-shell element requires both global and local coordinate systems for the description of shell geometry and the kinematics of deformation. A global coordinate system has Cartesian coordinates X,Y,Z while local orthogonal coordinate systems are given at each node and integration point on the shell midsurface. At a node, a triad of unit vectors, a_1, a_2 and a_3 in x,y,z coordinate directions, respectively, is supplied as an input to the element subroutine such that a_1, a_2 are tangent to the shell midsurface. On the other hand, a_3 is normal to the midsurface. At integration points, local orthogonal coordinates are defined and the unit vector a_1 (or x) is parallel to local coordinate ξ and a_3 (or z) is normal to the shell midsurface. The a_2 (or y) as well as a_1 vectors are tangent to the shell midsurface. Using global and local coordinate systems, the global coordinate of a material point in shell element can be expressed as

$$\begin{Bmatrix} X \\ Y \\ Z \end{Bmatrix} = \sum_{i=1}^{10} N_i(\xi,\eta) \begin{Bmatrix} X_o^i \\ Y_o^i \\ Z_o^i \end{Bmatrix} + \frac{\zeta}{2} \sum_{i=1}^{10} N_i(\xi,\eta)\, t_i \begin{Bmatrix} a_{31}^i \\ a_{32}^i \\ a_{33}^i \end{Bmatrix} \qquad (1)$$

where

N_i = ten-node shape function

ξ,η,ζ = parent coordinates (ζ=0 on the midsurface)

X_o^i, Y_o^i, Z_o^i = global coordinates of node i on the shell midsurface

t_i = shell thickness at node i

a_{3j}^i = j-th component of the unit vector a_3 at node i

The displacement component in the global coordinate system can be assumed in terms of nodal inplane displacements and rotational angles as following

$$\begin{Bmatrix} U \\ V \\ W \end{Bmatrix} = \sum_{i=1}^{10} N_i \begin{bmatrix} a_{11}^i & a_{21}^i & a_{31}^i \\ a_{12}^i & a_{22}^i & a_{32}^i \\ a_{13}^i & a_{23}^i & a_{33}^i \end{bmatrix} \begin{Bmatrix} u_i \\ v_i \\ w_i \end{Bmatrix} + \frac{\zeta}{2} \sum_{i=1}^{10} N_i\, t_i \begin{bmatrix} a_{11}^i & a_{21}^i \\ a_{12}^i & a_{22}^i \\ a_{13}^i & a_{23}^i \end{bmatrix} \begin{Bmatrix} \phi_i \\ \psi_i \end{Bmatrix} \quad (2)$$

where

U,V,W = displacement components in X, Y and Z directions respectively

u_i, v_i, w_i = inplane displacement components with respect to local coordinate system at node i

ϕ_i, ψ_i = rotational angles around $\underset{\sim}{a}_2$ and $\underset{\sim}{a}_1$ vectors respectively at node i

a_{1j}^i = j-th component of $\underset{\sim}{a}_1$ at node i

a_{2j}^i = j-th component of $\underset{\sim}{a}_2$ at node i

Symbolically Eq. (2) can be written in matrix form as

$$\underset{\sim}{U} = \underset{\sim}{N}\, \underset{\sim}{q}_e \quad (3)$$

where $\underset{\sim}{U}$ is the displacement vector in global coordinate, and $\underset{\sim}{q}_e$ is the element nodal displacement vector.

With the description of geometry and assumed displacement given above, the strain vector $\underset{\sim}{E}^G$ in the global coordinate system can be expressed in terms of nodal degrees of freedom as

$$\underset{\sim}{E}^G = \underset{\sim}{B}_1\, \underset{\sim}{q}_e + \zeta\, \underset{\sim}{B}_2\, \underset{\sim}{q}_e \quad (4)$$

neglecting higher order terms in ζ. The B_1 and B_2 matrices are independent of ζ. For a degenerated solid shell, it is necessary to express strain vector E^L with respect to local coordinate system in terms of q_e through strain transformation. Symbolically $\underset{\sim}{E}^L$ can be written as

$$\underset{\sim}{E}^L = \begin{Bmatrix} \underset{\sim}{\bar{\varepsilon}} + \zeta\, \underset{\sim}{\bar{\kappa}} \\ \underset{\sim}{\bar{\gamma}} \end{Bmatrix} \quad (5)$$

where

$$\underset{\sim}{\bar{\varepsilon}}_e = \begin{Bmatrix} \bar{\varepsilon}_{xx} \\ \bar{\varepsilon}_{yy} \\ \bar{\varepsilon}_{xy} \end{Bmatrix} = \underset{\sim}{B}_e\, \underset{\sim}{q}_e \quad (6)$$

is the inplane strain vector and

$$\bar{\gamma} = \begin{Bmatrix} \bar{\gamma}_{xz} \\ \bar{\gamma}_{yz} \end{Bmatrix} = B_\gamma \, q_e \qquad (7)$$

is the transverse shear strain vector and

$$\bar{\kappa} = \begin{Bmatrix} \bar{\kappa}_{xx} \\ \bar{\kappa}_{yy} \\ \bar{\kappa}_{xy} \end{Bmatrix} = B_\kappa \, q_e \qquad (8)$$

is a vector proportional to curvature strain vector. For want of a name, we will will call $\bar{\kappa}$ "curvature strain" vector.

(b) Mixed Formulation

The present TSHEL element is based on the modified Hellinger-Reissner principle with the functional expressed as

$$\Pi_{mR} = \int_A (\bar{\varepsilon}_e^T C_e \varepsilon_e - \frac{1}{2} \varepsilon_e^T C_e \varepsilon_e) dA + \int_A \frac{1}{2} \bar{\kappa}^T C_\kappa \bar{\kappa} \, dA + \int_A (\bar{\gamma}^T C_\gamma \gamma - \frac{1}{2} \gamma^T C_\gamma \gamma) \, dA - W \qquad (9)$$

In Eq. (9), all vector and matrix quantities are defined with respect to the local coordinate system. The strain vectors $\bar{\varepsilon}_e$, $\bar{\kappa}$ and $\bar{\gamma}$ are functions of inplane displacements and rotations. And also

$$\varepsilon_e = \begin{Bmatrix} \varepsilon_{xx} \\ \varepsilon_{yy} \\ \varepsilon_{xy} \end{Bmatrix} = \text{independent inplane strain vector}$$

$$\gamma = \begin{Bmatrix} \gamma_{xz} \\ \gamma_{yz} \end{Bmatrix} = \text{independent transverse shear strain vector}$$

W = applied load term

A = area of the shell midsurface

The elastic constant matrices C_e, C_κ, C_γ are defined as

$$C_e = \int_{-1}^{1} C_1 \, d\zeta \qquad (10)$$

$$C_\kappa = \int_{-1}^{1} \zeta^2 C_1 \, d\zeta \qquad (11)$$

$$\underset{\sim}{C}_\gamma = \int_{-1}^{1} \underset{\sim}{C}_2 \, d\zeta \tag{12}$$

where $\underset{\sim}{C}_1$ and $\underset{\sim}{C}_2$ are elastic constant matrices relating five components of stress to strain as follows

$$\begin{Bmatrix} \sigma_{xx} \\ \sigma_{yy} \\ \sigma_{xy} \end{Bmatrix} = \underset{\sim}{C}_1 \begin{Bmatrix} \varepsilon_{xx} \\ \varepsilon_{yy} \\ \varepsilon_{xy} \end{Bmatrix} \tag{13}$$

and

$$\begin{Bmatrix} \sigma_{xz} \\ \sigma_{yz} \end{Bmatrix} = \underset{\sim}{C}_2 \begin{Bmatrix} \gamma_{xz} \\ \gamma_{yz} \end{Bmatrix} \tag{14}$$

For finite-element approximation, $\bar{\varepsilon}_e$, $\bar{\kappa}$ and $\bar{\gamma}$ are assumed in terms of nodal degrees of freedom as in Eqs. (6)-(8). In addition, the independent strains $\underset{\sim}{\varepsilon}_e$ and $\underset{\sim}{\gamma}$ are assumed in terms of unknown coefficients such that

$$\underset{\sim}{\varepsilon}_e = \underset{\sim}{P}_\alpha \, \underset{\sim}{\alpha} \tag{15}$$

$$\underset{\sim}{\gamma} = \underset{\sim}{P}_\beta \, \underset{\sim}{\beta} \tag{16}$$

where $\underset{\sim}{P}_\alpha$ and $\underset{\sim}{P}_\beta$ are shape function matrices of assumed strains and $\underset{\sim}{\alpha}$ and $\underset{\sim}{\beta}$ are column vectors of unknown parameters which are eliminated at element level. In TSHEL, the assumed strains $\underset{\sim}{\varepsilon}_e$ and $\underset{\sim}{\gamma}$ have either linear or quadratic distribution. Further discussion on assumed strains will be given in the next section.

Substituting Eqs. (6)-(8), (10), and (16) into Eq. (9), Π_{mR} can be written symbolically as

$$\Pi_{mR} = \Sigma \left[\underset{\sim}{\alpha}^T \underset{\sim}{G}_\alpha \underset{\sim}{q}_e - \frac{1}{2} \underset{\sim}{\alpha}^T \underset{\sim}{H}_\alpha \underset{\sim}{\alpha} + \frac{1}{2} \underset{\sim}{q}_e^T \underset{\sim}{K}_B \underset{\sim}{q}_e + \underset{\sim}{\beta}^T \underset{\sim}{G}_\beta \underset{\sim}{q}_e \right.$$

$$\left. - \frac{1}{2} \underset{\sim}{\beta}^T \underset{\sim}{H}_\beta \underset{\sim}{\beta} - \underset{\sim}{q}_e^T \underset{\sim}{Q}_e \right] \tag{17}$$

where the summation notation implies assembly of elements and

$$\underset{\sim}{G}_\alpha = \int_A \underset{\sim}{P}_\alpha^T \underset{\sim}{C}_e \underset{\sim}{B}_e \, dA$$

$$\underset{\sim}{H}_\alpha = \int_A \underset{\sim}{P}_\alpha^T \underset{\sim}{C}_e \underset{\sim}{P}_\alpha \, dA$$

$$\underset{\sim}{K}_B = \int_A \underset{\sim}{B}_\kappa^T \underset{\sim}{C}_\kappa \underset{\sim}{B}_\kappa \, dA \tag{18}$$

$$\underset{\sim}{G}_\beta = \int_A \underset{\sim}{P}_\beta^T \underset{\sim}{C}_\gamma \underset{\sim}{B}_\gamma \, dA$$

$$\underset{\sim}{H}_\beta = \int_A \underset{\sim}{P}_\beta^T \underset{\sim}{C}_\gamma \underset{\sim}{P}_\beta \, dA$$

$\underset{\sim}{Q}_e$ = element load vector

Taking $\delta \Pi_{mR} = 0$ with respect to $\underset{\sim}{\alpha}$,

$$\underset{\sim}{G}_\alpha \underset{\sim}{q}_e - \underset{\sim}{H}_\alpha \underset{\sim}{\alpha} = 0 \tag{19}$$

and similarly taking $\delta \Pi_{mR} = 0$ with respect to β,

$$\underset{\sim}{G}_\beta \underset{\sim}{q}_e - \underset{\sim}{H}_\beta \underset{\sim}{\beta} = 0 \tag{20}$$

From Eqs. (19) and (20)

$$\underset{\sim}{\alpha} = \underset{\sim}{H}_\alpha^{-1} \underset{\sim}{G}_\alpha \underset{\sim}{q}_e \tag{21}$$

and

$$\underset{\sim}{\beta} = \underset{\sim}{H}_\beta^{-1} \underset{\sim}{G}_\beta \underset{\sim}{q}_e \tag{22}$$

Now substituting Eqs. (21) and (22) into Eq. (17)

$$\Pi_{mR} = \Sigma \left(\frac{1}{2} \underset{\sim}{q}_e^T \underset{\sim}{k}_e \underset{\sim}{q}_e - \underset{\sim}{q}_e^T \underset{\sim}{Q}_e\right) \tag{23}$$

where

$$\underset{\sim}{K}_e = \underset{\sim}{G}_\alpha^T \underset{\sim}{H}_\alpha^{-1} \underset{\sim}{G}_\alpha + \underset{\sim}{G}_\beta^T \underset{\sim}{H}_\beta^{-1} \underset{\sim}{G}_\beta + \underset{\sim}{K}_\beta \tag{24}$$

is the element stiffness matrix. For TSHEL, uniform 7 point rule is used for numerical integration of element stiffness matrix. In addition, the five degrees of freedom associated with the interior node are statically condensed out, resulting in an element with 45 degrees of freedom. After assembly of all elements, Π_{mR} can be written as

$$\Pi_{mR} = \frac{1}{2} \underset{\sim}{q}^T \underset{\sim}{K} \underset{\sim}{q} - \underset{\sim}{q}^T \underset{\sim}{Q} \tag{25}$$

where

$\underset{\sim}{q}$ = global nodal displacement vector
$\underset{\sim}{K}$ = global stiffness matrix
$\underset{\sim}{Q}$ = global load vector

Taking $\delta \Pi_{mR} = 0$ with respect to q leads to

$$\underset{\sim}{K} \underset{\sim}{q} = \underset{\sim}{Q} \tag{26}$$

which can be solved for $\underset{\sim}{q}$. With $\underset{\sim}{q}$ and thus $\underset{\sim}{q}_e$ determined, inplane forces and moments-per-unit length for isotropic shells are determined as follows

$$\underset{\sim}{N} = \begin{Bmatrix} N_{xx} \\ N_{yy} \\ N_{xy} \end{Bmatrix} = \frac{t}{2} \underset{\sim}{C}_e \underset{\sim}{\varepsilon}_e = \frac{t}{2} \underset{\sim}{C}_e \underset{\sim}{p}_\alpha \underset{\sim}{\alpha} \tag{27}$$

and

$$\underset{\sim}{M} = \begin{Bmatrix} M_{xx} \\ M_{yy} \\ M_{xy} \end{Bmatrix} = \frac{t^2}{4} \underset{\sim}{C}_{\kappa} \underset{\sim}{\kappa} = \frac{t^2}{4} \underset{\sim}{C}_{\kappa} \underset{\sim}{B}_{\kappa} \underset{\sim}{q}_e \tag{28}$$

where t is the shell thickness.

ASSUMED STRAINS

The choice of assumed strains is of paramount importance in mixed formulation. After all, proper choice of assumed strain distributions makes the mixed formulation element different from the usual assumed displacement formulation based on the principle of virtual work. Especially for the purpose of alleviating locking, it is desirable to choose assumed strain distribution as simple as possible [2]. However, an excessively simple form of assumed strain will trigger kinematic modes or spurious zero strain energy modes other than rigid-body modes. These modes are also found in other finite-element models such as hybrid stress formulation reduced and selective integration schemes. Of course reduced and selective integration is equivalent to mixed formulation in certain cases. Existence of spurious kinematic modes at the element level is not a serious problem as long as they are suppressed at the global structural level. On the contrary, it has been observed that an element with kinematic mode is less sensitive to the locking effect even for very thin plates under clamped boundary conditions [3]. In fact, reference 4 describes a modeling technique for plate bending where six-node mixed formulation elements with kinematic modes are combined with the other six-node elements without kinematic modes. These elements with kinematic modes are introduced to alleviate locking while those without kinematic modes are used to suppress kinematic modes. In the present paper, we apply the same concept to the TSHEL element. Depending upon the type of assumed strains, the TSHEL element may be divided into type A and type B. In type A, the independent strains are assumed to be linear within each element with unknown coefficients as follows:

a) Inplane Strains (linear 9α)

$$\varepsilon_{xx} = \alpha_1 + \alpha_2 \xi + \alpha_3 \eta$$

$$\varepsilon_{yy} = \alpha_4 + \alpha_5 \xi + \alpha_6 \eta$$

$$\varepsilon_{xy} = \alpha_7 + \alpha_8 \xi + \alpha_9 \eta$$

b) Transverse Shear Strains (linear 6β)

$$\gamma_{xz} = \beta_1 + \beta_2 \xi + \beta_3 \eta$$

$$\gamma_{yz} = \beta_4 + \beta_5 \xi + \beta_6 \eta$$

The assumed strains for type B are

a) Inplane Strains (quadratic 18α)

$$\varepsilon_{xx} = \alpha_1 + \alpha_2 \xi + \alpha_3 \eta + \alpha_4 \xi\eta + \alpha_5 \xi^2 + \alpha_6 \eta^2$$

$$\varepsilon_{yy} = \alpha_7 + \alpha_8 \xi + \alpha_9 \eta + \alpha_{10} \xi \eta + \alpha_{11} \xi^2 + \alpha_{12} \eta^2$$

$$\varepsilon_{xy} = \alpha_{13} + \alpha_{14} \xi + \alpha_{15} \eta + \alpha_{16} \xi \eta + \alpha_{17} \xi^2 + \alpha_{18} \eta^2$$

b) Transverse Shear Strains (quadratic 12β)

$$\gamma_{xz} = \beta_1 + \beta_2\,\xi + \beta_3\,\eta + \beta_4\,\xi\,\eta + \beta_5\,\xi^2 + \beta_6\,\eta^2$$

$$\gamma_{yz} = \beta_7 + \beta_8\,\xi + \beta_9\,\eta + \beta_{10}\,\xi\,\eta + \beta_{11}\,\xi^2 + \beta_{12}\,\eta^2$$

Note that one element subroutine is designed to handle both types of assumed strains. The linear strains in type A trigger spurious kinematic modes in the TSHEL element. If we consider, for simplicity, an element with flat geometry, in which shell behavior is decoupled into plane stress and plate bending, then for the plane stress case, linearly assumed inplane strains will result in eight spurious kinematic modes associated with inplane deformation. In addition, for the plate-bending case, linearly assumed transverse shear strains will result in four kinematic modes associated with normal deflection. These modes are compatible, hence an assembly of type A elements will exhibit unstable spurious kinematic modes. On the other hand, the type B element with quadratic inplane and transverse shear strains is free of kinematic modes and thus stable. As in reference 4, type A and B elements can be combined as shown in Fig. 2 in an attempt to eliminate both locking and kinematic modes simultaneously. Note that the kinematic modes in type A elements are suppressed by type B elements.

NUMERICAL TEST

In order to test the effectiveness of the present TSHEL element, simple example problems involving thin plates and shells were solved. Of particular interest was the performance of the finite-element model with type A and type B elements combined as explained in the previous section. An example of finite-element mesh patterns employed is shown in Fig. 3a. In this figure, each rectangle consists of four triangular elements. Note that, for the model with combination of type A and type B elements, finite-element mesh is arranged such that a type A element does not share a common side with another type A element. All computations were carried out in double precision on the UNIVAC 1100/82 machine at the University of Maryland.

(a) Square Plate Supported at Four Corners

A square plate supported at four corners is under uniformly distributed load p psi. This problem was chosen to illustrate the detrimental effect of spurious kinematic modes. Due to symmetry in geometry and loading, only a quarter of the plate was modeled by 2 x 2 regular mesh as shown in Fig. 3a. In the figure, symbol c represents the plate centroid. Elastic properties of the plate are $E = 10^7$ psi and $\nu = 1/6$, and side lengths are a = b = 2 inches.

Table 1 lists nondimensional deflection $\bar{w} = 10\,DW/PL^4$ along y = 0 line for a/t = 100. Symbols D and t represent bending rigidity and thickness respectively. The finite-element model with type A elements only shows excessively large values of $\bar{w}$, clearly indicating existence of unstable kinematic modes. On the other hand, as expected, the finite-element model with a combination of type A and type B elements is free of kinematic modes and gives reliable solutions. In fact computed maximum $\bar{w} = 0.2633$ at the plate centroid is very close to the analytical solution $\bar{w} = 0.263$ for the Kirchhoff thin-plate theory.

(b) Simply Supported and Clamped Plates

A quarter of the square (a/b = 1) and rectangular plates (a/b = 2) under uniformly distributed load were modeled by 1 x 1 regular mesh, 2 x 2 regular mesh and 2 x 2 irregular mesh. Figures 3a and 3b show 2 x 2 regular mesh and 2 x 2 irregular mesh respectively. Elastic property and geometry are as follows:

$E = 10^7$ psi
$\nu = 0.3$
a = 2 inches

Table 2 lists maximum nondimensional deflection for simply supported boundary. These values were normalized with respect to analytical thin-plate theory solution. The numbers in parentheses under 2 x 2 mesh are those for 2 x 2 irregular mesh. Others are solutions obtained with 1 x 1 and 2 x 2 regular meshes. It is observed that the finite-element model with combinations of type A and type B elements does not exhibit locking effect for a wide range of a/t ratios considered here. In addition, even the model with type B elements only is surprisingly free of locking and gives very accurate solutions. Table 3 shows maximum moment M_{xx} computed at the integration point nearest to the centroid of the simply supported plate. These values are normalized with respect to analytical thin-plate theory solution. Again, for both regular and irregular meshes, the model with combinations of type A and type B elements gives numerial results almost insensitive to a/t ratios. The model with type B elements only also gives reliable solutions except for a/b = 1 modeled with irregular mesh. Here, quite surprisingly, solutions for a/t = 100 and 1000 are not as accurate as those for thinner plates. At the moment there is no good explanation to this behavior.

Table 4 lists nondimensional maximum deflection for the clamped boundary condition. Again, computed solutions were normalized with respect to analytical solutions for thin-plate theory. Here the model with combinations of type A and type B elements gives reliable solution for both regular and irregular meshes. The model with type B elements only also gives good solutions for 2 x 2 mesh. However, in general, the model with type A and type B elements combined is slightly better than the model with type B elements only, especially for 1 x 1 regular mesh.

(c) Pinched Cylinderical Shell

A cylindrical shell is loaded at two symmetric points as shown in Fig. 4. Elastic property and geometry are given as follows [7]:

$E = 1.05 \times 10^7$ psi
$\nu = 0.3$
R = 4.953"
L = 2R
R/t = 100

Circular boundaries are either diaphragmed or fixed. Due to symmetry in geometry and loading, only the octant of the shell was modeled by 2 x 2 and 3 x 3 mesh shown in Fig. 5.

Table 5 lists nondimensional maximum deflection $\bar{w}_c = -w_c Et/p$ at the load point for both diaphragmed and fixed ends. Symbol w represents normal deflection and the subscript c stands for load point c. Here numerical results for the model with combinations of type A and type B elements are much better than those for the model with type B elements only. For diaphragmed ends, 3 x 3 mesh solution $\bar{w}_c = 163.88$ for the model with combination of type A and type B elements is close to $\bar{w}_c = 164.24$ reported in ref. 7. For fixed ends, 3 x 3 mesh solution $\bar{w}_c = 136.85$ for the model with type A and type B combined is close to $\bar{w}_c = 136.81$ obtained in ref. 8. On the other hand, solutions for the model with type B elements only are very poor compared with the model with type A and type B elements combined. This result is quite contrary to the plate-bending case where differences between two model types were quite small. As a check, an additional model called type E was also tested. In the

type E model, all elements employ assumed transverse shear strain with quadratic distribution while for inplane strain, elements with linear and quadratic distributions are combined as the model with type A and type B elements combined. As expected, numerical results for type E model are better than the model with type B elements only. However they are still far worse than the results from the model with type A and type B elements combined. This test shows that, although quadratic assumed transverse shear strain gives good solution for the flat plate, it is no longer true for curved shells.

Figures 6 and 7 show nondimensional normal deflection $\bar{w} = Etw/p$ along lines BC and DC respectively for both diaphragmed and fixed ends. Again these results agree with those given in refs. 7 and 8. More results obtained with the present TSHEL elements are reported in ref. 9.

(d) Pinched Spherical Shell

Figure 8 shows a spherical shell under concentrated force p at two opposite points. Elastic property and geometry of the shell [10] are:

$E = 1. \times 10^4$ psi
$\nu = 0.3$
$t = 1"$
$R/t = 50, 500$ and 1000

Two finite-element models were considered: model 1 with eight segments and model 2 with ten segments. Model 1 is shown in Fig. 8 with segment numbers as indicated. Here segment 1 consists of a single TSHEL element with type B assumed strains. On the other hand, other individual segments consist of four triangular elements. The segment angles in model 1 are 2°, 6°, 8°, 12°, 17°, 22.5°, and 22.5° starting from th first segment. Model 2 is obtained by equally dividing segments 1 and 2 of model 1.

Table 6 lists nondimensional maximum deflection $\bar{w} = Etw/p$ at the load point. Numerical solutions are compared with Koiter's solution [10]. For R/t = 500 and 1000, agreement is very good. For R/t = 50, the difference is slightly larger. The difference between the present solution and Koiter's solution might be due to differences in shell modeling. Especially for R/t = 50, the shell is relatively thick. Note that Koiter's solution is based on thin-shell theory which neglects the effect of transverse shear deformation.

Figures 9, 10, and 11 show nondimensional normal deflection, bending-moment, and inplane force distributions along ϕ obtained with mesh 2. For R/t = 50, they are in good agreement with those reported in ref. 10. The R/t = 500 and 1000 cases were not considered in ref. 10.

DISCUSSION AND CONCLUSION

Results of the numerical test show that for plate-bending problems, performance of finite-element models with type B elements only seems as good as that of the mode with type A and type B combined. However, for shells, only the model with type A and type B combined performs well.

In order to facilitate the use of the present modeling technique, it will be much more convenient to design a preprocessor which can identify type A and type B elements in the finite-element model.

REFERENCES

1. Ahmad, S., Irons, B. M., and Zienkiewicz, O. C., "Analysis of thick and thin shell structures by curved elements," Int. J. Num. Meth. Engng., Vol. 2, 419-451 (1970).

2. Lee, S. W. and Pian, T. H. H., "Improvement of plate and shell finite element by mixed formulations," AIAA J. 16, 29-34, (1978).

3. Lee, S. W. and Wong, S. C., "Mixed formulation finite elements for Mindlin theory plate bending," Int. J. Num. Meth. Engng. 18, 1297-1311, (1982).

4. Lee, S. W. and Zhang, J. C., "A six node finite element for plate bending," Int. J. Meth. Engng. (In Press).

5. Zienkiewicz, O. C., The Finite Element Method, 3rd Ed., McGraw-Hill, New York, 1977.

6. Cook, R. D., Concepts and Applications of Finite Element Analysis, 2nd Ed., John Wiley and Sons, New York, 1981.

7. Dawe, D. J., "Static analysis of diaphragm-supported cylindrical shells using a curved finite strip," Int. J. Meth. Engng., Vol. 11, 1347-1364 (1977).

8. Lee, S. W., Wong, S. C., and Rhiu, J. J., "Study of a nine-node mixed formulation finite element for thin plates and shells," Computers and Structures (In Press).

9. Dai, C. C., "A mixed formulation triangular finite element for thin shell analysis," Ph.D. Dissertation, Dept. of Aerospace Engineering, Univ. of Maryland, Sept. 1984.

10. Koiter, W. T., "A spherical shell under point loads at its poles." Progress in Appl. Mech., The Prager Anniversary Volume, MacMillan, 1963, pp. 155-169.

Table 1 -- Nondimensional deflection along y = 0 line for a square plate supported at four corners (2 x 2 regular mesh)

2x/a	A + B	B only	A only
0.	0.2633	0.2624	0.3262×10^{11}
0.125	0.2615	0.2606	0.6243×10^{10}
0.25	0.2561	0.2552	-0.2890×10^{10}
0.375	0.2474	0.2465	0.1043×10^{11}
0.5	0.2359	0.2349	0.2843×10^{11}
0.625	0.2220	0.2210	0.1048×10^{11}
0.75	0.2065	0.2054	-0.3017×10^{10}
0.875	0.1901	0.1890	0.6070×10^{10}
1.	0.1738	0.1726	0.3322×10^{11}

Table 2 -- Maximum nondimensional deflection for simply supported plate

a/b	1				2			
Type	A + B		B		A + B		B	
Mesh	1 x 1	2 x 2	1 x 1	2 x 2	1	2 x 2	1 x 1	2 x 2
$\frac{a}{t} = 10^2$	0.9985	1.0000 (0.9993)	0.9995	0.9999 (0.9970)	0.9974	0.9999 (0.9999)	1.0084	1.0000 (0.9979)
$\frac{a}{t} = 10^3$	0.9983	0.9999 (0.9992)	0.9992	0.9998 (0.9966)	0.9970	0.9998 (0.9999)	1.0089	1.0001 (0.9976)
$\frac{a}{t} = 10^4$	0.9983	0.9999 (0.9992)	0.9992	0.9998 (0.9967)	0.9970	0.9998 (0.9999)	1.0089	1.0001 (0.9978)
$\frac{a}{t} = 10^5$	0.9983	0.9998 (0.9992)	0.9992	0.9998 (0.9967)	0.9970	0.9998 (0.9999)	1.0089	1.0001 (0.9978)

ıble 3 -- Maximum nondimensional moment $\bar{M}_{xx}$ for simply supported plate (2 x 2 mesh)

a/b	1		2	
Type	A + B	B	A + B	B
$\frac{a}{t} = 10^2$	0.9994 (1.0077)	0.9923 (0.9741)	0.9999 (0.9999)	1.0000 (0.9979)
$\frac{a}{t} = 10^3$	1.0031 (1.0090)	0.9935 (0.9885)	0.9998 (.0.9999)	1.0001 (0.9976)
$\frac{a}{t} = 10^4$	1.0031 (1.0090)	0.9937 (0.9923)	0.9998 (0.9999)	1.0001 (0.9978)
$\frac{a}{t} = 10^5$	1.0031 (1.0090)	0.9937 (0.9923)	0.9998 (0.9999)	1.0001 (0.9978)

'able 4 -- Maximum nondimensional deflection for clamped plate

a/b	1				2			
Type	A + B		B		A + B		B	
Mesh	1 x 1	2 x 2	1 x 1	2 x 2	1 x 1	2 x 2	1 x 1	2 x 2
$\frac{a}{t} = 10^2$	0.9968	0.9995 (0.9992)	1.0328	0.9968 (0.9909)	0.9763	0.9961 (0.9960)	1.1118	0.9961 (1.0004)
$\frac{a}{t} = 10^3$	0.9966	0.9990 (0.9986)	1.0351	0.9974 (0.9898)	0.9764	0.9957 (0.9961)	1.1157	1.0001 (1.0063)
$\frac{a}{t} = 10^4$	0.9966	0.9990 (0.9986)	1.0351	0.9974 (0.9898)	0.9764	0.9957 (0.9961)	1.1157	1.0001 (1.0065)
$\frac{a}{t} = 10^5$	0.9966	0.9990 (0.9986)	1.0351	0.9974 (0.9892)	0.9764	0.9957 (0.9961)	1.115/	1.0001 (1.0062)

Table 5 -- Maximum deflection $\bar{w}_c$ for cylindrical shell ($\frac{R}{t} = 100$)

Mesh	Diaphragmed Ends			Fixed Ends		
	A + B	B	E	A + B	B	E
2 x 2	154.14	89.04	102.15	130.86	33.57	59.54
3 x 3	163.88	120.46	149.44	136.85	98.46	117.69

Table 6 -- Maximum deflection $\bar{w}$ at the pole for pinched sphere

$\frac{R}{t}$	1	2	Koiter [10]
50	23.39	23.72	21.20
500	211.98	210.32	207.32
1000	419.89	419.76	413.92

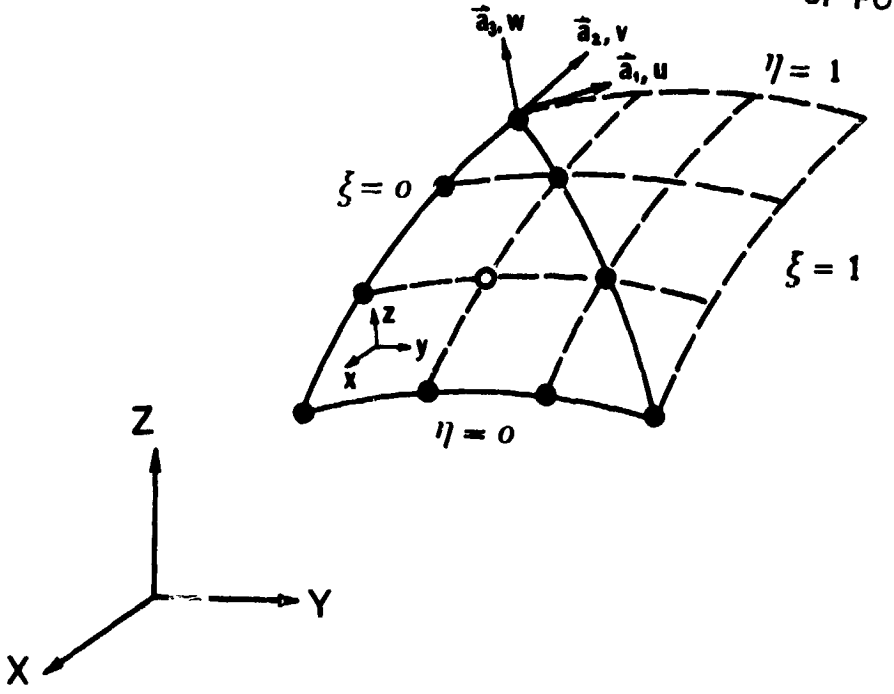

Figure 1. Triangular-shell element TSHEL.

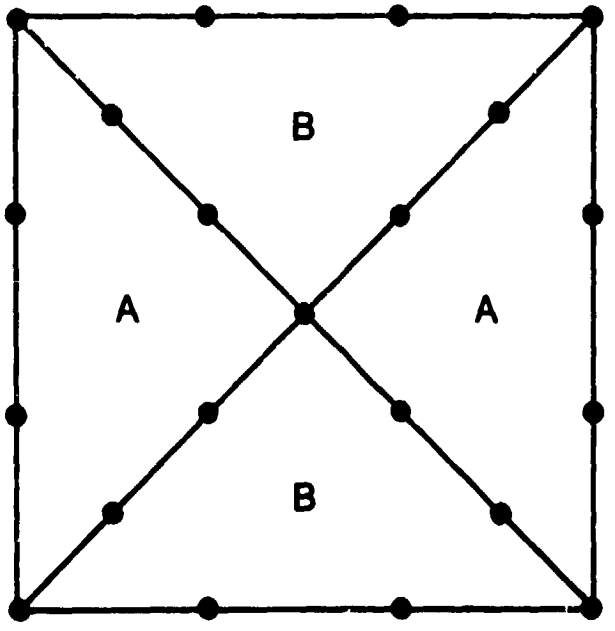

Figure 2. A stable combination of type A and type B.

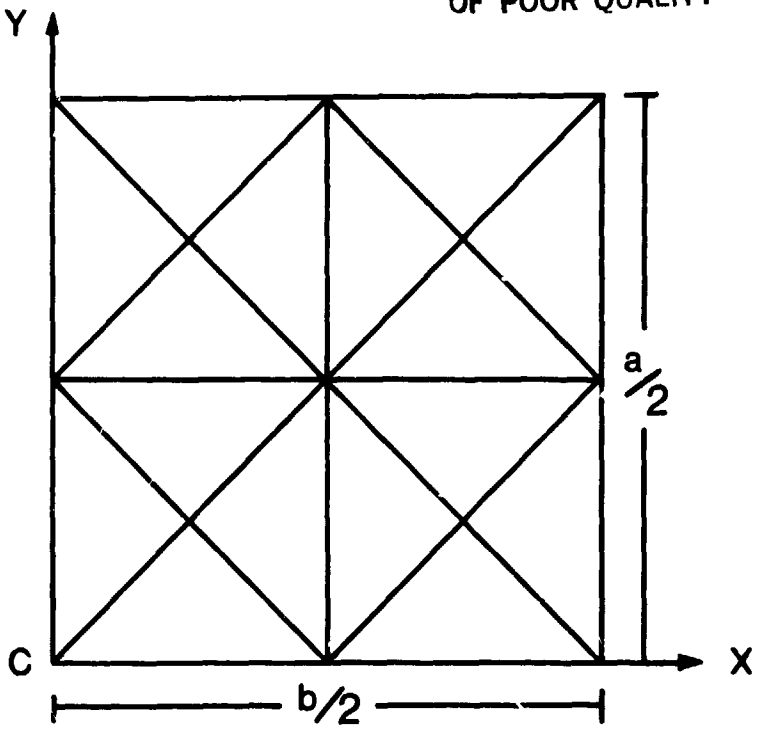

Figure 3(a). Regular 2 x 2 mesh.

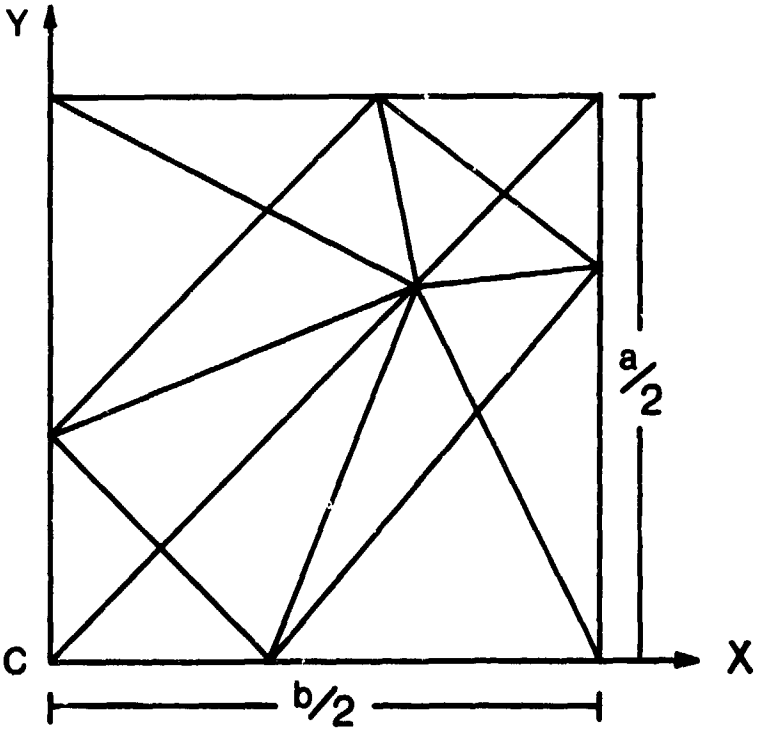

Figure 3(b). Irregular 2 x 2 mesh.

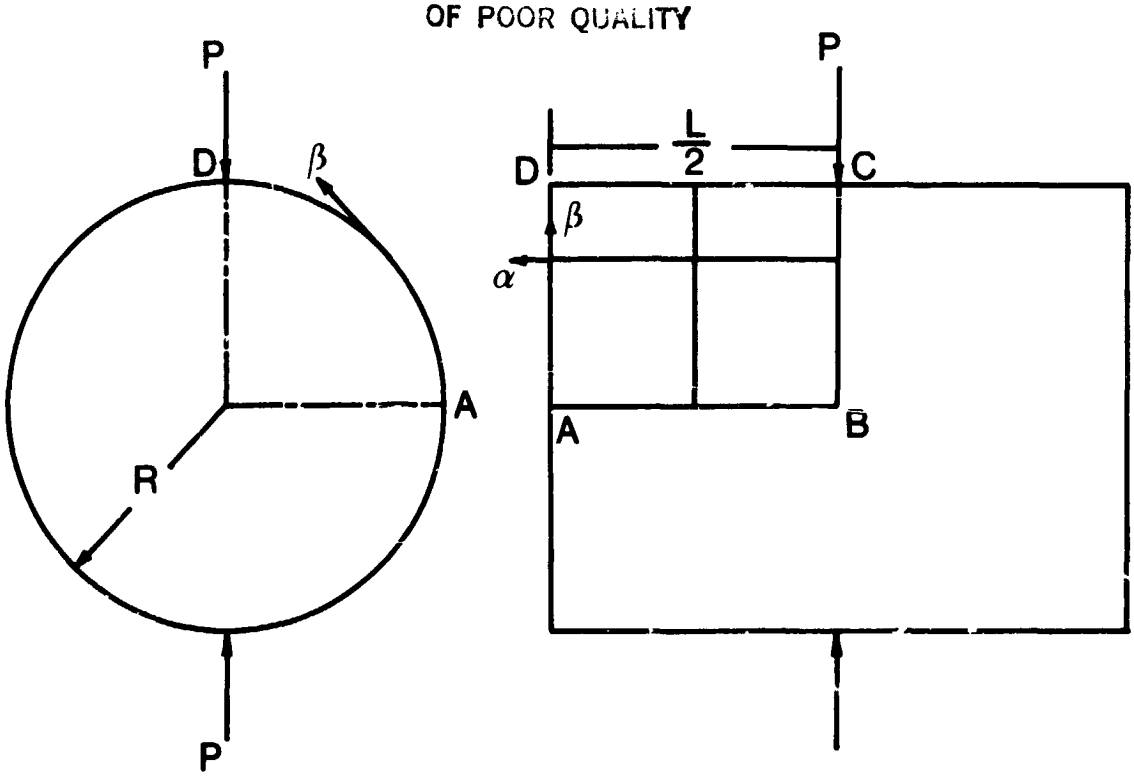

Figure 4. A pinched cylindrical shell.

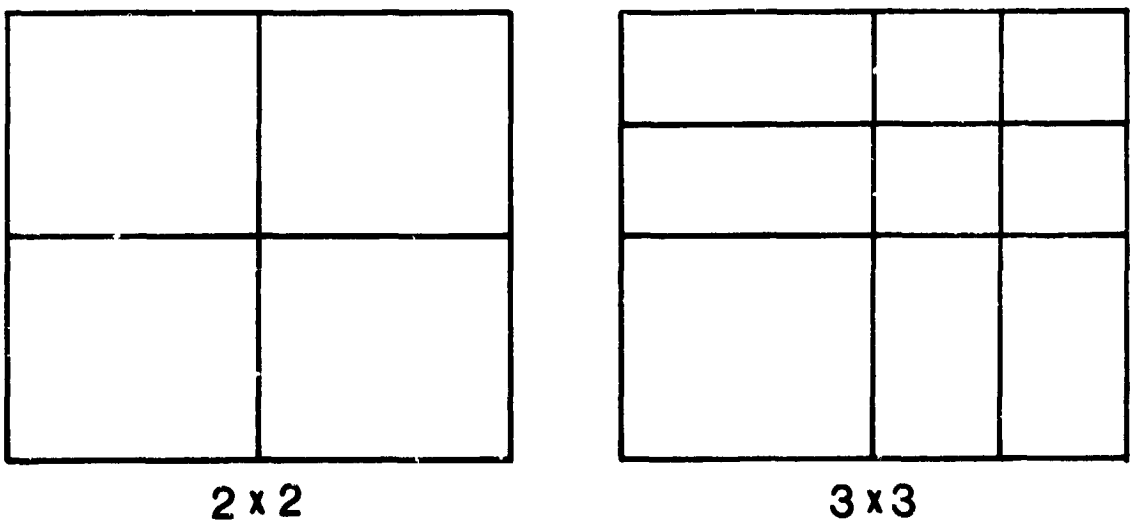

Figure 5. Finite-element meshes for cylindrical shell.

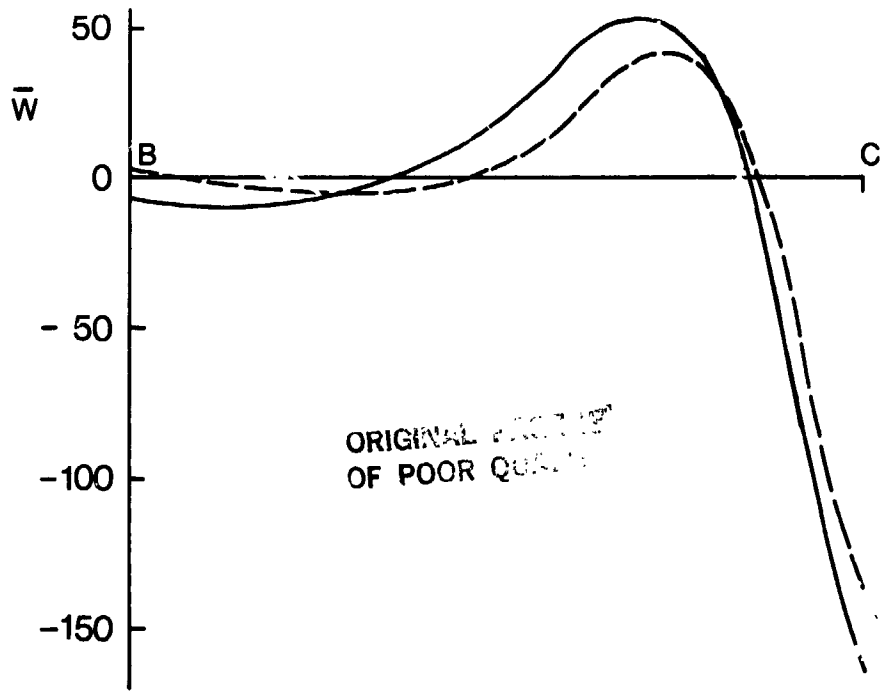

Figure 6. The deflection $\bar{w}$ along BC (cylindrical shell).

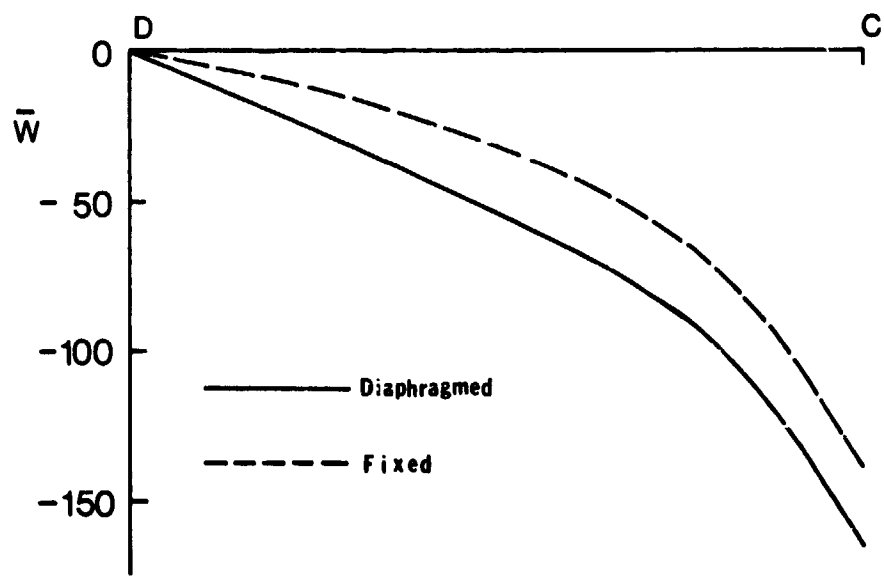

Figure 7. The deflection $\bar{w}$ along DC (cylindrical shell).

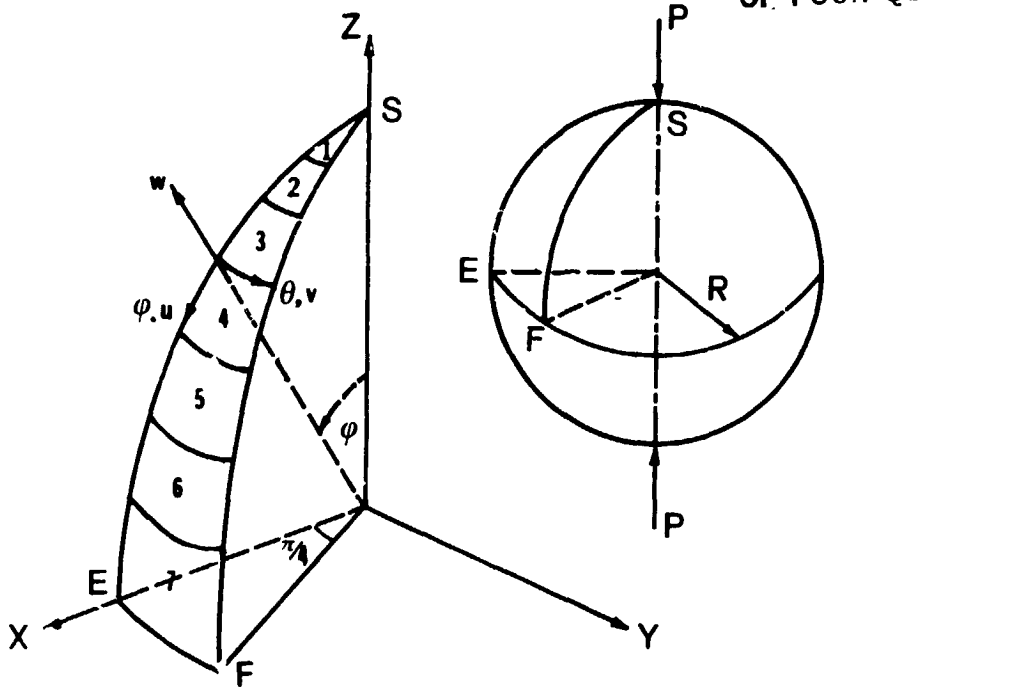

Figure 8. Pinched spherical shell.

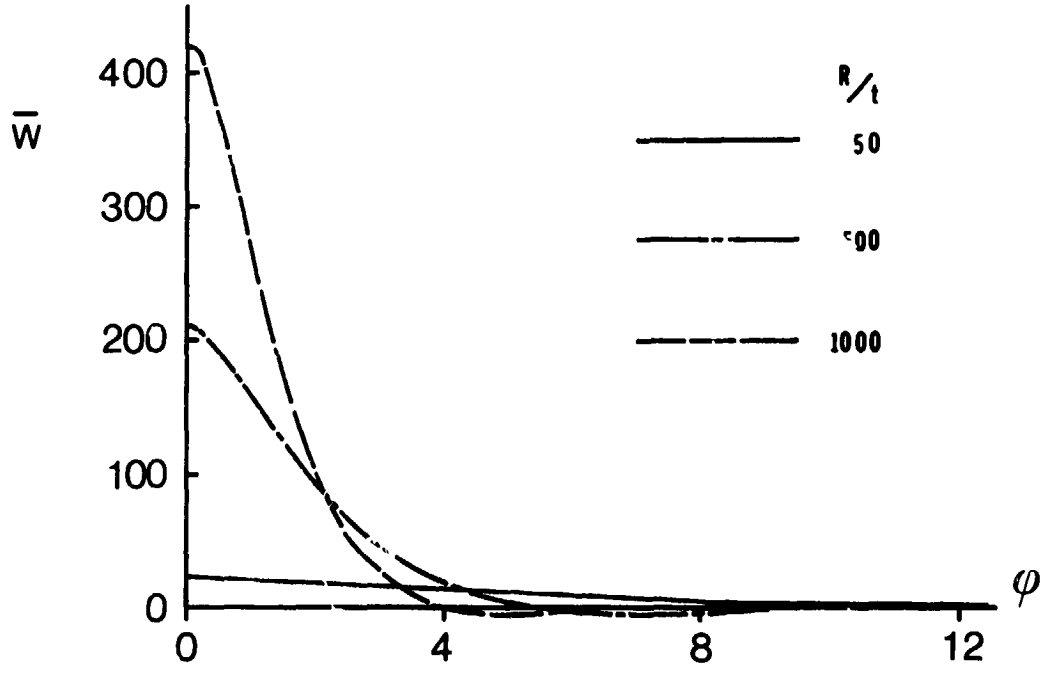

Figure 9. Nondimensional normal deflection $\bar{w}$ along ϕ for pinched spherical shell.

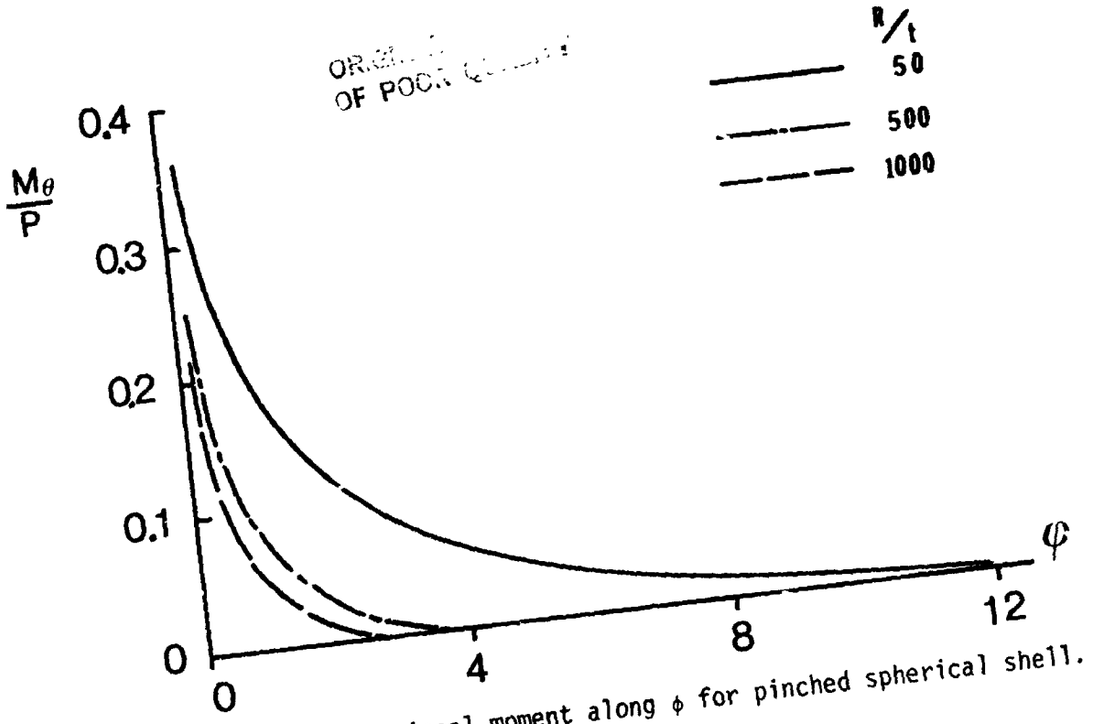

Figure 10. Nondimensional moment along ϕ for pinched spherical shell.

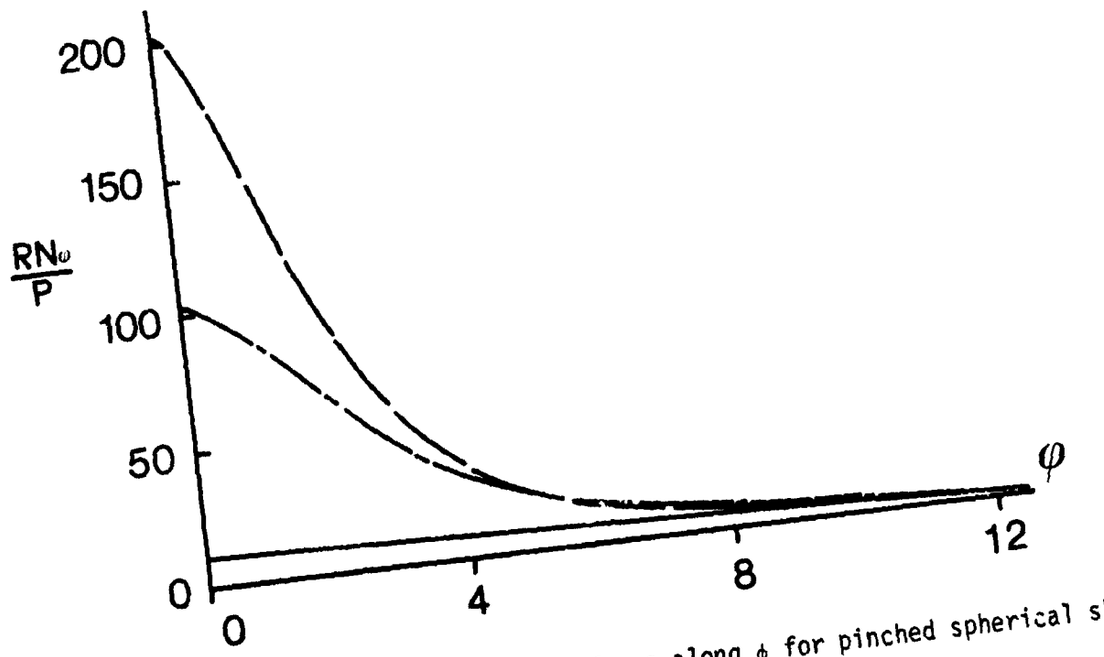

Figure 11. Nondimensional inplane force along ϕ for pinched spherical shell.

N85 10387

INTERACTIVE GRAPHICS NONLINEAR CONSTRAINED OPTIMIZATION*

Victor E. Saouma
Assistant Professor

Efthimios S. Sikiotis
Graduate Student

Dept. of Civil Engineering
University of Colorado, Boulder CO 80309

SUMMARY

An interactive computer graphics environment is used to perform non linear constrained optimization analysis. It is found that by combining the power of a digital computer with the subtlety of Engineering judgment during program execution, final results can be substantially better than the ones achieved by the numerical algorithm by itself.

INTRODUCTION

During its early development stage, great expectation was placed on structural optimization techniques. However, after almost twenty years of development [1], most engineers would agree that only limited success has been achieved. This can only be partly explained by the inherent complexity of the optimization formulation arising in practical structural design. Another important reason has been our approach to the problem and the working environment in which our numerical algorithms have been put to work. As such, one could hardly expect any substantial or quantum improvement in our optimization techniques, unless a radically new approach is followed.

A very promising new "discipline" is Artificial Intelligence (AI) [2]. It is anticipated that ultimately AI could produce robust and reliable expert systems which would blend mathematical formulation with Engineering Judgment and Experience in a single numerical code. Unfortunately, and despite some initial success, much work is yet to be performed before AI and structural optimization can be integrated into a comprehensive program for the analysis/design of engineering structures.

*This research has been supported by NSF Grant No: CEE-8405621 to the University of Colorado, Boulder.

Short of using AI, and as an alternative to the "black box" environment in which most, if not all, numerical alogorithms have been confined (during execution), it is proposed to take advantage of the rapidly developing techniques and hardware of computer graphics to enable the user to interact with the program. In this working environment, powerful optimization techniques can be "guided" by and combined with engineering judgment which shall always remain an integral part of structural design.

ADVANTAGES OF INTERACTIVE OPTIMIZATION

The interior penalty function, or SUMT (Sequential Unconstrained Minimization Technique) is based on the transformation of an objective function U(x) into an "augmented" objective function F({x}) such that:

$$F(\{x\},r) = U(\{x\}) + r \sum_{j=1}^{m} G(g(\{x\}))$$

where g({x}) are the inequality constraints. The function G is selected such that, if minimization is performed for a sequence of values of r, the solution will be forced to converge to that of the constrained problem. The factor r performs the weighting between the (real) objective function and the penalty term; it is called the response factor [3]. From this brief description of SUMT, it is apparent that its success would greatly depend on the judicious choice of: 1) the penalty function; 2) the initial response factor value; 3) the subsequent reduction of the response factor; and 4) the initial design point. Despite numerous attempts, there has not yet been any conclusive and general recommendation for the selection of these four parameters. As such the SUMT would greatly benefit from a working environment in which parametric studies could easily be performed, tested and evaluated and the best combination of parameters for a given problem easily identified.

Typically an optimization algorithm would scan a very large design space. It is expected that a good part of this search is spent in that portion of the design space which is mathematically feasible but practically unrealistic. By providing the design engineer with the capability to continuously monitor the program execution (through real time graphical displays of variables, constraint equations, and cost versus iterations), we would enable him to instantaneously use his Engineering Judgment, Experience, and why not intuition, to interrupt execution, "pull back" the design variables to a feasible and realistic region, and finally resume execution. As such computational time and efficiency might very well be enhanced.

PROGRAM ALGORITHM

IGNOP -Interactive Graphics Nonlinear Optimization Program- has been written with the above considerations in mind. In using the well known and proven interior penalty method [3,4,5] it certainly does not pretend to be an innovative optimization code per se. However it differs drastically from most, if not all, previous codes because it "liberates" the penalty method from the "black box" in which it has been confined, and enables it to communicate directly with the user.

The algorithm and execution mode of IGNOP are best described in conjunction with its detailed flow chart, Figure 1.

1. The program initially reads data from a disk file which includes the design variables and complete problem definition. Default values will be assigned if needed, and subsequently the user could overwrite any of these variables.

2. Initialize the graphical device and set default values to the attributes of the graphical displays (segments). The initial ranges of the x and y variables in the graphs are also defined here. There will be one arithmetic plot for each variable and one semi-logarithmic plot for each constraint inequality. Those plots are all with respect to number of iterations within a given unconstrained minimization process.

3. Set the upper and lower limits for each of the constraints in terms of user defined input data, and in accordance with the appropriate design code.

4. Check the initial design to make sure that it is a feasible one (as required by the interior penalty method).

5. If initial design is unfeasible, enable the user to modify it.

6. Through subroutine UREAL, evaluate the real objective function.

7. Through subroutine CONST, evaluate the inequality constraints.

8. Compute the initial value of the response factor by forcing the augmented objective function to be twice the initial real objective one.

9. Display the initial control page, Figure 2. It consists of 26 menus, 19 of them being detectable with a light pen. This control page is the one displayed during the numerical optimization. It would not only indicate the various graphs (discussed in 2), but also the iteration number, the unconstrained minimization number, the objective function values (both real and augmented), their variation

with respect to the previous iteration, the initial and current reduction factor, and the penalty function used. Also displayed are menu entries which would enable the user to interrupt, resume, or scan previous analyses.

10. At this stage IGNOP waits for a menu item to be picked up. When this is done, execution will then be transferred to any one of steps 11 to 23 and return subsequently to this one.

11. Problem definition, Figure 3. The "global" structure (as opposed to the structural element whose design is to be optimized) to be analysed is plotted, in this case a partially prestressed concrete beam. Also displayed are the material properties, costs, and design requirements. Any one of these values can be altered at any time.

12. Constraint inequalities limits, Figure 4. The upper and lower limits of each one of the behavior inequality constraints are displayed. These limits have been computed in step 3. By giving the user the possibility to overwrite those values, we are providing him with the capability to artificially "release" some of the constraints for a particular parametric study. This could easily be achieved by setting very large upper limits for a constraint, thus making sure that it will not be active or will not be the controlling one in the final design.

13. Design Geometry, Figure 5. The structure, the design of which is to be optimized, is graphically displayed along with all its dimensions (which constitute the variables) and some cross sectional properties. This would enable the user to inspect at any time the current design attempted by IGNOP, and if need be, directly alter it. Subsequent analysis resumption would then use the altered design. This is certainly one of the most interesting features of the program.

14. Design Evaluation, Figure 6. For each of the constraints, this would indicate their current value (such as stress, deflection, or others), their upper or lower allowable limit (as set by 12), and their PHI(x) ratio. This is an indication of the extend to which this constraint controls the design. A very small positive ratio indicates that the design is very close to this particular constraint, and a negative one implies that the constraint is being violated.

15. The user can select any of the three available penalty functions $G(g(\{x\}))$. These functions are :

a) $\dfrac{1}{g(\{x\})}$ b) $\dfrac{1}{g^2(\{x\})}$ c) $-\log [g(\{x\})]$

16. INTERRUPT. This menu item provides the capability to interrupt the program during the unconstrained minimization portion of IGNOP

and modify or simply inspect some of the optimization parameters and the design variables.

17. REVIEW. Any of the previous designs can be reviewed since all the intermediary data are saved in a disk file. This makes it possible to retrieve, examine and restart from any previous design.

18. RESET would reset the charts to their initial range.

19. A hard copy of the screen's contents may be obtained, if appropriate hardware is available.

20. We can zoom in a particular part of the display if more detailed information is needed.

21. Help can be obtained at any stage of the execution.

22. Again using the light pen we can modify the penalty function variables; i.e., maximum number of iterations, maximum number of penalty function evaluations, reduction factor, response factor, and others.

23. RESUME. Resume will start the optimization procedure or restart it should it have been previously interrupted.

24. Subroutine ZXMIN is a routine of the IMSL library [6] which performs the unconstrained minimization of the augmented objective function. It internally calls FUNCT which defines the augmented objective function in terms of the nine design variables.

25. Subroutine FUNCT evaluates the augmented objective in terms of the m constraint functions and controls the display of the data and the charts. This subroutine provides the critical link between IGNOP and a specific application. Thus the program is not written specifically for one particular problem, but rather to any one which can be mathematically formulated as a nonlinear constrained optimization design.

26. Subroutines UREAL and EQUAL evaluate the objective function and the equality constraints.

27. The augmented objective function is then evaluated.

28. The next step is to update some of the values displayed on the screen, such as current cost, current penalty term, number of iterations performed so far, current value of the augmented objective function, and their percentage change from the previous iteration.

29. The program makes a call to subroutine CHARTS which will update the graphs already on display using the data obtained from the last optimization iteration.

30. At this point the program will transfer the execution back to step 24 (ZXMIN) or if interrupt has been previously specified it will go on to the next step.

31. This step is the same as step 10 where the user is prompted to decide about the direction of the execution.

32. Any of the functions 11-23 that were mentioned previously can be accessed at this point. RESUME will restart the optimization procedure; otherwise, the program will wait for further instructions.

EXAMPLE PROBLEM

The general program that is described above has been applied to a particular problem, the optimization of partially prestressed, simply supported, uniformly loaded concrete beams, Figure 7. The problem has been formulated in terms of nine design variables and nineteen constraints. The cross section of the beam can have a general I shape with six geometrical variables and three areas of reinforcement, prestressed and non prestressed (top and bottom). It is assumed that for maximum efficiency the tendon eccentricity takes its largest allowable value at mid-span and that the initial prestressing force (after prestress transfer) is also at its maximum allowable value of 0.70 fpu (ACI 318-77 [7]).

The nineteen constraints are divided into two categories, ten behavior constraints and nine practical or geometrical constraints. The behavior constraints are the maximum compressive and tensile stresses in concrete at the initial and service stage (a total of 4 constraints, the initial camber, the dead and live load deflection, the ultimate and cracking moment capacity and the shear stress). The other nine constraints impose a lower limit on the values of the nine design variables. The objective function to be minimized is the total cost of the beam, which includes cost of concrete, cost of prestressed and non prestressed reinforcement and cost of forming. Both the objective function and the constraints are highly nonlinear functions. A detailed discussion and a derivation of the constraint equations can be found in reference [8] which was a batch implementation of this particular problem.

To assess the advantages of interactive optimization, an example design problem [9] was analysed through both batch and interactive method. Table 1 gives a complete description of the beam shown in Figure 7. Table 2 has the original design taken from reference [9], and shows the results obtained by the two approaches. It should be noted that the indicated batch solution was selected among numerous trials in which various combinations of parameters were tried, and this particular one gave the lowest cost. In this case, the initial response factor was such that the objective function was twice the penalty term, the reduction factor was 0.05, and the penalty function

used was 1/g(x). The interactive optimization was performed by primarily:

a) Moving designs from what appeared to be "unpractical" portions of the design space.

b) Accelerating the convergence by ncting trends in the optimization solution. In many instances it was clear that through numerous succesive iterations, one particular variable was monolithically converging by very small increments. This prompted the user to accelerate this trend by direcly assigning a larger/smaller value f`r this variable.

c) Trying and modifying various SUMT parameters. Two penalty functions were used along with a variety of response factors.

It should be noted that through numerous analyses, the user ended up having a "feeling" or intuition for the optimization process and trends. Though it seldom had any physical or engineering justification, it played a non-negligible role in the final design process.

By inspecting table 2 and the accompanying final designs in Figure 8, one can conclude that:

1) Interactive optimization yielded better results than batch ($4,034 versus $4,509) in designing a beam which would have cost $5,109 according to [9]

2) The design obtained interactively is "superior" to the one obtained by batch optimization (note the unpractical and inneficient bottom flange size in Figure 8.b)

PROGRAM IMPLEMENTATION

IGNOP is a highly modular program written in 18 subroutines and approximately 6,000 FORTRAN 77 executable statements. Through subroutine FUNCT and UREAL it can be linked to virtually any design problem which can be formulated mathematically as a nonlinear optimization minimization. (However, minor adjustments to some of the graphical displays would have to be made.) The graphics is supported by a device independent, Core based, graphical package (DI 3000) [10]. Thus IGNOP could be transportable to virtually any graphical device and system. Currently this program is running on an Apollo DN 300 workstation.

FUTURE EXTENSION

This research program shall be extended to include other

applications and to further take advantage of interactive graphics optimization.

Programs like IGNOP should have great potential in automotive and aerospace structural designs. The authors would greatly appreciate if, through this conference, such practical applications are brought to their attention.

Another feature of IGNOP and of most optimization programs is that literally hundreds of analyses are performed, and their results are only temporarily used and never saved. In practice, we know that numerous attempts are made before a final design is finally selected. This should prompt us to take further advantage of those analyses by keeping their results in an extensive data base which should be continuously updated. At the very end, and only as a complement to our previous analyses, one could attempt to use interactive graphics to selectively and intelligently plot those data and attempt to find a better design.

CONCLUSION

An interactive graphics program for the constrained optimization of nonlinear structural problems has been developed. It is found that such an approach will yield not only more economical designs, but also better ones.

REFERENCES

1. Lev, O. (ed.), "Structural Optimization, Recent Developments and Applications", ASCE, New York, 1981.

2. Dym, C.L., "Expert Systems: New Approaches to Computer-Aided Engineering", 25th AIAA/ASME/ASCE/AHS Structures, Structural Dynamics and Materials Conference, Palm Springs, CA, May 14-16, Part I, pp. 99-115, 1984.

3. Kirsch, U., 'Optimum Structural Design", McGraw-Hill, N.Y., 1981.

4. Avriel, M., "Nonlinear Programming: Analysis and Methods", Prentice-Hall Inc., Englewood Cliffs, N.J., 1981.

5. Gallagher, R.H., and Zienkiewicz, O.C. (ed.), "Optimum Structural Design, Theory and Applications", John Wiley, 1973.

6. IMSL Reference Manual, 8th Ed., International Mathematical and Statistical Library, Houston, TX, 1980.

7. "ANSI/ACI 318-77, Building Code Requirements for Reinforced Concrete", American Concrete Institute, Detroit, Mich., 1977.

8. Saouma, V.E., and Murad, R.S., "Partially Prestressed Concrete Beam Optimization", Journal of Structural Engineering, Vol 110, No 3, Paper No 18678, March 1984, pp. 589-604.

9. Nilson, A.H., "Design of Prestressed Concrete", John Wiley, New York, 1978.

10. DI300 User's Manual, Release No. 4, Precision Visual Inc., Boulder Co, 1984.

SPAN LENGTH.....	24.4 m	(80.0 ft)
SUPERIMPOSED DEAD LOAD.....	595.3 Kg/m	(0.4 K/ft)
SUPERIMPOSED LIVE LOAD.....	1785.8 Kg/m	(1.2 K/ft)
DENSITY OF CONCRETE.....	2322.7 Kg/m3	(145 PCF)
CONCRETE STRENGTH (Fc').....	34.5 MPa	(5000 PSI)
TRANSFER CONCRETE STRENGTH (Fci).....	27.6 MPa	(4000 PSI)
CREEP COEFFICIENT.....	2.32	
PRESTRESS LOSS.....	15.0 %	
ALLOW. COMP. INITIAL STRESS.....	0.0041 Fci	(0.6 Fci)
ALLOW. TENS. INITIAL STRESS.....	0.25 sqrt(Fci)	(3.0 sqrt(Fci))
ALLOW. COMP. SERVICE STRESS.....	0.0031 Fci	(0.45 Fci)
ALLOW. TENS. SERVICE STRESS.....	1.0 sqrt(Fc')	(12.0 sqrt(Fc'))
YIELD STR. OF NON-PRES. REINF.....	413.7 MPa	(60 KSI)
TYPE OF PRESTRESSING STEEL.....	1723.7 MPa STRAND	(250 KSI)
PRES. TENDON CONFIGURATION	PARABOLIC	
MIN. CONC. COVER OF PRES. STEEL.....	20.3 cm	(8.0 IN)
MIN. CONC. COVER OF NON-PRES. STL.....	7.6 cm	(3.0 IN)
MAXIMUM ALLOWABLE CAMBER.....	-12.7 cm	(-5.0 IN)
MAXIMUM D.L DEFLECTION.....	15.2 cm	(6.0 IN)
MAXIMUM L.L DEFLECTION.....	7.6 cm	(3.0 IN)
COST OF CONCRETE.....	104.6 $/m3	(80.0 $/CU.YD)
COST OF FORMING.....	21.5 $/m2	(2.0 $/FTSQ)
COST OF PRESTRESS STEEL.....	2.8 $/Kg	(1.28 $/LB)
COST OF NON-PRESST. STEEL.....	0.8 $/Kg	(0.37 $/LB)

Table 1. Characteristics of Example Problem

DESIGN VARIABLES	INITIAL	OPTIMIZED BATCH	OPTIMIZED INTERACTIVE
Top fl. width	177.8 cm (70.0 in)	185.6 cm (73.09 in)	101.6 cm (40.0 in)
Top fl. depth	15.2 cm (6.0 in)	10.3 cm (4.07 in)	12.7 cm (5.0 in)
Bot fl width	----------	29.5 cm (11.63 in)	----------
Bot fl depth	----------	10.1 cm (7.52 in)	----------
Web width	5.6 cm (14.0 in)	25.9 cm (10.18 in)	25.4 cm (10.0 in)
Total depth	121.9 cm (48.0 in)	146.1 cm (57.52 in)	134.6 cm (53.0 in)
Pres stl area	31.6 cm2 (4.9 in2)	22.9 cm2 (3.55 in2)	20.8 cm2 (3.23 in2)
Tens stl area	12.9 cm2 (2.0 in2)	4.1 cm2 (0.64 in2)	11.3 cm2 (1.75 in2)
Comp stl area	3.2 cm2 (0.5 in2)	6.0 cm2 (0.93 in2)	3.2 cm2 (0.5 in2)
Active Constraint	Compressive stress, initial	Ultimate Moment	Ultimate Moment
Total cost $	5109	4509	4034

Table 2. Comparison of Design Results

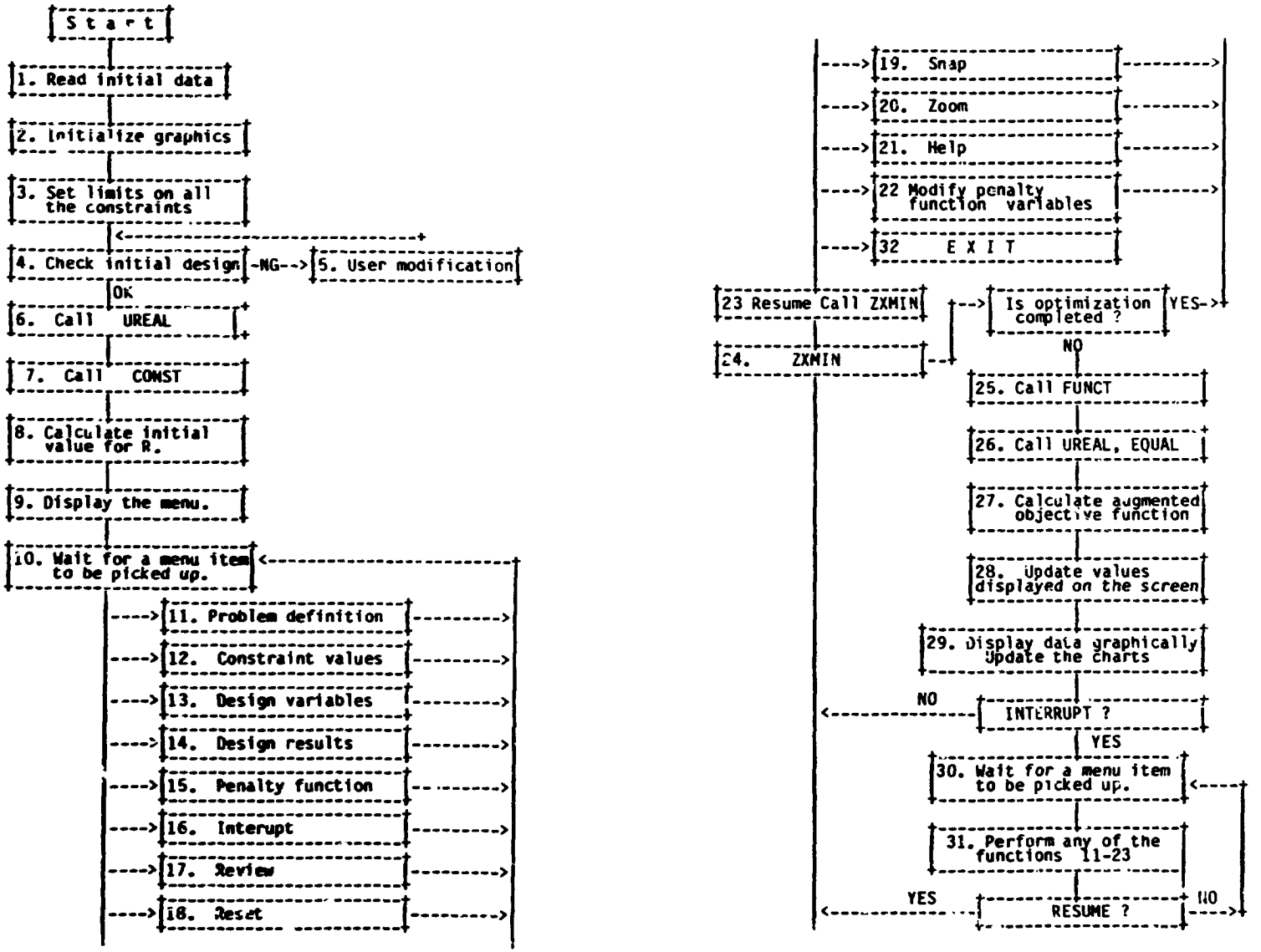

Figure 1. IGNOP Flowchart

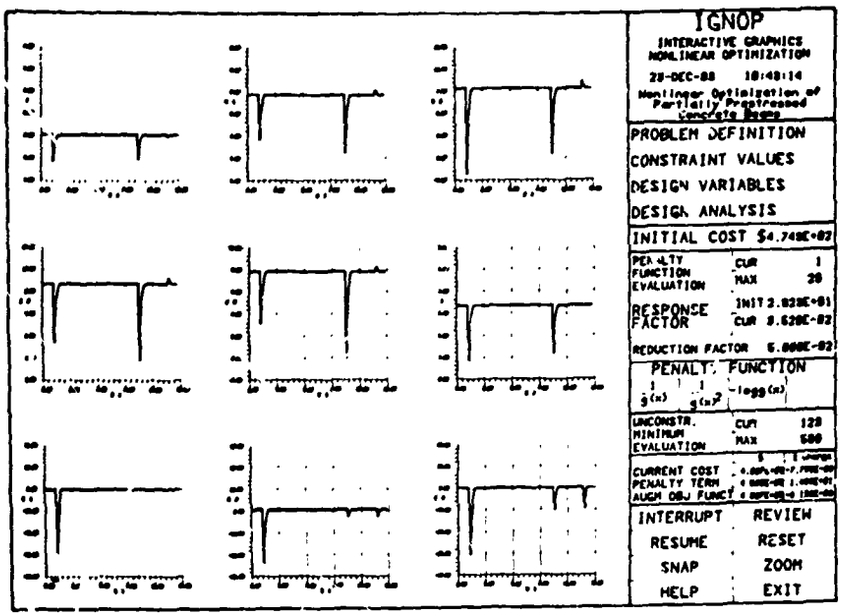

Figure 2. Control Page

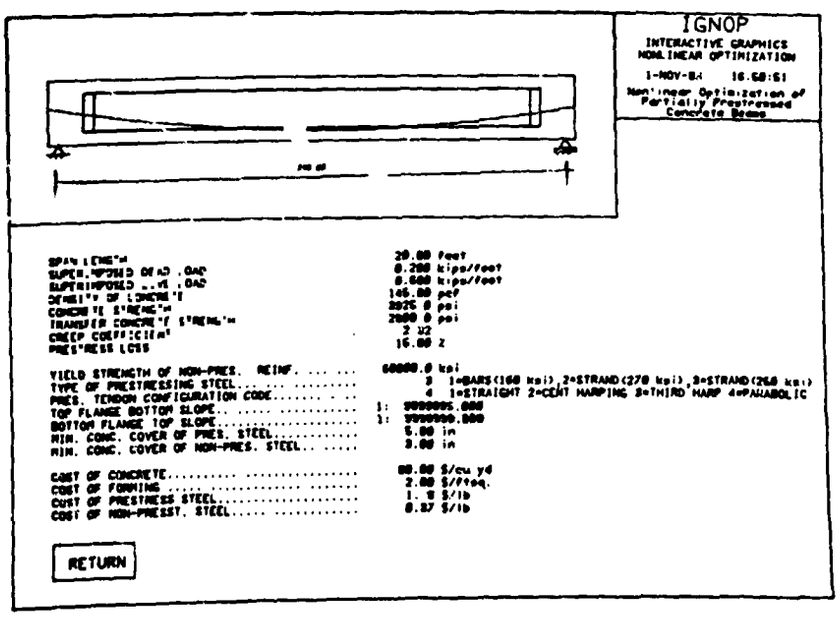

Figure 3. Problem Definition

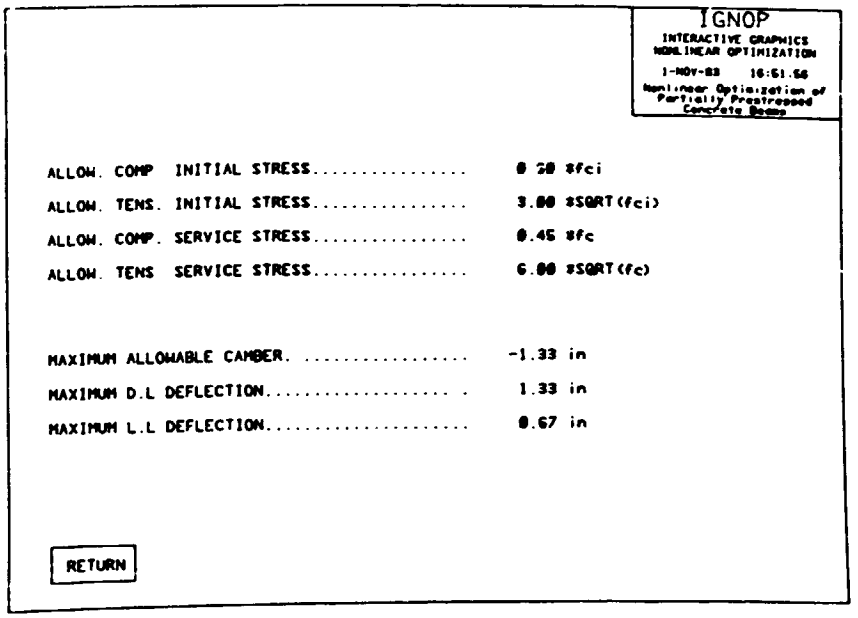

Figure 4. Constraint Inequalities Limits

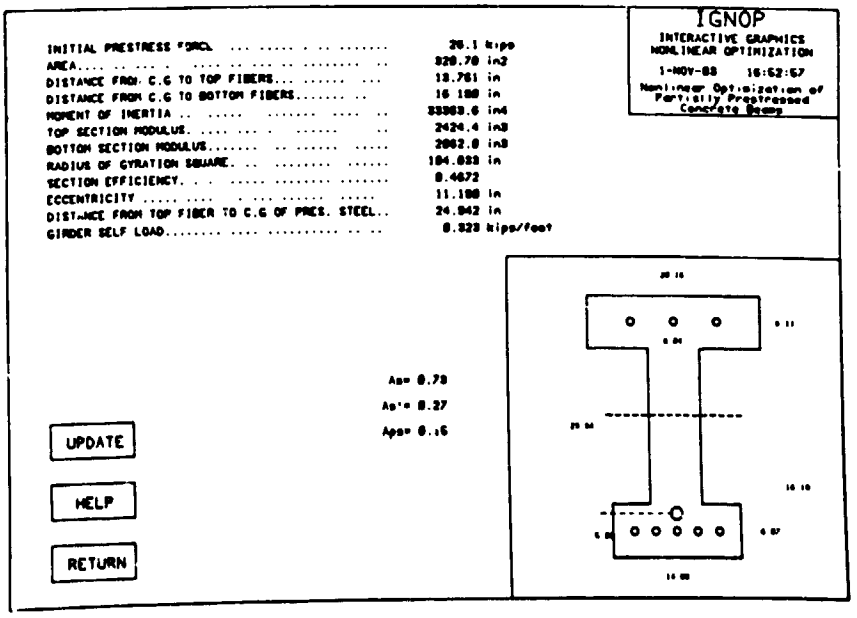

Figure 5. Design Geometry

IGNOP
INTERACTIVE GRAPHICS
NONLINEAR OPTIMIZATION
1-NOV-83 16:53 66
Nonlinear Optimization of Partially Prestressed Concrete Beams

INITIAL STAGE

TENSILE STRESS= -4.0814E+01 PSI
MAX. ALLOWABLE= 1.6875E+02 PSI
PHI= 0.1250+01

COMPRESSIVE STRESS= -1.2906E+02 PSI
MAX. ALLOWABLE= -1.6888E+03 PSI
PHI= 0.9230+00

SERVICE STAGE

TENSILE STRESS= -4.0868E-02 PSI
MAX. ALLOWABLE= 3.7508E+02 PSI
PHI= 0.6350+00

COMPRESSIVE STRESS= 0.3098E-03 PSI
MAX. ALLOWABLE= 1.7663E+03 PSI
PHI= 0.8610+00

INITIAL CAMBER
CAMBER= -4.8968E-03 IN
MAX. ALLOWABLE= -1.3333E+00 IN
PHI= 0.9960+00

DEAD LOAD DEFL.
DEFLECTION= 0.3098E-03 IN
MAX. ALLOWABLE= 1.3333E+00 IN
PHI= 0.9940+00

LIVE LOAD DEFL.
DEFLECTION= 1.7936E-02 IN
MAX. ALLOWABLE= 6.6667E-01 IN
PHI= 0.9730+00

CRACK./ULTIM. MOMENT
RATIO= 1.3401E+00
MIN. ALLOWABLE= 1.2000E+00
PHI= 0.1170+00

ULTIMATE MOMENT
ULTIMATE MOMENT= 2.7171E+02 K-FT
MAX. ALLOWABLE= 4.7188E+02 K-FT
PHI= 0.7330+00

SHEAR AT SPAN/4
RESISTING SHEAR AT L/4= 2.6231E+01KIPS
APPLIED SHEAR AT L/4= 1.0386E+01KIPSL
PHI= 0.1560+01

COST OR VOLUME= 4.2BE+02 $ OR CU-YD

RETURN

Figure 6. Design Evaluation

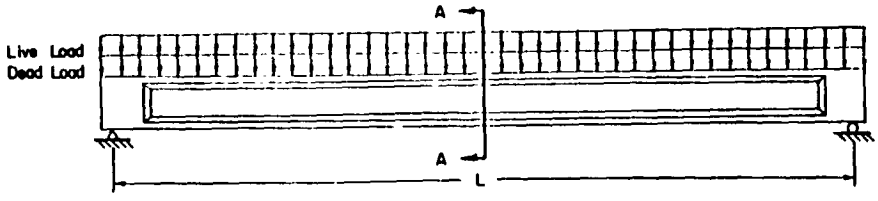

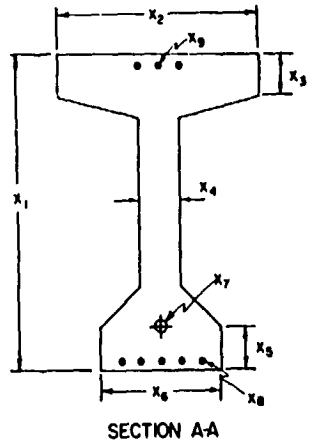

SECTION A-A

Figure 7. Example Problem

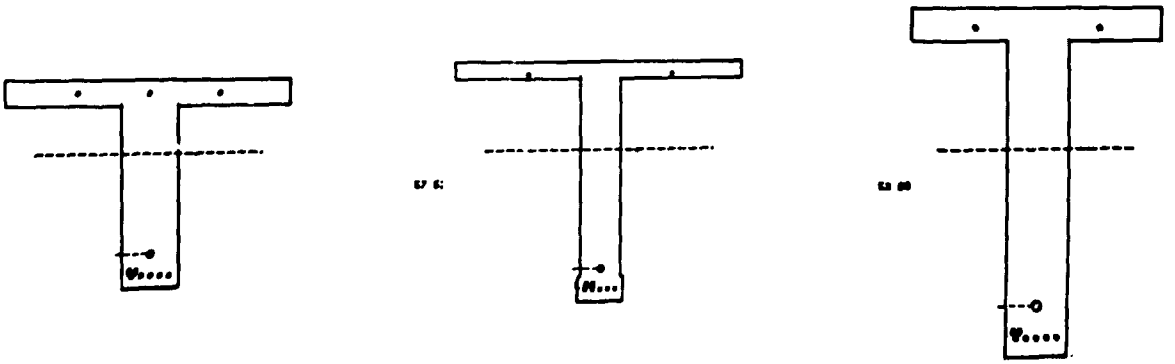

a. Initial Design [9]

b. Batch Optimization

c. Interactive Optimization

Figure 8. Final Designs

N85 10388

SENSITIVITY ANALYSIS OF LIMIT STATE FUNCTIONS FOR PROBABILITY-BASED PLASTIC DESIGN

Dan M. Frangopol

Department of Civil Engineering
University of Colorado, Boulder, Colorado 80309

SUMMARY

The evaluation of the total probability of a plastic collapse failure P_f for a highly redundant structure of random interdependent plastic moments acted on by random interdependent loads is a difficult and computationally very costly process. The evaluation of reasonable bounds to this probability requires the use of second moment algebra involving many statistical parameters. A computer program which selects the best strategy for minimizing the interval between upper and lower bounds of P_f is now in its final stage of development at the University of Colorado. For the purpose of investigating the relative importance of various uncertainties involved in the computational process on the resulting bounds of P_f, sensitivity analysis is used. Numerical examples are provided to illustrate response sensitivities for both mode and system reliability of an ideal-plastic portal frame.

BACKGROUND

As stated recently by Ellingwood and Galambos (ref. 1) "The development of probability-based limit states design has been motivated by a desire to quantify performance of structures and to treat uncertainties in loads, resistances and analysis in a more rational way". In probability-based limit states design probabilistic methods are used to guide the selection of statistical parameters which account for the different uncertainties underlying the various loads and strengths and give the desired level of risk against occurrence of each limit state of interest. The probability of failure (unfavorable performance) is used as a consistent measure of the level of risk. This probability has an absolute meaning (ref. 2) - "the likelihood of occurrence of some predefined limit state"; it may be a serviceability limit state (e.g., excessive deflection or rotation, initial yielding) or an ultimate limit state (e.g., partial or total collapse, instability). Since there is less danger of loss of life, a higher probability of occurrence may be tolerated for serviceability limit states than in the case of ultimate limit states (ref. 3).

The conceptual framework for probability-based limit states design is provided by the classical theory of structural reliability which is based on full-distribution procedures (refs. 4-7). In this context, the loads and resistances are assumed to be random variables and the probability of failure for the limit state of interest can be computed on the basis of assumed distribution functions.

Consider first a limit state which contains only two random variables R and Q. If R is the resistance of a structural member in this limit state, Q is the load effect (dimensionally consistent with R), and if R and Q are statistically

independent, then the probability that the limit state will be reached (probability of failure) P_f is computed as

$$P_f = P(R \leq Q) = \int_0^\infty F_R(q) f_Q(q) dq \qquad (1)$$

in which $P(R \leq Q)$ = probability of the failure event $(R \leq Q)$, $F_R(\cdot)$ = the cumulative probability distribution function of the resistance, and $f_Q(\cdot)$ = the probability density function of the load effect.

If both the resistance and the load effect are assumed to be normally (Gaussian) or lognormally distributed, P_f can be readily determined from standard tables. For other distributions a numerical integration is required to determine P_f.

In general, a limit state expression contains more than two random variables. As examples, consider the superposition of stresses in the beams or columns of a building due to gravity and wind loads, the total yield force of bars in a section of a concrete beam, and the ultimate capacity of a high-strength bolted connection. Therefore, R and Q are usually functions of other basic random variables

$$R = R(R_1, R_2, \cdots, R_m) \qquad (2.a)$$

$$Q = Q(Q_1, Q_2, \cdots, Q_n) \qquad (2.b)$$

Then, the limit state equation, which represents the boundary between the safe and failure regions, can be described in terms of a finite set of basic variables

$$g(X) = g(R_1, R_2, \cdots, R_m, Q_1, Q_2, \cdots Q_n) = 0 \qquad (3)$$

where R_i and Q_j indicate a basic resistance and load variable, respectively, and the vector X relates all these variables. The expression (3) is called the limit state surface, function or equation. By convention failure is said to occur when

$$g(X) \leq 0 \qquad (4)$$

The probability of failure P_f is the probability content of the failure domain $D = [g(X) \leq 0]$,

$$P_f = \int_D f_X(r_1, r_2, \cdots, r_m, q_1, q_2, \cdots q_n) dx \qquad (5)$$

in which $f_X(\cdot)$ is the joint density function of $R_1, R_2, \cdots, R_m, Q_1, Q_2, \cdots, Q_n$ and $dx = dr_1\, dr_2 \cdots dr_m\, dq_1 dq_2 \cdots dq_n$.

If the m+n basic variables are statistically independent, the probability of failure (5) can be written as the product of all the individual density functions $f_{R_i}(r_i)$ and $f_{Q_j}(q_j)$. Thus, the failure probability (equation 5), becomes

$$P_f = \int_D f_{R_1}(r_1) f_{R_2}(r_2) \cdots f_{R_m}(r_m)\, f_{Q_1}(q_1) f_{Q_2}(q_2) \cdots f_{Q_n}(q_n)\, dx \qquad (6)$$

Notice that the assumption of independence is not restrictive since any set of dependent variables can be transformed into a vector with independent components (ref. 8).

As is well known (refs. 9 and 10), because of scarcity of statistical data it is usually impossible to construct the joint density function $f_X(\cdot)$ associated with equation (5) and/or to determine each of the individual density functions associated with equation (6). Even in the case where statistical information may be sufficient to determine these functions, it is often impractical if not impossible to perform numerically the multidimensional integration over the failure domain D in order to evaluate P_f (refs. 3 and 11).

The difficulties outlined above have motivated the development of various approximate reliability methods. The present approaches take their origin in three papers published in 1969 by Cornell (refs. 12 to 14). The two central ideas underlying the theoretical basis of the method proposed by Cornell are: (a) the use of only first and second moments to characterize the entire set of random variables (R_1, R_2, $\cdots$, R_m, Q_1, Q_2, $\cdots$ Q_n), and (b) the linearization by means of a Taylor series expansion (truncated at the linear terms only) of the limit state function g(X) at some appropriate checking point (also called design point) $x^\circ = (r_1^\circ, r_2^\circ, \cdots, r_m^\circ, q_1^\circ, q_2^\circ, \cdots q_n^\circ)$ yielding a linear function $g_0(X) = g_0$ to be used in place of g(X) for purposes of performing the reliability analysis. The measure of reliability associated with a particular limit state i is given by the reliability (safety) index β_i, which is the reciprocal of the coefficient of variation of the linear function g_0:

$$\beta_i = \bar{g}_0/\sigma(g_0) = 1/V(g_0) \qquad (7)$$

in which $\bar{g}_0$ = mean value of $g_0(X)$, $\sigma(g_0)$ = standard deviation of $g_0(X)$, $V(g_0)$ = coefficient of variation of $g_0(X)$.

By linearizing the function g(X) at the mean values of the variables, as suggested in earlier first-order second-moment (FOSM) methods, in truncating the Taylor series expansion of the limit state expression (3) at the first-order (linear) terms, $\bar{g}_0$ and $\sigma(g_0)$ then are obtained as:

$$\bar{g}_0 = g(\bar{R}_1^\circ, \bar{R}_2^\circ, \cdots, \bar{R}_m^\circ, \bar{Q}_1^\circ, \bar{Q}_2^\circ, \cdots, \bar{Q}_n^\circ) = \bar{g} \qquad (8)$$

$$\sigma(g_0) = \left[\sum_{i=1}^{m} (\partial g/\partial R_i)_0^2\, \sigma^2(R_i) + \sum_{k=1}^{n} (\partial g/\partial Q_k)_0^2\, \sigma^2(Q_k)\right]^{1/2} \approx \sigma(g) \qquad (9)$$

in which $(\partial g/\partial R_i)_0$ and $(\partial g/\partial Q_k)_0$ indicate that the derivatives are evaluated at the checking point x° of coordinates ($\bar{R}_1^\circ$, $\bar{R}_2^\circ$, $\cdots$, $\bar{R}_m^\circ$, $\bar{Q}_1^\circ$, $\bar{Q}_2^\circ$, $\cdots$, $\bar{Q}_n^\circ$). Note that equation (9) is valid for statistically uncorrelated R_i and Q_k. More

generally, correlation among resistances variables R_i and load-effect variables Q_k, and independence among resistances and load-effect variables will lead to:

$$\sigma(g_0) = \Big[\sum_{i=1}^{m} (\partial g/\partial R_i)_0^2\, \sigma^2(R_i) + 2\sum_{i=1}^{m}\sum_{j=i+1}^{m} (\partial g/\partial R_i)_0\, (\partial g/\partial R_j)_0\, \mathrm{cov}\,(R_i, R_j)$$

$$+ \sum_{k=1}^{n} (\partial g/\partial Q_k)_0^2\, \sigma^2(Q_k) + 2\sum_{k=1}^{n}\sum_{\ell=k+1}^{n} (\partial g/\partial Q_k)_0\, (\partial g/\partial Q_\ell)_0\, \mathrm{cov}\,(Q_k, Q_\ell)\Big]^{1/2} \approx \sigma(g) \tag{10}$$

in which $$\mathrm{cov}(R_i, R_j) = \overline{R_i R_j} - \overline{R}_i \overline{R}_j = \sigma(R_i)\, \sigma(R_j)\, \rho(R_i, R_j) \tag{11.a}$$

$$\mathrm{cov}(Q_k, Q_\ell) = \overline{Q_k Q_\ell} - \overline{Q}_k \overline{Q}_\ell = \sigma(Q_k)\, \sigma(Q_\ell)\, \rho(Q_k, Q_\ell) \tag{11.b}$$

are the covariances among resistances variables and among load-effect variables, respectively, and $\rho(X_i, X_j)$ is the correlation coefficient between X_i and X_j.

This approximate technique sometimes yields excellent agreement with the exact solution $\beta_i = \overline{g}/\sigma(g)$. Notice that if g(X) is linear, equation (8) is exact, $\overline{g} = \overline{g}_0$, and equations (9) and (10) are also exact, $\sigma(g) = \sigma(g_0)$, for independent and correlated variables, respectively.

A serious drawback of the earlier FOSM methods is that the checking point represented by the mean values of the variables may not be informative for reliability evaluation of nonlinear limit state functions since significant errors may be introduced in approximating g(X) by the linearized form $g_0(X)$ (refs. 3, 8, 11 and 15). Furthermore, the use of mean-value point as linearization point fails to be invariant with respect to the reliability index for equivalent formulations of the same limit state failure event (i.e., $R - Q < 0$, $\ell n\,(R/Q) < 0$, $R/Q < 1$), (ref. 16). These two inconveniences (lack of accuracy for nonlinear limit state functions and lack of invariance) may be circumvented by selecting an appropriate checking point x^* and by obtaining a better approximation to the limit state surface at the design point. The selection procedure, which is one of the key considerations for improving the FOSM results, can be made by using one of the so-called advanced first-order second-moment (AFOSM) methods (e.g., Rackwitz iterative procedure (ref. 17)). Improved estimates of the probabilities of failure have been suggested for highly nonlinear limit states by approximating the limit state surface by a quadratic (instead of linear) surface at the design point (refs. 18 and 19). The approximation is such that the two surfaces have the same tangent hyperplane and second order derivatives at the design point. More accurate approximations are available if higher order terms are retained (ref. 20). However, these approximations are not computationally simple.

A review of the AFOSM methods was recently presented by Shinozuka (ref. 9), who also proposed a Lagrange multiplier formulation for evaluating the reliability index β and locating the checking point on the limit state surface. According to this formulation, the point on the limit state surface defined in the space of reduced (standardized) variables

$$X_i' = (X_i - \overline{X}_i)/\sigma(X_i) \tag{12}$$

with the minimum distance to the origin is the most probable failure point (point of maximum likelihood) if Gaussian variabilities are assumed. As a practical alternative to other methods, Shinozuka recommended the use of the most probable failure point as checking point even in the case of non-Gaussian variabilities.

The FOSM and AFOSM methods mentioned above give values of the reliability index β which sometimes may be directly related to the probability of failure P_f. For example, if R and Q are normal and statistically independent variates, then the probability of failure is

$$P_f = \Phi\left[-\frac{\overline{R} - \overline{Q}}{\sqrt{\sigma^2(R) + \sigma^2(Q)}}\right] = \Phi\left[-\beta_0\right] \tag{13}$$

in which $\Phi[\cdot]$ = the standardized normal distribution function. Similarly, if R and Q are lognormal variates, then P_f is

$$P_f = \Phi\left\{-\frac{\ell n\left\{\frac{\overline{R}}{\overline{Q}}\left[\frac{1 + V^2(Q)}{1 + V^2(R)}\right]\right\}^{1/2}}{\left\{\ell n[(1 + V^2(Q))(1 + V^2(R))]\right\}^{1/2}}\right\} = \Phi\left[-\beta_1\right] \tag{14}$$

In such cases, the reliability index β (denoted above by β_0 for normal variates, and β_1 for lognormal variates) is related to P_f through

$$\beta = -\Phi^{-1}\left[P_f\right] \tag{15}$$

in which $\Phi^{-1}[\cdot]$ = the inverse standardized normal distribution function.

In the absence of information as to the type of probability distribution of R and Q, the reliability index β is a useful measure of safety; the larger the β the smaller the probability of unsatisfactory performance P_f. In such cases, the failure probability in the i-th failure mode is usually approximated by

$$P_{f_i} \approx \Phi[-\beta_i] \tag{16}$$

in which β_i is the shortest distance between the origin and the limit state surface defined in the standard space of the reduced variables (12). In this manner, some guidance from equation (16) is available to relate the probability of failure to β when the probability laws of R and Q cannot be determined exactly.

LIMIT STATE PROBABILITIES OF STRUCTURAL SYSTEMS

Few structural problems of practical interest can be reduced to one failure mode problems. The individual failure modes are almost always possible failure

paths of a structural system so that additional probability analysis is required for an overall system reliability assessment. The general formulation of the overall system reliability of an m mode-of-failure structure is well known (refs. 5 to 7, 21 and 22) for both series and parallel systems.

A structure which belongs to the class of series (or 'weakest-link') systems will fail if any failure mode occurs. Then, the probability of failure of the system, P_f, can be written as

$$P_f = P(g_{system} \leq 0) = P[\bigcup_{i=1}^{m} (g_i \leq 0)] \tag{17}$$

where g_{system} is the system failure expression (or system safety margin) for an ideal series system, g_i is the i-th failure mode expression (mode safety margin), the event $g_{system} \leq 0$ represents the failure of the system, the event $g_i \leq 0$ means that the i-th failure mode has been realized, and U is the symbol of union of failure mode events. The equation $g_{system} = 0$ is denoted by the limit state function (or failure surface) of the system, and $g_i = 0$ is denoted by the limit state function of the i-th failure mode.

In contrast, an ideal ductile parallel (or 'fail-safe') system fails if all of its failure modes occur. Consequently, the probability of failure of the system, P_f, is

$$P_f = P(g_{system} \leq 0) = P[\bigcap_{i=1}^{m} (g_i \leq 0)] \tag{18}$$

where $\cap$ is the symbol of intersection of failure mode events ($g_i \leq 0$).

Many structures exhibit characteristics that are a combination of the series and parallel systems (refs. 23, 24, 25). For example, consider the steel ductile frame with its seven critical sections (1, 2, ..., 7) and ten possible collapse modes (a, b, ..., j) shown in Figure 1 (ref. 26). By considering rigid-plastic theory, assuming unlimited ductility for the critical sections of the structure and neglecting the influence of the axial load on the value of the plastic moment, the general linear expression for the safety margin of a collapse mode (failure mode expression) is

$$g_i = \sum_j A_{ij} M_j - \sum_\ell B_{i\ell} L_\ell \tag{19}$$

in which A_{ij} and $B_{i\ell}$ are constant coefficients, depending on frame geometry, M_j = random plastic moment at section j, and L_ℓ = random load that is active in producing failure mode i. Assuming that the plastic moments in positive and negative bending are the same at any of the seven critical sections (one plastic moment is associated with one critical section), then the safety margin expressions for the collapse modes of the frame shown in Fig. 1 are:

$$\left.\begin{aligned} g_a &= M_2 + 2M_4 + M_6 - 5P \\ g_b &= M_3 + 2M_4 + M_5 - 5P \\ g_c &= M_3 + 2M_4 + M_6 - 5P \\ g_d &= M_2 + 2M_4 + M_5 - 5P \end{aligned}\right\} \text{beam modes (3 hinges)} \qquad (20.a)$$

$$\left.\begin{aligned} g_e &= M_1 + M_3 + M_5 + M_7 - 4H \\ g_f &= M_1 + M_2 + M_6 + M_7 - 4H \\ g_g &= M_1 + M_2 + M_5 + M_7 - 4H \\ g_h &= M_1 + M_3 + M_6 \quad M_7 - 4H \end{aligned}\right\} \text{panel modes (4 hinges)} \qquad (20.b)$$

$$\left.\begin{aligned} g_i &= M_1 + 2M_4 + 2M_6 + M_7 - 5P - 4H \\ g_j &= M_1 + 2M_4 + 2M_5 + M_7 - 5P - 4H \end{aligned}\right\} \text{combined modes (4 hinges)} \qquad (20.c)$$

Each beam mode involves four active random variables at collapse (3 plastic moments and the gravity load), each panel model involves five active random variables (4 plastic moments and the lateral load), and each combined mode involves six active random variables (4 plastic moments and both the gravity and the lateral loads).

A failure mode can be modelled as a parallel system of plastic hinges, since failure via an individual mode is conditioned by the occurrence of all plastic hinges related to this mode. Therefore, if the event $g_{ij} \leq 0$ means that the j-th plastic hinge has been formed in the i-th failure mode, then the probability of plastic collapse of the frame shown in Figure 1 may be obtained by considering the probability that at least one of the ten possible collapse modes will occur:

$$P_f = P(g_{system} \leq 0) = P\left[\bigcup_{i=1}^{10} (g_i \leq 0)\right] \qquad (21.a)$$

or, equivalently, the probability that enough plastic hinges will occur to turn the structure or part of it into a collapse mode:

$$P_f = P\left[\bigcup_{i=1}^{10} \bigcap_{j=1}^{7} (g_{ij} \leq 0)\right] \qquad (21.b)$$

The equation (21.b) is the probability of failure of a system of parallel subsystems (plastic hinges) in series (failure modes).

For ductile systems the probability of failure in a given mode is independent of the sequence of plastic hinges occurrence (ref. 23, 25, and 27). In the case of brittle systems the failure sequences are path-dependent. Consequently, the probability that a brittle mode occurs is

$$P_{f_i} = P(g_i \leq 0) = P\left[\bigcap_{k=1}^{s} (g_{ik} \leq 0)\right] \tag{22}$$

where g_{ik} is the safety margin expression for the k-th component in the failure sequence comprising mode i, and s is the total number of possible failure events associated with this failure sequence.

For example, if the first mode in equation (17) involves brittle component failures, this equation should be modified to account for the presence of the brittle failure sequence associated with this mode, as follows

$$P_f = P(g_{system} \leq 0) = P\left[\bigcap_{k=1}^{s} (g_{1k} \leq 0) \cup (g_2 \leq 0) \cup \cdots \cup (g_m \leq 0)\right] \tag{23}$$

Consider the general case of a structural system consisting of structural subsystems modeled as a network of interconnected components. Employing the concepts of system reliability introduced above, it is possible now to write the general expression of the probability of failure of such a system.

The probability of failure of a system composed of m parallel subsystems connected in series is the probability of a union of intersections

$$P_f = P(g_{system} \leq 0) = P\left\{\bigcup_{i=1}^{m}\left[\bigcap_{j=1}^{m_i} (g_{ij} \leq 0)\right]\right\} \tag{24}$$

where g_{ij} is the safety margin expression (or 'performance function') of link ij, which is the j-th component in the i-th parallel connection.

For m series subsystems connected in parallel P_f can be written as the probability of an intersection of unions

$$P_f = P(g_{system} \leq 0) = P\left\{\bigcap_{i=1}^{m}\left[\bigcup_{j=1}^{m_i} (g_{ij} \leq 0)\right]\right\} \tag{25}$$

where g_{ij} is the safety margin expression of the j-th component in the i-th series connection.

APPROXIMATE RELIABILITY ANALYSIS OF SERIES SYSTEMS

The exact evaluation of limit state probabilities of various structural systems presented above (equations 17, 18, 23-25) is a very difficult process for non-trivial cases because the experimental data are often too poor to establish a joint probability distribution of the failure modes. The presence of statistical correlation between failure modes through loading and resistances complicates this process. Even if the joint probability distribution is available an exact calculation of P_f requires evaluation of multiple integrals which implies an enormous computational effort. For this reason methods for approximate reliability analysis have been developed. Some of these methods are briefly mentioned below for the particular class of series systems with dependent failure modes. This type of system may be used to compute the overall probability of

collapse of a plastic structure, as well as the overall probability of failure of structures in which system failure is deemed to occur if any one element reaches its critical capacity (e.g., statically determinate structures).

As an alternative to the exact evaluation of the total limit state probability of a series system, P_f (see equation 17), several approximate methods are available.

A first estimate of P_f in terms of lower and upper bounds was proposed by Cornell (ref. 6):

$$P_f \geq \max_{i=1}^{m} P_{f_i} \tag{26.a}$$

$$P_f \leq 1 - \prod_{i=1}^{m} (1 - P_{f_i}) \approx \sum_{i=1}^{m} P_{f_i} \tag{26.b}$$

in which $P_{f_i} = P(g_i \leq 0)$.

The lower bound (26.a) is obtained by assuming the mode failure expressions perfectly dependent:

$$\rho_{ij} = \rho(g_i, g_j) = 1 \qquad \text{for all } i \text{ and } j \tag{27.a}$$

in which ρ_{ij} is the correlation coefficient between the i-th and the j-th failure mode, while the upper bound (26.b) is derived by assuming statistical independence between mode failure expressions

$$\rho_{ij} = \rho(g_i, g_j) = 0 \qquad \text{for all } i \neq j \tag{27.b}$$

The Cornell bounds (eqns. 26) can be improved by taking into account the correlation between a pair of failure modes. In this context, Kounias (ref. 28) and Ditlevsen (refs. 29-31) proposed better bounds involving the intersections of any two failure mode events. These narrow bounds are as follows:

$$P_f \geq P_{f_1} + \sum_{i=2}^{m} \max(P_{f_i} - \sum_{j=1}^{i-1} P_{f_{ij}}, 0) \tag{28.a}$$

$$P_f \leq \sum_{i=1}^{m} P_{f_i} - \sum_{i=2}^{m} \max_{j<i} P_{f_{ij}} \tag{28.b}$$

in which $P_{f_1} = P(g_1 \leq 0)$, and $P_{f_{ij}}$ is the joint probability

$$P_{f_{ij}} = P(g_i \leq 0, g_j \leq 0) \tag{29}$$

that both failure modes i and j will simultaneously occur.

Note that the bounds given by equations (28) depend on the ordering of failure modes. The closest bounds are obtained by ordering the failure modes according to decreasing values of their probabilities of occurrence (i.e., $P_{f_1} \geq P_{f_2} \geq \cdots \geq P_{f_m}$). Therefore, in equation (28.a) it is convenient to define

$$P_{f_1} = \max_{i=1}^{m} P_{f_i}$$

The bounds (28) involve the evaluation of the probability of occurrence of intersection of events $P_{f_{ij}}$ for each pair of failure modes. This probability is difficult to obtain, since in general the joint distribution function of a pair of failure modes is not available. The basis of the evaluation of $P_{f_{ij}}$ is an advanced first-order second-moment system reliability analysis (ref. 31). This is accomplished by transforming the initial formulation space of the basic variables into a space of reduced normal variates. In this last space, the m limit state equations (or "the failure set") represent m intersecting hypersurfaces which are bounded by the respective tangent hyperplanes at the design points for the individual modes. The distance from the origin of the reduced variates to the i-th design point represents the i-th mode reliability index β_i. The joint failure probability $P_{f_{ij}}$ is then calculated as follows:

$$P_{f_{ij}} = \Phi(-\beta_i, -\beta_j; \rho_{ij}) \tag{30}$$

where $\Phi(-\beta_i, -\beta_j; \rho_{ij})$ is the distribution function for a bivariate normal vector with zero mean values, unit variances and correlation coefficient ρ_{ij}. The numbers β_i and β_j are the reliability indices of the i-th and j-th failure modes; therefore, the limit state probabilities for these modes are determined using equation (16). The correlation coefficient between the i-th and j-th failure mode, ρ_{ij}, is the cosine of the angle α_{ij} between the normal vectors to the hyperplanes which represent the approximations of the limit state equations of the i-th and j-th failure mode

$$\rho_{ij} = \cos \alpha_{ij} \tag{31}$$

Therefore, using the bivariate normal integral (30) the exact second-order bounds (28) are as follows:

$$P_f \geq \Phi(-\beta_1) + \sum_{i=2}^{m} \max \left[\Phi(-\beta_i) - \sum_{j=1}^{i-1} \Phi(-\beta_i, -\beta_j; \rho_{ij}), 0\right] \tag{32.a}$$

$$P_f \leq \sum_{i=1}^{m} \Phi(-\beta_i) - \sum_{i=2}^{m} \max_{j<i} \left[\Phi(-\beta_i, -\beta_j; \rho_{ij})\right] \tag{32.b}$$

An efficient method for computing the bivariate normal integral (30) has been presented by Owen (ref. 32). However, if needed, further approximation of this integral may be obtained when β_i, β_j, and ρ_{ij} are given, by using the conditional

bounding method of the bivariate normal probability (ref. 30). For example, the following bounds may be derived for positively correlated failure modes ($\rho_{ij} \geq 0$):

$$\Phi(-\beta_i, -\beta_j; \rho_{ij}) \geq \max [\Phi(-\beta_i)\, \Phi(-\beta_{j/i}), \Phi(-\beta_j)\, \Phi(-\beta_{i/j})] \tag{33.a}$$

$$\Phi(-\beta_i, -\beta_j; \rho_{ij}) \leq \Phi(-\beta_i)\, \Phi(-\beta_{j/i}) + \Phi(-\beta_j)\, \Phi(-\beta_{i/j}) \tag{33.b}$$

where

$$\beta_{i/j} = (\beta_i - \beta_j \rho_{ij})/(1 - \rho^2_{ij})^{1/2} \tag{34.a}$$

$$\beta_{j/i} = (\beta_j - \beta_i \rho_{ij})/(1 - \rho^2_{ij})^{1/2} \tag{34.b}$$

The bounds (33) on the bivariate normal probability (30) are then used in equations (32) as follows: for the lower bound of P_f (32.a) it is necessary to use the approximation of $\Phi(-\beta_i,-\beta_j; \rho_{ij})$ given by the upper bound (33.b), and for the upper bound of P_f (32.b) it is necessary to approximate $\Phi(-\beta_i,-\beta_j; \rho_{ij})$ by its lower bound (33.a). The advantage of using bounds on the bivariate probability (30) is their convenient computation solely by use of second moment algebra.

A different method for approximating the total failure probability (equation 17) of a series system with dependent failure modes was introduced by Vanmarcke (ref. 21). This method is based on the earlier work of Moses and Kinser (ref. 33), which has shown that equation (17) can be expressed as follows:

$$P_f = P_{f_1} + \sum_{i=2}^{m} a_i P_{f_i} \tag{35}$$

where

$$a_i = P[(g_1 > 0) \cap (g_2 > 0) \cap \cdots \cap (g_{i-1} > 0) \,|\, (g_i \leq 0)] \tag{36}$$

is the conditional probability that the first i-1 modes survive given that mode i occurs. Note that the failure modes are arranged so that $P_{f_1} \geq P_{f_2} \geq \cdots \geq P_{f_m}$ because the value of the conditional probability (36) depends on the ordering of failure modes.

The method introduced by Vanmarcke (ref. 21) by (upper) bounding the conditional probability a_i reduces in equation (36) the number of i-1 survival events, for which a joint probability distribution and a lengthy multiple integration are necessary, to only one:

$$a_i \leq \min_{j=1}^{i-1} P[(g_j > 0) \,|\, (g_i \leq 0)] = a_i^* \qquad \text{for all } j = 1,2,\cdots,i-1 \tag{37}$$

where $a_1^* = 1$ and $a_2^* = a_2$. Therefore, an upper bound of the system failure probability P_f is

$$P_f \leq P_{f_1} + \sum_{i=2}^{m} a_i^* P_{f_i} = P_{f_1} + a_2 P_{f_2} + \sum_{i=3}^{m} a_i^* P_{f_i} \qquad (38)$$

Further, using a first-order approach, Vanmarcke introduced a useful approximation of the conditional probability $P[(g_j > 0) | (g_i \leq 0)]$ in terms of the coefficient of correlation between the failure modes i and j, and of the safety indices β_i and β_j associated with these modes, as follows (ref. 21):

$$P[(g_j > 0) | (g_i \leq 0)] \approx 1 - G[\text{Max} (\frac{\beta_j}{|\rho_{ij}|}, \beta_i)]/G(\beta_i) \qquad (39)$$

in which it is assumed that the probability of occurrence of the i-th mode, $P_{f_i} = G(\beta_i)$, depends on β_i only.

A different method which avoids calculating conditional probabilities resulting from conditions leading to failure via pair of failure modes is the probabilistic network evaluation technique (PNET) of Ang and Ma (ref. 34). This method is based on the notion of demarcating correlation coefficient ρ_0, assuming those failure modes with high correlation ($\rho_{ij} \geq \rho_0$) to be perfectly correlated, and those with low correlation ($\rho_{ij} < \rho_0$) to be statistically independent. As might be expected, one of the key considerations is the selection of an appropriate value for ρ_0. The failure modes must be arranged in decreasing order of their probabilities of occurrence, and in each group the mode with the highest probability of occurrence is chosen as the "representative" failure mode. That is, the failure probability of the entire group is assumed to be the probability of the "representative" event of the group. Since the different groups are considered statistically independent, the overall probability of failure of the system is approximated by

$$P_f \leq 1 - \prod_{\text{groups}}^{\text{all}} (1 - P_{f,\text{group}}) \approx \sum_{\text{groups}}^{\text{all}} P_{f,\text{group}} \qquad (40)$$

References 35 and 36 discuss the PNET method in detail. Other methods for approximating P_f are reviewed in a recent benchmarck study (ref. 37). Although this study was intended only to assess and compare the computational accuracy and efficiency of different methods to determine collapse failure probabilities of simple plastic frames, it did demonstrate the need for a criterion for discerning the importance of approximations used in the evaluation of the limit state probabilities of series systems.

Coupled with the problems related to appropriate approximations used in the methods for reliability evaluation of series systems are problems related to the accuracy needed in describing the statistical information required for computation. This information is associated with (1) basic design variables (i.e., loads, strengths) such as mean values, dispersions, coefficients of correlation, and (2) other parameters such as the overall reliability level (given by the value of the global probability of failure). The main reason for needing this informa-

tion is to establish a measure of the way the limit state function associated with a prescribed reliability level varies with changes in the statistical parameters that define each problem. To obtain this information sensitivity analysis is required.

COMPUTER-AUTOMATED PLASTIC SENSITIVITY ANALYSIS

A reliability-based computer program based on the second moment reliability concept and using a matrix formulation of reliability analysis due to Vanmarcke (ref. 21) was prepared for evaluating the global probability of collapse of plastic frames. Failure of a frame structure is defined as a formation of at least one collapse mode due to transformation of a certain number of critical sections in plastic hinges. The program has the following essential features: (a) the engineering modeling which means identification, description and enumeration of the m possible collapse modes of a structure is generated by the computer; (b) probabilistic calculations to determine correlation coefficients between any two failure modes ρ_{ij} and individual collapse mode probabilities $P_i = \Phi(-\beta_i)$ are then automatically computed; (c) upper and lower bounds on the true probability of system failure P_f are evaluated and, if necessary, improved in an iterative manner until the bounds are sufficiently narrow for practical purposes (e.g., ± 1% error); and (d) sensitivity of the response quantities to change in problem parameters is evaluated.

The detailed description of this program is beyond the scope of this paper. Its conception was strongly influenced by the program for interactive reliability-based structural optimization of plastic structures described in ref. (38). The present program extends the reliability-based evaluation phase of the program presented in ref. (38) to other probabilistic methods, including Cornell's bounds (equations 26), Ditlevsen's bounds (equations 32 using the approximations 33 for the bivariate normal integral), exact second-order bounds (equation 32), Vanmarcke's upper bound (equation 38 using the approximation given in equation 39), and Ang and Ma's upper bound (equation 40). The basic idea of the evaluation technique is to compute lower and upper bounds on P_f sufficiently narrow for practical purposes. In reaching these bounds the evaluation technique begins with Cornell's bounds and proceeds from one bound to a better bound. It is noted that for some particular examples even the Cornell bounds are sufficiently narrow if the level of the admissible error is sufficiently high (e.g., ±5%).

Sensitivity evaluation is valuable for estimating the effect that changes in the input parameters will have on the safety index of an individual failure mode, and on the probability-based limit state function of the overall structure. The limit state function for a plastic structure with uncertain interdependent plastic moments and acted on by random interdependent loads is defined here as an iso-safety surface in the space of the mean values of the loads. Two different points on the limit state surface represent two different combinations of the mean values of the loads leading to the same value of the overall probability of plastic collapse P_f.

The information provided by sensitivity analysis of the limit state function is of vital importance for specifying the required exactness of statistical data used as input in the computation, so that a reasonable level of confidence in the resulting reliability level against plastic collapse can be achieved.

NUMERICAL EXAMPLE

Many sensitivity examples of limit state functions for probability-based plastic design of various framed structures have been studied. One of them is considered here. The example deals with the rectangular portal frame shown in Fig. 1. All random variables, including the loads P, H and the seven plastic moments M_1, M_2, ..., M_7 of the critical sections, are assumed to be modelled by second moment algebra (mean values, coeficients of variation, coefficients of correlation). The statistical dependence between loads and between plastic moments is accounted for through the coefficients of correlation $\rho(P,H)$ and $\rho(M_i, M_j)$, respectively. All plastic moments are assumed to have the same mean value $\overline{M}$ = 178.5kNm and coefficient of variation V(M), and to be equicorrelated $\rho(M_i, M_j) = \rho(M)$. The safety margin expressions for the ten failure modes (a, b, ..., j) shown in Fig. 1 are defined in equations (20).

Some sensitivity results concerning the individual collapse mode reliability, the correlation coefficient between pair of collapse modes and the limit state isosafety curves corresponding to plastic collapse of the frame shown in Figure 1 are plotted in Figures 2 to 11.

Figures 2 to 5 illustrate the influence of different statistical parameters that define the random structure and the random loading on the safety index β (equation 7) associated with each of the ten possible collapse modes shown in Figure 1. It is interesting to note that: (1) the combined failure modes i and j are the only ones influenced by the correlation coefficient between loads $\rho(P,H)$, since both P and H are active only for these modes; (2) the panel and the beam failure modes are insensitive to the coefficient of variation of the vertical and horizontal load, respectively (see Figs. 4 and 5); (3) the assumption of perfect positive correlation of plastic moments, $\rho(M_i, M_j) = 1$, leads to smaller mode reliabilities as compared to non-correlation; (4) the assumption of perfect negative correlation of the loads, $\rho(P,H) = -1$, leads to larger mode reliabilities as compared to non-correlation $\rho(P,H) = 0$, and/or to perfect positive loading correlation, $\rho(P,H) = 1$; (5) the reduction in the safety index of individual collapse modes with increasing plastic moment coefficient of variation V(M) (see Fig. 3) is more sensitive to the correlation between plastic moments in the high range of V(M); and (6) in some cases, the influence of the coefficient of correlation between loads $\rho(P,H)$ on the safety index β can be much more significant than the influence of the coefficient of variation of an individual load. (This is the case in Figure 5 where the assumption of a perfect negative loading correlation leads to an increase in the safety index of the combined failure modes with increasing coefficient of variation of the lateral load.)

Figures 6 to 8 show the influence of the coefficient of correlation among plastic moments $\rho(M_i, M_j)$ on the coefficient of correlation among a pair of failure modes $\rho(g_i, g_j)$, under the assumption that the loads are independent: $\rho(P,H) = 0$. The following remarks may be made regarding the sensitivity of $\rho(g_i, g_j)$ to $\rho(M_i, M_j)$ and to the type of failure modes: (1) even if all loads and plastic moments are statistically independent, collapse modes may be highly correlated through common loads and/or plastic moments; (2) the correlation coefficient between any pair of collapse modes increases with increasing values of $\rho(M_i, M_j)$; (3) the correlation coefficient between any two collapse modes of the same type (i.e., beam-beam, panel-panel, combined-combined) is always larger, for the same value of $\rho(M_i, M_j)$, than the coefficient of correlation between

different types of failure modes (i.e., beam-panel, panel-combined, beam-combined), and (4) the influence of $\rho(M_i, M_j)$ on $\rho(g_i, g_j)$ decreases with the increasing values of $\rho(M_i, M_j)$.

The influence of different parameters on the plastic limit state isosafety curves ($P_f = 10^{-5}$) evaluated according to three different methods including Cornell's upper bound method, Ditlevsen's upper bound method and Vanmarcke's method is presented in Figures 9, 10, and 11, respectively. Figure 9 gives plots of the limit state curve for four combinations of cases of correlation among plastic moments and among loads. It is important to observe that the safe loading space increases as the statistical dependence between plastic moments and/or between loads decreases. For a given correlation among plastic moments the sensitivity of the limit state curve to the correlation among loads is present only when the combined failure modes, i and/or j, are dominant. This sensitivity increases with decreasing values of the correlation coefficient between plastic moments. Figure 10 shows the influence of the coefficients of variation of loads on the plastic limit state isosafety curves corresponding to statistical independence among all variables. As expected, the safe loading space increases with decreasing values of the load coefficients of variation. The limit state curves become less sensitive to V(P) (or V(H)) for larger $\overline{H}$ (or $\overline{P}$). The reason for this is that increasing $\overline{H}$ (or $\overline{P}$) leads to a higher probability of occurrence of the panel (or beam) failure modes, for which the random load P (or H) is inactive. Limit state curves corresponding to three reliability levels against plastic collapse of the portal frame example with statistically independent loads and plastic moments are plotted in Figure 11. As expected, the safe loading space decreases with increasing values of the reliability level (or, equivalently, with decreasing values of P_f).

CONCLUSION

A sensitivity analysis capability for probability-based limit states design of plastic structures has been presented. It combines a probabilistic representation of the strengths and the loading acting on the structure, an approximate (first-order second-moment) reliability analysis formulation including the correlation between mode failure events, and a rigorous sensitivity analysis formulation. Sensitivity studies of the type shown in the numerical example are useful in assessing the parameter perturbation effects on the resulting limit state reliability. This sensitivity information is of considerable importance, since it can illustrate the accuracy needed in describing the statistical data required in probabilistic computations, which is a major goal in limit states design.

REFERENCES

1. Ellingwood, B.; Galambos, T.V.: Probability Based Criteria for Structural Design. Struct. Safety, vol. 1, 1982, pp. 15-26.

2. Ang, A.H-S.; Cornell, C.A.: Reliability Bases of Structural Safety and Design. J. Struct. Div., ASCE, vol. 100, no. ST9, Sept. 1974, pp. 1755-1769.

3. Ellingwood, B.; Galambos, T.V.; MacGregor, J.G.; Cornell, C.A.: Development of a Probability Based Load Criterion for American National Standard A58. Building Code Requirements for Minimum Design Loads in Buildings and Other Structures. National Bureau of Standards, Washington D.C., 1980.

4. Freudenthal, A.M.: Safety and the Probability of Structural Failure. Trans. ASCE, vol. 121, 1956, pp. 1337-1397.

5. Freudenthal, A.M.; Garrelts, J.M.; Shinozuka, M.: The Analysis of Structural Safety. J. Struct. Div., ASCE, vol. 92, no. ST1, Feb. 1966, pp. 267-325.

6. Cornell, C.A.: Bounds on Reliability of Structural Systems. J. Struct. Div., ASCE, vol. 93, no. ST1, Feb. 1967, pp. 171-200.

7. Ang, A.H-S.; Amin, M.: Reliability of Structures and Structural Systems. J. Eng. Mech. Div., ASCE, vol. 94, no. EM2, Apr. 1968, pp. 671-691.

8. Hohenbichler, M.; Rackwitz, R.: Non-Normal Dependent Vectors in Structural Safety. J. Eng. Mech. Div., ASCE, vol. 107, no. EM6, Dec. 1981, pp. 1227-1238.

9. Shinozuka, M.: Basic Analysis of Structural Safety. J. Struct. Eng., ASCE, vol. 109, no. 3, Mar. 1983, pp. 721-740.

10. Kam, T-Y.; Corotis, R.B.; Rossow, E.C.: Reliability of Nonlinear Framed Structures. J. Struct. Eng., ASCE, vol. 109, no. 7, July 1983, pp. 1585-1601.

11. Grigoriu, M.: Methods for Approximate Reliability Analysis. Struct. Safety, vol. 1, 1982, pp. 155-165.

12. Cornell, C.A.: Structural Safety Specifications Based on Second-Moment Reliability Analysis. IABSE Symposium on Concepts of Safety of Structures and Methods of Design, London, 1969, pp. 235-245.

13. Cornell, C.A.: Probability-Based Structural Code. Journal of the Amer. Concr. Inst., vol. 66, no. 12, Dec. 1969, pp. 974-985.

14. Cornell, C.A.: A First-Order Reliability Theory for Structural Design. Structural Reliability and Codified Design, Study no. 3, Univ. of Waterloo, Ontario, Canada, 1969.

15. Dolinski, K.: First-Order Second-Moment Approximation in Reliability of Structural Systems: Critical Review and Alternative Approach. Structural Safety, vol. 1, 1983, pp. 211-231.

16. Hasofer, A.M.; Lind, N.C.: Exact and Invariant Second Moment Code Format. J. Eng. Mech. Div., ASCE, vol. 100, no. EM1, Feb. 1974, pp. 111-121.

17. Rackwitz, R.: Practical Probabilistic Approach to Design. First Order Reliability Concepts for Design Codes. Comité Européan du Beton, Bull., d'Inf., no. 112, Munich, West Germany, July 1976.

18. Fiessler, B.; Neumann, H.-J.; Rackwitz, R: Quadratic Limit States in Structural Reliability. J. Eng. Mech. Div., ASCE, vol. 105, no. EM4, August 1979, pp. 661-676.

19. Madsen, H.O.: First Order vs. Second Order Reliability Analysis of Series Structures, submitted for publication, Struct. Safety.

20. Tvedt, L.: Two Second Order Approximations to the Failure Probability. Det Norske Veritas RDIV/20-004-83, 1983.

21. Vanmarcke, E.H.: Matrix Formulation of Reliability Analysis and Rel ..ility-Based Design. Comput. Struct., vol. 3, 1973, pp. 757-770.

22. Hohenbichler, M.; Rackwitz, R.: First-Order Concepts in System Reliability. Struct. Safety, vol. 1, 1983, pp. 177-188.

23. Rashedi, R.; Moses, F: Studies on Reliability of Structural Systems. Dept. of Civil Engineering, Case Western Reserve University, Report no. R83-3, Cleveland, Dec. 1983.

24. Moses, F.: Reliability of Structural Systems. J. Struct. Div., ASCE, vol. 100, no. ST9, Sept. 1974, pp. 1813-1820.

25. Moses, F.: System Reliability Developments in Structural Engineering. Struct. Safety, vol. 1, 1982, pp. 3-13.

26. Frangopol, D.M.: Sensitivity Studies in Optimum Reliability-Based Design of Plastic Structures. Proc. AIAA/ASME/ASCE/AHS 25th Structures, Structural Dynamics, and Materials Conf., Part 1, 1984, pp. 21-33, AIAA Paper 84-0854.

27. Bennett, R.M.; Ang, A. H-S.: General Structural System Reliability Analysis. Recent Advances in Engineering Mechanics and Their Impact on Civil Engineering Practice, vol. I, W.F. Chen and A.D.M. Lewis, eds., ASCE, Engr. Mech. Div., 1983, pp. 839-842.

28. Kounias, E.G.: Bounds for the Probability of a Union with Applications. Annals of Math. Stat., vol. 39, no. 6, 1968, pp. 2154-2158.

29. Ditlevsen, O.: Narrow Reliability Bounds for Structural Systems. J. Struct. Mech., vol. 7, no. 4, 1979, pp. 453-472.

30. Ditlevsen, O.: System Reliability Bounding by Conditioning. J. Eng. Mech. Div., ASCE, vol. 108, no. EM5, Oct. 1982, pp. 708-718.

31. Ditlevsen, O.: Model Uncertainty in Structural Reliability. Structural Safety, vol. 1, 1982, pp. 73-86.

32. Owen, D.B.: Tables for Computing Bivariate Normal Probabilities. Annals of Math. Stat., vol. 27, no. 4, Dec. 1956, pp. 1075-1090.

33. Kinser, D. E.; Moses, F.: Optimum Structural Design with Failure Probability Constraints, AIAA J., vol. 5, no. 6, 1967, pp. 1152-1158.

34. Ang, A. H-S.; Ma, H-F.: On the Reliability of Structural Systems. Proc. 3rd Int. Conf. on Struct. Safety and Reliability, Trondheim, Norway, June 1981.

35. Ang, A. H-S.; Tang, W.H.: Probability Concepts in Engineering Planning and Design, vol. 2, John Wiley and Sons, 1975.

36. Chou, K.C.; McIntosh, C.; Corotis, R.B.: Observations on Structural Reliability and the Role of Modal Correlations. Struct. Safety, vol. 1, 1983, pp. 189-198.

37. Grimmelt, M.J.; Schueller, G.I.: Benchmark Study on Methods to Determine Collapse Failure Probabilities of Redundant Structures. Struct. Safety, vol. 1, 1982/1983, pp. 93-106.

38. Frangopol, D.M.: Interactive Reliability-Based Structural Optimization. Comput. and Struct., in press, 1984.

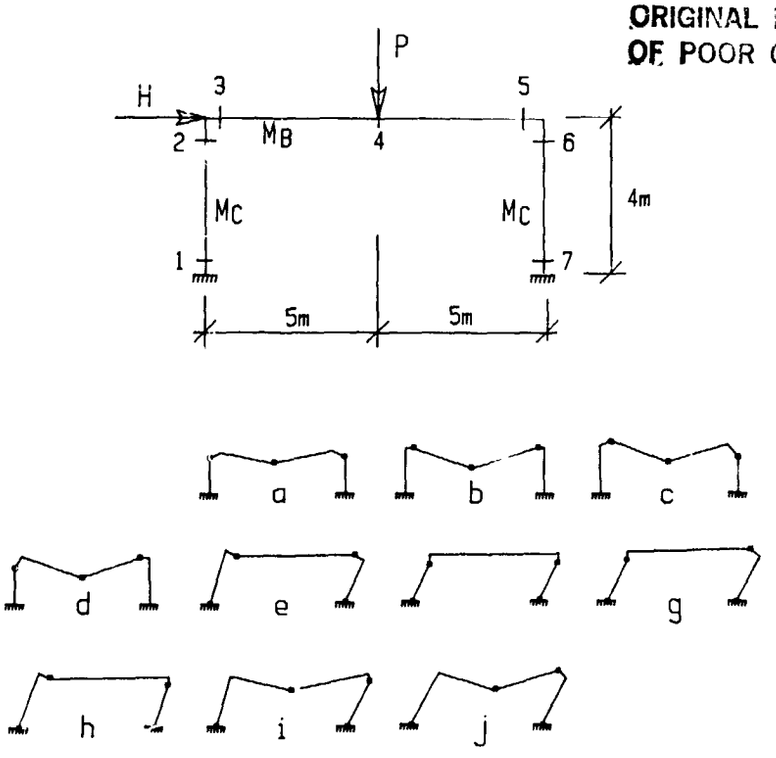

Figure 1 - Portal frame example

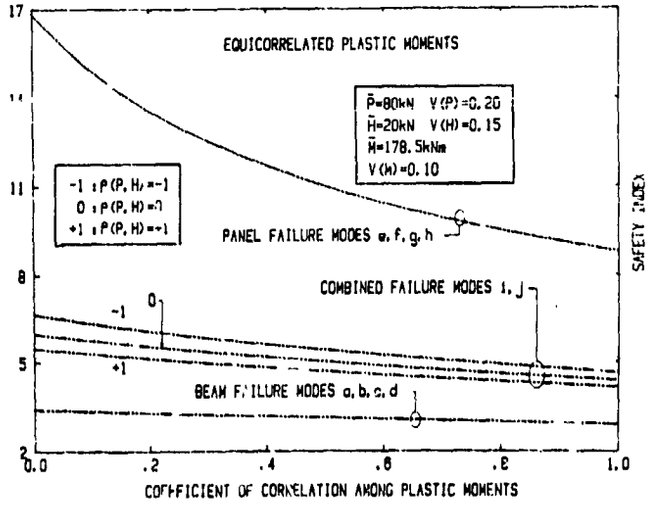

Figure 2 - Effect of correlation coefficients on the modal safety

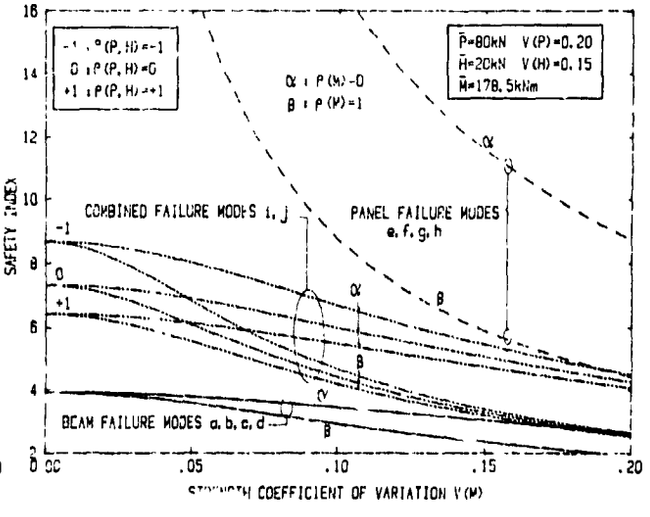

Figure 3 - Effect of V(M) on the modal safety for various ρ(P,H)

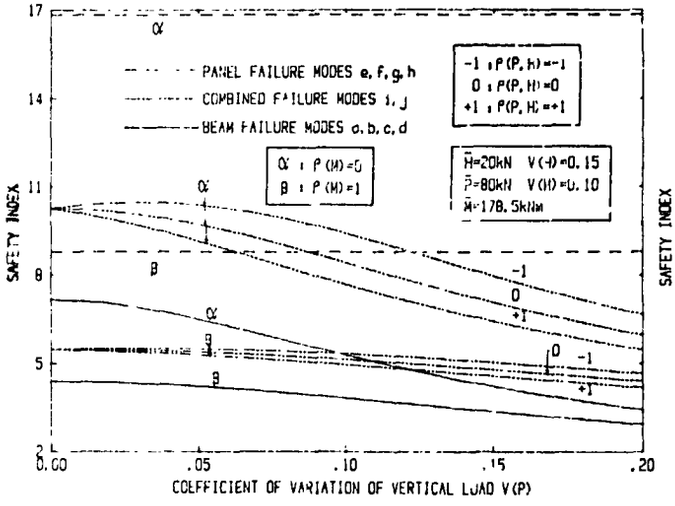

Figure 4 - Effect of V(P) on the modal safety for various correlation coefficients

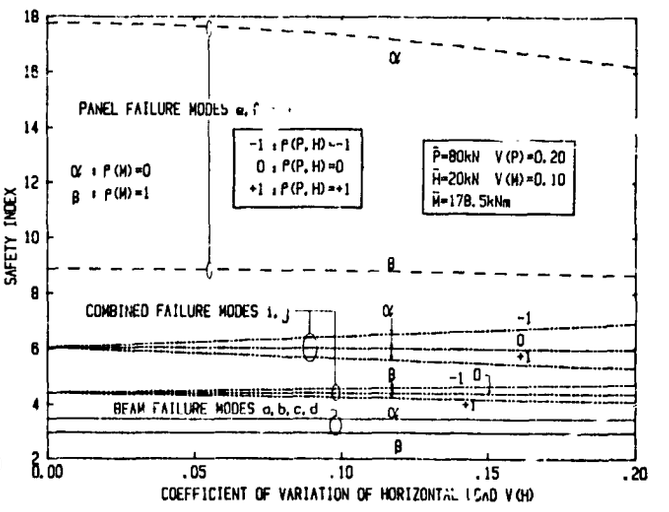

Figure 5 - Effect of V(H) on the modal safety for various correlation coefficients

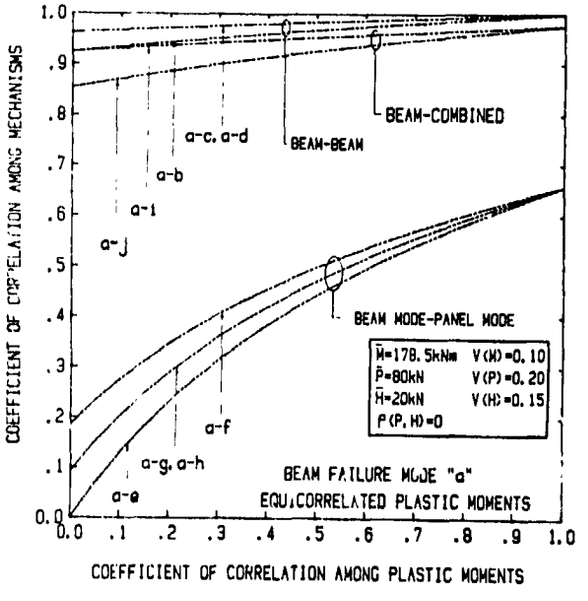

Figure 6 - Effect of plastic moments correlation on modes correlation - beam mode "a"

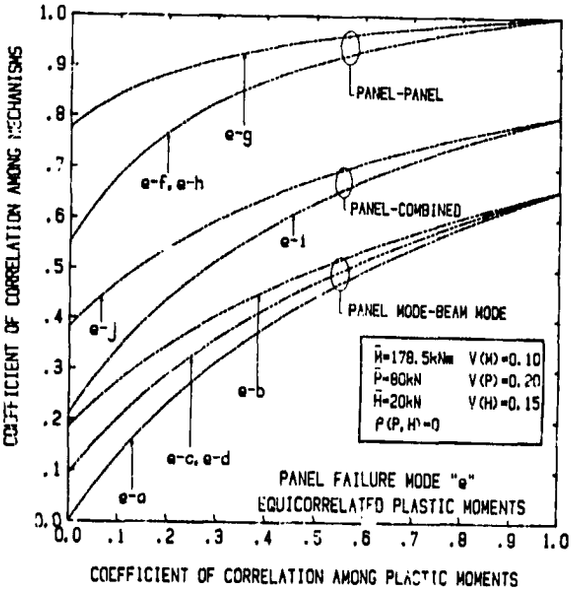

Figure 7 - Effect of plastic moments correlation on modes correlation - panel mode "e"

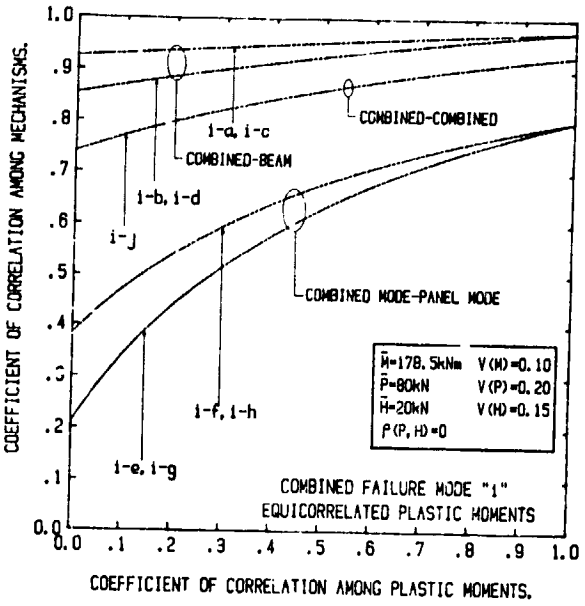

Figure 8 - Effect of plastic moments correlation on modes correlation - combined mode "i"

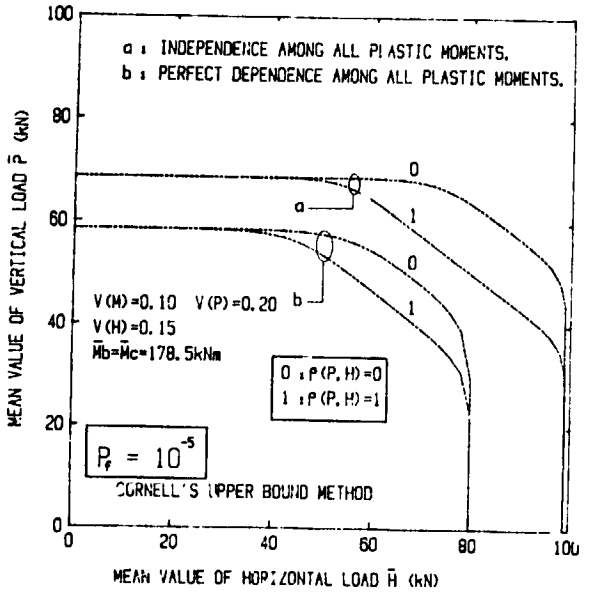

Figure 9 - Effect of correlation on the limit state curves

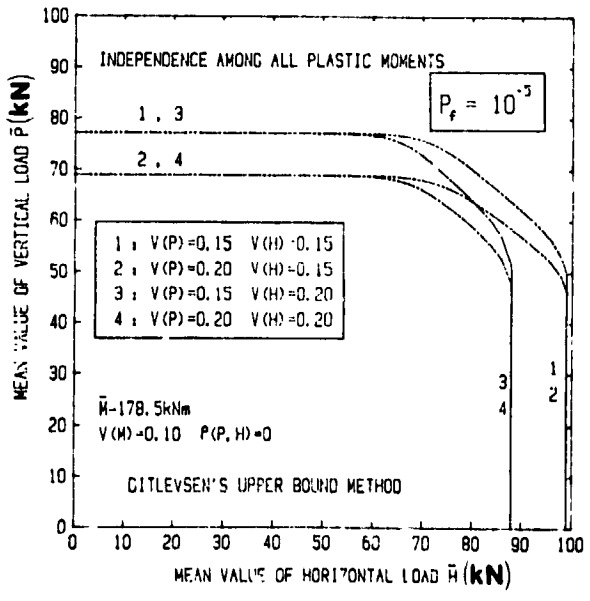

Figure 10 - Effect of load coefficients of variation on the limit state curves

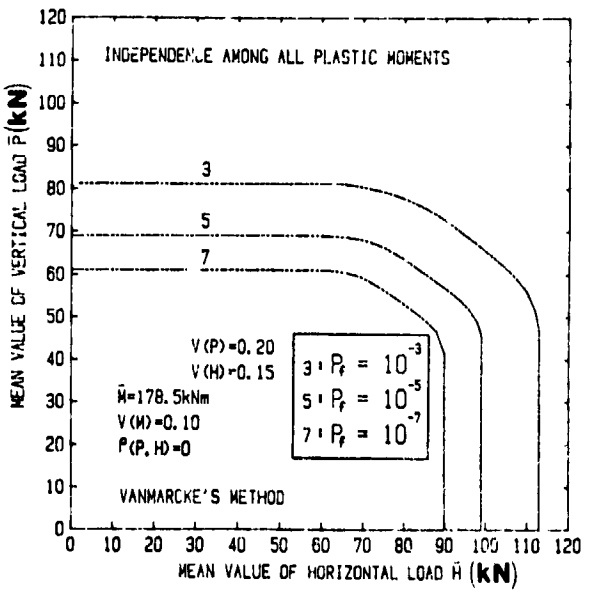

Figure 11 - Effect of reliability level on the limit state curves

N85 10389

COMPOSITE LAMINATE OPTIMIZATION PROGRAM

SUITABLE FOR MICROCOMPUTERS

Gerald V. Flanagan
Grumman Aerospace Corporation
Bethpage, New York

and

Anthony N. Palazotto, Professor
Department of Aeronautics and Astronautics
Air Force Institute of Technology
Wright-Patterson AFB, OH

SUMMARY

The design of a composite panel requires some way of finding the minimum thickness laminate which will withstand the load requirements without failure. The mathematical complexity of this problem dictates the use of nonlinear optimization techniques. Although there are sophisticated optimization programs available capable of solving for the ply ratios, these programs are not often used in preliminary design because they require a large computer and some knowledge of the program's operation. As an alternative, specialized laminate optimization programs were developed which are compact and efficient enough to run on microcomputers. Only stresses at a point and inplane loads and deflections are considered. The programs are simple to use and require no knowledge of optimization. Techniques are developed in this paper that find minimum thickness laminates with either ply ratios or ply angles as design variables. In addition, a method is presented for finding the optimimum orientation for the axis of symmetry of an orthotropic laminate. The orthotropic laminate program uses an approximate failure theory, as suggested by Tsai and Hahn (ref. 1), which has been found to speed computations dramatically.

INTRODUCTION

Optimization techniques are needed for even the simplest design problems when a minimum weight composite structure is desired. The designer needs to know desirable fiber orientations and the percentage of the total fiber volume to be aligned along each orientation (referred to as the "ply ratio"). For a single required loading condition, the proper ply ratios can be tabulated for common combinations of ply orientations, but there are no available guidelines when the design must meet multiple independent load requirements. To encourage the use of composites in situations involving complex and charging load conditions, easy access to an optimization program by designers was felt to be desirable. The program presented in this paper is made accessible by being written in an easy to use format and by being available on microcomputers. Since the program requires only about 15 kilo-bytes of memory, it can run on some of the least expensive portable and hand-held computers. Furthermore, the algorithm has been made efficient enough that run times are reasonable (1-10 minutes) even when using interpretive BASIC.

DISCUSSION

The program developed herein is used to design a laminate subject to strength constraints under multiple independent loading conditions at a point. Only in-plane loads and deflections are considered. A first-ply failure criterion is used, specifically the Tsai and Wu (ref. 2) quadratic interaction criterion. Design variables are the ply ratios and orientations that result in a minimum thickness design. The two design variables are handled separately. The user has the option of choosing which variable is to be optimized, or both can be optimized sequentially. The user only needs to select a material system from the material library and enter loads and initial ply angles.

Ply ratio optimization is by a modification of the method of feasible directions. The total thickness of a laminate with constant ply ratios can be calculated analytically so that one constraint is exactly satisfied as an equality. The modification of the method of feasible directions uses this analytic result to speed the algorithm, making operation on a microcomputer more practical. The program also allows for a percentage of fibers at some particular angle to reach zero. When this happens, the constraints associated with that orientation are dropped so that the failure of a zero thickness ply group cannot control the final laminate thickness.

Selection of angles by optimization methods is a more difficult problem because the objective function (total thickness) is not a direct function of the design variables. Also, the trigonometric functions form many local minima. The approach presented in this paper is to form an unconstrained function which when minimized as a function of the ply angles will also decrease the total laminate thickness (while holding ply ratios constant). The best function was found to be the variance of all the failure constraints. As the variance approaches its minimum of zero, the laminate approaches a simultaneous failure condition. The assumption is made that laminate thickness will approach a minimum at the simultaneous failure condition. The approach has been found that after the angle optimization process, the ply ratio optimization often cannot make any further changes. Similarly, after ply ratio optimization, the angle routine will often not make any changes. Thus, the designer has a choice of design variables which for many biaxial loading conditions will give equally efficient laminates.

CONCLUSIONS

A series of effective laminate optimization programs have been developed and thoroughly tested. The programs have been designed to be compact and efficient enough to operate on some of the smallest microcomputers. Although not as general or sophisticated as some of the optimization code currently available, these programs offer good performance and are very easy to use even for those unversed in optimization. No program in the literature has been found that can perform angle optimization or the orthotropic axis optimization. Thus, much greater flexibility is now available to the designer.

The gains due to optimization have been found to be substantial, with typically a 30% weight savings as compared to quasi-isotropic laminates. Surprisingly, these large gains can be made with either of a couple of design parameters. The designer can either optimize the ply ratios, or the angles and usually efficient laminates; or, he may choose to constrain the laminate to be orthotropic after

optimization. If the orthotropic axis is free to change, efficient laminates can be designed.

By trying many example cases, it has been found that $\pi/4$ laminate is a good starting laminate. By starting with quasi-isotropic laminates, no knowledge of desired starting orientations for the particular loads is needed. Increasing the number of initial orientations does not seem to improve the final laminates.

An approximate failure criteria has been found to give good results while substantially decreasing the computation times needed. The approximate criteria could be particularly important when the optimization procedure is tied into a finite-element code on an iterative basis, where the repeated optimizations could become excessively time consuming.

REFERENCES

1. Tsai, S. W., and Hahn, H. T.: Introduction to Composite Materials. Technomic Publishers, Westport, Conn., 1980, pp. 315-325.

2. Tsai, S. W., and Wu, E. M.: A General Theory of Strength for Anisotropic Materials. J. Comp. Mat., vol. 5, Jan. 1971, pp. 58-81.

FRACTURE, FAILURE, AND FRAGMENTATION

John K. Dienes
Theoretical Division, Group T-3
Los Alamos National Laboratory
Los Alamos, New Mexico 87545

SUMMARY

Though continuum descriptions of material behavior are useful for many kinds of problems, particularly those involving plastic flow, a more general approach is required when the failure is likely to involve growth and coalescence of a large number of fractures, as in fragmentation. Failures of this kind appear frequently in rapid dynamic processes such as those resulting from impacts and explosions, particularly in the formation of spall fragments. In the first part of this paper an approach to formulating constitutive relations that accounts for the opening, shear and growth of an ensemble of cracks is discussed. The approach also accounts for plastic flow accompanying fragmentation. The resulting constitutive relations have been incorporated into a Lagrangian computer program.

In the second part of this paper a theoretical approach to coalescence is described. The simplest formulation makes use of a linear Liouville equation, with crack growth limited by the mean free path of cracks, assumed constant. This approach allows for an anisotropic distribution of cracks. An alternative approach is also described in which the decrease of the mean free path with increasing crack size is accounted for, but the crack distribution is assumed isotropic. A reduction of the governing Liouville equation to an ordinary differential equation of third order is possible, and the result can be used to determine how mean free path decreases with increasing crack size.

INTRODUCTION

As used here, fracture refers to the mechanical instability of a single flaw, failure describes the last stages of plastic flow before ductile rupture, and fragmentation involves breakage into small pieces following an impact or explosion. In this paper an approach to characterizing material response that incorporates all of these processes is outlined. The underlying idea is to generalize the elastic-plastic relations described by Reuss in reference 1 by considering the stretching (the symmetric part of the velocity gradient) as the sum not only of elastic and plastic parts, but also of contributions resulting from crack opening, shear, and growth. The crack sizes are assumed to be randomly distributed with a simple distribution function, so that a sample can have random behaviour with a theoretically predictable mean and variance.

CONSTITUTIVE RELATIONS

The velocity gradient $u_{i,j}$ can always be represented as the sum of a symmetric part, the stretching d_{ij}, and an antisymmetric part, the vorticity w_{ij}, so that

$$u_{i,j} = d_{ij} + w_{ij} \tag{1}$$

or, in matrix notation,

$$C = D + W \tag{2}$$

where we employ Truesdell's notation in reference 2. Contributions to the stretching can arise from small changes in the lattice structure of a solid, D^e; from motion of slip planes and dislocations whose macroscopic contribution can be considered as the plastic stretching D^p; from shearing of closed cracks denoted as D^s; from opening of cracks, denoted as D^o; from the unstable growth of either open or closed cracks, D^g; and from nonlinear interatomic and thermal effects represented by D^n. These mechanisms can be considered approximately independent, and each one has to be represented by an appropriate constitutuve law. In particular, we can consider the average stretching due to changes in the crystalline lattice to be unaffected by plastic flow. Thus we may write

$$D = D^e + D^p + D^o + D^s + D^g + D^n \tag{3}$$

It is shown by Dienes in reference 3 that the stretching D in spatial coordinates is related to the stretching in material coordinates $\bar{D}$ by

$$\bar{D} = R^T D R \tag{4}$$

where R is the matrix characterizing material rotation, and that the strain rate in material coordinates $\dot{\bar{E}}$ is related to the stretching by

$$\dot{\bar{E}} = \bar{V}\bar{D}\bar{V} \tag{5}$$

where $\bar{V}$ is the stretching in material axes (Truesdell's U). The strain is related to the Cauchy-Green tensor $\bar{B}$ (Truesdell's C) by

$$\bar{E} = \frac{1}{2}(\bar{B} - I) \tag{6}$$

These relations are appropriate for a coordinate system rotating with the material. Care must be taken to use suitable rates when the matrices refer to tensors specified

in spatial axes, as illustrated by Dienes in references 3 and 4. Throughout this paper material and spatial representations will be related by the transformation indicated in equation (4).

The energy of deformation e can be separated into a sum of terms since

$$\dot{e} = \mathrm{tr}\,(\bar{\bar{\sigma}}\bar{\bar{D}}) = \dot{e}^e + \dot{e}^p + \dot{e}^o + \dot{e}^s + \dot{e}^g + \dot{e}^n \qquad (7)$$

where $\bar{\sigma}$ represents the stress in material axes and each term represents the rate of work associated with a particular deformation mechanism. For each crack the stress σ is the approximate far-field stress. It is not implied that the stresses in the neighborhood of a crack are constant. Since the strain rate $\dot{\bar{E}}$ and $\bar{D}$ are related by (5), we can also separate $\bar{E}$ into a sum of terms

$$\bar{E} = \bar{E}^e + \bar{E}^p + \bar{E}^o + \bar{E}^s + \bar{E}^g + \bar{E}^n \qquad (8)$$

The condition that e^e represents an elastic strain energy is that

$$\dot{e}^e = \mathrm{tr}\,\bar{\bar{\sigma}}\bar{\bar{D}}^e/\rho = \mathrm{tr}\,\sigma D^e/\rho \qquad (9)$$

be an exact differential, where ρ denotes material density. In view of equation 5 it is straightforward to show that for an elastic process the constitutive relation must have the form

$$\bar{\sigma} = 2\rho\bar{V}\bar{\tau}\bar{V}$$

where

$$\bar{\tau} = (\bar{\tau}_{ij}) = \left(\frac{\partial f}{\partial \bar{B}_{ij}}\right) \qquad (11)$$

is an exact differential. This relation is equivalent to that discussed by Rivlin in reference 5. In that paper advantage is taken of material isotropy, and the derivatives are taken with respect to strain invariants. In this more general formulation, materials do not remain isotropic, and nothing is gained by choosing the strain invariants as independent variables. Because of possible anisotropy, the formulation is best left in terms of material axes for simplicity. It is possible to carry out the analysis in spatial axes, but care must be taken about material rotation. Discussion of that subject, primarily of a mathematical character, is eschewed in this brief paper.

In previous work on statistical crack mechanics (SCM) it was tacitly assumed that deformation is associated only with elastic and fracture mechanisms, essentially a brittle behaviour. In many calculations this appears to make the material stiffer than is observed in experiments, and it now appears probable that this is because ductile aspects of deformation are ignored. In principle a micromechanical treatment of slip planes analogous to that for shear cracks could be developed, but it is not entirely clear how the details of slip plane behaviour should be characterized. An excellent review of the current status of this approach is provided by Asaro in reference 6. An alternative is to represent plastic flow with a suitable phenomonological law. The simplest such law, ideally plastic flow, requires a constant value of the second stress invariant, a constraint incompatible with the assumptions made in connection with the general SCM fracture model, which assumes arbitrary stress levels. Thus, a hardening plasticity rule is required. The simplest such theory is isotropic hardening, but an alternative, kinematic hardening, appears to be more realistic. It permits the yield surface to translate in stress space, while constrained to remain cylindrical in shape. I have outlined a theory in which the yield surface depends on mean stress in reference 7, but it seems premature to incorporate those complications into the fracture process, so only a simple version of that theory is summarized here.

The stress is considered to lie on a cylindrical yield surface whose generator is given by the back stress $\bar{\alpha}$. Its history is governed by

$$\dot{\bar{\alpha}} = b\bar{D}^p \tag{12}$$

with b a (constant) hardening modulus. As in equation (4), bars denote variables in material axes. The deviator stress $\bar{S}$ is then the sum of the back stress $\bar{\alpha}$ and a relative deviator $\tilde{\bar{S}}$, so that

$$\bar{S} = \tilde{\bar{S}} + \bar{\alpha} \tag{13}$$

The total stress is the sum of the deviator and a mean whose negative is usually taken as a pressure, that is

$$\sigma = S - pI \tag{14}$$

where I denotes the unit matrix. If the relative deviator lies within the yield surface,

$$\mathrm{tr}\ \tilde{\bar{S}}^2 < Y^2 \tag{15}$$

the flow is treated as elastic, the plastic strain rate is set to zero, and the back stress remains constant. Otherwise, the plastic flow is governed by the above equa-

tion, with D^p obtained by subtracting $\bar{D}^e$, $\bar{D}^s$, $\bar{D}^o$, $\bar{D}^g$, and $\bar{D}^n$ from the total strain rate, as indicated by equation (3). In addition to the kinematic hardening postulates outlined above, we have the usual kinematic hardening relation

$$\bar{D}^p = \lambda \bar{\bar{S}}/2Y \tag{16}$$

By combining these relations it is possible to show that

$$\lambda = \frac{\text{tr } \bar{\bar{S}}(\bar{D}^e + \bar{D}^p)}{Y(1 + b/2\mu)} \tag{17}$$

It is shown in references 8 and 9 that the average strain rate due to opening of an ensemble of cracks, assuming no change in material density, is

$$\bar{d}^o_{ij} = \beta^o \bar{Z}^o_{ijkl} \dot{\bar{\sigma}}_{kl} \tag{18}$$

where

$$\beta^o = 8(1 - \nu)/3\mu \tag{19}$$

here ν represents Poisson's ratio, μ is the shear modulus, and the open-crack compliance is

$$\bar{Z}^o_{ijkl} = -\int_\Omega d\Omega n_i n_j n_k n_l \int_0^\infty dc \frac{\partial N^o}{\partial c} c^3 \tag{20}$$

The integral over Ω represents integration over all crack orientations here n_i is the crack normal, and $N^o(\Omega,c)$ represents the number of open cracks with radius larger than c as a function of orientation. Cracks are considered open when the normal component of traction is tensile. Similarly, the strain rate due to crack shear is

$$\bar{d}^s_{ij} = \beta^s \bar{Z}^s_{ijkl} \dot{\bar{\sigma}}_{kl} \tag{21}$$

where

$$\bar{Z}^s_{ijkl} = -\int_\Omega d\Omega\ S(1-\alpha) b_{ijkl} \int_o^\infty dc\ \frac{\partial N^s}{\partial c}\, c^3 \tag{22}$$

$$\beta^s = \frac{8}{3\mu}\,\frac{1-\nu}{2-\nu} \tag{23}$$

and

$$\alpha = \bar{\mu}|B|/\sqrt{A-B}^2 \tag{24}$$

In reference 8 it is shown that the quantity α appears when the effect of crack friction is accounted for. $S(x)$ is x for x positive and zero otherwise. The function

$$A - B^2 = \sigma_{ij} n_i \sigma_{kj} n_k - (\sigma_{ij} n_i n_j)^2 \tag{25}$$

represents the square of the tangential traction on a shear crack, $1-\alpha$ is the factor by which shear deformation is reduced when the frictional stress is accounted for, and $\bar{\mu}$ denotes the coefficient of friction. The crack orientation is accounted for by

$$b_{ijkl} = n_i n_k \delta_{jl} + n_j n_k \delta_{il} - 2 n_i n_j n_k n_l \tag{26}$$

FLAW STATISTICS

Though a few cracks in a highly stressed solid can grow independently, if the number density is large, intersections will develop and the statistics and crack effects will be strongly modified as a result. A detailed theory would present enormous complications since materials are neither homogeneous nor isotropic on a small scale, and cracks tend to bend and bifurcate as they grow. Still, it is possible to formulate a limited theory by making simplifying assumptions about growth and intersection. In the current approach we consider two kinds of flaws, those that are isolated and can grow unstably, and those that have intersected a number of others and are no longer capable of unstable growth. The density of the former is denoted by $L(c,\Omega,t)$, the latter by $M(c,\Omega,t)$, and the sum by $N(c,\Omega,t)$, with c the radius of an equivalent penny-shaped crack, Ω a symbolic representation of crack orientation, and t the duration of crack growth.

The number L of isolated (active) cracks at time $t + \Delta t$ whose radii exceed $c + \Delta c$ is equal to the number at time t whose radii exceed c, less the number that have been converted from active to inactive (stable) status, i.e.

$$L(c + \Delta c,\ t + \Delta t) = L(c,t) - \dot{M}(c,t)\Delta t$$

The dependence on Ω is dropped here since crack orientation is considered fixed in the course of crack growth. In the limit of small Δt this becomes

$$L_t + \dot{c}L_c = -M_t \tag{27}$$

where the subscripts denote differentiation and $\dot{c}$ the speed of crack growth. For high stresses $\dot{c}$ is typically about a third of sound speed, but for lower stresses $\dot{c}$ depends on stress level. In propellant calculations $\dot{c}$ is made to vary as $(\sigma/\sigma_o)^n$, with n=10, following data provided in reference 10. By making the change of variable

$$\gamma = \int_o^t \dot{c}\, dt \tag{28}$$

the governing equation is simplified to

$$L_c + L_\gamma = -M_\gamma \tag{29}$$

We have been able to proceed in two ways. In the first, the cracks in each orientation are allowed to behave independently, while the mean free path is assumed constant. The cracks intersect at a rate $\dot{c}N/\lambda$, where λ is the mean free path, assumed constant at its initial value. Then

$$\dot{M} = kL/\alpha \quad , \quad k = \pi^2 L_c^{-2}\dot{c} \tag{30}$$

where α is the number of intersections required to make a crack inactive, a number generally taken as 4. This representation is important where anisotropic effects are sought. For example, in cavity formation in oil shale by explosives, an initially spherical cavity becomes pill-shaped at later times because of the weakness (i.e. large cracks) in the bedding planes, as discussed in reference 11. Even in the absence of any initial anisotropy, however, cracks tend to develop radially near an explosive charge and circumferentially far from the charge, inducing a strong local anisotropy.

In the first method the governing equation is linear and has a particularly simple integral when the initial distribution is assumed exponential:

$$L(c,o) = L_o e^{-c/\bar{c}} \tag{3}$$

an assumption that has been fairly well justified in reference 12 by observation. Then

$$L(c,t,\Omega) = L_o e^{-c/\bar{c}+\beta\gamma} \tag{3}$$

where

$$\beta = 1/\bar{c} - k/\dot{c}\alpha \tag{3}$$

The anisotropy due to crack growth arises because its extent, γ, depends strongly on orientation. The parameters may also depend on Ω if the material is anisotropic.

In the second approach in which crack isotropy is assumed L and M are independe of Ω, but the rate of formation of inactive cracks is not assumed linear in L. A pr liminary description of the theory is given in reference 8. In this approach the rate of innactive crack formation is given by

$$\dot{M} = \ell\dot{c}n/\alpha \tag{3}$$

where $\ell(c,t)$ is the edge length of all active cracks with radius exceeding c per uni volume and $\eta(t)$ is the number of cracks per unit area. Then, if we put

$$z = 2\pi L_c \quad , \quad j = \pi/2\alpha \tag{3}$$

the governing equation, (29), reduces to

$$z_\gamma + z_c + 4jcn(\gamma)z = 0 \tag{3}$$

This equation can be integrated with the following result:

$$L = e^{-4j(J-\gamma J')} \int_{c-\gamma}^{\infty} du\ h(u)e^{4juJ'(\gamma)} \tag{3}$$

where J is related to η by

$$J_{\gamma\gamma} = -\eta \quad , \quad J(0) = J'(0) = C \tag{38}$$

An additional relation is required to complete the solution. This can be obtained by geometrical considerations in the following way. Let η_i denote the number of isolated crack intercepts per unit area and η_c the number of connected crack intercepts per unit area. Then, following the approach of reference 13,

$$\eta_i = \frac{\pi}{2}\int_{\gamma}^{\infty} dc\ L(c) \quad , \quad \eta_c = \frac{\pi}{2}\int_{o}^{\infty} dc\ M(c) \tag{39}$$

With these results, it follows after a lengthy calculation that $\eta = \eta_i + \eta_c$ is given by

$$\eta = \frac{\pi}{2}\left[\int_{o}^{\infty} dc\ L(o,c) + \int_{o}^{\infty} dc\ L(c,c) - \gamma L(\gamma,\gamma)\right] \tag{40}$$

Differentiating this result with respect to γ and combining with equations (37) and (38) results in the ordinary differential equation

$$J''' = \pi j \gamma L_o J'' \frac{\bar{c} + \gamma - 4j\bar{c}\gamma J'}{(1 - 4_j\bar{c}J')^2} e^{-4j(J-\gamma J')} \tag{41}$$

assuming the initially exponential distribution of equation (31).

RESULTS

The theory described herein has been incorporated into SCRAM, a computer program developed for analysis of fragmentation. Results of a propellant impact calculation without plastic flow are illustrated in figure 1 and with plastic flow are illustrated in figure 2. Incorporating a plastic flow component into the strain rate makes the deformation appear significantly more like that observed in experiments such as those illustrated in reference 14.

REFERENCES

1. Reuss, A.: Elastic Deformation According to Theory of Plasticity. Zeit. Ang Math. Mech., vol. 10, May-June 1930, pp. 266-274.

2. Truesdell, C.: The Elements of Continuum Mechanics. Springer-Verlag, 1966.

3. Dienes, J. K.: On the Analysis of Rotation and Stress Rate in Deforming Bodies. Acta Mechanica, vol. 32, 1979, pp. 217-232.

4. Dienes, J. K.: The Effect of Finite Rotation on a Problem in Plastic Deformation. Proceedings of the International Symposium on Plasticity, University of Oklahoma, Norman, OK, July 30-August 3, 1984.

5. Rivlin, R. S.; and Ericksen, J. L.: Stress-Deformation Relations for Isotropic Materials. J. Rational Mechanics and Analysis, vol. 4, no. 2, March 1955, pp. 323-425.

6. Asaro, R.: Crystal Plasticity. J. Appl. Mech., vol. 50, Dec. 1983, pp. 921-934.

7. Dienes, J. K.: A High-Pressure Kinematic Hardening Model for Rocks and Soils. J. Geophysical Research, vol. 80, no. 26, Sept. 1975, pp. 3749-3754.

8. Dienes, J. K.: Statistical Crack Mechanics. Proceedings of the Colloque International du CNRS no. 351, Failure Criteria of Structured Media, Villard-de-Lans, France, June 21-24, 1983.

9. Dienes, J. K.; and Margolin, L. G.: A Computational Approach to Rock Fragmentation. Proceedings of the 21st Symposium on Rock Mechanics, Univ. of Missouri, 1980, p. 390.

10. Schapery, R. A.: Mechanical Behavior of Solid Propellent. Proceedings of the ONR/AFOSR Workshop on Deflagration-to-Detonation Transition, Atlanta, GA, January 11-13, 1978, pp. 39-46.

11. Dienes, J. K.: On the Effect of Anisotropy in Explosive Fragmentation. Proceedings of the 22nd U.S. Symposium on Rock Mechanics, M.I.T., 1981, p. 164.

12. Seaman, L.; Curran, D. R.; and Shockey, D. A.: Computational Models for Ductile and Brittle Fracture. J. Appl. Phys., vol. 47, no. 11, 1976, pp. 4814-4826.

13. Dienes, J. K.: On the Inference of Crack Statistics from Observations on an Outcropping. Proceedings of the 20th U.S. Symposium on Rock Mechanics, Univ. of Texas, Austin, 1979, p. 259.

14. Jensen, R. C.; Blommer, E. J.; and brown, B.: An Instrumented Shotgun Facility to Study Impact Initiated Explosive Reactions. Proceedings of the Seventh Symposium (International) on Detonation (J. M. Short, Ed.) Naval Surface Weapons Center, White Oak, MD, 1982, pp. 299-307.

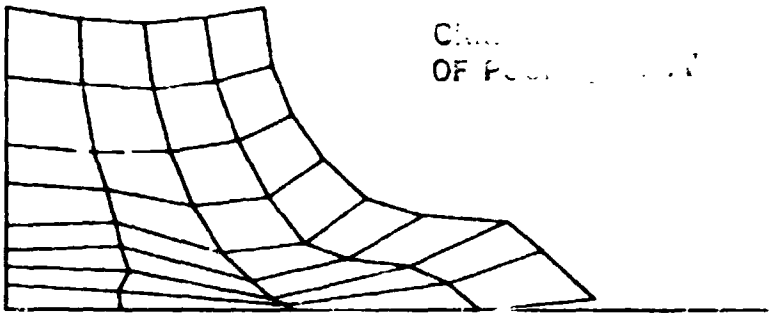

Fig. 1. Impact of a propellant cylinder onto a rigid target accounting for crack opening, shear, growth and intersection.

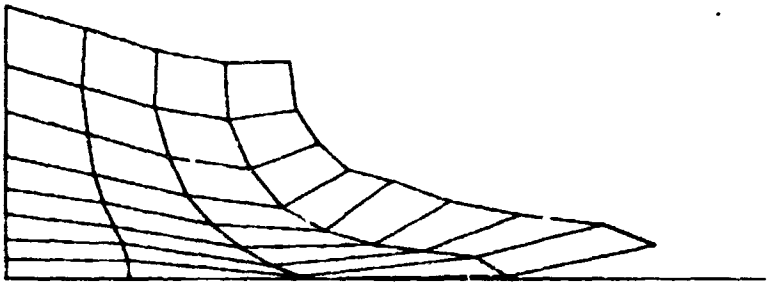

Fig. 2. Impact of the same propellant cylinder as in Fig. 1 onto a rigid target, allowing for plastic deformation in addition to the crack mechanisms described above.

N85 10391

SHEAR DEFORMATION PLATE CONTINUA

OF

LARGE DOUBLE-LAYERED SPACE STRUCTURES*

Mohamed Samir Hefzy
Grand Valley State College
Allendale, Michigan 49401

Adnan H. Nayfeh
University of Cincinnati
Cincinnati, Ohio 45221

1. INTRODUCTION

The last decade has witnessed a dramatic increase in the research activities dealing with the possibility of utilizing space for various commercial and scientific needs. Large lattice-type structures are analyzed as candidates to meet such applications. In order to assess the utility of such structures, complete understanding of their mechanical and thermal behavior is needed. Continuum approximations provide practical means for achieving this understanding.

In three recent papers (ref. 1-3) we derived the stiffness coefficients of equivalent continua by using a building block approach consisting of obtaining the effective properties of the smallest unit cell of the repeating structure and then using orthogonal transformation teachniques to obtain the overall properties. In (ref. 1-2) we constructed the equivalent continuum for discrete pinjointed repetitive structures using the rod's unidirectional property as our building block unit. In a more recent paper (ref. 3) we derived the effective properties of rigid jointed (frame type) repetitive structures. This differed substantially from the truss-like structures in that the influence of in-plane bending rigidities to the structure are included. The fact that the individual rod in a rigid-jointed array can resist in-plane bending dictated that the smallest sub-cell of the structure which was used as the building block unit was no longer unidirectional and thus had to be two-dimensional substructure. The most degenerate basic two dimensional frame structures were found to be the $(0^\circ, 90^\circ)$ and the $(0^\circ, \pm 60^\circ)$ layups. Effective properties for these sub-cells were constructed using simple strength of materials approaches such as the matrix structural analysis methods (ref. 4-6). This resulted in two-dimensional generalization of the one-dimensional area weighted properties needed in the analysis of pinned-jointed structures (ref. 1-2). The analysis of (ref. 1-3) gave exact results for the constitutive relations of one-dimensional (unidirectional) layups, "strictly" two-dimensional (in the forms of 0°, 90°, 0°, $\pm 60^\circ$) layups and the "strictly" three-dimensional layups as we defined in (ref. 2).

By invoking the classical plate theory assumptions the results of the strictly three-dimensional structures were successfully reduced to those of the quasi-three-dimensional problem (ref. 2) only for the case of pin-jointed

* This work was supported by NASA grant NSG1185.

structures. Here, a quasi-three-dimensional model consists of two surface sheets separated by a thickness h and are connected by diagonals to form a plate. In attempting to obtain the equivalent plate continuum for discrete frame-like structure, expressions for its general bending rigidities were not possible to obtain by the techniques described in (ref. 1-3). Therefore, we need to use another approach to develop these requirements. The energy equivalence technique presents a way of developing such properties. As a by-product of using the energy equivalence approach, we obtain, besides the bending rigidities, the information for the stiffness coefficients. The results obtained by the energy method will also help in assessing the accuracy of the building block approach described in (ref. 3).

In this paper we use the energy equivalence to construct equivalent continua for the actual lattice structure. An energy equivalent continuum is defined as that which has the same amount of strain and kinetic energies stored in it as the original lattice structure when both are subjected to the same loading conditions. The equivalent continuum is characterized by its strain and kinetic energies from which the constitutive relations and the equations of motion can be derived.

The basic concept in the energy approach is the existence of kinematic variables which are functions of continuous spatial coordinates as opposed to those in the lattice theory which are defined at discrete points or members. To relate both the discrete and continuum models, Taylor series expansion has been commonly used in constructing the equivalent continuum.

Previous studies which utilize the energy equivalence approach, such as those carried out by Sun and Yang in (ref. 7); Noor, Greene and Anderson in (ref. 8-9); Bazant and Christensen in (ref. 10, 11); and Nemeth in (ref. 12) are available in the literature. Bazant and Christensen derived an equivalent micro-polar continuum for large grid frameworks in order to solve the extensional buckling of a multi-story, multi-bay rectangular frame. Sun and Yang in (ref. 7) established a two-dimensional in-plane continuum model with couple-stress for a $(0^{\circ}, 90^{\circ})$ layup. Noor et al. constructed in (ref. 8) the equivalent continuum of a double layer grid assuming all joints to be pinned. Also, in (ref. 13) Noor developed micropolar models for large repetitive beam-like planar lattices with rigid joints. Nemeth in (ref. 12) derived the strain energy of the single layer grids with rigid joints in terms of its beam member strains and curvatures. These are then expressed in terms of the strains and curvatures of the continuum.

The present study takes a somewhat different energy approach and presents a simple method to model large rigid-jointed lattices as continuous media with couple-stresses. In our analysis the transition from the discrete system to the continuous medium is achieved by expanding the displacements and the rotations of the nodal points in a Taylor series about a suitable chosen origin. Here basic kinematic assumptions are introduced to insure that the assumptions used in deriving the governing equations of the modeled continuum are satisfied. Accordingly, the number of terms retained in the Taylor series expansion will depend upon the properties to be evaluated. This implies that one has first to determine what kind of continuum is needed to model from the discrete lattice, before the actual properties are derived.

In Section 2 we present our analysis followed in Section 3 by a comparison between our approach and those reported in the literature. Finally, in Section 4 we present a variety of applications.

2. ANALYSIS

2.1 Linearized Constitutive Equations for Elastic Materials with Couple-Stresses

The internal energy of an elastic material without couple-stresses may be expressed as a function of the material strain tensor. Toupin, in (ref. 14), has shown that when couple-stresses are taken into consideration, the energy function will be a homogeneous quadratic function of the material strain tensor ε_{ij} and the curvature twist tensor κ_{ij} which are defined as

$$\varepsilon_{ij} = \frac{1}{2}\left(\frac{\partial u_i}{\partial x_j} + \frac{\partial u_j}{\partial x_i}\right) \tag{1}$$

$$\kappa_{ij} = \frac{1}{2} e_{j\ell k}\, u_{k,\ell i} \tag{2}$$

where u_i are the components of the displacement vector and $e_{j\ell k}$ is the permutation symbol.

The strain energy function describing the general constitutive equations for a linear elastic material with couple-stresses can be obtained, as per (ref. 15), as:

$$W = \frac{1}{2} C_{ijk\ell}\,\varepsilon_{ij}\,\varepsilon_{k\ell} + B_{ijk\ell}\,\varepsilon_{ij}\,\kappa_{k\ell} + \frac{1}{2} E_{ijk\ell}\,\kappa_{ij}\,\kappa_{k\ell} \tag{3}$$

where W is the strain energy function. This strain energy expression would describe an elastic material without couple-stresses when all the $B_{ijk\ell}$ and $E_{ijk\ell}$ coefficients vanish.

2.2 Determination of the Characteristics of the Equivalent Continuum Models

The steps used in the construction of the equivalent continuum are as follows:

i. Isolate the smallest repeating element from the lattice.
ii. Write the stiffness matrix of this repeating element and calculate its strain energy in terms of its nodal displacements and rotations.
iii. The displacements and the rotations of the nodal points are then expanded in a Taylor series about a suitable chosen origin. Basic kinematic assumptions are then introduced to insure that the assumptions used in deriving the governing equations of the modeled continuum are satisfied.
iv. The displacement expansions obtained in (iii) are substituted in the energy expression of the repeating element to obtain the energy expression of the equivalent continuum, from which we can determine the characteristics of the equivalent continuum model.

The strain energy of the repeating element of a lattice with rigid joints is given by (ref. 16):

$$U = \sum_{\text{members}} \frac{1}{2}\{\Delta\}^T [\Gamma^{(m)}]^T [K^{(m)}] [\Gamma^{(m)}] \{\Delta\} \tag{4}$$

where $\{\Delta\}$ is the vector of nodal displacements and rotations of a typical member, $K^{(m)}$ is the elemental stiffness matrix of the typical beam in local coordinates, $\Gamma^{(m)}$ is the member transformation matrix in local coordinates, the superscripts m and T denote the mth member in the repeating element and transposition, respectively. As mentioned earlier, the transition from the discrete lattice to the equivalent continuous medium is done by expanding the nodal displacements and rotations about the origin of the repeating element by Taylor series. The number of the terms retained in the Taylor series expansion and the kinematic assumptions used on the continuous displacement and rotation variables will depend upon the properties to be evaluated.

This implies that we have first to determine what kind of continuum we need to model from the discrete lattice: a linear elastic material without couple-stresses where the motion is treated as a three-dimensional problem of stress analysis or an equivalent plate continuum where the fundamental equations of plate are used.

2.3 Kinematic Assumptions Used to Model a Linear Elastic Material Without Couple-Stresses

Here we evaluate the stiffness coefficients, $C_{ijk\ell}$, for the equivalent elastic linear continuum whose strain energy is

$$W = \frac{1}{2} C_{ij\,\ell}\, \varepsilon_{ij}\, \varepsilon_{k\ell} \qquad i,j,k,\ell = 1,2,3 \tag{5}$$

This will be constructed from a single layer grid or multi layer grids. For this case, the nodal displacements of the repeating element are expanded up to the second order Taylor series expansion, whereas the nodal rotations follow a one-term expansion. This implies that the rotations are considered to be constant for all the nodal points of the repeating element. Hence for a typical node (x_i, y_i, z_i) these expansions are affected as follows:

$$u_i = u + x_i \frac{\partial u}{\partial x} + y_i \frac{\partial u}{\partial y} + z_i \frac{\partial u}{\partial z} \tag{6a}$$

$$v_i = v + x_i \frac{\partial v}{\partial x} + y_i \frac{\partial v}{\partial y} + z_i \frac{\partial v}{\partial z} \tag{6b}$$

$$w_i = w + x_i \frac{\partial w}{\partial x} + y_i \frac{\partial w}{\partial y} + z_i \frac{\partial w}{\partial z} \tag{6c}$$

$$\theta_{x_i} = \Theta_x, \quad \Theta_{y_i} = \Theta_y, \quad \Theta_{z_i} = \Theta_z \tag{7}$$

where u, v, w, Θ_x, Θ_y and Θ_z are the displacement and the rotation continuous functions which assume the values of the displacements and the rotations at the origin of the repeating element. Furthermore, the rotation functions θ_x, θ_y and θ_z are the component rotations defining the rotation of the rigid equivalent

continuum; therefore, they are expressed in terms of the displacement functions u, v, w as:

$$\theta_x = \frac{1}{2}\left(\frac{\partial w}{\partial y} - \frac{\partial v}{\partial z}\right), \quad \theta_y = \frac{1}{2}\left(\frac{\partial u}{\partial z} - \frac{\partial w}{\partial x}\right), \quad \theta_z = \frac{1}{2}\left(\frac{\partial v}{\partial x} - \frac{\partial u}{\partial y}\right) \tag{8}$$

The strain energy of the equivalent continuum is obtained by substituting the expressions for the displacement and rotation given by equations (6-8) into the expression for the strain energy of the repeating element given in equation (4). By differentiating according to equation (5), we obtain the three-dimensional stiffness coefficients of the continuum.

2.4 Kinematic Assumptions Used to Model a Shear Deformation Plate Continuum

The strain energy function for a repeating element governed by the shear deformation plate theory is given in appendix A, equation (A.1) (ref. 9). Notice that the plate curvature, $\kappa_{\alpha\beta}$, are components of the general curvature-twist tensor, κ_{ij}, defined in equation (2); specifically, we have:

$$\kappa_{12} \rightarrow K_{11}, \quad \kappa_{21} \rightarrow K_{22}, \quad 2(\kappa_{22} - \kappa_{11}) \rightarrow K_{12} \tag{9}$$

Therefore, and by examining the governing equations of the shear deformation plate continuum, we establish the following procedure, using the superposition principle, to evaluate the different characteristic coefficients for that continuum.

i) Evaluate all the $A_{ijk\ell}$ stiffness coefficients as if the equivalent continuum were a three-dimensional linear elastic media with couple-stresses; the stiffness coefficients $A_{\alpha\beta\gamma\rho}$ of the reduced model are determined in terms of $A_{ijk\ell}$ as per equation (A.4) in Appendix A. The stiffness coefficients $A_{ijk\ell}$ are defined to be:

$$A_{ijk\ell} = h\, C_{ijk\ell} \tag{10}$$

where h is the plate thickness.
[Notice that $i,j,k,\ell = 1,2,3$ and $\alpha,\beta,\gamma,\rho = 1,2$]

ii) Evaluate the bending stiffness coefficients $D_{ijk\ell}$ and the coupling coefficients $F_{\alpha\beta\gamma\rho}$ of the equivalent continuum as if it were governed by the classical plate theory contitutive equations. The stiffness coefficients $A_{\alpha 3\beta 3}$ and $2A_{\alpha 3\beta\gamma}$ which represent the shear deformation contribution to the governing equations of the plate continuum are determined from the first step. The coupling and bending coefficients of the reduced model are then evaluated using equations (A.5) and (A.6) in Appendix A.

Specifically, we determine the strain energy expression for the equivalent continuum as if it is a linear elastic material with couple-stresses, as required by Toupin's constitutive equations. This is followed by specializing this strain energy expression to obtain the corresponding one for an equivalent plate continuum using the same assumptions used to obtain the governing equations for the plate continuum from the governing equations for the linear elastic continuum with couple-stresses. This is done by retaining the following expansion forms:

$$u_i = u + x_i \frac{\partial u}{\partial x} + y_i \frac{\partial u}{\partial y} + z_i \frac{\partial u}{\partial z} + \frac{1}{2} + (y_i^2 \frac{\partial^2 u}{\partial y^2} + z_i^2 \frac{\partial^2 u}{\partial z^2} + 2x_i y_i \frac{\partial^2 u}{\partial x \partial y}$$
$$+ 2y_i z_i \frac{\partial^2 u}{\partial y \partial z} + 2x_i z_i \frac{\partial^2 u}{\partial x \partial z}) \qquad (11a)$$

$$v_i = v + x_i \frac{\partial v}{\partial x} + y_i \frac{\partial v}{\partial y} + z_i \frac{\partial v}{\partial z} + \frac{1}{2} (x_i^2 \frac{\partial^2 v}{\partial x^2} + z_i^2 \frac{\partial^2 v}{\partial z^2} + 2x_i y_i \frac{\partial^2 v}{\partial x \partial y}$$
$$+ 2y_i z_i \frac{\partial^2 v}{\partial y \partial z} + 2x_i z_i \frac{\partial^2 v}{\partial x \partial z}) \qquad (11b)$$

$$w_i = w + x_i \frac{\partial w}{\partial x} + y_i \frac{\partial w}{\partial y} + z_i \frac{\partial w}{\partial z} + \frac{1}{2} (x_i^2 \frac{\partial^2 w}{\partial x^2} + y_i^2 \frac{\partial^2 w}{\partial y^2} + 2x_i y_i \frac{\partial^2 w}{\partial x \partial y}$$
$$+ 2y_i z_i \frac{\partial^2 w}{\partial y \partial z} + 2x_i z_i \frac{\partial^2 w}{\partial x \partial z}) \qquad (11c)$$

$$\theta_{x_i} = \theta_x + x_i \frac{\partial \theta_x}{\partial x} + y_i \frac{\partial \theta_x}{\partial y} + z_i \frac{\partial \theta_x}{\partial z} \qquad (12a)$$

$$\theta_{y_i} = \theta_y + x_i \frac{\partial \theta_y}{\partial x} + y_i \frac{\partial \theta_y}{\partial y} + z_i \frac{\partial \theta_y}{\partial z} \qquad (12b)$$

$$\theta_{z_i} = \theta_z + x_i \frac{\partial \theta_z}{\partial x} + y_i \frac{\partial \theta_z}{\partial y} + z_i \frac{\partial \theta_z}{\partial z} \qquad (12c)$$

where u, v, w, θ_x, θ_y and θ_z are the displacement and rotation continuous functions which assume the values of the displacements and the rotations at the origin of the repeating element. The rotation functions θ_x, θ_y, and θ_z are expressed in terms of the displacement variables u, v and w as per equation (8).

The strain energy of the equivalent linear elastic continuum with couple-stresses is obtained by substituting the above expressions for the displacements and rotation expansions into the expression of the strain energy of the repeating element given in equation (4). In order to obtain the equivalent classical continuum plate from the linear elastic media with couple-stresses, one has to impose the following two assumptions on the expression of the strain energy of that media. Firstly, by assuming bending to occur in the x-y plane only, some terms in the curvature-twist tensor of the elastic media do not contribute in the strain energy of that model and will be nonexistant. These terms are:

$$\frac{\partial^2 u}{\partial y^2}, \quad \frac{\partial^2 u}{\partial x \partial y}, \quad \frac{\partial^2 v}{\partial x^2}, \quad \frac{\partial^2 v}{\partial x \partial y}, \quad \frac{\partial^2 w}{\partial y \partial z}, \quad \frac{\partial^2 w}{\partial x \partial z}$$

And secondly, following the classical plate theory assumption, the transverse shear strains ϵ_{23} and ϵ_{13} are negligible. These lead to the following constraints:

$$\frac{\partial u}{\partial z} = - \frac{\partial w}{\partial x}, \qquad \frac{\partial v}{\partial z} = - \frac{\partial w}{\partial y} \tag{13}$$

The expressions for the rotation functions thus become

$$\theta_x = \frac{\partial w}{\partial y} \qquad \theta_y = - \frac{\partial w}{\partial x} \tag{14}$$

The plate curvatures are expressed as (ref. 16):

$$K_{11} = - \frac{\partial^2 w}{\partial x^2}, \quad K_{22} = - \frac{\partial^2 w}{\partial y^2}, \quad K_{12} = - 2\frac{\partial^2 w}{\partial x \partial y} \tag{15}$$

Using the relations (13) and (14) in the expression of the strain energy of the linear elastic media with couple-stresses we end with the strain energy of the classical plate continuum.

3. COMPARISON WITH OTHER ENERGY METHODS

At this point, we would like to compare our energy equivalence approach for continuum modeling of the large discrete structures with those reported in the literature.

1. Nemeth in (ref. 12) derived the strain energy of the single layer grid in terms of its beam member's strains and curvatures, and consequently expressed in terms of the strains and curvatures of the continuum.
2. Noor et al. in (ref. 9) derived the equivalent continuum for double layer grids with pinned joints. The strain energy of the plate continuum was obtained by replacing the axial strain in each member of the repeating element by its expression in terms of the strain components in the coordinate directions evaluated at the center of each member, and then expanding these strain components in Taylor series about a suitably chosen origin.
3. Noor et al. in (ref. 8) derived the equivalent continuum for double layer grids with pinned joints using an approach similar to the one proposed here. In their theory, a linear variation in the normal coordinate z was assumed for the displacement components; the nodal displacements were then expanded in a two term Taylor series expansion. Therefore, at a typical node (x_i, y_i, z_i) of the repeating element they obtained, as an example, the following expression for the nodal displacement w_i in the z direction:

$$w_i = (w + z_i \frac{\partial w}{\partial z}) + x_i (\frac{\partial w}{\partial x} + z_i \frac{\partial^2 w}{\partial x \partial z}) + y_i (\frac{\partial w}{\partial y} + z_i \frac{\partial^2 w}{\partial y \partial z}) \tag{16a}$$

and rearranging terms they obtained

$$w_i = w + (x_i \frac{\partial w}{\partial z} + y_i \frac{\partial w}{\partial y} + z_i \frac{\partial w}{\partial z}) + (x_i z_i \frac{\partial^2 w}{\partial x \partial z} + y_i z_i \frac{\partial^2 w}{\partial y \partial z}) \qquad (16b)$$

The difference between both approaches can be seen by comparing equation (16b) with equation (11c).

Here we would like to add that it is easier to write the strain energy of the repeating element in terms of its nodal displacements than to write it in terms of its beam members strains and curvatures; furthermore, the modeling of linear elastic media with couple-stresses for large lattice structures with rigid joints has not been presented before.

4. APPLICATIONS

4.1 Single Layer Grids

In this section an application of the energy method to determine the characteristics of the equivalent plate continuum of single layer grids is presented. The grids are considered to be rigidly connected and to have both bending and torsional rigidities. We notice here that the terms containing $(\frac{\partial}{\partial z})$ and $(\frac{\partial^2}{\partial z^2})$ in the expansion of the nodal displacements and rotations do not appear since all the grid joints lie in the same plane.

The repeating element for the $(0^\circ, 90^\circ)$ grid, the triangular mesh grid, the diagonally braced mesh grid and the hexagonal mesh grid (Figure 1) at any arbitrary point are shown in Figure 2. The areas of the repeating element for these mesh grids are L^2, $(\sqrt{3}\ L^2)/2$, $2L^2$ and $(3\sqrt{3}\ L^2)/2$, respectively.

The stiffness coefficients and the bending rigidities of the equivalent plate continuum for the $(0^\circ, 90^\circ)$, $(0^\circ, \pm 60^\circ)$ and $(0^\circ, 90^\circ, \pm 45^\circ)$ lattices are given in Table I. The stiffness coefficients and the bending rigidities characterizing the equivalent plate continuum for the hexagonal planar lattice are found to be one third of those corresponding to the $(0^\circ, \pm 60^\circ)$ layup. This result, obtained using the energy equivalence, confirms the results obtained in (ref. 17) using the 'building block' approach.

4.2 Three Dimensional Structures and Double Layered Structures

In our analysis we shall differentiate between the three dimensional structures and the double layered structures. The representative candidate in our study is the octetruss structure (ref. 18). We shall first obtain the properties of its equivalent linear elastic continuum without couple-stresses. After that, we shall model the plate continuum of the double layered tetrahedral grid (which is the quasi-three-dimensional model of the octetruss structure).

(i) Three Dimensional Octetruss Structure

This structure is shown in Fig. 3. We shall assume that all the beams have the same geometric properties. In view of the periodic nature of the structuring, we shall focus attention on joint (x_1, y_1, z_1). A typical beam assembly element at this point is displayed in Fig. 4.

In order to derive the effective stiffness properties of this repeating element, we have to determine the directions of the principal axes of the cross section of its beam elements, oy and oz, with respect to the fixed directions X_1, X_2 and X_3. The member transformation matrix in local coordinates, $[\Gamma]$, (of order 12 x 12) is given in (ref. 16) as

$$[\Gamma] = \begin{bmatrix} T & & \\ & T & \\ & & T \end{bmatrix} \tag{17}$$

where $[T]$ represents the matrix of direction cosines of the ox, oy and oz directions, respectively. It is measured in the global system X_1, X_2, and X_3, and is given by

$$[T] = \begin{bmatrix} \ell_{ox} & m_{ox} & n_{ox} \\ \ell_{oy} & m_{oy} & n_{oy} \\ \ell_{oz} & m_{oz} & n_{oz} \end{bmatrix} \tag{18}$$

For the repeating element of Figure 3, the octetruss is considered to be constructed from three single squared layers having different orientations in space. The local oz principal axis of each beam is defined to be the one which is perpendicular to the single layer grid containing that particular beam. Therefore, and with reference to Figure 3, the coordinates of the seven nodes of the repeating element are given by:

Joint	X_1	X_2	X_3
1	0	0	0
2	L	0	0
3	L/2	$L\sqrt{3}/2$	0
4	L/2	$-L\sqrt{3}/2$	0
5	0	$-L\sqrt{3}/3$	$L\sqrt{2}/\sqrt{3}$
6	L/2	$L\sqrt{3}/6$	$L\sqrt{2}/\sqrt{3}$
7	-L/2	$L\sqrt{3}/6$	$L\sqrt{2}/\sqrt{3}$

The matrices of the direction cosines, $[T]$, for the different beam members in this element are give by:

$$[T]_{1-2} = \begin{bmatrix} 1 & 0 & 0 \\ 0 & -1/\sqrt{3} & \sqrt{2}/\sqrt{3} \\ 0 & -\sqrt{2}/\sqrt{3} & -1/\sqrt{3} \end{bmatrix} \qquad [T]_{1-3} = \begin{bmatrix} 1/2 & \sqrt{3}/2 & 0 \\ -1/2 & \sqrt{3}/6 & \sqrt{2}/\sqrt{3} \\ 1/\sqrt{2} & -1/\sqrt{6} & 1/\sqrt{3} \end{bmatrix}$$

$$[T]_{1-4} = \begin{bmatrix} 1/2 & -\sqrt{3}/2 & 0 \\ -1/2 & -\sqrt{3}/6 & -\sqrt{2}/\sqrt{3} \\ 1/\sqrt{2} & 1/\sqrt{6} & -1/\sqrt{3} \end{bmatrix} \qquad [T]_{1-5} = \begin{bmatrix} 0 & -1/\sqrt{3} & 2/\sqrt{3} \\ -1 & 0 & 0 \\ 0 & -\sqrt{2}/\sqrt{3} & -1/\sqrt{3} \end{bmatrix}$$

$$[T]_{1-6} = \begin{bmatrix} 1/2 & \sqrt{3}/6 & \sqrt{2}/\sqrt{3} \\ 1/2 & -\sqrt{3}/2 & 0 \\ 1/\sqrt{2} & 1/\sqrt{6} & -1/\sqrt{3} \end{bmatrix} \qquad [T]_{1-7} = \begin{bmatrix} -1/2 & \sqrt{3}/6 & \sqrt{2}/\sqrt{3} \\ -1/2 & -\sqrt{3}/2 & 0 \\ 1/\sqrt{2} & -1\sqrt{6} & 1/\sqrt{3} \end{bmatrix}$$

The analysis described in section 2 is carried out. The strain energy of the repeating element is evaluated; the nodal displacements and rotations are expanded according to the two-term and to the one-term expansion, respectively, with respect to the nodal joint (x_i, y_i, z_i) as the suitable chosen origin; the continuous rotation functions are expressed according to equation (8); and finally the effective properties of the equivalent elastic linear continuum without couple-stresses are evaluated. These are found identical to those reported in (ref. 3 and 17).

We have confirmed in (ref. 17) that for the repeating element of Figure 4, the structure can be considered to be constructed from four $(0^\circ, \pm 60^\circ)$ layups with the restriction of using circular cross-sectional beams. This was actually done and the results were found to be identical to those reported in (ref. 17).

(ii) Double-Layered Grids

The double-layered grids are also known to be the quasi-three-dimensional structures (ref. 2). Here, the double-layered tetrahedral grid is studied. It consists of two parallel layers of $(0^\circ, \pm 60^\circ)$ beams connected by diagonal members which form three-sided pyramids as shown in Figure 5. In this double-layered grid, all the members have the same length L. In order to differentiate between the role of the upper and lower chords and the diagonals, we shall assume that the two

layers and the diagonals have different geometric and material properties from each other. If the upper and lower layers and the diagonals are designated by the subscripts 1, 2 and d, respectively, their geometric properties will be designated by $(A_1, I_{y1}, I_{z1}, J_1)$, $(A_2, I_{y2}, I_{z2}, J_2)$ and $(A_d, I_{yd}, I_{zd}, J_d)$, respectively while their material properties are designated by (E_1, G_1), (E_2, G_2) and (E_d, G_d), respectively.

Since we intend to derive the characteristics of the equivalent plate continuum for this quasi-three-dimensional structure, we must have the origin of its repeating element at the middle of the distance separating its upper and lower layers.

In what follows, we shall derive the equivalent plate continuum for this structure as if it were constructed from three different $(0^o, 90^o)$ single layers.

The area of the repeating element of the double-layered tetrahedral grid shown in Figure 6 is $(\sqrt{3}\, L^2)/2$.

The strain energy of the repeating element is evaluated. The nodal displacements and rotations are expanded according to the three-term and to the two-term expansions, respectively; the continuous rotation functions are expressed according to equation (8); the assumptions of the classical plate theory are introduced; and finally, the effective properties of the equivalent plate continuum are evaluated.

The characteristics describing the equivalent plate continuum for the double-layered tetrahedral grids are listed in Table II. Notice that Table II constitutes a modification of our previously reported results in (ref. 2) which are reflected in the appearance of the bending and torsional rigidities of the members. Examinationn of the results in Table II indicates that $C_{1212} = (C_{1111} - C_{1122})/2$ $F_{1212} = (F_{1111} - F_{1122})/2$ and $D_{1212} = (D_{1111} - D_{1122})/2$ and hence the octetruss is transversely isotropic, as is expected.

The algebraic expressions in this analysis were obtained using the algebraic programming system Reduce 2 written by Hearn (ref. 19).

REFERENCES

1. A.H. Nayfeh and M.S. Hefzy, "Continuum Modeling of Three-Dimensional Truss-Like Space Structures," AIAA J. Vol. 16, 1978, pp. 779-787.

2. A.H. Nayfeh and M.S. Hefzy, "Continuum Modeling of the Mechanical and Thermal Behavior of Discrete Large Structures," AIAA J. Vol. 19, 1981, pp. 766-773.

3. A.H. Nayfeh and M.S. Hefzy, "Effective Constitutive Relations for Large Repetitive Frame-Like Structures," Int. J. Solids Structures, Vol. 18, 1982, pp. 975-987.

4. H.C. Martin, Introduction to Matrix Methods of Structural Analysis, McGraw Hill, New York, 1966.

5. M.D. Vanderbilt, Matrix Structural Analysis, Quantum Publishers Inc., 1974.

6. L. Kollar, "Analysis of Double-Layer Space Truss with Diagonally Square Mesh by the Continuum Method," Acta Technica Academiae Scientiarum Hungaricae, Tomus 76, pp. 273-292 (1974).

7. Sun, C.T. and Yang, T.Y., "A Continuum Approach Toward Dynamic of Gridworks," Journal of Applied Mechanics, Vol 40, Series E, March 1973, pp. 186-192.

8. Noor, A.K., Greene, W.H. and Anderson, M.S., "Continuum Models for Static and Dynamic Analysis of Repetitive Lattices," presented at the AIAA/ASME/SAE 18th Structures, Structural Dynamics and Materials Conference, San Diego, California, March 21-23, 1977. (AIAA paper no 77-414.)

9. Noor, A.K., Anderson, M.S. and Greene, W.H., "Continuum Models for Beam- and Platelike Lattice Structures," AIAA Journal, Vol. 16, No. 12, December 1978, pp. 1219-1228.

10. Bazant, Z.P. and Christensen, M., "Analogy Between Micropolar Continuum and Grid Frameworks under Initial Stress," Int. J. of Solids and Structures, Vol. 8, 1972, pp. 327-346.

11. Bazant, Z.P. And Christensen, M., "Continuum Solutions for Long-Wave Extensional Buckling of Regular Frames," Int. J. of Eng. Sciences, Vol. 11, pp. 1255-1263.

12. Nemeth, Micheal P., "Continuum Models for Repetitive Lattice Structures with Rigid Joints," M.S. Thesis, George Washington University, 1979.

13. Noor, A.K. and Nemeth, M.P., "Micropolar Beam Models for Lattice Grids with Rigid Joints," Computer Methods in Applied Mechanics and Engineering, Vol. 21, 1980, pp. 249-263.

14. Toupin, R.A., "Elastic Materials with Couple-Stresses," Arch. Rational Mech. Anal., Vol. 11, 1962, pp. 385-414.

15. Tiersten, H.F. and Bleustein, J.L., "Generalized Elastiac Continua," in R.D. Mindlin and Applied Mechanics, edited by Herrmann, G., Pergamon Press, Inc., NY, 1974.

16. Przemieniecki, J.S., Theory of Matix Structural Analysis, McGraw Hill Book Company, 1968.

17. M.S. Hefzy, "Continuum Modeling and Analysis of Discrete Repetitive Large Structures," Ph.D. Dissertation, University of Cincinnati, Cincinnati, Ohio, 1981

18. Nayfeh, A.H. and Hefzy, M.S., "Continuum Modeling of Three-Dimensional Truss-Like Discrete Structures," NASA CR-145248, September 1977.

19. Hearn, A.C., "Reduce User's Manual," University of Utah, Salt Lake City, Utah, 2nd edition.

TABLE I.- Stiffness Coefficients for Plate Continuum from Single-Layered Grids

	$(0^\circ, 90^\circ)$ Grid	$(0^\circ, 60^\circ)$ Grid	$(0^\circ, 90^\circ, +45^\circ)$ Grid
$A_{1111} = A_{2222}$	$\frac{EA}{L}$	$\frac{3\sqrt{3}}{4}\frac{EA}{L} + 3\sqrt{3}\frac{EI_z}{L^3}$	$\frac{EA}{L} + \frac{\sqrt{2}}{4}\frac{E_dA_d}{L} + \frac{3\sqrt{2}}{2}\frac{E_dI_{z_d}}{L^3}$
A_{1122}	0	$\frac{\sqrt{3}}{4}\frac{EA}{L} - 3\sqrt{3}\frac{EI_z}{L^3}$	$\frac{\sqrt{2}}{4}\frac{E_dA_d}{L} - \frac{3\sqrt{2}}{2}\frac{E_dI_{z_D}}{L^3}$
A_{1212}	$\frac{6EI_z}{L^3}$	$\frac{\sqrt{3}}{4}\frac{EA}{L} + 3\sqrt{3}\frac{EI_z}{L^3}$	$\frac{6EI_z}{L^3} + \frac{\sqrt{2}}{4}\frac{E_dA_d}{L}$
$A_{1313} = A_{2323}$	$\frac{3EI_y}{L^3}$	$3\sqrt{3}\frac{EI_y}{L^3}$	$\frac{3EI_y}{L^3} + \frac{3\sqrt{2}}{4}\frac{E_dI_{y_d}}{L^3}$
$D_{1111} = D_{2222}$	$\frac{EI_y}{L}$	$\frac{3\sqrt{3}}{4}\frac{EI_y}{L} + \frac{\sqrt{3}}{4}\frac{GJ}{L}$	$\frac{EI_y}{L} + \frac{\sqrt{2}}{4}\frac{E_dI_{y_d}}{L} + \frac{\sqrt{2}}{4}\frac{G_dJ_d}{L}$
D_{1122}	0	$\frac{\sqrt{3}}{4}\frac{EI_y}{L} - \frac{\sqrt{3}}{4}\frac{GJ}{L}$	$\frac{\sqrt{2}}{4}\frac{E_dI_{y_d}}{L} - \frac{\sqrt{2}}{4}\frac{G_dJ_d}{L}$
D_{1212}	$\frac{GJ}{2L}$	$\frac{\sqrt{3}}{4}\frac{EI_y}{L} + \frac{\sqrt{3}}{4}\frac{GJ}{L}$	$\frac{GJ}{2L} + \frac{\sqrt{2}}{4}\frac{E_dI_{y_d}}{L}$

TABLE II.- Stiffness Coefficients for Plate Continuum of the Double-Layered Tetrahedral Grids Constructed Using Three Siugle Layers

$A_{1111} = A_{2222}$	$\frac{9(E_1A_1 + E_2A_2 + \frac{1}{9}E_dA_d)}{4\sqrt{3}\,L} + \frac{6\,(E_1I_{y_1} + E_2I_{y_2} + E_dI_{y_d})}{\sqrt{3}\,L^3} + \frac{\sqrt{3}\,(E_1I_{z_1} + E_2I_{z_2} + E_dI_{z_d})}{L^3}$
A_{1122}	$\frac{3(E_1A_1 + E_2A_2 + \frac{1}{9}E_dA_d)}{4\sqrt{3}\,L} - \frac{6(E_1I_{y_1} + E_2I_{y_2} - \frac{1}{3}E_dI_{y_d})}{\sqrt{3}\,L^3} - \frac{\sqrt{3}\,(E_1I_{z_1} + E_2I_{z_2} + E_dI_{z_d})}{L^3}$
A_{1212}	$\frac{3(E_1A_1 + E_2A_2 + \frac{1}{9}E_dA_d)}{4\sqrt{3}\,L} + \frac{6(E_1I_{y_1} + E_2I_{y_2} + \frac{1}{3}E_dI_{y_d})}{\sqrt{3}\,L^3} + \frac{\sqrt{3}\,(E_1I_{z_1} + E_2I_{z_2} + E_dI_{z_d})}{L^3}$
$A_{1133} = A_{2233}$	$\frac{2\,E_dA_d}{3\sqrt{3}\,L} - \frac{8\,E_dI_{y_d}}{\sqrt{3}\,L^3}$
A_{3333}	$\frac{8\,E_dA_d}{3\sqrt{3}\,L} + \frac{16\,E_dI_{y_d}}{\sqrt{3}\,L^3}$
$A_{1123} = -A_{2223} = A_{1312}$	$\frac{\sqrt{2}\,E_dA_d}{6\sqrt{3}\,L} + \frac{\sqrt{6}\,(E_1I_{y_1} + E_2I_{y_2} + \frac{1}{3}E_dI_{y_d})}{L^3} - \frac{\sqrt{6}\,(E_1I_{z_1} + E_2I_{z_2} + E_dI_{z_d})}{L^3}$
$A_{2323} = A_{1313}$	$\frac{2\,E_dA_d}{3\sqrt{3}\,L} + \frac{\sqrt{3}\,(E_1I_{y_1} + E_2I_{y_2} + \frac{1}{3}E_dI_{y_d})}{L^3} - \frac{2\sqrt{3}\,(E_1I_{z_1} + E_2I_{z_2} + E_dI_{z_d})}{L^3}$

Table II.- (cont'd)

$F_{1111} = F_{2222}$	$\frac{3\sqrt{2}}{8}(E_1A_1 - E_2A_2) + \frac{\sqrt{2}}{L^2}(E_1I_{y_1} - E_2I_{y_2}) + \frac{\sqrt{2}}{2L^2}(E_1I_{z_1} - E_2I_{z_2})$
F_{1122}	$\frac{\sqrt{2}}{8}(E_1A_1 - E_2A_2) - \frac{\sqrt{2}}{L^2}(E_1I_{y_1} - E_2I_{y_2}) - \frac{\sqrt{2}}{2L^2}(E_1I_{z_1} - E_2I_{z_2})$
F_{1212}	$\frac{\sqrt{2}}{8}(E_1A_1 - E_2A_2) + \frac{\sqrt{2}}{L^2}(E_1I_{y_1} - E_2I_{y_2}) + \frac{\sqrt{2}}{2L^2}(E_1I_{z_1} - E_2I_{z_2})$
$F_{3311} = F_{3322} = F_{3312}$	0
$D_{1111} = D_{2222}$	$\frac{3L}{8\sqrt{3}}(E_1A_1 + E_2A_2) + \frac{3(G_1J_1 + G_2J_2 + \frac{1}{9}G_dJ_d)}{4\sqrt{3}L} + \frac{7(E_1I_{y_1} + E_2I_{y_2} + \frac{3}{7}E_dI_{y_d})}{4\sqrt{3}L} + \frac{2(E_1I_{z_1} + E_2I_{z_2} + \frac{1}{12}E_dI_{z_d})}{\sqrt{3}L}$
D_{1122}	$\frac{L}{8\sqrt{3}}(E_1A_1 + E_2A_2) - \frac{3(G_1J_1 + G_2J_2 + \frac{1}{9}G_dJ_d)}{4\sqrt{3}L} - \frac{3(E_1I_{y_1} + E_2I_{y_2} - \frac{1}{3}E_dI_{y_d})}{4\sqrt{3}L} - \frac{E_dI_{z_d}}{6\sqrt{3}L}$
D_{1212}	$\frac{L}{8\sqrt{3}}(E_1A_1 + E_2A_2) + \frac{3(G_1J_1 + G_2J_2 + \frac{1}{9}G_dJ_d)}{4\sqrt{3}L} + \frac{5(E_1I_{y_1} + E_2I_{y_2} + \frac{1}{5}E_dI_{y_d})}{4\sqrt{3}L} + \frac{(E_1I_{z_1} + E_2I_{z_2} + \frac{1}{6}E_dI_{z_d})}{\sqrt{3}L}$

Appendi . A

The strain energy for a repeating element governed by the shear deformaton plate theory is:

$$U = \frac{1}{2} a \Big[A_{\alpha\beta\gamma\rho}\, \varepsilon_{\alpha\beta}\, \varepsilon_{\gamma\rho} + 2A_{\alpha\beta 33}\, \varepsilon_{\alpha\beta}\, \varepsilon_{33} + 2F_{\alpha\beta\gamma\rho}\, \varepsilon_{\alpha\beta}\, K_{\gamma\rho}$$

$$+ 2A_{\alpha\beta\gamma 3}\, \varepsilon_{\alpha\beta}\, (2\varepsilon_{\gamma 3}) + 2F_{\alpha\beta 33}\, \varepsilon_{33}\, K_{\alpha\beta} + D_{\alpha\beta\gamma\rho}\, K_{\alpha\beta}\, K_{\gamma\rho} \qquad (A.1)$$

$$+ A_{\alpha 3\beta 3}(2\varepsilon_{\alpha 3})\, (2\varepsilon_{\beta 3}) + A_{3333}\, \varepsilon_{33}^{2} \Big]$$

where a is the platform area of the repeating element. If the transverse normal stress resultant is neglected, then the transverse normal strain ε_{33} is given by:

$$\varepsilon_{33} = -\frac{A_{33\gamma\rho}}{A_{3333}}\, \varepsilon_{\gamma\rho} - \frac{F_{33\gamma\rho}}{A_{3333}} K_{\gamma\rho} \qquad (A.2)$$

The strain energy for the repeating element of the reduced model becomes

$$U = \frac{1}{2} a \Big[\overline{A_{\alpha\beta\gamma\rho}}\, \varepsilon_{\alpha\beta}\, \varepsilon_{\gamma\rho} \qquad \text{Extensional strain energy}$$

$$+ \overline{D_{\alpha\beta\gamma\rho}}\, K_{\alpha\beta}\, K_{\gamma\rho} \qquad \text{Bending strain energy}$$

$$+ \underline{A_{\alpha 3\beta 3}}\, (2\varepsilon_{\alpha 3})\, (2\varepsilon_{\beta 3}) \qquad \text{Transverse shear strain energy} \qquad (A.3)$$

$$+ 2\, \underline{A_{\alpha 3\beta\gamma}} (2\varepsilon_{\alpha 3})\, \varepsilon_{\beta\gamma} \qquad \text{Transverse shear-extensional coupling}$$

$$+ 2\, \overline{F_{\alpha\beta\gamma\rho}}\, \varepsilon_{\alpha\beta}\, K_{\gamma\rho} \Big] \qquad \text{Bending extensional coupling}$$

(the underlined terms represent the shear deformation contribution in the governing equations) where

$$\overline{A_{\alpha\beta\gamma\rho}} = \left[A_{\alpha\beta\gamma\rho} - \frac{(A_{33\alpha\beta})(A_{33\gamma\rho})}{(A_{3333})^{2}} \right] \qquad (A.4)$$

$$\overline{F_{\alpha\beta\gamma\rho}} = \left[F_{\alpha\beta\gamma\rho} - \frac{(A_{33\alpha\beta})(F_{33\gamma\rho})}{(A_{3333})^{2}} \right] \qquad (A.5)$$

$$\overline{D_{\alpha\beta\gamma\rho}} = \left[D_{\alpha\beta\gamma\rho} - \frac{(F_{33\alpha\beta})(F_{33\gamma\rho})}{(A_{3333})^{2}} \right] \qquad (A.6)$$

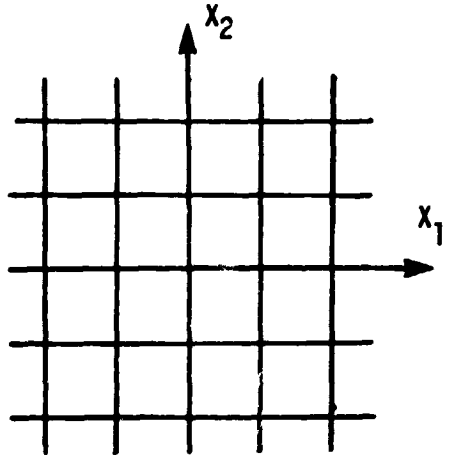

(a) $(0^{o},90^{o})$ grid.

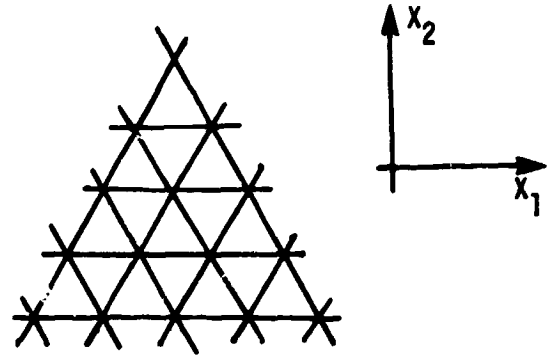

(b) Triangular mesh grid.

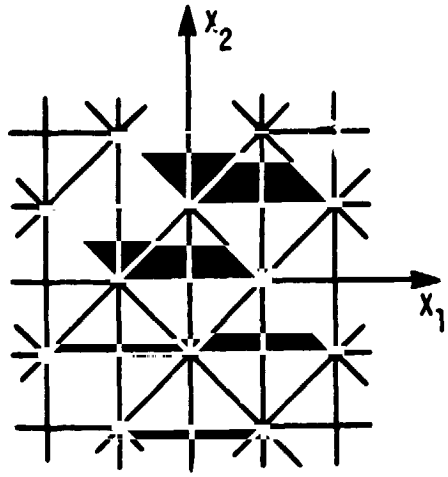

(c) Diagonally braced mesh grid.

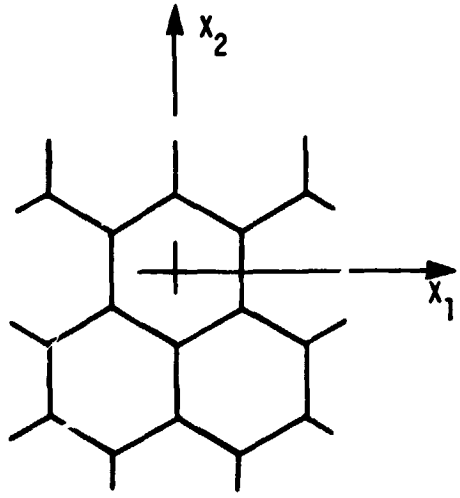

(d) Hexagonal mesh grid.

Figure 1. Four different single layer lattice grids.

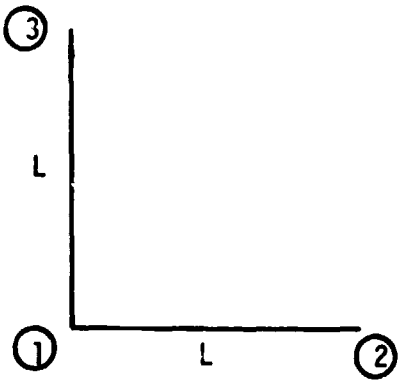

(a)

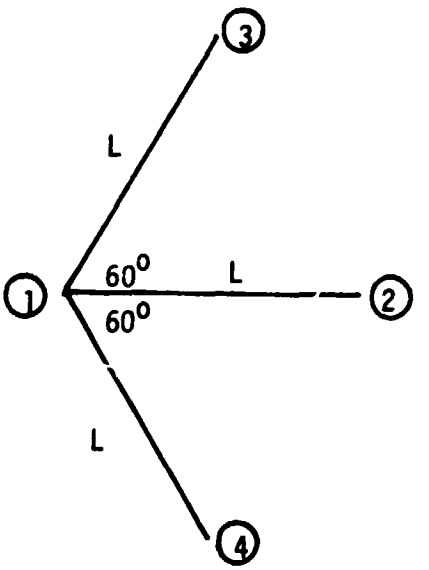

(b)

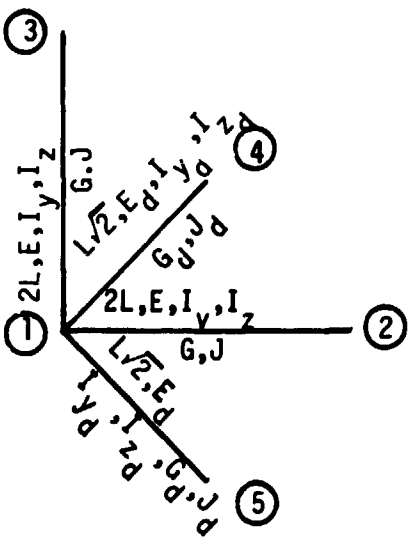

(c)

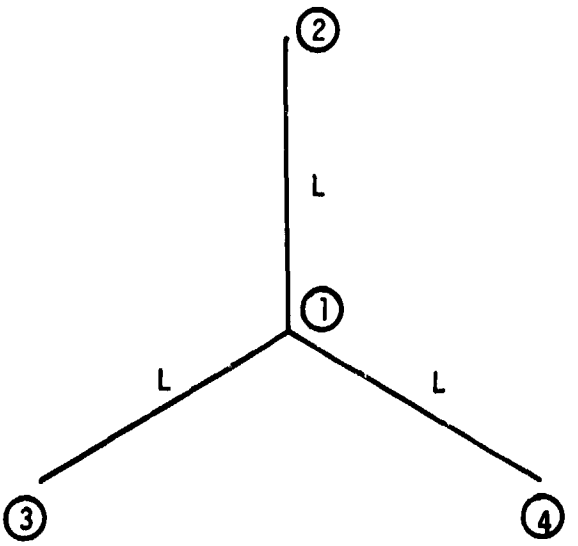

(d)

Figure 2. Repeating elements for $(0^{\circ},90^{\circ})$, $(0^{\circ},\pm60^{\circ})$, $(0^{\circ},90^{\circ},\pm45^{\circ})$ and hexagonal grids.

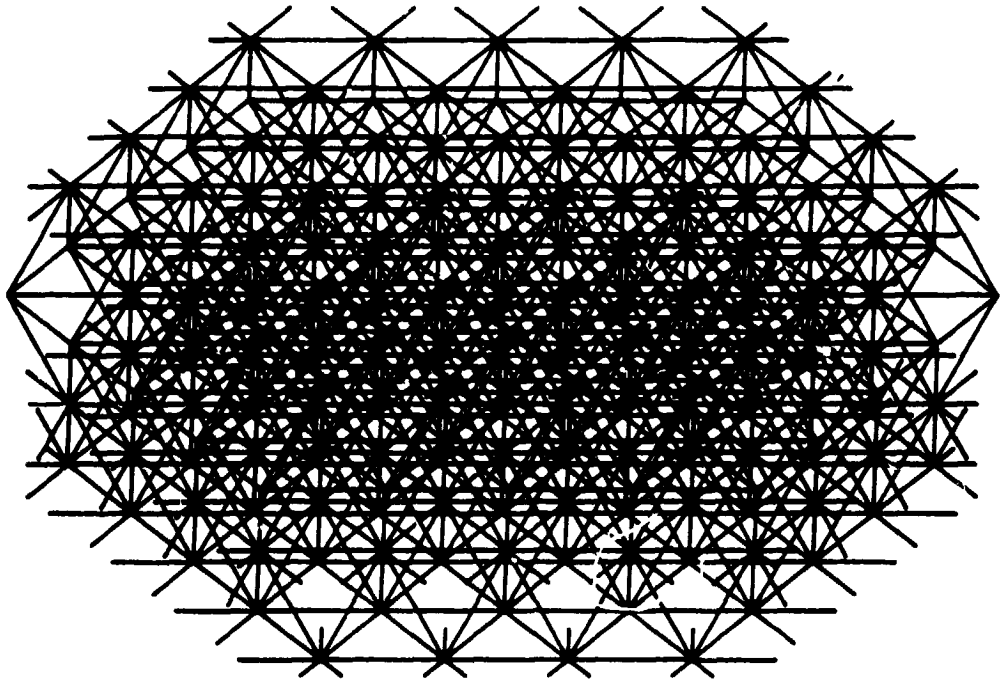

Figure 3. Three-dimensional octetruss structure.

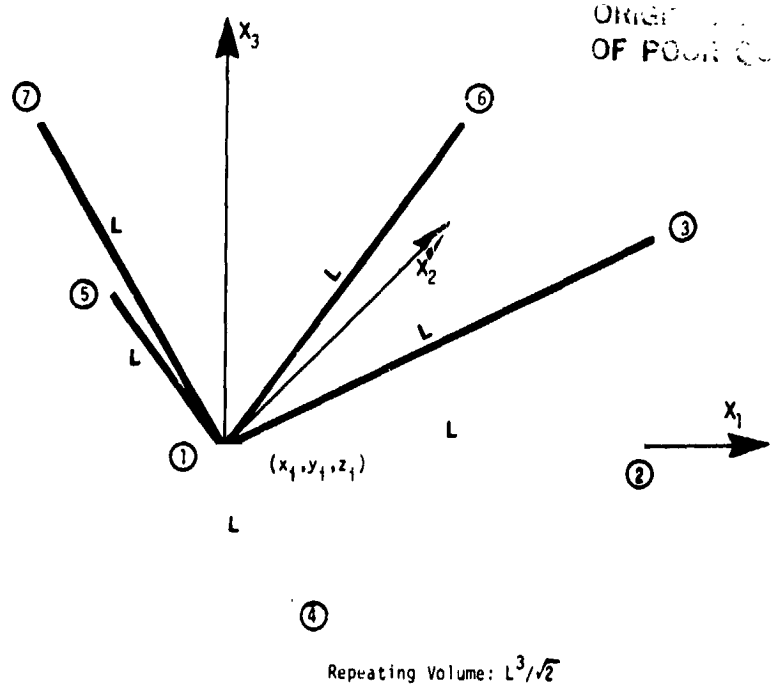

Figure 4. Repeating element of the octetruss structure.

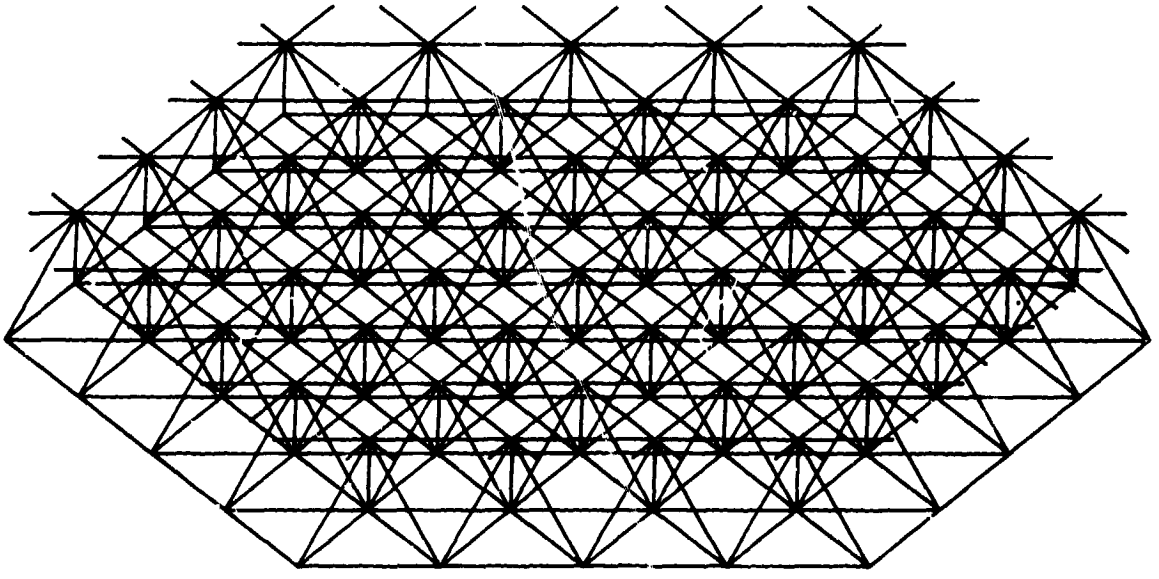

Figure 5. Quasi-three-dimensional octetruss structure corresponding to figure 3.

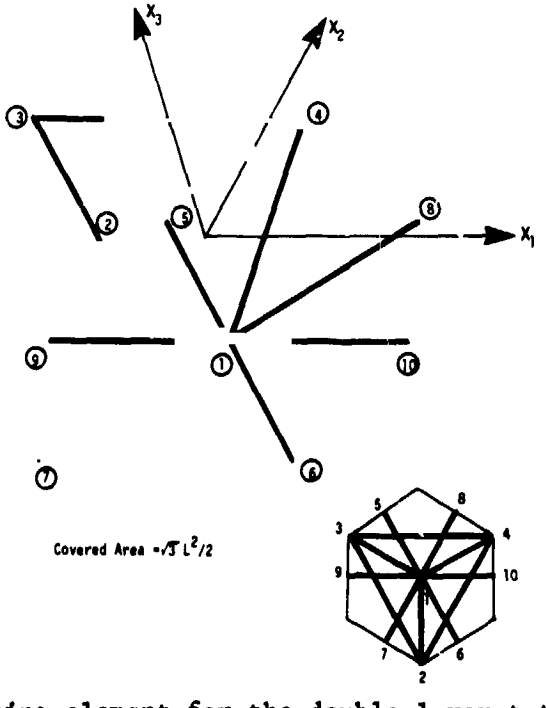

Figure 6. The repeating element for the double-layer tetrahedral grids.

INTERACTIVE BUCKLING OF THIN-WALLED STRUCTURAL COMPONENTS UNDER STATIC AND DYNAMIC LOADS*

Srinivasan Sridharan
Washington University, St. Louis, MO

Rafael Benito
Nutech International, Madrid, Spain

SUMMARY

The paper summarizes the recent advances in the study of interactive buckling of thin-walled structural components achieved with the aid of finite-strip technique used in conjunction with the theory of mode interaction. The interaction of the primary local mode with Euler buckling (in columns) and flexural-torsional buckling (in columns and beams) is of primary interest in the present study. The interaction of two companion local modes with the overall mode is also considered briefly for the columns with doubly symmetric cross-sections. The effect of dynamic loads in the form of suddenly applied end compression is also investigated.

INTRODUCTION

In recent years the subject of interactive buckling of thin-walled structures has received considerable attention. While some valuable insight has been gained (ref. 1-6), only **limited progress has been achieved towards a unified treatment of the variety of both the interactive buckling phenomena that can occur and the** cross-sectional shapes that are currently employed in various forms of engineering construction. Further, in the context of interactive buckling, thin-walled members are imperfection-sensitive so that the sudden application of axial load cannot but reduce their load carrying capacity. This aspect has not received much attention so far. In this paper a summary of the progress achieved in Washington University in the last two years towards filling these voids in the literature is presented.

The objectives of this research effort have been:

1. To develop an analytical approach that will be applicable to prismatic thin-walled members of arbitrary cross-sectional configurations for an investigation of nonlinear interaction of local and overall buckling

2. To investigate the imperfection sensitivity, especially under coincident buckling of members with typical cross-sections

3. To study the effect of dynamic application of axial loads

Only a summary of the salient features of this study is presented here and the interested reader is referred to publications listed under ref. 7-12.

* The work reported in the paper was supported by a grant from NSF (Grant No. CEE-8204673).

THEORY

The basic strategy of the present study has been to employ the finite-strip to determine the participating modes of buckling as well as the relevant higher order fields and then generate a single potential energy expression in terms of the scaling factors of the participating modes of buckling and the load parameter. Thus the number of degrees of freedom are condensed to only as many as there are modes of buckling.

In the course of the study, several versions of this basic approach were developed and these will be described briefly in the sequel.

Version I

This version is designed for a study of local and Euler buckling interactions in columns which fall in either of the following categories.

1. The column is simply supported at its ends and has a doubly symmetric cross-section and is compressed by prescribing the axial displacement of the centroid of the end section of the column.

2. The column has at least one axis of symmetry and is compressed uniformly at its ends.

The description of the first order terms is taken in the form (ref. Fig. 1):

$$u_i = \bar{u}_i(y)\ \cos(m_i \pi x/\ell)$$

$$v_i = \bar{v}_i(y)\ \sin(m_i \pi x/\ell)$$

$$w_i = \bar{w}_i(y)\ \sin(m_i \pi x/\ell) \qquad \text{(no sum on 'i')} \quad (i = 1 \text{ or } 3) \qquad 1(a\text{-}c)$$

in which 'i' takes on values of 1 and 3 and thus identifies a buckling mode (the subscript '1' refers to the primary local mode and '3' refers to the overall mode), m_i gives the number of half-waves of the buckling mode, $\bar{u}_i$..., etc. are appropriate functions of 'y'. The overall buckling of a clamped column is modelled by taking m_3=2 and a suitable shift of the origin - a valid procedure when the cross-section suffers little or no distortions.

The second order displacement field for each mode can be extracted from the governing differential equations in the form (ref. 13):

$$u_{ii} = \bar{u}_{ii}(y)\ \sin(2m_i \pi x/\ell)$$

$$v_{ii} = \bar{v}_{ii,0}(y) + \bar{v}_{ii,2}(y)\ \cos(2m_i \pi x/\ell)$$

$$w_{ii} = \bar{w}_{ii,0}(y) + \bar{w}_{ii,2}(y)\ \cos(2m_i \pi x/\ell) \quad \text{(no sum on 'i', i = 1 or 3)} \quad 2(a\text{-}c)$$

Similarly the mixed second order displacement field may be obtained in the form:

$$u_{13} = u^*_{13}(y)\ \sin\{(m_1-m_3)\pi x/\ell\} + \bar{u}_{13}(y)\ \sin\{(m_1+m_3)\pi x/\ell\}$$

$$v_{13} = v^*_{13}(y)\ \cos\{(m_1-m_3)\pi x/\ell\} + \bar{v}_{13}(y)\ \cos\{(m_1+m_3)\pi x/\ell\}$$

$$w_{13} = w^*_{13}(y)\ \cos\{(m_1-m_3)\pi x/\ell\} + \bar{w}_{13}(y)\ \cos\{(m_1+m_3)\pi x/\ell\} \qquad 3(a\text{-}c)$$

in which the barred and starred functions of 'y' are determined from a finite strip analysis (ref. **13**).

The displacement functions in eqn. 2(b-c) and 3(b-c) do not satisfy the kinematic boundary conditions for 'v' and 'w' but can be shown to be justifiable approximations. Note that $m_1 >> 1$, and m_3 is either 1 or 2. **Thus, for the second order, local and mixed second order fields are made up of so many half waves that the influence** of kinematic boundary conditions is localized near the ends. Again, for the case of overall buckling, the cross-sections remain sufficiently undistorted so that $v_{33} \approx 0$ and $w_{33} \approx 0$. It is now possible to set up a potential energy function in the form:

$$\Pi = a_1\xi_1^2\{1-\lambda/\lambda_1\} + a_3\xi_3^2\{1-\lambda/\lambda_3\} + b_{11}\xi_1^4 + b_{13}\xi_1^2\xi_3^2 + b_{33}\xi_3^4$$

$$- 2a_1(\lambda/\lambda_1)\xi_1^{(0)}\xi_1 - 2a_3(\lambda/\lambda_3)\xi_3^{(0)}\xi_3 \qquad 4$$

where ξ_1 and ξ_3 are scaling factors, $a_1 \ldots\ldots b_{33}$ are constants which can be evaluated once the displacement fields are **available, and λ is the load parameter, which in this case is the end shortening. Note that the eqn. 4 contains linear terms which contain the lowest order effect of initial imperfections. Equilibrium equations are** produced invoking the principle of stationary potential energy and solving the resulting equations by prescribing any one of (ξ_1, ξ_3, λ) and computing the other two by a standard numerical procedure such as the Newton-Raphson method.

In the case of columns of category 1, it can be shown (ref. 12) that the mixed second order field takes the character of a local mode (henceforth called 'secondary') whose wavelength tends to be the same as the primary local mode for sufficiently large values of m_1. In other words, the overall bending of the column triggers the secondary mode by its interaction with the primary mode. The secondary mode is antisymmetric (symmetric) with respect to the axis of overall buckling if the primary mode is symmetric (antisymmetric). Thus it aggravates the displacements on the compression side of the axis of bending and alleviates the same on the tension side. Examples of the two companion modes are shown for an I- and square box cross-sections in Fig. 2(a-b). The existence of a secondary local mode poses a singularity problem in the evaluation of the mixed second order field if it eigenvalue is close to that of the primary one. In this version of our approach, this problem is simply bypassed by seeking an upperbound solution (for the stiffness of the structure) by deleting the geometric stiffness terms associated with λ in the evaluation of the mixed second order field.

While this version has the advantage of simplicity, the procedure would lead in general to an overestimate of the stiffness of the structure for values of λ in the vicinity of λ_2, the critical value of λ corresponding to the secondary local mode.

Version II

This is an extension of Versions I for columns of category 1 to account precisely for the destabilizing influence of the secondary local mode. The singularity problem arises in Version I because the secondary local mode appears as a higher order field. This problem is eliminated in this version by treating the secondary mode as an additional participating mode with the full complement of higher order terms taken into account. (The scaling factor of the secondary mode (ξ_2) is assumed to be of the same order of magnitude as that of the primary.) In the analysis, it is not necessary to compute the mixed second order field arising from an interaction of each local mode with overall buckling, as this is given by the other local mode. However the mixed second order field arising from the interaction of the two local modes is taken into account and in this respect this version of the analysis is more accurate than any available in the literature so far. The potential energy for the perfect structure takes the form:

$$\Pi = a_1(1-\lambda/\lambda_1)\ \xi_1^2 + a_2(1-\lambda/\lambda_2)\ \xi_2^2 + a_3(1-\lambda/\lambda_3)\ \xi_3^2 + \underline{c\xi_1\xi_2\xi_3} + b_{11}\xi_1^4$$

$$+ b_{22}\xi_2^4 + b_{12}\xi_1^2\xi_2^2 + (b_{33}\xi_3^4 + b_{32}\xi_3^2\xi_2^2 + b_{31}\xi_3^2\xi_1^2) \qquad 5$$

The most significant feature of this function is the presence of a non-vanishing cubic (or trilinear) term underlined in eqn. 5 which usurps the role of the b_{13} term of eqn. 4. The last three terms enclosed inside the parentheses in eqn. 5, though retained in the analysis, are only of minor significance.

Version III

This version is designed to be applicable to prismatic members of arbitrary cross-section simply supported at their ends in a study of interaction of a local mode with an overall mode which may either be purely flexural (Euler) or flexural-torsional. The mode of loading is one of prescribed stress which can be uniform or linearly varying across the section.

The displacement functions for the eigenvalue problem are taken in the same form as in eqn. 1(a-c).

The second order local field is represented in the form:

$$u_{11} = \tilde{u}_{11}(y)\sin(2m_1\pi x/\ell) + \underline{u_{11,0}(y)\left(\frac{\ell}{2}-x\right)}$$

$$v_{11} = \tilde{v}_{11,0}(y) + \tilde{v}_{11,2}(y)\cos(2m_1\pi x/\ell) + \underline{v^*x(\ell-x)}$$

$$w_{11} = 0 \qquad 6(a\text{-}c)$$

The underlined terms are familiar expressions in the post-local-buckling analysis under prescribed end compression [eqn. 2(a-b)]. The additional terms have now been included to allow for:

1. The additional longitudinal compression for a given level of compressive stress which occurs due to local buckling

2. The inplane rotation of each constituent plate and thus of the entire cross-section which would occur in members whose cross-sections are not doubly symmetric, as a result of the shift of the "effective centroid" which is a consequence of local buckling. The degrees of freedom v* number as many as there are constituent plates in the structure. The second order contribution to normal displacements have been neglected for simplicity because of the smallness of flexural rigidity in comparison to their extensional rigidity.

The second order overall field is represented by Fourier series supplemented by corrective functions so as not to violate the natural boundary condition of the prescribed axial stresses at the ends:

$$u_{33} = u_{33}^{(p)}(y)\cos(p\pi x/\ell) + u_{33}^{*}(\tfrac{\ell}{2} - x)$$

$$v_{33} = v_{33}^{(p)}(y)\sin(p\pi x/\ell)$$

$$w_{33} = w_{33}^{(p)}(y)\sin(p\pi x/\ell) \qquad (p = \ldots, m_3-2, m_3, m_3+2, \ldots) \qquad 7$$

where u_{33}^{*} is a known function given by

$$u_{33}^{*} = \frac{1}{2}\{(m_3^2\pi^2/\ell^2)[\bar{v}_3^2 + \bar{w}_3^2] + \overline{vu}_{3,y}^2\}$$

Similarly the mixed second order field is given by:

$$u_{13} = u_{13}^{(q)}(y)\cos(q\pi x/\ell) + u_{13}^{*}(\ell/2 - x)$$

$$v_{13} = v_{13}^{(q)}(y)\sin(q\pi x/\ell)$$

$$w_{13} = w_{13}^{(q)}(y)\sin(q\pi x/\ell)$$

$$q = \ldots, (m_1-m_3-2),\ (m_1-m_3), (m_1-m_3+2), (m_1+m_3-2), (m_1+m_3), (m_1+m_3+2), \ldots$$

$$8(a\text{-}c)$$

Again u^*_{13} is a known function given by:

$$u^*_{13} = (m_1 m_3 \pi^2/\ell^2) w_1(y) w_2(y)$$

(m_1 and m_3 are assumed to be both even or both odd)

A simplifying factor in the analysis is the uncoupling of harmonics which occurs in the determination of the second order overall and mixed second order fields. The orthogonality conditions between each of the second order fields with both of the eigenmodes are enforced by the use of a Lagrangian multiplier technique in the computations. In the evaluation of the second order fields, the value of the load parameter was set equal to λ_o, a constant equal to smaller of the two values, viz. (i) λ_{max} (the maximum value of λ, attainable in the presence of imperfections) and (ii) Min $|\lambda_1, \lambda_3|$. The energy function in this version includes a full complement of cubic and quartic terms in the two degrees of freedom.

Dynamic Interaction

Dynamic behavior under suddenly applied loads is investigated neglecting the axial modes of vibration. A kinetic energy expression is written in the form of a homogeneous quadratic of the scaling factors ($T=m_i \dot{\xi}_i^2$). Langrangian equations of motion are set up in terms of ξ_i for any given level of axial load. These equations are then solved using an implicit method (Newmark's 'β' method) in conjunction with Newton-Raphson iteration to obtain the dynamic response. Dynamic buckling is signaled when the deflections grow indefinitely with time.

EXAMPLES

In what follows, examples are presented to illustrate the type of results that can be produced using the different versions of the method and some salient features of interactive buckling of thin-walled structural components.

Interaction in Clamped Stiffened Panels

A wide plate carrying equispaced narrow rectangular stiffeners is considered. Because of the symmetry with respect to the longitudinal center lines of each panel, only the action of a typical panel included between any two successive center lines is considered. Table 1 summarizes the details of the panels under study. Of these Panel A has a considerably slender stiffener ($d_s/t=25$) which therefore initiates the buckling process. Panel B has a more realistic stiffener with $d_s/t=15$, typically used in offshore construction. The panels exemplify the case of near coincident buckling. Twenty-four strips are employed in the finite strip analysis to represent the panel and these appear to be certainly adequate as judged from earlier convergence studies (ref. 7).

Fig. 3(a-b) shows the imperfection-sensitivity surfaces of the panels. These surfaces give the maximum load carried by the structure as a fraction of σ_{c_1}, the local critical stress of the structure. A common feature of the behavior of the

panels is that there exists a limit on the end shortening on the natural loading path in the presence of imperfections. Very often this limit is reached before the structure begins to shed the load and there follows a catastrophic form of failure under controlled end shortening.

The more acute imperfection-sensitivity of Panel A in comparison to Panel B is in conformity with the general view (ref. 1) **that the greater the slenderness of the web** the greater the imperfection sensitivity. The other factor which controls the imperfection sensitivity is of course $\sigma_{c_3}/\sigma_{c_1}$ the ratio of overall to the local critical stress. Panel C has the same cross-section as A but with its length reduced so that $\sigma_{c_3}/\sigma_{c_1}$=1.52. The imperfection sensitivity continues to be severe, but there occurs an increase in the maximum load of 11% over the local critical load for the perfect panel (not shown).

Interaction in I-Section and Box Section Columns: Version II

Fig. 4 shows the cross-sectional dimensions of the I-section columns investigated. Fig. 2(a) illustrates the primary local mode. The interaction of overall bending about the xx-axis aggravates the deflections on the compression side and alleviates the same on the tension side leading to the triggering of the secondary local mode also illustrated in Fig. 2(a). Columns having two different lengths are considered:

(a) ℓ = 2000t, $\sigma_{c_3}/\sigma_{c_1}$ = 1.06, $\sigma_{c_2}/\sigma_{c_1}$ = 1.21

(b) ℓ = 1200t, $\sigma_{c_3}/\sigma_{c_1}$ = 2.90, $\sigma_{c_2}/\sigma_{c_1}$ = 1.21

Fig. 5(a) shows the variation of the maximum load that can be carried by the column (a) expressed in the form σ_u/σ_{c_1} with overall imperfection amplitudes. The effect of introducing a given imperfection in the local mode equal to 0.2t is also illustrated in the same figure. These results are compared with the upperbound solution produced by Version I. The latter values are consistently higher because of the destabilizing influence of the secondary local mode duly considered in Version II. In Fig. 5(b) the same results are plotted for the column (b). Here the differences between the two sets of results are more pronounced. Because of the considerably higher value of the overall critical stress, λ can now approach closer to λ_2 than in case (a) and so the secondary local mode causes an increased destabilization.

Comparison with Koiter's Results on Square Box Columns

Square box columns with various values of $\sigma_{c_3}/\sigma_{c_1}$ and different levels of initial imperfections have been studied using Version II. Fig. 6a shows the variation of σ_u/σ_{c_1} with $\sigma_{c_3}/\sigma_{c_1}$ for two different levels of local imperfection ($\xi_1^{(0)}$t), viz. t/80 and t/20 as obtained by the present theory and as obtained by Koiter (ref. 14). In Fig. 6b similar results are presented for columns having a fixed value of local imperfection equal to t/40 and two different values of overall imperfections, viz. 1% and 8% of the radius of gyration (r) of the cross-section. In the range of $\sigma_{c_3}/\sigma_{c_1}$ considered, Koiter's theory gives results which exceed those of the present theory by a maximum of 7%. Koiter used a mechanical model to which he built in the degrees of freedom corresponding to local buckling and postbuckling deformation in an approximate manner. A major approximation in his approach is the complete **neglect of the** mixed second order field arising out of interaction of the two local modes - an

approximation which overestimates the coefficient b_{12} in the energy function (ref. eqn. 5) which in turn overestimates the stiffness of the structure. This field, if taken into account, gives additional freedom to the plate elements to 'pull in' (in the compression zone) or to 'relax' (in the tension zone) in their own plane. The results of the present theory must be deemed more accurate.

Interaction of Local and Lateral-Torsional Buckling

In order to illustrate the scope of the analysis in Version III, we consider a problem not so far studied in a rational manner: the interaction of local and lateral-torsional buckling in a beam subjected to end moments. We consider a set of three T-section beams having near coincident critical stresses. The details are shown in Fig. 7(a). The load-displacement characteristics are shown in Fig. 7(b) for the imperfection magnitudes given by $\xi_1^{(0)}=0.1$, $\xi_3^{(0)}=1/2000\cdot\ell/t$. For shorter d/b (=1.0) the interaction does not produce any catastrophic effects; the local buckling displacements decrease after having increased initially and there occurs a gradual increase in the overall buckling amplitudes as we approach the combined critical load. The behavior of the section with d/b=2.0 is, on the other hand, quite the opposite. There occurs a rapid increase in both the local and overall buckling amplitudes around 80% of the critical load, followed closely by a limit point type of failure. It is evident that the structure is now imperfection sensitive. As d/b increases, the torsional component in the overall buckling deformation diminishes and the flexural component increases. It appears that the torsional buckling and local buckling modes merely 'interfere' with each other (as would do two local modes) leading to imperfection insensitivity. When flexural component is dominant in the overall buckling deformation, then there results an imperfection-sensitive behavior. This finding is of considerable practical importance as some proposed design approaches have assumed that the interactions of both types of overall buckling, viz. lateral torsional and purely flexural buckling, with local buckling are equally serious problems (15).

Interaction Under Dynamic Loading

An I-section column with B/t=80 and D/t=80, ℓ/t=2000 (Fig. 4) was chosen to study the effect of suddenly applied end compression. Table 2 gives the static and dynamic buckling values of λ (viz. λ_S and λ_D) as a fraction of λ_1 for various imperfection amplitudes. Figure 8(a) shows the variation of local and overall (spatial) amplitudes with nondimensional time $\tau(=\omega_1 T\times 10^3)$ for a value of $\lambda<\lambda_D$. It is found that the column vibrates essentially about the static equilibrium position in both the modes. The local amplitude varies in the form of a slowly varying function which itself is periodic, its maxima synchronizing with the maxima of vibration in the overall mode. Figure 8(b) shows the variation of ξ_1 and ξ_3 with respect to time, again for a value of λ greater than λ_D by 1%. In this case, the amplitudes continue to increase with time signalling dynamic instability. It is evident from a study of Table 2 that the additional loss of capacity to carry loads resulting from their sudden application is primarily influenced by overall imperfections, which makes their consideration in design and fabrication especially important. For an overall imperfection of magnitude of L/1000, the drop in the limit end compression is about 8% from the static case. In many practical cases, plastic yielding would be triggered due to huge oscillations that build up for end compressions significantly smaller than λ_D.

CONCLUSION

Significant progress has been made in the prediction of behavior under interactive buckling of prismatic thin-walled column and beams using the finite-strip technique and the theory of mode interaction. The approaches developed can deal with a variety of problems of practical interest. The effect of sudden application of the axial load has been investigated and it is shown that the dynamic buckling load can be significantly smaller than the static buckling load in the presence of imperfections.

NOTATION

B	width of flange at I-section
D	depth of web of I-section
T	kinetic energy; also time
b	width of flange of T-section; width of panel
d	depth of web of T-section
d_s	depth of stiffener
m_1, m_3	the number of half waves of buckling in the local and overall modes
t	thickness of a certain plate element (t_s = thickness of stiffener)
u,v,w	the displacement components in the x,y,z directions
x,y,z	the coordinate axes in the longitudinal, transverse and normal directions of a plate strip
Π	potential energy
λ	load parameter
λ_{max}	value of λ corresponding to λ_{max}
$\lambda_1, \lambda_2, \lambda_3$	critical value of λ corresponding to buckling in the primary local, secondary local and overall modes respectively
λ_S, λ_D	maximum value of λ corresponding to buckling under static and dynamic application of load
ξ_1, ξ_2, ξ_3	scaling factors for the primary local, secondary local and overall modes respectively
$\xi_1^{(0)}, \xi_2^{(0)}, \xi_3^{(0)}$	initial imperfections in the buckling modes
$\sigma_{c_1}, \sigma_{c_2}, \sigma_{c_3}$	critical stresses in axial compression

τ dimensionless time ($\omega_1 T \times 10^3$)

ω_1 natural frequency in the primary local mode

REFERENCES

1. Neut, van der, A.: Mode Interaction with Stiffened Panels Z-Z in Buckling. Buckling Structures, B. Budiansky (Ed.), Springer-Verlag, Berlin, 1976, pp. 117-132.

2. Tvergaard, V.: Imperfection-Sensitivity of a Wide Integrally Stiffened Panel Under Compression. International Journal of Solids and Structures, vol. 9, 1973, pp. 177-192.

3. Kotter, W. T.; and Pignataro, M.: An Alternative Approach to the Interaction Between Local and Overall Buckling in Stiffened Panels. Buckling of Structures, B. Budiansky (Ed.), Springer-Verlag, Berlin, 1976, pp. 133-148.

4. Kotter, W. T.; and Pignataro, M.: A General Theory for the Interaction Between Local and Overall Buckling of Stiffened Panels. Technische Hogeschool, Delft, report no. WTHD-83 FR-556, 1976. (Avail. NTIS HC-A04/MF-A01.)

5. Graves-Smith, T. R.: The Ultimate Strength of Locally Buckled Columns of Arbitrary Length. Thin-Walled Steel Construction, Ed. K. C. Rockey and H. V. Hill, Crosby Lockwood, London, 1967.

6. Thompson, J. M. T.: Instabilities and Catastrophies in Science and Engineering. John Wiley and Sons, 1982.

7. Sridharan, S.: Doubly Symmetric Interactive Buckling of Plate Structures. International Journal of Solids and Structures, vol. 19, no. 7, 1983, pp. 625-641.

8. Sridharan, S.; and Benito, R.: Columns: Static and Dynamic Interactive Buckling. Journal of Engineering Mechanics, ASCE, vol. 110, no. 1, Jan. 1984, pp. 49-65.

9. Benito, R.: Static and Dynamic Interactive Buckling of Plate Assemblies. D.Sc. Dissertation, Washington University in St. Louis, 1983.

10. Benito, R.; and Sridharan, S.: Interactive Buckling Analysis with Finite Strips. International Journal of Numerical Methods in Engineering, in press, 1984.

11. Benito, R.; and Sridharan, S.: Mode Interaction in Structural Members. Journal of Structural Mechanics, in press, 1984.

12. Sridharan, S.; and Ali, M. A.: Response of Frames Having Thin-walled Columns. Research Report no. 59, Washington University, Dept. Civil Engineering, Aug. 1984.

13. Sridharan, S.: A Semianalytical Method for the Post-Local-Torsional Buckling Analysis of Prismatic Plate Structures. International Journal for Numerical Methods in Engineering, vol. 18, 1982, pp. 1685-1697.

14. Kotter, W. T.; and Neut, van der, A.: Interaction Between Local and Overall Buckling of Stiffened Compression Panels. Thin-Walled Structures, J. Rhodes and A. C. Walker (Eds.), John Wiley and Sons, 1980, pp. 61-85.

15. Wang, S. T.; and Pao, H. Y.: Torsional-Flexural Buckling of Locally Buckled Columns. Computers and Structures, vol. 11, 1980, pp. 127-136.

TABLE 1.-GEOMETRY AND INITIAL BUCKLING DATA OF STIFFENED PANELS

Identification of Panel	GEOMETRY				BUCKLING MODES AND CRITICAL STRESSES*		
	b	$t(=t_s)$	d_s	ℓ	m_1	$\left(\frac{\sigma_{c_1}}{E}\right)\times10^3$	$\left(\frac{\sigma_{c_3}}{E}\right)\times10^3$
A	50	1	25	1320	22	1.157	1.190
B	50	1	15	600	12	1.526	1.513
C	50	1	25	1080	18	1.157	1.762

* The subscripts 1 and 3 refer to the local and Euler modes; $m_3=2$ for all cases.

TABLE 2.-DYNAMIC BUCKLING COMPRESSION VALUES OF THE I-SECTION COLUMN

Initial Imperfections $\xi_3^{(0)}$	Initial Imperfections $\xi_1^{(0)}$	λ_S/λ_1	λ_D/λ_S	λ_D/λ_1
0.0	0.1	0.92	1.0	0.92
	0.2	0.85	1.0	0.85
	0.5	0.75	1.0	0.75
1.0	0.1	0.80	0.96	0.77
	0.2	0.75	0.96	0.72
2.0	0.1	0.74	0.92	0.68
	0.2	0.70	0.92	0.64

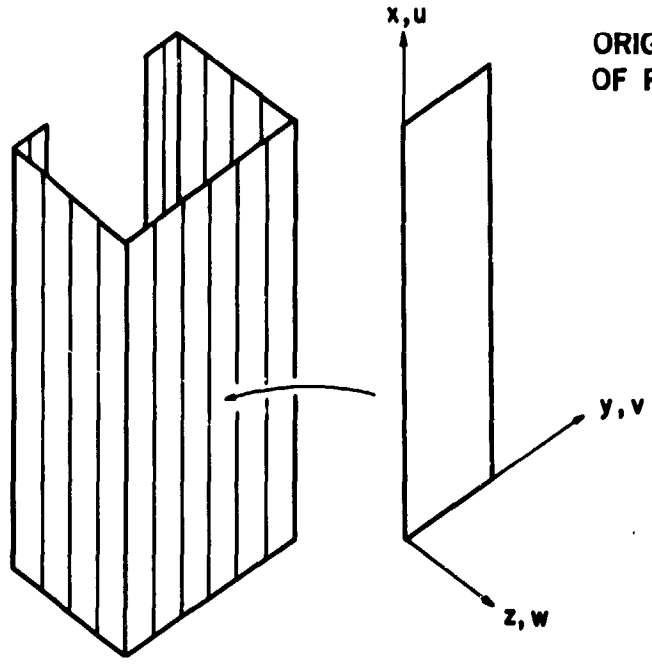

Figure 1.- Finite strip configuration and the local coordinate system.

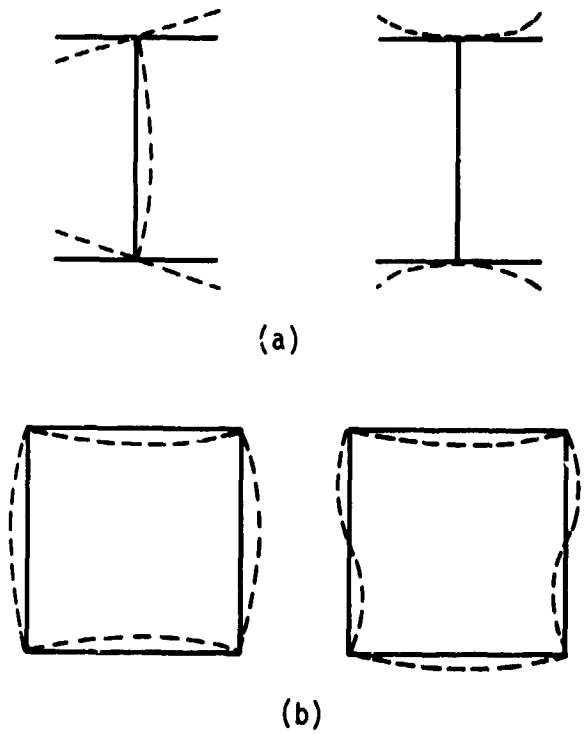

Figure 2.- The primary and secondary local modes of buckling for an I-section (a) and a square box (b) column.

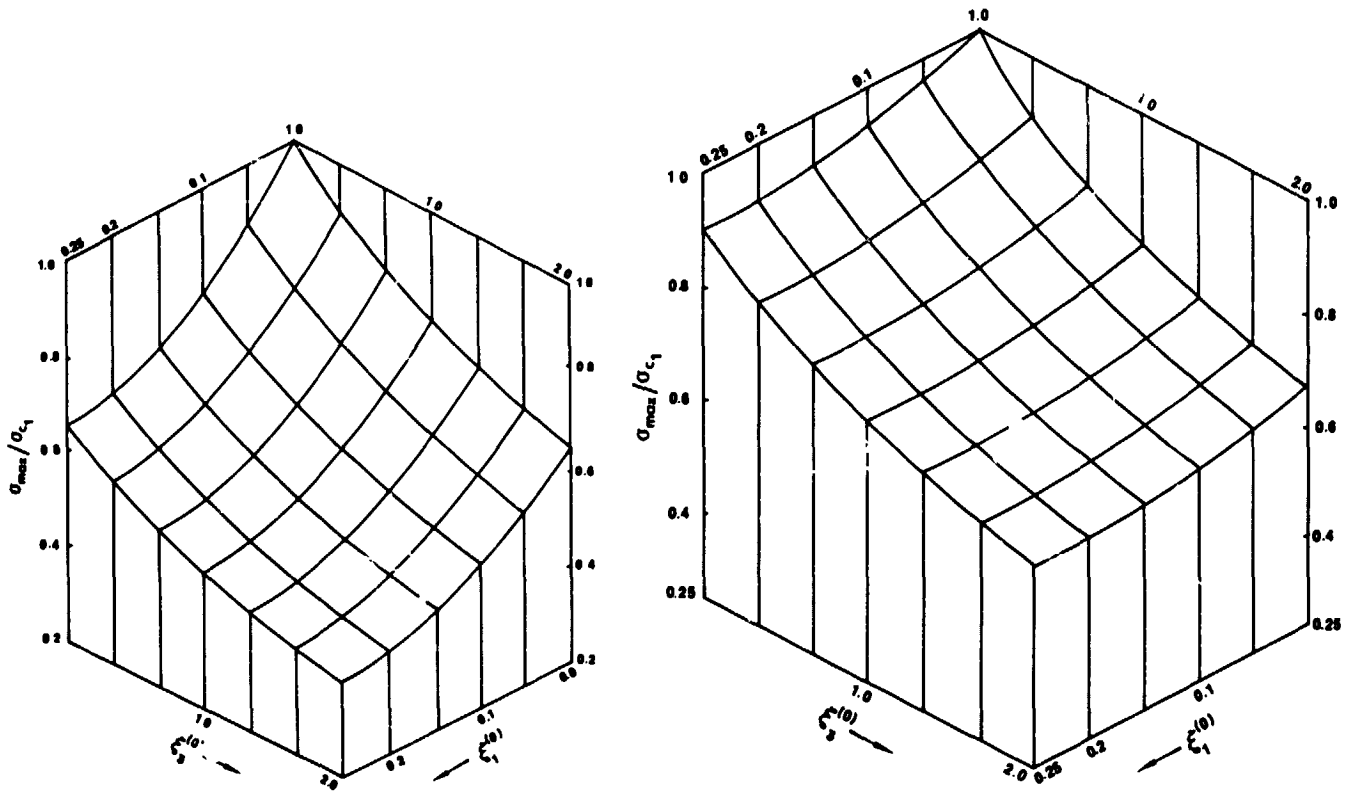

(a) Stiffened panel A. (b) Panel B.

Figure 3.- Imperfection-sensitivity surface of panels A and B. (See Table 1.)

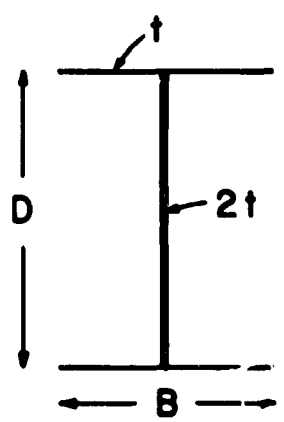

Figure 4.- The dimensions of the I-section column studied (B=D=80t, ℓ=2000t and 1200t).

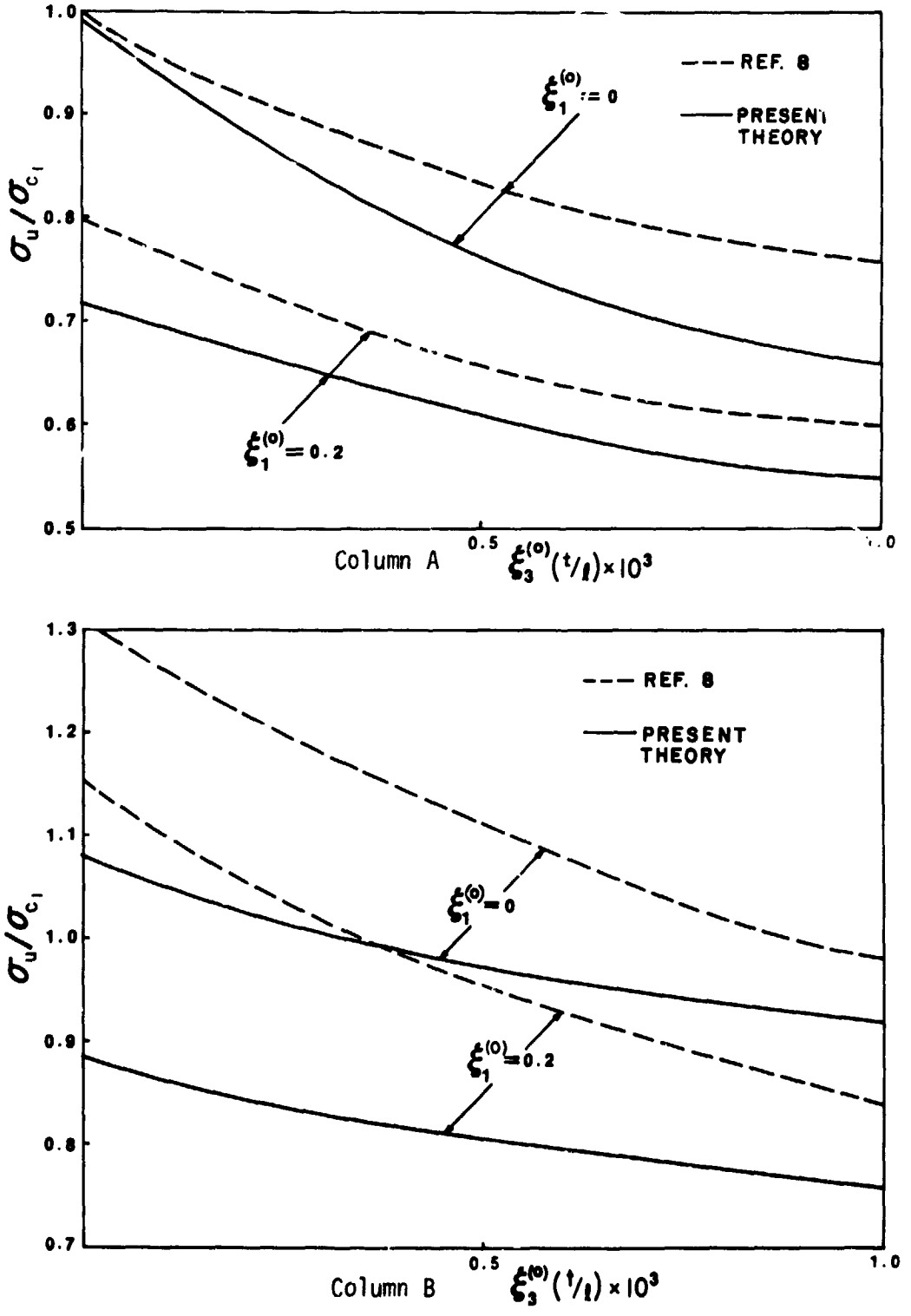

Figure 5.- The variation of maximum load supported by I-section column with overall imperfections for a specified local imperfection for columns A and B.

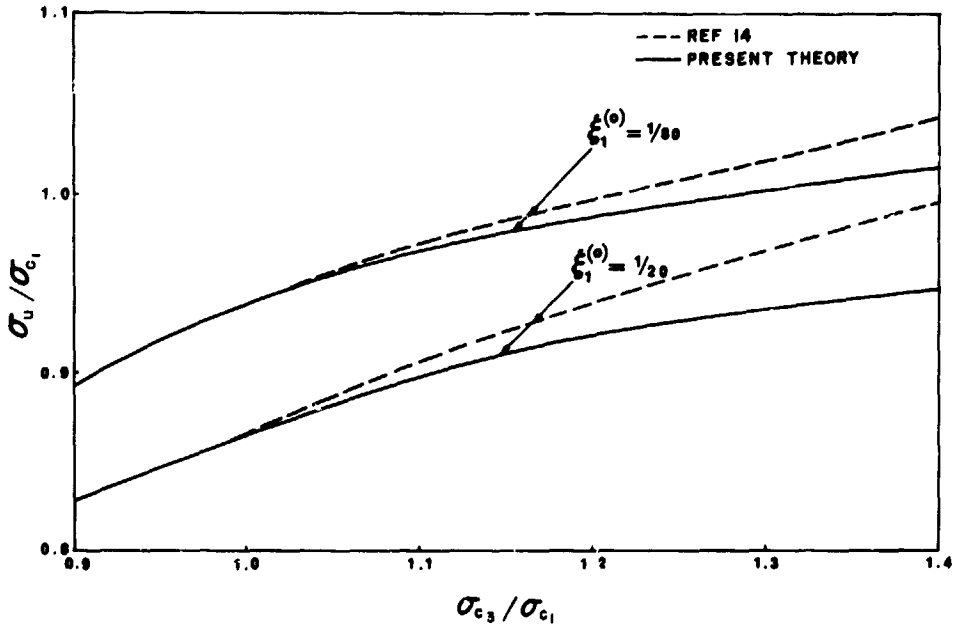

(a) Local imperfections only.

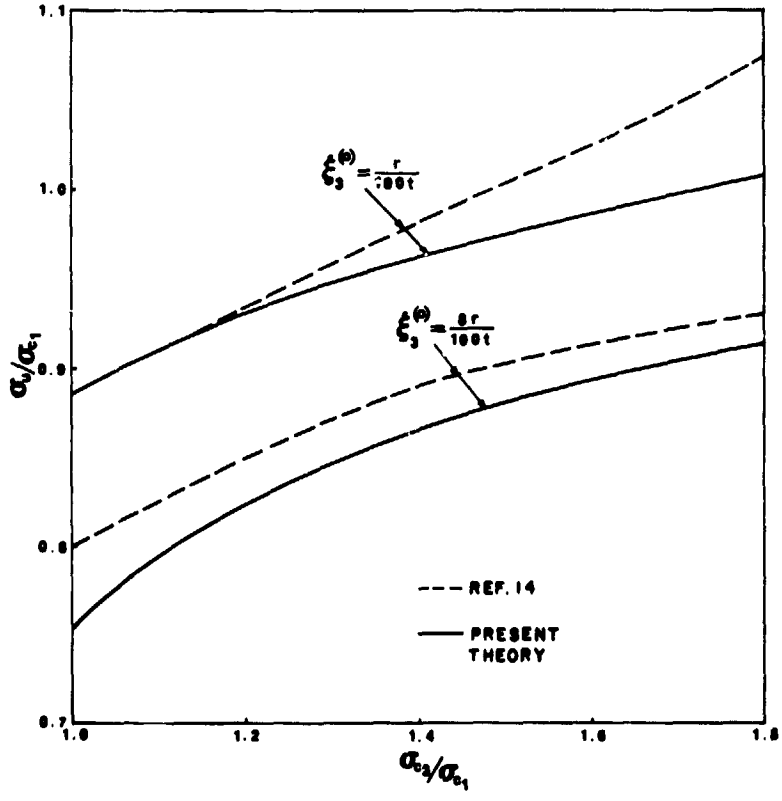

(b) Combined imperfections ($\xi_j^{(0)} = 1/40$).

Figure 6.- Variation of maximum support load with the ratio of critical stresses for square box column.

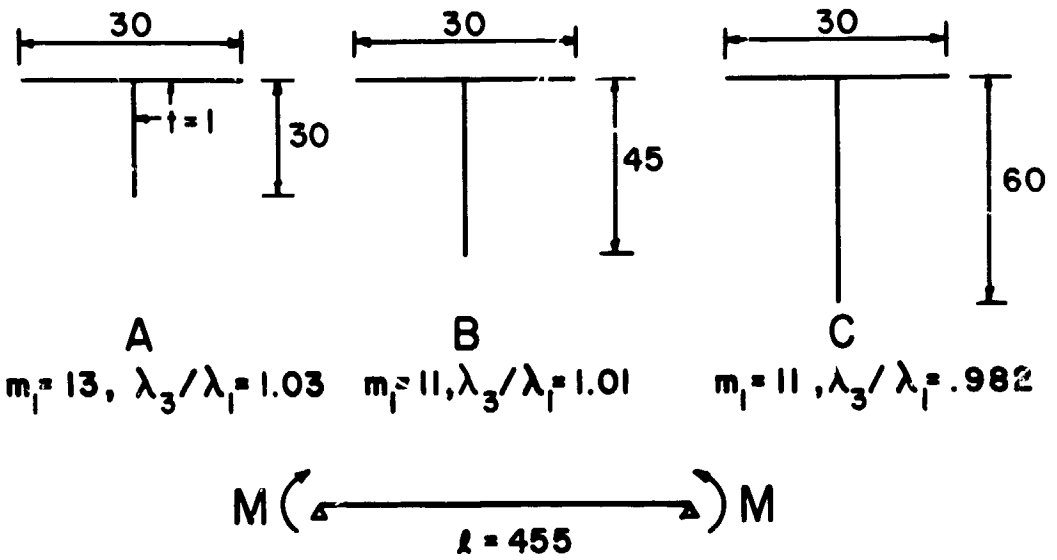

(a) The details of the T-section beam carrying end moments of M. $\xi_1^{(0)}$ = local imperfection amplitude at the tip of the tip of the flange divided by t = 0.1; $\xi_3^{(0)}$ = overall imperfection amplitude at the junction of the flange and web divided by t, = 1/2000(ℓ/t).

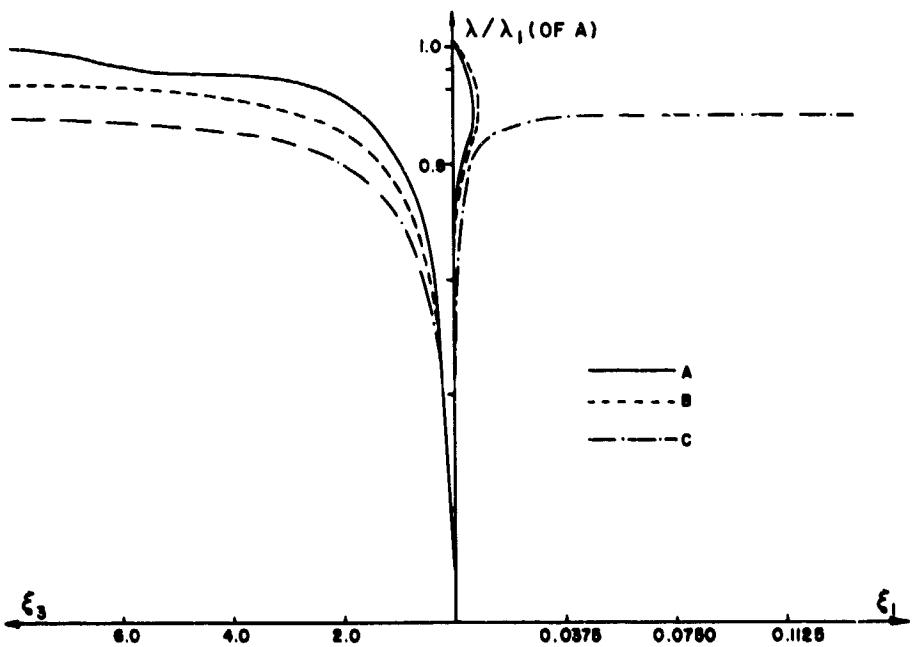

(b) The load deflection characteristics of the T-section beams.

Figure 7.- Details and load displacement characteristics of T-section beam.

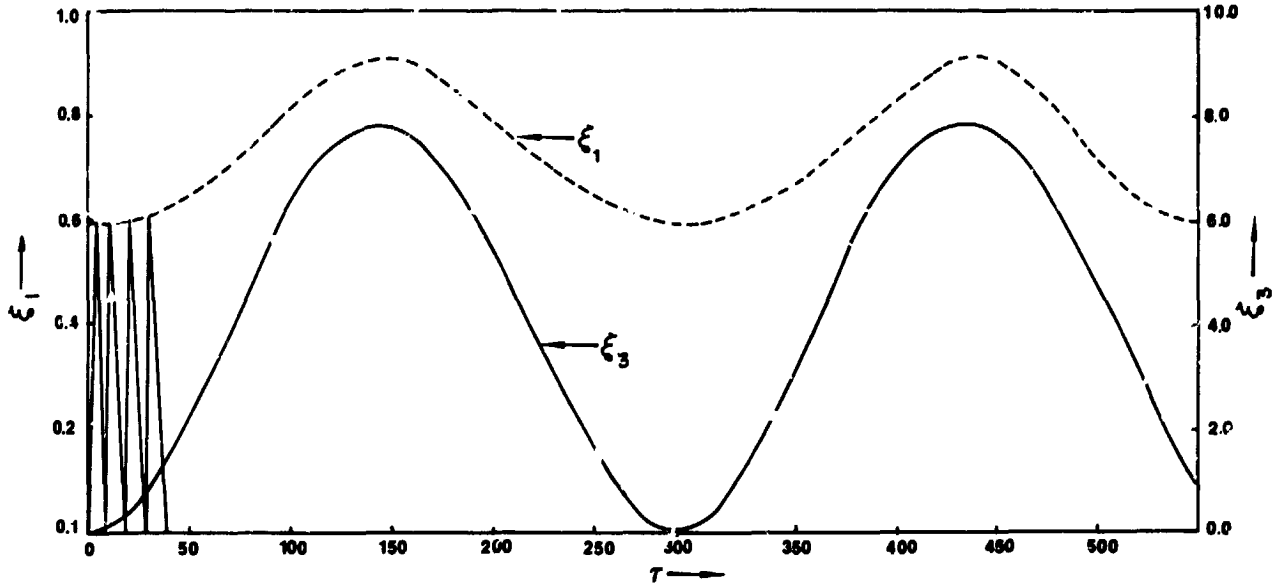

(a) $\lambda = 0.4 \times 10^{-3}$.

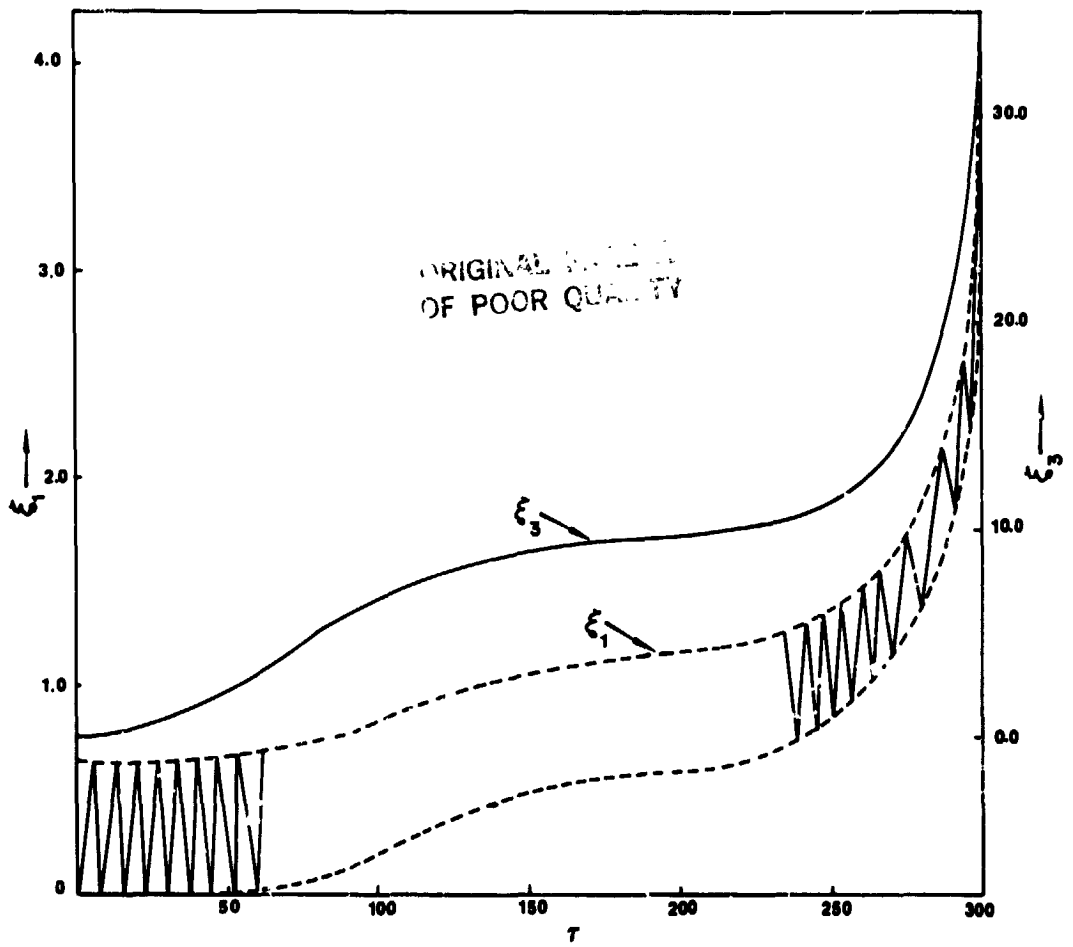

(b) $\lambda = 0.407 \times 10^{-2}$.

Figure 8.- Dynamic response of I-section column (ref. Fig. 4) with $\xi_1^{(0)} = 0.2$, $\xi_3^{(0)} = 2.0$ under suddenly applied end compression.

INITIAL POSTBUCKLING ANALYSIS OF ELASTOPLASTIC THIN-SHELL STRUCTURES

E. G. CARNOY and G. PANOSYAN

Novatome, la Boursidière RN.186

92357 Le Plessis Robinson Cedex

ABSTRACT

The design of thin-shell structures with respect to elastoplastic buckling requires an extended analysis of the influence of initial imperfections. For conservative design, the most critical defect should be assumed with the maximum allowable magnitude. This defect is closely related to the initial postbuckling behavior. The paper presents an algorithm for the quasi-static analysis of the postbuckling behavior of structures that exhibit multiple buckling points. The algorithm based upon an energy criterion allows the computation of the critical perturbation which will be employed for the definition of the critical defect. For computational efficiency, the algorithm uses the reduced basis technique with automatic update of the modal basis. The method is applied to the axisymmetric buckling of cylindrical shells under axial compression, and conclusions are given for future research.

INTRODUCTION

The design of LMFBR slender vessels involves complex and possibly stiffened shell structures that are submitted to pressure loads and large temperature gradients. The design requires an extended buckling analysis which takes into account geometrical and material non-linearities as well as the influence of initial imperfections.

In most cases, however, initial imperfections are not known except for their global order of magnitude which can be obtained from fabrication tolerances. For conservative design, the most critical imperfection should be assumed with the maximum allowable magnitude. Then, the difficulty consists of defining the most critical imperfection pattern.

For small imperfections, asymptotic theories (1 to 3) describe the critical imperfection as parallel to the initial postbuckling behavior of the actual structure. In the elastoplastic range, determination of the initial postbuckling behavior is a quite difficult task since the buckling point is generally multimodal; namely, a relatively large number of deformation modes exhibit null or small stiffnesses, and depending upon the initial perturbation, several postbuckling paths can be obtained.

Moreover, the elastic criterion of the minimum of the total potential energy should be extended to non-conservative systems, such as elastoplastic materials.

Although a quasi-static approach is employed, the mass matrix is the only physical norm that can be used for defining the perturbation amplitude (4). Then, considering a small but finite perturbation, the critical postbuckling path is defined by the perturbation that minimizes the work of internal forces.

The purpose of this paper is the description of methods that allow approximate solution of this complex minimum problem. The first issue consists of defining a suitable reduced modal basis for the description of the structural behavior around the buckling point. The use of a reduced subspace, while not necessary for the solution of the minimization problem, allows saving of computer time and improves the understanding of the structural behavior.

Much work has been done on the reduced basis technique, especially for conservative systems (5 to 9). Some of these works concern the elastic buckling and imperfection sensitivity of thin shell structures (6, 7). The mixed finite element approach also improves the reduced basis technique for elastic behaviors (10, 11). The introduction of plasticity requires special care for the definition of a suitable subspace, since possible unloading in the early postbuckling path may drastically change the structural behavior with respect to the initial modal bases. The proposed approach that involves a continuous update of the reduced subspace is presented in the next section.

The next issue consists of defining the critical perturbation for a given amplitude by applying the minimum criterion to the reduced subspace. Employing Crisfield's method (12), we search for the equilibrium path in the reduced basis that corresponds to a given initial direction. The internal work is also evaluated along this postbuckling path. The third section presents the algorithm for defining the suitable initial direction in the reduced subspace.

Simple numerical examples corresponding to the axisymmetric buckling of cylindrical shell under axial compression are given in the fourth section and conclusions for future research are presented in the last section.

REDUCED BASIS TECHNIQUE

Fundamental path

Before analysing the postbuckling behavior, the fundamental path has to be computed up to the buckling point. An efficient procedure consists of employing the arc-length method of Riks-Wempner (13) in conjunction with an incremental bifurcation analysis (14). The stability matrix of the bifurcation problem is the sum of the geometrical stiffness matrix, the load stiffness matrix and the material stiffness matrix that accounts for the change of tangent modulus along the linear approximation of the fundamental path (15).

By giving an estimate of the buckling load, the incremental bifurcation analysis allows adaptive step-size increments so that the buckling point is attained within a few steps. Indeed, in the prebuckling range, large increments can be employed with good accuracy with respect to the integration of the constitutive equations, since the condition of radial loading is usually locally satisfied.

Buckling modes

When a state of equilibrium has been obtained in the neighbourhood of the buckling point, the buckling modes are computed by solving the following eigenvalue problem:

$$\underset{\sim}{K}_T^o \underset{\sim}{q}_i = \omega_i^2 \underset{\sim}{M} \underset{\sim}{q}_i \qquad (1)$$

with

$\underset{\sim}{K}_T^o$ tangent stiffness matrix at the reference state

$\underset{\sim}{M}$ mass matrix, possibly diagonalised

$\underset{\sim}{q}_i$ eigenmode

ω_i pulsation

An efficient algorithm for solving (1) is given by the Lanczos method (16), or even better, the block Lanczos method (17). The choise of (1) for defining the buckling modes is related to the choice of the mass matrix as a norm of the perturbation amplitude. The lowest frequency eigenmode is also the solution of the minimum criterion for an infinitessimal amplitude.

The initial modal basis corresponds to the lowest frequency eigenmodes along with the deformation mode tangent to the fundamental path, $\underset{\sim}{q}_o$

$$\underset{\sim}{K}_T^o \underset{\sim}{q}_o = \lambda \underset{\sim}{G} \qquad (2)$$

where λ denotes the load factor and $\underset{\sim}{G}$ the unit external load. In the following, the modal basis, denoted by $\underset{\sim}{\Gamma}$, is assumed to be orthonormalised with respect to the mass matrix:

$$\underset{\sim}{\Gamma} = \{\underset{\sim}{q}_o, \underset{\sim}{q}_1, \cdots, \underset{\sim}{q}_n\} \qquad (3)$$

with

$$\underset{\sim}{q}_i^T \underset{\sim}{M} \underset{\sim}{q}_j = J_{ij} \qquad \text{for} \qquad i,j = 0,1,\ldots,n \qquad (4)$$

J_{ij} (Kronecker symbol)

so that a finite perturbation is defined by the relation

$$\underset{\sim}{q} = \underset{\sim\sim}{\Gamma}\underset{\sim}{a} \tag{5}$$

and its amplitude is given by the euclidian norm of the reduced vector a:

$$\underset{\sim}{q}^T\underset{\sim\sim}{M}\underset{\sim}{q} = \underset{\sim}{a}^T\underset{\sim}{a} = \alpha^2 \tag{6}$$

Crisfield's method in the reduced subspace

For a given perturbation, $\underset{\sim}{a}$, of the reference equilibrium, we seek convergence in the reduced subspace, at first. The iterative procedure employs Crisfield's method (12) and the correction of displacements, $\dot{\underset{\sim}{a}}$, is computed as follows:

$$\underset{\sim\sim}{k}\dot{\underset{\sim}{a}} = \underset{\sim}{r} + \dot{\lambda}\underset{\sim}{g} \tag{7}$$

$$\dot{\underset{\sim}{a}} = \dot{\underset{\sim}{a}}_1 + \dot{\lambda}\underset{\sim}{a}_2 \tag{8}$$

$$(\underset{\sim}{a} + \dot{\underset{\sim}{a}})^T(\underset{\sim}{a} + \dot{\underset{\sim}{a}}) = \alpha^2 \tag{9}$$

where the tangent stiffness matrix, $\underset{\sim\sim}{k}$, the residual load vector, $\underset{\sim}{r}$, and the unit external load, $\underset{\sim}{g}$, are restricted into the modal basis:

$$\underset{\sim\sim}{k} = \underset{\sim\sim}{\Gamma}^T\underset{\sim\sim}{K}_T\underset{\sim\sim}{\Gamma} \tag{10}$$

$$\underset{\sim}{r} = \underset{\sim\sim}{\Gamma}^T\underset{\sim}{R} \tag{11}$$

$$\underset{\sim}{g} = \underset{\sim\sim}{\Gamma}^T\underset{\sim}{G} \tag{12}$$

This projection can be performed at the finite element level so that no triangularisation of the complete stiffness matrix is required. During the iterations, the total inertia is kept constant by the relation (9), which allows computation of the correction, $\dot{\lambda}$, to the load factor by solving a second order algebraic equation (12). The relation (5) with the corrected reduced displacement gives the displacement vector in the complete system which is employed to compute the stress correction by integration of the constitutive equations.

Update of the reduced basis

When convergence is attained in the reduced subspace, the convergence criterion in the complete system may not be satisfied and modification to the modal basis has to be performed.

Considering, for example, a simply supported plate under axial compression, the lowest frequency eigenmodes correspond to bending deformations, but the initial postbuckling behavior also involves membrane contribution that makes the structure stiffer (1, 18). These membrane deformations are associated with much higher eigenfrequencies than the allowable cut-off frequency employed for choosing the initial modal basis with problem (1). This membrane contribution could be recovered in the elastic case by a perturbation process such as the one employed by Koiter (1) or Noor (9). However, since the occurrence of plasticity and possible unloading may drastically change this contribution, a more efficient procedure has to be employed.

A simple way for updating the initial reduced basis consists of defining an additional deformation mode associated with the residual vector of the complete system by the relation

$$\underset{\sim}{K}_T^o \underset{\sim}{q}_n + 1 = \underset{\sim}{R} \qquad (13)$$

The solution of (13) is orthonormalised to the previous modal basis following relation (4) with incrementation of the reduced subspace.

$$n \leftarrow n + 1 \qquad (14)$$

It is worth noting that the solution of (13) does not require the triangularisation of a new tangent stiffness matrix, but only employs the triangularisation of the reference tangent stiffness matrix used in (1). The incrementation of the modal basis is performed up to convergence in the complete system.

CRITICAL POSTBUCKLING PATH

Energy criterion

The critical perturbation is assumed to be the solution of the minimisation problem

$$\omega_\alpha^2 = \min_{\underset{\sim}{q}} \frac{\int_o^{\underset{\sim}{q}} \underset{\sim}{F}_{int}^T \, d\underset{\sim}{q}}{\underset{\sim}{q}^T \underset{\sim}{\underset{\sim}{M}} \underset{\sim}{q}} \qquad (15)$$

under the constraint (6). The integration of the work of the internal forces, F_{int}, is performed along an equilibrium path. The quotient in (15) has the dimension of a pulsation and its minimum value can be positive or negative. The criterion (15) does not allow verification of the stability of the postbuckling path but this check can be deduced from the sign of the load factor increment. Assuming that the applied load remains constant at the buckling point, the perturbation defined by (15) makes the kinematic energy maximum for an unstable postbuckling behavior. The minimum value of (15) may be considered as a measure of the degree of instability of the structure, which depends on the perturbation amplitude.

Within the framework of the reduced basis technique, the criterion is also given by

$$\omega_\alpha^2 = \min_{\underset{\sim}{d}} \frac{\int_o^\alpha \underset{\sim}{f}_{int}^T \underset{\sim}{d}\, d\alpha}{\hat{\alpha}^2} \qquad (16)$$

with

$$\underset{\sim}{f}_{int} = \underset{\sim}{\Gamma}^T \underset{\sim}{F}_{int} \qquad (17)$$

and the current tangent direction to the postbuckling path

$$\underset{\sim}{d} = \frac{d\underset{\sim}{a}}{d\alpha} \qquad (18)$$

Algorithm initialization

When the cut-off frequency has been defined, the initial direction, $\underset{\sim}{d}_o$, in the reduced subspace is chosen as the tangent to the fundamental path with the equation (7):

$$\underset{\sim}{k}\underset{\sim}{d}_o = \underset{\sim}{g} \qquad (19)$$

which yields with (9)

$$\hat{\lambda} = \frac{\alpha}{\sqrt{\underset{\sim}{d}_o^T \underset{\sim}{d}_o}} \; ; \quad \hat{\underset{\sim}{a}} = \hat{\lambda}\underset{\sim}{d}_o \qquad (20)$$

The load factor increment is taken positive since the reduced stiffness matrix is positive definite by the choice of the reference equilibrium state on the fundamental path. The initial amplitude, α, is chosen small enough in order to keep good accuracy in the integration of the constitutive equations. Indeed, in this integration, the strain rate is assumed to be constant during the increment so that plastic loading followed by elastic unloading is precluded within the same increment (19). Such a behavior may occur when a bifurcation appears within the increment.

From the first guess (20), iterations are performed up to convergence in the complete system with possible updating of the modal basis. The smallness of the increment size allows computation of the work of internal forces in (16) by applying the simple trapezoidal integration rule.

Check of the initial direction

Before proceeding to the next increment, we have to check if the energy criterion is satisfied with the current perturbation. It is assumed that the criterion is satisfied provided that the number of negative or null pivots in the triangularisation of the reduced tangent stiffness matrix is less than or equal to one. Otherwise, the eigenmodes associated with negative or null eigenvalues are computed in the reduced basis:

$$\underset{\sim}{k}\underset{\sim}{d}_i = \omega_i^2 \underset{\sim}{d}_i \quad \text{for} \quad \omega_i^2 < 0 \tag{21}$$

The new direction is chosen as the one that makes the maximum angle with the current initial direction. After normalisation with respect to the euclidian norm

$$\underset{\sim}{d}_j : \; |\underset{\sim o}{d}^T \underset{\sim}{d}_j| = \min_i |\underset{\sim o}{d}^T \underset{\sim}{d}_i| \tag{22}$$

the new direction is defined by the relation

$$\underset{\sim}{d}_o + \{\underset{\sim}{d}_j - (\underset{\sim o}{d}^T \underset{\sim}{d}_j)\underset{\sim}{d}_o\} \sin(\underset{\sim o}{d}^T \underset{\sim}{d}_j) \tag{23}$$

and the current increment is reinitialised with

$$\dot{\underset{\sim}{a}} = \gamma \underset{\sim}{d}_o ; \quad \dot{\lambda} = 0 \tag{24}$$

$$\gamma = \frac{\sqrt{B^2 + \Delta\alpha^2 A} - B}{A} \tag{25}$$

$$B = \underset{\sim o}{d}^T \underset{\sim}{a} ; \quad A = \underset{\sim o}{d}^T \underset{\sim o}{d} \tag{26}$$

where $\Delta\alpha^2$ is the current increment size. This procedure is employed up to satisfaction of the energy criterion. Then, we can proceed to the next increment, the direction of which is given by the equation (19). The increment size $\Delta\alpha^2$ is updated by taking into account the number of iterations required to get convergence.

Remarks about the cut-off frequency

The choice of the cut-off frequency for the definition of the initial modal basis is the main issue for the convergence of the algorithm and its accuracy. This frequency should not be too large in order to keep a suitable number of modes for algorithm efficiency with respect to computer time. On the other hand, too small a frequency could yield convergence difficulties in the complete system or give a bad approximation of the lowest eigenvalues of the complete tangent stiffness matrix far away from the reference state. Indeed, the algorithm is based on the solution of the eigenvalue problem (21) and the reduced modal basis has to contain the current eigenmodes of lowest eigenvalues of the complete system, at best.

The cut-off frequency depends on the proximity of the reference state with respect to the buckling point and also on the total magnitude of the considered perturbation. This amplitude is not very large since the definition of the critical defect is only based on the initial postbuckling behavior. The cut-off frequency should be defined with respect to the lowest eigenfrequency of the structure in its unstressed configuration. Preliminary results indicate that these frequencies should be of the same order of magnitude.

AXISYMMETRIC BUCKLING OF CYLINDRICAL SHELLS UNDER AXIAL COMPRESSION

The proposed method has been applied to the axisymmetric buckling of two circular cylindrical shells under axial compression. The cylinders are clamped at both ends and the material is elastic - perfectly plastic (table 1). Both shells have the same value for the Euler buckling load and the linear limit load. The structure is modeled by 50 2-node thin-shell elements with one integration point on the lamina and 5 Gauss points over the thickness (20).

Both shells exhibit about the same postbuckling behavior; namely, an asymmetric bifurcation is nearly coincident with a symmetric limit point type of buckling. The bifurcation path yields the largest energy release while elastic unloading takes place at one end of the cylinder. The shell 2 is slightly more unstable than the shell 1 since the instability occurs even with controlled displacement in this case. The deformation patterns of both shells are represented in the figures 1 and 2.

The reference equilibrium state is chosen on the fundamental path slightly below the buckling point. By taking the cut-off frequency of the same order as the eigenfrequency of the unstressed configuration, we choose for the initial modal basis the first 6 or 8 eigenmodes, respectively, for the two shells in addition to the tangent to the fundamental path (table 2). In the step 1, convergence is attained on the symmetric postbuckling path at first, and the definition of a new initial direction then yields convergence on the asymmetric bifurcation path with a decrease of the energy criterion. The results are summarized in tables 3 and 4. The final number of modes in the reduced subspace is also indicated for each step.

CONCLUSIONS

In this paper we have presented an algorithm for the definition of the critical perturbation in the postbuckling behavior of elastoplastic thin-shell structures. The algorithm is based upon an automatic reduced basis technique to improve its efficiency with respect to computer time. This approach also allows better understanding of the postbuckling behavior. Simple numerical examples illustrate the method and the energy criterion gives some insight into the degree of structural instability.

Further research is necessary to clarify some important issues; namely, a good criterion for the definition of the cut-off frequency in the selection of the initial modal basis; and application of the critical perturbation to the definition of the critical defect, especially with respect to the relation between the perturbation amplitude to be considered and the maximum allowable magnitude of the initial defect. In this work, the usual J2 flow theory has been employed to model the plastic behavior, but other theories are more suitable for buckling analysis (21). Finally, the present approach should be applied to more complex postbuckling behaviors than the ones considered up to now.

Acknowledgment

The support of this research provided by the French Ministry of Industry and Research is gratefully acknowledged.

REFERENCES

1. Koiter, W. T.: The Stability of Elastic Equilibrium. AFFDL-TR-70-25, 1970. (Transl. of Ph.D. Thesis, Technische Hogeschool, Delft, 1945.)

2. Maewal, A.; and Nachbar, W.: A Perturbation Analysis of Mode Interaction in Postbuckling Behavior and Imperfection Sensitivity. Int. J. Solids Structures, Vol. 13, 1977, pp. 937-946.

3. Hutchinson, J. W.: Plastic Buckling - Post-Bifurcation and Imperfection Sensitivity. Adv. Appl. Mech., Vol. 14, 1974, pp. 67-144.

4. Hoffman, A.; and Verpeaux, P.: Plasticité et Postflambage, Position du Problème et Exemples. Flambage Elastique et Plastique des Coques Minces, Institut Pour la Promotion des Sciences de l'Ingenieur, Paris, April 1982.

5. Almroth, B. O.; Stern, P.; and Brogan, F. A.: Automatic Choice of Global Shape Functions in Structural Analysis - Nonlinear Static and Dynamic Finite Element Programs. AIAA J., Vol. 16, 1978, pp. 525-528.

6. Besseling, J. F.; Ernst, L. J.; van der Werff, K.; de Koning, A. U.; and Riks, E.: Geometrical and Physical Nonlinearities - Some Developments in the Netherlands - Finite Element Analysis for Crack Growth and Other Structural Problems. Comp. Meth. Appl. Mech. Engrg., Vol. 17/18, 1979.

7. Carnoy, E.: Postbuckling Analysis of Elastic Structures by the Finite Element Method. Comp. Meth. Appl. Mech. Engeg., Vol. 23, 1980, pp. 143-174.

8. Nagy, D. A.; and Konig, M.: Geometrically Nonlinear Finite Element Behavior Using Buckling Mode Superposition. Comp. Meth. Appl. Mech. Engrg., Vol. 19, 1979.

9. Noor, A. K.; and Peters, J. M.: Reduced Basis Technique for Nonlinear Analysis of Structures. AIAA J., Vol. 4, 1980, pp. 455-462.

10. Carnoy, E.; and Sander, G.: Stability and Postbuckling Analysis of Nonlinear Structures. Comp. Meth. Appl. Mech. Engrg., Vol. 32, 1982, 329-363.

11. Noor, A. K.; and Peters, J. M.: Instability Analysis of Space Trusses. Comp. Meth. Appl. Mech. Engrg., Vol. 40, 1983, pp. 199-218.

12. Crisfield, M. A.: An Arc-Length Method Including Line Searches and Accelerations. Int. J. Num. Meth. Engrg., Vol. 19, 1983, pp. 1269-1289.

13. Riks, E.: The Application of Newton's Method to the Problem of Elastic Stability. ASME Trans., Series E, J. Appl. Meth., Vol. 39, 1972, pp. 1060-1065.

14. Carnoy, E.; and Panosyan, G.: Numerical Methods in Buckling Analysis of Elasto-plastic Thin Shell Structures. Third Int. Colloquium on Stability of Metal Structures, Centre Technique Industriel de la Construction Metallique, Paris, 16-17 Nov. 1983, p. 347 (ISBN 2-902720-13-0).

15. Carnoy, E.; and Panosyan, G.: Approximation of the Plastic Buckling Load as the Solution of an Eigenvalue Problem. Nucl. Engr. Design, Vol. 78, 1984, pp. 347-353. Presented at International Seminar on Computational Aspects of the Finite Element Method (CAFEM-7), Chicago, Aug. 29-30, 1983.

16. Carnoy, E.; and Geradin, M.: On the Practical Use of the Lanczos Algorithm in Finite Element Applications to Vibration and Bifurcation Problems, Matrix Pencils, Lecture Notes in Mathematics, No. 973, Springer-Verlag, 1983, pp. 156-173.

17. Golub, G. H.; and Underwood, R.: The Block Lanczos Method for Computing Eigenvalues, Mathematical Software 3, Publ. Math. Res. Center, no. 39, Academic Press, New York, 1977, pp. 361-377.

18. Carnoy, E.; and Sander, G.: Stability and Postbuckling Behavior of Thin Walled Structures. LTAS-SA-97, University of Liège, Belgium, Sept. 1981.

19. Nyssen, C.: An Efficient and Accurate Iterative Method, Allowing Large Incremental Steps, To Solve Elasto-Plastic Problem. Comp. Struct., Vol. 13, 1981, pp. 63-71.

20. Carnoy, E.; and Panosyan, G.: Elastoplastic Buckling Analysis of Slender Vessels by Finite Elements Expanded in Fourier Series. Numerical Methods for Nonlinear Problems, Vol. 2, C. Taylor, E. Hinton, D. J. R. Owen, and E. Onate (Eds.), Pineridge Press, Swansea, U. K., 1984, pp. 215-223.

21. Tvergaard, V.: Plastic Buckling of Axially Compressed Circular Cylindrical Shells. Thin-Walled Structures, Vol. 1, 1983, pp. 139-163.

TABLE I : GEOMETRIC AND MATERIAL DATA

	Shell 1	Shell 2
Young Modulus (MPa)	210 000	210 000
Poisson ratio	0.3	0.3
Yield stress (MPa)	210.	420.
Radius (mm)	150.	150.
Length (mm)	40.	100.
Thickness (mm)	0.25	0.50
Mass density (kg/m^3)	7 800.	7 800.

TABLE 2 : CHOICE OF THE INITIAL MODAL BASIS

A : antisymmetric mode S : symmetric mode

		Shell 2		Shell 1	
Initial eigenfrequency (Hz)		146		158	
Load level (daN)		16 690.		4 093.	
Eigenfrequencies (Hz)	1	6.3	A	6.7	S
	2	38.4	S	62.3	A
	3	67.3	S	89.5	A
	4	81.3	A	123.	S
	5	89.1	A	152.	S
	6	106.	S	169.	A
	7	121.	S	210.	
	8	133.	A		
	9	150			

TABLE 3 : RESULTS FOR SHELL 1

	Reference state	Step 1	Step 1
Load level (daN)	4093.	4006.	3994.
Axial end-shortening (mm)	0.0335	0.0348	0.0346
Perturbation amplitude (kg)	-	$3.65\ 10^{-6}$	$3.65\ 10^{-6}$
Number of modes	-	13	16
Number of negative pivots	0	2	1
Criterion	-	$2.2\ 10^{6}$	$1.9\ 10^{6}$

TABLE 4 : RESULTS FOR SHELL 2

	Reference state	Step 1	Step 1	Step 2	Step 3	Step 4	Step 5
Load level (daN)	16690	16680	16680	16440	16200	15850	15320
Axial end-shortening (10^{-2}mm)	17.01	17.26	17.09	17.05	16.99	16.93	16.91
Perturbation amplitude (kg)	-	$1.15\ 10^{-5}$	$1.15\ 10^{-5}$	$2.43\ 10^{-5}$	$5.15\ 10^{-5}$	$9.09\ 10^{-4}$	$2.31\ 10^{-4}$
Number of modes	-	11	13	14	15	17	19
Number of negative pivots	0	2	1	1	1	1	1
Criterion	-	$5.8\ 10^{6}$	$1.8\ 10^{6}$	$4.4\ 10^{5}$	$-9.8\ 10^{4}$	$-1.9\ 10^{5}$	$-1.1\ 10^{5}$

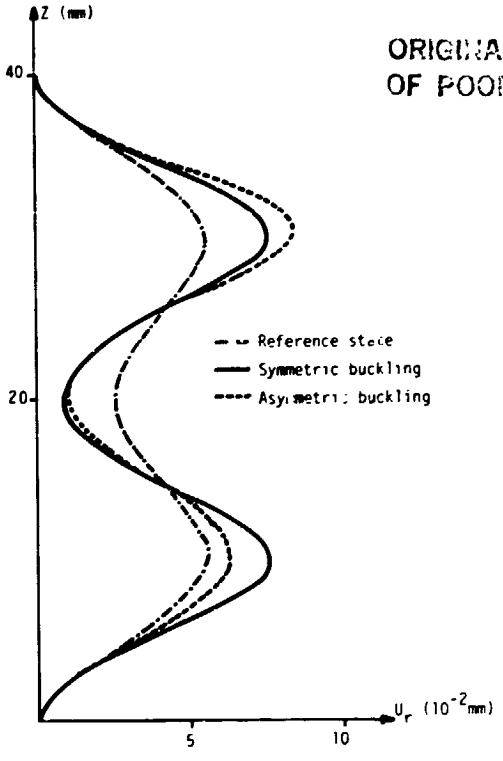

Figure 1. Radial displacement of shell 1.

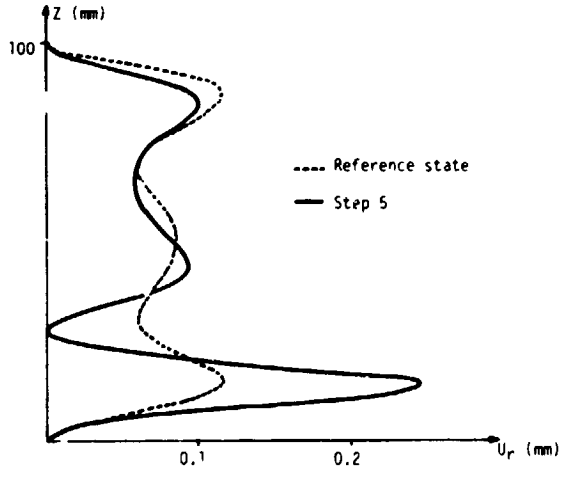

Figure 2. Radial displacement of shell 2.

NONLINEAR DYNAMIC ANALYSIS OF SANDWICH PANELS

Allen M. Lush
Kaman AviDyne, Burlington, MA

SUMMARY

This paper demonstrates two analytical techniques applicable to large deflection dynamic response calculations for pressure-loaded composite sandwich panels. One technique utilizes finite element modeling with a single equivalent layer representing the face sheets and core. The other technique utilizes the modal analysis computer code DEPROP (Reference 1), which has recently been modified to include transverse shear deformation in a core layer. The example problem consists of a simply-supported rectangular sandwich panel. Included in the paper are comparisons of linear and nonlinear static response calculations, in addition to dynamic response calculations.

INTRODUCTION

Sandwich panels can be designed to withstand large dynamic pressure loads. For example, the latest generation of Command, Control, and Communication military shelters employs sandwich panel walls designed to survive severe blast loading (References 2, 3, 4). An important step in the design process is to predict accurately the response (stresses and deflections) for the expected loads, thus ensuring design adequacy and efficiency. One approach is to test either full size or scaled models, but this can be time consuming and expensive, especially if many configurations are being considered. Alternatively, an analytical model of the sandwich panel can be constructed. This paper demonstrates two different analytical techniques applicable to geometrically nonlinear (large deflection) dynamic response calculations for composite sandwich panels with honeycomb cores. Of primary concern are the in-plane face stresses and the transverse shear stresses in the core. This information permits a survivability determination to be made by the designer.

The first analytical technique presented utilizes finite element modeling, with an equivalent layer representing the stiffness properties of the sandwich cross section. The equivalent layer modeling theory has been developed recently (Reference 5), and is summarized in the paper. It is considered to have wide applicability and to offer optimal efficiency for many sandwich panel analyses. For sandwich panels having thin face sheets and possessing a neutral surface decoupling bending and stretching, the equivalent layer representation is essentially exact, except for the effects of rotary inertia. For this paper, the equivalent layer calculations were done with computer code ADINA (Reference 6). It was intended to use the transverse shear deformable thick shell element (type 7) for the dynamic response calculations, but this was not possible due to difficulties with the 1981 version of the code. Consequently, the 3D solid isoparametric elements (type 3) were used. Geometrically nonlinear dynamic analysis with the ADINA code was done using a total Lagrangian motion description and the Newmark-Beta implicit method of time integration.

A second analytical technique presented for comparison uses a modified version of the modal analysis computer code DEPROP (Reference 1) (Dynamic Elastic Plastic Response Of Panels). It is formulated to model multilayer panels. This code uses orthogonal spatial functions with time-dependent coefficients to describe the deformation of the panel. Governing equations of motion are obtained from the principle of virtual work, with the volume and surface integrations for energy terms performed numerically. In its documented form, the DEPROP analysis is based on the Novozhilov nonlinear strain-displacement relations for large displacement response of thin panels, based on the assumption of undeformable normals. Recently, this code was modified to incorporate transverse shear deformation in the core layer. Time integration is done using the central difference explicit method.

The example problem was chosen to demonstrate the important features of large deflection dynamic sandwich panel response. Figure 1 describes the panel, which has orthotropic face sheets and a honeycomb core. The panel boundaries are simply supported. With the chosen panel dimensions, transverse shear deformation in the core is an important contributor to the dynamic response. The first comparison is for linear static response with uniform pressure loading, for which an accurate analytical solution adapted from Chapter 7 of Allen (Reference 7) is available. Both modeling techniques are shown to approach the reference solution. The second comparison is for large deflection static response. No accurate reference solution is available for this problem, but the two analytical results are shown to be in good agreement. Finally, dynamic response predictions are compared for the two techniques, and reasonable agreement is again shown.

EQUIVALENT LAYER SANDWICH PANEL MODEL

Reference 5 presented an equivalent layer theory for sandwich panels with thin laminated composite facings and honeycomb cores. The fundamental approach to equivalence consists of three basic steps. First, a kinematic correspondence is established between equivalent layer and sandwich panel such that the work of the external forces is reproduced exactly. This dictates, for example, that the transverse displacement be the same for both. Additionally, the face sheet midsurface displacements should be matched, resulting in matching of the work done by in-plane external forces applied to the face. An added advantage of matching the face sheet midsurface displacements is that it becomes much easier to calculate the face sheet stresses and strains in the output. The second step consists of equating the strain energies in the equivalent layer and sandwich panel, which leads to equivalent layer elastic moduli determination. Exact equivalence of stiffnesses is possible if the sandwich panel possesses a neutral surface decoupling bending and stretching. Finally, the density of the equivalent layer is calculated to match the mass per unit area of the panel. Thus, the primary contribution to the kinetic energy is represented.

Thin composite face sheet laminates can be modeled using laminated plate theory (Reference 8), which neglects transverse shear strains and uses a plane stress model for each layer. As a result, the moments and membrane forces in the face sheet are related to its midsurface stretches and curvatures via the membrane, coupling, and bending stiffnesses $\underset{\sim}{A}$, $\underset{\sim}{B}$, and $\underset{\sim}{D}$, respectively. In the following derivation only the membrane stiffnesses are incorporated for the thin

facings, introducing a small error that depends on the relative thicknesses of the core and face sheets. For example, the error in ignoring face sheet bending stiffnesses is less than 1% if they are homogeneous and less than 21% of the core thickness.

For the honeycomb core, the "antiplane" model (Reference 7) is adopted here. This means that the in-plane core stresses are neglected. Consequently, the transverse shear stresses and strains can be modeled as constant through the core thickness. It is also reasonable to ignore transverse normal strains in the core (Reference 9), although this precludes modeling of face wrinkling instability.

The equivalent layer is assumed to behave like a Mindlin plate composed of an orthotropic or monoclinic elastic material. Thus, a straight line drawn through the undeformed equivalent layer remains straight during the response, i.e., the transverse shear stresses and strains do not vary through the thickness. Three dimensional solid isoparametric elements can meet this requirement. Alternatively, "thick shell" elements such as the one in ADINA (Reference 10) can be used.

Figure 2 illustrates that the equivalent layer matches displacements at the face sheet midsurfaces and at an additional surface in the core, designated the "reference surface". In the following derivation, superscripts 1, 2, c, r, n, and e refer to the inner face sheet, outer face sheet, core, reference surface, neutral surface, and equivalent layer, respectively. The thickness of layer k (k = 1,2,c,e) is denoted $h^{(k)}$. With respect to the reference surface, the face sheet midsurfaces are located at (see Figure 2):

$$z_{ms}^{(2)} = \frac{h^{(c)}h^{(2)}}{h^{(1)}+h^{(2)}} + \frac{h^{(2)}}{2}$$

$$z_{ms}^{(1)} = \frac{-h^{(c)}h^{(1)}}{h^{(1)}+h^{(2)}} - \frac{h^{(1)}}{2}$$

This information allows the reference surface location to be calculated. Note that the transverse shear strains in the equivalent layer are smaller than those in the core by the factor:

$$R = 1/\left\{ 1 + \frac{h^{(1)} + h^{(2)}}{2h^{(c)}} \right\}$$

Three reference surface displacements ($u_1^{(r)}$, $u_2^{(r)}$, $u_3^{(r)}$) plus two core transverse shear strains ($\gamma_{31}^{(c)}$, $\gamma_{23}^{(c)}$) are sufficient to describe the deformed sandwich panel geometry completely. In terms of these quantities, the sum of the strain energies in the two faces can be written:

$$U_{faces} = \tfrac{1}{2}\underset{\sim}{e}^{(r)T}\underset{\approx}{A}^{(r)}\underset{\sim}{e}^{(r)} + \underset{\sim}{e}^{(r)T}\underset{\approx}{B}^{(r)}\underset{\sim}{\kappa}^{(r)} + \tfrac{1}{2}\underset{\sim}{\kappa}^{(r)T}\underset{\approx}{D}^{(r)}\underset{\sim}{\kappa}^{(r)}$$

where $\underset{\sim}{e}^{(r)} = \begin{bmatrix} u^{(r)}_{1,1} \\ u^{(r)}_{2,2} \\ u^{(r)}_{1,2} + u^{(r)}_{2,1} \end{bmatrix}$

and $\underset{\sim}{\kappa}^{(r)} = \begin{bmatrix} R\gamma^{(c)}_{31,1} - u^{(r)}_{3,11} \\ R\gamma^{(c)}_{23,2} - u^{(r)}_{3,22} \\ R\gamma^{(c)}_{31,2} + R\gamma^{(c)}_{23,1} - 2u^{(r)}_{3,12} \end{bmatrix}$

The sandwich panel membrane, coupling, and bending stiffnesses are

$$\underset{\approx}{A}^{(r)} = \underset{\approx}{A}^{(1)} + \underset{\approx}{A}^{(2)}$$

$$\underset{\approx}{B}^{(r)} = z^{(1)}_{ms}\underset{\approx}{A}^{(1)} + z^{(2)}_{ms}\underset{\approx}{A}^{(2)}$$

$$\underset{\approx}{D}^{(r)} = z^{(1)^2}_{ms}\underset{\approx}{A}^{(1)} + z^{(2)^2}_{ms}\underset{\approx}{A}^{(2)}$$

A sufficient and necessary condition for a neutral surface decoupling bending and stretching to exist is that the ratios c_{ij} given by

$$c_{ij} = A^{(1)}_{ij}/A^{(2)}_{ij}$$

be equal for all ij terms of importance. The neutral surface is then located at

$$z_{ns} = (c_{ij}z^{(1)}_{ms} + z^{(2)}_{ms})/(1 + c_{ij})$$

If the c_{ij} values differ slightly, it is best to use a weighted average $\bar{c}_{ij}$, emphasizing the most important terms. If the c_{ij} values differ considerably, then an equivalent layer representation is not advisable. With respect to the special neutral surface, the bending stiffnesses are

$$\underset{\approx}{D}^{(n)} = \underset{\approx}{D}^{(r)} - 2z_{ns}\underset{\approx}{B}^{(r)} + z^2_{ns}\underset{\approx}{A}^{(r)}$$

The membrane stiffnesses $\underset{\approx}{A}^{(n)}$ are the same as $\underset{\approx}{A}^{(r)}$.

The transverse shear strains and stresses do not vary through the thickness of the core. Consequently, the core strain energy can be written:

$$U_{core} = \tfrac{1}{2}\underset{\sim}{\gamma}^{(c)T}\underset{\approx}{F}^{(c)}\underset{\sim}{\gamma}^{(c)}$$

where $$\underset{\sim}{\gamma}^{(c)T} = \begin{bmatrix} \gamma_{31}^{(c)} & \gamma_{23}^{(c)} \end{bmatrix}$$

and $$\underset{\approx}{F}^{(c)} = h^{(c)} \begin{bmatrix} Q_{55}^{(c)} & Q_{45}^{(c)} \\ Q_{45}^{(c)} & Q_{44}^{(c)} \end{bmatrix}$$

The strain energy in the equivalent layer can be written in exactly the same form as the strain energy in the sandwich panel, with the following stiffnesses:

$$A_{ij}^{(e)} = Q_{ij}^{(e)} h^{(e)} \qquad (i,j = 1,2,6)$$

$$B_{ij}^{(e)} = z_{ms}^{(e)} A_{ij}^{(e)} \qquad (i,j = 1,2,6)$$

$$D_{ij}^{(e)} = \left\{ \frac{h^{(e)2}}{12} + z_{ms}^{(e)2} \right\} A_{ij}^{(e)} \qquad (i,j = 1,2,6)$$

$$F_{ij}^{(e)} = R^2 h^{(e)} Q_{ij}^{(e)} \qquad (i,j = 4,5)$$

where $z_{ms}^{(e)}$ is the location of the midsurface. For exact equivalence, these twenty-one stiffnesses must all equal their counterparts for the sandwich panel, which is possible provided a neutral surface exists in the sandwich panel.

The midsurface (which is the neutral surface) of the equivalent layer is always placed at the same x_3 location as the neutral surface of the sandwich panel, i.e.,

$$z_{ms}^{(e)} = z_{ns}$$

The thickness $h^{(e)}$ is given by

$$h^{(e)} = (h^{(c)}/R)\sqrt{12\bar{c}_{ij}}/(1 + \bar{c}_{ij})$$

In-plane equivalent layer moduli $Q_{11}^{(e)}$, $Q_{22}^{(e)}$, $Q_{12}^{(e)}$, $Q_{66}^{(e)}$, $Q_{16}^{(e)}$, and $Q_{26}^{(e)}$ are equal to

$$Q_{ij}^{(e)} = A_{ij}^{(n)}/h^{(e)} \qquad (i,j = 1,2,6)$$

If only approximate equivalence is possible, the optimal choice for these in-plane moduli may depend on the problem being solved because it will not be possible to match both the bending and stretching stiffnesses. Therefore, weighting factors α_{ij} should be chosen to reflect the relative importance of matching bending versus stretching stiffnesses, as follows:

$$Q_{ij}^{(e)} = \alpha_{ij}(12D_{ij}^{(n)}/h^{(e)^3}) + (1-\alpha_{ij})A_{ij}^{(n)}/h^{(e)} \qquad (i,j = 1,2,6)$$

Equivalent layer transverse shear moduli $Q_{44}^{(e)}$, $Q_{55}^{(e)}$, and $Q_{45}^{(e)}$ are equal to

$$Q_{ij}^{(e)} = F_{ij}^{(c)}/R^2h^{(e)} \qquad (i,j = 4,5)$$

For dynamic analysis, the equivalent layer density is determined by matching the mass per unit area of the sandwich panel. Consequently, the rotational inertias of the sandwich panel can not be matched. It can be shown that with a symmetrical cross section, the rotational inertia contributions from the face sheets are matched exactly, and the rotational inertia contribution from the core is off by a factor of three (too high in the equivalent layer). With an unsymmetrical cross section, the results are not so simple. For most sandwich panel problems, the rotational inertia is very small, and the error in the equivalent layer representation is negligible.

Care should be taken in modeling the edge conditions for an equivalent layer because the outer and inner surfaces do not coincide with the sandwich panel face sheets. For example, if the sandwich panel edge support consists of restricted motion in one face only, then it is necessary to constrain the motion of the equivalent layer outer and inner surfaces such that the correct point within the equivalent layer remains fixed. The more conventional simply supported boundary condition shown in Figure 9.3c of Reference 7 can be implemented with the equivalent layer by restraining the neutral surface (midsurface) displacements and leaving the rotations free. For the clamped boundary condition shown in Figure 9.3d of Reference 7, the face sheet midsurface displacements are both restrained. The panel midsurface becomes sloped when transverse shear strains occur in the core, causing the thin face sheets to appear kinked at the edge. In reality, the face sheets experience a localized region of bending and shearing strains, which are not modeled in the equivalent layer analysis.

For the example problem specified in Figure 1, the equivalent layer properties are:

$$R = .941176$$

$$h^{(e)} = 0.0934874 \text{ m} \quad (3.68061 \text{ in.})$$

$$E_1^{(e)} = E_2^{(e)} = 2.10742 \times 10^9 \text{ N/m}^2 \quad (3.05656 \times 10^5 \text{ psi})$$

$$\nu_{12}^{(e)} = \nu_{21}^{(e)} = 0.1$$

$$G_{12}^{(e)} = 1.40495 \times 10^8 \text{ N/m}^2 \quad (2.03771 \times 10^4 \text{ psi})$$

$$G_{23}^{(e)} = 8.03602 \times 10^7 \text{ N/m}^2 \quad (1.16553 \times 10^4 \text{ psi})$$

$$G_{31}^{(e)} = 3.80653 \times 10^7 \text{ N/m}^2 \quad (5.52091 \times 10^3 \text{ psi})$$

$$\rho^{(e)} = 1.23322 \times 10^2 \text{ kg/m}^3 \quad (1.195 \times 10^{-5} \text{ lb-sec}^2/\text{in}^4)$$

DEPROP SANDWICH PANEL MODEL

DEPROP was described in detail in Reference 1. Some features of this code have already been described in the introduction. Additional details are as follows. For elastic analysis, DEPROP performs integration through the panel thickness in closed form for the volume integrals appearing in the principle of virtual work. Therefore, the problem is reduced to a distribution of five parameters over a reference surface fixed in the core. The five parameters are the three reference surface displacements plus two core shear angles. The distributions of these parameters are modeled in DEPROP using combinations of two-dimensional spatial modes, chosen to meet the boundary conditions. Each mode is the product of two shape functions: one for each direction. The choice of modal contributions to be included in a calculation is part of the DEPROP input. DEPROP includes the bending stiffnesses of the faces. It does not model rotary inertia effects associated with slope of the reference surface. Finally, deformation dependent pressure loading (nonconservative) is accounted for in this code.

EXAMPLE 1: LINEAR STATIC RESPONSE

For simply supported sandwich panels, an accurate analytical solution for linear static response to uniform pressure loading was presented in Chapter 7 of Reference 7. This solution used assumed modes for the transverse deflection and core shear strains. The resulting equations were programmed on the VAX 11/750 computer at Kaman AviDyne. It was found that a tremendous number of modal contributions could be incorporated in a reasonable amount of computer time. This was fortunate because slow convergence was found for the transverse shear strains. Approximately 0.1% accuracy was obtained for these strains by

including all modes up to number 801 (only odd modes contribute) in each direction, for a total of 160,000 modes for each quantity. The following maxima were obtained for unit pressure loading (1.0 psi) on the panel specified in Figure 1:

Center Displ. = 1.3681×10^{-3} m (0.053862 in.)

Face Sheet Strains: $e_1 = \pm.0079490\%$

$e_2 = \pm.020929\%$

$\gamma_{12} = \pm.035629\%$

Core Strains: $\gamma_{23} = .057274\%$

$\gamma_{31} = .076241\%$

The maximum strains e_1 and e_2 occurred at the panel center, whereas the maximum strain γ_{12} occurred in the corner. The maximum core shear strains occurred at the panel mid-edges. It is worth noting that core shear flexibility contributed 11.4% of the total deflection for this example.

Equivalent layer results for comparison were generated with ADINA using the isoparametric thick shell element (Reference 10). This isotropic element was modified to accommodate an anisotropic material law for plate problems by redefining matrix C in subroutine MAT1. Two versions of the element were investigated. Elements with 16 midsurface nodes (cubic interpolation functions) were studied first because they describe transverse shear well, without the need for special integration schemes. Elements with 9 midsurface nodes (quadratic interpolation functions) were also studied because they require less computer time for a given number of nodes in the model. It was necessary to use a 2 x 2 x 2 Gaussian quadratures integration scheme with these elements, which is "underintegration". Comparison of the cubic and quadratic elements was done to determine which one gives the best balance of accuracy and cost. Table I gives the relevant data for the ADINA equivalent layer calculations. For all cases, the element mesh was uniform. The specified number of DOF includes in-plane displacements of the midsurface, which were zero for this linear response problem but became important for the subsequent nonlinear response calculations.

Referring to Table I, it is seen that both versions (cubic and quadratic) of the shell element converge very closely to the analytical Allen solution for center displacement and all strains. It is also seen that for a given number of DOF in the model, the quadratic shell element is cheaper and generally less accurate. It is worth noting, though, that the core shear strains were generally more accurate with the quadratic shell element. The element meshes with 2832 DOF were included primarily to demonstrate convergence. For the dynamic calculations, the 6 x 6 mesh of 9 node shells was chosen as representing a good balance of accuracy and cost. Of particular interest were the accurate core shear strain results with this mesh.

Case LU16 in Table I had the same element mesh as Case LU6, except that underintegrated 16 node 3D solid isoparametric elements were used instead of the 9 node shell elements. The 3D solid elements had 8 nodes each on the inner and outer surfaces. Constraint equations in ADINA were used to relate the inner and outer surface displacements at the edge such that a simply supported boundary condition was represented exactly. Case LU16 was done after attempts at running the ADINA shell element dynamically were unsuccessful. It demonstrates that 3D solid elements can give essentially the same results as the shell elements. With the 3D solid elements, though, it is necessary for the two Poisson's ratios governing thickness change for in-plane stresses to be zero. The elastic modulus in the thickness direction was arbitrarily set equal to the in-plane modulus because it has little effect on the results. All other elastic constants were the same as for the shell element cases.

The DEPROP result in Table I was produced using 32 total spatial modes for each of the 5 parameters (3 displacements and two shears). It is seen that this calculation agrees quite well with the finite element and Allen solutions. The observed slight inaccuracy in the core shear strain results can be attributed to the same sort of slow convergence as was noted in the Allen solution.

EXAMPLE 2: NONLINEAR STATIC RESPONSE

The panel specified in Figure 1 was designed to withstand a step pressure load of 1.2411×10^5 N/m^2 (18 psi). Therefore, in keeping with the approximate concept of a dynamic overshoot doubling the deflection and strains, the panel was analyzed for a static pressure load of 2.4821×10^5 N/m^2 (36 psi). The response was found to contain appreciable geometrical nonlinearity. Every case in Table I except for LU4 was rerun nonlinearly for the 36 psi pressure load. Table II presents the results.

A total Lagrangian formulation was used for the ADINA results in Table II. The pressure load was applied incrementally in 9 steps. ADINA handles rotational increments additively, so the load step size should be limited to preserve accuracy in nonlinear analysis. With the 9 steps used, the maximum angular increment was less than one degree, ensuring accuracy. For each load step, equilibrium iterations were performed using the BFGS method, and the stiffness matrix was reformed to account for nonlinearities.

An accurate geometrically nonlinear analytical solution was not available for evaluating the results in Table II. The ADINA equivalent layer solutions appear to converge fairly rapidly, but they do not converge exactly to the DEPROP result, although they are pretty close. The most severe disagreement is for $\gamma_{23}^{(c)}$, which differs by around 10% from the DEPROP solution. Much of the discrepancy between ADINA and DEPROP can be attributed to the pressure load not adjusting to the surface deformation in the 1981 version of ADINA. An additional factor is the relatively small number of modes in the DEPROP solution. This solution has not fully converged.

Table II includes an accurate linear solution based on the Allen solution in Example 1. Comparing with case LU14, it is seen that goemetrical nonlinearity has reduced the center deflection by 28%, the maximum face sheet compressive strain by 56%, and the core shear stresses by 24% and 15%, respectively. It may be concluded that for this problem, the design would be too conservative without the inclusion of nonlinearity in the analysis. Accurate prediction of the face sheet compressive stresses and the core shear stresses is important because compressive laminate failure and core shear failure tend to be the most severe limitations on the survivability of a light-weight composite sandwich panel subjected to large transverse loads.

EXAMPLE 3: NONLINEAR DYNAMIC RESPONSE

The two analytical techniques were used to calculate the dynamic response of the sandwich panel specified in Figure 1 for a step pressure load of 1.2411×10^5 N/m^2 (18 psi). For the ADINA equivalent layer calculation, a 6 x 6 mesh of underintegrated 16 node brick elements was used. This model was identical to the one used in case LU17 of Table II, where it was shown to be in good agreement with the more accurate case LU14. As stated earlier, it was necessary to use 3D solid elements instead of thick shell elements because the thick shell element did not work dynamically in the 1981 version of ADINA. For time integration, the Newmark beta scheme available in ADINA was used. Although this scheme is unconditionally stable, the accuracy deteriorates as the timestep becomes too large. Therefore, two dynamic response calculations were done with differing timesteps (0.1 and 0.02 msec) to check the numerical accuracy. These calculations were carried out to 8 msec and 4 msec, respectively. Equilibrium iterations were done for each timestep, and the stiffness matrix (used in restoring equilibrium) was reformed every 0.2 and 0.04 msec, respectively. Total solution time for 200 timesteps was 750 seconds on a Cyber 176 computer running NOS 2.1 with MTOT=29800 in ADINA. The most important results are shown in Figures 3, 4, and 5 for the calculation with a timestep of 0.02 msec. The results with a 0.1 msec timestep differed by less than 1% for the curves in Figures 3, 4, and 5.

DEPROP results for comparison were obtained using a central difference scheme with a 5.0 microsecond timestep to integrate the equations of motion. Two calculations were done. In the first, the same modal combinations were used as for the static results in Tables I and II. It was felt that the inclusion of more modes in the solution would be advantageous, so a second calculation was done with the number of modes per parameter increased from 32 to 36. This caused less than 1% change in all of the strain and displacement results. Figures 3, 4, and 5 contain the more accurate DEPROP results. Very good agreement with ADINA is seen.

Comparing the DEPROP and ADINA dynamic results, the peak deflection was 0.04189 m at 3.0 msec for DEPROP, and 0.04052 m at 3.1 msec for ADINA. These deflections differ by only 3.4%. The peak face sheet strains e_2 for ADINA were +.905% at 3.0 msec and -.383% at 2.8 msec. The DEPROP results were very close (about 0.5% less). The peak ADINA core shear strain γ_{23} was 1.689% at 3.2 msec,

whereas DEPROP predicted a peak value of 1.894% at the same time. These values differ by 12.2%, although the time histories in Figure 5 are in good agreement except for the peaks. An explanation for the difference between ADINA and DEPROP was offered following example 2. Basically, ADINA (1981 version) does not account for surface deformation affecting the load, whereas DEPROP does. Some effect can also be attributed to limited convergence in both calculations.

Comparing the peak dynamic results to the nonlinear static results in Table II, it is seen that the dynamic calculation predicts higher strains and displacements than the static calculation. In other words, the dynamic overshoot is greater than two for this problem. To be safe, a designer is well advised to perform dynamic analyses of a structure unless the true dynamic overshoot is reliably known.

Direct comparison of solution times for DEPROP and ADINA for this example problem was not possible because limited core size prevented running DEPROP on the CYBER 176 with the number of modes used. The DEPROP calculations were done on the VAX 11/750 at Kaman AviDyne. Past experience at Kaman AviDyne with slightly smaller DEPROP calculations done on a CYBER 176 computer has shown that DEPROP and ADINA consume comparable amounts of computer time for a given accuracy.

FURTHER DISCUSSION

To design a sandwich panel for large transverse loads, it is necessary to select a face sheet laminate, core material and thickness, and face-to-core bond mechanism. The two analytical techniques demonstrated in this paper are applicable to calculating face sheet and core stresses, permitting a survivability evaluation to be made by the designer. Neither technique is without limitations, though. For example, the equivalent layer method cannot be used for materially nonlinear analysis. In addition, the equivalent layer inner and outer surfaces are displaced from the actual face sheet surfaces. Consequently, it is difficult to model additional components attaching directly to the face sheets. The DEPROP code can model only single panels. If it is desired to model a box-like structure such as a communication shelter, it is necessary to make crude assumptions about "representative" boundary supports. Two other approaches to sandwich panel modeling are mentioned here.

Reference 11 outlines a finite element method whereby separate elements are used for the face sheets and core. This approach may not achieve the most efficient model in terms of degrees of freedom or minimum number of elements, but the above-mentioned difficulties with the equivalent layer and DEPROP models are avoided.

A second approach is to formulate a special sandwich panel element for a finite element code. An example of such an element is given in Reference 12. This element is kinematically similar to the thick shell element in ADINA

(Mindlin plate), except that the internal integrations have been modified to allow for separate face sheet and core material regions within the element. A new sandwich panel element is currently being developed at Kaman AviDyne that differs somewhat from the Reference 12 element by positioning all nodes within the face sheets. Instead of having midsurfaces nodes with rotational DOF, this element has only translational DOF at the faces. It will thus be well suited for modeling face sheet attachments. This element and the Reference 12 element are both formulated for materially nonlinear analysis.

REFERENCES

1. Mente, L.J.; and Lee, W.N.: "Dynamic Elastic-Plastic Response of Unstiffened and Stiffened Panels to Pressure Loadings", Proceedings of the Army Symposium on Solid Mechanics. **Designing for Extremes: Environment,** Loading, and Structural Behavior, AMMRC MS 80-4, Sept. 1980.

2. Schuman, W.J.; Zartarian, G.; Yeghiayan, R.P.; and Allison, W.D.: "C^3 Shelter Designs for the Tactical Battlefield", Proceedings of the Army Symposium on Solid Mechanics. **Designing for Extremes: Environment,** Loading, and Structural Behavior, AMMRC MS 80-4, Sept. 1980.

3. Zartarian, G.; Yeghiayan, R.P.; and Lush, A.M.: "Nuclear Blast Simulation Tests on HATS Type A Shelters in Event MILL RACE and in the CEG Shock Tube - Response Results and Correlations with Analysis", Kaman AviDyne Technical Report KA-TR-203, Feb. 1983, prepared for US Army Electronics Research and Development Command, Harry Diamond Laboratories, Adelphi, MD, Contract DAAK 21-80-C-0012.

4. Milligan, [illegible] A.; and Crenshaw, W.L.: "Blast Response of a Hardened Army ISO Shelter", Supplement to the Proceedings of the Army Symposium on Solid Mechanics, 1982: Critical Mechanics Problems in Systems Design, AMMRC MS 82-4, Sept. 1982.

5. Lush, A.M.: "An Equivalent Layer Sandwich Panel Model", Computers and Structures, submitted, 1984.

6. "ADINA: A Finite Element Program for Automatic Dynamic Incremental Nonlinear Analysis", ADINA Engineering Report AE 81-1, Sept. 1981.

7. Allen, H.G.: Analysis and Design of Structural Sandwich Panels, Pergamon Press, Oxford, 1969.

8. Ashton, J.E.; and Whitney, J.M.: Theory of Laminated Plates, Progress in Materials Science Series, vol. 4, Technomic, Stamford, CT, 1970.

9. Reissner, E.: "Finite Deflections of Sandwich Plates", J. Aeronautical Sci. 15(7), 435-440, July 1948.

10. Bathe, K.J.; and Bolourchi, S.: "A Geometric and Material Nonlinear Plate and Shell Element", Comput. Structures 11, 23-48 (1980).

11. Brockman, R.A.: "Nonlinear Finite Element Analysis of Sandwich Composites", AFWAL-TR-81-3008, March 1981.

12. Chang, T.Y.; and Sawamiphakdi, K.: "Large-Deformation Analysis of Laminated Shells by Finite Element Method", Comput. Structures 13, 331-340 (1981).

TABLE I. LINEAR STATIC RESPONSE OF PANEL IN FIGURE 1

Case	Mesh**	Nodes / Elem.	#DOF	CPU* Time	Percent Error					
					Center Displ.	$e_1^{(f)}$	$e_2^{(f)}$	$\gamma_{12}^{(f)}$	$\gamma_{23}^{(c)}$	$\gamma_{31}^{(c)}$
LU1	1x1	16	39	.55	+.008	-8.533	+1.635	+2.140	+3.721	+14.217
LU2	2x2	16	168	1.74	.000	-.696	+.115	+1.167	+3.226	+1.903
LU3	4x4	16	696	21.40	.000	-.045	+.007	+.637	+.679	+.303
LU4	8x8	16	2832	***	.000	-.003	+.001	+.280	+.202	+.084
LU5	3x3	9	168	.43	+.023	+2.153	+3.718	+4.687	-1.532	+1.384
LU6	6x6	9	696	4.96	+.001	+.490	+.907	+1.938	-.276	+.357
LU7	12x12	9	2832	***	.000	+.119	+.225	+.776	+.030	+.126
LU16	6x6	16 (3D Solid)	647	4.56	-.001	+.489	+.907	+1.709	-.276	+.348
DEPROP			160		+3.287	+.162	+1.124	-.747	+11.736	+1.105

*CYBER 176 Computer with NOS 2.1; ADINA set with MTOT = 29800

**Isoparametric thick shell elements except for case LU16.

***Solution time unrealistic because 408 blocks were required to store stiffness matrix due to small MTOT.

TABLE II. NONLINEAR STATIC RESPONSE OF PANEL IN FIGURE 1 FOR 2.4821 BARS

Case	Mesh*	Nodes / Elem.	#DOF	Maximums: Center Displ. (m)	$e_2^{(2)}$ (%)	$e_2^{(1)}$ (%)	$\gamma_{23}^{(c)}$ (%)	$\gamma_{31}^{(c)}$ (%)
Linear Solution				.049251	-.7534	+.7534	2.0619	2.7447
LU8	1x1	16	39	.035280	-.3163	+.7664	1.7918	2.5846
LU9	2x2	16	168	.035300	-.3325	+.7414	1.5915	2.4371
LU10	4x4	16	696	.035301	-.3338	+.7394	1.5656	2.3598
LU12	3x3	9	168	.035305	-.3470	+.7629	1.5674	2.2999
LU13	6x6	9	696	.035301	-.3369	+.7449	1.5618	2.3348
LU14	12x12	9	2832	.035301	-.3346	+.7406	1.5613	2.3422
LU17	6x6	16 (3D Solids)	647	.035116	-.3354	+.7392	1.5672	2.3444
DEPROP			160	.036338	-.3308	+.7447	1.7132	2.3198

*Isoparametric thick shell elements except for case LU16.

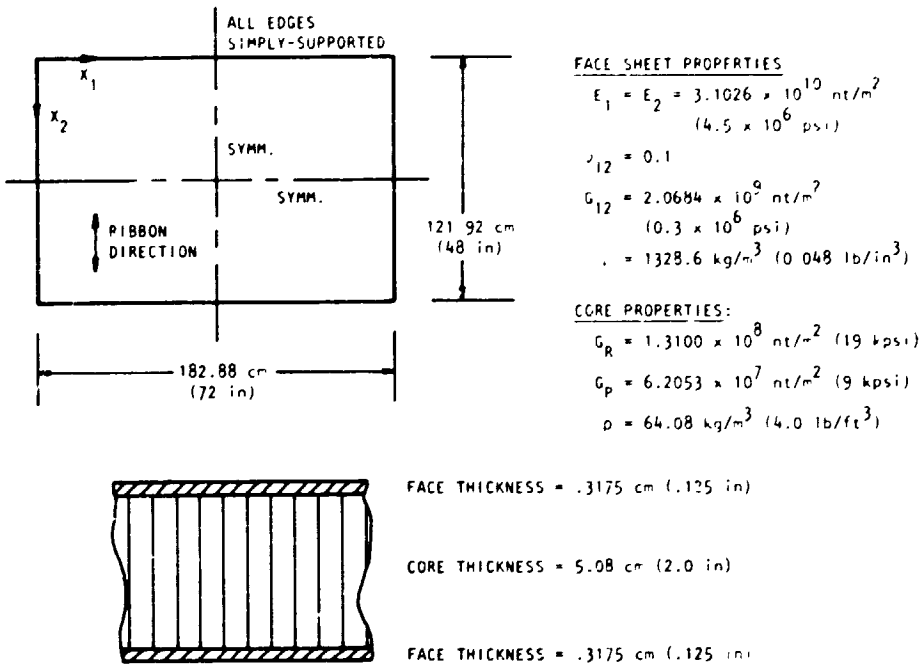

Figure 1.- Properties for sandwich panel example problem.

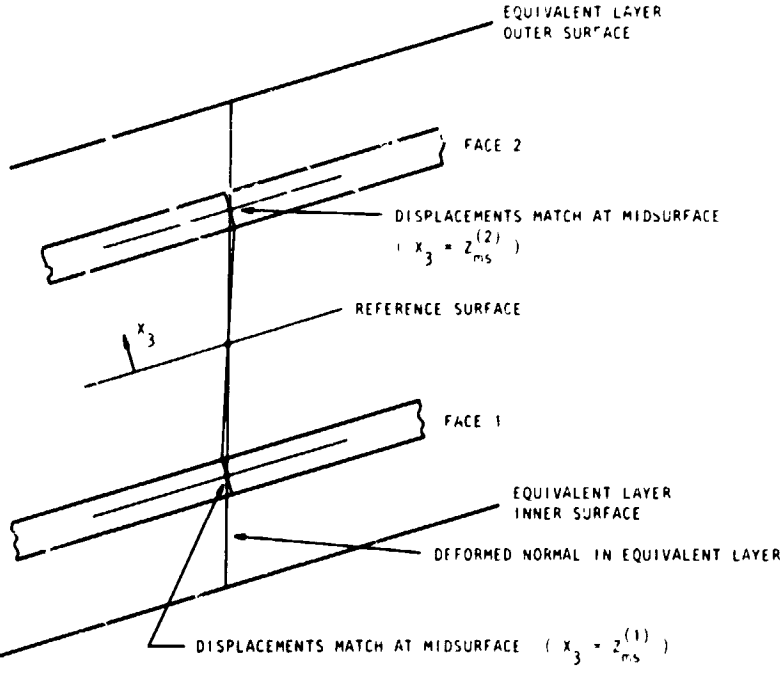

Figure 2.- Face sheet midsurface displacements matched by equivalent layer.

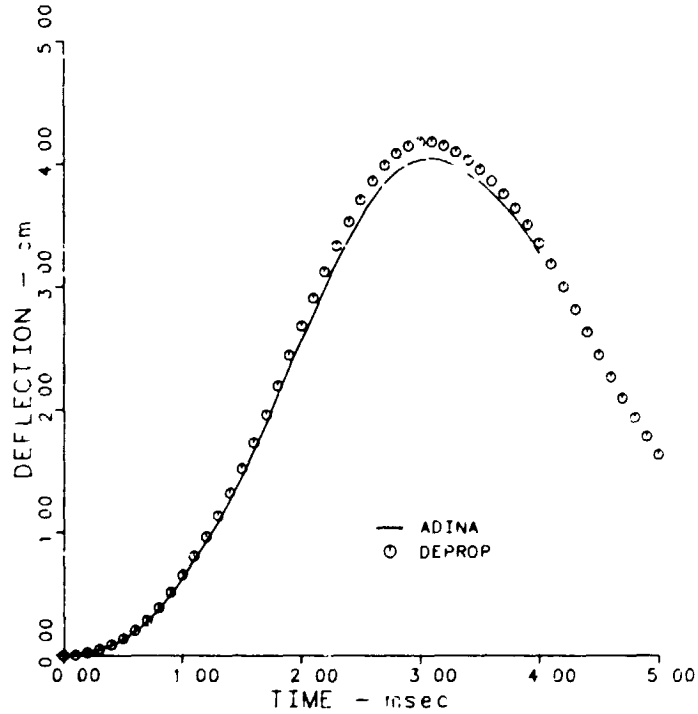

Figure 3.- Comparison of deflection for ADINA and DEPROP dynamic response calculations.

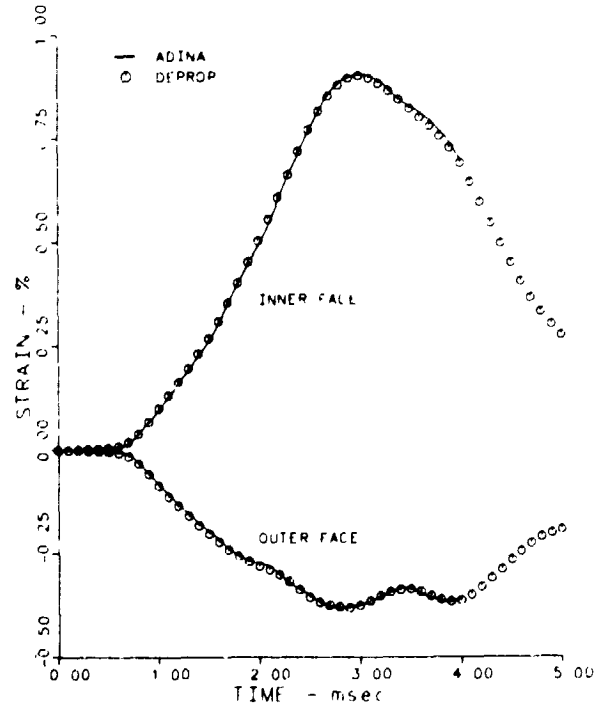

Figure 4.- Comparison of face strain E_2 for ADINA and DEPROP dynamic response calculations.

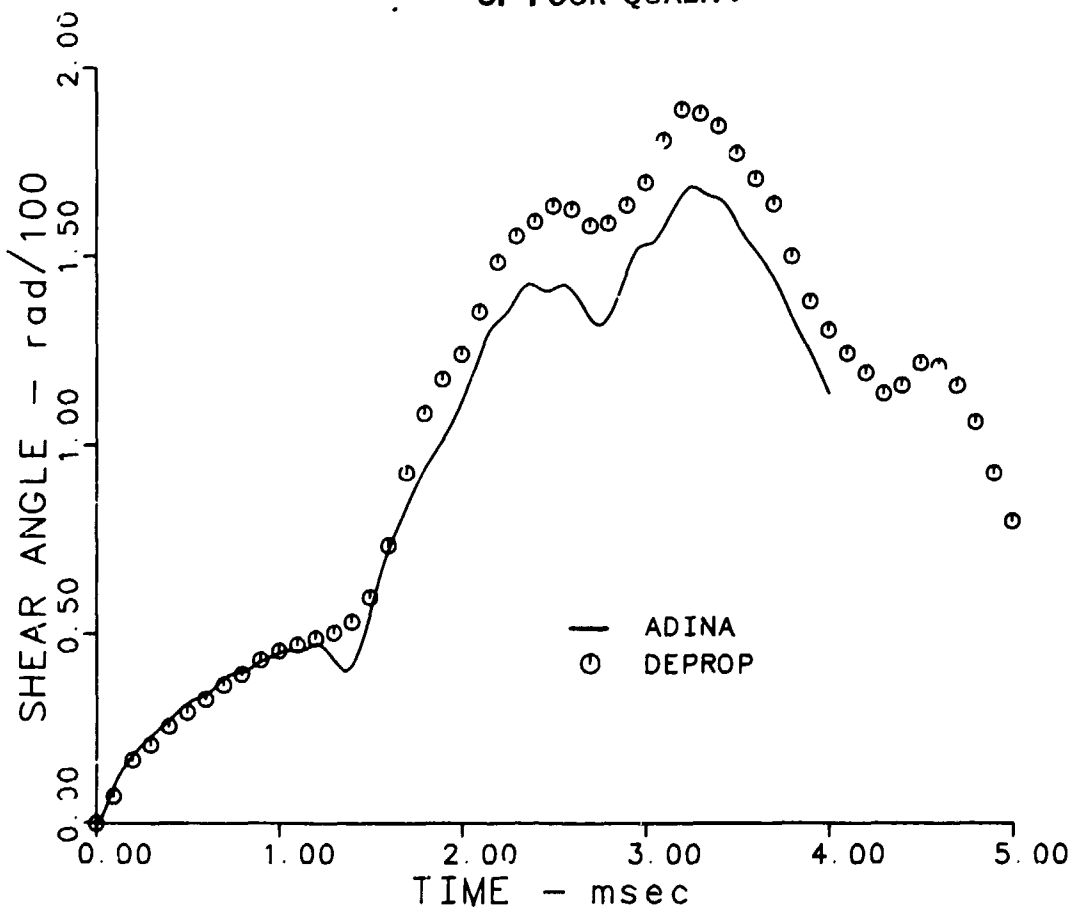

Figure 5.- Comparison of core shear strain γ_{23} for ADINA and DEPROP dynamic response calculations.

NON-GAUSSIAN APPROACH FOR PARAMETRIC RANDOM VIBRATION OF NON-LINEAR STRUCTURES*

R. A. Ibrahim and A. Soundararajan
Texas Tech University
Department of Mechanical Engineering
Lubbock, Texas 79409

SUMMARY

The dynamic response of a non-linear, single-degree-of-freedom structural system subjected to a "physically" white noise parametric excitation is investigated. The Itô stochastic calculus is employed to derive a general differential equation for the moments of the response coordinates. The differential equations of moments of any order are found to be coupled with higher order moments. A non-Gaussian closure scheme is developed to truncate the moment equations up to fourth order. The statistics of the stationary response are computed numerically and compared with analytical solutions predicted by a Gaussian closure scheme and the stochastic averaging method. It is found that the computed results exhibit the jump phenomenon which is typical of the characteristics of deterministic non-linear systems. In addition, the numerical algorithm leads to multiple solutions all of which give positive mean squares. However, two of these solutions are found to violate the properties of high order moments. One solution preserves the moments properties and demonstrates that the system achieves a stationary response.

INTRODUCTION

The flutter of aeroelastic structural components and their response to various types of aerodynamic loading are of main concern to aerospace engineers. The dynamic analysis of such systems in the transonic flight regime is often the most critical and difficult task (reference 1). The flutter problem of two- and three-dimensional plates undergoing limit cycle oscillations in a high supersonic flow has been investigated by Dowell (reference 2). The plate amplitude is limited by the non-linear membrane forces induced by the plate motion. In a series of investigations (references 3-7) Dżygadło analyzed the coupled parametric and self-excited (flutter) vibrations of plates subjected to periodic varying in-plane forces. It was found that plate flutter may occur as a result of pressure difference acting on the plate. In supersonic gas flow the Mach number for which self-excited vibration occurs is referred to as the critical Mach number M_{cr}. The influence of the Mach number on the size and location of the parametric instability regions has been considered. The general trend is that the instability region of the harmonic resonance shrinks and moves towards

*This research is supported by a grant from the National Science Foundation under grant No. MEA-8313572.

higher excitation frequencies and amplitudes as the Mach number M increases. On the other hand, the first region of parametric instability expands and moves towards a lower excitation frequency as M increases, provided $M<M_{cr}$. For $M>M_{cr}$ these regions shrink and reverse location towards larger frequency and amplitude of the parametric excitation.

Eastep and McIntosh (reference 8) investigated panel flutter under random excitation and linear aerodynamic loading. The limit cycle oscillation was determined by representing the modal amplitudes by a Fourier series and applying the Galerkin averaging for the temporal solution. The existence of a limit cycle was predicted by investigating the stability of small perturbations about the limit cycle solution. The excitation was represented by a random field (reference 9) which is described by a process which depends upon space and time. The panel motion was described by a coupled set of linear non-homogeneous differential equations with harmonic coefficients. They extended the study to determine the response of the panel under non-linear aerodynamic loading in the absence of any random excitation. Two non-linear mechanisms were considered. The first is the non-linear interaction between in-plane panel stresses and transverse transformation. This interaction provides a stabilizing influence on the panel motion in that it acts to restrain further deformation. The second is the non-linear aerodynamic loading, which has a destabilizing effect.

Recently Lee (reference 10) obtained the response of an elastic wing to random loads using rigid model wind tunnel pressure fluctuation measurements. The coupling between the structural dynamics and aerodynamics of a vibrating wing was taken into account by using the doublet lattice method for computing the unsteady aerodynamic force. The linear modeling showed that the acceleration and displacement response spectra, which were computed for the F-4E aircraft, were most affected by changes in dynamic pressure and Mach number.

To the authors' knowledge the random response of aeroelastic systems possessing structural and other types of non-linearities has not been examined properly. According to Bolotin (reference 11) and Barr (reference 12) non-linearity can enter the dynamic model through the elastic restoring forces, through the inertial terms, and through other internal or external agencies such as friction. In most cases the in-plane turbulent flow component acts as a source of random parametric excitation to the system. Thus the dynamic response of structural elements such as beams, columns, and plates may be described by a partial differential equation usually in one spatial dimension and time. This in turn can be reduced, by using the assumed mode method for example, to a finite set of ordinary differential equations (in the time) for the various modes of interest. Considering the fundamental mode as a first step to study the stochastic behaviour of these systems, the non-linear differential equation is obtained in the general form:

$$\ddot{Y} + 2\zeta\omega\dot{Y} + \omega Y = \psi\{W(t),\ Y,\dot{Y},\ddot{Y}\} \qquad (1)$$

where Y represents the generalized displacement of the system mode in question, ζ and ω are the linear damping ratio and natural frequency of the system, respectively. The function $\psi(\ )$ includes the relevant non-linear terms and the random parametric excitation W(t). It may be noted that equation (1) is identical in form to the equation of motion of the liquid propellant sloshing under random longitudinal excitations (references 13, 14).

The response analysis of system (1) is not a simple task mainly because of the limited capability of the available techniques (references 15,16). For example, if the random excitation is assumed to be a "physically" white noise process, the response coordinates constitute a Markov process for which the Fokker-Planck equation, or the Itô stochastic calculus, can be employed. In most cases it is not possible to derive an analytical solution for the stationary probability density. Instead one can generate a system of differential equations for the joint moments of the response. However, these equations form an infinite coupled set in the sense that the moment equations of a certain order are coupled with higher order moments. It is obvious that in order to determine the response statistics the moment equations must be closed. In view of the non-linear nature of system (1) the response process will not be Gaussian distributed even if the excitation is Gaussian white noise. In this case all Gaussian closure schemes (reference 16) are not applicable. A non-Gaussian closure scheme must be developed to truncate the moment equations.

In this paper a non-Gaussian closure scheme based on higher order cumulants (semi-invariants) will be developed. The first and second order cumulants represent the mean and the variance of the process, respectively. Higher order cumulants are statistical functions and, if they do not vanish, give a measure of the deviation of the random processes from being Gaussian distributed. A non-Gaussian probability density can then be represented by the Edgeworth expansion (reference 17). The first term of the series is the Gaussian probability density, while the rest of the expansion consists of functions of Hermite polynomials and higher order cumulants (of order greater than 2). These terms represent the deviation of the process from being non-Gaussian distributed. As a first order approximation, the fifth and sixth order cumulants will be set to zero and the fifth and sixth order joint moments can then be expressed in terms of lower order moments. Thus the dynamic moment equations up to fourth order will be closed and solved numerically for the stationary response statistics. The numerical solution will be compared with analytical solutions obtained previously by the authors. One remarkable feature of the non-Gaussian solution is that the response statistics experience the jump phenomenon known in deterministic vibration theory of non-linear systems. It will be noticed that the jump occurs at an excitation level below the threshold level of the condition of almost sure stability, and above the excitation level of the mean square stability of the linearized system.

SYMBOLS

$B(t)$	Brownian motion (Wiener) process
C_i	Coefficients of equations (24)
$2D$	Spectral density of the white noise
$E[\ ]$	Expectation of the argument $[\ ]$
$F_{\underset{\sim}{x}}(\underset{\sim}{\theta})$	The characteristic function
$H_n(X)$	Chebytchev-Hermite polynomial

K_i	Coefficients of the system equation (23)
M	Mach number
$m_{k,\ell}$	Joint moment of order K + ℓ
$p^*(\underset{\sim}{X},t)$	Gaussian probability density
$p(\underset{\sim}{X},t)$	Non-Gaussian probability density
q_i	Coefficients of the Edgeworth expansion
$R(\Delta t)$	Autocorrelation function, Δt = correlation time
$W(t)$	White noise process
X_1, X_2	Coordinates of the response Markov process
Y	Structure spatial coordinate
$\delta(\ )$	The Dirac delta function
ζ	The structure damping factor
$\underset{\sim}{\theta}$	Arbitrary real valued vector (θ_1,θ_2)
Φ	Scalar function of the response coordinates
$\psi(\ )$	Non-linear function of equation (1)
ρ	Correlation coefficient
τ	Non-dimensional time parameter = ωt
σ	Standard deviation
λ_K	the K-th order cumulant of the response
ω	Natural frequency of the system

STATISTICS OF THE NON-GAUSSIAN RESPONSE

Structural systems described by non-linear stochastic differential equations of the type (1) can be written in a state Markov vector if the non-linear terms involving $\ddot{Y}$ are eliminated by expanding the terms of $\psi\{W(t),Y,\dot{Y},\ddot{Y}\}$ into an asymptotic series approximation. Introducing the response coordinate transformation $Y = X_1$ and $\dot{X}_1 = X_2$, equation (1) can be written in terms of the two first order differential equation of the vector form:

$$\dot{\underset{\sim}{X}} = \underset{\sim}{f}(\underset{\sim}{X},t) + \underline{\underline{G}}(\underset{\sim}{X},t)\underset{\sim}{W}(t) \qquad (2)$$

where $\underset{\sim}{f}(\underset{\sim}{X},t)$ is a vector whose elements are non-linear functions of the state coordinates X_1 and X_2, $\underline{G}(\underset{\sim}{X},t)$ is a 2×2 matrix whose elements are also non-linear and $\underset{\sim}{W}(t)$ is a white noise vector. The elements of $\underset{\sim}{W}(t)$ have the following statistical properties:

$$E[W_i(t)] = 0$$

$$R_{W_iW_j}(\Delta t) = E[W_i(t)W_j(t+\Delta t)] = 2D_{ij}\,\delta(\Delta t) \tag{3}$$

It is customary to write $W_i(t)$ as the "formal" derivative of the Brownian motion process as:

$$W_i(t) = \sigma_i \frac{dB_i(t)}{dt} \tag{4}$$

where σ_i is the spectral density such that $\sigma_i^2 = 2D_i$.
Equation (2) may be written as a stochastic differential equation of Stratonovich type:

$$dX_i = f_i(\underset{\sim}{X},t)dt + \sum_{j=1}^{2} G_{ij}(\underset{\sim}{X},t)dB_j(t) \tag{5}$$

Alternatively equation (2) may in turn be transformed into the Itô type equation:

$$dX_i = \left\{f_i(\underset{\sim}{X},t)dt + \frac{1}{2}\sum_{k=1}^{2}\sum_{j=1}^{2} G_{kj}\frac{\partial G_{ij}}{\partial X_k}\right\}dt + \sum_{j=1}^{2} G_{ij}dB_j(t) \tag{6}$$

where the double summation expression in (6) is referred to as the Wong-Zakai correction term (reference 18).

The dynamic response statistical functions can be expressed in terms of moments, semi-invariants (cumulants) or quasi-moments. Information about one of these functions can be used to determine the other functions. However, for a highly non-Gaussian response it is convenient to deal with statistic functions whose values diminish faster as their order increases. If the process is Gaussian the Edgeworth expansion is reduced to the fundamental term since all higher order terms vanish identically. It will be shown later that the higher order cumulants (which appear as coefficients in the expansion) do not vanish for non-Gaussian response. In the present analysis we will deal with the response joint moments and joint cumulants. Applying the Itô rule for the stochastic differential (reference 19)

$$d\phi(\underset{\sim}{X}) = \left\{\frac{\partial\phi(\underset{\sim}{X})}{\partial X_i}\right\}^T \{d\underset{\sim}{X}\} + \frac{1}{2}\,\text{Trace}\,\underline{G}\,\underline{Q}\,\underline{G}\left(\frac{\partial^2\phi(\underset{\sim}{X})}{\partial X_i \partial X_j}\right)dt \tag{7}$$

where $\Phi(\underset{\sim}{X})$ is a general scalar function of the response coordinates.

Taking the expectation of both sides of (7) and dividing by dt gives

$$\frac{d}{dt} E[\phi] = E\left[\left\{\frac{\partial \phi}{\partial X_i}\right\}^T \{f(\underset{\sim}{X},t)\}\right] + \frac{1}{2} E\left[\text{Trace } \underline{G}\, \underline{Q}\, \underline{G} \left(\frac{\partial^2 \phi}{\partial X_i \partial X_j}\right)\right] dt \tag{8}$$

The choice of $\Phi(\underset{\sim}{X})$ depends mainly upon the type of the statistical function to be evaluated. If the joint moments of response are required, the following expression may be used:

$$\Phi(\underset{\sim}{X}) = \left(X_1^{k_1} X_2^{k_2}\right) \tag{9}$$

The joint moments of (9) are related to the cumulants through the characteristic function:

$$\begin{aligned} F_{\underset{\sim}{X}}(\underset{\sim}{\theta}) &= E\left[\exp\left(i\theta_1 X_1 + i\theta_2 X_2\right)\right] \\ &= \int_{-\infty}^{\infty} \int_{-\infty}^{\infty} \exp\left(i\theta_1 X_1 + i\theta_2 X_2\right) p(X_1, X_2)\, dX_1\, dX_2 \end{aligned} \tag{10}$$

where θ_1 and θ_2 are arbitrary real valued parameter and $i = \sqrt{-1}$. The moments and joint moments can be generated by taking derivatives of $F_{\underset{\sim}{X}}(\underset{\sim}{\theta})$ with respect to θ_1 and θ_2:

$$E\left[X_1^{k_1} X_2^{k_2}\right] = \left(\frac{1}{i}\right)^K \left(\frac{\partial^K F_{\underset{\sim}{X}}(\underset{\sim}{\theta})}{\partial \theta_1^{k_1} \partial \theta_2^{k_2}}\right|_{\underset{\sim}{\theta} = 0}\Bigg), \quad K = k_1 + k_2 \tag{11}$$

Expanding the characteristic function in a Maclaurin series gives

$$F_{\underset{\sim}{X}}(\underset{\sim}{\theta}) = 1 + \sum_{n=1}^{\infty} \frac{1}{n!} E\left[\left(i\theta_1 X_1 + i\theta_2 X_2\right)^n\right] \tag{12}$$

This expansion suggests that $F_{\underset{\sim}{X}}(\underset{\sim}{\theta})$ can be written as an exponential function whose argument is a series of the joint cumulants $\lambda_K\left(X_1^{k_1}, X_2^{k_2}\right)$:

$$F_{\underset{\sim}{X}}(\underset{\sim}{\theta}) = \exp\left\{ \sum_{j=1}^{2} (i\theta_j)\lambda_1(X_j) + \frac{1}{2!} \sum_{j=1}^{2} \sum_{\ell=1}^{2} (i\theta_j)(i\theta_\ell)\lambda_2(X_j X_\ell) \right.$$

$$\left. + \frac{1}{3!} \sum_{j=1}^{2} \sum_{\ell=1}^{2} \sum_{r=1}^{2} (i\theta_j)(i\theta_\ell)(i\theta_r)\lambda_3(X_j X_\ell X_r) + \ldots \right\} \tag{13}$$

The joint cumulants of order K are generated by taking the K-th derivative of the principal logarithm of $F_{\underset{\sim}{X}}(\underset{\sim}{\theta})$:

$$\lambda_K[X_1^{k_1} X_2^{k_2}] = \left(\frac{1}{i}\right)^K \left. \frac{\partial^K \ell n\, F_{\underset{\sim}{X}}(\underset{\sim}{\theta})}{\partial\theta_1^{k_1}\, \partial\theta_2^{k_2}} \right|_{\underset{\sim}{\theta} = 0} \tag{14}$$

Definition (14) and relations (11) and (12) reveal that the joint cumulant of order K is related to the K-th and lower order joint moments.

In order to clarify the influence of higher order cumulants on the probability density, consider the case of one-dimensional random process. The Gaussian probability density of the random variable X is

$$p^*(X) = \frac{1}{\sqrt{2\pi}\,\sigma} \exp\left\{ -\frac{(X-m)^2}{2\sigma^2} \right\} \tag{15}$$

where $m = E[X]$, and $\sigma^2 = E[(X-m)^2]$.

The characteristic function of a Gaussian process X can be established by taking the inverse Fourier transform of (15) (reference 20):

$$F_x(\theta) = \exp\left\{ im\theta - \frac{1}{2}\sigma^2\theta^2 \right\} \tag{16}$$

The logarithm of (16) is

$$\ell n\, F_x(\theta) = im\theta - \frac{1}{2}\sigma^2\theta^2 \tag{17}$$

Comparison of (17) with the logarithm of the characteristic function (13) of an arbitrary random process.

$$\ln F_x(\theta) = i\theta\lambda_1 - \frac{1}{2!}\theta^2\lambda_2 - \frac{i}{3!}\theta^3\lambda_3 + \frac{\theta^4}{4!} + \ldots \tag{18}$$

reveals that for Gaussian processes all cumulants of order greater than 2 must vanish identically. If the process is not Gaussian it will possess higher order cumulants. Thus, for non-Gaussian processes one must express the probability density in terms of the Edgeworth asymptotic expansion. For a one-dimensional case p(X) takes the form (reference 17)

$$p(X) = q_o p^*(X) + \frac{1}{1!} q_1 \frac{\partial p^*(X)}{\partial X} + \frac{1}{2!} q_2 \frac{\partial^2 p^*(X)}{\partial X^2} + \ldots \tag{19}$$

where q_i are constant coefficients and $p^*(X)$ is the normal Gaussian density function given by (15). When $q_o = 1$ and all other coefficients vanish the process is purely normal distributed. The coefficients q_i are related to the Chebytchev-Hermite polynomials $H_n(X)$ defined by the relation

$$H_n(X) = (-1)^n \exp\left(\frac{X^2}{2}\right) \frac{d^n}{dX^n}\left(\exp\left(-\frac{X^2}{2}\right)\right), \quad H_0(X) = 1 \tag{20}$$

For two-dimensional problems the Edgeworth expansion can be written in terms of the Hermite polynomials and the joint cumulants in the form (reference 21)

$$\begin{aligned} p(X_1,X_2) = p^*(X_1,X_2)\Bigg\{ & \sum_{k=0}^{\infty} \frac{\rho^k}{k!} H_k\left(\frac{y_1}{\sigma_1}\right) H_k\left(\frac{y_2}{\sigma_2}\right) \\ & + \sum_{i+j=3} \frac{1}{i!j!} \frac{\lambda_{ij}}{\sigma_1^i \sigma_2^j} \sum_{k=0}^{\infty} \frac{\rho^k}{k!} H_{k+i}\left(\frac{y_1}{\sigma_1}\right) H_{k+j}\left(\frac{y_2}{\sigma_2}\right) \\ & + \sum_{i+j=4} \frac{1}{i!j!} \frac{\lambda_{ij}}{\sigma_1^i \sigma_2^j} \sum_{k=0}^{\infty} \frac{\rho^k}{k!} H_{k+i}\left(\frac{y_1}{\sigma_1}\right) H_{k+j}\left(\frac{y_2}{\sigma_2}\right) \\ & + \frac{1}{2} \sum_{\substack{i+j=3 \\ \ell+m=4}} \frac{1}{i!j!\ell!m!} \frac{\lambda_{ij}}{\sigma_1^i \sigma_2^j} \frac{\lambda_{\ell m}}{\sigma_1^\ell \sigma_2^m} \sum_{k=0}^{\infty} \frac{\rho^k}{k!} H_{k+i+\ell}\left(\frac{y_1}{\sigma_1}\right) H_{k+j+m}\left(\frac{y_2}{\sigma_2}\right) \Bigg\} \end{aligned} \tag{21}$$

where

$$p^*(X_1,X_2) = \frac{1}{2\pi\sigma_1\sigma_2} \exp\left\{-\frac{1}{2}\left(\frac{y_1}{\sigma_1}\right)^2 - \frac{1}{2}\left(\frac{y_2}{\sigma_2}\right)^2\right\} \tag{22}$$

$$\rho = \frac{\lambda_{11}}{\sigma_1 \sigma_2}$$

$$y_i = X_i - E[X_i]$$

It is seen from expansion (21) that higher order cumulants (of order greater than 2) give a measure for the deviation of the response distribution from being Gaussian. It is expected that the expansion converges as the cumulant order increases up to a degree where their contribution becomes negligible.

NON-LINEAR SINGLE FREEDOM STRUCTURE

Equation of Motion and Its Markov Vector

The equation of motion of structural elements such as beams (reference 22) and plates (reference 23) and liquid free surface motion (reference 14), subjected to random parametric excitation may be written in the non-dimensional form:

$$\ddot{Y} + 2\zeta\dot{Y} + [1-W(\tau)]Y(1-K_1Y-K_2Y^2) + K_3\dot{Y}^2 + K_4Y\ddot{Y} + K_5Y\dot{Y}^2 + K_6Y^2\ddot{Y} = 0 \tag{23}$$

where Y, $\dot{Y}$, and $\ddot{Y}$ represent a characteristic displacement, velocity and acceleration of the system response, respectively, ζ is the viscous damping, K_i are constants and the dot denotes differentiation with respect to the dimensionless time parameter $\tau = \omega t$, ω is the structure natural frequency, and $W(\tau)$ is the random parametric loading which is assumed to be stationary, Gaussian white noise and possesses the statistical properties given by (3). Thus it is possible to treat the response as a Markov process. To generate the Markov vector the double derivative $\ddot{Y}$ must be successively eliminated from the non-linear terms $K_4Y\ddot{Y}$ and $K_6Y^2\ddot{Y}$. Keeping terms up to cubic order and introducing the transformation $Y = X_1$, $\dot{X}_1 = X_2$, equation (23) may be written in the state vector form:

$$\begin{aligned}
\dot{X}_1 &= X_2 \\
\dot{X}_2 &= -2\zeta X_2 + C_1X_1X_2^2 + C_2X_2^2 + C_3\zeta X_1^2X_2 + C_4\zeta X_1X_4 \\
&\quad - [1-W(\tau)](X_1 - C_6X_1^2 - C_5X_1^3)
\end{aligned} \tag{24}$$

where C_i depend on K_i.

Dynamic Moments Equation

Using equation (8) and letting $\phi = (X_1^k X_2^\ell)$, the following general differential equation of the moments of order $n = k + \ell$ is

$$\begin{aligned}\dot{m}_{k,\ell} &= k m_{k-1,\ell+1} + \ell\{-2\zeta m_{k,\ell} + C_1 m_{k+1,\ell+1} + C_2 m_{k,\ell+1} + C_3\zeta m_{k+2,\ell} \\ &+ C_4\zeta m_{k+1,\ell} + C_5 m_{k+3,\ell-1} + C_6 m_{k+2,\ell-1} - m_{k+1,\ell-1}\} \\ &+ \ell(\ell-1)D\{m_{k+2,\ell-2} - 2C_6 m_{k+3,\ell-2} + C_7 m_{k+4,\ell-2}\}\end{aligned} \tag{25}$$

where

$$m_{k,\ell} = \int_{-\infty}^{\infty}\int_{-\infty}^{\infty} X_1^k X_2^\ell \, p(\underset{\sim}{X},t)\,dX_1\,dX_2 \tag{26}$$

and $C_7 = C_6^2 - 2C_5$. For a typical dynamic system the following constants are obtained:

$C_1 = -203.060$ $\quad C_2 = -14.189$ $\quad C_3 = -174.380$

$C_4 = -14.419$ $\quad C_5 = 16.364$ $\quad C_6 = 9.909$

It is seen that the moment equation of order $n = k+\ell$ contains moments of higher order $(n+1, n+2, \ldots)$, and the system of dynamic moment equations generated from (26) forms an "infinite hierarchy" coupled equations. Since the system (23) is non-linear and includes random parametric coefficients, then all cumulants of order higher than two will not vanish and the joint probability density, $p(\underset{\sim}{X},t)$, of the response will not be Gaussian.

Considering dynamic moment equations up to the fourth order, the following coupled equations are obtained.

The first order moment equations are:

$$\begin{aligned}\dot{m}_{10} &= m_{01} \\ \dot{m}_{01} &= -2\zeta m_{01} + C_1 m_{12} + C_2 m_{02} + C_3\zeta m_{21} + C_4\zeta m_{11} \\ &+ C_5 m_{30} + C_6 m_{20} - m_{10}\end{aligned} \tag{27}$$

The second order moment equations are:

$$\dot{m}_{20} = 2m_{11}$$

$$\dot{m}_{02} = -4\zeta m_{02} + 2C_1 m_{13} + 2C_2 m_{03} + 2C_3\zeta m_{22} + 2C_4\zeta m_{12} + 2C_5 m_{31}$$
$$+ 2C_6 m_{21} - 2m_{11} + 2Dm_{20} - 4DC_6 m_{30} + 2DC_7 m_{40} \qquad (28)$$

$$\dot{m}_{11} = m_{02} - 2\zeta m_{11} + C_1 m_{22} + C_2 m_{12} + C_3\zeta m_{31} + C_4\zeta m_{21} + C_5 m_{40}$$
$$+ C_6 m_{30} - m_{20}$$

The third order moment equations are:

$$\dot{m}_{30} = 3m_{21}$$

$$\dot{m}_{03} = -6\zeta m_{03} + 3C_1 m_{14} + 3C_2 m_{04} + 3C_3\zeta m_{23} + 3C_4\zeta m_{13}$$
$$+ 3C_5 m_{32} + 3C_6 m_{22} - 3m_{12} + 6Dm_{21} - 12DC_6 m_{31} + 6DC_7 m_{41}$$

$$\dot{m}_{21} = 2m_{12} - 2\zeta m_{21} + C_1 m_{32} + C_2 m_{22} + C_3\zeta m_{41} + C_4\zeta m_{31} \qquad (29)$$
$$+ C_5 m_{50} + C_6 m_{40} - m_{30}$$

$$\dot{m}_{12} = m_{03} - 4\zeta m_{12} + 2C_1 m_{23} + 2C_2 m_{13} + 2C_3\zeta m_{32} + 2C_4\zeta m_{22}$$
$$+ 2C_5 m_{41} + 2C_6 m_{31} - m_{21} + 2Dm_{30} - 4DC_6 m_{40} + 2DC_7 m_{50}$$

The fourth order moments are:

$$\dot{m}_{40} = 4m_{31}$$

$$m_{04} = -8\zeta m_{04} + 4C_1 m_{15} + 4C_2 m_{05} + 4C_3\zeta m_{24} + 4C_4\zeta m_{14}$$
$$+ 4C_5 m_{33} + 4C_6 m_{23} - 4m_{13} + 12Dm_{22} - 24DC_6 m_{32} + 12DC_7 m_{42}$$

$$\dot{m}_{31} = 3m_{22} - 2\zeta m_{31} + C_1 m_{42} + C_2 m_{32} + C_3\zeta m_{51} + C_4\zeta m_{41}$$

$$+ C_5 m_{60} + C_6 m_{50} - m_{40}$$

$$\dot{m}_{13} = m_{04} - 6\zeta m_{13} + 3C_1 m_{24} + 3C_2 m_{14} + 3C_3 \zeta m_{33} + 3C_4 \zeta m_{23}$$

$$+ 3C_5 m_{42} + 3C_6 m_{32} - 3m_{22} + 6Dm_{31} - 12Dm_{41} + 6DC_7 m_{51} \qquad (30)$$

$$\dot{m}_{22} = 2m_{13} - 4\zeta m_{22} + 2C_1 m_{33} + 2C_2 m_{23} + 2C_3 \zeta m_{42} + 2C_4 \zeta m_{32}$$

$$+ 2C_5 m_{51} + 2C_6 m_{41} - 2m_{31} + 2Dm_{40} - 4DC_6 m_{50} + 2DC_7 m_{60}$$

NON-GAUSSIAN CUMULANT CLOSURE

A first order non-Gaussian closure can be established by setting the fifth and sixth order cumulants obtained by using definition (14) to zero. This results in a set of relations between fifth and sixth order joint moments, in equations (30) and (31), and lower order moments. Thus the fifth and sixth joint moments in (30) and (31) are replaced by the following expressions:

$$m_{50} = 5m_{10}m_{40} - 20m_{20}^2 m_{30} - 30m_{10}m_{20}^2 + 60m_{10}^3 m_{20} + 10m_{20}m_{30} - 24m_{10}^5$$

$$m_{05} = 5m_{01}m_{04} - 20m_{01}^2 m_{03} - 30m_{01}m_{02}^2 + 60m_{01}^3 m_{02} + 10m_{02}m_{03} - 24m_{01}^5$$

$$m_{41} = 4m_{10}m_{31} + m_{01}m_{40} - 4m_{10}(2m_{01}m_{30} + 3m_{10}m_{21}) - 6m_{20}(m_{01}m_{20}$$

$$+ 4m_{10}m_{11} - m_{21}) + 12m_{10}^2(3m_{01}m_{20} + 2m_{10}m_{11} - 2m_{10}^2 m_{01}) + 4m_{11}m_{30}$$

$$m_{14} = 4m_{01}m_{13} + m_{10}m_{04} - 4m_{01}(2m_{10}m_{03} + 3m_{01}m_{12}) - 6m_{02}(m_{10}m_{02}$$

$$+ 4m_{01}m_{11} - m_{12}) + 12m_{01}^2(3m_{10}m_{02} + 2m_{01}m_{11} - 2m_{01}^2 m_{10}) + 4m_{11}m_{03}$$

$$m_{32} = 3m_{10}m_{22} - 6m_{10}(m_{10}m_{12} + 2m_{01}m_{21} + m_{02}m_{20} + 2m_{11}^2 - 6m_{10}m_{01}m_{11}$$

$$- 3m_{01}^2 m_{20} - m_{10}^2 m_{02} + 4m_{10}^2 m_{01}^2) - 2m_{01}(m_{01}m_{30} + 6m_{11}m_{20} - m_{31})$$

$$+ m_{02}m_{30} + 6m_{11}m_{21} + 3m_{20}m_{12}$$

$$\mu_{23} = 3\mu_{01}\mu_{22} - 6\mu_{01}(\mu_{01}\mu_{21} + 2\mu_{10}\mu_{12} + \mu_{02}\mu_{20} + 2\mu_{11}^2 - 6\mu_{01}\mu_{10}\mu_{11}$$
$$- 3\mu_{10}^2\mu_{02} - \mu_{01}^2\mu_{20} + 4\mu_{01}^2\mu_{10}^2) - 2\mu_{10}(\mu_{10}\mu_{03} + 6\mu_{11}\mu_{02} - \mu_{13})$$
$$+ \mu_{20}\mu_{03} + 6\mu_{11}\mu_{12} + 3\mu_{02}\mu_{21}$$

$$\mu_{60} = 15\mu_{20}(\mu_{40} - 4\mu_{10}\mu_{30} - 2\mu_{20}^2 + 6\mu_{10}^2\mu_{20}) + 10\mu_{30}^2 - 24\mu_{10}^6$$

$$\mu_{06} = 15\mu_{02}(\mu_{04} - 4\mu_{01}\mu_{03} - 2\mu_{02}^2 + 6\mu_{01}^2\mu_{02}) + 10\mu_{03}^2 - 24\mu_{01}^6$$

$$\mu_{51} = 5\mu_{11}\mu_{40} + 10\mu_{20}(\mu_{31} - \mu_{01}\mu_{30} - 3\mu_{21} - 3\mu_{20}\mu_{11} + 3\mu_{10}\mu_{01}\mu_{20}$$
$$+ 6\mu_{10}^2\mu_{11}) + 10\mu_{30}(\mu_{21} - 2\mu_{10}\mu_{11}) - 24\mu_{10}^5\mu_{01}$$

$$\mu_{15} = 5\mu_{11}\mu_{04} + 10\mu_{02}(\mu_{13} - \mu_{10}\mu_{03} - 3\mu_{01}\mu_{12} - 3\mu_{02}\mu_{11} + 3\mu_{01}\mu_{10}\mu_{02}$$
$$+ 6\mu_{01}^2\mu_{11}) + 10\mu_{03}(\mu_{12} - 2\mu_{01}\mu_{11}) - 24\mu_{01}^5\mu_{10} \qquad (31)$$

$$\mu_{42} = \mu_{02}\mu_{40} + 8\mu_{11}\mu_{31} + 6\mu_{20}\mu_{22} - 4\mu_{01}(2\mu_{11}\mu_{30} + 3\mu_{20}\mu_{21} - 1.5\mu_{01}\mu_{20}^2$$
$$- 12\mu_{10}\mu_{20}\mu_{11} + 6\mu_{01}\mu_{10}^4) - 4\mu_{10}(3\mu_{20}\mu_{12} + \mu_{02}\mu_{30} + 6\mu_{11}\mu_{21}$$
$$- 3\mu_{10}\mu_{20}\mu_{02} - 6\mu_{10}\mu_{11}^2) + 4\mu_{12}\mu_{30} + 6\mu_{21}^2 - 6\mu_{20}^2\mu_{02} - 24\mu_{11}^2\mu_{20}$$

$$\mu_{24} = \mu_{20}\mu_{04} + 8\mu_{11}\mu_{13} + 6\mu_{02}\mu_{22} - 4\mu_{10}(2\mu_{11}\mu_{03} + 3\mu_{02}\mu_{12} - 1.5\mu_{10}\mu_{02}^2$$
$$- 12\mu_{01}\mu_{02}\mu_{11} - 6\mu_{10}\mu_{01}^4) - 4\mu_{01}(3\mu_{02}\mu_{21} + \mu_{20}\mu_{03} + 6\mu_{11}\mu_{12}$$
$$- 3\mu_{01}\mu_{02}\mu_{20} - 6\mu_{01}\mu_{11}^2) + 4\mu_{21}\mu_{03} + 6\mu_{12}^2 - 6\mu_{02}^2\mu_{20} - 24\mu_{11}^2\mu_{02}$$

$$\mu_{33} = 3\mu_{20}\mu_{13} + 3\mu_{02}\mu_{31} + 9\mu_{11}\mu_{22} - 3\mu_{10}(\mu_{20}\mu_{03} + 6\mu_{11}\mu_{12} + 3\mu_{02}\mu_{21}$$
$$- 6\mu_{10}\mu_{11}\mu_{02} - 12\mu_{01}\mu_{11}^2 + 8\mu_{10}^2\mu_{01}^3) - 3\mu_{01}(\mu_{02}\mu_{30} + 3\mu_{20}\mu_{12}$$
$$+ 6\mu_{11}\mu_{21} - 6\mu_{01}\mu_{11}\mu_{20} - 6\mu_{10}\mu_{02}\mu_{20}) - 6\mu_{11}(3\mu_{02}\mu_{20} + 2\mu_{11}^2)$$
$$+ \mu_{03}\mu_{30} + 9\mu_{12}\mu_{21}$$

It is obvious that the first order non-Gaussian closure scheme presented by relations (31) increases the degree of non-linearity of the dynamic moment equations (27-30). Therefore, the stationary solution, obtained by setting the left-hand side of equations (27-30) to zero, will have more than one solution. The resulting fourteen non-linear, algebraic equations are solved numerically by using the IMSL (International Mathematical and Statistical Library) Subroutine ZSPOW. This subroutine is based on the MINPACK subroutine HYBRD1, which uses a modification of the M.J.D. Powell's hybrid algorithm described in reference (24). This algorithm is a variation of Newton's method which uses a finite difference approximation to the Jacobian and takes precautions to avoid large step sizes or increasing residuals.

The numerical algorithm gives five solutions. Each solution is obtained as a result of a set of initial guessing values. All solutions give positive mean squares for the response displacement and velocity. However, two of these solutions are rejected because the associated higher even moments (such as m_{40} or m_{04}) are found to be negative for the whole range of excitation level $D/2\zeta$. A third solution exhibits positive mean squares and higher even moments over a limited range of excitation level $1.2 \leq D/2\zeta \leq 27$. This solution is associated with numerical instability in the higher order moments and the algorithm indicates that the iteration has not made good progress. The fourth solution demonstrates successful numerical iteration with a very high degree of accuracy. In addition, the response preserves most of the moment properties for which all even order moments (up to fourth order) are positive over an excitation level range $D/2\zeta > 1.86$. However, this solution does not satisfy the Schwartz inequality and it is found that $m_{10} > m_{20}$. The results of this solution are shown in fig. (1). The fifth solution is believed to be the most realistic as it satisfies all moments properties and Schwartz's inequality over the excitation level range $D/2\zeta > 1.5$ as shown in fig. (2).

Figure (3) provides a comparison between the mean square values of the response displacement as computed by the non-Gaussian closure schemes (the last three solutions are plotted) and as predicted analytically by the Gaussian closure method (reference 14) and the stochastic averging (reference 14). Unlike the predicted solutions of reference (14), the non-Gaussian closure scheme exhibits the jump characterstic which is common in deterministic non-linear vibration theory. Furthermore, it is seen that the computed results are stationary and begin at excitation levels varying between $D/2\zeta = 1.2$ and 1.86. The mean square m_{20} of the fifth solution is almost over 80% of the predicted solutions of reference (14). This difference is not surprising since the non-Gaussian closure scheme increases the degree of non-linearity of the dynamic moment equations. In deterministic theory of non-linear vibration it is known that the non-linearity stabilizes the original unstable linear system.

CONCLUDING REMARKS

A non-Gaussian closure scheme has been developed and worked successfully for non-linear structural systems subjected to wide-band random parametric excitation. Multiple solutions have been obtained and examined for their validity based on the behavior of kurtosis and higher even joint moments. The method

predicted the jump phenomenon, for all mean squares, at an excitation level very close to the threshold level of the condition of almost-sure stability. In view of the additional degree of non-linearity resulting from the non-Gaussian closure scheme, the mean square of the response displacement has been found to be less than those values obtained by other methods such as the Gaussian closure or the stochastic averaging.

REFERENCES

1. Borland, C. J. and Rizzetta, D. P.: Non-linear Transonic Flutter Analysis. AIAA Journal, vol. 20, no. 11, Nov. 1982, pp. 1606-1615.

2. Dowell, E. H.: Non-linear Oscillations of a Fluttering Plate. AIAA Journal, vol. 4, no. 7, July 1966, pp. 1267-1275.

3. Dżygadlo, Z.: Parametric Self-Excited Vibration of a Simply Supported Plate in Supersonic Flow. Proc. Vibr. Probl., vol. 6, no. 4, 1965, pp. 353-365.

4. Dżygadlo, Z.: Parametric Self-Excited Vibration of a Plate of Finite Length in Plane Supersonic Flow. Proc. Vib. Probl., vol. 7, no. 4, 1966, pp. 287-309.

5. Dżygadlo, Z.: Non-stationary Parametric and Parametric Self-Excited Vibration of a Plate of Finite Length in Plane Supersonic Flow. Proc. Vibr. Probl., vol. 8, no. 4, 1967, pp. 381-394.

6. Dżygadlo, Z.: Forced Parametrically-Excited Vibration of a Plate of Finite Length in Plane Supersonic Flow. Part I - Theory. Proc. Vibr. Probl., vol. 10, no. 2, 1969, pp. 231-245.

7. Dżygadlo, Z.: Forced Parametrically-Excited Vibration of a Plate of Finite Length in Plane Supersonic Flow. Part II - Numerical Analysis. Proc. Vibr. Probl., vol. 10, no. 4, 1969, pp. 407-423.

8. Eastep, F. E. and McIntosh, S. C. Jr.: Analysis of Non-linear Panel Flutter and Response Under Random Excitation or Non-linear Aerodynamic Loading. AIAA Journal, vol. 9, no. 3, March 1971, pp. 411-418.

9. Vanmarcke, E.: Random Fields, analysis and synthesis. The MIT Press, Cambridge, Mass., 1983.

10. Lee, B. H. K.: Aeroelastic Response of an Aircraft Wing to Random Loads. National Aeronautical Establishment of Canada, Aeronautical Report LR-613, NRC No. 21230, Ottawa, April 1983.

11. Bolotin, V. V. and Weingarten, V. I.: The Dynamic Stability of Elastic Systems. Holden-Day, Inc., San Francisco, Calif., 1964.

12. Barr, A. D. S.: Some Developments in Parametric Stability and Non-linear Vibration. Recent Advances in Structural Dynamics, Proc. Int. Conf., Institute of Sound and Vibration Research, Univ. of Southhampton, England, pp. 545-567, 1980.

13. Woodward, J. H. Jr.: Fluid Motion in a Cylindrical Tank of Sector-Annular Cross Section When Subjected to Longitudinal Excitation. Ph.D. Thesis, Georgia Institute of Technology, 1966.

14. Ibrahim, R. A. and Soundararajan, A.: Non-linear Parametric Liquid Sloshing Under Wide Band Random Excitation. J. Sound Vib., vol. 91, no. 1, 1983, pp. 119-134.

15. Ibrahim, R. A. and Roberts, J. W.: Parametric Vibration, Part V: Stochastic Problems. The Shock and Vibration Digest, vol. 10, no. 5, 1978, pp. 17-38.

16. Ibrahim, R. A.: Parametric Vibration, Part VI: Stochastic Problems (2). The Shock and Vibration Digest, vol. 13, no. 9, 1981, pp. 23-35.

17. Cramer, H.: Mathematical Methods of Statistics. Princeton University Press, Princeton, 1946.

18. Wong, E. and Zakai, M.: On the Relation Between Ordinary and Stochastic Differential Equations. Int. J. Eng. Sci., vol. 3, no. 2, 1965, pp. 213-229.

19. Jazwinski, A. H.: Stochastic Processes and Filtering Theory. Academic Press, New York, 1970.

20. Lin, Y. K.: Probabilistic Theory of Structural Dynamics. Robert E. Krieger Publishing Company, Huntington, N. Y., 1976.

21. Assaf, Sh. A. and Zirkle, L. D.: Approximate Analysis of Non-linear Stochastic Systems. Int. J. Control, vol. 23, no. 4, pp. 477-492, 1976.

22. Baxter, G. K.: The Non-linear Response of Mechanical Systems to Parametric Random Excitation. Ph.D. Thesis, University of Syracuse, Syracuse, N. Y., 1971.

23. Schmidt, G.: Vibrations Caused by Simultaneous Random Forced and Parametric Excitations. (in German) Z. Angew. Math. Mech., vol. 60, no. 9, pp. 409-419, 1980.

24. Moré, J.; Garbow, B.; and Hillstrom, K.: User Guide for MINPACK-1. Argonne National Laboratory Report ANL-80-74, Argonne, Ill., Aug. 1980.

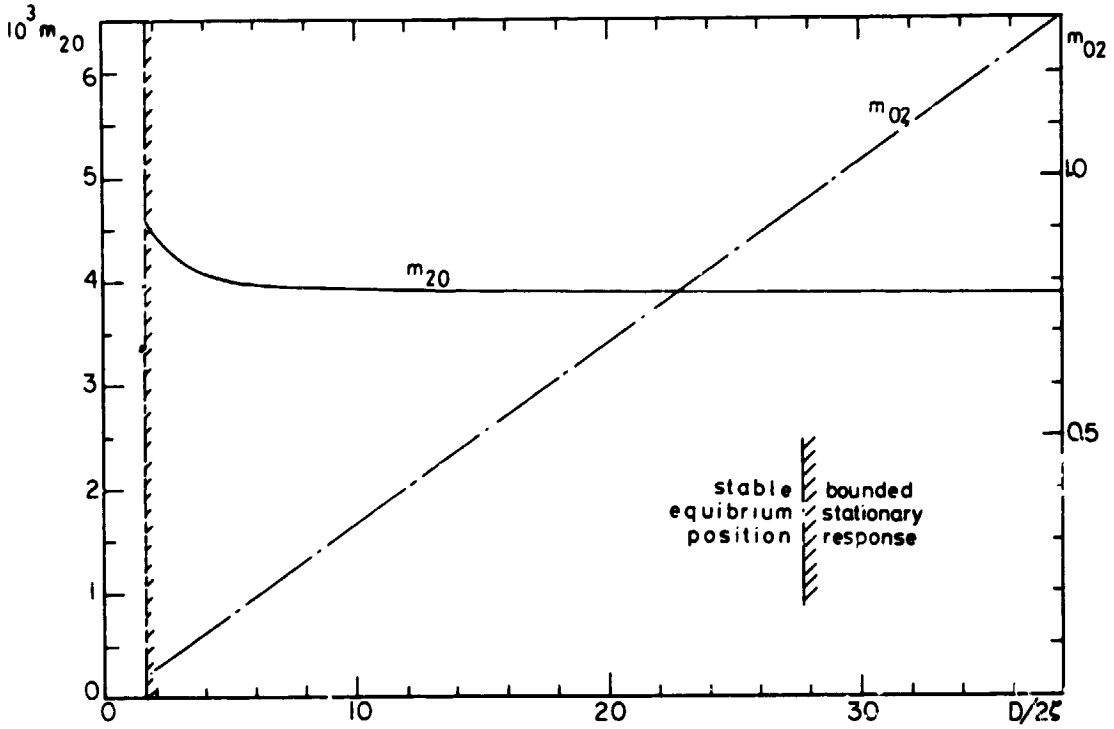

(a) Stationary mean squares of response.

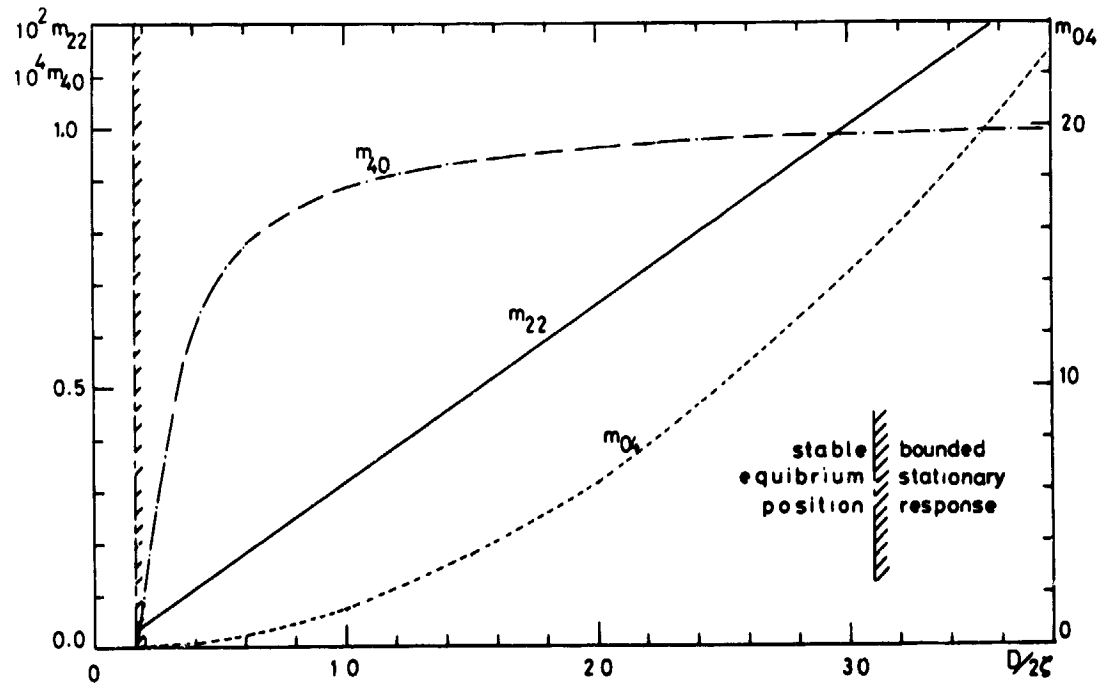

(b) Fourth-order moments of response.

Figure 1. Fourth numerical solution of non-Gaussian response.

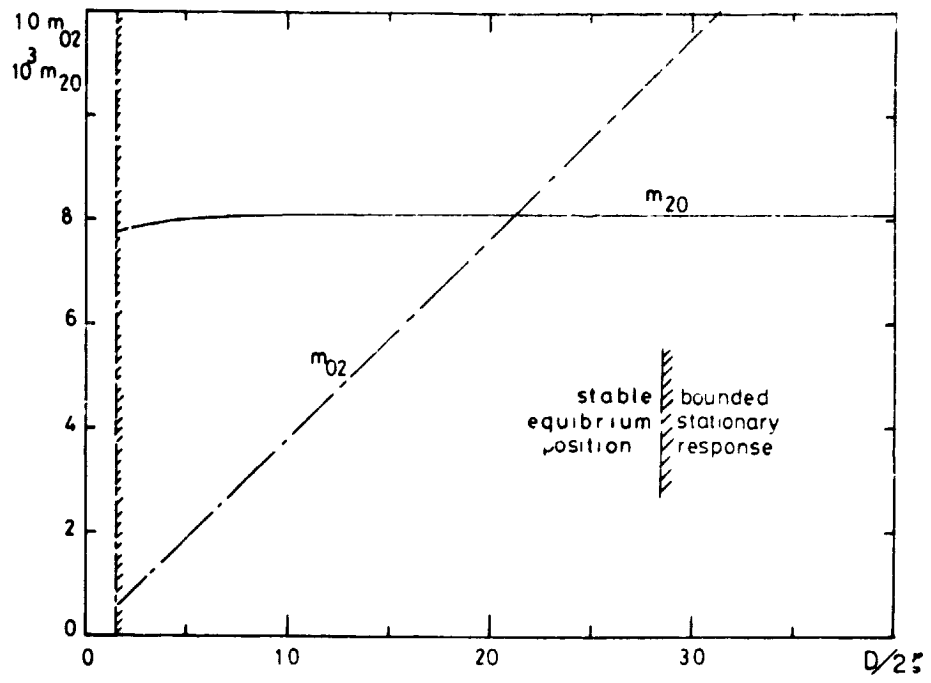

(a) Stationary response of mean squares.

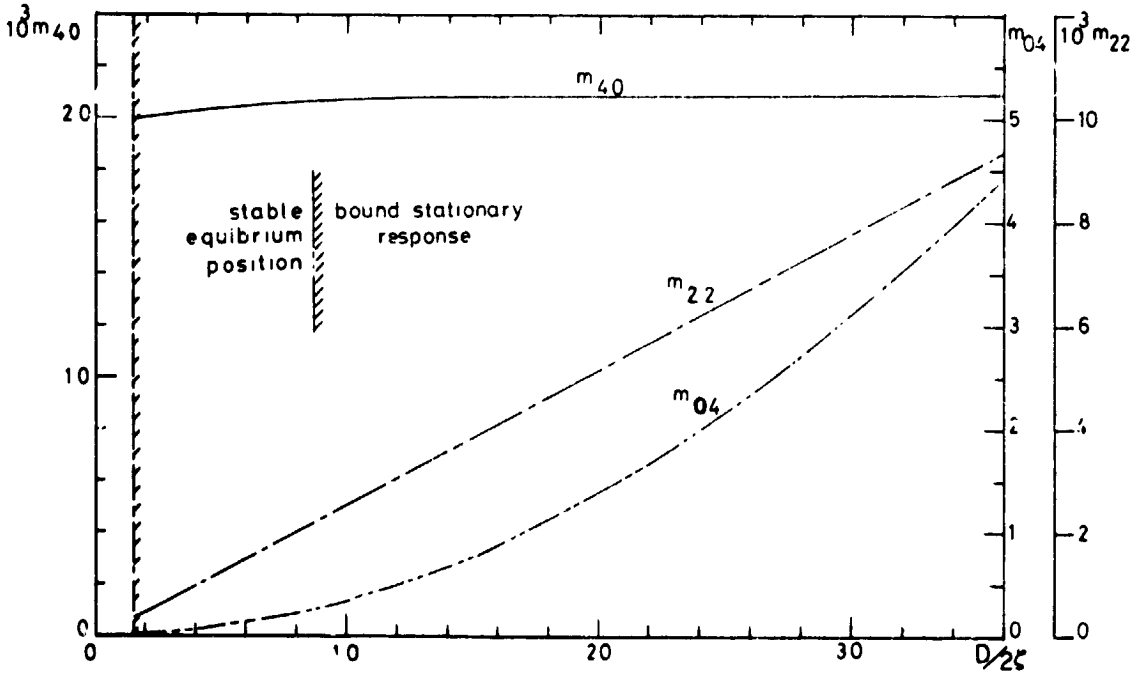

(b) Stationary fourth-order moments of response.

Figure 2. Fifth numerical solution of non-Gaussian response.

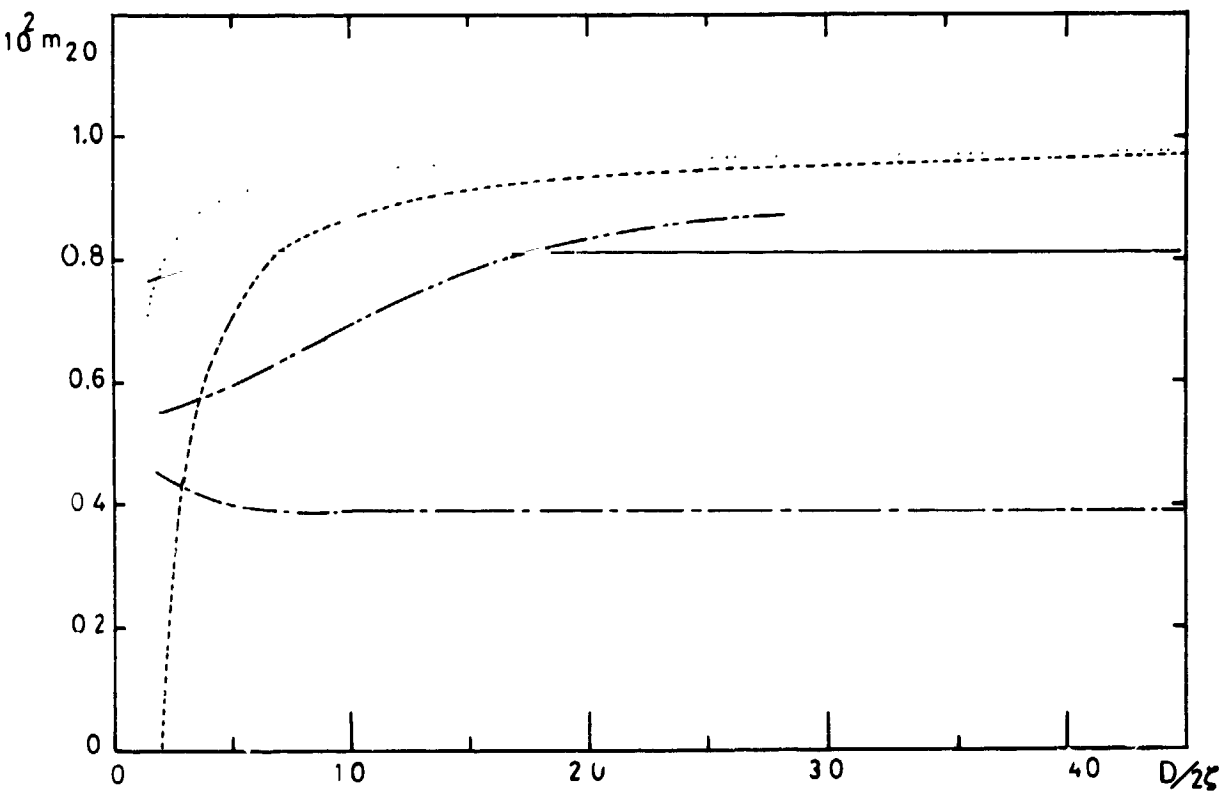

Figure 3. Comparison of mean square response as obtained by Gaussian closure (···), stochastic averaging (---), and third (— -- —), forth (— - —), and fifth (—) non-Gaussian solutions.

RESPONSE AND CHARACTERISTICS OF STRUCTURES SUBJECTED TO S-H WAVES

Spencer T. Wu
National Bureau of Standards
Washington, D.C.

SUMMARY

This paper presents a study of the dynamic characteristics of a coupled translational-rotational system. The formulation of the problem considers the soil-structure interaction effects by utilizing the impedance functions at the foundation of a structure. Due to the fact that the coefficient matrix in the characteristic equation is frequency dependent in nature, iterations have to be performed to find the nature frequencies of the system. Examples and discussions are presented in this paper. Comparisons of the analytical results from various approaches are also given.

INTRODUCTION

The coupling effects in translational-rotational structures subjected to seismic waves have been investigated extensively, e.g., references 1-3. However, the interactions between the foundations and the surrounding medium were not included in these studies. In an earlier paper (4), a simple approach was proposed for computing the responses of structures by utilizing the impedance functions for the foundations. There have been many analytical models developed for evaluating the impedance functions, e.g., references 5-7. The impedance functions used in reference 4 were based on the solutions in reference 8 developed for rigid foundations subjected to non-vertically propagated seismic waves. In this paper, approximate solutions of the natural frequencies of such structural systems are evaluated. Due to the fact that impedance functions are frequency dependent in nature, the frequency solutions have to be computed based on iterative procedures. Comparisons between the results of this approach against the others are shown with a numerical example. The formulation of the problem is also briefly described.

APPROACH

Formulation of the Problem

Assuming a one-story structural system with geometric eccentricity equal to e between the center of rigidity (C. R.) and the center of mass (C. M.) at the first floor as shown in figure 1, the governing equations of the system for coupled lateral-torsional motions under consideration may be written as:

$$m_t \ddot{U}_{yt} + e\, m_t \ddot{U}_{\phi t} + k_y U_{yd} + c_y \dot{U}_{yd} = 0 \tag{1}$$

$$m_t e \ddot{U}_{yt} + I_{\phi t} \ddot{U}_{\phi t} + k_\phi U_{\phi d} + c_\phi \dot{U}_{\phi d} = 0 \tag{2}$$

$$m_b \ddot{U}_{yb} + m_t \ddot{U}_{yt} + m_t e \ddot{U}_{\phi t} = f_y(t) \tag{3}$$

$$m_t e \ddot{U}_{yt} + I_{\phi t} \ddot{U}_{\phi t} + I_{\phi b} \ddot{U}_{\phi b} = f_\phi(t) \tag{4}$$

where m, c, k, and U = the mass damping, stiffness and displacement, respectively. Subscript t or b denotes that the term is related to the top or the base floor; subscript y or ϕ denotes that the term is related to the translational or rotational movements; subscript d denotes that the term is equal to the difference between the related terms of first floor and the base floor, e.g., $U_{yd} = U_{yt} - U_{yb}$; $I_{\phi t}$ and $I_{\phi b}$ are the rotational mass moments of inertia taken with respect to Z-axis passing C. R. as shown in figure 1 for the top and bottom floors, respectively; and f_y and f_ϕ are the earthquake excitation forces at the foundation. If U and f are transformed into the frequency domain, and f is expressed in terms of the impedance function, i.e.,

$$\{f(s)\} = [K_f]\,[\{U_f\} - \{U_f^*\}] \tag{5}$$

where (K_f) represents the impedance matrix; (U_f) represents the foundation motion; and (U_f^*) represents the input motion; the subscript f denotes terms related to foundation mat; equations 1-4 can be rearranged and written in matrix form for each ω_s as:

$$\begin{bmatrix} -m_t\omega_s^2 & -em_t\omega_s^2 & -m_b\omega_s^2+k_{fy} & 0 \\ -em_t\omega_s^2 & -I_{\phi t}\omega_s^2 & 0 & -I_{\phi b}\omega_s^2 + K_{f\phi} \\ -m_t\omega_s^2+k_y + c_y 2\omega_s & -e\omega^2 m_t & -k_y - c_{yi}\omega_s^2 & 0 \\ -em_t\omega_s^2 & -I_{\phi t}\omega^2+K_\phi + C_{\phi i}\omega_s & 0 & -k_\phi - c_{\phi i}\omega_s \end{bmatrix} \begin{bmatrix} U_{yt} \\ U_{\phi t} \\ U_{bt} \\ U_{b\phi} \end{bmatrix} = \begin{bmatrix} k_{fy}U_{fy}^* \\ k_{f\phi}U_{f\phi}^* \\ 0 \\ 0 \end{bmatrix} \tag{6}$$

The response of the structure may be computed for each ω_s based on equation 6.

Characteristics of the System

To have a more clear depiction of the system characteristics, eigenvalues as well as the eigenvectors are needed to be evaluated. The effects on structural response due to the input motions are not considered here.

For simplicity, the frequency equation of the system under consideration is expressed as:

$$[A - \lambda B] = 0 \qquad (7)$$

where λ represents the eigenvalues of the system (ω_s in equation 6); B is the complex matrix relating ω terms in equation 6 and A is the rest of the complex matrix in equation 6. To avoid the possibility that B may be nearly singular, a stable algorithm (9, 10) was selected in the evaluation of the eigenvalues. The procedures are as follows: (1) to reduce A to upper Hessenberg form and B to upper triangular form, (2) to reduce A to quasi-triangular form, and (3) to reduce the quasi-triangular form into a triangular form and compute the eigenvalues and eigenvectors. Due to the frequency-dependent nature of the matrix A, the eigenvalues cannot be found directly. Iterative process is taken here in this paper for determining the approximate solutions of the system, i.e., based on the assumed frequencies of the system initially, the terms related to the impedance functions are determined. The procedures are repeated if the eigenvalues are different from the assumed ones.

EXAMPLES AND DISCUSSIONS

A structure is assumed to have a rigid foundation subjected to horizontal incident shear waves (S-H waves).

The general properties of the system are assumed as: $m_t = 3.63 \times 10^7$ kg, $m_b = 1.85 \times 10^8$ kg, $I_{\phi t} = 3.03 \times 10^9$ kg-m^2, $I_{\phi t} = 1.52 \times 10^{10}$ kg-m^2, $K_y = 1.44 \times 10^9$ N/m, $K_\phi = 2.70 \times 10^{11}$ N-m/rad. The soil in a uniform elastic half-space is assumed to have the Poisson's ratio equal to 0.33, the hysteretic damping ratio equal to 0.05 and the shear modulus of the medium equal to 2.15×10^8 N/m. In this example, it is assumed that the geometric eccentricity is 2.70 m. The structure is assumed to have a square foundation mat of 25.9 m x 25.9 m. The real and imaginary parts of the impedance functions and the input motions used in this study are shown in figures 2 and 3 based on the solutions in reference 8. By assuming the input Fourier spectra to be constant, dynamic eccentricity, E(t), of the first floor system can be obtained as shown in figure 4 by solving equation 6 and transformed into the time domain. The E(t) is defined as the torsional moment divided by the transverse shear. This variable could be the best single parameter to represent the coupling behavior of the system.

To find the eigenvalue of the system, equation 7 has to be solved. The initial values of the impedance functions are estimated based on the uncoupled translational and rotational frequencies as if the structure were fixed at the foundation mat. The uncoupled frequencies are approximately equal to 1.0 Hz and 1.5 Hz for the translational and the rotational modes, respectively. Following the procedures described above, the frequencies of the system are found only after a few iterations. It may be worthy pointing out that the impedance functions are quite smooth in the frequency range of interest. This could be the reason that the true solutions converged very rapidly in this analysis. Four frequencies are obtained. The lower frequencies for the corresponding lateral and rotational modes are 0.92 Hz and 1.45 Hz, respectively. If the structure is considered to be fixed at the foundation level, the corresponding frequencies can be computed as 1.17 Hz and 1.36 Hz, respectively, based on references 2 and 3. These results are tabulated in table 1.

CONCLUDING REMARKS

Dynamic characteristics of a coupled lateral-torsional system subjected to seismic shear waves are investigated. The formulation of the problem is based on the simple approach presented in reference 4 that made use of the impedance functions developed in reference 8. Due to the frequency-dependent nature of the coefficient matrix, iterative procedures are needed in the evaluation of eigenvalues of the system or the frequencies of the structures. An illustrative example is given to show how the frequencies of the structure are shifted based on this approach in comparison with the analytical results from the previous studies.

REFERENCES

1. Hoerner, J.B., "Modal Coupling and Earthquake Response of Tall Buildings," Earthquake Engineering Research Laboratory, EERL 71-07, California Institute of Technology, 1971.

2. Kan, C.L. and Chopra, A.K., "Coupled Lateral Torsional Response of Buildings to Ground Shaking," Report EERC 76-13, University of California, Berkeley, 1976.

3. Tso, W.K. and Dempsey, K.M., "Seismic Torsional Provisions for Dynamic Eccentricity," Earthquake Engineering and Structural Dynamics, vol. 8, no. 3, May-June 1980, pp. 275-289.

4. Wu, S.T. and Leyendecker, E.V., "Determining Dynamic Eccentricity: A Simple Approach," Recent Advances in Engineering Mechanics and Their Impact on Civil Engineering Practice, vol. I, Proc. of 4th Engineering Mechanics Division Specialty Conf., ASCE, 1983.

5. Bycroft, G.N., "Forced Vibrations of a Rigid Circular Plate on a Semi-Infinite Elastic Space and on Elastic Stratum," Phil. Trans. of the Royal Society, vol. 248, no. 948, 1956, pp. 327-368.

6. Luco, J.E., "Impedance Functions for a Rigid Foundation on a Layered Medium," Nuclear Engineering and Design, vol. 31, no. 2, 1974, pp. 204-217.

7. Ljunggren, S., "Generation of Waves in an Elastic Plate by a Torsional Moment and a Horizontal Force," J. of Sound and Vibration, vol. 93, no. 2, 1984, pp. 161-187.

8. Wong, H.L. and Luco, J.E., "Tables of Impedance Functions and Input Motions for Rectangular Foundations," No. CE 78-15, University of Southern California, 1978.

9. Kaufman, L., "Algorithm 496. The LZ Algorithm to Solve the Generalized Eigenvalue Problem for Complex Matrices [F2]," ACM Transactions on Mathematical Software, vol. 1, no. 3, Sept. 1975, pp. 271-281.

10. Moler, C.B. and Stewart, G.W., "An Algorithm for Generalized Matrix Eigenvalue Problems," SIAM J. on Numer. Anal., vol. 10, no. 2, April 1973, pp. 241-256.

Table 1. Frequencies of the Translational-Rotational System Selected in the Case Study

	Case 1 Based on the presented model	Case 2 Based on the models in refs. 2 and 3	Case 3 Based on the uncoupled systems by assuming base as fixed
Translational Frequency (Hz)	0.92	1.17	1.00
Rotational Frequency (Hz)	1.45	1.36	1.50

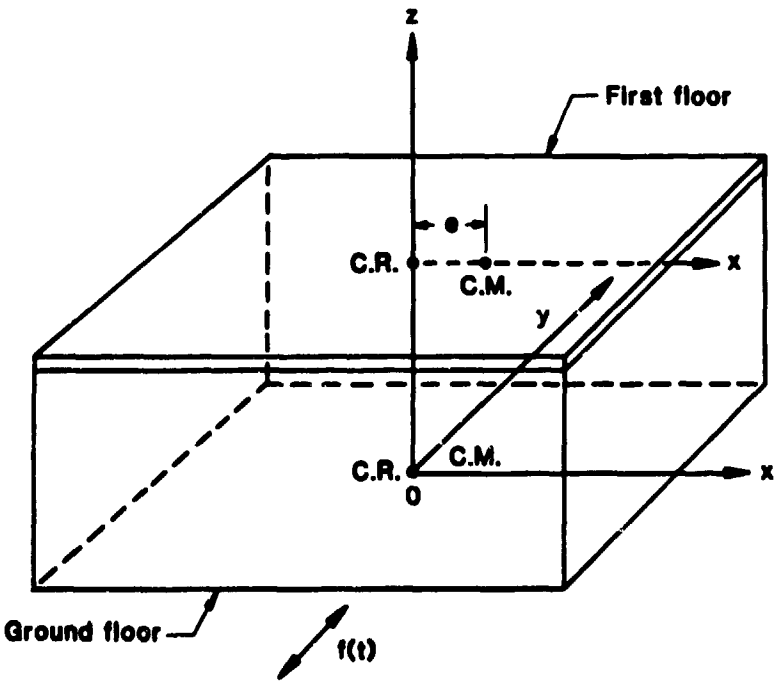

Figure 1.- A sketch of a one-story building system subjected to earthquake excitations.

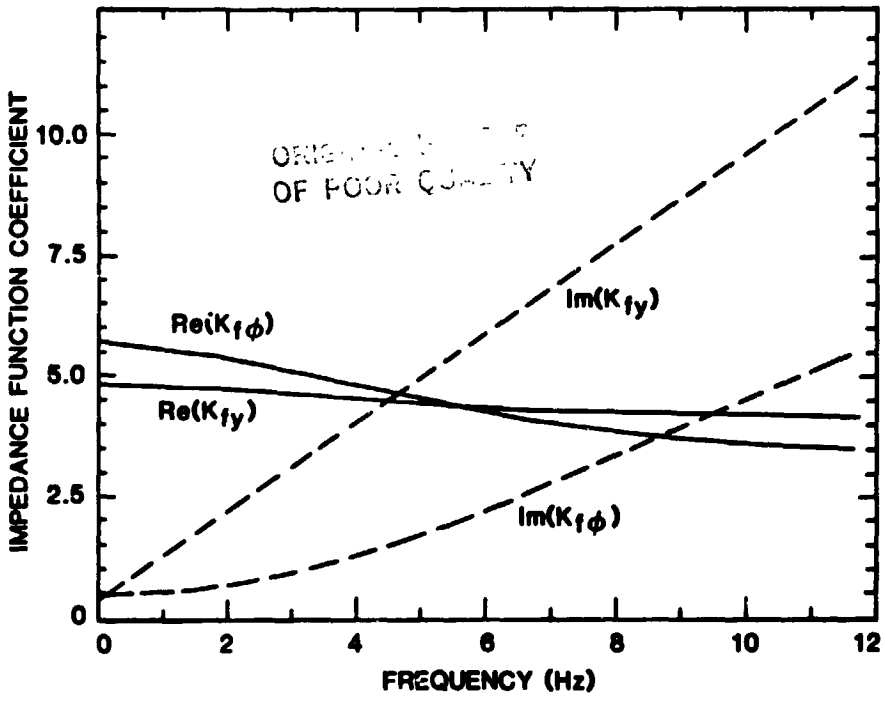

Figure 2.- The impedance functions for the selected example (computed based on ref. 8).

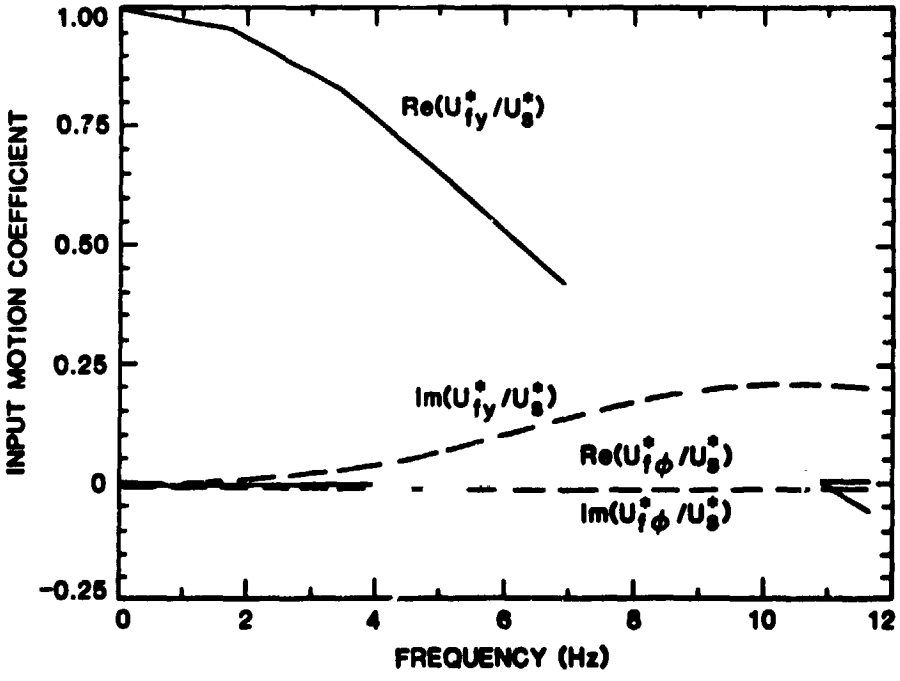

Figure 3.- The input motions for the selected example (computed based on ref. 8).

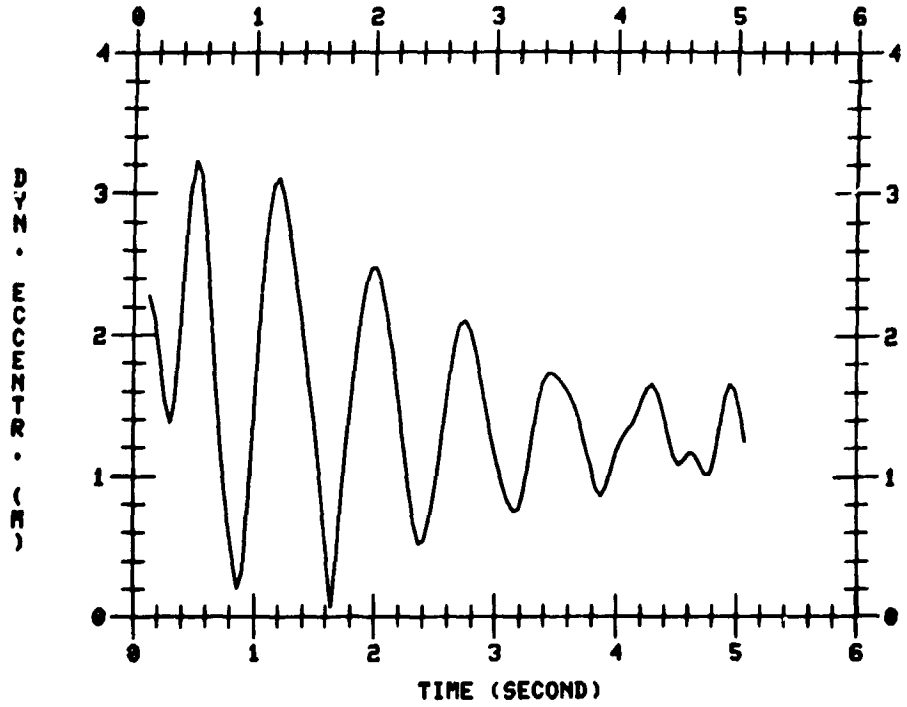

Figure 4.- Dynamic eccentricity computed based on equation 6 for the selected example.

NUMERICAL ANALYSIS OF SOME PROBLEMS RELATED TO THE MECHANICS OF PNEUMATIC TIRES: FINITE DEFORMATION/ROLLING CONTACT OF A VISCOELASTIC CYLINDER AND FINITE DEFORMATION OF CORD-REINFORCED RUBBER COMPOSITES*

J. Tinsley Oden and Eric B. Becker
and
T.L. Lin and K.T. Hsieh
The University of Texas at Austin
Austin, Texas

SUMMARY

The formulation and numerical analysis of several problems related to the behavior of pneumatic tires are considered. These problems include the general rolling contact problem of a rubber-like viscoelastic cylinder undergoing finite deformations and the finite deformation of cord-reinforced rubber composites. New finite element models are developed for these problems. Numerical results obtained for several representative cases are presented.

INTRODUCTION

The study of the behavior of pneumatic tires under various loading conditions constitutes one of the most challenging and difficult collections of nonlinear problems in the mechanics of solids. It is our aim in this paper to investigate two subclasses of problems related to tire mechanics which encompass some significant and complex features of tire behavior:

1) The general rolling contact problem of finite deformation of a flexible, viscoelastic cylinder in steady-state motion on a rough foundation (roadway)

2) The finite deformation of cord-reinforced rubber composites

---

* The work reported here was supported by the NASA Langley Research Center under Contract NAS1-17359 as a part of the National Tire Modelling Program, with the Computational Mechanics Co., Inc. The encouragement and support of this work by Mr. John Tanner of NASA is gratefully acknowledged.

In all of the formulations considered here, we place no limitations on the order of magnitude of deformations; if strains are "small or moderate", as is sometimes the case in cord-reinforced tires, then the prediction of small or moderate strains should be a natural outcome of our analysis. Moreover, we also incorporate the effects of non-conservative loads such as those encountered in the pressurization of flexible surfaces.

For problem class 1, the rolling contact problem, we present a new and general variational principle governing steady-state rolling of a cylindrical body, with finite deformations, unilateral contact, friction, viscoelastic response, and possibly standing waves at certain critical angular velocities. This principle involves a highly nonlinear variational inequality with the motion of the cylinder relative to a natural reference configuration as the unknown. This variational principle represents a generalization of our earlier work (ref. 1) to viscoelastic materials, viscoelastic effects being included to provide a model of rolling resistance in tires. We use this variational principle, or rather a regularized form of it, as a basis for the development of two-dimensional finite element models. We discuss algorithms for solving the resulting systems of nonlinear equations, locating bifurcations and limit points, and following solution paths which are based on continuation methods of the Riks, Wempner, Keller type. Numerical solutions of several representative problems are presented.

For problem class 2, the finite deformation of cord-reinforced rubber composites, new finite element models are developed which employ anisotropic membrane elements to model the cord layer and quadratic isoparametric elements to model the rubber matrix. The rubber can be modelled as an incompressible or compressible material and Halpin-Tsai or Gough-Tangorra-type representations (see, e.g., ref. 2) can be used as a basis for the model of the cord layers. An interesting feature of such composite models is that they can predict the change in "optimum" ply angles with finite uniaxial stretching, a phenomenon well outside the scope of linear models of composite materials. Some representative numerical solutions are presented.

MECHANICS OF FINITE ROLLING CONTACT OF A VISCOELASTIC CYLINDER

Our first objective is to formulate the equations and inequalities governing the deformation of a cylindrical body rolling at a constant angular velocity ω on a rough rigid roadway, as indicated in figure 1. A key consideration is the kinematics: we compare the geometry of the deformed cylinder in its current configuration C with that of a rigid cylinder spinning at the same angular velocity ω, the latter characterizing the reference configuration C_0. Polar cylindrical coordinates (r, θ, z) of a particle with labels (R, Θ, Z) at some arbitrary reference time $\tau = 0$ are defined by

$$r = R \ , \ \theta = \Theta + \omega t \ , \ z = Z \quad (t \geq 0) \tag{1}$$

or, alternatively, we can employ the cartesian reference coordinates

$$X_1 = r \cos \theta \ , \ X_2 = r \sin \theta \ , \ X_3 = z \tag{2}$$

The reference coordinates (r, θ, z) or (X_1, X_2, X_3) are thus time dependent, but this dependence is only formal since the shape of the deformed cylinder is the same at all times t to any observer fixed to the axle of the cylinder The geometry is illustrated in Figure 1.

The motion $\underset{\sim}{u}$ of the cylinder is defined by an invertible, twice differentiable map $\underset{\sim}{\chi}$ that takes the configuration C_0 into the configuration C.
In particular, the cartesian components of $\underset{\sim}{u}$ relative to the fixed spatial frame of reference are given by

$$u_i = \chi_i(r, \theta, z) = \bar{\chi}_i(X_1, X_2, X_3) \tag{3}$$

Thus, time enters our description of motion only implicitly as $\theta = \Omega + \omega t$. Henceforth, we shall not distinguish between the values $\underset{\sim}{u}$ (or u_i) of the map $\underset{\sim}{\chi}$ and the map itself, unless confusion is likely.

With this kinematical convention, we can easily write down expressions for the deformation gradient $\underset{\sim}{F}$, the right (left) Cauchy-Green deformation tensor $\underset{\sim}{C}$ ($\underset{\sim}{B}$), the displacement field $\underset{\sim}{d}$, the velocity $\underset{\sim}{v}$, and the acceleration $\underset{\sim}{a}$:

$$\begin{aligned}
&\underset{\sim}{F} = \underset{\sim}{\nabla u} \; ; \; F^{i}_{\cdot j} = \{\partial u_i / \partial X_j\} \\
&\underset{\sim}{C} = \underset{\sim}{F}^T \underset{\sim}{F} \; , \; \underset{\sim}{B} = \underset{\sim}{F} \, \underset{\sim}{F}^T \\
&\underset{\sim}{d} = \underset{\sim}{u} - \underset{\sim}{r} \\
&v_i = \frac{\partial u_i}{\partial t} = \dot{u}_i = \omega \partial u_i / \partial \theta \\
&a_i = \frac{\partial v_i}{\partial t} = \ddot{u}_i = \omega^2 \, \partial^2 u_i / \partial \theta^2
\end{aligned} \tag{4}$$

Here $\underset{\sim}{r}$ is the position vector of the particle with reference coordinates (r, θ, z), $1 \leq i, j \leq 3$. The time rate of change of $\underset{\sim}{F}$ is

$$\begin{aligned}
\dot{\underset{\sim}{F}} &= \omega \frac{\partial}{\partial \theta} \left\{ \frac{\partial u_i}{\partial r} , \frac{\partial u_i}{\partial \theta} , \frac{\partial u_i}{\partial z} \right\} \quad 1 \leq i \leq 3 \\
&= \omega \frac{\partial}{\partial \theta} \underset{\sim}{F}
\end{aligned} \tag{5}$$

or, since

$$\frac{\partial X_\alpha}{\partial t} = \omega \, \varepsilon_{\beta\alpha} \, X_\beta \; , \; \frac{\partial X_3}{\partial t} = 0 \; , \; \alpha, \beta = 1, 2 \tag{6}$$

where $\varepsilon_{\alpha\beta}$ is the two-dimensional permutation symbol ($\varepsilon_{11} = \varepsilon_{22} = 0$, $\varepsilon_{12} = \varepsilon_{21} = -1$), we have

$$\dot{F}^{\alpha\beta} = X_\gamma \varepsilon_{\gamma\rho} u_{\alpha,\rho\beta} , \quad 1 \le \alpha, \beta, \gamma, \rho \le 2$$

$$\dot{F}^{3j}_{,j} = \dot{F}^{j3}_{,3} = 0 , \quad j = 1,2,3 \tag{7}$$

where $u_{\alpha,\rho\beta} = \partial^2 u_\alpha / \partial X_\rho \, \partial X_\beta$, and

$$\dot{C}_{\alpha\beta} = \omega X_\gamma \varepsilon_{\gamma\rho} (u_{\mu,\rho\alpha} u_{\mu,\beta} + u_{\mu,\rho\beta} \ldots) \tag{8}$$

$$\dot{C}_{j3} = 0 , \quad 1 \le j \le 3 , \quad 1 \le \alpha, \beta, \gamma, \rho, \mu \le 2$$

Thus, time derivatives of such deformation measures are characterized by functions of second derivatives of the motion with respect to the referential coordinates X_I.

The cylinder is assumed to be composed of a viscoelastic material characterized by a constitutive equation for the Cauchy stress $\underset{\sim}{\sigma}$ of the form

$$\underset{\sim}{\sigma} = \underset{\sim}{F}(X; \underset{\sim}{C}, \dot{\underset{\sim}{C}}) \tag{9}$$

where the response functional $\underset{\sim}{F}(\cdot)$ is of a generalized Kelvin-Voight type; e.g.,

$$S_{ij} = G^1_{ij}(\underset{\sim}{X}, \underset{\sim}{C}) + G^1_{ij}(\underset{\sim}{X}, \dot{\underset{\sim}{C}}) \tag{10}$$

where $\underset{\sim}{S} = \det \underset{\sim}{F} \; \underset{\sim}{\sigma} \; \underset{\sim}{F}^{-T}$ is the Piola-Kirchhoff stress tensor and F^1 and G^2 are response functionals of the deformation and deformation rate, respectively. In certain applications, we may also impose the incompressibility constraint

$$\det \underset{\sim}{F} = 1 \tag{11}$$

VARIATIONAL FORMULATION

Space limitations prevent a full discussion of the derivation of our variational formulation of the rolling contact problem; see reference 1 for more details. It can be demonstrated that the steady-state motion u of the rolling viscoelastic cylinder satisfies the following nonlinear variational inequality:

$$u \in K ;$$

$$A(\underset{\sim}{u}, \underset{\sim}{v} - \underset{\sim}{u}) + j(\underset{\sim}{u}, \underset{\sim}{v}) - j(\underset{\sim}{u}, \underset{\sim}{u}) \ge \omega^2 B(\underset{\sim}{u}, \underset{\sim}{v} - \underset{\sim}{u}) + f(\underset{\sim}{v} - \underset{\sim}{u}) \tag{12}$$

$$\text{for every } v \text{ in } K$$

where

$A(\underset{\sim}{u}, \underset{\sim}{v})$ = virtual power

$$= \int_{\Omega} S_{ij}(\underset{\sim}{X}, \nabla\underset{\sim}{u}, \omega)\, v_{i,j}\, dV_0$$

$j(\underset{\sim}{u}, \underset{\sim}{v})$ = the virtual power of the frictional forces

$$= \int_{\Gamma} \nu |\underset{\sim}{S}(\underset{\sim}{X}, \nabla\underset{\sim}{u}, \omega) \cdot \underset{\sim}{n}_0 \cdot \underset{\sim}{i}_2| \; |\underset{\sim}{w}_T(\underset{\sim}{v})| dA_0$$

$B(\underset{\sim}{u}, \underset{\sim}{v})$ = the power developed by inertial forces

$$= \int_{\Omega} \rho_0 \, \partial_\theta \underset{\sim}{u} \cdot \partial_\theta \underset{\sim}{v} \, d V_0$$

$f(\underset{\sim}{v})$ = the virtual power of external forces

$$= \int_{\Omega} \rho_0 \, \underset{\sim}{b} \cdot \underset{\sim}{v} \, d V_0 + \int_{\Gamma_F} \underset{\sim}{t} \cdot \underset{\sim}{v} \, d A_0 \qquad (13)$$

Here Ω is the reference domain in the rigid spinning cylinder, Γ is its exterior (contact) boundary with unit exterior normal $\underset{\sim}{n}_0$, Γ_F is a portion of the boundary on which tractions $\underset{\sim}{t}$ are applied (e.g. pressurization loads), and $S_{ij}(\underset{\sim}{X}, \nabla\underset{\sim}{u}, \omega)$ is the Piola-Kirchhoff stress which is given as a function of $\underset{\sim}{X}$, $\nabla\underset{\sim}{u}$, and ω by constitutive laws of the type (10). For example,

$$S_{ij}(\underset{\sim}{X}, \nabla\underset{\sim}{u}, \omega) = {}^{1}_{ij}(\underset{\sim}{X}, \; u_{k,\ell}\, u_{\ell,k}) + {}^{2}_{ij}(\underset{\sim}{X}, \; \omega X_\gamma \, \varepsilon_{\gamma\rho} u_{\mu,\rho\alpha} u_{\mu,\beta} + u_{\mu,\rho\beta} u_{\mu,\alpha})) \qquad (14)$$

Note that, again, time t does not appear explicitly in this formulation, but the presence of deformation-rate terms in the constitutive equations leads to second derivatives of the motion in the virtual power. In (12), K is the set of admissible motions

$$K = \{\underset{\sim}{v} = (\omega \, \partial_\theta v_1, \; v_2, \; \omega \, \partial_\theta v_3) \; , \; \underset{\sim}{v} \quad \underset{\sim}{V} \; , \; v^2 \leq H\} \qquad (15)$$

where H is the distance from the axle of the deformed cylinder to the roadway and V is a space of functions on which the energy is well defined (e.g. $V = W^{2,p}(\Omega)$). In (13), ν is the coefficient of friction, $\underset{\sim}{w}_T = \underset{\sim}{v}_T - v_0 \underset{\sim}{i}_1$ is the slip velocity, v_0 being the speed with which the cylinder moves along the roadway, ρ_0 is the reference mass density, and $\underset{\sim}{b}$ is the body force density.

We reduce (12) to a nonlinear variational equality by regularization: the friction term is regularized by the smoothing scheme discribed in reference 3 (see also ref. 1) and the unilateral contact condition is relaxed by the use of an exterior penalty approximation, as described in reference 1. If the material is incompressible, we also include the incompressibility constraint (11) by the introduction of an appropriate penalty approximation.

SOLUTION OF THE DISCRETE PROBLEM

We now consider finite element approximations of a class of two-dimensional (plane strain) rolling contact problems in which the motion $\underset{\sim}{u}$ is approximated over a mesh of Q_2 (biquadratic) elements. When the regularized version of the variational principle (12) is approximated by finite elements, we obtain a system of nonlinear equations of the form

$$\underset{\sim}{F}(\underset{\sim}{x}, \rho) = \underset{\sim}{0} \tag{16}$$

where $\underset{\sim}{F}$ is an N-vector of nonlinear momentum equations governing the discrete model, $\underset{\sim}{x} = (x_1, x_2, \ldots, x_N)^T$ is a vector of N degrees of freedom representing the nodal values of the motion, and ρ is a parameter representing, for example, the indentation distance H .

We solve (16) using variants of the Riks Keller continuation methods. For example, we regard $(\underset{\sim}{x}, \rho)$ as functions of a real arc-length parameter s , $s \propto [0,1]$, and derive from (10) the system of differential equations,

$$F_i(\underset{\sim}{x}(s), \rho(s)) = 0 \qquad s \propto [0,1] \tag{17}$$

$$\left.\begin{aligned} J_{ij}(\underset{\sim}{x}, \rho)\dot{x}_j + g_i(\underset{\sim}{x}, \rho)\dot{\rho} &= 0 \\ \dot{x}_j \dot{x}_j + \dot{\rho}^2 &= 1 \end{aligned}\right\} \tag{18}$$

where

$$\left.\begin{aligned} J_{ij}(\underset{\sim}{x}, \rho) &= \frac{\partial F_i(\underset{\sim}{x}, \rho)}{\partial x_j} \\ g_i(\underset{\sim}{x}, \rho) &= \frac{\partial g_i(\underset{\sim}{x}, \rho)}{} \\ \dot{x}_j &= \frac{dx_j}{ds} \\ \dot{\rho} &= \frac{d\rho}{ds} \end{aligned}\right\} \tag{19}$$

Equations (17) and (18) hold on the path $\Gamma = \{(\underset{\sim}{x}, \rho) \mid \underset{\sim}{x} = \underset{\sim}{x}(s), \ \rho = \rho(s), \ 0 \leq s \leq 1\}$ in N+1-dimensional space. Repeated indices are summed from 1 to N. The second member of (18) is, of course, the definition of arc length of Γ .

The system of nonlinear ordinary differential equations (18) is equivalent to the system

$$J_{ij}(\underset{\sim}{x}, \rho)v_j = g_i(\underset{\sim}{x}, \rho)$$

$$\dot{\rho}^2 = \frac{1}{1+v_i v_i} \qquad (20)$$

$$\dot{x}_j = -\dot{\rho} v_j$$

Equations (20) are sufficient to determine directions $(\dot{\underset{\sim}{x}}, \dot{\rho})$ which define a hyperplane tangent to Γ. These can be used to define a linear extrapolation of the solution into this plane. It then makes sense to correct this approximate solution so that a point on the solution path Γ is obtained. One algorithm for such a procedure is given as follows:

Step 1 (tangent Hyperplane)

With initial data $\underset{\sim}{x}_0$, ρ_0, $(\Delta\rho)_0$, compute

$$J_{ij}(\underset{\sim}{x}_0, \rho_0)v_j^{(1)} = g_i(\underset{\sim}{x}_0, \rho_0)$$

$$\dot{\rho}_i = 1 \Big/ \sqrt{1 + v_j^{(1)} v_j^{(1)}}$$

$$\dot{x}_{1j} = -\dot{\rho}_1 v_j^{(1)}$$

Step 2 (Extrapolation)

Compute

$$(\Delta s)_1 = (\Delta\rho)_0/\dot{\rho}_1$$

$$\underset{\sim}{x}_1 = \underset{\sim}{x}_0 + \dot{\underset{\sim}{x}}_1(\Delta s)_1$$

$$\rho_1 = \rho_0 + \dot{\rho}_1(\Delta s)_1$$

Step 3 (Correction)

$$J_{ij}^{(r)} w_j^{(r)} = -F_i^{(r)}$$

$$J_{ij}^{(r)} v_j^{(r)} = g_i^{(r)}$$

$$(\Delta\rho)^{(r)} = \frac{-\dot{\underset{\sim}{x}}_1 \cdot \underset{\sim}{w}}{\dot{\rho}_1 - \dot{\underset{\sim}{x}}_1 \cdot \underset{\sim}{v}^{(r)}}$$

$$(\Delta\underset{\sim}{x})^{(r)} = \underset{\sim}{w}^{(r)} - \underset{\sim}{v}^{(r)}(\Delta\rho)^{(r)}$$

with

$$J_{ij}^{(r)} = J_{ij}(\underset{\sim}{x}^r, \rho^r) \ , \ F_i^{(r)} = F_i(\underset{\sim}{x}^r, \rho^r)$$

$$\underset{\sim}{x}^r = \underset{\sim}{x}_1 + \sum_{k=1}^{r} (\Delta \underset{\sim}{x})^{(k)}$$

$$\rho^r = \rho_1 + \sum_{k=1}^{r} (\Delta\rho)^{(k)}$$

$$(\Delta \underset{\sim}{x})^k = \underset{\sim}{x}^{k+1} - \underset{\sim}{x}^k \ ; \ (\Delta\rho)^k = \rho^{k+1} - \rho^k$$

$$1 \leq i,j \leq N \ , \ 1 \leq r \leq R$$

Set

$$\underset{\sim}{x}_1' = \underset{\sim}{x}_1 + \sum_{r=1}^{R} \Delta \underset{\sim}{x}^r = \underset{\sim}{x}^R$$

$$\rho_1' = \rho_1 + \sum_{r=1}^{R} (\Delta\rho)^{(r)} = \rho^R$$

Step 4

Return to Step 1 and continue the process with $(\underset{\sim}{x}_0, \rho_0)$ replaced by $(\underset{\sim}{x}_1', \rho_1')$.

In Step 1, it is, in general, inappropriate to set $(\underset{\sim}{x}_0, \rho_0) = (0, 0)$ since this is not a point on the solution path. The starting point $(\underset{\sim}{x}_0, \rho_0)$ is computed by specifying a small initial value of ρ_0 and computing $\underset{\sim}{x}_0$ by Newton's method.

The procedure in Step 2 was advocated by Keller (reference 4) and has the attractive feature of preserving the symmetry and bandwidth of J_{ij} (when symmetry exists) as opposed to treating the full system (16) at once.

The algorithm given in Step 3 is also a Keller-type scheme, similar in structure to that of Step 2, and is equivalent to the constrained Newton-Raphson scheme,

$$\begin{aligned} J_{ij}(\underset{\sim}{x}^r, \rho^r)\Delta x_j^r + g_i(\underset{\sim}{x}^r, \rho^r)\Delta\rho^r \\ = - F_i(\underset{\sim}{x}^r, \rho_i^r) \qquad (21) \\ \dot{\underset{\sim}{x}}_1 \cdot \Delta \underset{\sim}{x}^r + \rho_1(\Delta\rho)^{(r)} = 0 \end{aligned}$$

The second equation is a constraint on the Newton-Raphson process which forces the scheme to progress toward the solution path Γ in a direction normal to the tangent plane. Some acceleration of this iterative process can be realized by

using alternative constraints which make the iterative scheme follow a spherical path (Crisfield (reference 5)), or an elliptical path (Padovan (reference 6)), and such variants are easily implemented.

Algorithms such as that above can be used to determine limit points and bifurcations in solution paths. Multiple branches can also be determined and followed. While our working program can handle these features, space limitation prevents a discussion of details.

SAMPLE CALCULATION OF A VISCOELASTIC CYLINDER

As a representative example of some of our numerical results, we consider the finite deformation of a viscoelastic cylinder for which the Piola-Kirchhoff stress is given by

$$S_{ij} = \frac{\partial W}{\partial u_{i,j}} + \mu D_{ij}$$

where

$$W = C_1(I_1 - 3) + C_2(I_2 - 3)$$

$$D_{ij} = \tfrac{1}{2}(v_{i,j} + v_{j,i})$$

We choose for the Mooney-Rivlin constants C_1 and the viscosity μ,

$$C_1 = 80 \text{ psi}, \quad C_2 = 20 \text{ psi}, \quad \mu = 0.0016 \text{ lb sec}^2/\text{in}^2$$

The coefficient of friction is taken to be $\nu = 0.3$ and the density $\rho_0 = 1$. We consider a solid cylinder of initial (undeformed) radius of 2.0 units spinning at an angular velocity $\omega = 5$ rad/sec. The axle load is gradually increased so that contact is made and H is, successively, $H = 1.75, 1.694, 1.649, 1.600, 1.579, 1.545$, and 1.532.

For these choices of parameters, the rolling contact problem was solved using the formulation and methods discussed earlier on a rather coarse mesh of Q_2-biquadratic elements. Computed deformed shapes together with principal stress contours are shown in Figures 2-5 for various values of H and ω. Figure 3 contains the computed variations in maximum stress components with angular velocity ω for a fixed contact length $H = 1.75$ and Figure 4 indicates the variation in axle load with ω for $H = 1.75$. The computed variation of axle load with vertical displacement $d = 2 - H$ is shown in Figure 5. We have also computed contact pressure profiles as a function of H (or F) and ω but do not include these results here.

CORD-REINFORCED RUBBER COMPOSITES

We shall now direct our attention to the construction of a finite element

model of cord-reinforced rubber composites of a type representative of those found in modern pneumatic tires. Two special properties of such composites that influences features of our model are:

i) the ratio of cord to matrix modulus is high (or, in other words, the matrix (rubber) is very soft in comparison with the cord)

ii) the ratio of cord to rubber volume is small

These properties are reflected in a model in which the composite is represented by an anisotropic, Hookean membrane of vanishing thickness attached to a thick layer of isotropic, hyperelastic, rubber matrix (figure 6). The membrane is in a state of plane stress and has no transverse stiffness. Both the membrane and the rubber matrix can withstand finite deformations.

In the models discussed here, the cord membrane element is modelled, using the Gough-Tangorra theory, as an orthotropic sheet with cords oriented at an angle θ, indicated in Figure 6 (see reference 2) and the rubber matrix is assumed to be a Mooney-Rivlin material.

As a sample calculation, consider the reinforced thin cylindrical shell, shown in Figure 7, constructed of two polyester cord layers and a rubber matrix. The end $z = 0$ of the shell element is fixed and the end at $z = H$ is stretched uniformly an amount U in the z-direction. In calculating elasticities of the cord layer using the Gough-Tangorra theory, we take d = number of cord ends/cm = 102 and E_c = Young's modulus = 3.97 GPa while the matrix is a 60NR/40 SBR rubber with a Young's modulus $C_1 + C_2 = 5.5$ MPa. Other dimensions are given in Figure 7.

Since this composite element can undergo finite extensions, the "optimum" cord angle θ^* (the ply angle corresponding to a minimum axial force F_z for a given stretch U/H) may vary with deformations. To study this behavior, we have calculated solutions to finite element approximations of this problem for values of $\theta = 0^\circ, 10^\circ, 20^\circ, \ldots, 90^\circ$ and U/H of 1% to 20%.

It is first noted that stretching of the sheet changes the cord angle orientation throughout the specimen. The amount of angle change $\nabla\theta$ depends upon the initial orientation θ and the amount of stretch, and for $U/H = .10$ and the material properties assumed, the maximum change occured for an orientation of $\theta = 70^\circ$, as indicated in Figure 7b.

One problem of practical interest is to determine θ for given U/H, the value of θ at which the inter-laminar shear stress τ is minimized. For the example computed here, τ was found to be zero for $U/H = .10$ at a ply angle of around 35° (see Figure 8). The results of other calculations are illustrated in Figures 9 and 10. The total cord force versus cord angle for various stretches is illustrated in Figure 9 while the net axial force F_z for various cord angles and stretches is given in Figure 10. It is interesting to note that the minimum F_z is roughly independent of the amount of stretch and occurs for a ply angle of around $\theta \approx 35^\circ$.

We have performed similar calculations for reinforced shell elements subjected to internal radial pressures, simulating pressurization of a tire. Because of space limitations, these results are not given here.

REFERENCES

1. Oden, J.T.; Becker, E.B.; Lin, T.L.; and Demkowicz, L.: Formulation and Finite Element Analysis of a General Class of Rolling Contact Problems with Finite Elastic Deformations. Mathematics of Finite Elements with Applications, Vol. V, edited by J.R. Whiteman, Academic Press Ltd., London, 1984.

2. Walter, J.D.: Cord Reinforced Rubber Section 3.1, Mechanics of Pneumatic Tires, Revised Edition; edited by S.K. Clark, U.S. Dept. of Transportation, Washington, D.C., 1981, pp. 123-177.

3. Campos, L.T.; Oden, J.T.; and Kikuchi, N.: A Numerical Analysis of a Class of Contact Problems with Friction in Elastostatics, Comp. Meth. in Appl. Mech. & Engrg. 34, 1982, pp. 821-845.

4. Keller, H.B.: Practical Procedures in Path Following Near Limit Point, in Computing Methods in Applied Sciences and Engineering, R. Glowinski and J.L. Lyons, eds., North-Holland Publ. Inc., 1982.

5. Crisfield, M.A.: A Fast Incremental/Iterative Solution Procedure that Handles 'Snap-Through', Comput. & Struct. 13, 1981, pp. 55-62.

6. Padovan, J. and Arechaga, T.: Formal Convergence Characteristics of Elliptically Constrained Incremental Newton-Raphson Algorithms, Int. J. Eng. Sci. 20(10), 1982, pp. 1077-1097.

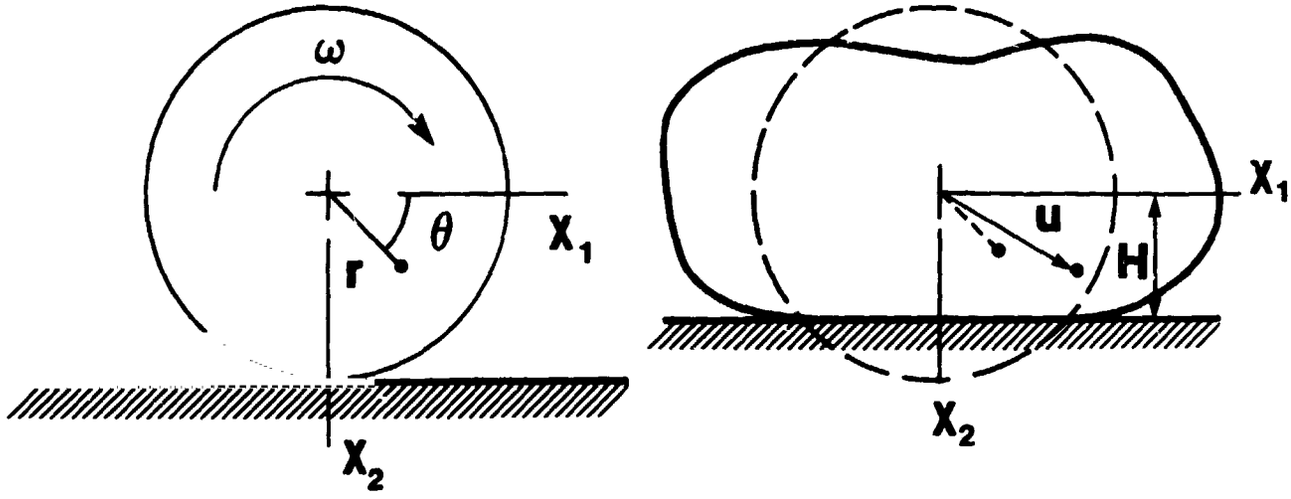

Figure 1. Finite deformation of a rolling viscoelastic cylinder.

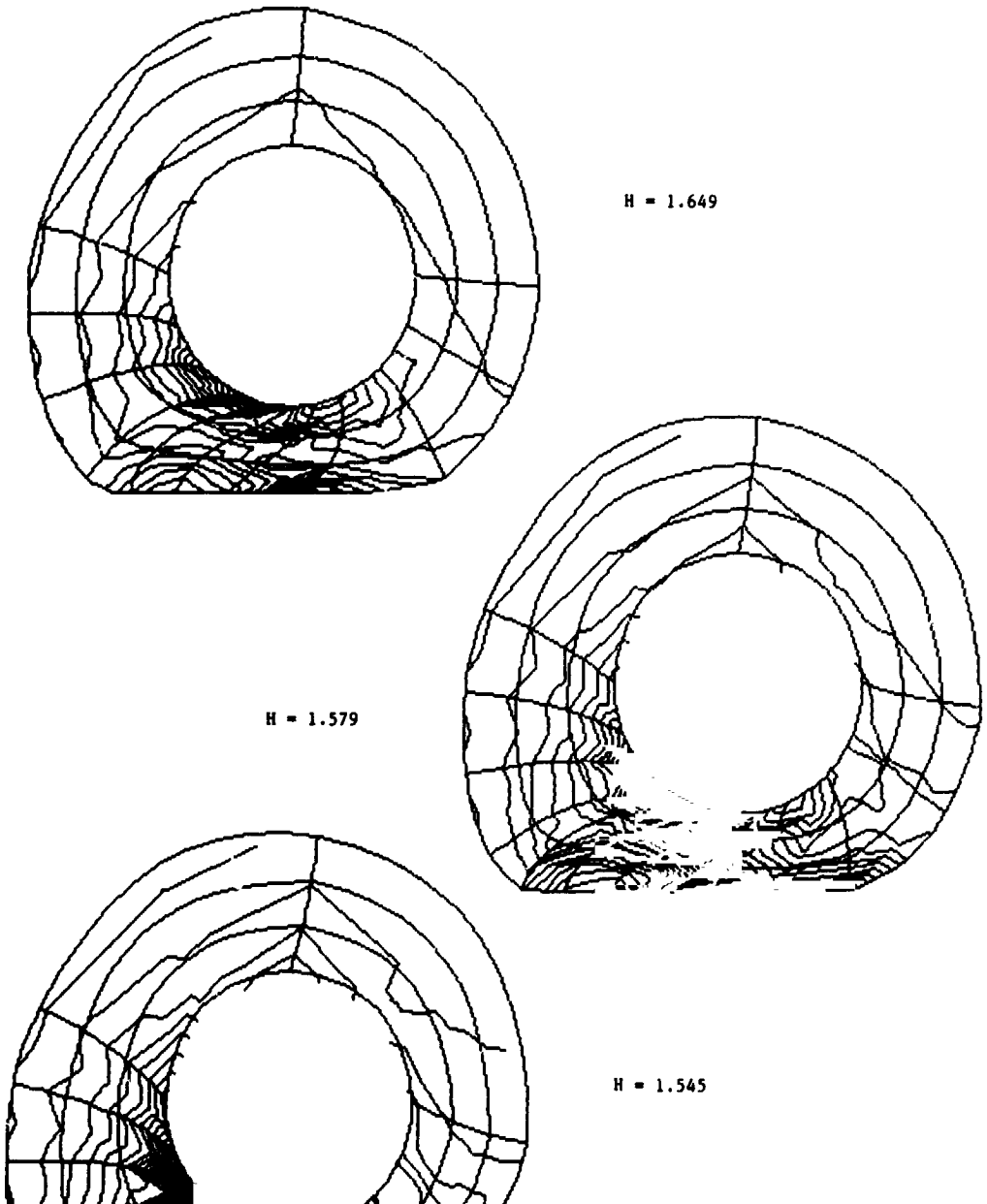

Figure 2. Computed generated deformed shapes and stress contours for viscoelastic cylinder.

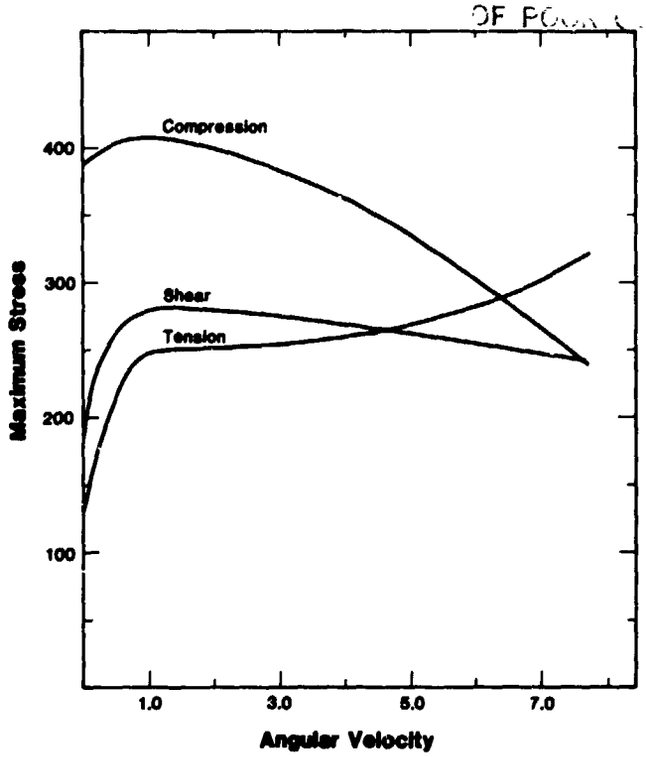

Figure 3. Maximum stress variation with angular velocity (rad/sec).

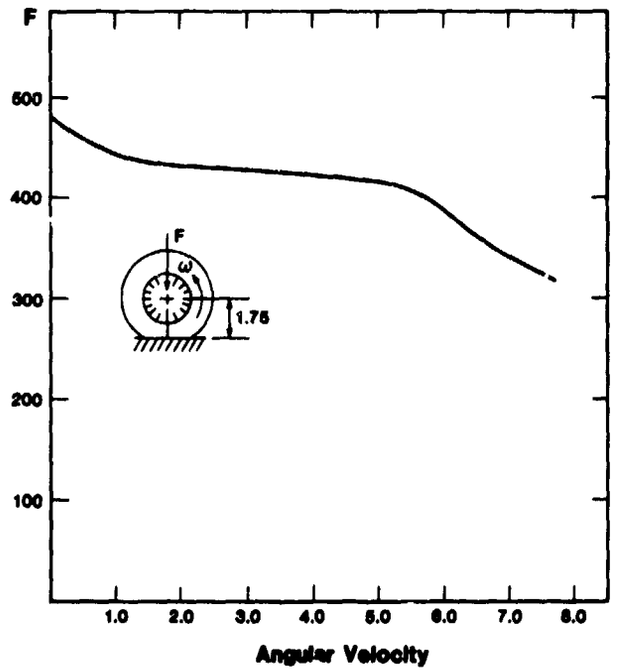

Figure 4. Axle load versus angular velocity (rad/sec).

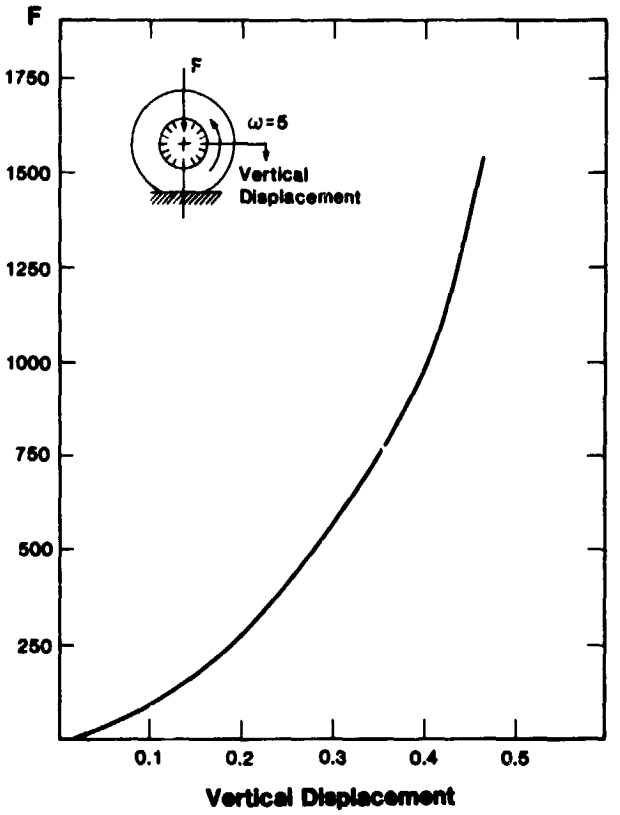

Figure 5. Axle load F versus displacement d = 2.0 - H.

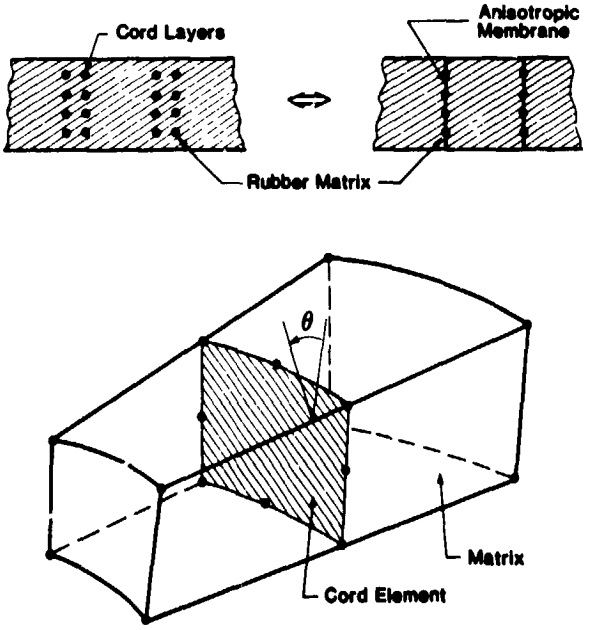

Figure 6. Model of a cord-reinforced rubber composite.

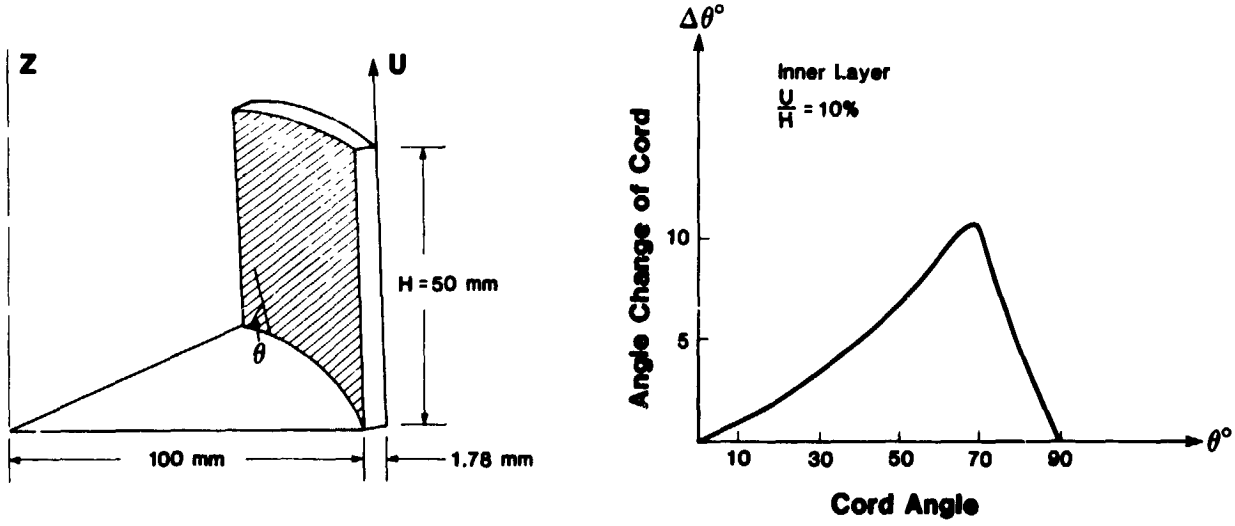

(a) A cord-reinforced shell. (b) Change in cord angle due to stretching.

Figure 7. Reinforced thin cylindrical shell.

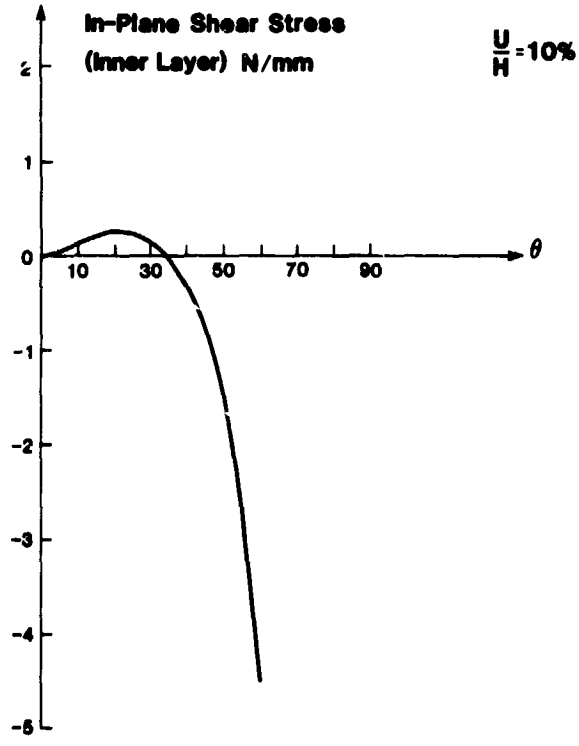

Figure 8. Interlaminar shear stress as a function of cord angle for U/H = .10.

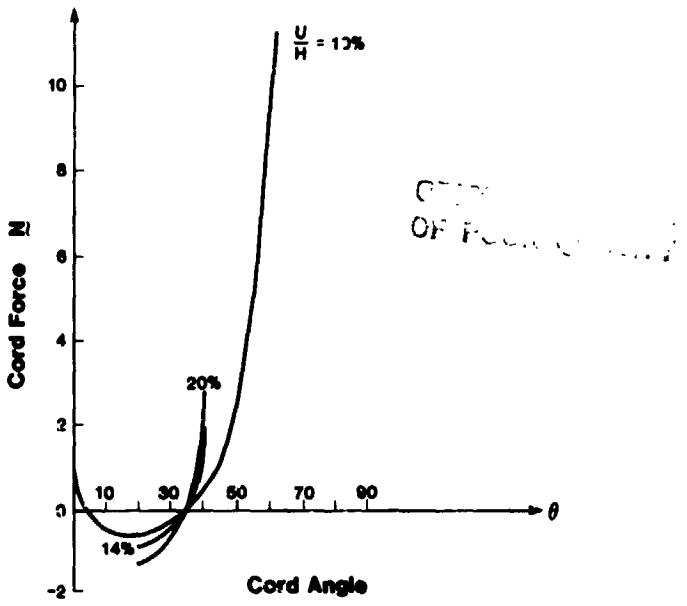

Figure 9. Computed variation of cord force N with cord angle for different stretch ratios.

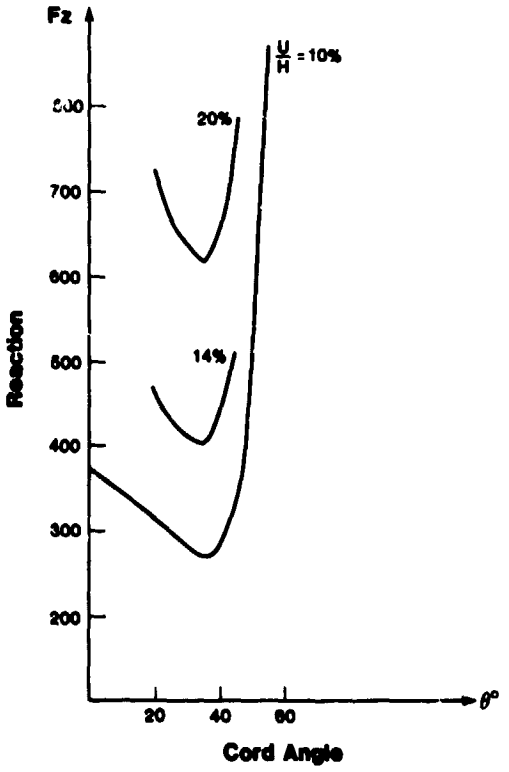

Figure 10. Calculation of dependence of axial stiffness for various cord angles at different stretch ratios.

SIMULATION OF CONTACT SURFACE EROSION FOR IMPACT PROBLEMS

K. D. Kimsey and J. A. Zukas
US Army Ballistic Research Laboratory
Aberdeen Proving Ground, MD

SUMMARY

This paper outlines an algorithm for the simulation of contact surface erosion for impact problems. The algorithm dynamically relocates the contact surface as projectile and target materials exceed their failure criterion. Example computations of axisymmetric and oblique impacts are compared with experimental data.

INTRODUCTION

The mechanic of penetration and perforation of solids has long been of interest for military applications and is currently being applied to a number of industrial applications such as the integrity of nuclear reactor pressure vessels, crashworthiness of vehicles, protection of spacecraft from meteoroid impact, and explosive forming and welding of metals.

Impacts at velocities in excess of 1 km/s excite the high frequency modes of the colliding solids. The response is confined to a localized region (typically 2 to 3 projectile diameters) and is characterized by the presence of shock waves and high hydrodynamic pressures which, on contact, can exceed the material strength by an order of magnitude. For ordnance velocity impacts (1-3 km/s) the pressures decay rapidly due to the presence of free surfaces and the effects of material strength and, except at the interface, oscillate at values comparable to the material strength. Under hypervelocity conditions (4-12 km/s), hydrodynamic pressure dominates the behavior of the solids for the bulk of the penetration process. Material strength effects become significant only in the very late stages of the process. Superimposed on these are extensive plastic deformation, large localized heating and material failure due to a number of mechanisms (i.e., petalling, spall, adiabatic shear). The failure mechanism(s) activated depend on geometry, loading history and material constitution. Strain rates of $10^5\ s^{-1}$ at the impact interface and $10^2 - 10^3\ s^{-1}$ elsewhere are not uncommon. Penetration and perforation are formidable physical problems and it is not surprising that the bulk of the research in this area has been experimental in nature.

A complete mathematical description of the dynamics of impacting solids must account for the geometry of the interacting bodies; elastic, plastic, and shock wave propagation; hydrodynamic flow, finite strains and deformations; thermal and frictional effects, and the initiation and propagation of failure in the colliding solids. During the past decade, rapid progress has been achieved in computational penetration mechanics (ref. 1). Today, two- and three-dimensional simulations of high velocity impact phenomena are routinely performed in conjunction with experimental studies in terminal ballistics.

Numerical simulation of penetration phenomena can be performed with both Lagrangian (mass reference) and Eulerian (laboratory reference) descriptions. In the laboratory reference scheme, the computational mesh remains stationary with material being transported through it based on velocity gradients present in the flow field. Such a description is ideally suited for modeling severe material deformations that occur in hypervelocity impacts, explosive-metal interactions and the penetration of thick targets (i.e., situations wherein the ratio of target thickness to penetrator diameter, t/d, exceeds 3). In the mass reference description the computational mesh is fixed in the material and distorts with it in accordance with applied loads. The Lagrangian approach offers the advantages of being conceptually straightforward (due to the lack of convective terms to represent mass flow) and permitting material boundaries to be delineated without ambiguity. However, irregular mesh shapes arising from severe material deformations lead to inaccuracies in the numerical approximation which can grow to unacceptable levels. In addition, since almost all Lagrangian wave propagation codes use explicit temporal integration schemes (in which the maximum time step is limited to satisfy a stability condition), violent distortion of the computational mesh leads to a reduction of the time step to such a low value that continuing the calculation becomes economically prohibitive. These problems can be overcome through the use of rezoning, coupled Lagrangian-Eulerian descriptions, and contact surface erosion algorithms.

In rezoning, a new Lagrange computational mesh is overlaid on the old one and a rezone algorithm maps mesh quantitites of the severely distorted mesh onto the new mesh such that conservation of mass, momentum, total energy and the constitutive relationship are satisfied. Rezoning can be a costly and nontrivial process. For very thick target penetration studies (plate thickness to projectile diameter ratios greater than 10) 30 to 50 rezones are not uncommon. Frequent rezoning renders the computational mesh semi-Eulerian in that large distortions are realized but material history and location of material boundaries are diffused.

Many impact situations are not simulated very well with Lagrangian or Eulerian descriptions alone (i.e., fluid-structure interaction problems). Coupling methodologies for combining Lagrangian and Eulerian descriptions exploit the respective

advantages of each. In general, the Eulerian portion of the computational mesh behaves as a pressure boundary acting on the Lagrangian regions, while the Lagrangian regions represent obstacles in the Eulerian flow field. This technique does not circumvent the possibility of excessive diffusion of material history. While cumbersome and time-consuming logic for abating diffusion of material interfaces and histories has been demonstrated, the computational penalties for such logic are high.

A most promising technique to extend the capability of Lagrangian codes to deep penetration and spaced plate perforation problems is the concept of contact surface erosion. The Lagrangian codes developed in the seventies required that the contact surface or sliding interface specified at the beginning of the problem remain unchanged throughout. This requirement was imposed not from physical considerations but to simplify the interface logic. Its effect was to prohibit total failure of material dictated by the physical problem, resulting either in unrealistic distortions of the computational mesh leading to large truncation errors or in temporal integration increments which render further computation uneconomical.

The eroding contact surface concept has been under active investigation at a number of centers since 1978 and is now finding its way into production codes. The most comprehensive treatment is to be found in the DYSMAS/L code developed by Massmann, Poth and their associates at Industrieanlagen-Betriebsgesellschaft mbH (Ottobrun, W. Germany). The contact processor in DYSMAS/L (ref. 2-4) is based on a generalized master-slave concept. Structural surfaces which are to be controlled by the contact processor are defined as master planes and slave points. Both master surface erosion and internal cracking can be treated. In the case of element separation (crack opening) the separated nodal masses of the affected elements are designated as slave points to permit calculation of momentum exchange in case of further contact. Redefinition of the contact surface in case of erosion or cracking is treated automatically, requiring no user intervention.

Methods for dynamic redefinition of sliding interfaces in the presence of total element failure have also been developed by Johnson (ref. 5-6). The earlier approach, implemented in the EPIC-3 (ref. 5) code, had several limitations and restrictions (i.e., only obliquities of 45° or less could be treated and users had to specify a priori the extent of target damage) and has not been used extensively. Many of these have been removed from the techniques now used in current versions of EPIC-2 and EPIC-3. Snow (ref. 7) implemented logic to dynamically redefine the master surface as element failure occurs in the EPIC-2 code. The approach retained the requirement in the original version of the code that the master surface remain continuous and employed an asymmetric interface treatment. Most recently Belytschko and Lin[1] have introduced eroding contact surface concepts into the EPIC-3 code, making use of eight-node hexahedral elements and hourglass viscosity to stabilize spurious deformation modes caused by one point integration.

[1]Work done under contract to Ballistic Research Labs.

CONTACT SURFACE EROSION FOR LAGRANGIAN COMPUTATIONS

Contact surfaces or sliding interfaces are appropriate in situations where large relative motions can be expected at material boundaries. Situations involving the interactions of gases and fluids with solid walls, the penetration of targets by projectiles, and contact between colliding bodies require the use of sliding interfaces. They prove useful also in regions where large shears or fractures develop. Most sliding interface methods are based on the decomposition of acceleration and velocity into components normal and tangential to the interface. Motions in the normal direction are continuous when materials are in contact but independent when they are separated. Tangential motions are independent when materials are separated or the interface is frictionless but are modified if there is contact and a frictional force is present. Materials on either side of an interface may separate if a user-specified criterion is exceeded or if materials are in tension, and may collide again if previously separated. A comprehensive discussion of sliding interface treatments is given by Hallquist (ref. 8-9).

The sliding interface algorithm in the EPIC-2 code (ref. 7) has been restructured to simulate contact surface erosion during impact. Initially, a series of nodes lying on the interface are identified and labelled as either master or slave nodes. Designation of master and slave is arbitrary since a symmetric treatment at the interface is used. In the method employed here, a set of nodal points that define element edges or segments which have both nodes declared to be master nodes define unique master segments of the master surface on which slave nodes are not permitted to intrude. These master segments are not required to define the master surface in a continuous manner. When penetration of a slave node through the master surface occurs, the velocities of the master and slave nodes are adjusted to conserve angular and linear momentum as described in reference 10. Once the intrusions are removed, the designation of master and slave is interchanged and the procedure is repeated. Each temporal integration increment is comprised of the following steps.

1. Determine master segments on one side of the interface that circumscribe elements which have not exceeded the user-specified failure criterion.

2. For each slave node find the master segment whose search radius, R', in Figure 1 contains the slave node.

3. Determine the sign of the cross product of the vectors M_1M_2 and M_1S^t defined in Figure 1. A requirement of the interface logic outlined here is that slave nodes must remain to the left of the master segment. A negative sign of the cross product indicates penetration of the master segment by a slave node and requires corrective action.

4. If there is intrusion, position the slave node on the master segment in a direction normal to the segment.

5. Update master and slave node velocities to conserve linear and angular momentum.

6. Update nodal forces to account for change in nodal velocities.

7. Interchange master and slave designations and repeat steps 1-6.

Figure 2 shows results obtained with this method for the penetration of a steel plate by a 65 gram, hemispherically nosed steel rod with a striking velocity of 1103 m/s. Figure 3 shows similar results for a plane strain simulation at an obliquity of 60° and striking velocity of 1647 m/s. Table I shows a comparison of computed residual masses and velocities with those obtained experimentally by Lambert (ref. 11) from radiographic data. The agreement is quite good for the normal impact case. The higher residual mass and velocity computed for the oblique impact is characteristic of plane strain analyses of high velocity impacts. The utility of plane strain analyses of high velocity impacts has been examined by Zukas et al. (ref 12) who concluded that the fundamental difference in the formulation of the computational elements between the plane strain approximation and the exact (axisymmetric) computation of penetration is sufficient reason to expect different energy displacement relationships for the two formulations.

CONCLUSIONS

The simulation of contact surface erosion in Lagrangian analyses of high velocity impacts appears to be a most promising refinement which extends the capabilities of Lagrangian codes for problems involving perforation of solids. The methodology permits simulation of deep penetration which previously was limited to Eulerian codes. Furthermore, the methodology has been demonstrated to yield residual parameters that are in good agreement with experimental data at a considerable reduction in cpu time and memory requirements for a comparable Eulerian analysis.

REFERENCES

1. Zukas, J. A., Jonas, G. H., Kimsey, K. D., Misey, J. J., and Sherrick, T. M., "Three-Dimensional Impact Simulations: Resources and Results," in K. C. Park and R. F. Jones, Jr., eds., Computer Analysis of Large-Scale Structures, AMD, Vol. 49, American Society of Mechanical Engineers, 1981.

2. Poth, A., et al., "Experimental and Numerical Investigation of the Ricochetting of Projectiles from Metallic Surfaces," Proceedings of the Sixth International Symposium on Ballistics, Joseph E. Backofen, Jr., ed., American Defense Preparedness Association, October 1981.

3. Poth, A., et al., "Failure Behavior of an Aluminum Plate Under Impact Loading," Proceedings of the International Conference on Application of Fracture Mechanics, Kluwer Acad. Publ., The Hague, 1984.

4. Schwartz, R., et al., "Analysis of Reinforced Concrete Structures Subjected to Aircraft Impact Loading," Proceedings of the Seventh International Conference on Structural Mechanics in Reactor Technology, Chicago, Illinois ,1983.

5. Johnson, G. R., et al., "Three Dimensional Computer Code for Dynamic Response of Solids to Intense Impulsive Loads," International Journal for Numerical Methods in Engineering, Vol. 14, No. 12, 1979, pp. 1865-1871.

6. Johnson, G. R., et al., "Lagrangian Computations for Projectile Penetration into Thick Plates," to appear in Applied Computer Methods in Ballistics session at the 1984 ASME International Computers in Engineering Conference and Exhibit, Las Vegas, Nevada, August 12-16, 1984.

7. Snow, P., "KEPIC-2", Kaman Sciences Corporation Report K82-46U (R), August, 1982.

8. Hallquist, J. O., "A Numerical Treatment of Sliding Interfaces and Impact," in K. C. Park & D. K. Gartling, eds., Computational Techniques for Interface Problems, AMD Vol. 30, ASME, New York, 1978.

9. Hallquist, J. O., "A Numerical Procedure for Three-Dimensional Impact Problems", Preprint 2956, ASCE National Convention and Exposition, San Francisco, Oct. 1977.

10. Johnson, G. R., "EPIC-2, A Computer Program for Elastic-Plastic Impact Computations in 2 Dimensions Plus Spin," Ballistic Research Laboratory Contract Report No. ARBRL-CR-00373, June 1978. (Avail. from NTIS as AD-A058786.)

11. Lambert, J. P., "The Terminal Ballistics of Certain 65 Gram Long Rod Pentrators Impacting Steel Armor Plate, Ballistic Research Laboratory Report No. ARBRL-TR-02072, May 1978.

12. Zukas, J. A., et al., "On the Utility of Plane Strain Approximations for Oblique Impact Computations," Ballistic Research Laboratory Report No. ARBRL-MR-02969, October 1979. (Avail. from NTIS as AD-A081120.)

TABLE I. - COMPARISON OF CALCULATED AND MEASURED RESIDUAL PARAMETERS

Obliquity (degrees)	Striking Velocity (m/s)	Residual Velocity (m/s)		Residual Mass (g)	
		Calculated	Measured*	Calculated	Measured*
0	1103	709	690	32.1	32.7
60	1647	1202	1145	22.9	16.8

* - Reference 11

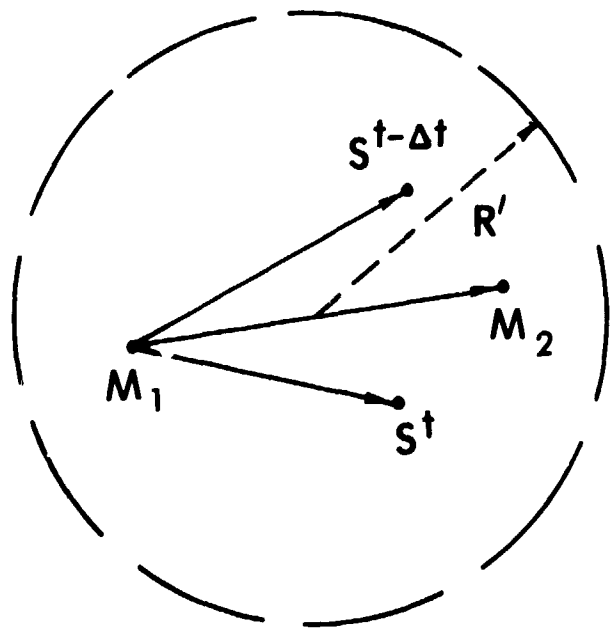

FIGURE 1. - TEST FOR SLAVE NODE INTRUSION OF MASTER SEGMENT M_1M_2: VECTOR CROSS PRODUCT $M_1M_2 \times M_1s^t<0$.

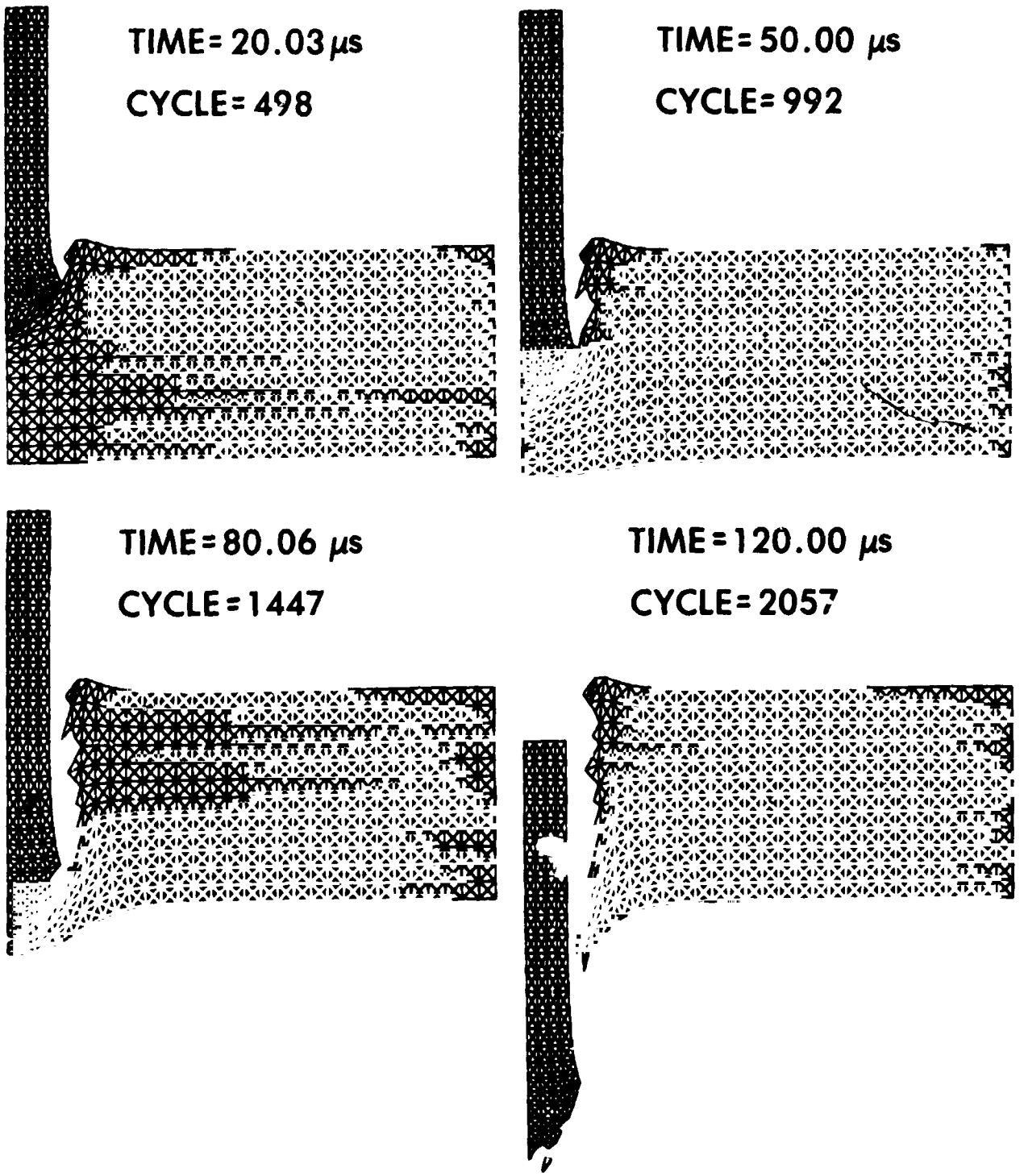

FIGURE 2. - EVOLUTION OF CONTACT SURFACE EROSION FOR AN AXISYMMETRIC IMPACT

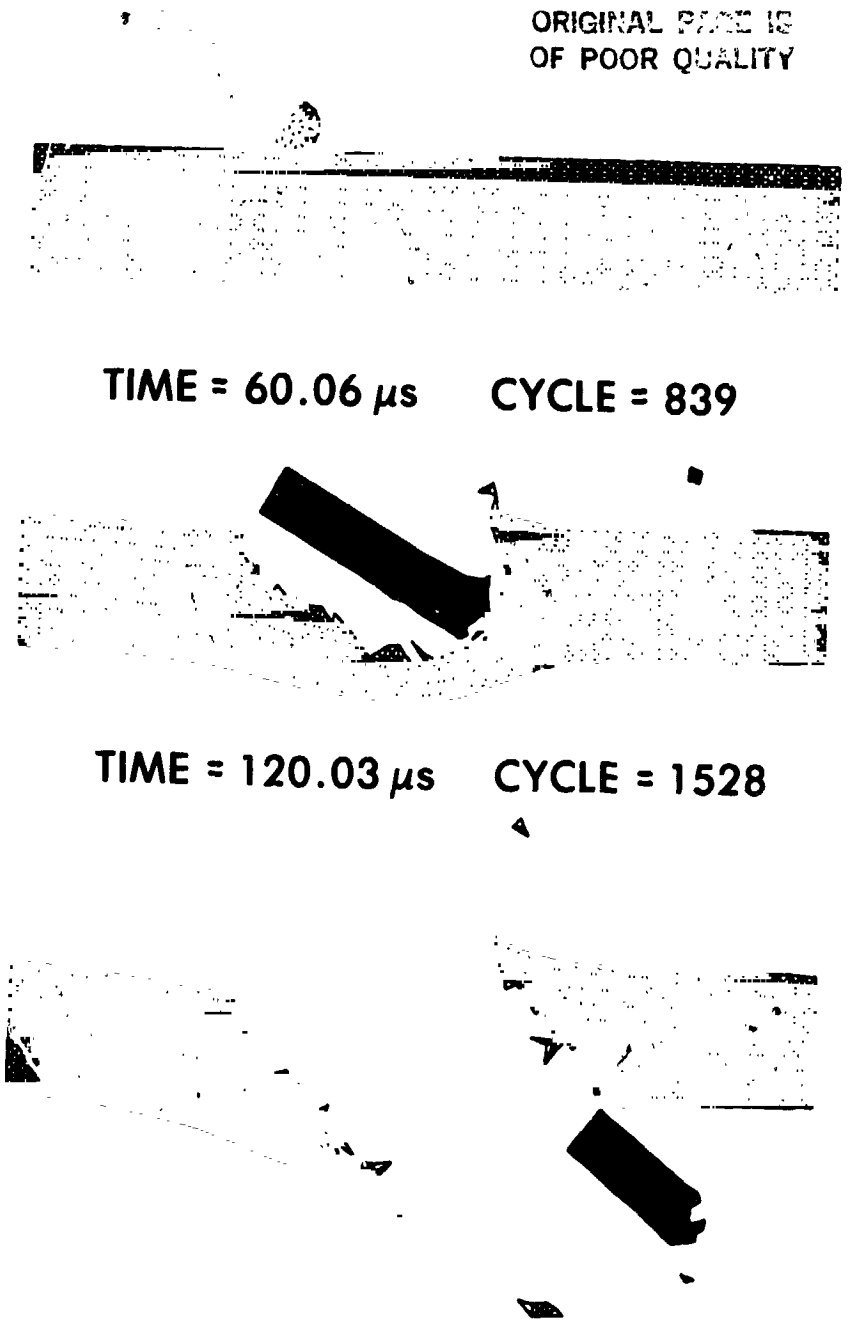

FIGURE 3. - EVOLUTION OF CONTACT SURFACE EROSION FOR AN OBLIQUE IMPACT

CRASHWORTHINESS OF LIGHT AIRCRAFT FUSELAGE STRUCTURES: A NUMERICAL AND EXPERIMENTAL INVESTIGATION

A.P. Nanyaro, R.C. Tennyson and J.S. Hansen
University of Toronto, Institute for Aerospace Studies

SUMMARY

A comprehensive program was undertaken to investigate both analytically and experimentally the dynamic behaviour of aircraft fuselage structures subject to various impact conditions. An analytical model was developed based on a self-consistent finite element (CFE) formulation utilizing shell, curved beam and stringer type elements. Equations of motion were formulated and linearized (i.e. for small displacements), although material nonlinearity was retained to treat local plastic deformation. The equations were solved using the implicit Newmark-Beta method with a 'frontal' solver routine. Free-flight testing of stiffened aluminum fuselage models was also undertaken using the UTIAS pendulum crash test facility. Data were obtained on dynamic strains, g-loads and transient deformations (using high speed photography in the latter case) during the impact process. Correlations between tests and predicted results are presented, together with computer graphics, based on the CFE model. These results include level and oblique angle impacts as well as the free-flight crash test.

Finally, comparisons are also made with a hybrid, lumped mass finite element computer model. It is demonstrated that the CFE formulation provides the best overall agreement with impact test data for comparable computing costs.

INTRODUCTION

In evaluating the crashworthiness of aircraft structures, it is essential to utilize computer analyses to aid the aircraft designer during the preliminary design phase. Designing a crash-resistant structure and seat configuration necessitates an understanding of the behaviour of a complex structure deforming under various impact loads. Testing of full scale aircraft or scale models is extremely expensive and difficult. Consequently, the experimental approach alone is undesirable. Computer techniques are needed which adequately consider large deflections, elastic-plastic material response, local buckling and post-buckling behaviour, as well as isolated component fractures. From an economic view, it is desirable to develop the simplest feasible mathematical model representation of the actual structure, while maintaining an acceptable level of accuracy. The cost restrictions place constraints on the total number of degrees of freedom that can be retained in the model, the number of elements that may exhibit material and/or structural non-linearity, and the number of times the system stiffness matrix can be re-assembled, inverted, and/or transformed in a dynamic analysis. Consequently, two analytical approaches were considered. The first model developed was based on a lumped mass finite element (LMFE) representation of the structure using flat, straight elements. The intention was to approximate the structure in such a manner as to obtain a low cost, efficient and accurate analysis that would be attractive as a preliminary design code. Results of this effort have been

well documented elsewhere (refs. 1,2). At the same time, a more accurate, more cost effective and consistent finite element (CFE) formulation was recently developed to provide a basis for comparison, details of which are provided in the following section.

Clearly, regardless of which model is utilized, the analysis must be capable of providing accurate estimates of the g-loads, volume reduction, and associated gross failure modes of the structure for certain crash conditions. Of particular importance is the accurate prediction of g-loads transferred to the passenger seat structure in order to improve seat design and minimize occupant injury. Also of vital concern is the prediction of structural g-loading of large masses which, in the case of high wing aircraft, can crush the fuselage. Finally, in order to select a reliable computer model, validation of its predictions is only possible via credible tests on realistic structural configurations subjected to simulated impact loadings that reflect a range of likely aircraft crash conditions which are potentially survivable.

This report presents a brief summary of the finite element formulation together with a description of the experimental program and comparisons with test data. For further details, the reader is referred to ref.3.

DERIVATION AND SOLUTION OF MOTION EQUATIONS FOR AN IMPACTING AIRCRAFT

The motion equations appropriate for the present problem have been developed from the method of virtual work and are given by

$$\mu \frac{\partial^2 W}{\partial t^2} + B^T \sigma = F \tag{1}$$

where μ is the mass density, W is a column matrix of displacements, B is a matrix of non-linear differential operators, σ is the column stress matrix and F is a column matrix of applied forces acting on the system. Equation (1) does not explicitly contain the impact forces that result from ground contact.

However, this characteristic is obtained in the computer code by imparting appropriate moments to various nodes when ground contact occurs. In addition, dissipation resulting from contact is included through the use of an appropriate coefficient of restitution.

Finite Element Motion Equations

In this section, the development of the consistent mass and stiffness matrices that correspond to the finite element discretized motion equations is presented. As the fuselage structure is complex, the differential equations the describe the motion are not dealt with directly. Rather, the aircraft is idealized as an assembly of flexible structural elements (figure 1) comprised of curved ribs, stringers, (two nodes, 6 degrees of freedom (DOF) per node) and shell segments (4 nodes, 6 DOF per node). All elements can exhibit plasticity if required.

In the following analysis, three basic reference frames are considered:

1. I, an inertial frame
2. B, a fuselage centre of mass, body-fixed frame
3. E_i, an element centre of mass frame (i refers to the i-th element)

These reference frames are shown schematically in figure 2. Note that the fuselage centre of mass has been assumed to remain fixed even as the fuselage deforms. This is justified on the basis that the predominant mass in the analysis is that of the wing, which is assumed rigid, and therefore changes in shape of the fuselage cause very minor changes in the centre of mass location.

The discretized motion equations that result from the application of the finite element procedure take the general form,

$$M\ddot{x} + C\dot{x} + Kx = F(t) \tag{2}$$

where M, C, K are the mass, damping and stiffness matrices, respectively, and x and F(t) correspond to the response and forcing column matrices, respectively. The following sections present the development of each of these quantities at the elemental level; these are then assembled to form the matrix or vector of interest.

The basis functions used in the analysis are polynomials and the model deformations are represented by d_i, with i ranging over the number of displacement degrees of freedom. In the continuum representation, the displacements are defined by W:

$$W = [u, v, w]^T \tag{3}$$

with the discretized representation (trial function) taking the form

$$W = P_b\Gamma \tag{4}$$

Here P_b is the matrix of polynomial functions which for the cylindrical shell element is given by

$$P_b = \begin{bmatrix} 1 & \xi & \eta & \xi\eta & 0 & 0 & \multicolumn{4}{c}{\multirow{2}{*}{\hrulefill}} \\ 0 & 0 & 0 & 0 & 1 & \xi & \eta & \xi\eta & 0 & 0 & \multicolumn{4}{c}{} \\ 0 & \multicolumn{9}{c}{\hrulefill} & 1 & \xi & \eta & \xi\eta & \xi^2 & \eta^2 & \cdots \end{bmatrix} \tag{5}$$

where ξ and η are the axial and circumferential shell coordinates, respectively, and Γ is the vector of polynomial coefficients. The nodal variables d are related to Γ by substituting the coordinates into the trial functions and equating to the nodal degrees of freedom. This yields

$$W(\xi_i, \eta_i) = W_i = P_1(\xi_i, \eta_i)\Gamma \tag{6}$$

for the nodal displacements while the nodal slope and twist degrees of freedom are obtained from

$$\begin{bmatrix} \frac{\partial}{\partial \xi} \\ \frac{\partial}{\partial \eta} \\ \frac{\partial^2}{\partial \xi \partial \eta} \end{bmatrix} w|_i = \begin{bmatrix} \frac{\partial}{\partial \xi} \\ \frac{\partial}{\partial \eta} \\ \frac{\partial^2}{\partial \xi \partial \eta} \end{bmatrix} [0 \ldots 0 \quad 1 \quad \xi \quad \eta \quad \xi\eta \quad \xi^2 \quad \eta^2 \ldots] \Gamma|_i \qquad (7)$$

which can be expressed as

$$\beta_i = P_2 \Gamma \qquad (8)$$

thereby providing a relationship of the form

$$d_i = \begin{bmatrix} w_i \\ \beta_i \end{bmatrix} = \begin{bmatrix} P_1 \\ P_2 \end{bmatrix} \Gamma = P\Gamma \qquad (9)$$

The inversion of P then provides the required relationship

$$\Gamma = P^{-1} d_i = C d_i \qquad (10)$$

The elemental stiffness matrix is composed of two parts; the elastic component given by

$$K_s^c = \int_s C^T B^T D B C \, dv \qquad (11)$$

and the non-linear, induced stress component resulting from plasticity,

$$K_s^p = \int_s C^T B^T \sigma' dv \qquad (12)$$

In these, D is the constitutive matrix, given by

$$\sigma = D\varepsilon \qquad (13)$$

where σ and ε are the stress and strain column matrices, respectively, and B is a matrix of differential operators which relates strains and displacements,

$$\varepsilon = BW \tag{14}$$

Also, σ represents the plastic increment in stress. It should be noted that the above matrices are evaluated with respect to the element reference frame.

The contribution to the element matrices that results from the mass properties of an element requires evaluation with respect to an inertial reference frame. The acceleration of an element in the inertial reference frame is written as

$$A \triangleq \frac{d^2}{dt^2}[x + R_c + p + w] \tag{15}$$

where the vectors on the right are as follows (see figure 3)

1. Equation (16) gives the position of the fuselage centre of mass with respect to the inertial frame:

$$x \triangleq \{i\}^T x \tag{16}$$

2. Equation (17) gives the position of an element with respect to the fuselage centre of mass:

$$R_c \triangleq \{b\}^T R_c \tag{17}$$

3. Equation (18) gives the position of a particle in an element:

$$P \triangleq \{e\}^T p \tag{18}$$

4. Equation (19) is the deformation of a point in an element:

$$w \triangleq \{c\}^T W = \{b\}^T W_i \tag{19}$$

In the above, $\{i\}$, $\{b\}$, $\{e\}$, and $\{c\}$ are the matrices of unit vectors corresponding to the inertial, fuselage centre of mass, element centre of mass and position frames, respectively, while x, R_c, p, W and W_i are column matrices which are the components of the corresponding vector in the indicated reference frame. Thus, the acceleration in terms of the body-fixed reference frame becomes

$$\begin{aligned} A = \{e\}^T \{ & cc^T \ddot{x} + c[\omega_b^x(R_c + c^T p) + \omega_b^x \omega_b^x (R_c + c^T p)] + \ddot{W} \\ & + c[2\omega_b^x c^T \dot{W} + (\dot{\omega}_b^x + \omega_b^x \omega_b^x) c^T W\} \end{aligned} \tag{20}$$

where c is the transformation matrix given by

$$\{e\}^T = \{b\}^T c \tag{21}$$

and c^T represents the transpose of c, while ω_b is the column matrix of angular velocities of b with respect to 1. Further ω_b^x is defined by

$$\omega_b^x = \begin{bmatrix} 0 & -\omega_3 & \omega_2 \\ \omega_3 & 0 & -\omega_1 \\ -\omega_2 & \omega_1 & 0 \end{bmatrix} \tag{22}$$

where ω_b is given by

$$\omega_b = \begin{bmatrix} \omega_1 \\ \omega_2 \\ \omega_3 \end{bmatrix} \tag{23}$$

It should be noted that, in the above, the angular velocity of the element with respect to the body reference frame is neglected. That is, in the relation $\omega_e = \omega_b + c\dot{c}^T$, the effect of $\dot{c}$ has been neglected. Thus, the inertia terms yield the final result

$$\begin{aligned} &\{\int_s C^T c c^T \mu dv\}\ddot{x} + \int_s C^T c[(\dot{\omega}_b^x + \omega_b^x \omega_b^x)(R_c + c^T p)]\mu dv + \int_s C^T C \mu dv \ddot{d} \\ &+ \{\int_s 2C^T c \omega_b^x c^T C \mu dv\}\dot{d} + \{\int_s C^T c(\dot{\omega}_b^x + \omega_b^x \omega_b^x) c^T C \mu dv\} d \end{aligned} \tag{24}$$

where the coefficients of d, $\dot{d}$, $\ddot{d}$ may be identified by

$$\begin{aligned} K_a &\triangleq \int_s C^T c \dot{\omega}_b^x c^T C \mu dv \\ K_c &\triangleq \int_s C^T c \omega_b^x \omega_b^x c^T C \mu dv \\ G &\triangleq 2 \int_s C^T c \omega_b^x C \mu dv \\ M &\triangleq \int_s C^T C \mu dv \end{aligned} \tag{25}$$

These relations define the matrix for the angular acceleration of the elements, the acceleration matrix, the gyroscopic coupling matrix and the mass matrix, respectively. Thus, the contribution to the motion equation from a single element is given by

$$L_s = M\ddot{d} + G\dot{d} + [K_E + K_p + K_a + K_c]d + \int \mu C^T c(\dot{\omega}_b^x + \omega_b^x \omega_b^x) c^T p dv$$

$$+ \left\{ \int_s \mu C^T c c^T dv \right\} \ddot{x} + \left\{ \int_s \mu C^T c(\dot{\omega}_b^x + \omega_b^x \omega_b^x) dv \right\} R_c \qquad (26)$$

The motion equations are coupled by suitably orienting each element contribution, summing over all the elements and then adding external forces. Hence, the motion equation takes the form

$$\sum_s (c_s L_s - f_s) = 0 \qquad (27)$$

where f_s defines the column matrix for the consistent element force. With these assembled equations, a number of observations can be made. First, the motion of the centre of mass is unaffected by the motion of the fuselage relative to the centre of mass. This implies that a solution for $\ddot{x}$ corresponds to that of a free falling mass with appropriate rebound conditions included. Similarly, the angular momentum of the system is conserved during the free fall and rebound phases if suitable account is taken of the impact duration with the ground. Inclusion of these effects means that $\ddot{x}$, ω_b and $\dot{\omega}_b$ can be directly solved and thus they appear as forcing functions in equation (27). The final contribution to the motion equation from the structural element is of the form

$$L_s = M\ddot{d} + G\dot{d} + Kd \qquad (28)$$

where the remaining terms in equations (26) and (27) can be determined from free fall calculations for the centre of mass.

Solution by Time Integration

The motion equations have been integrated in the time domain using the Newmark-β method (ref.4) which relates d_{I+1}, v_{I+1} and a_{I+1} (i.e. the displacement, velocity and acceleration, respectively) at the $(I+1)^{st}$ time step by equations (29):

$$a_{I+1} = \frac{4}{\Delta t^2}(d_{I+1} - d_1 - \Delta t v_1 - \frac{1}{4}\Delta t^2 a_1)$$

$$v_{I+1} = v_1 + \frac{1}{2}\Delta t(a_1 + a_{I+1}) \qquad (29)$$

where β, the integration parameter, has been taken as 1/4. Substituting the expressions for a_{I+1} and v_{I+1} into the assembled motion equation yields

$$d_{I+1} = d_I + [M^a + \frac{1}{4} t^2 K_I^a]^{-1} \{M^a [\Delta t v_1 + \frac{1}{4} \Delta t^2 a_1] + \frac{1}{4} \Delta t^2 [F_{I+1} - K_I^a d_I]\} \quad (30)$$

where M^a and K_I^a are the assembled mass and tangent stiffness matrices, respectively, and F_{I+1} is the assembled force column matrix. This integration scheme has the advantage of unconditional stability and accuracy (ref.5) and also allows the use of a 'Frontal Solver' technique (ref.6).

Fuselage Model Analysis

As noted earlier, the fuselage model shown in figure 1 consists of shell, curved beam and stringer elements. The derivation of the cylindrical shell element is described in detail in ref. 7. Of interest is that rigid body displacements are considered while maintaining interelement compatibility. Consequently, the free-body motion of the fuselage during free-flight does not result in structural strains.

The model investigated in this report has 383 nodes and 1626 degrees of freedom. This compares to 368 degrees of freedom provided by the LMFE computer model utilizing 79 nodes, which are 'statically condensed' to provide 138 degrees of freedom before integration is performed. For the first time step, during the integration, the matrices are found and inverted. The element mass and stiffness matrices are stored on disks to be used in energy growth checks. Gaussian elimination is performed and information necessary for back-substitution in the first and subsequent time steps is stored on disks as well. For every time step, the external forces, plastic and corrective forces are found and used to obtain displacements, velocities and accelerations. The external forces include gravitational weight whereas the corrective forces include errors after iteration and the buckling forces. Subroutines are employed to evaluate the stiffness and mass-'creating' subroutines for the different elements. This is done during the first time step. The matrices are assembled into the body coordinate system and transformations are then performed from curved coordinates to Cartesian body coordinates. The displacement change is found in the inertial reference frame with components in the body axis directions at each step. Integration to find accelerations and velocities is done in the inertial reference frame. The angular velocity is included in the model together with centripetal, angular acceleration and gyroscopic forces about the fuselage centre of mass. These forces at the element level are neglected. Thus the element centrifugal, gyroscopic and angular acceleration matrices are assumed to have a negligible contribution to the element displacements about its own centre of mass.

The time step, (Δt), during the integration is chosen to maintain little energy growth in time, thus ensuring stability. In this study, $\Delta t = 0.001$ sec was employed. For every time step, negative strain energy is checked. If the energy is negative despite several iterations at the step, the integration is abandoned. On contact with the ground, velocity components are imparted to the appropriate nodes, equal in magnitude but opposite to the initial impact values. A rebound coefficient can be introduced at this point together with a coefficient of friction which will change the velocities parallel to the ground at the point of contact. These coefficients have not been used in this program, although they

were used in the LMFE analysis.

EXPERIMENTAL PROGRAM

Fuselage Test Model

The experimental fuselage model was chosen to characterize a large number of typical general transport, light aircraft fuselages withir a weight range of 3,000 to 24,000 kg. The model has a geometric scale factor of about a third for this category of aircraft. A high wing configuration was selected since it provided the worst case situation for an impacting fuselage. The objective behind the choice of the model was to perform credible experiments on realistic fuselage structures to demonstrate the validity of the computer codes, which then could be used to analyse an actual aircraft. The test models were fabricated from 0.305 mm thick 2024-T3 aluminum skin stiffened with twelve light rib frames and two solid cross-section, heavy main frames (bulkheads) to pick up the wing loads. A floor support structure was also added for completeness together with longitudinal stringers mounted on the exterior of the fuselage. The dimensions of the models were nominally 0.914 m in diameter, 2.31 m long and with a mass of approximately 16.4 kg. Figures 4 and 5 show photographs of a test model.

Wing loading for the free-flight configuration consisted of two longitudinal stiff beams (see fig.4) with end weights. This structure was attached to a rigid mounting fixture which itself was bolted to both interior main frames. This particular design was necessary to properly simulate the pitch moment of inertia and lower the centre of gravity within the fuselage cross-section.

In a flight test simulation, it should be noted that in reality, the loading on the aircraft fuselage will differ from the drop-test values due to aerodynamic lift in a "controlled" crash landing. The forces from the control surfaces will also affect the torques on the fuselage. A simple correction factor should be determined, by equating total energy at impact of the model and that of the fully 'lifted' aircraft using the appropriate nondimensional parameters. In this way, model data can be related to an actual aircraft fuselage using these nondimensional factors.

Crash Test Facility

Experimental tests were performed inside the geodetic dome (50 m diameter) of the University of Toronto Institute for Aerospace Studies. The facility consisted of a pendulum gantry constructed over a 12.2 m by 3.7 m reinforced concrete runway, as shown in the schematic of figure 6. The gantry was about 7 m high and stood on four legs, with the fuselage suspended from the gantry top 'frictionless' pivot by a rigid swing arm. The fuselage was then drawn back above the impact surface by a cable attached to the dome roof. Between this cable and the fuselage was a manual release mechanism. The fuselage mounting fixture was attached to the rigid swing arm by a pyrotechnic bolt tension separator. A free-flight test sequence was initiated when the fuselage was released from the pullback cable, permitting the model to swing 'pendulum style' above the impact surface. The fuselage was then separated from the swing arm by the pyrotechnic device, when the swinging arm was perpendicular to the ground or at the lowest point in its swinging path. This trigger mechanism was

activated when the fuselage passed through a laser beam as shown in fig.6. An electrical signal was then relayed to the pyrotechnic firing system, details of which can be found in refs. 7 and 8.

Data Acquisition System

Data acquisition during the crash tests was accomplished with photographic coverage using low and high speed cameras and with onboard strain gauges and accelerometers. The strain gauges were bonded to the inner edges of the main load carrying frames while strain gauge type miniature accelerometers were positioned on the fuselage to measure normal and/or longitudinal acceleration on the wing mass and on the floor structure. The accelerations on the wing mass result in loads being applied to the main frames and the accelerations of the floor can be used to assess the loads transmitted to the seat structure.

Both accelerometer and strain gauge signals were sent through a SE Bridge conditioning unit and a SE Galvo conditioning unit before being output on a Honeywell Visicorder oscillograph (Model 1508). The accelerometer signals were also filtered using a 200 Hz low pass filter and taped on a Bruel and Kjaer 7003 FM-tape recorder. The analog data on the FM-tape were digitized using a PDP 1140 computer and GT44 graphic terminal. The Visicorder contained type M200-350 (electromagnetic damped) miniature galvanometers having a resistance of 350 ohms and a flat frequency response from 0 to 180 Hz. Further details can be found in ref.7.

Impact Tests

Prior to the free-flight test, a series of level and oblique angle vertical drop tests were conducted. Some experimental g-load results are presented in tables I-II.

Subsequently, a free-flight test was performed with a wing mass of 244 kg. The initial release parameters at a height of 0.17 m were: angle of incidence, 3°; nose-up pitch rate (counter-clockwise) equal to 1.18 rad/sec; horizontal velocity of 6.58 m s^{-1}. At initial impact, the angle of incidence was about 9.6° and the centre of mass sink rate was 0.88 m s^{-1}. Selected high speed photographs presented in figure 7 ($\sim$ 400 pps) show portions of the 'free-flight' impact test. For further details, refer to ref.7. From post-crash pictures shown in figures 8 and 9, one can see modest collapse of the aft end (due to the first impact) and substantial collapse of the forward end. The floor failure is symmetric and local fracture was observed together with interior rib failures. No failure of the main rib occurred although some plastic deformation was evident.

Table III summarizes the measured peak g-loads for this case.

COMPARISON OF COMPUTER MODEL PREDICTIONS WITH TEST DATA

As noted earlier, two computer models were developed, one a hybrid based on a lumped mass - finite element approach (LMFE) and the other, which forms the basis of this report, a consistent finite element formulation (CFE). Details

on the former model can be found in refs 1 and 2, for example. Both model predictions of peak g-loads and times of occurrence are presented in tables I, II, and III for level, oblique and 'free-flight' impact tests, respectively. Although the available experimental data are somewhat limited, in general the CFE model provides better correlation than the LMFE analysis. Figure 10 provides a comparison of the CFE predicted acceleration - time response with the recorded output for the level impact case. Quite good correlation is observed.

Selected graphics depicting the initial 'free-flight' impact behaviour of the fuselage are presented in fig.11. These results can be compared with the high-speed photographs in fig.7 where the same general dynamic response is evident in the form of aft end transient collapse. For more complete photographic coverage of the free-flight test together with computer graphics, refer to refs. 7 and 8.

CONCLUSIONS

A consistent finite element computer code has been developed to analyse fuselage structures for a typical high wing passenger aircraft. The analysis was carried out for various impact configurations and energy levels. Vertical drop and 'free-flight' experimental tests were performed on scale model stiffened aluminum fuselage sections at the UTIAS Crashworthiness Facility. The test data obtained from realistic structural configurations provided a basis of comparison for two analytical models. It has been demonstrated in this report that the consistent finite element formulation provides the best overall agreement in terms of peak g-load predictions.

In summary, the computer code has the following capabilities:

(1) determines dynamic response in terms of displacements, velocities and accelerations for all the points on the fuselage model

(2) allows variation of initial conditions which consist of vertical and horizontal velocities, pitch rate, angular velocity, position and orientation relative to the surface of impact

(3) permits changes of coordinates and geometry, numbering of nodes, introduction of new elements, internal and external forces and changes in materials

(4) presents views of deformed fuselage structure in the form of computer graphics

REFERENCES

1. Tennyson, R.C., Hansen, J.S., Teichman, H., Nanyaro, A.P., and Mabson, G.E., "Crashworthiness of Light Aircraft Structures", TP 2616, Transport Canada, Research and Development Centre, Montreal, P.Q., March 1980.

2. Tennyson, R.C., Teichman, H., Nanyaro, A.P., and Mabson, G.E., "Study of the Crashworthiness of Light Aircraft Structures", in Proc. Twenty Second Structures, Structural Dynamics and Materials Conf., Part 1, pp. 276-285, AIAA/ASME/ASCE/AHS, Atlanta, Georgia, 1981.

3. Tennyson, R.C., Nanyaro, A.P., Teichman, H.C., and Hansen, J.S., "Crashworthiness of Light Aircraft Structures", Contractor Rept., TP 3927E, Transportation Development Centre, Montreal, P.Q., October 1982.

4. Newmark, M.N., "A Method of Computation For Structural Dynamics", Journal of Engineering, Mechanical Division, ASCE, 85, pp. 67-94, 1959.

5. Belytschko, T. and Schoeberle, D.F., "On the Unconditional Stability of an Implicit Algorithm for Nonlinear Structural Dynamics", Journal of Applied Mechanics, Series E, 42, pp. 865-869, 1975.

6. Irons, B.M., "A Frontal Solution Program for Finite Element Analysis", International Journal for Numerical Methods in Engineering, 2, pp. 5-32, 1970.

7. Nanyaro, A.P., "A Study of Crashworthiness of Light Aircraft Fuselage Structures: A Numerical and Experimental Investigation", University of Toronto Institute for Aerospace Studies TR #286, 1984.

8. Tennyson, R.C. and Hansen, J.S., "Study of the Crash Behaviour of Aircraft Fuselage Structures", "Structural Crashworthiness", Chapter 8, pp 218-258, N. Jones and T. Wierzbicki, Eds., Butterworths Pub., 1983.

TABLE I: SUMMARY OF PEAK g-LOADS (AND TIME OF OCCURRENCE - SEC) FOR LEVEL IMPACT V_o = 1.33 m s^{-1}, WING MASS = 244 kg. (VERTICAL ACCELERATION)

LOCATION OF ACCELEROMETERS	WING LOAD (RIB 6) #1+[211]**(27)***	WING LOAD (RIB 9) #3[215](21)	FLOOR (RIB 5) #4[61](43)	FLOOR (RIB 10) #6[137](46)
EXPERIMENT	11(.02)	13.9(.02)	11.2(.02)	20(.00)
LMFE	7.(.02)	7.(.02)	9.(.06)	9.(.06)
CFE	14(.02)*	14(.02)*	14(.02)*	14.4(.02)*

* FILTERED USING FIFTH-ORDER CHEBYSHEV LOWPASS FILTER WITH A PASSBAND OF 62.5Hz AND STOPBAND EDGE OF 125Hz

\+ ACCELEROMETER NUMBER

** CFE MODEL NODE NUMBER

*** LMFE MODEL NODE NUMBER

TABLE II: SUMMARY OF PEAK g-LOADS (AND TIME OF OCCURRENCE - SEC) FOR OBLIQUE IMPACT

V_o = 0.88 m s^{-1}

ANGLE = 2.0° WINGMASS = 244 kg (VERTICAL UNLESS STATED)

LOCATION OF ACCELEROMETERS	WING LOAD (MIDPOINT) HORIZONTAL ACC. #1+[215]**(27)***	FLOOR RIB 5 #2[61](12)	WING (MIDPOINT) #3(211)(27)	FLOOR RIB 5 HORIZONTAL #5[62](43)	FLOOR RIB 10 #6[136](46)
EXPERIMENT	2.8(.037)	23.5(.016)	7.9(.049)	5.2(.04)	20.6(.028)
LMFE	0.4(.02)	5.(.11)	4.(.07)	-	-
CFE	2.3(.01)	27(.016)*+	8.3(.03)	5.8(.035)	24(.027)*+

\+ ACCELEROMETER NUMBER

** CFE MODEL NODE NUMBER

*** LMFE MODEL NODE NUMBER

*+ FILTERED USING LOWPASS FIFTH ORDER CHEBYSHEV FILTER (A PASSBAND = 62.5 Hz STOPBAND = 125 Hz)

TABLE III: SUMMARY OF PEAK MEASURED g-LOADS (AND TIME OF OCCURRENCE - SEC)

FOR 'FREE-FLIGHT' CRASH TEST

LOCATION OF ACCELEROMETERS	WING (HORIZONTAL) RIB 6 #1+[211]**(27)***	FLOOR RIB 5 VERTICAL #2[61](43)	WINGLOAD RIB 9 VERTICAL #3[21](27)	FLOOR RIB 10 VERTICAL #4[181](43)	FLOOR RIB 5 HORIZONTAL #5[61](46)	FLOOR RIB 10 VERTICAL #6[136](46)
EXPERIMENT	0.76(.056)	8.3(.07)	3.7(.057)	8.1(.08)	2.8(.017)	4.0(.02)
LMFE	1.0(.068)	-	3.5(.06)	-	-	27.5(.17)
CFE	1.0(.04)*+	10(.05)*+	3.8(.05)**	-	4.1(.02)**	3.9(.02)**

\+ ACCELEROMETER POSITION

** CFE MODEL NODE NUMBER

*** LMFE NODE NUMBER

*+ FILTERED USING 5TH ORDER LOW PASS CHEBYSHEV FILTER (PASSBAND = 62.5 Hz)
(STOPBAND = 125 Hz)

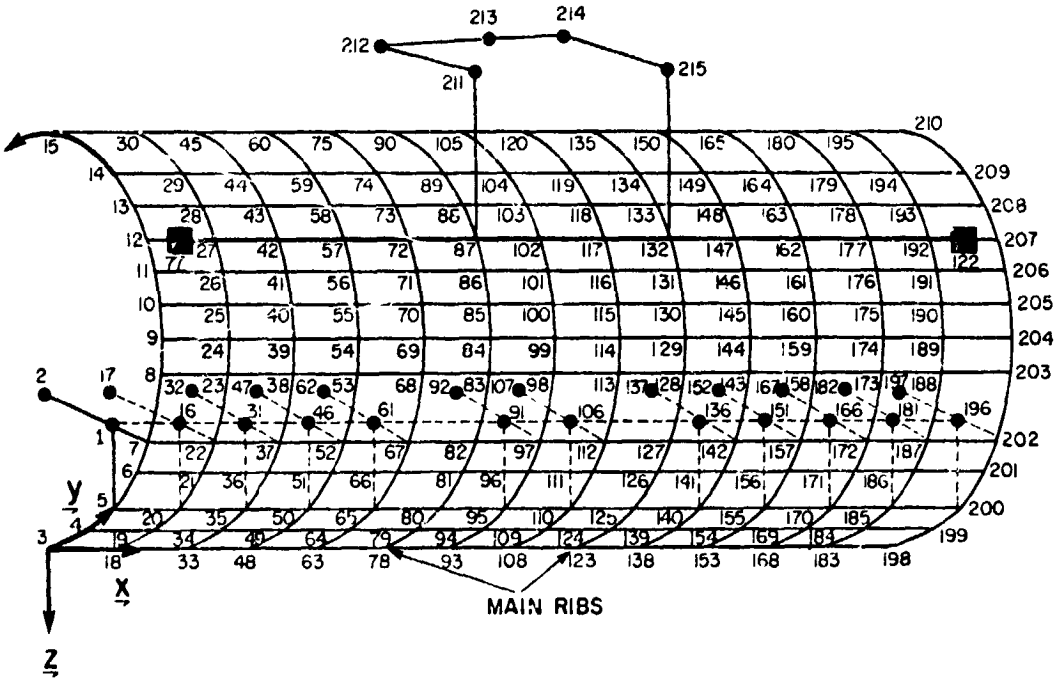

Figure 1. Half-fuselage nodes.

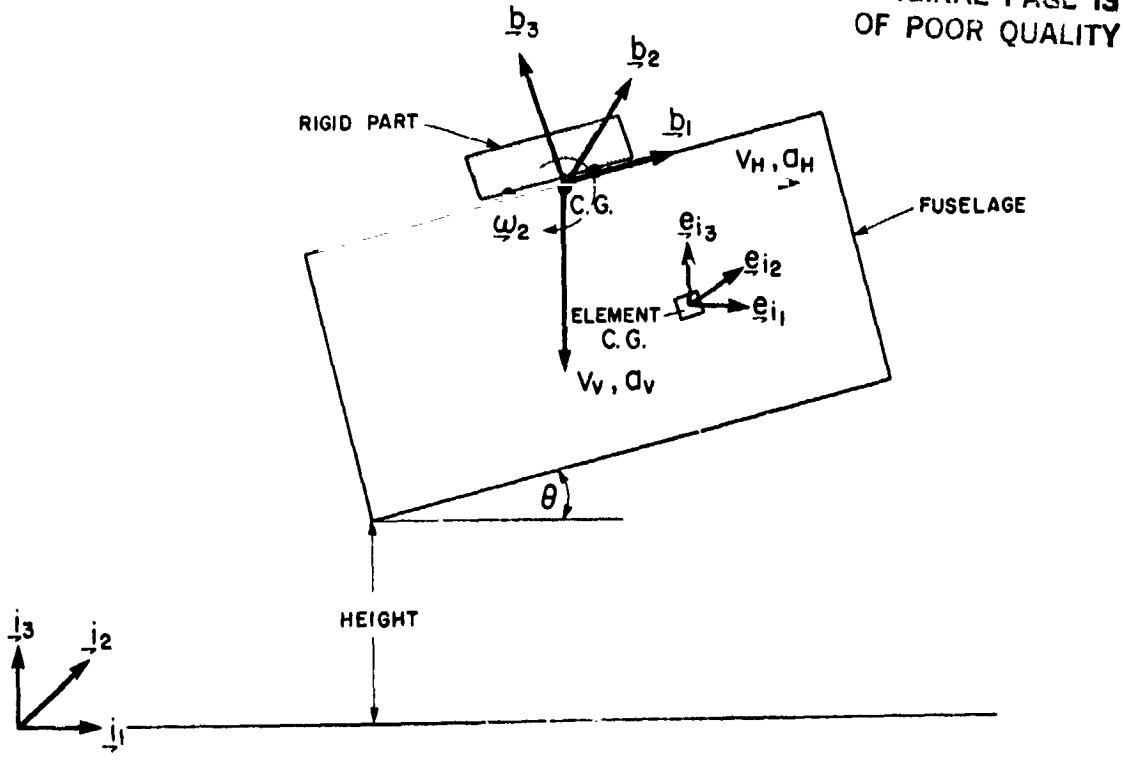

Figure 2. Reference frames.

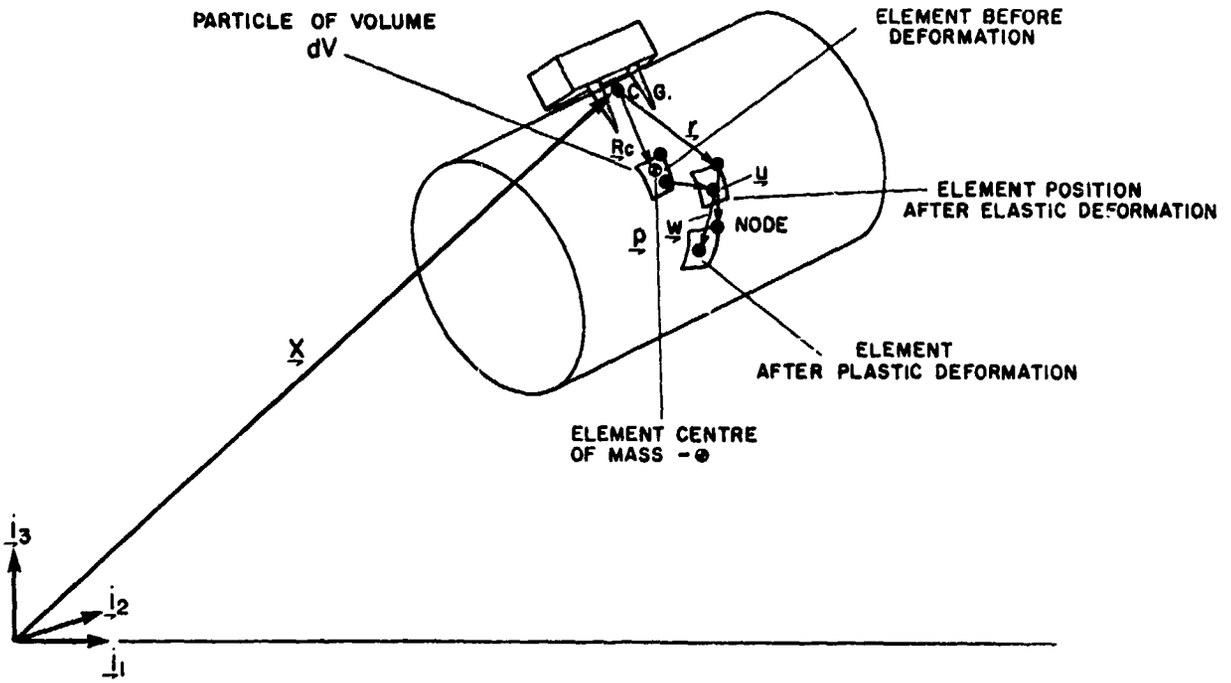

Figure 3. Vector position of the particle dV.

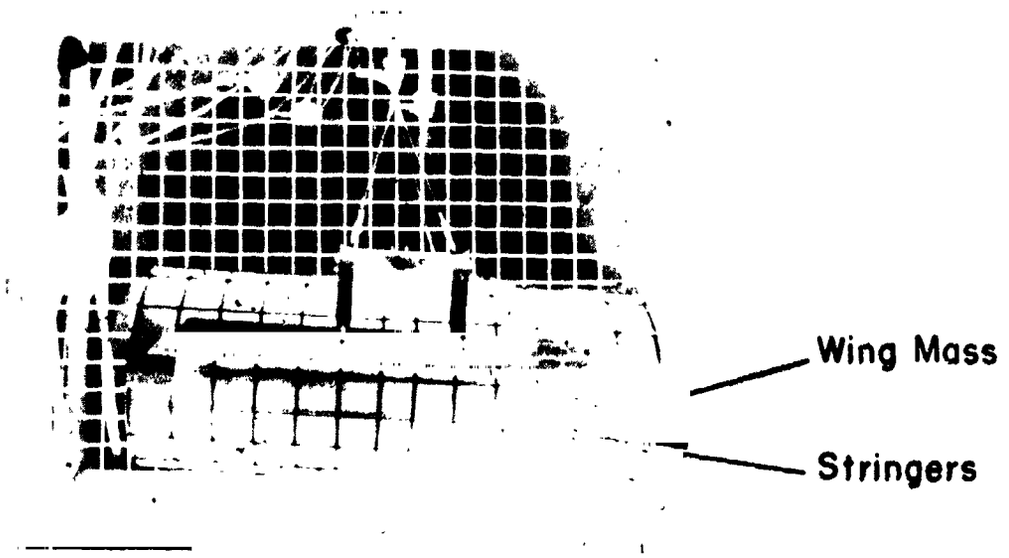

Figure 4. View of rib/stringer stiffened fuselage with high wing load attachment.

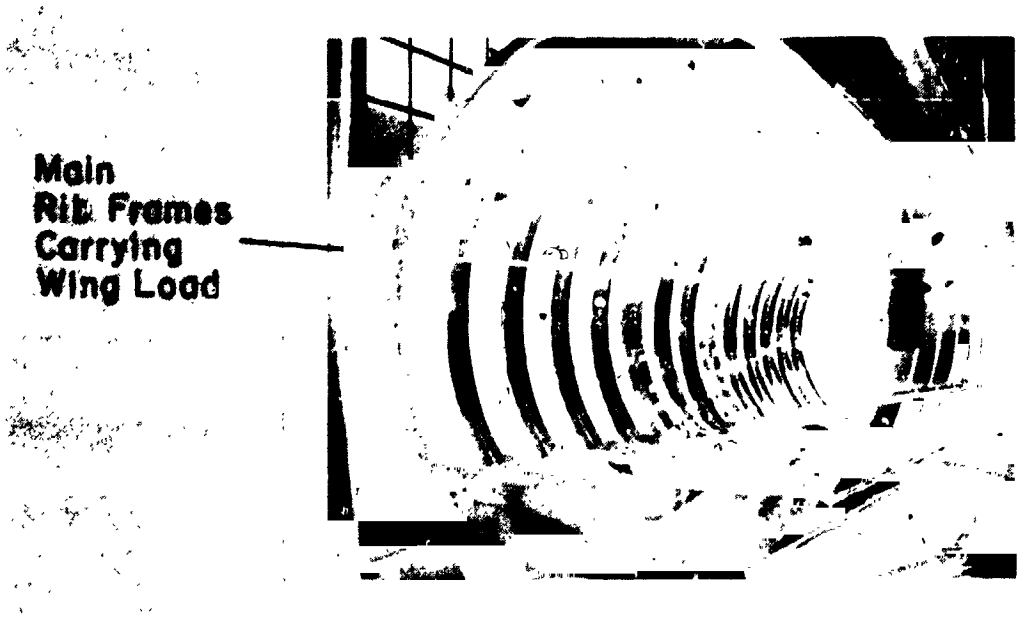

Figure 5. Interior view of ribs and floor frame structure.

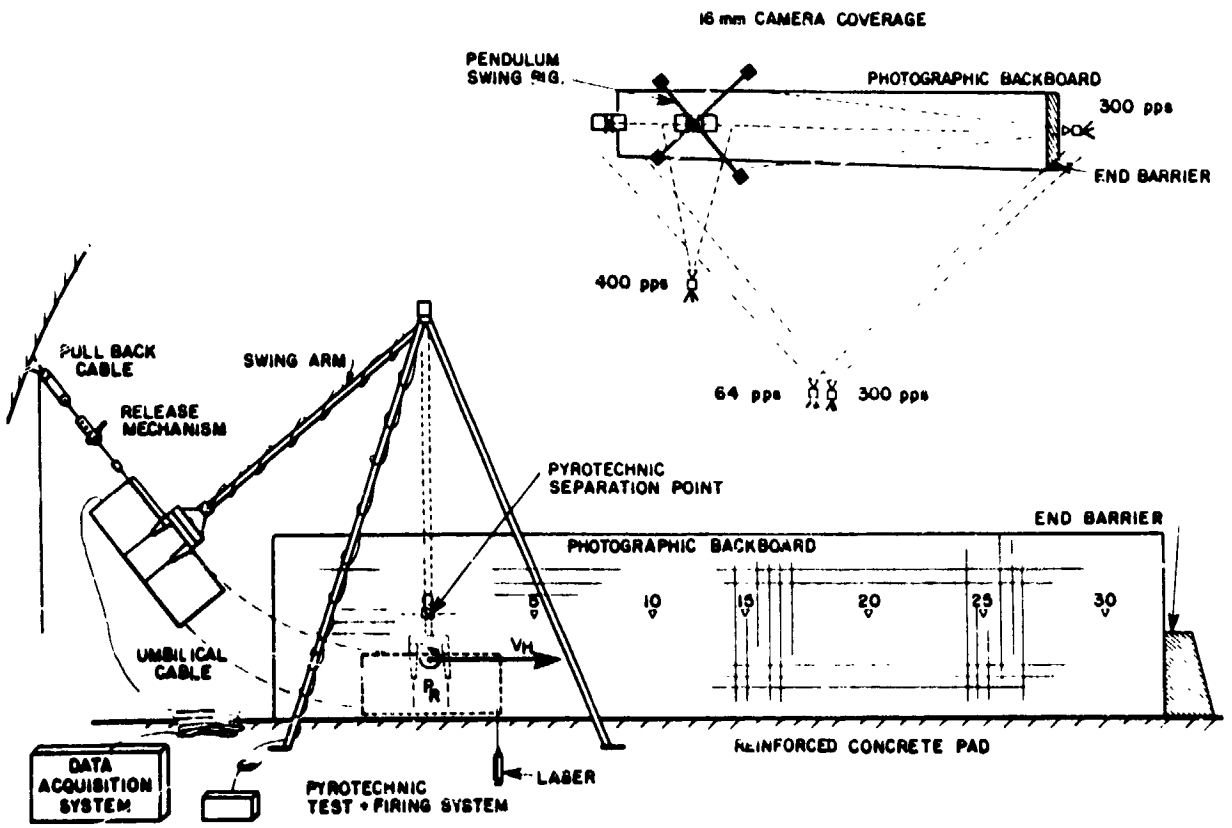

Figure 6. Schematic of pendulum gantry for free-flight tests.

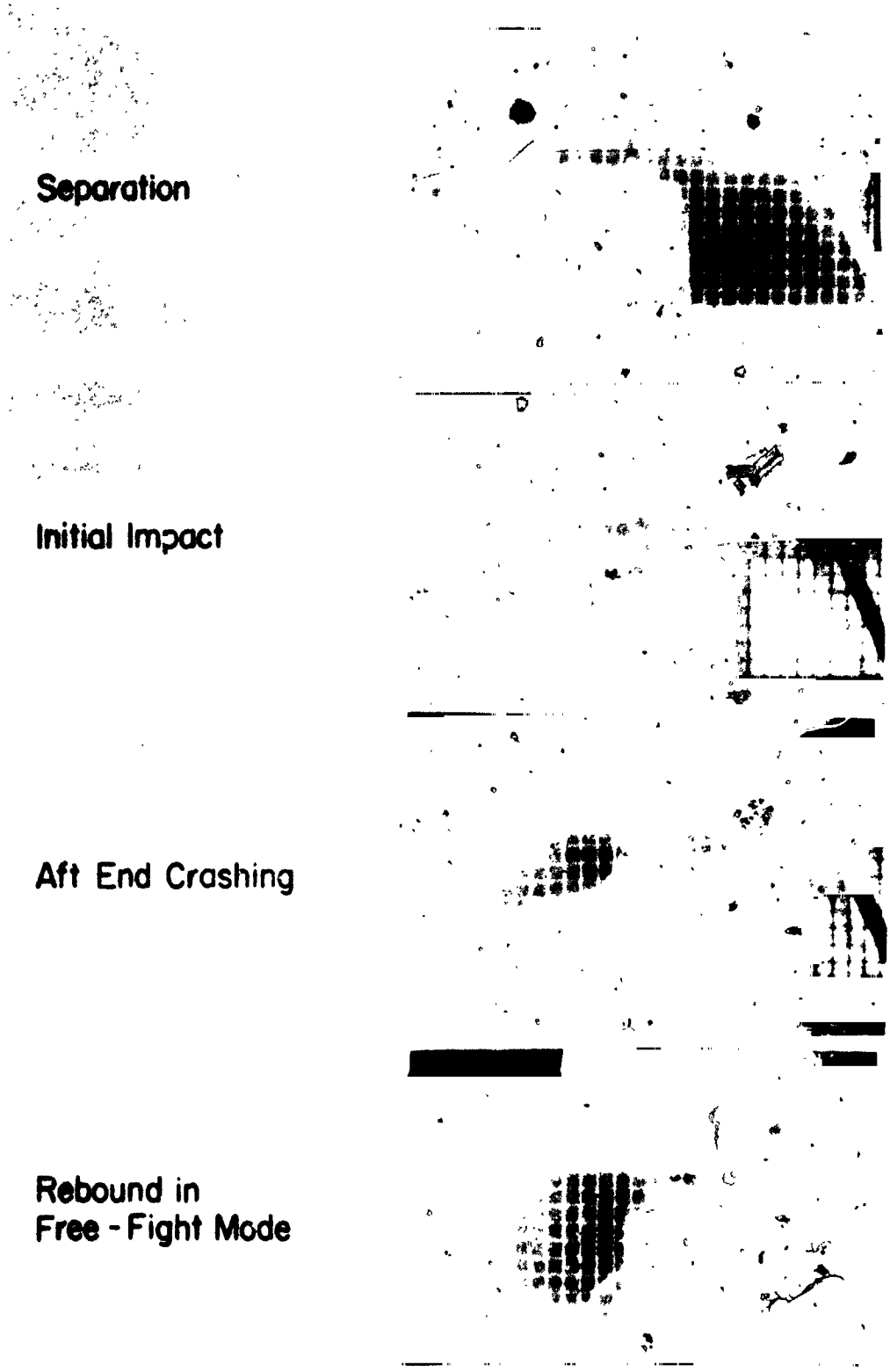

Figure 7. Selected high speed photographs of initial impact phase during free-flight test.

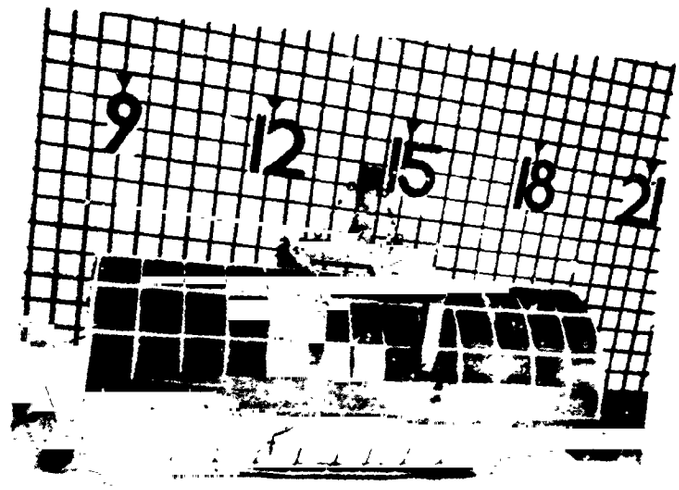

Figure 8. Post-crash side view of fuselage after free-flight test.

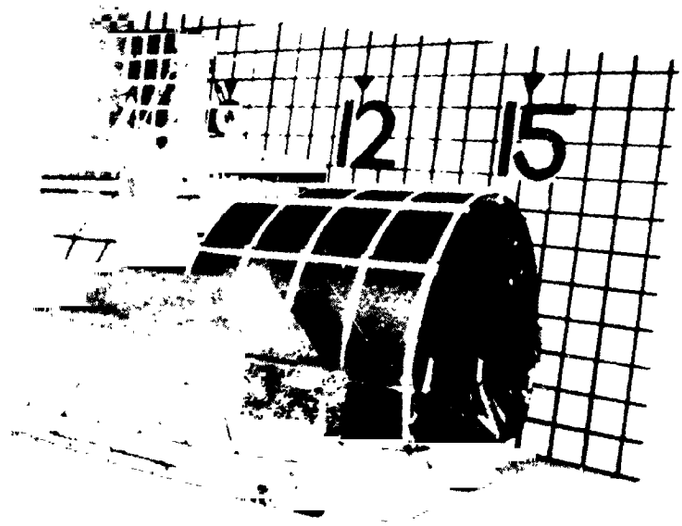

Figure 9. Post-crash end view of fuselage after free-flight test.

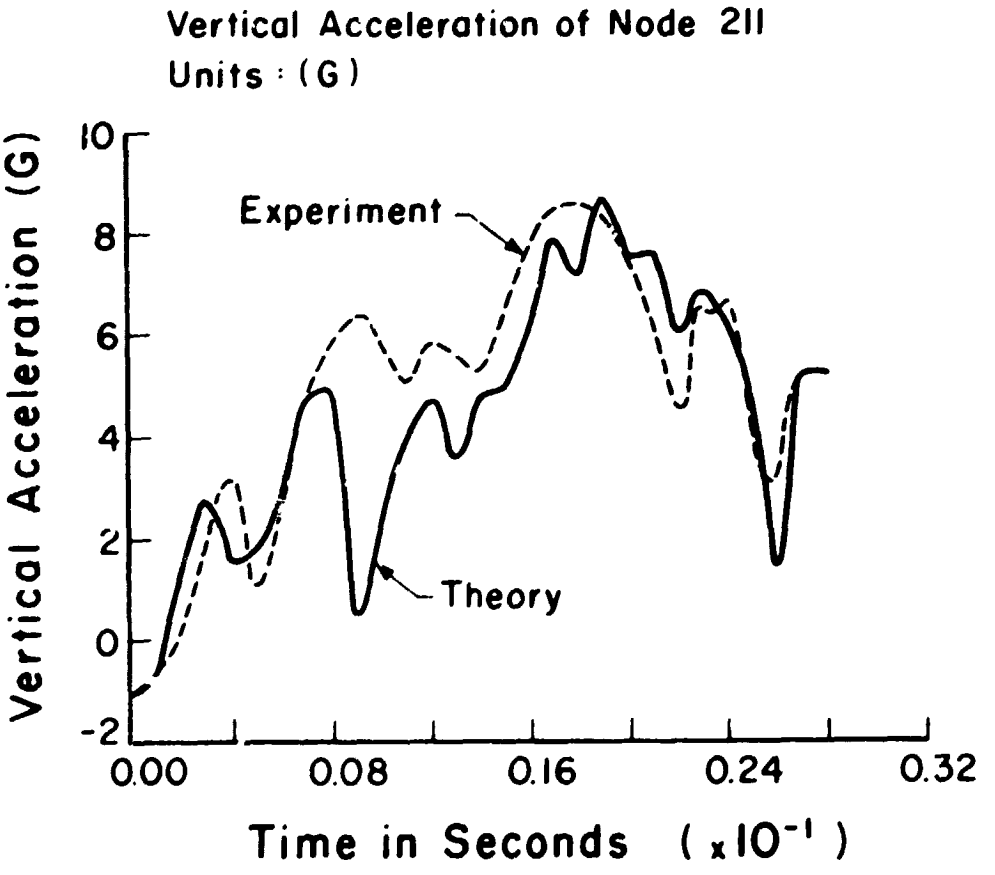

Figure 10. Level impact acceleration from CFE model (wing-load) V_o = 0.88 m s^{-1}.

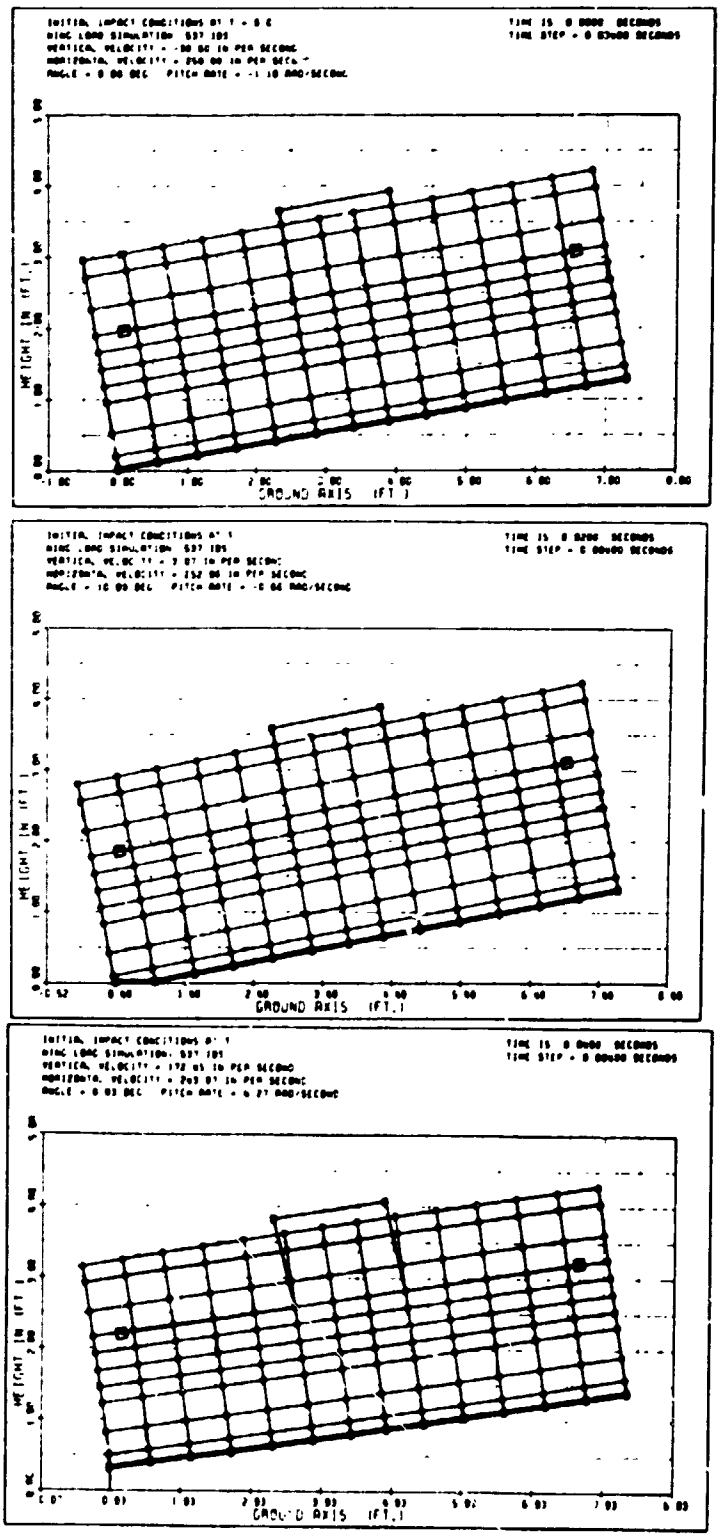

Figure 11. Selected computer graphics of initial free-flight impact phase.

ANALYSIS OF A TRANSPORT FUSELAGE SECTION DROP TEST

E. L. Fasanella
Kentron International, Inc., Hampton, Va.

R. J. Hayduk and M. P. Robinson
NASA Langley Research Center, Hampton, Va.

E. Widmayer
Boeing Commercial Airplane Company, Seattle, Wa.

SUMMARY

Transport fuselage section drop tests have provided useful information about the crash behavior of metal aircraft in preparation for a full-scale Boeing airplane Controlled Impact Demonstration (CID). The fuselage sections have also provided an operational test environment for the data acquisition system designed for the CID test, and data for analysis and correlation with the DYCAST nonlinear finite-element program.

The correlation of the DYCAST section model predictions was quite good for the total fuselage crushing deflection (22 - 24 inches predicted versus 24 - 26 inches measured), floor deformation, and accelerations for the floor and fuselage. The DYCAST seat and occupant model was adequate to approximate dynamic loading to the floor, but a more sophisticated model would be required for good correlation with dummy accelerations. Although a full-section model using only finite elements for the subfloor was desirable, constraints of time and computer resources limited the finite-element subfloor model to a two-frame model. Results from the two-frame model indicate that DYCAST can provide excellent correlation with experimental crash behavior of fuselage structure with a minimum of empirical force-deflection data representing structure in the analytical model.

INTRODUCTION

The FAA and NASA will conduct a full-scale air-to-surface impact-survivable Controlled Impact Demonstration (CID) (see figure 1) with a remotely piloted Boeing 720 aircraft at NASA's Dryden Flight Research Facility. The principal purposes of the impact demonstration are

. to verify that antimisting fuel can preclude ignition of the airborne fuel mist or suppress the ignited fireball growth rate and demonstrate an operational fuel/propulsion system capability; and

. to acquire metal structural baseline data to better understand transport crash behavior and to permit comparisons with any future composite aircraft structure crash data

A series of three transport fuselage section drop tests were performed at the Impact Dynamics Research Facility of NASA Langley Research Center, Hampton, Virginia, as part of the joint NASA/FAA Full-Scale Transport Controlled Impact Demonstration program (Reference 1). The sections were

from Boeing 707 aircraft fuselages (figure 2) and thus are representative of modern, all-metal aircraft fuselage construction.

The fuselage section drop tests were performed to provide structural crush data for the nonlinear subfloor springs of a finite-element beam and nonlinear-spring model being used to predict the overall crash impact behavior of the Boeing 720 aircraft. The drop tests were also used for the data acquisition system and the photographic system built by Langley Research Center for the Controlled Impact Demonstration. Additionally, the tests generated structural response data for comparison with the DYCAST computer program predictions.

This paper describes the first fuselage section drop test, some capabilities of the DYCAST computer program, the DYCAST finite-element models, and comparisons of experimental and analytical results from the research effort.

TEST SPECIMEN AND APPARATUS

Forward Fuselage Section

In figure 3 the forward fuselage section is shown suspended in the Vertical Test Apparatus (VTA) of the Impact Dynamics Research Facility at the NASA Langley Research Center. Because of the difficulty in locating a Boeing 720, nearly identical (structurally) 707 fuselage sections were used for test specimens. The 12-foot-long fuselage section, cut ten inches forward of Body Station (BS) 600 and ten inches aft of BS 600J, weighed 5051 pounds including the seats, anthropomorphic dummies, and instrumentation (fig. 2) (Ref. 2). The structural beams and paneling of the lower bulkhead, closing off the cargo bay at BS 600J, were removed to make the subfloor structural strength more uniform lengthwise in the section. As shown in figure 3, the fuselage section is open on both ends. Since the interactions of this fuselage section with the remainder of the airplane structure are very difficult to predict and simulate, a simple end restraint tension cable system was used to provide outward radial restraint only.

Figure 4 presents the floor layout of seats, instrumentation junction box, simulated power distribution pallet (for proper ballast) and a battery for camera power. Seats were located on the test section approximately as anticipated on the Controlled Impact Demonstration. Eight 50th percentile, 165 lb, Part 572 anthropomorphic dummies (Ref. 3), restrained with standard lap belts, were seated among the five triple seats as shown in figure 4. All dummies had vertical (aligned with the spine) and longitudinal (fore-and-aft perpendicular to the spine) accelerometers in their heads and pelvises. An uninstrumented 95th percentile dummy (195 lb), restrained with a standard lap belt, occupied the inboard location of seat F. Ballast (see fig. 5) was used to load the remaining six occupant locations. Table I gives the weight and coordinates of all articles and ballast onboard the section. The origin of the coordinate system (0,0,0) was arbitrarily chosen to be at BS 600F, centered at floor level (see fig. 4).

NASA Langley VTA Facility

The Vertical Test Apparatus (VTA) (fig. 3) was used to provide a stable guide mechanism for the vertical impact test of the transport section. The VTA, located at the northwest leg of the gantry structure at the Impact Dynamics Research Facility (Ref. 4), is 70 ft high and consists of a 7 1/2 ton hoist platform on two support columns. Each column has rails to guide the vertical motion of a lift frame to which a specimen can be attached for drop testing. The specimen impacts a steel-reinforced concrete pad at the bottom of the VTA, whereas, the support frame is decelerated by impacting two shock absorbers. An electrically activated quick-release hook is used to lift the support frame and specimen to the desired drop height.

For the transport section test, the section was suspended by a series of cables with turnbuckles to allow adjustment of the cable lengths and to control the impact attitude. The vertical impact velocity was 20 ft/sec and the impact attitude was 0 degree pitch, yaw, and roll.

INSTRUMENTATION AND DATA REDUCTION

Figures 6 and 7 show the locations and the positive axis directions of the DC accelerometers used on the aircraft structure to obtain continuous acceleration histories during the dynamic drop test. All data were transmitted to a tape recorder through an umbilical cable that was hard-wired to the data acquisition system. Reference 5 contains a complete set of the experimental data traces from the drop test.

Both the experimental data and the analytical DYCAST results show a large degree of high-frequency, high-amplitude acceleration data. In order to determine the relevant low-frequency accelerations that contribute to velocity change and large deflections, low pass filtering is necessary. To make reasonable comparisons between the experimental data and analytical calculations, the same digital filter program was used to filter both the analytical and experimental results. The filter program uses an inverse Fourier transform of the filter gain function in the frequency domain to transform to a smoothing function in the time domain (Ref. 6). Figure 8 presents the actual and ideal filter response for the 20-Hz filter. The finite transform distorts from the ideal as shown.

The analog signals were filtered with a 600-Hz low pass filter during recording and were subsequently digitized at 4000 samples per second. The digitized accelerometer data for the dummy head, dummy pelvis, and airplane structure were filtered at 600 Hz, 180 Hz, and 20 Hz, respectively, with a low pass digital filter.

DYCAST ANALYTICAL PROGRAM

DYCAST Features

DYCAST is a nonlinear structural dynamic finite-element computer code developed by Grumman Aerospace Corporation with principal support from NASA and the FAA as part of the combined NASA/FAA program for aircraft

crashworthiness. The major DYCAST features are described briefly in the following paragraphs (Ref. 7).

The basic element library consists of: (1) stringers with axial stiffness only; (2) beams with axial, two shear, torsional, and two bending stiffnesses; (3) isotropic and orthotropic membrane skin triangles with in-plane normal and shear stiffnesses; and, (4) isotropic plate-bending triangles with membrane and out-of-plane bending stiffnesses.

The nonlinear spring element provides axial stiffness with a user-specified force-displacement curve. It can be used as either elastic or dissipative, and as a gap element such as a ground-contact spring. The changing stiffnesses in the structure are accounted for by plasticity (material nonlinearity) and very large deflections (geometric nonlinearities). Material nonlinearities are accommodated by one of three options: (1) elastic-perfectly plastic, (2) elastic-linear hardening plastic, or (3) elastic-nonlinear hardening plastic of the Ramberg-Osgood type. The second option has been used exclusively for this modeling effort. Geometric nonlinearities are handled in an updated Lagrangian formulation by reforming the structure into its deformed shape after small time increments while accumulating deformations, strains, and forces. The nonlinearities due to combined loadings (such as beam-column effects) are maintained, and the stiffness variations due to structural failures are computed. The failure option is imposed automatically whenever a material failure strain criterion is met, or manually by the user at a restart.

The problem size is only limited by the computer resources needed to invert the stiffness matrix at least twice for each time step. A restart feature permits a large problem, or one of long event duration, to be run as a sequence of smaller time segments. This minimizes dedication of computer facilities, allows the user to examine the response as it progresses, and permits termination of the simulation if critical structural damage occurs.

The numerical time integrators available are fixed-step central difference, modified Adams, Newmark-beta, and Wilson-theta. The last three have a variable time step capability, which is controlled internally by a solution convergence error measure. Thus, the size of the time step is increased and decreased as required during the simulation. The Newmark-beta time integrator was used exclusively for the models presented in this paper.

Two postprocessors provide the user with output data graphics capability. GRAFIX plots histories of displacement, velocity, and acceleration at chosen nodes. SATLIT will generate time-sequenced drawings of the deforming structure from any viewing angle.

Modeling Considerations

The fuselage section mass is distributed 37% to the fuselage shell, 52% to the seat-occupant simulation, and 11% to equipment and ballast. Since 52% of the test specimen mass is located in seats, the anthropomorphic dummy response should be closely approximated. Furthermore, plastic deformation of the seat structures during the impact may alter the overall section response and the damage to the floor system. However, to accurately simulate the dynamic response of the anthropomorphic dummies and the effective mass at the floor track requires capability not currently available in DYCAST. As a first approach, the seat-occupant mass for each triple seat was distributed between the floor and the seat pan with the masses assigned to end nodes of the seat legs.

The seat-occupant and equipment mass is asymmetrically distributed throughout the section. This absence of symmetry requires a full seven-frame model to accurately represent the complete test section.

Various structural failure mechanisms must be accommodated analytically for accurate modeling of the structural behavior. For example, the lower lobe of the fuselage section resists vertical loading through deformation of the frames, whereas the longitudinal stringers and skin offer little resistance to crush. The lower frames could be expected to fail in bending and/or in shear and to develop points of inflection and "snap through" due to the ground reaction forces. The ground reaction might also impose high transverse shear loads on the frame cross sections. In addition, plastic hinges might develop in the frames between the floor level and the fuselage bottom. If the frames do not rupture while undergoing these types of deformations, large impulsive moments would be applied to the floor and the upper frame. Thus the analytical formulation needs to provide for many basic failure mechanisms.

Additionally, it often is desirable to include certain details in a finite-element model that could influence expected permanent deformations. For example, the fuselage floor consists of inch-deep built-up beams having T-section caps and stiffener reinforced webs. Where the seat tracks (which resemble an I-section) cross a floor beam, the lower part of the "I" has been beveled to the upper flange to straddle the floor beam. Some detailed modeling of this region would be desirable. However, for the current level of crash analysis development and computer resources, it is necessary to judiciously limit the number of degrees of freedom (nodes) and the number of structural elements in the crash model. As the degrees of freedom increase, model debugging, verification of the dynamic behavior, and interpretation of the results become increasingly difficult. Consequently, it is desirable to understand the behavior of less complicated components prior to formulation of the complete structural model.

BOEING STUDIES

One such study which utilized the component analysis approach has been undertaken by Boeing Commercial Airplane Company, Seattle, Washington. Under NASA contract NAS1-16076, Boeing has developed DYCAST models to simulate the fuselage section drop tests. A typical fuselage frame subjected to ground impact and a typical seat frame subjected to vertical loading were modeled. The results of the component studies were incorporated into a more general model of the fuselage section.

Single-Frame Model

The single-frame half model took advantage of symmetry about the fuselage center line. The frame was constrained to in-plane deflections with boundary conditions applied at crown, floor, and keel. The half-frame model had 62 nodes, 102 elements and 103 degrees of freedom. Efforts were made to model the variations of the frame cross sections from crown to keel (figure 9). The DYCAST offset beam capability allowed proper behavior of multiple beams connecting two nodes. Individual components could be monitored as

they experienced plasticity and ruptured. The frame model gave an assessment of the significant dynamic response of the floor and upper lobe, and identified problems and solutions with snap-through of the lower frame and shear failure of the frame web in the vicinity of the lightening holes near the fuselage bottom.

On the basis of frame solutions, an approximation of the lower fuselage crushing characteristics was obtained which permitted simplification of the fuselage section model. Each half, lower frame below the floor level could be represented as a vertical spring having known force-deflection characteristics, thus replacing many finite elements with a single nonlinear spring element.

Seat Model

The transport seat structure illustrated in figure 10 was a reinforced tubular aluminum frame consisting of three welded leg trusses connected to each floor track, two transverse tubes supporting four seat cross-bearers that carry loads into the leg trusses, and three seat pans that load the cross-bearers. As shown in figure 10, the triple seat is not centered on the leg trusses. This results in unequal vertical loading of the inboard and outboard leg trusses. Further, the inboard and outboard seats overhang the leg trusses which introduce bending moments over the leg yoke attachments. Depending on the joint fixity at the leg yokes, these bending moments may be introduced into the leg frames causing the frame to resist as a beam-column or as a simple column element.

A seat model, developed for the static vertical load condition, contained 36 nodes, 35 beam elements and 164 degrees of freedom. Using full fixity resulted in a collapse load of 4922 pounds for the triple seat. The aft legs in each truss developed plastic hinges at their mid points and buckled out of plane. In contrast, in tests conducted at NASA Langley Research Center, the seat trusses carried in excess of 12000 pounds applied vertically at the leg yokes. The 2.4 factor on vertical loads suggests a strong sensitivity to end fixity.

DYCAST Full-Section Model

Using the single frame and seat model results, a simplified DYCAST full-section model (figure 11) of the seven frames, floor beam-seat track structure, and seat-occupant with asymmetric mass distribution was formulated. The model had 106 nodes, 156 elements and 422 degrees of freedom. Nonlinear crush springs were used to represent the lower fuselage structure and the seat with anthropomorphic dummies. A beam framework modeled the upper fuselage. For simplicity, the seat springs and dummy masses were suspended below the floor level. The seat and occupant model in the full-section model used 4 springs and 4 masses that were uncoupled.

The full transport section model was used to develop transverse crush characteristics for the soft fuselage areas for the Controlled Impact Demonstration model. These characteristics were adjusted to account for failure events observed in the frame analysis and to match the total dynamic deflection of the test section.

LANGLEY RESEARCH CENTER STUDIES

Two-Frame DYCAST Model

In addition to the analytical studies by Boeing under contract NAS1-16076, a full two-frame model with sufficient detail to model the floor, two seats with lumped mass occupants, and the fuselage structure without using nonlinear springs (except for the seat and ground properties) was formulated at the Langley Research Center for research purposes. Although symmetry was lacking for the full section, two forward frames had two seats located symmetrically about the x-z plane. Thus a symmetric, two-frame, half model (which executed in core on the computer) provided results comparable to the full two-frame model and therefore was used for computations on the section.

The finite-element full two-frame model is shown schematically in figure 12. Stiff ground springs simulated the concrete pad impact surface. Each frame of the lower fuselage below the floor was modeled using eight beam elements. The floor and seat rails were modeled using appropriate beam elements. The upper fuselage structure above the floor (not expected to deform plastically) was modeled in much less detail to keep the model as small as possible. The triple seat-occupant model consisted of 4 lumped masses connected by horizontal stringer elements supported by 4 nonlinear springs representing the vertical legs. The force deflection curves were based on an experimentally determined maximum vertical seat failure load of 12,000 pounds. The mass of the three occupants was distributed using a 2 to 1 ratio with the inboard legs supporting two occupants and the outboard seat legs supporting only one occupant due to the asymmetry of the seat pan with respect to the legs.

The smaller two-frame symmetric half model (right half side of section in figure 12) consisted of 16 lumped masses, 32 beams, 4 stringers, 6 ground springs, 4 seat-occupant springs, and a total of 105 degrees of freedom. To simulate end constraints and strengthen the section, motion was not allowed in the fore-and-aft (x-axis) direction. Initially, the time step was allowed to vary, but was later held constant to 250 microseconds to correspond to the sample rate (4000 per second) used to digitize the experimental accelerations. Consequently, the same digital low pass filter used to filter the experimental data could be used to filter the DYCAST calculated accelerations without requiring an interpolation algorithm before filtering. The 250 microsecond time step was conservative for this problem compared to a minimum time step of 500 microseconds when a variable time step was allowed. To run 901 constant time increments (.225 sec total) required 1620 CPU seconds on a CDC Cyber 175 with a maximum field length of 303 K.

Nonlinear material properties used for the critical subfloor aluminum frame beam elements were elastic-plastic with a small amount of linear strain hardening. The yield stress initially chosen was 83,000 psi with a failure strain level of 11 percent.

RESULTS AND DISCUSSION

Figures 13 through 14 present photographs which illustrate the structural behavior/damage experienced by the fuselage section during the

vertical impact test at 20 ft/s. Figures 15 and 16 present DYCAST predictions of the fuselage behavior determined during the analytical studies and figures 17 to 22 present a comparison of typical experimental and analytical accelerations and displacement of the fuselage.

Gross Structural Damage

As shown in figure 13, gross structural damage to the fuselage was primarily confined to the lower fuselage below the floor level. All seven frames ruptured near the bottom contact point. The total post-test crushing distance measured from the floor level to the impact surface varied from a maximum of 22-23 inches for the forward end (frame 600) to 18-19 inches for the rearward end (frame 600I). Motion picture analysis of the forward frame at body station 600 indicated a maximum deflection of approximately 26 inches occurred at 0.21 seconds after impact. Plastic hinges (see figure 14) formed in each frame along both sides of the fuselage. The vertical acceleration histories showed two distinct peaks. The first peak corresponded to the deceleration at contact. When the bottom frames ruptured, the load was relieved and the acceleration decreased. The second peak occurred at the time the frame hinge point impacted the concrete.

Floor Deformation

The floor was surveyed post-test to determine the extent of permanent deformation. The right side (viewed from a passenger's reference) tracks, which had 3 triple seats, showed the most permanent deformation. The maximum downward plastic deformation, measured post-test, was slightly less than 1/32 inch. This occurred between seats D and F (see figure 23).

DYCAST Analytical Results

Analytical predictions from the DYCAST program for the fuselage section models are presented in figures 15 through 22. The initial two-frame model (subfloor frames yield stress of 83,000 psi and 11 percent failure strain) predicted crushing of the lower fuselage of approximately 16 inches as compared to a measured 24 inches. Since these initial yield stress and failure strain values gave less crushing than the experiment, the yield stress was reduced to 50,000 psi and the failure strain was varied to assess the effect on responses. The effects of varying the failure strains of the frames for the two-frame model are shown in figures 15 and 16. For a failure strain of 8%, good correlation with experiment was achieved (see figure 15). When the failure strain was reduced to 5%, premature failure of the frames at the contact point occurred and excessive deformation of over 35 inches was predicted (figure 16). Consequently, a yield stress of 50,000 psi and a failure strain of 8% were used in the two-frame model for all comparisons with experimental data in figures 17 - 22.

Fuselage Crush.-The seven-frame full-section model (nonlinear springs represented the lower frames) and the two-frame model (beam elements with 8 % failure strain represented the lower frames) predicted similar total

crush for a common lower fuselage region. For both models figure 17 shows the displacement of the floor (after impact) at body station 600. The full model predicted approximately 24 inches of displacement (crush), whereas the two-frame model predicted 22 inches of crush. An experimental vertical acceleration trace was integrated once to obtain the velocity curve and the resulting velocity curve was then integrated to give the experimental displacement curve shown in figure 17 for comparison with the predicted crush.

Floor/Fuselage Intersection Accelerations.-Figure 18 compares the predicted and measured vertical accelerations for node 31 located at the intersection of the floor and fuselage wall. The acceleration for the two DYCAST models is in good agreement with the experimental data. The full section model gave reasonably good results except for times greater than .15 seconds where a high acceleration was predicted. Although no study was made to identify the cause of the high peak acceleration, it is believed to be the result produced by a combination of the subfloor spring and seat-occupant spring characteristics.

Inboard Seat-Track Acceleration.-The vertical floor accelerations located at the inboard seat track at node 112 are shown in figure 19. The two-frame model and the experimental data compare well; however, the full-section model predictions again deviate dramatically from the experimental data starting at .12 seconds. Although the seat-occupant model is oversimplified, a comparison of the dummy response in seat location A (front left seat) is given in figure 20 which shows that the prediction for the first peak is close to the magnitude of the experimental acceleration, but the model overpredicts the amplitude of the second peak and also has a higher frequency of oscillation. The occupant representation in the full-section model underpredicted the occupant acceleration magnitude of both peaks observed in the experimental data.

Roof and Ground Contact Accelerations.-The experimental and analytical roof accelerations at node 231 are shown in figure 21. The predicted and experimental magnitudes agree quite well, but the analytical frequency response is incorrect probably due to the coarseness of the model for the upper fuselage. Finally, in figure 22, there are comparisons of the experimental and analytical two-frame accelerations at node 451 which correspond to the contact point with the concrete surface (bottom of frame 600). Only two-frame model results are given since the full model represented the lower fuselage with crush springs. As shown in figure 22 the predicted contact acceleration is higher than the experimental but overall characteristics of the response are in good agreement.

Based upon the experience gained using the analytical research models of this paper, implications are that for engineering applications, larger more complete models are required that would necessitate using larger and faster computers. Engineering models need to be detailed enough to represent the failure criteria at the element level and should be able to handle symmetric and asymmetric conditions.

CONCLUSIONS

Transport fuselage section drop tests have provided useful information about the crash behavior of metal aircraft in preparation for a full-scale Boeing airplane Controlled Impact Demonstration (CID). The fuselage sections have also provided an operational test environment for the data

acquisition system designed for the CID test, and data for analysis and correlation with the DYCAST nonlinear finite-element program.

The correlation of the DYCAST section model predictions was quite good for the total fuselage crushing deflection (22 - 24 inches predicted versus 24 - 26 inches measured), floor deformation, and accelerations for the floor and fuselage. The DYCAST seat and occupant model was adequate to approximate dynamic loading to the floor, but a more sophisticated model would be required for good correlation with dummy accelerations. Although a full-section model using only finite elements for the subfloor was desirable, constraints of time and computer resources limited the finite-element subfloor model to a two-frame model. Results from the two-frame model indicate that DYCAST can provide excellent correlation with experimental crash behavior of fuselage structure with a minimum of empirical force-deflection data representing structure in the analytical model.

REFERENCES

1. Thomson, Robert G., and Caiafa, Caesar: Designing for Aircraft Structural Crashworthiness. J. of Aircraft, Vol. 19, Number 10, Oct. 1982, pp 868-874.

2. Boeing 707-720 Reference Guide D6-40942, Boeing Commercial Airplane Company, March 1980.

3. U. S. Code of Federal Regulations, Title 49, Chapter 5, Part 572: Anthropomorphic Test Dummy. Government Printing Office, Washington, D.C., Oct. 1, 1983.

4. Vaughan, Victor L., and Alfaro-Bou, Emilio: Impact Dynamics Research Facility for Full-Scale Aircraft Crash Testing. NASA TN-D-8179, Apr [illegible]

5. Williams, M. Susan, and Hayduk, Robert J.: Vertical Drop Test of a Transport Fuselage Section Located Forward of the Wing. NASA TM-85679, August 1983.

6. Graham, R.J.: Determination and Analysis of Numerical Smoothing Weights. NASA TR-R-179, December 1963.

7. Hayduk, R.J.; Winter, R., Pitko, A.B. , and Fasanella, E.L.: Application of the Non-linear Finite Element Computer Program 'DYCAST' to Aircraft Crash Analysis. Structural Crashworthiness, Edited by N. Jones and T. Wierzbicki, Butterworth & Co. Ltd., 1983, pp 283-307.

TABLE I.- TRANSPORT SECTION TEST WEIGHT DISTRIBUTION

Item	Weight(lbs.)	X(in)	Y(in)	Z(in)
Empty weight	1870	0	0	0
Seat A: inboard	146	42	-19	-24
center	188	42	-38	-24
outboard	154	42	-57	-24
Seat B: inboard	154	42	19	-24
center	188	42	38	-24
outboard	148	42	57	-24
Seat C: inboard	187	-18	-19	-24
center	188	-18	-38	-24
outboard	187	-18	-57	-24
Seat D: inboard	154	12	19	-24
center	188	12	38	-24
outboard	187	12	57	-24
Seat F: inboard	217	-47	19	-24
center	188	-47	38	-24
outboard	146	-47	57	-24
Junction box	60	21	-36	-4
Pallet	145	-48	-36	-5
Camera 1 & mount	30	50	-31	-78
Light 1	6	54	-23	-84
Camera 2 & mount	30	50	47	-66
Light 2	6	54	38	-78
Camera 3 & mount	30	0	-42	-9
Light 3	6	14	-45	-72
Camera 4 & mount	30	0	43	-60
Light 4	6	6	44	-72
Time code box & battery	8	30	-70	-12
Battery	18	28	-55	-3
Camera timing pa[illegible]	4	10	-70	-12
Ballast	20	-65	-54	43
Ballast	20	-50	-54	43
Ball[illegible]	40	-65	-48	50
Bal[illegible]	20	-50	-48	50
Ballast	40	-65	-37	61
Ballast	40	-65	0	72

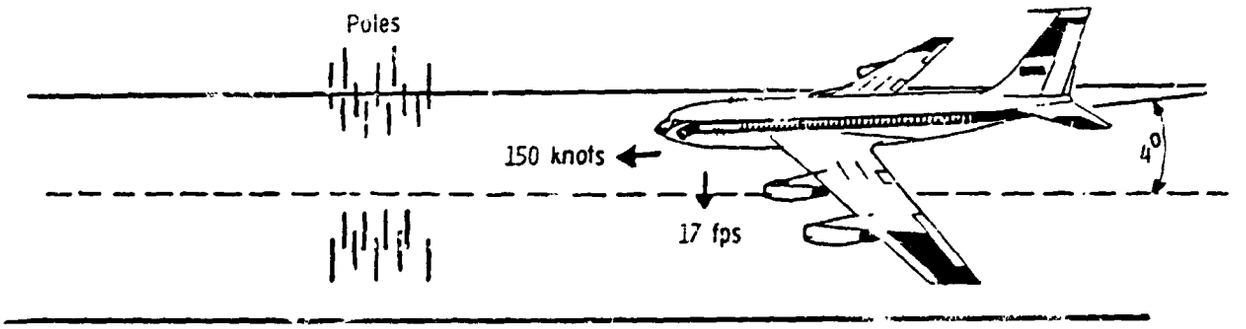

Figure 1.- Proposed controlled impact demonstration crash scenario for the remotely piloted Boeing 720.

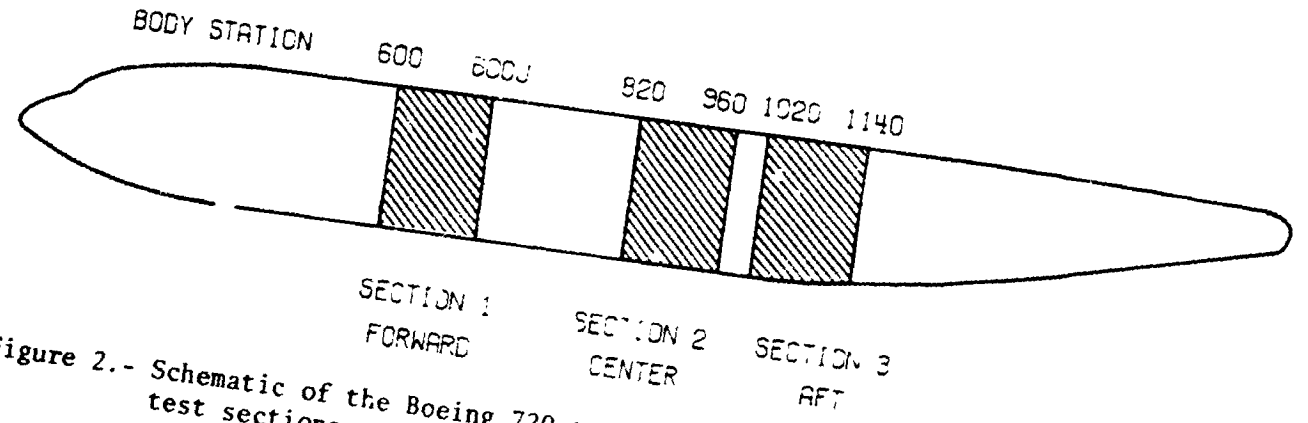

Figure 2.- Schematic of the Boeing 720 transport showing locations of three fuselage test sections.

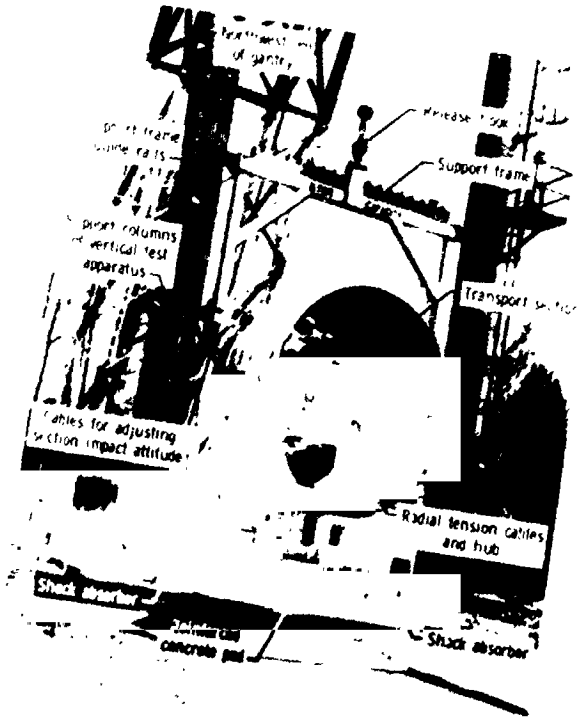

Figure 3.- Forward transport section suspended in Vertical Test Apparatus.

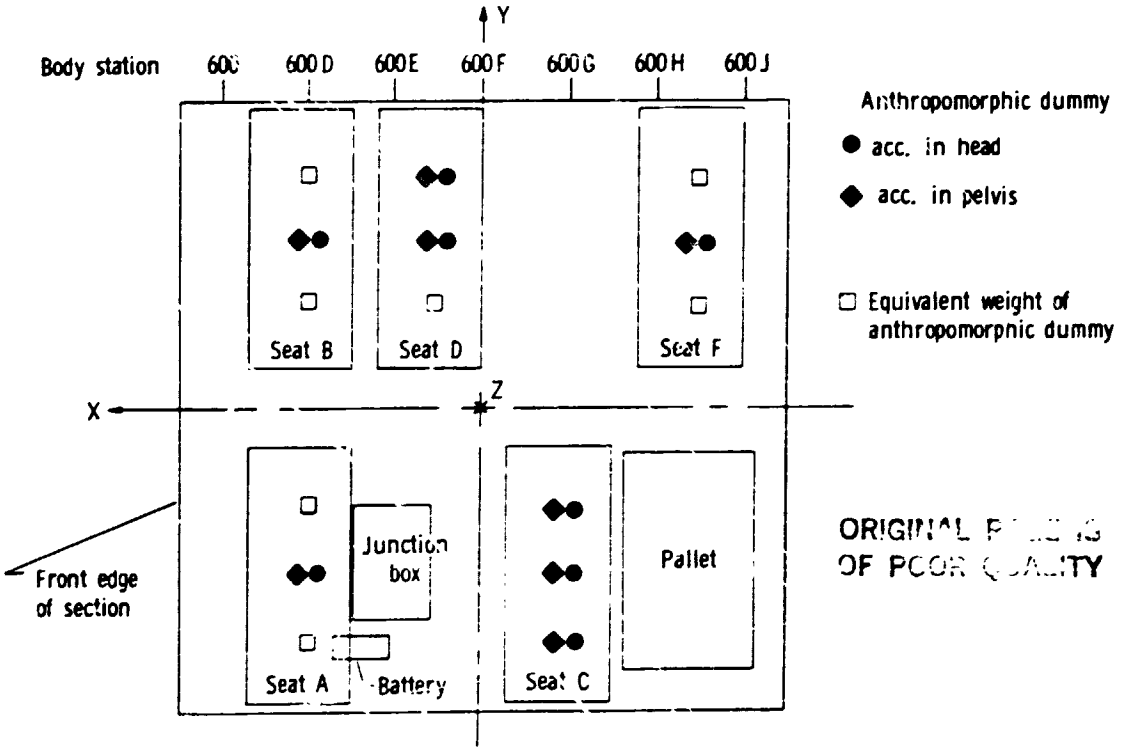

Figure 4.- Seat and dummy arrangement for the transport section test.

Figure 5.- Ballast used to load seats (not occupied by dummies).

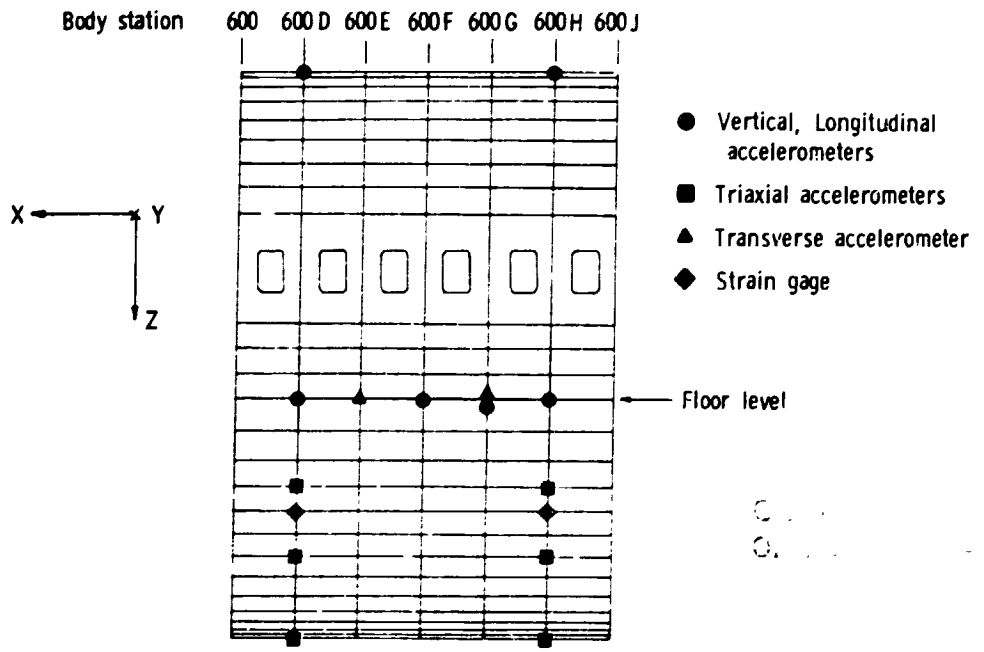

Figure 6.- Instrumentation locations for transport section test (side view).

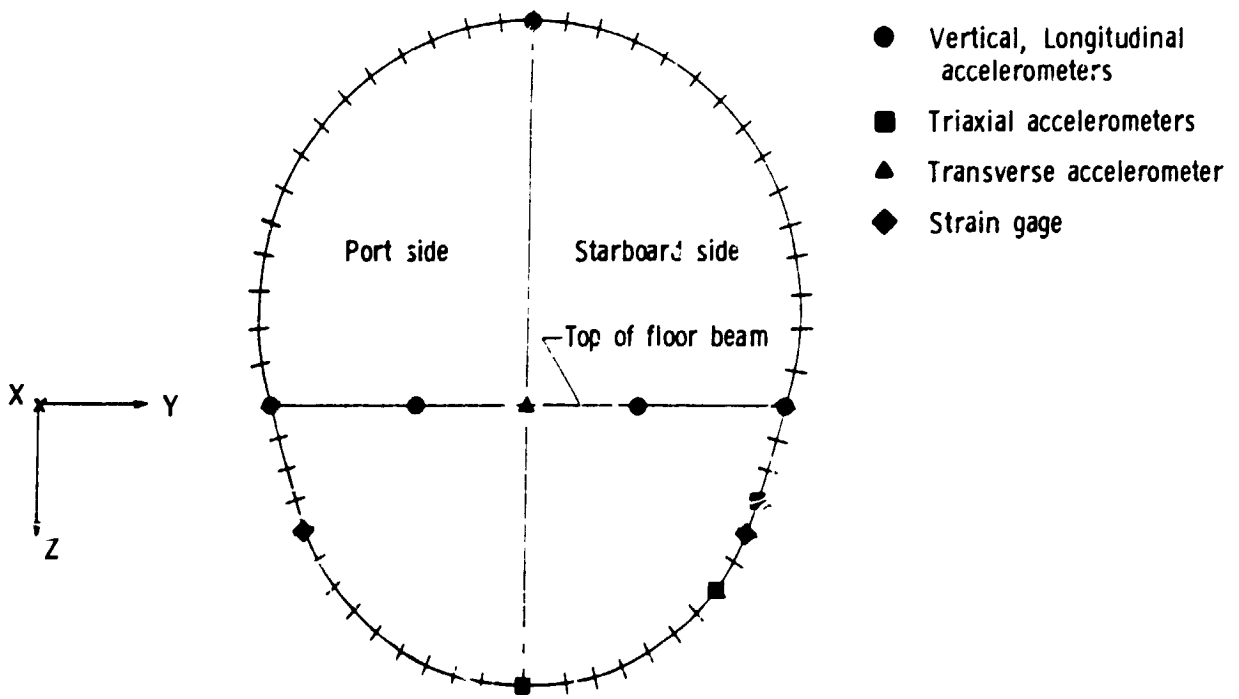

Figure 7.- Instrumentation locations for transport section test (end view).

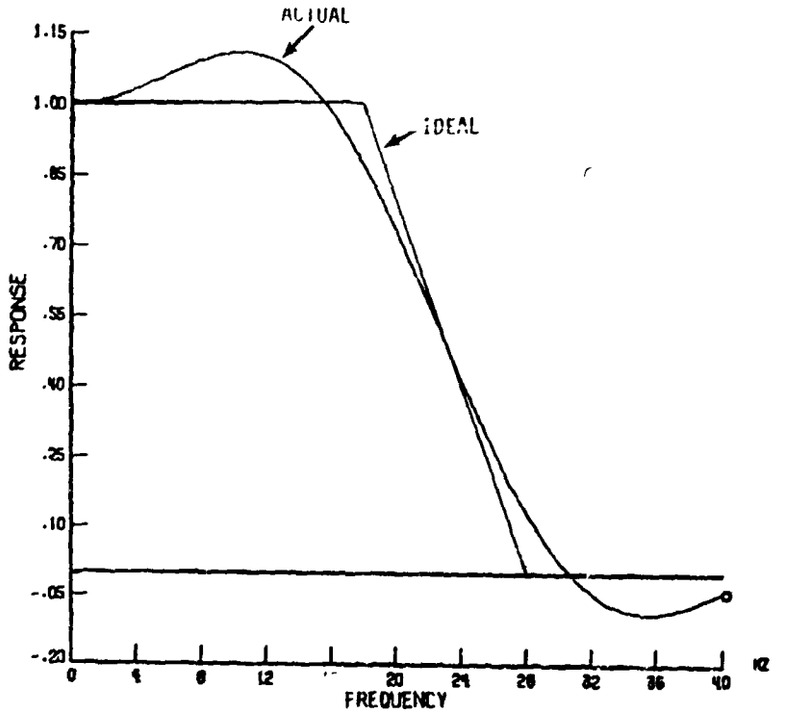

Figure 8.- Actual and ideal 20-hertz filter response.

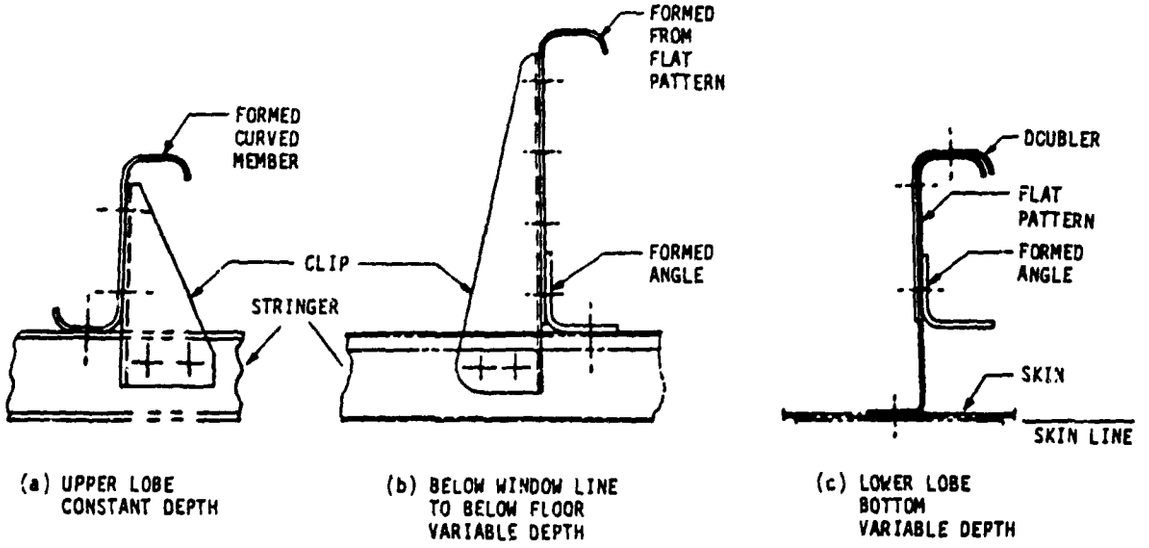

TYPICAL FRAME SECTIONS

Figure 9.- Typical frame cross sections from upper lobe to lower lobe.

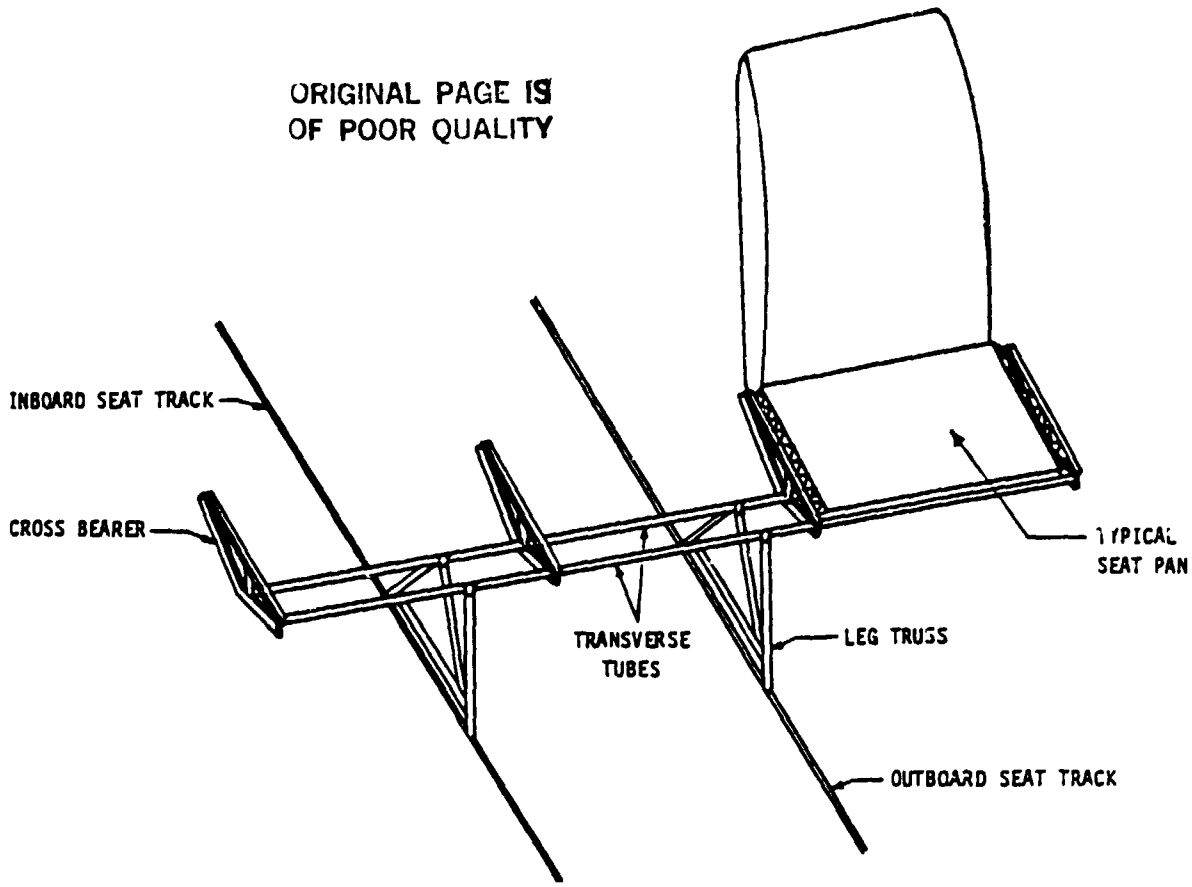

Figure 10.- Transport triple seat showing structural asymmetry (two seats removed for clarity).

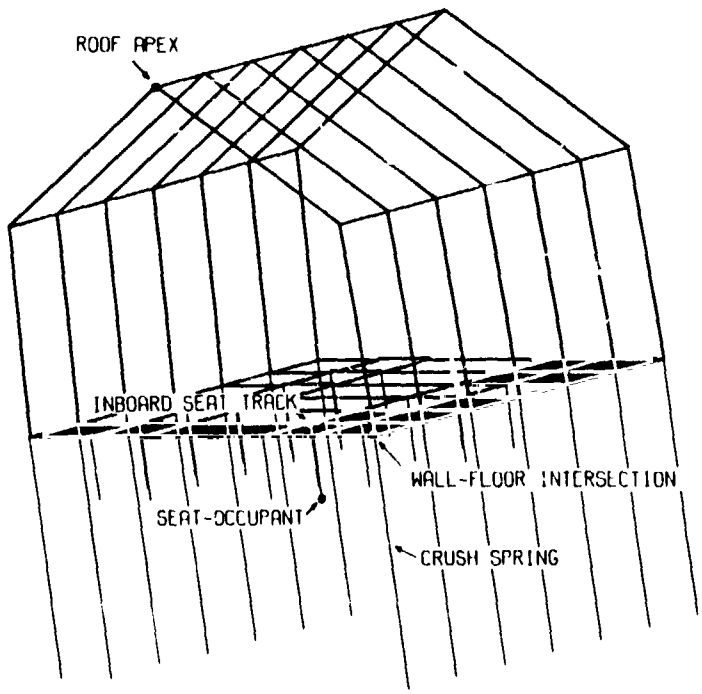

Figure 11.- Full-section model showing nodes where responses are compared.

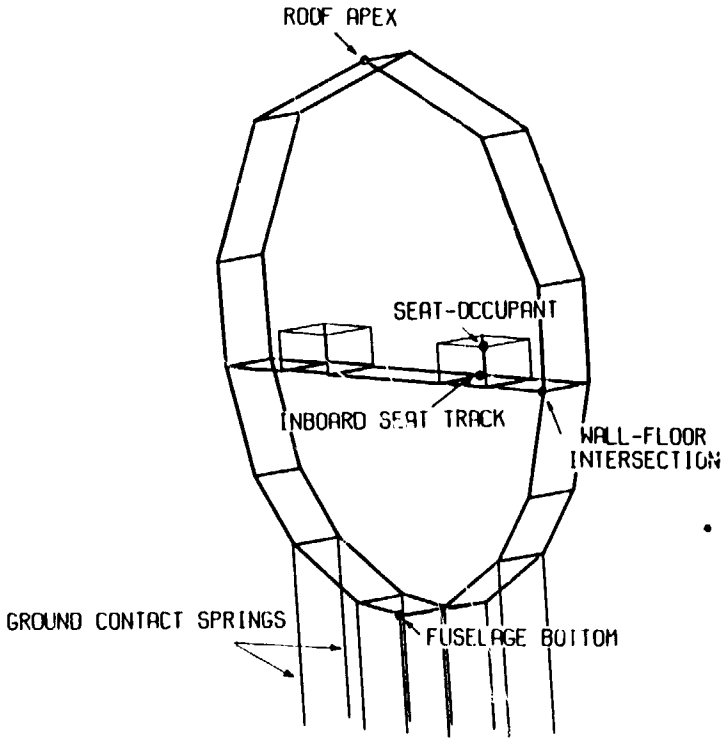

Figure 12.- Two-frame model showing nodes where responses are compared.

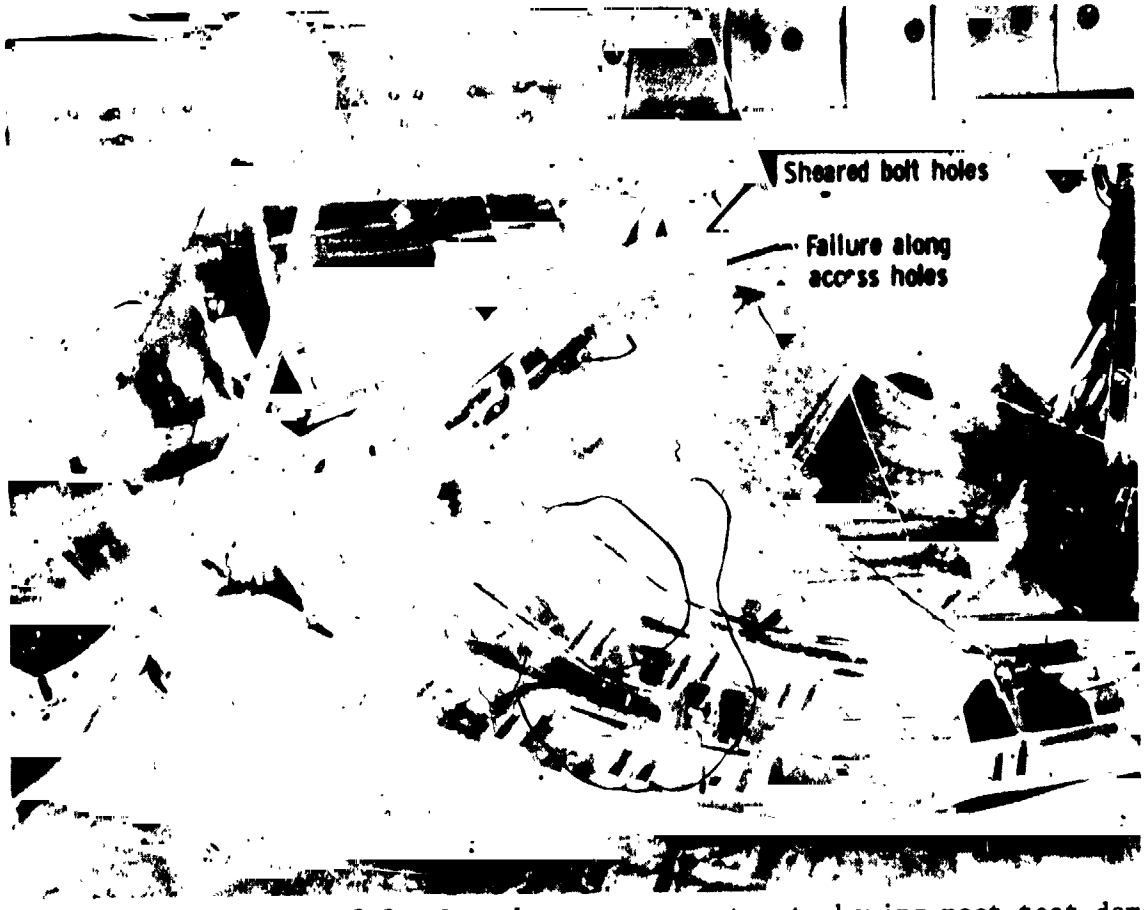

Figure 13.- Rear view of fuselage baggage compartment showing post-test damage.

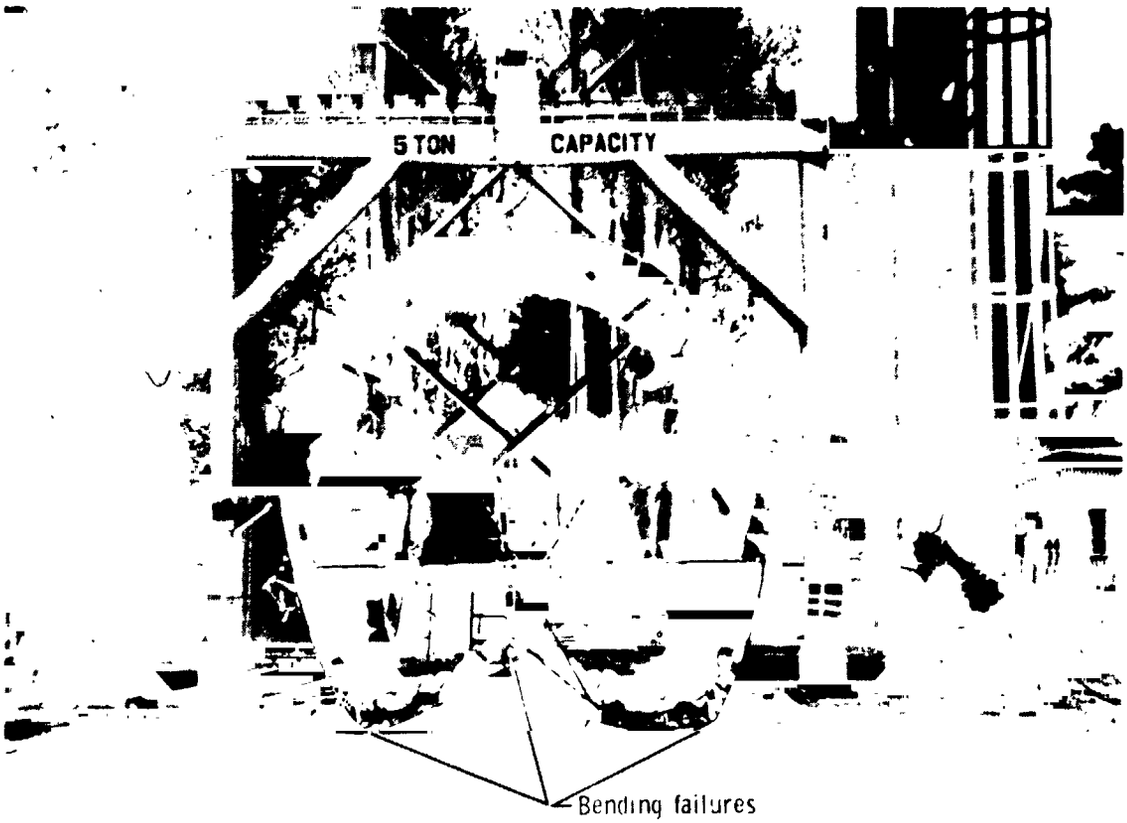

Figure 14.- Front view of fuselage section showing post-test damage.

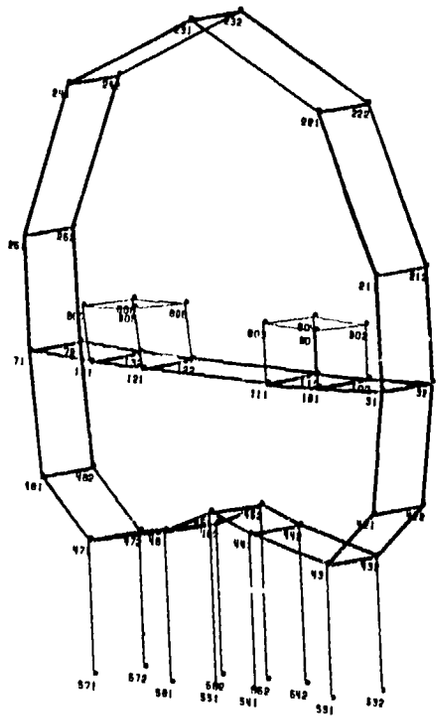

Figure 15.- Computer graphics of the two-frame model at time 0.236 seconds with a subfloor beam failure of 8 percent.

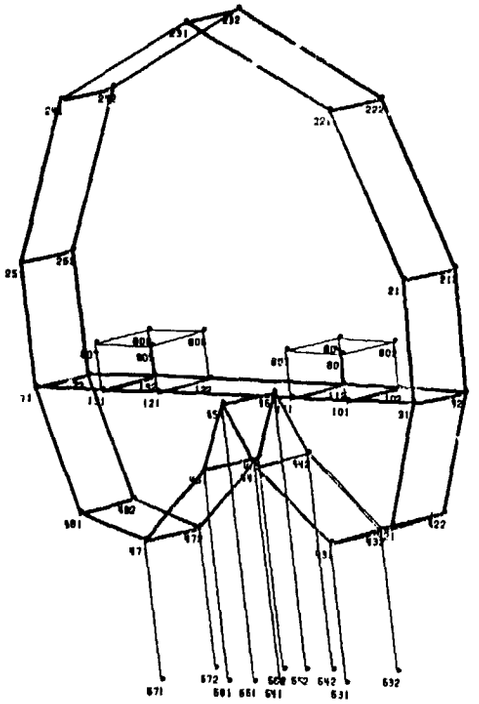

Figure 16.- Computer graphics of the two-frame model at time 0.225 seconds with a subfloor beam failure strain of 5 percent.

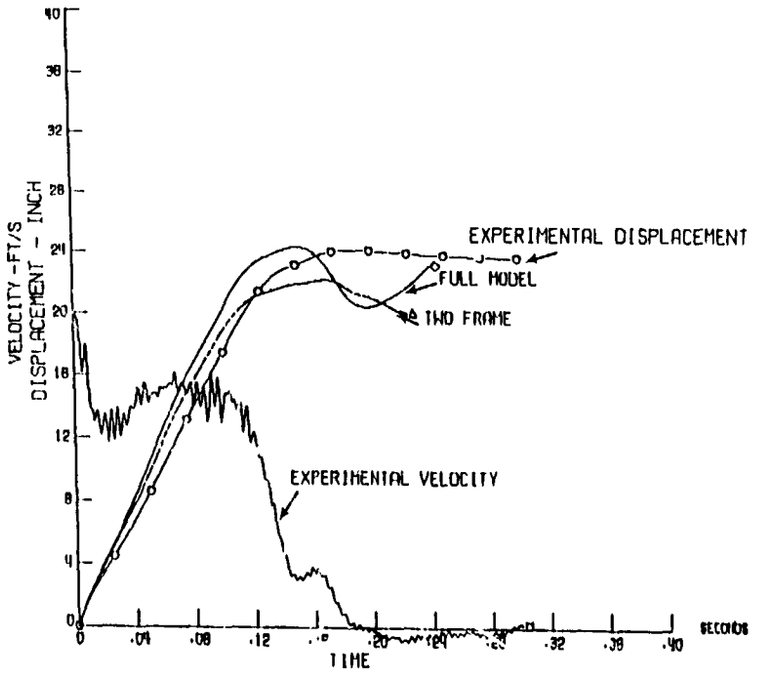

Figure 17.- Comparison of experimental floor vertical displacement of the section (from the integrated velocity trace) to the analytical models.

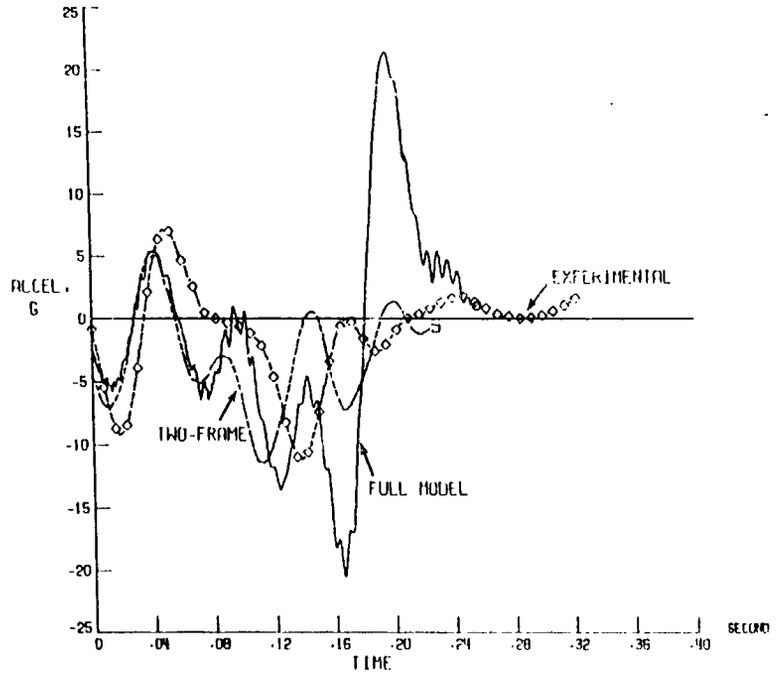

Figure 18.- Comparison of experimental and analytical section accelerations at the front, port wall-floor intersection.

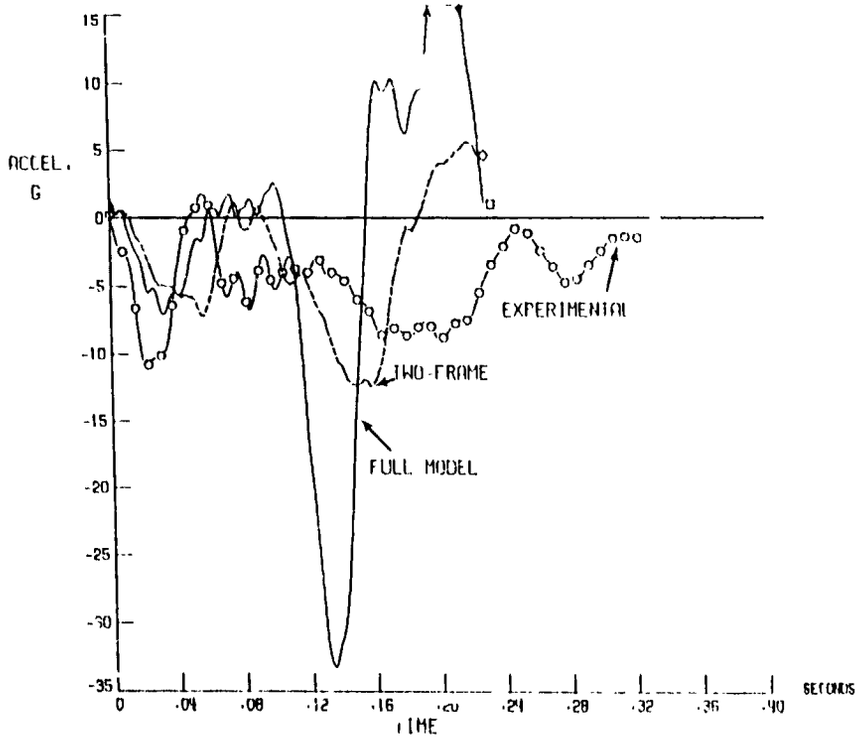

Figure 19.- Comparison of experimental and analytical vertical accelerations at the front, port, and inboard seat track.

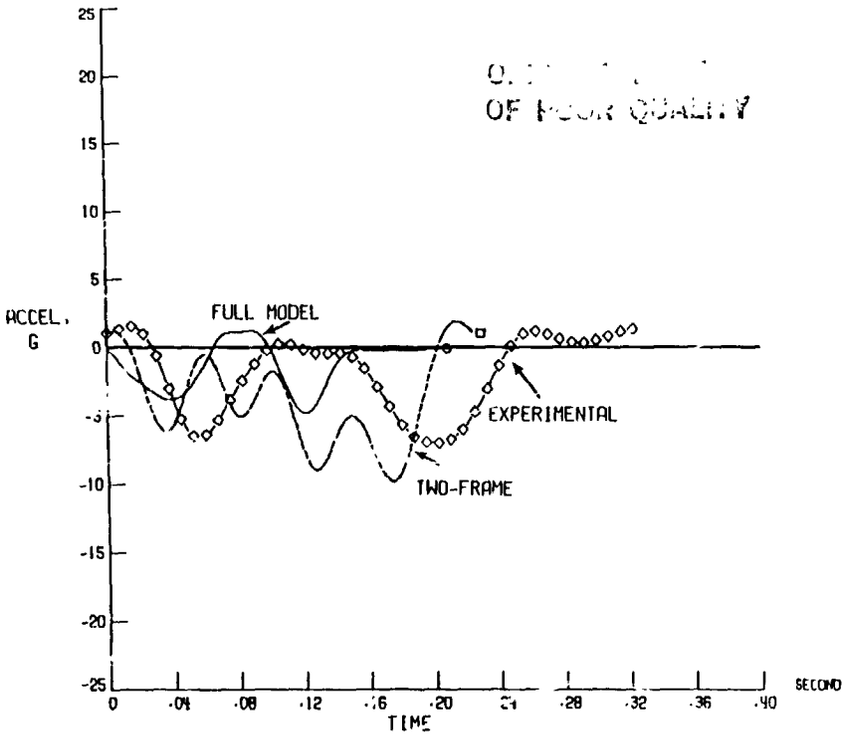

Figure 20.- Comparison of experimental and analytical vertical pelvis accelerations of the dummy seated in front port seat.

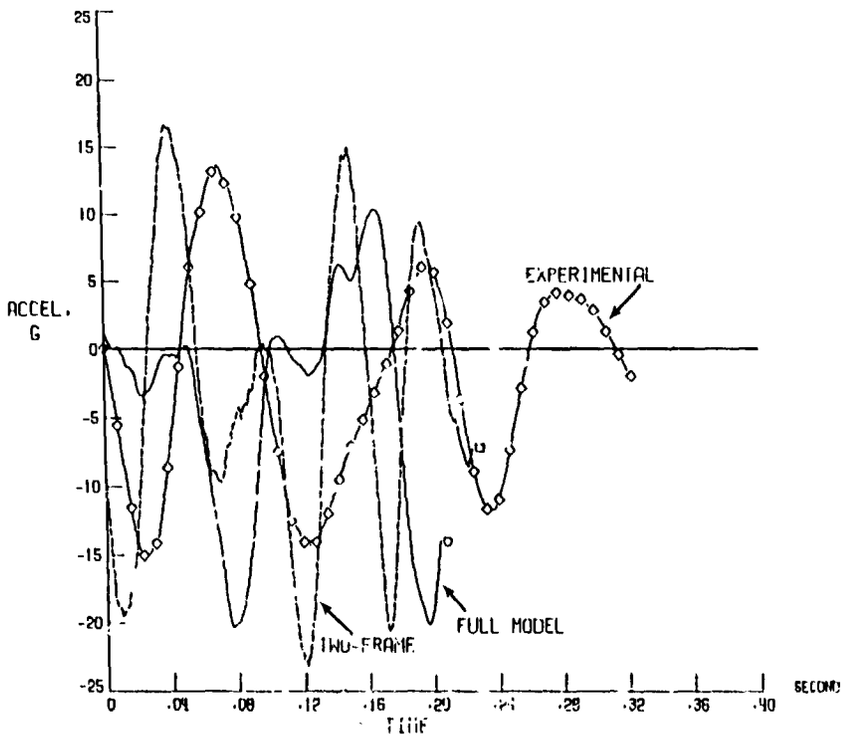

Figure 21.- Comparison of experimental and analytical vertical accelerati . at the apex of the front roof.

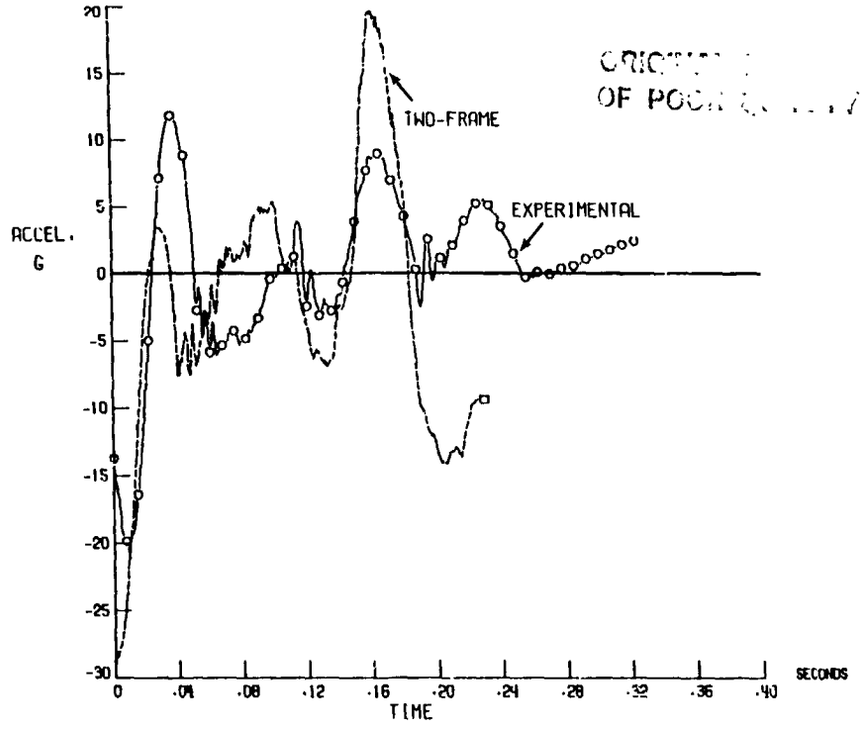

Figure 22.- Comparison of experimental and two-frame analytical vertical accelerations at the bottom of fuselage frame 600.

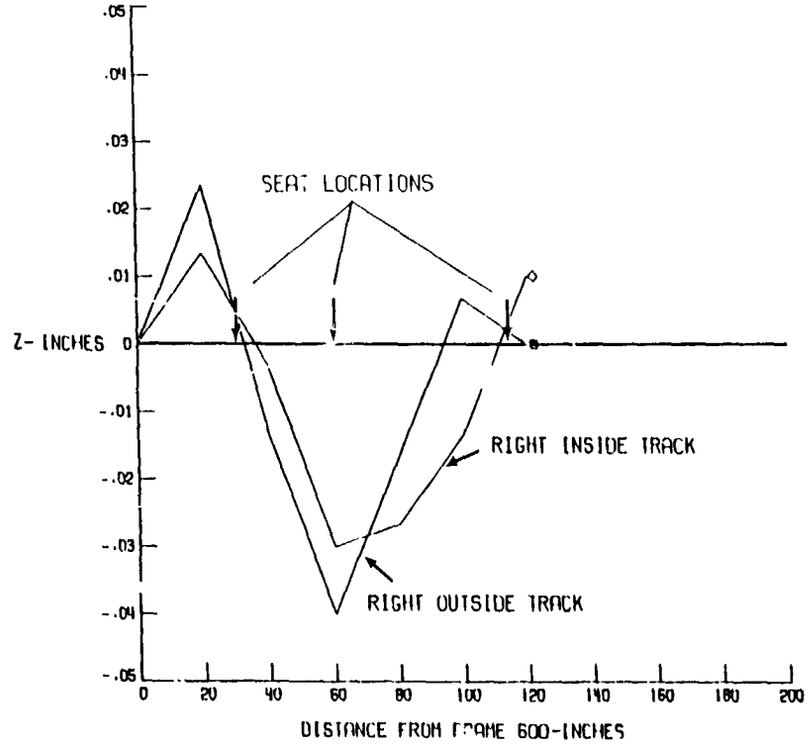

Figure 23.- Permanent vertical floor deformation of fuselage section right floor tracks.

STRUCTURAL ANALYSIS OF THE SPACE SHUTTLE ORBITER

Henry R. Grooms and James H. Johnson, Jr.
Rockwell International
Downey, California

INTRODUCTION

The Space Shuttle (figure 1) consists of a reusable orbiter mounted on top of an expendable external tank (ET) and two solid rocket boosters (SRB). The ET contains liquid hydrogen and liquid oxygen that are used as fuel for the Space Shuttle main engines (SSME). The Shuttle is launched like a rocket and returns to earth like a glider (figure 2).

The structural analysis of the Space Shuttle orbiter was planned with two concepts in mind: use derivatives or subsets of the same basic finite element model whenever feasible, and substantiate the model's predictive capability by performing ground tests. The analysis cycle (model modal loads stress [MMLS]) starts with the finite element model conception and ends with the detailed stress analysis and margins of safety.

The structural analysis of the orbiter encompasses a variety of static and dynamic problems. This paper will explain the salient features of the problems and their solutions.

OVERALL LOGIC

The Space Shuttle structure was designed so that its structural integrity would be established by analysis and the analytical methods would be verified by ground tests. This is contrary to what is usually done with aircraft, which is to establish the structural integrity by analysis and then verify it by flight tests.

The orbiter structure was designed to meet the following criteria:

- All of the primary structure should exhibit a factor of safety ≥ 1.4 for limit loads.
- All of the primary structure should have a fatigue life ≥ 400 missions (100 missions times a scatter factor of 4).
- All structural parts should exhibit a safe life (from fracture mechanics considerations) for 400 missions (100 x 4), or those parts should be inspected or replaced at necessary intervals (ref. 1).

Figures 3, 4, and 5 show how various ground tests and analyses fit into the structural certification scheme: figure 3, the events that preceded the first captive flight (FCF) and the first approach and landing (FAL), figure 4, the ground tests and analyses leading to the first vertical flight, and figure 5, the work that led to the first operational (OPNL) flight.

MODEL MODAL LOADS STRESS (MMLS) CYCLE

The MMLS cycle (figure 6) is a loose collection of computer programs that encompasses the work from calculating external loads to computing margins of safety. A finite element model was made for each element of the Shuttle transportation system: SRB's, ET, and orbiter. With compatible interfaces, these models were integrated and used to compute external loads for liftoff and boost. No further mention of the SRB and ET models will be made since this paper deals with the orbiter.

A finite element model, with approximately 40,000 degrees of freedom, was created to simulate the Space Shuttle orbiter. This model was used in its entirety for static analysis, and a reduced version was used for dynamic analysis. The

basic orbiter finite element model was set up using a computer program called the Automatic System for Kinematic Analysis (ASKA). Three levels of substructuring were used (ref. 2). The lowest level substructures were assembled to form sections such as the wing and tail (figure 7). These sections, which were second level substructures, were then joined to form the orbiter (see figure 8). The assembled orbiter is shown as 301 in figure 8. (The numbers in rectangles in figure 8 correspond to the numbers in hexagons in figure 7.)

The models contain four types of elements:

1. Beams

2. Triangular membranes

3. Quadrilateral membranes

4. Quadrilateral shear panels

Derivatives of the finite element model were used at various places in the MMLS cycle. The aero model, the outer surface of the finite element model, was used in smoothing the aerodynamic data obtained from wind tunnel tests. The weights model, which consists of a weight associated to every node in the finite element model, was used to set up the inertial loads.

Thermal data were obtained for certain discrete locations on the orbiter and then interpolated and extrapolated to create a temperature distribution all over the vehicle. Some of the automated routines used for smoothing wind tunnel data were also used for thermal data.

The external loads were computed using different methods for liftoff,boost, reentry, and landing. A dynamic model was used for each of these phases of flight. This model consisted of a reduced stiffness matrix and a reduced mass matrix.

Figure 9 shows the relationship between the various models and figure 10 shows their uses.

The orbiter was modeled as a symmetric structure. Only one side was represented and appropriate boundary conditions were used at the X-Z plane. All load cases, including thermal conditions, were decomposed into symmetric and antisymmetric parts. Separate solutions were obtained for thermal loads, mechanical loads, and compartment pressures. The internal loads for these solutions were combined using a series of programs called the post-processor.

The post-processed data were searched and the most critical conditions were identified on an element by element basis. These elemental data were used to perform a detailed stress analysis and compute a margin of safety. More MMLS information can be found in ref. 2.

ACOUSTIC FATIGUE

Showing that the orbiter structure had adequate fatigue life was a formidable task. Most jet aircraft have a few local areas where the acoustic environment is pronounced, but every area of the orbiter is exposed to a severe acoustic environment. The largest acoustic loads occur during main engine ignition, liftoff, and boost. The reentry acoustic loads are negligible.

In lieu of a complete acoustic environment test on the orbiter, it was decided to subject a batch of small test articles to acoustic environments. These articles were selected to represent different regions of the orbiter and different types of construction. The 16 test articles are listed in table I and shown in figure 11.

The certification logic was to conduct a complete modal survey on each test article before subjecting them to design acoustic environments. Strain gages were used to measure the responses at critical locations. These data allowed test-verified dynamic models to be generated. These models were used to combine acoustical and other flight environments for life certification of the spacecraft.

A NASTRAN finite element structural model was built for each of the test articles and mode shapes and frequencies were computed. Boundary conditions were used to simulate the test support conditions. The analytical mode shapes and frequencies were compared with test results. The analytical boundary conditions usually had to be altered to bring the analytical results in line with the test results. This process will be referred to as tuning the model.

After the model was tuned, a NASTRAN Solution 30 was run. This computes root mean square (RMS) stresses for a given acoustic environment. The RMS stresses were then surveyed and the number of missions that a part could sustain at this stress level was computed. The parts with the shortest lives were identified. Actual measured strains were available from the first four flights. In any locations where the measurements indicated a higher stress level than the analysis, the measured values were used for calculating the life.

A few structural failures occurred during the acoustic fatigue test program. Some of the failures were attributed to test boundary conditions that were not representative of the flight hardware, while others indicated flaws in the structural design that were subsequently changed. Table II gives some representative results. and ref. 3 gives additional details of the Shuttle acoustic fatigue work. The analysis logic is given in figure 12.

STATIC STRUCTURAL TESTS

An orbiter structure (also called static test article [STA]) was used to perform an overall static test in 1979. It was originally planned to dedicate one complete vehicle structure to a static test program to demonstrate that the design could sustain ultimate loads. As the program developed, it was concluded that significant cost savings could be achieved by limiting this complete structure to loads below the elastic limit and then reusing the structure as a flight article. This was done for the Space Shuttle Challenger (see table III). A series of structural component tests were defined and implemented to demonstrate the ultimate strength capability. These tests, called the STA Supplemental Test Program, totaled 36. Table IV lists the more complex test articles.

The test of the complete airframe (figure 13) consisted of 37 limit plus conditions, which were chosen such that each element of the structure was tested to its critical design loads for each phase of the mission. There were 25 ascent, 8 reentry, and 4 landing conditions. All conditions applied distributed airloads, inertial loads, discrete mass loads, and internal delta pressures. Loads were applied such that the structure was in a balanced state. Slight inbalances occurred because the load distributions were not perfect; these inbalances were reacted at the ET interface fittings. There were 32 real flight conditions and 5 hybrid conditions. The hybrid conditions were formulated to subject two or more elements to a critical condition with one test setup. No attempt was made to either apply temperatures or thermal strains during the reentry or landing conditions. It was impractical to heat the entire structure and it was judged an over-test to mechanically simulate thermal strains; however, a thermal stress test of the forward fuselage section was performed in combination with a landing condition to verify the ability of ASKA to predict thermal effects. This test has been reported elsewhere (ref. 4).

The test article was held in a horizontal position and supported at the three ET attach points. Around 4,000 strain gages were used, which were distributed as follows:

- Axial — 60%
- Biaxial — 5%
- Shear — 10%
- Rosette — 25%

The test article was a regular orbiter with some exceptions. The following elements were simulated by loading fixtures to provide proper load paths and stiffnesses at their interfaces:

- Crew module
- Nose landing gear (NLG) assembly
- Main landing gear (MLG) assemblies
- Actuators for the elevons, body flap, and rudder/speed brake
- OMS pods (OMS pods were tested to ultimate loads in separate tests off the vehicle)
- Left-hand elevons

The test objectives were to show that the orbiter was capable of experiencing significant (approximately 120% of limit) structural loads without damage occurring, and to show that the finite element model was a good predictor of stresses.

A pretest analysis was performed for the STA and for each specimen in the STA supplemental test program. A finite element model of the test article was created and subjected to boundary conditions that simulated the test support system. The planned test loads were then applied to the finite element model and stresses and deflections computed. If the computed stresses were acceptable, the test was run as planned. If not, the proposed test loads were altered and the process repeated.

DYNAMIC STRUCTURAL TESTS

Structural tests were performed to help determine vehicle mode shapes and frequencies and to verify the analytical (dynamic model) results. A quarter-scale model of the orbiter was subjected to dynamic testing in Downey, California, in the spring of 1977. In several areas (e.g. OMS pods and ET feedlines), the quarter-scale orbiter had more fidelity than the full-scale orbiter (OV 101), which was used for the later dynamic tests (horizontal ground vibration test [HGVT] and mated vertical ground vibration test [MVGT]).

The quarter-scale model replicated the stiffness and mass distribution of Orbiter 102. Its linear dimensions were one-fourth of full-scale, while its weight was 1/64th; therefore, the natural frequencies of the quarter-scale model were four times as great as the regular structure.

The quarter-scale orbiter was mounted horizontally in a test support structure. The vehicle was suspended on three air springs to decouple it from the support structure. A total of 224 accelerometers and 9 shakers were used to acquire all elastic modes up to 200 Hz. The usual data obtained for each mode were:

- Amplitude, phase, and co-quad raw data
- Kinetic energy distribution for certain components
- Orthogonality matrix
- Generalized mass
- Isometric vector plots

The posttest correlation was done using the Craig-Bampton method of component mode synthesis. Five components with a total of 1,900 degrees of freedom were utilized. The correlation work was based on kinetic energy considerations supplemented by a least-squared error modal displacement analysis. Table V compares the analytical and test results for the quarter-scale ground vibration test (QSGVT). Additional details on the dynamic tests and the application of the results are given in refs. 5 and 6.

The results for HGVT and MVGVT were very similar to those obtained for QSGVT. The HGVT used the same orbiter (OV 101) that was used for MVGVT. HGVT was an orbiter-only test while MVGVT included the orbiter, ET, and SRB's.

ABBREVIATED STRESS ASSESSMENTS

A complete MMLS cycle has taken two years or more to complete. As the Space Shuttle moved from late in the development phase into the early operational phase, it became apparent that a much shorter analysis cycle was needed to answer certain questions. Three types of abbreviated stress assessments evolved:

1. Day of launch
2. Flight by flight
3. Orbiter capability assessment (OCA)

The day of launch assessment was a set of calculations that were performed at specified prelaunch time points to predict the stress levels in the more responsive structural elements. A Monte Carlo analysis was performed on 150 wind profiles when the trajectory was devised to determine this most critical list. At specified times during the prelaunch activities, a weather balloon was used to measure the wind velocity components relative to the planned trajectory. These data were used to calculate external loads that were then used in the load indicator equations. The equations were evaluated on a time history basis. The peak values were compared to the structural allowables. The ten most critical load indicators were reviewed and used to help decide whether to launch or not. The typical time required to go from balloon release to load indicator evaluation was three hours.

The flight-by-flight assessment was a set of simplified analyses that were required when the vehicle was going to be flown outside the design envelope. The things that required the most evaluations were reentry thermal conditions and special uses of the SSME's. Once a reentry trajectory was established, thermal math models were run to determine the structural temperature distributions at selected locations in the forward, mid, and aft fuselage. These temperature distributions were then used to perform two-dimensional stress analyses at those locations. A typical temperature distribution and the resulting stresses are shown in figures 14 and 15.

The OCA was conceived as a relatively quick way of determining whether or not the vehicle was capable of flying outside the design envelope. The orbiter was designed, analyzed, and certified to fly within a particular set of loads, which are referred to as the 5.4 loads. The OCA work was initiated to determine what conditions outside the 5.4 loads envelope the orbiter could fly safely.

The idea behind the OCA work was to be more accurate than the load indicator equations or the flight-by-flight analyses, but not as time consuming as the MMLS cycle. It was decided to do an internal loads analysis but compute margins of safety for approximately 10 percent of the structural elements. The 10 percent was selected because it is most representative and includes a number of the most critical elements.

The time involved in each type of abbreviated stress assessment is shown in table VI.

CONCLUSIONS

The structural analysis approach and philosophy for the Space Shuttle orbiter have been presented, and an overview of ground tests and analytical procedures discussed. It has been shown how these tests and analyses fit together to demonstrate that the orbiter is structurally sound.

REFERENCES

1. Forman, R.G.; and Hu, T.: "Application of Fracture Mechanics on Space Shuttle," *Damage Tolerance of Structures*. ASTM (to be published).

2. Grooms, H.R.; Burnbaum, H.; and Rodgers, C.T.: *Orbital Thermal Deflections of the Space Shuttle*, Fifth International Seminar on the Computational Aspects of the Finite Element Method, West Berlin, Germany, Aug. 1979.

3. Cheng, J.S.; Dunham, M.J.; and Joanides, J.C.: *Acoustic Test Response Analysis of the Space Shuttle Orbiter*, International Modal Analysis Conference II, Orlando, Florida, Feb. 1984.

4. Grooms, H.R.; Gibson, W.F., Jr.; and Benson, P.L.: *Thermal Stresses in the Space Shuttle Orbiter: Analysis Versus Tests*, Seventh International Seminar on the Computational Aspects of the Finite Element Method, Chicago, Illinois, Aug. 1983.

5. Ujihara, B.H.; Dosoky, M.M.; and Tong, E.T.: *Improving a NASTRAN Dynamic Model With Test Data Using Linwood*, Tenth NASTRAN Users' Colloquium, New Orleans, Louisiana, May 1982.

6. Andrew, L.V.: *An Automated Application of Ibrahim's Time Domain Method to Responses of the Space Shuttle*, Proceedings of the AIAA/ASME/ASCE/AHS 22nd Structures, Structural Dynamics and Material Conference, Atlanta, Georgia, Apr. 1981.

TABLE I. ACOUSTIC FATIGUE TEST ARTICLE

Number	Test	Description
1	FFA01	Nose cap system test
2	FFA03	Window area with seals
3	FFA04	Underbody panel ($\approx$ 10 ft x 11 ft)
4	FFA05	Beany cap
5	FFA06	Forward RCS
6	PBA07	Payload bay doors with radiators
7	MFA08	Mid fuselage sidewall with frames
8	AFA11	Aft fuselage sidewall with frames
9	AFA12	Base heat shield with seals
10	AFA26	Complete APS pod
11	AFA15	1/2 body flap with seals
12	VSA16	Upper half of tail
13	VSA17	Tail lower trailing edge
14	WA18	Outer wing tip
15	WA19	Wing leading edge and skin stringer
16	AFA25	Aft RCS module

TABLE II. TYPICAL RESULTS FROM ACOUSTIC FATIGUE ANALYSIS

Test article	Section	Minimum life*	Part description
AFA26	OV 102 OMS pod	156	Frame, aft closure P/N 73A310069
AFA25	OV 102 aft RCS pod	1244	Forward bulkhead frame P/N 73A320134
FFA04	OV 102 lower forward fuselage	152	Lateral stability strut support end rivets
FFA04	OV 099 lower forward fuselage	Infinite	Mini frame X_0 522 CTD P/N V070-320765
FFA03 and FFA05	OV 099, OV 103, OV 104 forward fuselage window FF beany cap	523	Frame Y_0 28 P/N V0[illegible]31104-005
AFA11	OV 102 aft fuselage	590	Frame Cap X_0 1456 and X_0 1473 P/N V070-352279

*Any part with a life $\geqslant$ 100 missions is satisfactory

TABLE III. USES OF EARLY ORBITERS

Orbiter	Name	Uses
OV 101	Enterprise	HGVT, MVGVT, ALT
OV 099	Challenger	STA, Flight article
OV 102	Columbia	Flight article

TABLE IV. MAJOR STA SUPPLEMENTAL TESTS

Item	Description
1	1/2 body flap
2	Segment of wing box
3	Segment of wing and elevon
4	Upper vertical tail and rudder/ speed brake
5	Wing/mid fuselage/aft fuselage interface
6	Vertical tail/aft fuselage interface

TABLE V. CORRELATION OF QUARTER-SCALE RESULTS

Mode	Symmetric or antisymmetric	Test frequency (Hz)	Analytical frequency (Hz)
1S	Symmetric	19.2	17.8
2S	Symmetric	21.6	19.8
3S	Symmetric	25.6	29.9
4S	Symmetric	26.6	26.9
5S	Symmetric	27.2	26.9
1A	Antisymmetric	14.3	14.2
2A	Antisymmetric	24.4	22.9
3A	Antisymmetric	26.2	26.3
4A	Antisymmetric	29.7	34.2
5A	Antisymmetric	34.1	34.8

TABLE VI. ABBREVIATED STRESS ASSESSMENTS

Item	Name	Time required	Description
1	Day of launch	2 hours	Load indicator equations used
2	Flight by flight	2 weeks	2D analyses at selected locations
3	OCA	6 months	10% of complete internal loads used

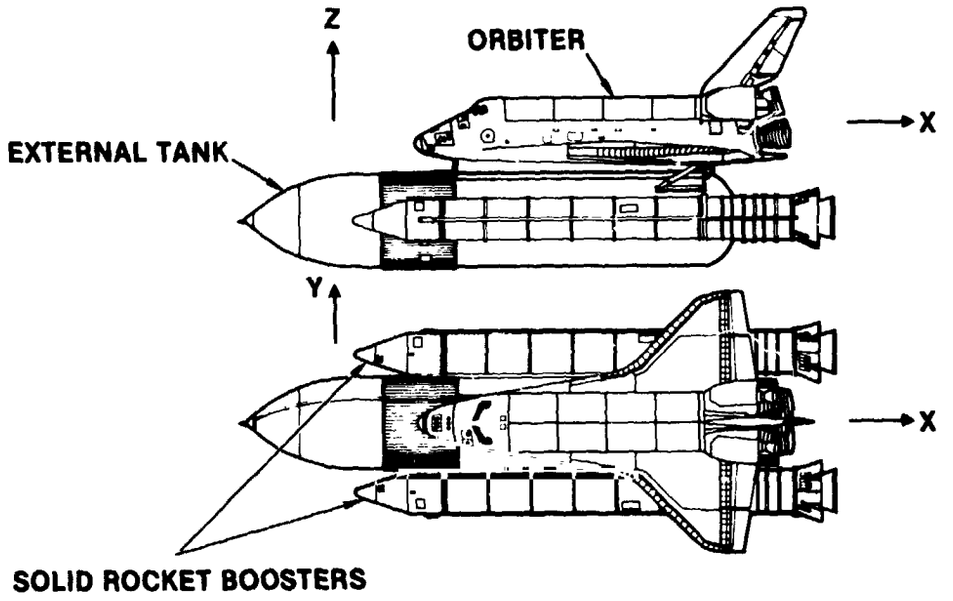

Figure 1. Space Shuttle

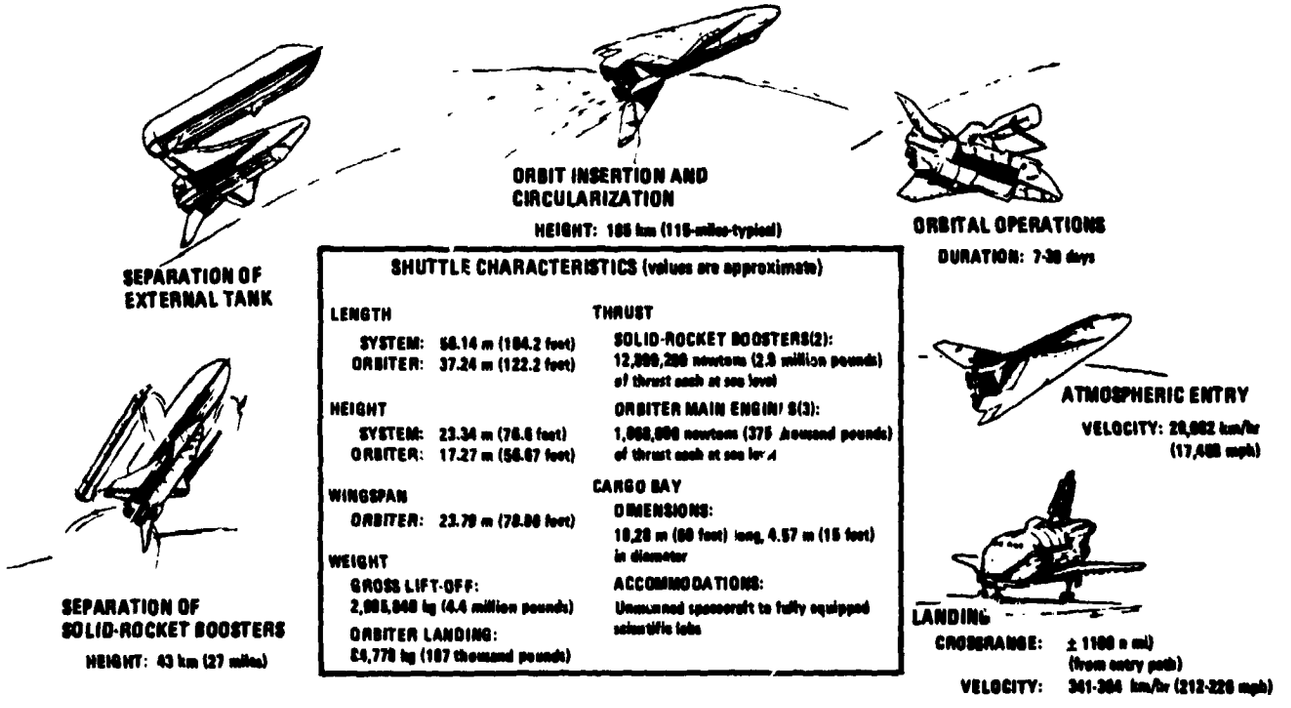

Figure 2. Profile of Shuttle Mission

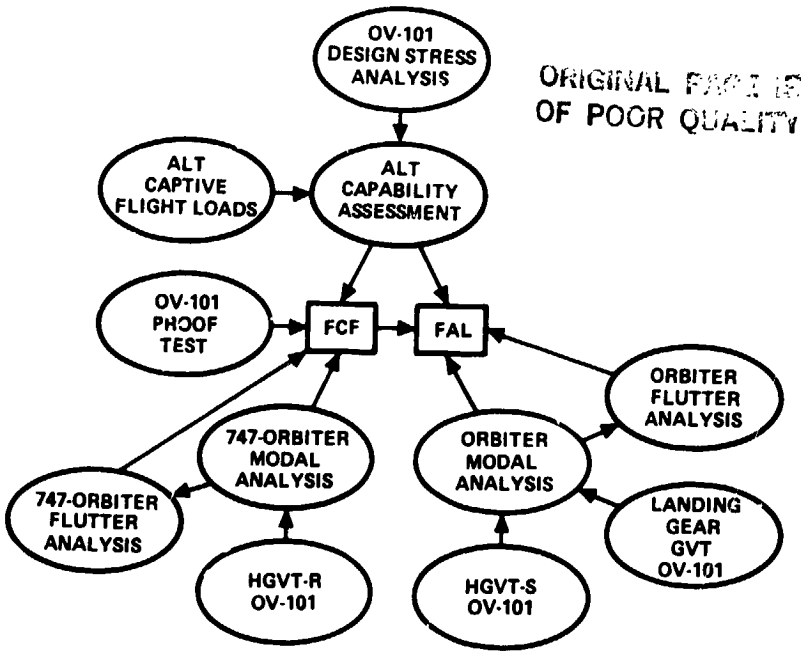

Figure 3. FCF and FAL Certification Logic

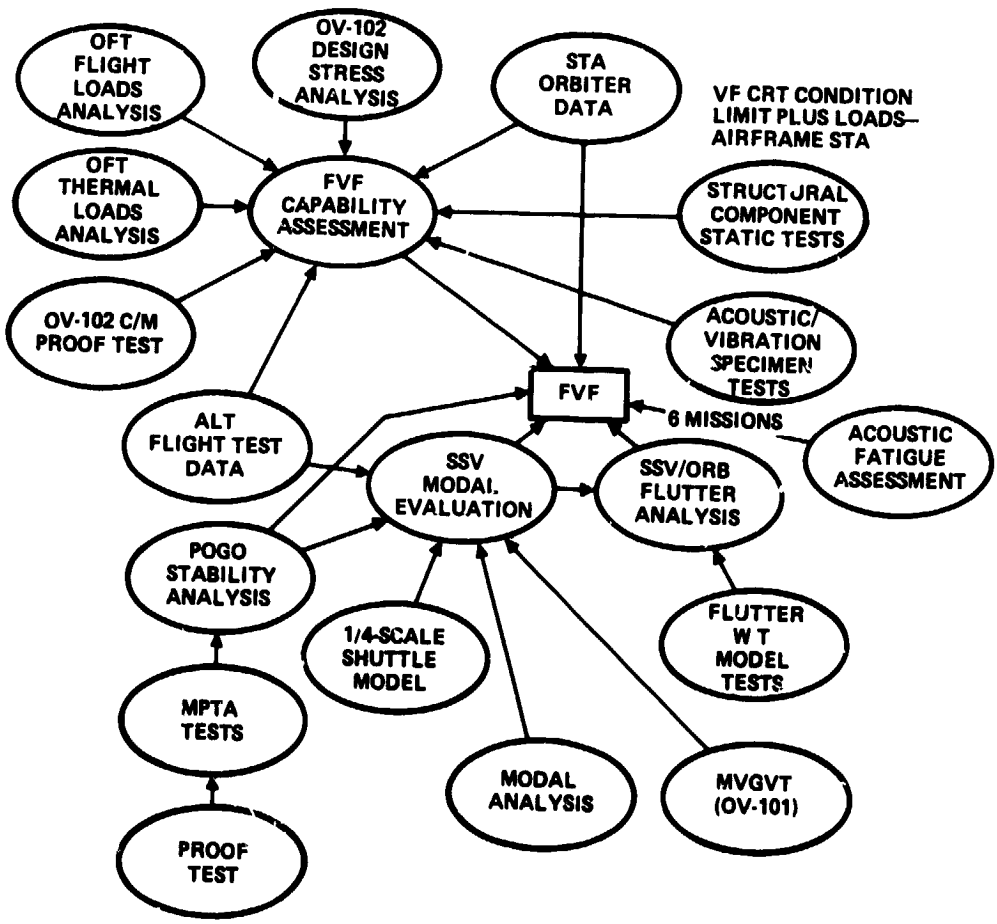

Figure 4. First Vertical Flight Certification Logic

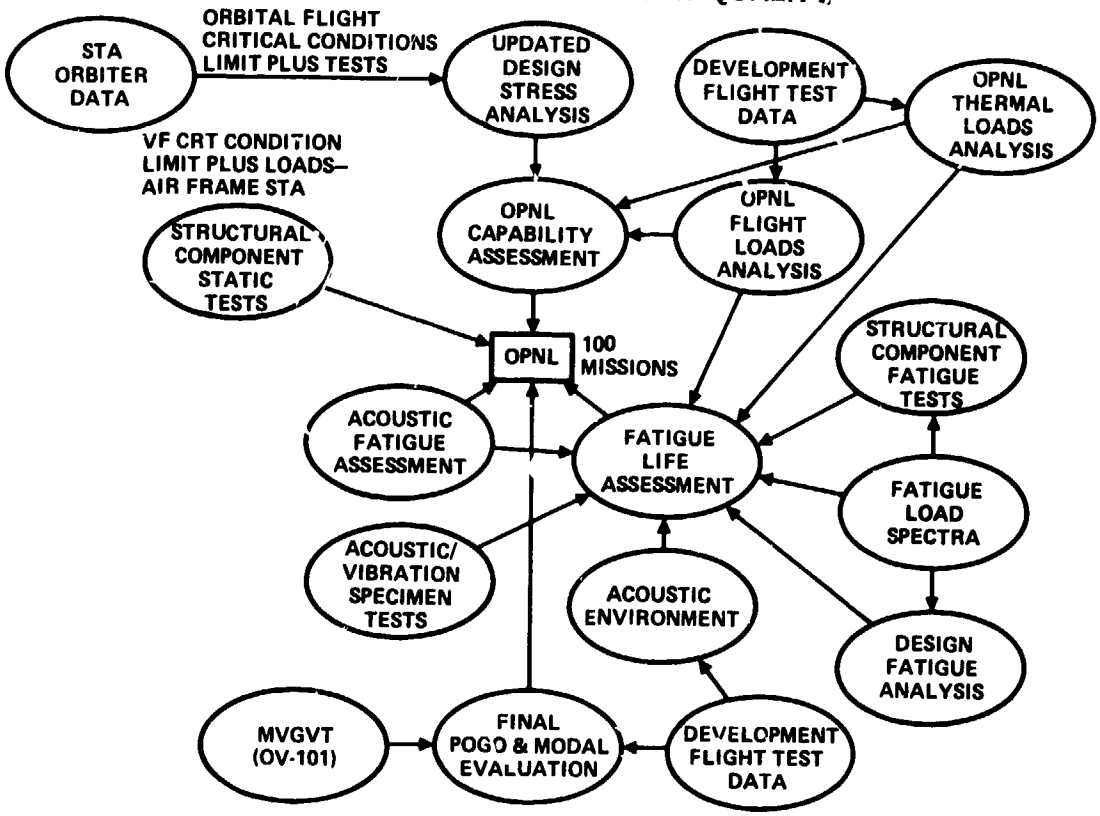

Figure 5. First Operational Flight Certification Logic

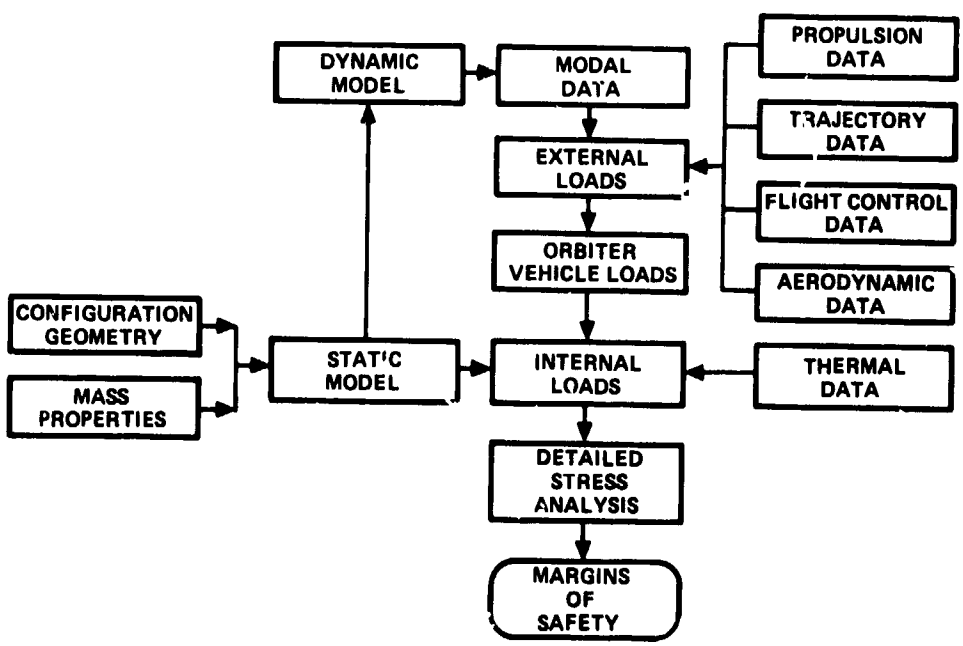

Figure 6. MMLS Cycle

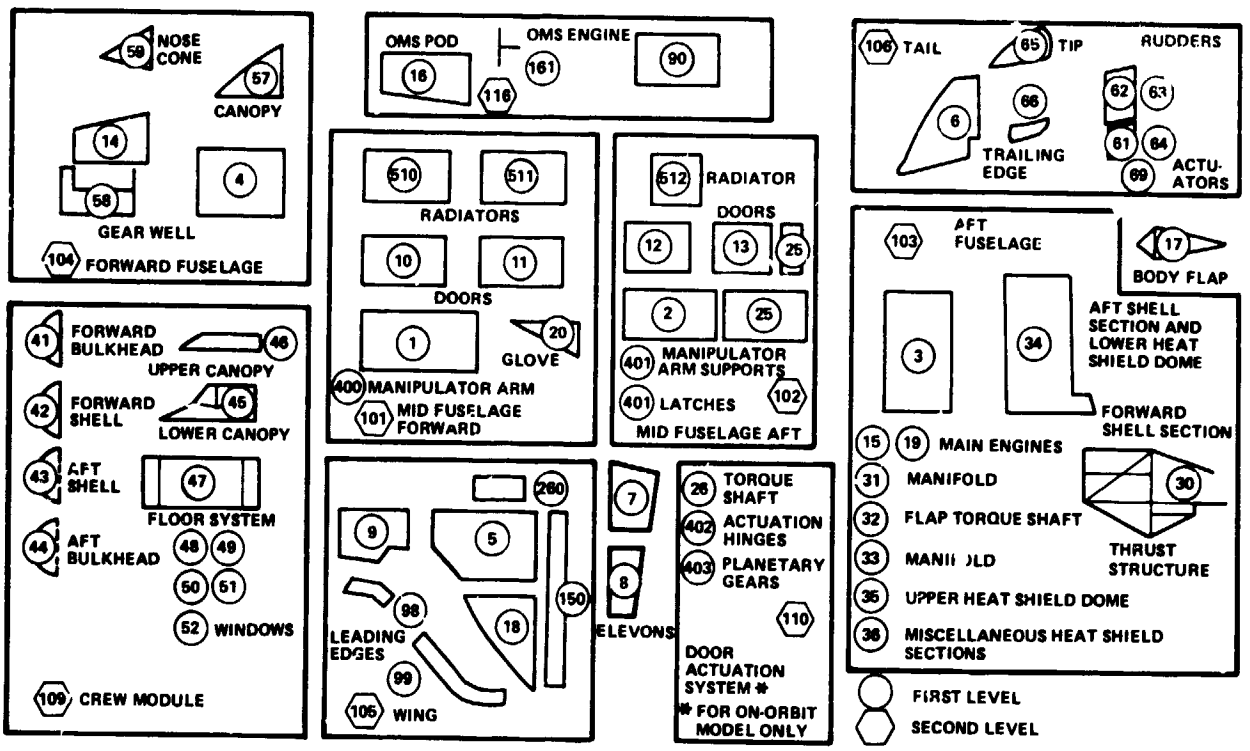

Figure 7. Orbiter Components

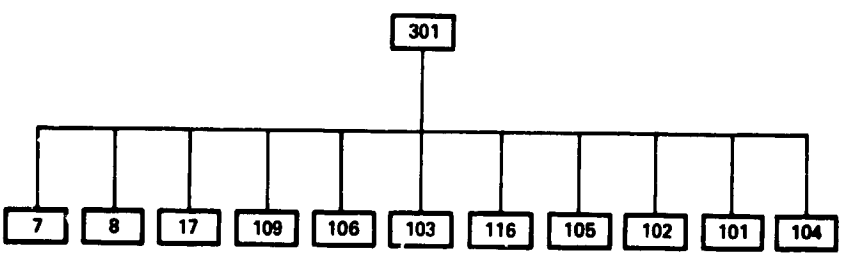

Figure 8. Substructure Assembly

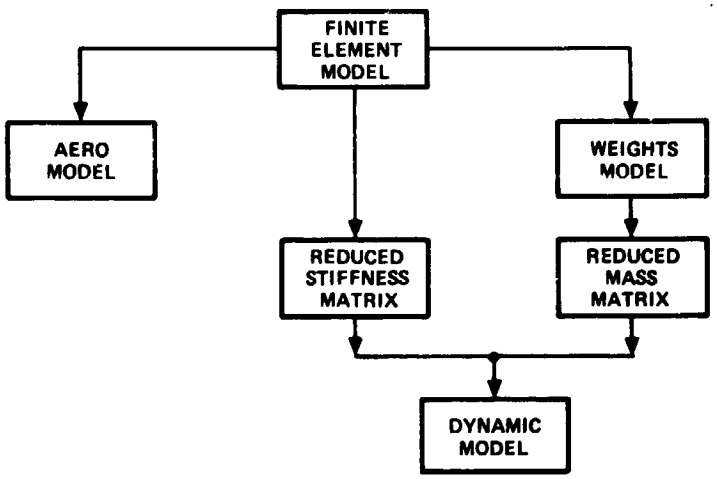

Figure 9. Relationship Between Models

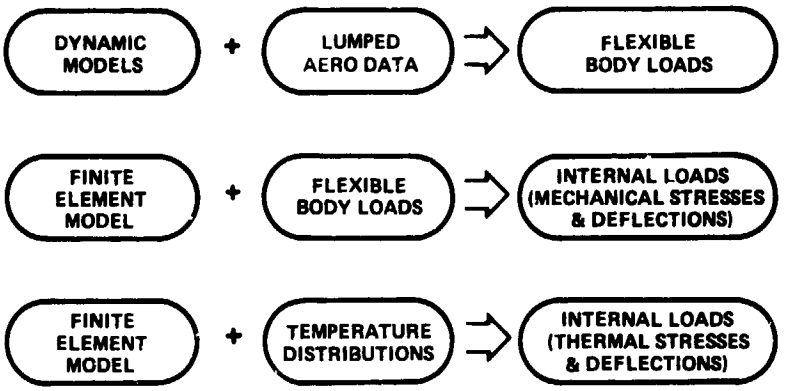

Figure 10. Model Uses

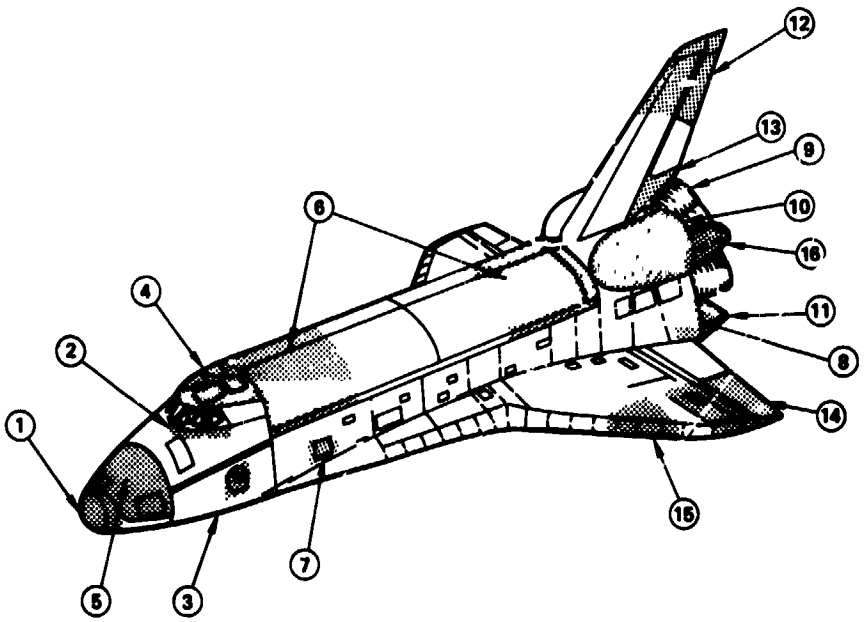

Figure 11. Location of Acoustic Test Articles

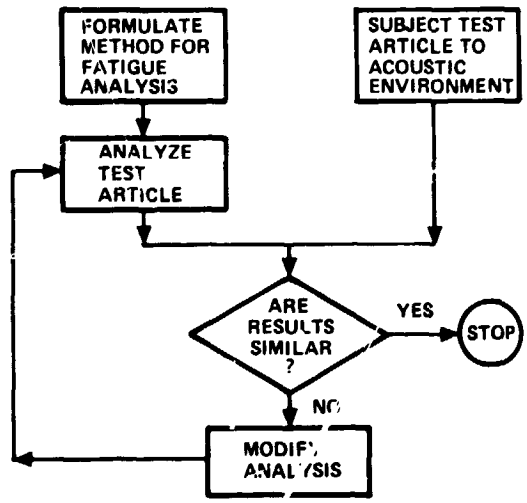

Figure 12. Acoustic Fatigue Logic

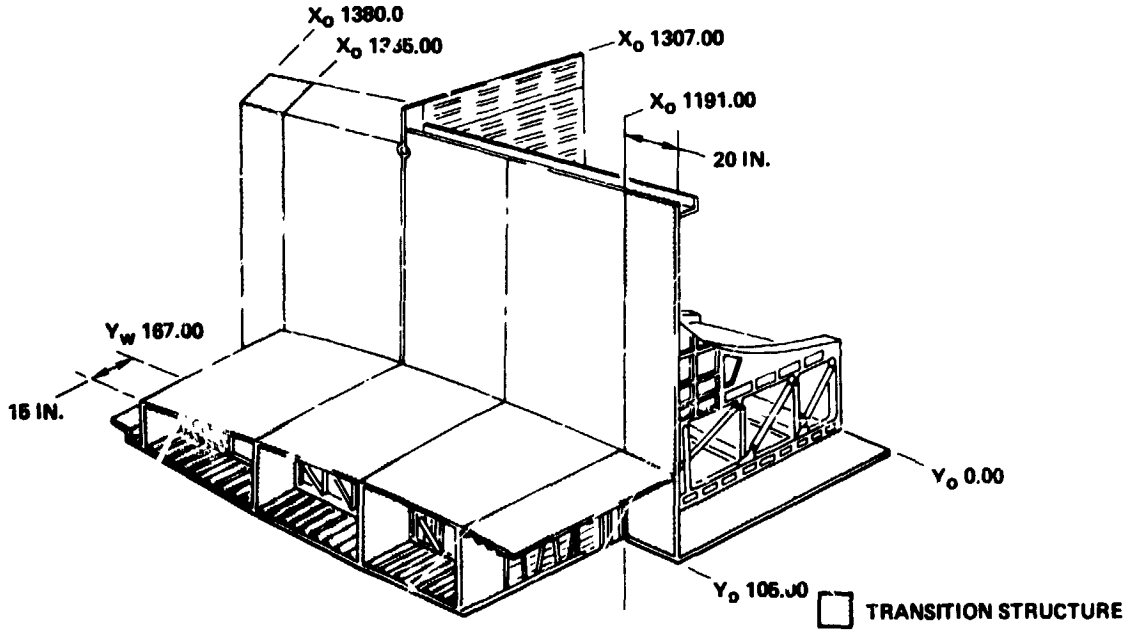

Figure 13. Test Article 36

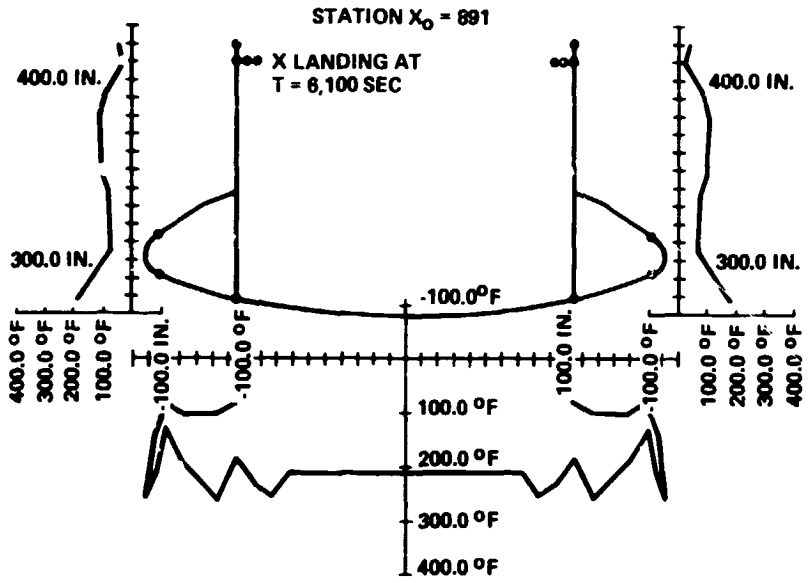

Figure 14. Preflight Temperatures—STS-4 EOM Landing Condition

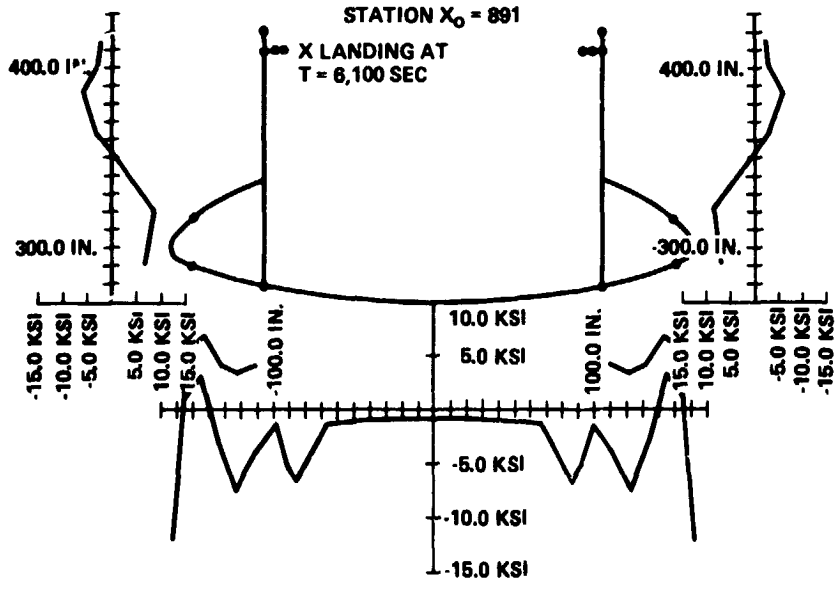

Figure 15. Preflight Thermal Analysis—STS-4 EOM Landing Condition

SINGLE-DROP IMPACT DAMAGE PREDICTION FOR LOW DENSITY, COATED CERAMIC MATERIALS

David Mustelier
Rockwell International
Downey, California

SUMMARY

A technique utilizing finite element analysis, liquid impact kinematics, and momentum theory is described and compared to single-drop impact test data performed on various configurations of coated ceramic material. The method correlates well with test data and is useful in predicting the single-drop impact damage velocity threshold for low-density, coated ceramic materials.

INTRODUCTION

The state of the art in rain erosion analysis is essentially that rain impact damage cannot be accurately predicted except by experimental evaluation. This method is extremely prohibitive when numerous combinations of materials and test conditions are to be evaluated. The development of an analytical and/or empirical methodology for predicting rain impact damage becomes an important means for minimizing testing by providing a means to prescreen materials prior to a more costly test evaluation. In addition, analytical simulation aids in the understanding and optimization of material properties for impact durability enhancement.

Single-drop ballistic impact tests were performed to evaluate the impact performance of various material configurations and to identify damage threshold velocities as a function of drop diameter. While single-drop tests by themselves are not necessarily indicative of the material performance in the multidrop environment, they do provide substantial insight into the impact phenomena. These items are:

- Establish upper limits for damage threshold velocities
- Provide controlled method for evaluating the effect of individual material property changes on damage thresholds
- Identify damage mechanisms
- Determine quantitative and qualitative ranking of material performance

Variations in incident angle, drop size, coating thickness, substrate density, and substrate sonic velocity were evaluated.

SINGLE-DROP IMPACT TESTING

Specimens 19 mm in diameter were cored from several glass-coated ceramic materials at various incident angles and mounted in sabots for testing. The sabot then was propelled through the test apparatus by a small charge of gunpowder where the sample impacted a single drop dispensed by a hypodermic needle. Immediately prior to impact, the drop was photographed for measurement and the specimen velocity measured. The sample was then recovered and inspected for damage. A schematic of the water drop impact apparatus is shown in figure 1. Testing was performed by General Research of Santa Barbara, Calif.

The maximum impact velocity without failure (V_{max}) and the minimum velocity with failure (V_{min}) bound the damage threshold velocity for the material, as shown in figure 2. Inspection of the specimens showed cracks radiating

from a central location as the initial mode of failure. As impact velocity increased above the initial failure velocity, damage progressed in order of severity: (mode 2) radial and circumferential cracking; (mode 3) radial/circumferential cracking with substrate penetration/removal. The progression of damage is illustrated in figures 3 and 4.

The initial failure mode is indicative of coating bending to failure; this type of failure has been previously observed in solid impact testing (refs. 1, 2). In the case of angular impact, cracks distinctly inclined to the coating normal axis are more evident. The damage indicated a more significant shear load contribution to coating failure not generally present in normal impacts. In addition, it was noted that the damage threshold for angular impacts was not simply related to the sine of the impact angle but was also dependent on the drop diameter. Overall, the coating damage appears to be primarily the result of direct pressure loading and lateral liquid movement. Stress wave effects within the solid appear to be of secondary importance at the low damage velocities for these materials.

FINITE ELEMENT ANALYSIS FAILURE PREDICTION

Approach

A method was developed to predict initial coating failure: the technique used liquid impact kinematics and momentum theory to define loads and NASTRAN finite element analysis to define a characteristic coating stress at failure.

The finite element model approach to predicting failure was based on several assumptions and simplifications:

- Two-dimensional finite element model assumed
- Only loading prior to the initiation of lateral drop outflow considered
- Uniform loading over drop contact area assumed
- Static rather than dynamic analysis used
- Predictions fixed relative to a single test data point

This approach was compatible with techniques used by other researchers (refs. 3, 4) and the correlation with test data indicates that the methodology is useful for predicting material performance around the test drop size/velocity range.

Load Model

During drop impact, loading of the coating resulted from three major sources: normal pressure loading, stress waves, and shear loads from lateral outflow. The single-drop tests indicated that initial coating failure was primarily the result of coating bending (oblique impacts indicated a more significant radial outflow induced shear contribution); therefore, for this analysis, only normal pressure was accounted for.

The sequence of events in the water drop collision with a solid can be divided into two phases: an expanding contact zone where pressure rises to a maximum within the droplet, followed by a pressure release phase characterized by high-velocity lateral liquid jetting along the target surface. Identifying the point of onset of lateral flow becomes important for distinguishing the material response from the two different phenomena.

The widely referenced equation for the onset of lateral flow (ref. 5) is:

$$A_c = V_0 R / U_w \qquad (1)$$

where

A_c = critical contact radius at onset of jetting

V_o = impact velocity

R = droplet radius

U_w = liquid compression wave velocity

Eq. 1 can be modified to account for the influence of impact velocity on the critical radius (ref. 6), yielding:

$$A_c = V_o R/(C_w + 2V_o) \tag{2}$$

where

C_w = liquid sonic velocity

Eq. 2 represents the radial location where the expanding drop/target contact radius is overtaken by the compression wave traveling in the liquid. It also describes the radius of the drop/solid contact area where compression within the liquid can be expected to generate maximum pressures prior to the pressure release phase associated with the lateral jetting of the drop.

The water hammer pressure given by

$$P_w = \rho_w C_w V_o \tag{3}$$

represents the interface pressure for the simplest case of the one-dimensional planar impact of the two semi-infinite bodies: a liquid and a rigid solid. This equation can be generalized to account for liquid impact on elastic surfaces (ref. 5) where

$$P_w = \rho_w U_w V_o/(1 + \rho_w U_w/ \rho_s U_s) \tag{4}$$

where

ρ_w = water density

ρ_s = solid density

U_s = solid compression wave velocity

and $P_w = P_s$ because of continuity at the liquid-solid interface. Again, accounting for the influence of impact velocity, the interfacial pressure equation becomes

$$P_w = \rho_w V_o (C_w + 2V_o)/(1 + \rho_w (C_w + 2V_o)/ \rho_s U_s) \tag{5}$$

with the solid compression wave velocity approximated by the solid acoustic velocity and the liquid compression wave velocity approximated by the liquid acoustic velocity.

Eqs. 2 and 5 were used to define the load model for input to the finite element analysis. This approach was selected for simplicity and neglects the observed pressure spike at the periphery of the drop contact radius (ref. 3) and inertial effects in the material. The assumption in this approach was that these defined loads would be proportional to actual loads and that the relative relationship between the predicted response of different materials will be maintained.

Finite Element Model

A two-dimensional slice of the coated ceramic material adjacent to the axis formed by the drop center and the initial point of impact (figure 5) was modeled in lieu of a more complex three-dimensional representation. For actual NASTRAN analysis, the model possessed constant thickness, which was an approximation of a thin symmetric wedge and eliminated the singularity along the drop impact axis (Y axis).

The finite element model detailed in figure 6 had overall dimensions of 12.5×12.5 mm^2. The mesh size varied from 1/3 along the outside edges to 1/500 at the substrate/coating interface and the loaded coating surface adjacent to the axis of symmetry. The model consisted of 190 individual grid points. It was constrained for out-of-plane translations and all rotations. In addition, the axis of symmetry was constrained for all but Y-axis translation. The remaining model boundaries, exclusive of the coating surface, were rigidly fixed. The entire model was constructed of quadrilateral and triangular membrane elements.

Load inputs to the model were derived from coating element thickness, coating/drop interface radius (eq. 2), and interface pressure (eq. 5) derived from measured coating material properties and measured impact parameters. The constant pressure load was reduced to discrete in-plane point loads for application to grid points along the coating surface.

Finite Element Analysis

A static stress analysis of the loaded model was performed to define a reference case, a single pair of test data points for which the velocity range between failure and no damage was the least. From this analysis, the "characteristic" principal tensile stress was determined for the coating element at the coating/substrate interface along the drop axis where bending failure would initiate. This stress differed considerably from reported values for the coating σ_{tu}. Sources for this discrepancy were attributed to neglecting inertial effects, two dimensional modeling, and the generally observed trend that dynamic loading often results in higher apparent failure stresses (refs. 2, 7). Finite element models were constructed based on test specimen material properties. A trial and error approach was used to bracket the velocity (within ± 4 m/s) for a given drop size that resulted in generating the same "characteristic" stress observed in the reference case previously described.

Results and Discussion

Damage threshold velocity predictions were generated for the normal impact tests and are plotted in figure 7 relative to their respective test cases. The predicted velocity ranges overlap the test result ranges in seven out of ten cases. The three outstanding cases represent a variation in coating composition and two cases for which V_{max} (maximum velocity without damage) was not determined. Nevertheless, the predictions for these two cases are in the right direction.

The correlation between test data and the semi-empirical finite element model approach indicates that this technique is valid within the drop size and velocity range of existing results and could be expected to provide a first order approximation of failure beyond these limits. Errors using this technique can be expected to be more significant for small drop size, high-velocity impacts where inertial effects are expected to predominate. Expanding the methodology to account for oblique impacts is currently being attempted as is statistical analysis of the significance of the correlation.

REFERENCES

1. Varner, J.R. and Ono, K.: *Damage Resistance of Space Shuttle Orbiter Thermal Protection Tiles.* Final Report for NASA Ames, Interchange No. NCA2-OR390-901-1979.

2. Green, D.J.: *Impact Behavior of Coated Low-Density Bodies.*To be published in the Journal of the American Ceramics Society, 1984.

3. Adler, W.F. and James, T.W.: *Localized Deformation and Fracture of Transparent Ceramics.* Report for Office of Naval Research, Contract N00014-76-C-0744, Mar. 1980.

4. Ito, Y.M. et al.: *Analysis of Water Drop Erosion Mechanisms in Infrared-Transparent Materials Using Microphysical Fracture Models.* AFML-TR-77-219, July 1977.

5. Adler, W.F.: "The Mechanics of Liquid Impact," *Treatise on Materials Science and Technology*, Vol. 16. Preece, C.M. ed., Academic Press, 1979, pp. 127-178.

6. Heymann, F.J.: "On the Shock Wave Velocity and Impact Pressure in High-Speed Liquid-Solid Impact," *ASME Transactions.* J. Bas. Eng. Vol. 90, 1968, pp. 400-402.

7. Roark, R.J.: *Formulas for Stress and Strain.* New York: McGraw-Hill Book Co. Inc., 1954.

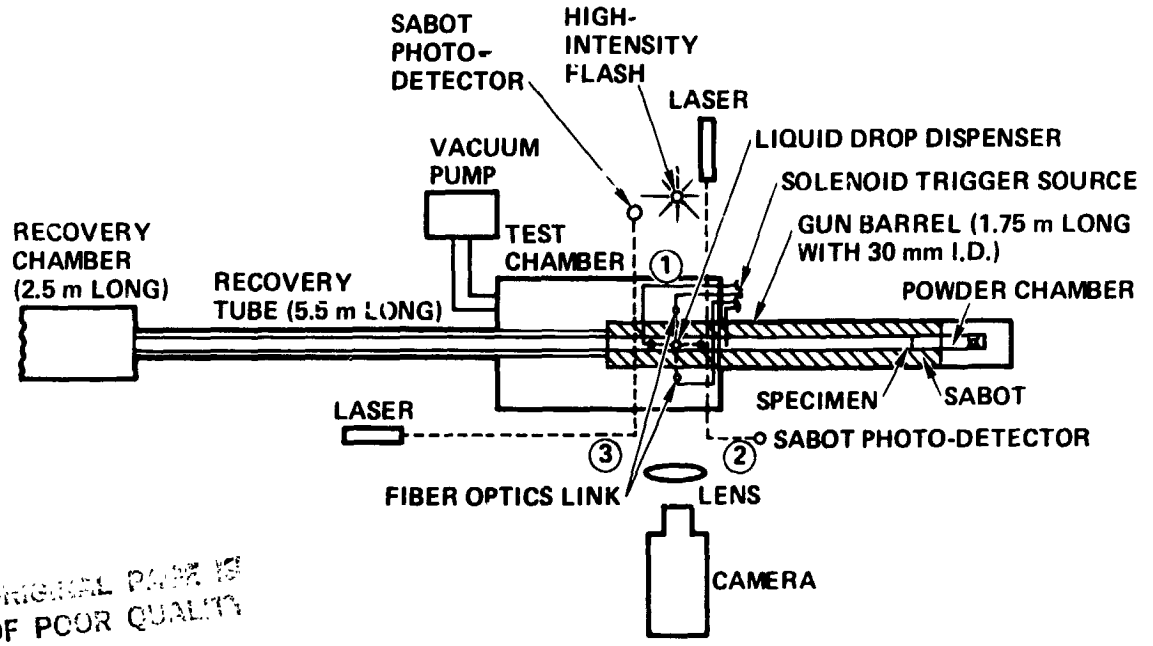

Figure 1. Schematic of Water Drop Impact Facility

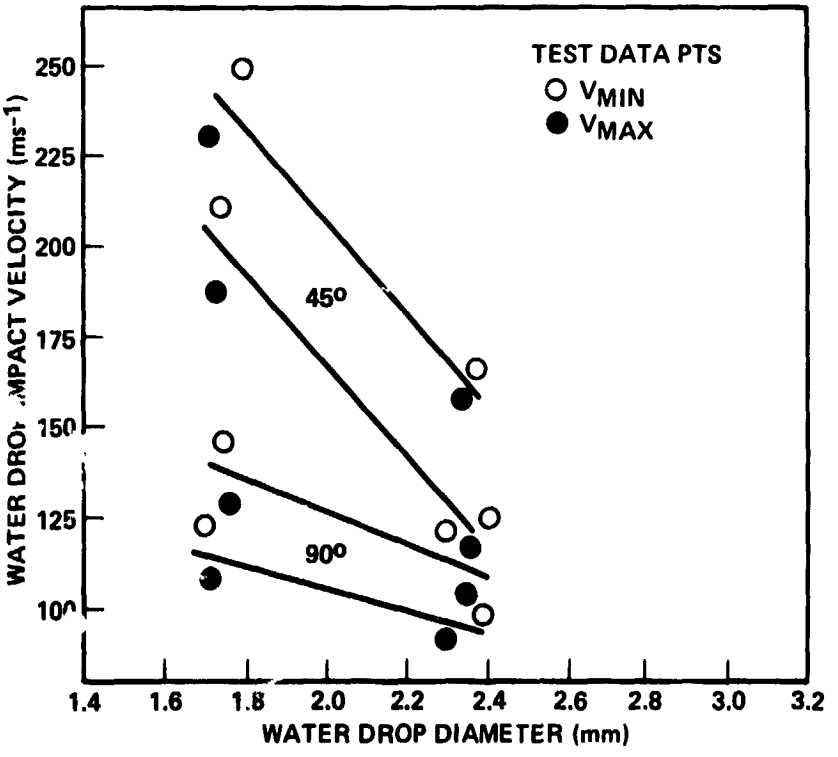

Figure 2. Single-Drop Damage Threshold Velocity Range

FIRST MODE: BENDING AT IMPACT SITE; RADIAL CRACKS

SECOND MODE: BENDING AT RADIUS FROM IMPACT SITE;
RADIAL AND CIRCUMFERENTIAL CRACKS

THIRD MODE: HYDRAULIC PENETRATION AND REMOVAL

$V_1 < V_2 < V_3$ V - VELOCITY

Figure 3. Single-Drop Impact Damage Modes (Deflections Exaggerated)

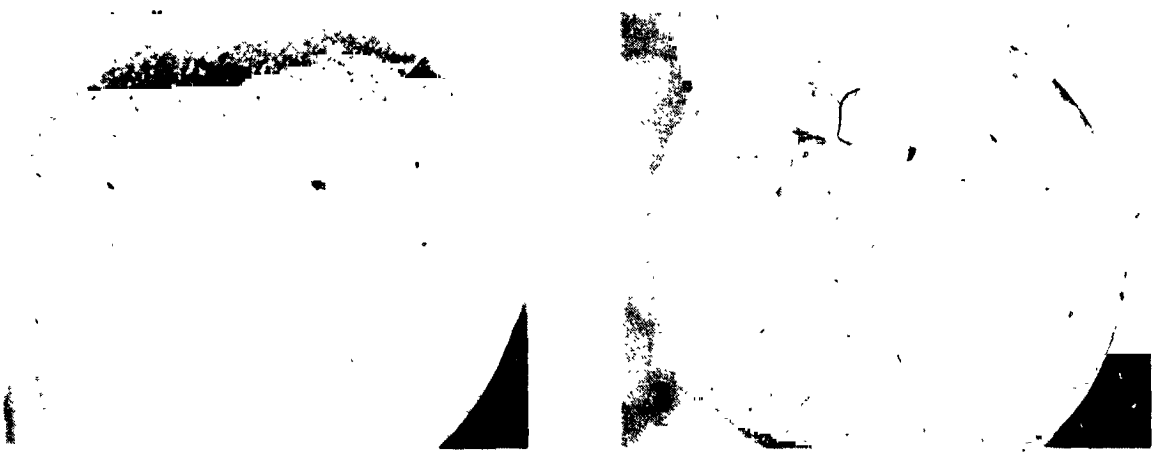

Figure 4. Specimen Photographs of Typical Water Drop Damage Modes

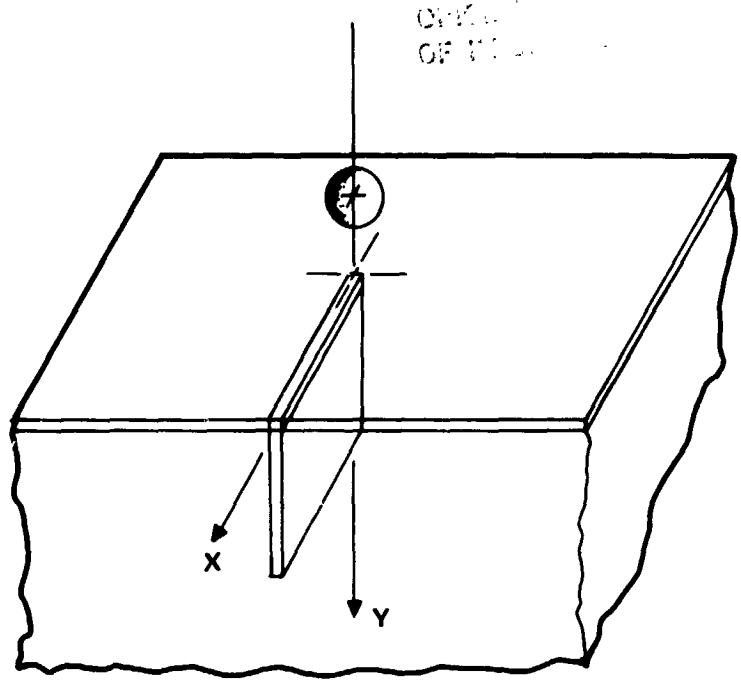

Figure 5. Representation of Coated Ceramic Material

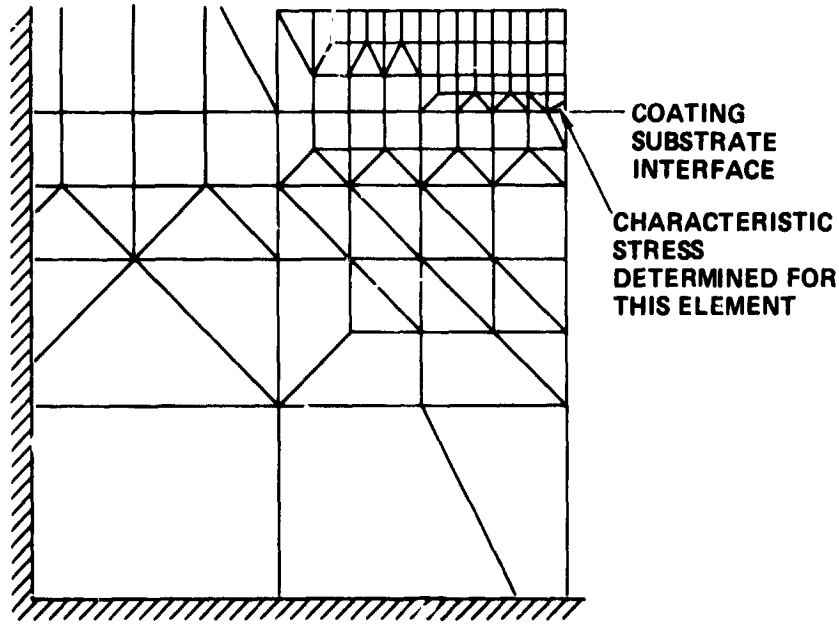

Figure 6. Detail of Finite Element Model at Coating-Substrate Interface

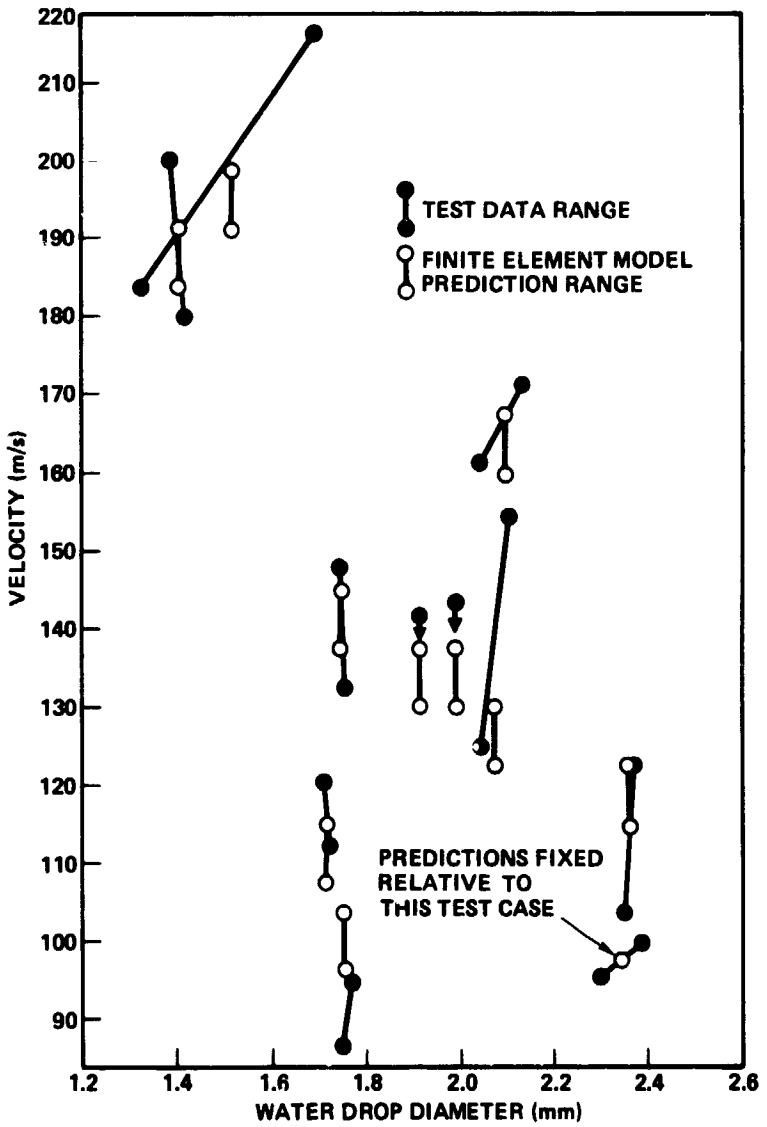

Figure 7. Single-Drop Damage Threshold Test Data Versus Finite Element Model Predictions

FINITE ELEMENT MODELLING OF BURIED STRUCTURES

David K. Playdon and Sidney H. Simmonds
Department of Civil Engineering, The University of Alberta

SUMMARY

In many structures the final stress states are dependent on the sequence of construction or the stress states at various stages of construction are of interest. Such problems can be analysed using finite element programs that have the capability of adding (birthing) elements to simulate the progress of construction. However the usual procedure of assembling elements may lead to numerical instabilities or stress states that are unrealistic. Both problems are demonstrated in the analysis of a structure using the program ADINA. A technique which combines application of a preload with element birthing to overcome these problems is described and illustrated.

INTRODUCTION

Analyses obtained from the finite element method are only as good as the correspondence of the modelling to the physical problem being solved. This is particularly true for those structures where the final stress states are dependent on the construction sequence. Such a structure is the arch-beam culvert where loads are carried by a complex soil-structure interaction. Being able to model accurately each step of the construction such as compaction of soil and placing of concrete is essential.

A number of modelling techniques were developed to determine the structural response of a prototype arch-beam culvert using the finite element method. From instrumentation placed and readings taken during construction it was possible to evaluate these techniques by comparing the results from analysis with field measurements. This paper first describes the structure analysed to indicate the nature of the problems encountered and then presents the techniques used to model three of the construction steps.

ARCH-BEAM CULVERT

Arch-beam culverts are large span corrugated steel culverts that have only a shallow soil cover and so are provided with a bonded concrete shell over the upper portion to distribute the effects of applied wheel loadings. The use of large span steel culverts in highway construction in regions that experience severe winter conditions has the advantage over traditional bridges in that the problems associated with deck deterioration due to salt and frost action are eliminated. Normally the depth of soil above the culvert relative to the culvert dimensions is sufficient that the strength and rigidity of the structure is provided through interaction with the surrounding soil and the steel culvert resists load primarily by membrane action. Highway loading is distributed by the soil and the effects of individual wheel loads acting on the culvert need not be considered. This is not the case when the soil cover is small compared to the culvert span.

For a stream crossing on a major highway in southern Alberta the peak flow

requirements were met by using a culvert with an elliptical cross-section having a span of 8.53 metres (28 ft) and a height of 4.27 metres (14 ft). The highway alignment was such that the difference in elevation between the highway surface and the top of the culvert varied from only 600 mm (2 ft) to 1500 mm (5 ft). To distribute wheel loadings, a reinforced concrete slab was poured over the upper portion of the culvert and extended beyond the culvert as shown in figure 1. This slab was of constant thickness and was bonded to the corrugated steel pipe using stud connectors to ensure composite behaviour.

At the time of the design, two possible structural actions for the concrete cover were postulated. The first action is that the concrete would act as a cylindrical shell with the horizontal wings acting to provide the horizontal stiffness. With this behaviour only a relatively thin concrete section is required. The second action considers the geometry to be sufficiently flat that the primary action is that of a one-way slab with the wings acting as reaction points. This behaviour requires a thicker concrete section. Due to the importance of the structure and the time constraints imposed for construction the more conservative behaviour of slab action was assumed during the design, resulting in a slab thickness of 500 mm (20 in.). Since it is expected that several hundred similar structures will be built in the next few years it was decided to obtain a better understanding of the structural behaviour by placing instrumentation, conducting load tests on the completed structure and undertaking a comprehensive program of analysis.

During construction, control points were established to measure distortion of the culvert cross-section using a tape extensometer. Pressure cells were placed adjacent to the culvert both above and below the spring line to measure the pressure between the culvert and soil. At selected critical locations electric resistance strain gages were applied to the reinforcement. Readings of all instrumentation were taken at various stages of construction and during load tests on the completed structure.

METHOD OF ANALYSIS

Analyses were obtained using the program ADINA (ref. 1). Considerable time was spent selecting a finite element mesh that truly modelled the concrete section and steel culvert while giving realistic stresses in the surrounding soil. The mesh used for the preliminary two-dimensional analysis of a cross-section through the structure is given in figure 2 and contains 486 nodes and 226 elements.

The corrugated steel pipe with a true thickness of 5 mm is modelled as a uniform sheet with a thickness of 60 mm but with transformed material properties that are equivalent to the corrugated material. An appropriate elastic-plastic stress-strain curve is used. Reinforcing bars are modelled as truss elements and elastic-plastic behaviour assumed using the Von Mises yield criteria. The constitutive relationship for the concrete is based on an approximation of the tri-axial failure surface and is obtained by entering values at discreet points with linear interpolation between points. Cracking of the concrete is controlled by entering an allowable uniaxial tensile stress. The soil is modelled as a two-dimensional solid using the Drucker-Prager yield criteria with tension cut-off.

A typical analysis considers the following construction steps

a) soil excavated to receive culvert
b) placing of culvert with erection cables in place
c) compaction and placing of soil prior to placing concrete

d) placing of wet concrete
e) placing of soil above hardened concrete
f) application of wheel loading

The construction steps described in detail in the following sections correspond to steps c, d and e above.

COMPACTION AT SPRING LINE

During construction the in situ material is shaped to permit placing the steel culvert on a prepared bedding. Due to the size and flexibility of the culvert section horizontal erection cables are required to prevent collapse under its self weight. Soil is then placed in the cavity on each side of the culvert. For circular culverts of usual dimensions buried at significant depth the compaction of this material is extremely important and constitutes a major source of the strength of the completed structure. However due to the extreme flexibility of the culvert being analysed, the overall stability of the culvert is extremely sensitive to the lateral pressures applied near the spring lines. It was found that when the usual procedure of birthing soil elements in the cavity was used the movement of the culvert was sufficient to cause the soil to fail in yielding thus preventing further analysis. Hence a different modelling technique was required. This behaviour was also observed in the field where the initial backfill in this region had to be placed very carefully by hand and essentially no compaction could be achieved without excessive uplift of the crown.

To overcome the numerical problems caused by yielding of the soil the compaction at the spring line was modelled in the following manner. After the construction had proceeded to placing the culvert (see figure 3), a lateral linearly varying pressure, referred to as the preload, was applied to the culvert in the region of the side cavity. The magnitude of this preload was determined by trial and error but was sufficient to lift the crown just slightly above its desired position. This preload was approximately 80% of the at rest lateral pressure of the soil. The next step in the analysis was to give birth to the elements in the cavity and to remove the preload. The resulting pressure between soil and culvert was found to be distributed differently with depth but at the two locations measured by the pressure cells in the field (see figure 3b) the pressure intensities agreed closely. To determine the sensitivity of the final pressure distributions to the initially assumed preload distribution a further analysis was obtained with an initial preload distribution that was almost uniformly distributed with depth (figure 3c). The resulting pressure distribution after giving birth to the cavity elements and removing the preload had a similar shape (figure 3d) to that obtained using the linearly varying preload distribution. Agreement of the pressure values at the two locations where field measurements were obtained was excellent. It was concluded that the vertical distribution of the initial preload is not critical when using this technique to obtain final pressure.

PLACING OF CONCRETE

Using the ADINA program it is not possible to alter the stiffness properties of an element once they have been assigned for the initial run. For the concrete slab the elements at the time of placing have essentially no stiffness but upon curing achieve a stiffness greater than that of the surrounding soil.

Modelling of placement of the concrete was again done in two steps in the analysis. The first step consisted of applying a preload to the elements below the

concrete equal to the mass of the concrete (figure 4). This produced a state of stress in the existing structure corresponding to the placing of the concrete. The next step involved giving birth to the concrete (and reinforcement) elements with their final stiffnesses and removal of the preload. Since the weight of the concrete is then carried primarily in the steel culvert, concrete elements are essentially unstressed at this construction stage.

It was noted that the crown deflections obtained from the analyses were less than those observed in the field. This was attributed to the soil at the spring line being too stiff compared to that achieved in the field due to the problems of placing as noted earlier. Analyses were then rerun for the previous construction stage but the soil elements placed in the cavity region at the spring line were given orthotropic properties. The modulus of elasticity in the vertical direction was maintained at the value of the surrounding soil but in the lateral direction was reduced to only one-fifth of that in the vertical direction. If the same initial preload for modelling compaction at the spring line was used the drop in the crown deflection due to this decreased lateral stiffness was on the order of 1 mm and could be ignored although naturally this difference could have been compensated for by increasing slightly the initial preload. However the effect of using cavity elements with orthotropic properties permitted obtaining much closer agreement with observed crown displacements for the placing of the concrete and later construction stages. It is felt that the problem of obtaining compaction in this region noted in the field record is closely modelled using this orthotropic feature.

PLACING SOIL ABOVE HARDENED CONCRETE

Following an initial curing of the concrete, soil is then compacted in layers to the road surface. The first attempt at modelling was to give birth to all of the elements for this construction step at one time. No numerical problems were encountered but the final stresses in the soil included zones of tension and yielding near the surface which again could not be in agreement with those in the field.

A second modelling technique was to give birth to the elements in each layer of the mesh to simulate this phase of the construction. No problems were encountered in considering the first layer; that is, the layer immediately to the side of the concrete wing. However, tensile stresses were indicated in the element adjacent to the concrete. In attempting to consider the second layer it was not possible to reformulate the stiffness matrix with the new elements indicating a failure in the soil near the end of the concrete. Obviously no further analysis was possible. Clearly, even if numerical problems had not been encountered, this form of modelling does not give an indication of the stress in the soil that has just been compacted.

A technique similar to that used for the previous construction step was then tried which proved to be successful. To explain this technique and to give an indication of results a simpler patch test is discussed rather than the actual arch-beam culvert analysis.

The problem encountered was attributed to the different compressibility properties of the concrete and surrounding soil. When two elements are side by side, one of concrete and the other of soil, the addition of other soil elements above will, due to the forced compatibility of deformation at their common boundary, cause large tensile stresses in the soil which may lead ultimately to failure. The rate at which this occurs is dependent on the depth of soil below the concrete layer. Thus the problem will occur whenever one has a partial layer of elements that have a

significantly greater stiffness than the surrounding elements.

The patch test used is shown in figure 5. Soil elements between lines A and G represent the soil in place prior to pouring the concrete. The first three elements from the left between lines G and H represent the concrete wing and the soil elements above line G represent the soil placed after the concrete hardens. The boundaries for the patch test are fixed against deformation along line A and fixed against lateral deformation along the two vertical sides (roller joints). The top surface is free.

All runs for the patch test began by obtaining a gravity load solution for the soil below line C in place followed by birthing of the three concrete elements. The analyses differ only in the way the soil above line G is modelled.

To duplicate the phenomena observed in the prototype structure the first analysis consisted of birthing all soil elements above line G at one time. The principal stresses above line F are shown in figure 6. Here zones of tension and yielding at the surface similar to those obtained for the prototype are observed.

The second modelling procedure was to place the soil in layers beginning with the soil between lines G and H. The principal stresses for the region between lines F and H are shown in figure 7 where yielding was observed at three Gauss integration points in the element adjacent to the concrete and tension failure was observed at the other Gauss integration point. This was similar to that obtained in the prototype analysis. Elements between lines H and J were then birthed but although the stiffness matrix was reformulated no convergence was obtained after 10 iterations when normally only 1 or 2 interations are required. This was again considered indicative of the numerical problems encountered with the prototype analysis.

Having essentially reproduced the problems encountered with the prototype in the patch test, two techniques were tried to overcome these difficulties. The first involved applying a preload along line G under the soil elements only equal to the weight of these elements between lines G and H. The next step involved giving birth to these elements and at the same time removing the preload applied in the previous step. Thus the soil elements are created with stresses due only to their self weight since the deformations of all supporting elements due to this self weight being added are not included when computing the induced stresses. The process was repeated for the next layer of soil by again using two steps, the first preloading along line H equal to the weight of soil between lines H and I and then giving birth to the elements in this layer but removing the preload. The process is then repeated for all remaining layers. At no stage were tensile stresses or yielding of the soil obtained. The final principal stresses are shown in figure 8a. The stresses are considered representative of those that would be obtained in the field for the prototype.

Since the compression stresses in the upper layer being modelled at any construction stage were small it was thought prudent to try another modelling technique whereby when modelling the soil elements between lines G and H a preload was applied along line G under these soil elements and along line H above the concrete elements equal in magnitude to the weight of all soil to be placed above these lines. The soil elements between lines G and H were then birthed and the preload applied to line G reduced by the self weight of these elements and applied to line H. This process was then repeated layer by layer to the surface. The final stresses using this procedure are given in figure 8b and are seen to be essentially

identical to those obtained using the previous technique of applying a preload equal only to the weight of the next layer of elements. While the final stresses are essentially identical the stresses at intermediate steps are much greater as expected. Thus if the stresses at various stages of construction are of interest the first technique is required.

CONCLUDING REMARKS

For finite element analyses, where nonlinear material behavior is used and where elements are formed at later stages to simulate a construction sequence, the stress state within the elements at the time of birth can be very unrealistic. This is due primarily to the deformation of the existing structure under the self weight of the newly formed elements. This deformation also occurs in the field, however at this stage many materials are still being remolded by the construction procedure and no permanent stresses are induced.

Within the finite element program the elements have their stiffnesses formulated based upon the input geometry. For all elements, deflections of the nodes prior to the time of their birth are subtracted in all strain calculations. Applying the preload to the interface nodes causes them to deflect to their equilibrium position under the weight of the elements that will be birthed in the next stage. Giving birth to these elements with self weight and removing the preload effectively causes the deflections of the existing structure due to this self weight to be ignored. Hence, stresses in the birthed elements are obtained only from their internal displacements resulting in more realistic stress distributions and the elimination of many of the associated numerical difficulties.

Solutions are presented for three very different problems involving modelling stages of construction of an arch-beam culvert using the preload-birthing technique. This technique can also be used for a wide range of similar problems in other buried structures.

REFERENCE

1. ADINA Users Manual: ADINA Engineering Inc. Report AE81-1, Watertown, Mass. 1981.

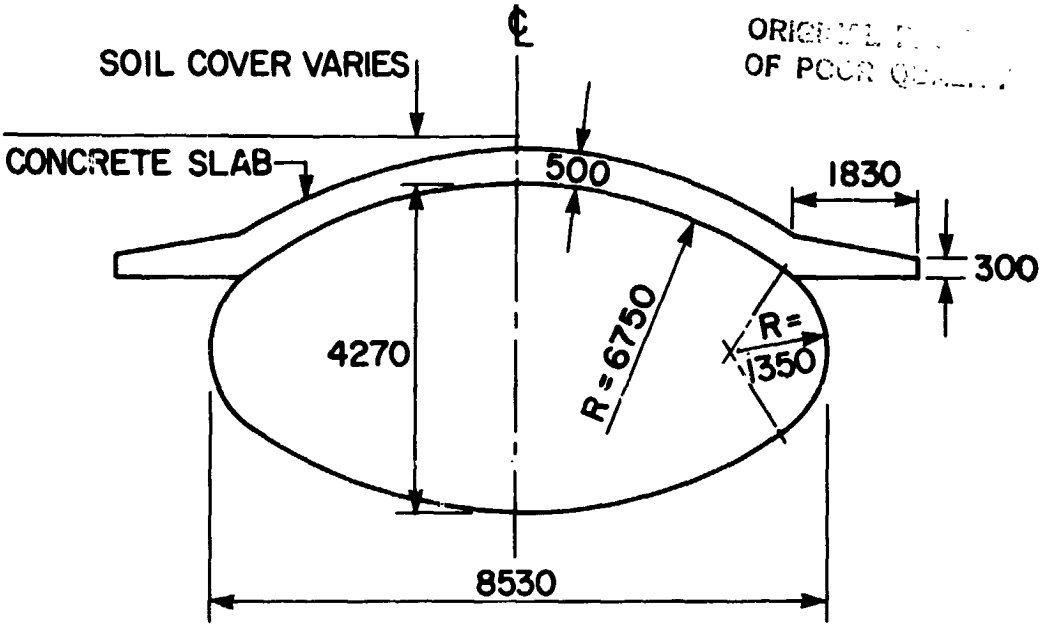

Figure 1. Cross section of arch-beam culvert prototype.

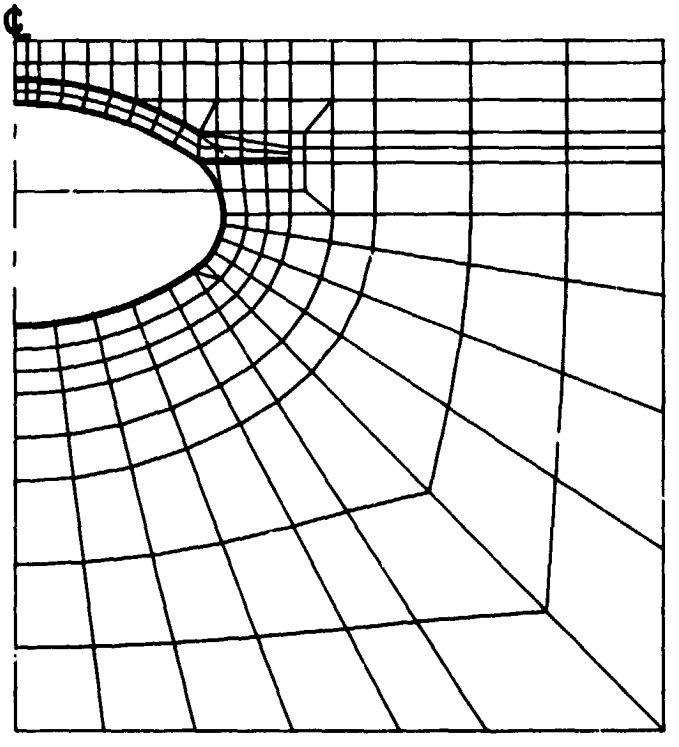

Figure 2. Mesh used to analyse arch-beam culvert prototype.

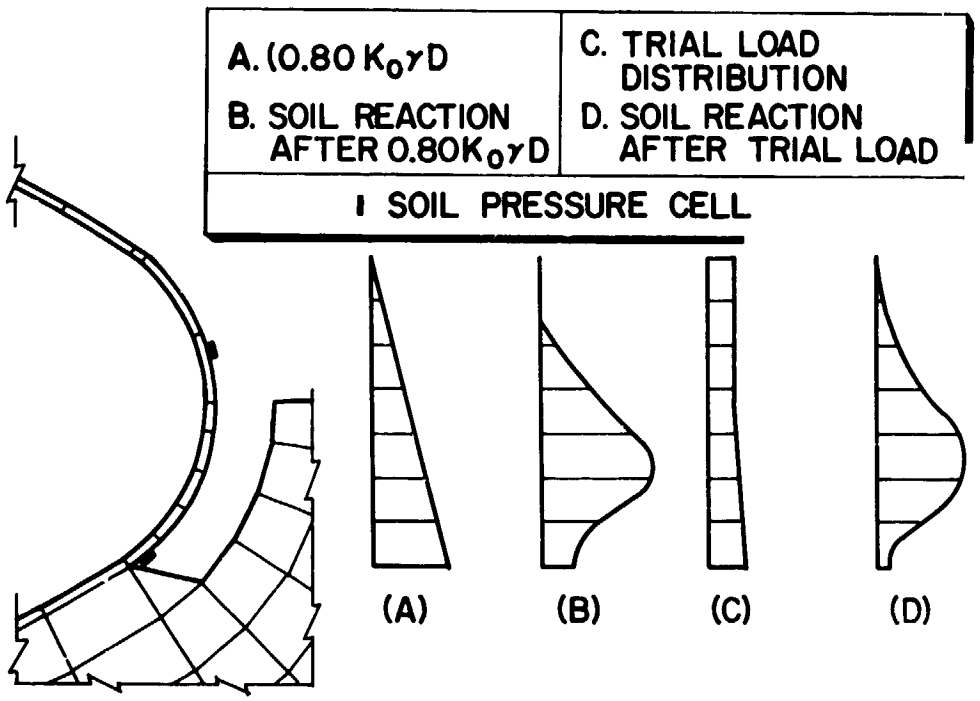

Figure 3. Preload distribution for placing soil near spring line.

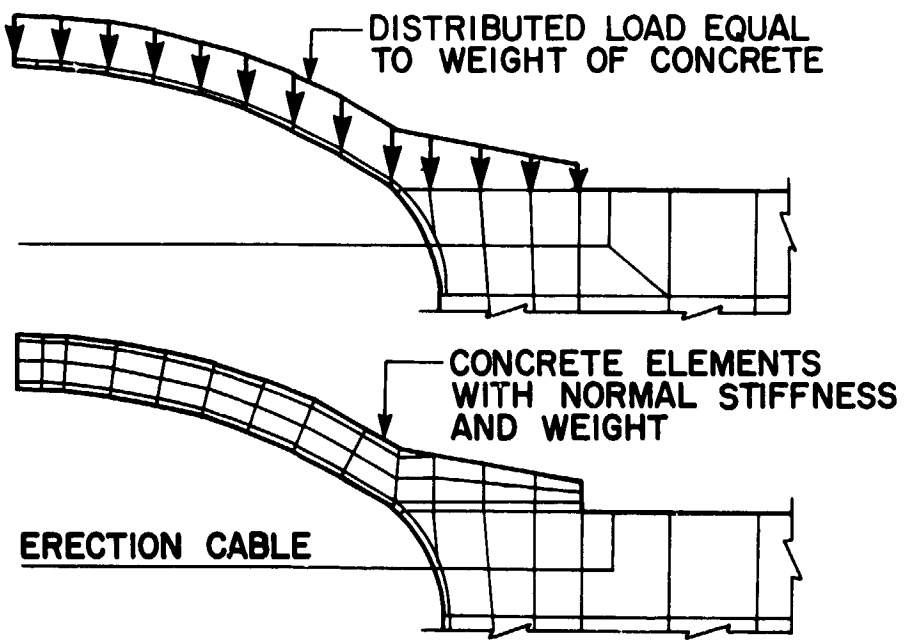

Figure 4. Preload distribution for placement of concrete.

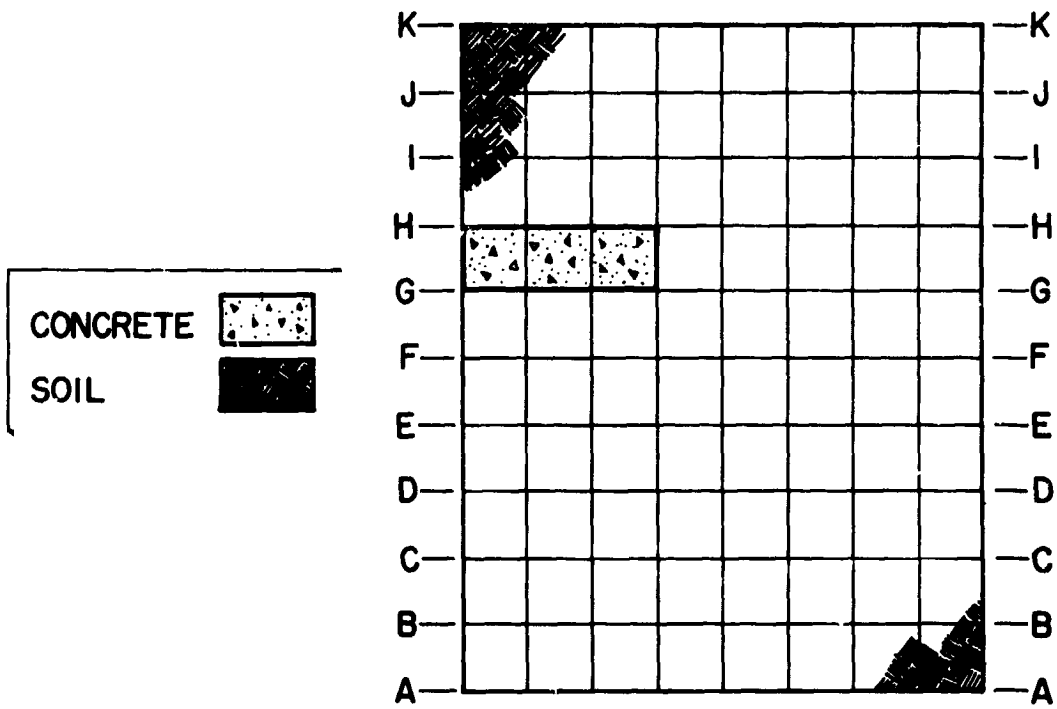

Figure 5. Mesh used for patch test to evaluate modelling the placing of soil.

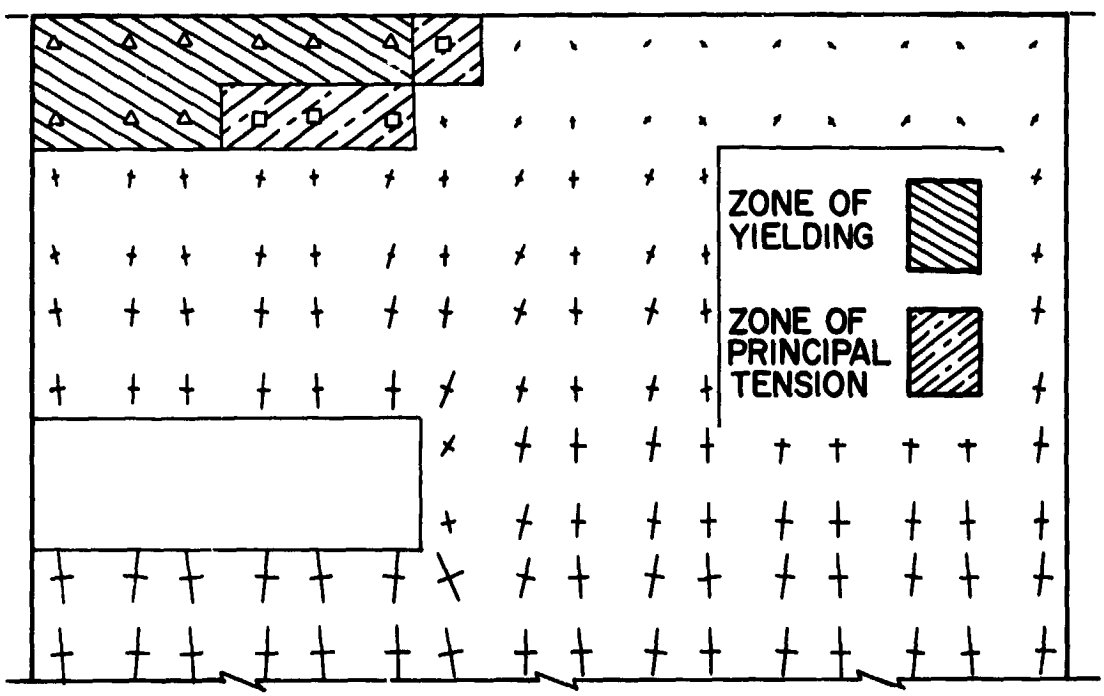

Figure 6. Principal stress due to placing soil without preload.

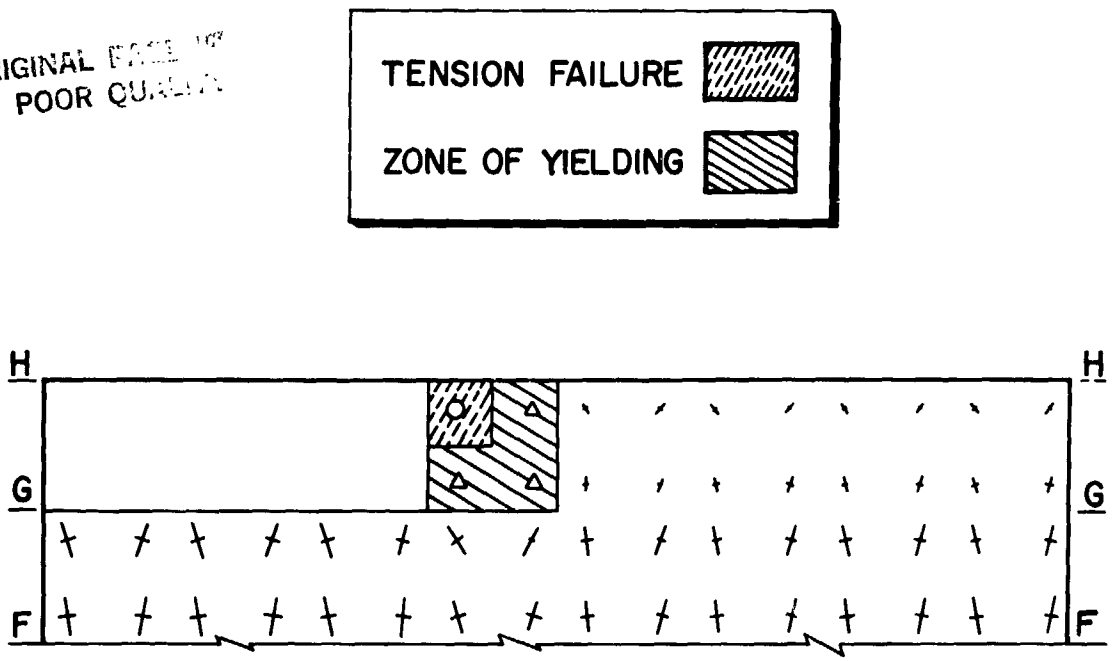

Figure 7. Principal stress due to placing single layer of soil without preload.

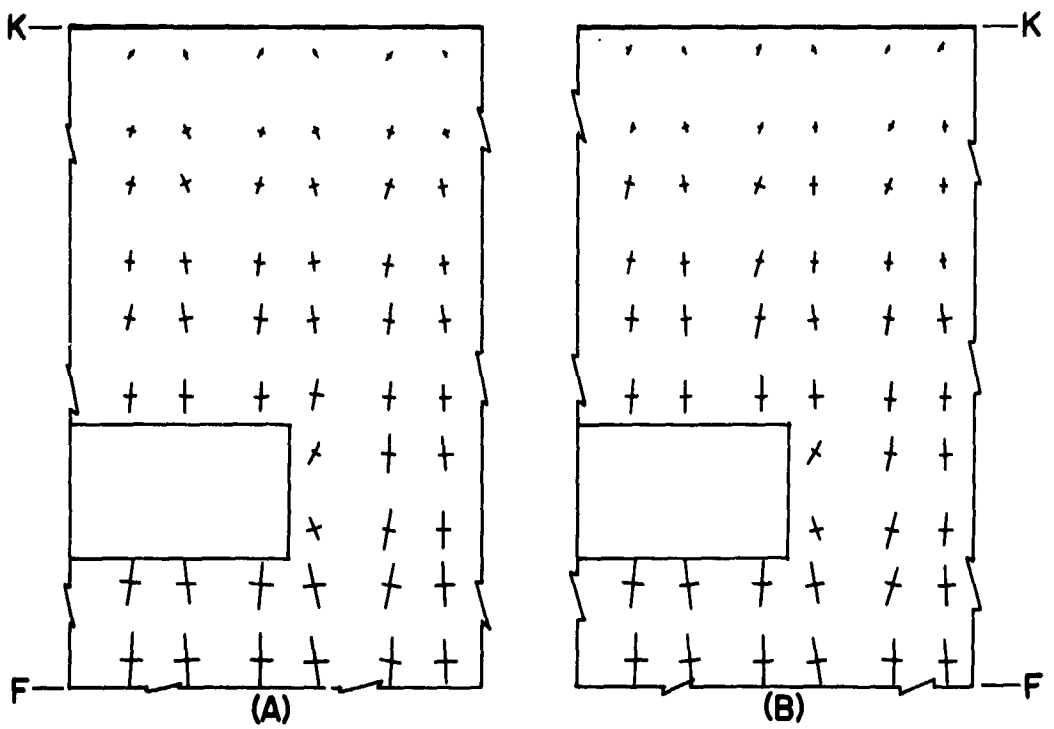

Figure 8. Principal stresses from two procedures of preload.

N85 10404

ON THE COMPUTER ANALYSIS OF STRUCTURES AND MECHANICAL SYSTEMS

Bruce E. Bennett
Bennett Computational Mechanics
Pleasant Hill, CA

Abstract

The governing equations for the analysis of open branch-chain mechanical systems are developed in a form suitable for implementation in a general purpose finite-element computer program. Lagrange's form of d'Alembert's principle is used to derive the system mass matrix and force vector. The generalized coordinates are selected as the unconstrained relative degrees of freedom giving the position and orientation of each "slave" link with respect to their "master" link. Each slave link may have from zero to six degrees of freedom relative to the reference frames of its master link. A strategy for automatic generation of the system mass matrix and force vector is described.

1. INTRODUCTION

Many problems in mechanics involve the interaction between separate bodies of matter. In general, individual material bodies deform under the action of applied forces. In special cases, however, solid bodies may be sufficiently unyielding that they may be considered rigid. Whether rigid or deformable, there is a need to predict the response of individual material bodies and the response and interaction between multiple bodies.

Recently, in a historical sense, the finite-element method has become a major extension of our ability to predict the response of a continuum of material, whether solid or fluid. The popularization of the digital computer has made the finite-element method readily available as a practical and useful tool. The development and use of this method have, however, been primarily directed at the analysis of individual material bodies. It is the intention of this paper to address the extension of the finite-element method to enable the direct analysis of general assemblies of rigid and deformable bodies.

The finite-element method can be thought of as a technique for approximating a continuum of matter by discrete rigid particles connected by finite "elements." Consistent with this perspective is the approximation of a general continuum of matter by discrete particles and finite rigid bodies connected by finite elements. Certain constraints may, in general, exist between the degrees of freedom associated with these particles and rigid bodies. For example, certain degrees of freedom might be "supported" with a prescribed and constant value. In other cases, certain degrees of freedom may be constrained to other degrees of freedom to form a "mechanical system."

A mechanical system is an organization of interconnected mechanical components. Machines and mechanisms are examples of mechanical systems. A machine is a mechanical system that "does work;" a mechanism is a mechanical system that "achieves a desired motion." Any of the mechanical components comprising the system may be considered rigid or deformable. The interconnection of these components, called kinematic pairs, is the distinguishing

feature between a mechanical system and a structure.

There has been, and continues to be, considerable interest in the analysis of mechanical systems. Much of this interest has focused on both open and closed kinematic branch-chain mechanical systems. One of my favorite papers is that published by Chace and Bayazitoglu [1] wherein the authors presented a complete development of closed branch-chain mechanical systems and described the application of this development in a 2-dimensional computer program. However, their development does not seem to lend itself to easy implementation in 2 dimensions, and would be very complex in 3 dimensions. More recently, Huston and Passerello [2, 3, 4], and others, have published papers describing their approach to this same problem. Of particular interest is the paper by Kamman and Huston [5], in which the authors present what appears to be a new approach to the elimination of the constrained degrees of freedom associated with a closed branch-chain mechanical system.

This paper is restricted to discussion of open branch-chain mechanical systems. The problem of interest is a formulation for the governing equations for this class of mechanical systems that will lead to practical and efficient implementation in a 3-dimensional finite-element program. It is the hope of the author that the insight garnered from this development will lead to a complete implementation for closed branch-chain mechanical systems.

The remainder of this paper is organized as follows. After a brief discussion concerning the mathematical notation employed herein, a thorough statement of the problem is given. Next a detailed investigation of the equations of motion for a simple kinematic chain is presented. The results of this investigation are a set of equations that provide the basis for the discussion, in the next part, of the system equations for a general open branch-chain mechanical system. An example problem is then considered, followed by some concluding remarks.

2. NOTATION

The dyadic notation for vectors and tensors is used throughout this paper. This notation is well suited for working with 3-dimensional vectors and tensors. Because of the need to work simultaneously with related pairs of vectors and tensors (for example, forces and moments, and velocities and angular velocities), I have also employed a "blend" of matrix notation and dyadic notation.

To illustrate, the velocity vector $\underline{v}$ and the angular velocity vector $\underline{\omega}$ are "associated" to form a special velocity vector

$$\{\underline{u}\} = \begin{Bmatrix} \underline{v} \\ \underline{\omega} \end{Bmatrix}$$

where the braces indicate the special nature, in this case a vector (in the matrix sense) of vectors (in the dyadic sense).

Similarly, the mass matrix $[\underline{\underline{M}}]$ (in the matrix sense) is defined as

$$[\underline{\underline{M}}] = \begin{bmatrix} m\underline{\underline{\delta}} & \underline{\underline{C}} \\ \underline{\underline{C}}^t & \underline{\underline{I}} \end{bmatrix}$$

where $\underline{\underline{\delta}}$, $\underline{\underline{C}}$, and $\underline{\underline{I}}$ are the usual dyadic tensors (the superscript "t" indicating that the transpose is to be taken) and where the brackets indicate the special nature, in this case a matrix of tensors.

Operationally, standard matrix and dyadic concepts apply, for example

$$\{\underline{u}\}^t \cdot \{\underline{u}\} = \underline{v} \cdot \underline{v} + \underline{\omega} \cdot \underline{\omega}$$

and

$$[\underline{\underline{M}}] \cdot \{\dot{\underline{u}}\} = \begin{Bmatrix} m\dot{\underline{v}} + \underline{\underline{C}} \cdot \dot{\underline{\omega}} \\ \underline{\underline{C}}^t \cdot \dot{\underline{v}} + \underline{\underline{I}} \cdot \dot{\underline{\omega}} \end{Bmatrix}$$

3. STATEMENT OF THE PROBLEM

The objective of this paper is to describe a methodology that provides for the computer analysis of problems in mechanics that involve structures and/or mechanical systems. This methodology is a natural extension of a finite-element program to include the description and the analysis of mechanical systems.

A finite-element program generates finite-element stiffness and mass matrices and force vectors at the element nodal points, or nodes. These matrices and the force vector are then assembled and accumulated at the system degrees of freedom associated with the "joints." The joints are particles which may possess inertia and may be subjected to applied forces. Many finite-element programs provide for the concept of a finite-size joint, or rigid body, through "eccentricities" or rigid "master/slave" constraints. For example, the joint is considered to be the origin of the rigid body and a finite-element node is at a fixed location with respect to the joint. A simple geometric transformation matrix transforms the element stiffness, mass, and force from the nodal location to the joint. With very little effort, then, a finite-element program can be easily extended to solve problems containing multiple non-interconnected rigid bodies.

A mechanical system is an organization of interconnected rigid bodies, which are called rigid links. The connectivity of the rigid links in the mechanical system can be represented by a hierarchical, tree-structured, or branch-chain organization (see figure 1). A branch-chain system is also referred to as a complex kinematic chain. A simple kinematic chain is a mechanical system with only a single branch. A closed branch-chain system

contains at least one closed loop, otherwise it is an open system.

Because of the complexity of the closed branch-chain mechanical systems, it was necessary to first fully understand the simpler but still complex open branch-chain mechanical systems. The remainder of this paper is concerned with the problem of developing the equations of motion for an arbitrary open branch-chain mechanical system in a form suitable for implementation in a general purpose finite-element computer program. These equations of motion are formulated using Lagrange's form of d'Alembert's principle [6]. From these equations a system mass matrix and force vector are extracted.

Consider an arbitrary open branch-chain mechanical system. Let the "upper-most" link (see figure 1) be the reference link. Any link in the system, except the "lowest" level links, can have any number of links "slaved" to it. Any link in the system, except the reference link, is itself slaved to only one "master" link.

The motion of each slave link is measured relative to its master link (figure 2). The motion of the reference link is measured with respect to an inertial reference frame. The generalized coordinates are selected as the unconstrained relative degrees of freedom. Five lower kinematic pairs [7] are easily modeled: 1) pin, 2) slider, 3) cylindric, 4) spheric, and 5) planar. The sixth lower kinematic pair, the helical pair, involves a coupling between rotation about an axis (the pin) and translation along that axis (the slider).

The development of the equations of motion for an arbitrary open branch-chain mechanical system proceeds as follows. The equations of motion for a simple kinematic chain are developed in a form in which the generalized active forces and inertia forces corresponding to the generalized coordinates of a particular rigid link are determined completely from the forces applied directly to that link and from the forces applied through the kinematic pair of the rigid link that is slaved to it. Clearly, then, the contribution of any number of slave links can be obtained by summing the contribution of each slave link.

4. EQUATIONS OF MOTION: SIMPLE KINEMATIC CHAIN

In this section the dynamical equations of motion for a simple open kinematic chain are developed in a form suitable for automatic generation by a digital computer. Lagrange's form of d'Alembert's principle [6] is used. This principle states that

$$Q_i + Q_i^* = 0 \qquad (1)$$

where Q_i and Q_i^* are the generalized active force and the generalized active inertia force, respectively, for the i-th generalized coordinate.

4.1 Description of the Model

With reference to figure 2, a simple kinematic chain which is comprised

of N rigid links is considered. One of the end links is selected as the reference link, and the links are numbered consecutively from the reference link, 1 through N. The reference link is considered to have only one link slaved to it. All other links are considered to be slaved to one master link. That is, referring to figure 2, the k+1 link is the slave link and the k-th link is the master link. Of course, the k-th link is itself a slave to the k-1 link.

4.2 Kinematics

Let $\underline{r}^k$ be the vector fixed in the k-th link that defines the reference origin of the k+1 link with respect to the origin of the k-th link. Let ${}^{k-1}\underline{x}^k$ be the relative displacement vector of the origin of the k-th link with respect to the reference origin of the k-th link which is fixed in the k-1 link. Similarly, define $\{{}^{k-1}\theta^k\}$ as the set of three Euler angles which defines the orientation of the k-th link with respect to an arbitrary set of axes fixed in the k-1 link.

The position of the origin of the k-th link in an inertial reference frame R is given by

$$ {}^R\underline{p}^k = \sum_{j=1}^{k} {}^{j-1}\underline{p}^j \qquad (2) $$

where

$$ {}^{k-1}\underline{p}^k = \underline{r}^k + {}^{k-1}\underline{x}^k $$
$$ {}^0\underline{p}^k = {}^R\underline{p}^k \qquad (3) $$

The orientation of the k-th link with respect to an arbitrary set of axes fixed in the k-1 link is completely defined by the unique rotation matrix

$$ {}^{k-1}\underline{\underline{R}}^k = {}^{k-1}\underline{\underline{R}}^k(\{{}^{k-1}\theta^k\}) $$

It follows that the orientation of the k-th link with respect to an arbitrary set of axes fixed in R is defined by

$$ {}^R\underline{\underline{R}}^k = {}^R\underline{\underline{R}}^1 \ldots {}^{k-1}\underline{\underline{R}}^k \qquad (4) $$

The angular velocity of the k-th link with respect to the arbitrary set of axes fixed in R is

$$ {}^R\underline{\omega}^k = \sum_{j=1}^{k} {}^{j-1}\underline{\omega}^j \qquad (5) $$

where ${}^{j-1}\underline{\omega}^{j}$ is the angular velocity of the j-th link with respect to the j-1 link. The vector ${}^{j-1}\underline{\omega}^{j}$ is related to the first derivative of the Euler angles $\{{}^{j-1}\theta^{j}\}$ through the equality

$$\{{}^{j-1}\dot{\theta}^{j}\} = [\Omega^{j}]\ \{{}^{j-1}\omega^{j}\} \tag{6}$$

where the matrix $[\Omega^{j}]$ is obtained directly from the definition of the Euler angles.

Finally, the velocity of the origin of the k-th link is obtained from

$$R_{\underline{v}}{}^{k} = \sum_{j=1}^{k} {}^{j-1}\underline{v}^{j} + \sum_{j=1}^{k-1} R_{\underline{\omega}}{}^{j} \times {}^{j}\underline{p}^{j+1} \tag{7}$$

where

$$R_{\underline{v}}{}^{k} = R_{d(R_{\underline{p}}{}^{k})/dt}$$

$$^{j-1}\underline{v}^{j} = {}^{j-1}d_{(^{j-1}\underline{x}^{j})/dt}$$

Since

$$\sum_{j=1}^{k-1} R_{\underline{\omega}}{}^{j} \times {}^{j}\underline{p}^{j+1} = \sum_{j=1}^{k-1} {}^{j-1}\underline{\omega}^{j} \times {}^{j}\underline{p}^{k} \tag{8}$$

and introducing the antisymmetric tensor $\underline{\underline{C}}(\underline{r})$ such that

$$\underline{\underline{C}}(\underline{r})\cdot\underline{\omega} = \underline{\omega} \times \underline{r} \tag{9}$$

then equation (7) can be written as

$$R_{\underline{v}}{}^{k} = \sum_{j=1}^{k} {}^{j-1}\underline{v}^{j} + \sum_{j=1}^{k-1} \underline{\underline{C}}({}^{j}\underline{p}^{k}).{}^{j-1}\underline{\omega}^{j} \tag{10}$$

Introduce, now, the geometric transformation matrix

$$[{}^{j}\underline{\underline{T}}^{k}] = \begin{bmatrix} \underline{\underline{\delta}} & \underline{\underline{C}}({}^{j}\underline{p}^{k}) \\ 0 & \underline{\underline{\delta}} \end{bmatrix}, \quad (j \leq k) \tag{11}$$

where ${}^{k}\underline{p}^{k} = 0$, and where $\underline{\underline{\delta}}$ is the idem factor (or "identity" tensor). Also let

$$\{^{k-1}\underline{u}^{k}\} = \begin{Bmatrix} ^{k-1}\underline{v}^{k} \\ ^{k-1}\underline{\omega}^{k} \end{Bmatrix} \qquad (12)$$

Then equation (10) can be written in the symbolic form

$$\{^{R}\underline{u}^{k}\} = \sum_{j=1}^{k} [^{j}\underline{T}^{k}] \cdot \{^{j-1}\underline{u}^{j}\} \qquad (13)$$

4.3 Generalized Coordinates

The position of the origin of the slave link with respect to the reference origin fixed in the master link, and the Euler angles defining the orientation of the set of axes fixed in the slave link with respect to the set of axes fixed in the master link are selected as the generalized coordinates. There may be from zero to six generalized coordinates relating the position and orientation of the slave link with respect to the master link. Let $\{^{k-1}q^{k}\}$ be the set of generalized coordinates, and let $^{k-1}\underline{x}_{t}^{k}$ and $\{^{k-1}\theta_{t}^{k}\}$ be the prescribed values such that the actual position and orientation of the k-th link with respect to the k-1 link are given by

$$\begin{Bmatrix} ^{k-1}\underline{x}^{k} \\ \{^{k-1}\theta^{k}\} \end{Bmatrix} = \{^{k-1}q^{k}\} + \begin{Bmatrix} ^{k-1}\underline{x}_{t}^{k} \\ \{^{k-1}\theta_{t}^{k}\} \end{Bmatrix} \qquad (14)$$

Following Kane [6], it is convenient to introduce $\{^{k-1}\underline{u}_{q}^{k}\}$ as linear combinations of the $\{^{k-1}\dot{q}^{k}\}$, that is

$$\{^{k-1}\underline{u}_{q}^{k}\} = \begin{Bmatrix} ^{k-1}\underline{v}_{q}^{k} \\ ^{k-1}\underline{\omega}_{q}^{k} \end{Bmatrix}$$

where $^{k-1}\underline{v}_{q}^{k}$ and $^{k-1}\underline{\omega}_{q}^{k}$ are the relative velocity and angular velocity corresponding to the generalized coordinates $\{^{k-1}\dot{q}^{k}\}$. Let $^{k-1}\underline{v}_{t}^{k}$ and $^{k-1}\underline{\omega}_{t}^{k}$ similarly correspond to the prescribed values $^{k-1}\dot{\underline{x}}_{t}^{k}$ and $\{^{k-1}\dot{\theta}_{t}^{k}\}$ so that

$$\{^{k-1}\underline{u}^{k}\} = \{^{k-1}\underline{u}_{q}^{k}\} + \begin{Bmatrix} ^{k-1}\underline{v}_{t}^{k} \\ ^{k-1}\underline{\omega}_{t}^{k} \end{Bmatrix} \qquad (15)$$

4.4 Lagrangian Base Vectors

The Lagrangian base vectors, also known as the partial rates of change

of position and orientation [6], that span the multi-dimensional vector space defined by the generalized coordinates can be determined "by inspection" when the velocity and angular velocity are expressed as a linear function of the $\{u_{q's}\}$. These Lagrangian base vectors are simply the coefficients of the $\{u_{q's}\}$ in that linear expression. Referring to equation (13), the Lagrangian base vectors are obtained as follows:

Decompose the matrix $[{}^{j}\underline{\underline{T}}^{k}]$ as

$$[{}^{j}\underline{\underline{T}}^{k}] = [{}^{j}\underline{\underline{T}}^{k}_{q}] + [{}^{j}\underline{\underline{T}}^{k}_{t}], \quad (j \leq k) \tag{16}$$

where

$$[{}^{j}\underline{\underline{T}}^{k}_{q}]\cdot\{{}^{j-1}\underline{u}^{j}\} = [{}^{j}\underline{\underline{T}}^{k}]\cdot\{{}^{j-1}\underline{u}^{j}_{q}\}, \quad (j \leq k) \tag{17}$$

and

$$[{}^{j}\underline{\underline{T}}^{k}_{t}]\cdot\{{}^{j-1}\underline{u}^{j}\} = [{}^{j}\underline{\underline{T}}^{k}]\cdot\begin{Bmatrix} {}^{j-1}\underline{v}^{j}_{t} \\ {}^{j-1}\underline{\omega}^{j}_{t} \end{Bmatrix}, \quad (j \leq k) \tag{18}$$

Then,

$$\{{}^{R}\underline{u}^{k}\} = \sum_{j=1}^{k} ([{}^{j}\underline{\underline{T}}^{k}_{q}] + [{}^{j}\underline{\underline{T}}^{k}_{t}])\cdot\{{}^{j-1}\underline{u}^{j}\} \tag{19}$$

and by inspection the Lagrangian base vectors are simply the columns of the submatrices of the geometric transformation matrix $[{}^{j}\underline{\underline{T}}^{k}_{q}]$, $j \leq k$.

4.5 Generalized Active Forces

The contribution of the forces acting on the k-th link to the generalized active forces associated with the i-th link is

$$\{{}^{i}\underline{Q}^{k}\} = [{}^{i}\underline{\underline{T}}^{k}_{q}]^{t}\cdot\{\underline{F}^{k}\}, \quad (i=1,\ldots,k) \tag{20}$$

where $[{}^{i}T^{k}_{q}]^{t}$ is the array of Lagrangian base vectors, and

$$\{\underline{F}^{k}\} = \begin{Bmatrix} \underline{f}^{k} \\ \underline{g}^{k} \end{Bmatrix}$$

and where $\underline{f}$ and $\underline{g}$ are the applied forces and moments, respectively, acting on the k-th link.

The total of the generalized active forces associated with the i-th link is the sum

$$\{\underline{Q}^i\} = \sum_{k=i}^{N} \{{}^i\underline{Q}^k\}$$

$$= \sum_{k=i}^{N} [{}^i\underline{\underline{T}}_q^k]^t \cdot \{\underline{F}\} \tag{21}$$

Using the property that

$$[{}^i\underline{\underline{T}}_q^k]^t = \prod_{\ell=i+1}^{k} [{}^{\ell-1}\underline{\underline{T}}_q^\ell]^t, \quad (k > i) \tag{22}$$

then

$$\{\underline{Q}^i\} = [{}^i\underline{\underline{T}}_q^i]^t \cdot \{\underline{F}^i\} + \sum_{k=i+1}^{N} \left(\prod_{\ell=i+1}^{k} [{}^{\ell-1}\underline{\underline{T}}_q^\ell]^t \right) \cdot \{\underline{F}^k\} \tag{23}$$

When this seemingly intractable expression is expanded it can be seen that it can be replaced with the folowing equivalent simple recursive equations:

$$\{\underline{Q}^N\} = [{}^N\underline{\underline{T}}_q^N]^t \cdot \{\underline{F}^N\} \tag{24}$$

$$\{\underline{Q}^i\} = [{}^i\underline{\underline{T}}_q^i]^t \cdot \{\underline{F}^i\} + [{}^i\underline{\underline{T}}_q^{i+1}]^t \cdot \{\underline{Q}^{i+1}\}, \quad (i=N-1,N-2,\ldots,1) \tag{25}$$

These equations are used to compute the total generalized active forces associated first with the N-th link, then the N-1 link, etc., in subsequent steps until all N links have been considered.

4.6 Generalized Active Inertia Forces

The generalized active inertia forces are determined in a process similar to the generalized active forces. Specifically, the contribution of the inertia forces acting on the k-th link to the generalized active inertia forces associated with the i-th link is

$$\{{}^i\underline{Q}^{*k}\} = [{}^i\underline{\underline{T}}_q^k]^t \cdot \{\underline{F}^{*k}\}, \quad (k \geq i) \tag{26}$$

where $\underline{F}^{*k}$ is the vector of inertia forces and moments acting on the k-th link, that is,

$$\{\underline{F}^{*k}\} = -[\underline{\underline{M}}^k] \cdot \begin{Bmatrix} R\dot{\underline{v}}^k \\ R\dot{\underline{\omega}}^k \end{Bmatrix} - \begin{Bmatrix} {}^R\underline{\omega}^k \times (\underline{\underline{C}}^k \cdot {}^R\underline{\omega}^k) \\ {}^R\underline{\omega}^k \times (\underline{\underline{I}}^k \cdot {}^R\underline{\omega}^k) \end{Bmatrix} \tag{27}$$

The link mass matrix is

$$[\underline{\underline{M}}^k] = \begin{bmatrix} M^k \underline{\underline{\delta}} & \underline{\underline{C}}^k \\ (\underline{\underline{C}}^k)^t & \underline{\underline{I}}^k \end{bmatrix} \tag{28}$$

where M^k, $\underline{\underline{C}}^k$, and $\underline{\underline{I}}^k$ are the rigid link mass, mass coupling tensor, and inertia tensor, respectively.

The accelerations can be expressed in terms of the first derivative of the $\{u_q's\}$ as

$$\begin{matrix} {}^{R\cdot k}\underline{v} \\ {}^{R\cdot k}\underline{\omega} \end{matrix} = \sum_{j=1}^{k} [{}^{j}\underline{\underline{T}}_q^k + {}^{j}\underline{\underline{T}}_t^k] \cdot \begin{Bmatrix} {}^{j-1\cdot j}\underline{v} \\ {}^{j-1\cdot j}\underline{\omega} \end{Bmatrix} + \{\underline{A}^k\} \tag{29}$$

where

$$\{\underline{A}^k\} = \begin{Bmatrix} \underline{a}^k \\ \underline{b}^k \end{Bmatrix} \tag{30}$$

and

$$\underline{b}^k = \sum_{j=1}^{k} {}^{R}\underline{\omega}^j \times {}^{j-1}\underline{\omega}^j \tag{31}$$

$$\underline{a}^k = \sum_{j=1}^{k-1} [{}^{R}\underline{\omega}^j \times {}^{j}\underline{v}^{j+1} + ({}^{R}\underline{\omega}^j \times {}^{j-1}\underline{\omega}^j) \times {}^{j}\underline{p}^k \tag{32}$$

$$+ {}^{R}\underline{\omega}^j \times {}^{R}d({}^{j}\underline{p}^{j+1})/dt], \quad k > 1$$

The inertia force on the k-th link can be written as

$$\{\underline{F}^{*k}\} = - [\underline{\underline{M}}^k] \cdot \sum_{j=1}^{k} [{}^{j}\underline{\underline{T}}_q^k] \cdot \{{}^{j-1\cdot j}\underline{u}\} + \{\tilde{\underline{F}}^k\} \tag{33}$$

where

$$\{\tilde{\underline{F}}^k\} = - [\underline{\underline{M}}^k] \cdot [(\sum_{j=1}^{k} [{}^{j}\underline{\underline{T}}_t^k] \cdot \{{}^{j-1\cdot j}\underline{u}\}) + \{\underline{A}^k\}] \tag{34}$$

$$- \begin{Bmatrix} {}^{R}\underline{\omega}^k \times (\underline{\underline{C}}^k \cdot {}^{R}\underline{\omega}^k) \\ {}^{R}\underline{\omega}^k \times (\underline{\underline{I}}^k \cdot {}^{R}\underline{\omega}^k) \end{Bmatrix}$$

The total of the generalized inertia forces associated with the i-th link is obtained using the recursive formulas derived above for the generalized active forces. That is,

$$\{\underline{Q}^{*N}\} = [\underline{\underline{T}}_q^{N\,N}]^t \cdot \{\underline{F}^{*N}\} \tag{35}$$

$$\{\underline{Q}^{*i}\} = [\underline{\underline{T}}_q^{i\,i}]^t \cdot \{\underline{F}^{*i}\} + [\underline{\underline{T}}_q^{i\,i+1}]^t \cdot \{\underline{Q}^{*i+1}\}, \quad (i=N-1,N-2,\ldots,1) \tag{36}$$

4.7 First-Order Differential Equations

The dynamical equations of motion are typically solved numerically with the aid of an explicit time integration scheme, and such a scheme is considered here. Toward this end the dynamical equations are considered as a first-order system of ordinary differential equations of the form

$$[A]\ \{\dot{y}\} = \{b\}$$

where

$$\{\dot{y}\} = \begin{Bmatrix} \{\dot{q}\} \\ \{\dot{u}_q\} \end{Bmatrix}$$

Actually, the $\{\dot{u}_q\}$ are uncoupled from the $\{\dot{q}\}$ and are obtained from the solution of the system of equations

$$[M]\ \{\dot{u}_q\} = \{F\} \tag{37}$$

Once the $\{\dot{u}_q\}$ are computed, the $\{\dot{q}\}$ are computed directly from the equations

$$^{k-1}\dot{\underline{x}}^k = {}^{k-1}\underline{v}^k, \quad (k=1,\ldots,N) \tag{38}$$

$$\{^{k-1}\dot{\theta}^k\} = [\Omega^k]\ \{^{k-1}\omega^k\}, \quad (k=1,\ldots,N) \tag{39}$$

5. SYSTEM EQUATIONS: OPEN BRANCH-CHAIN SYSTEMS

Using the results obtained for the simple kinematic chain, the dynamical equations for open branch-chain mechanical systems can be automatically generated and solved with the use of a digital computer. This result follows directly from the form of the equations derived for the simple kinematic chain. In particular, the recursive equation (25) is readily generalized to

$$\{\underline{Q}^i\} = [\underline{\underline{T}}_q^{i\,i}]^t \cdot \{\underline{F}^i\} + \sum_{\text{slaves}} [\underline{\underline{T}}_q^{i\,i+1}]^t \cdot \{\underline{Q}^{i+1}\} \tag{40}$$

where the sum is over all links that are slaved to the i-th link.

A strategy for automatic generation of the dynamical equations, i.e.,

generation of the system force vector and the system mass matrix, has been developed and implemented as an integral part of a general-purpose finite-element computer program. In this implementation the rigid links are processed by the program as joints with rigid body mass. The system mass matrix and force vector are assembled including contributions from both finite elements and joints/links. The assembly strategy for the joints/links within an open branch-chain mechanical system is described below. It is worth noting that the assembly of a tangent stiffness matrix is completely analogous to the assembly of the mass matrix.

5.1 Assembly of the Force Vector

The generalized active forces and certain terms from the generalized active inertia forces must be assembled to form the system force vector. Because the necessary terms from the generalized active inertia forces can be combined directly with the applied forces for each rigid link, it is sufficient to consider that this has been done.

Because the generalized active forces associated with the generalized coordinates of the i-th link are dependent only on the forces applied to the i-th link and to the generalized active forces associated with the i+1 link [equation (25)], it follows that the generalized active forces associated with all links at the i+1 level of links in the branch-chain system can be summed directly at the i-th link.

The assembly procedure is therefore straightforward. Beginning at the lowest level, that is, the links to which no other slave links are attached, assemble the contribution of the forces applied to those links to their generalized active forces using equation (24). For these links, transform their generalized active forces and accumulate the contribution to the master link to which each slave link is attached. The procedure is repeated until all links have been considered.

5.2 Assembly of the Mass Matrix

The system mass matrix can be assembled using an extension of the procedure used to assemble the system force vector. Because of the symmetry of the mass matrix, only the upper triangle needs to be assembled. Referring to equations (33), (35), and (36), it can be seen that the geometric transformation matrix $[{}^{j}\underline{T}^{k}_{q}]$ transforms the right side of the mass matrix $[\underline{\underline{M}}^{k}]$ from the k-th column to the j-th column. Similarly, with reference to equations (35) and (36), the transpose of the geometric transformation matrix $[{}^{i}\underline{T}^{i+1}_{q}]$ transforms the mass matrix $[\underline{\underline{M}}^{k}]$ from the i+1 row to the i-th row.

Using these concepts, the assembly procedure is as follows. Referring to figure 3, the mass matrix for each of the lowest level links is assembled at the row and column locations associated wholly with each link. This mass matrix is then transformed up to the row associated with the master link. Before assembling at this location, and before performing the successive transformations and assemblies that complete the entire column, a copy of this mass matrix is transformed over one column, transposed, and accumulated at that master

link. This procedure is repeated for all rigid links at the lowest level.

At the next level of links, the accumulated mass matrix is added to the actual mass matrix for each link, and the same procedure, as described above, is repeated. All levels of links are processed in the same manner.

6. EXAMPLE PROBLEM

The purpose of this example problem is to further examine the nature of the formulation presented in this paper and to compare results obtained from this formulation with those derived from an alternate approach. In particular, a 3-degree of freedom translating compound pendulum is considered. The dynamical equations are derived explicitly using Lagrange's equations. These derived equations are compared numerically with the computer-generated equations as described in this paper.

The problem considered consists of three rigid links as depicted in figure 4. The first link is the reference link. The origin of the first link is free to translate along the x-axis of the inertial reference frame R, and a set of axes fixed to this link at the origin are free to rotate about the z-axis of the frame R.

The reference origin for the second link is fixed in the first link at a location of $-\ell_1 \underline{e}^1_y$ with respect to the origin of the first link, where $\underline{e}^1_x$, $\underline{e}^1_y$ are orthogonal unit vectors fixed in the first link. A set of axes fixed to the second link are free to rotate about the z-axis of the first link, which is coincident with the z-axis of the reference frame R.

The third link is rigidly attached to the second link at a location $-\ell_2 \underline{e}^2_y$ with respect to the origin of the second link, where $\underline{e}^2_x$, $\underline{e}^2_y$ are orthogonal unit vectors fixed in the second link. Each of the rigid links has a mass of m_i and a moment of inertia at the link origin of I_i, where $i = 1, 2, 3$.

The generalized coordinates for this system are

$$\{q\} = \{x, \theta_1, \theta_2\}^t$$

and

$$\{u\} = \{\dot{q}\} = \{v, \omega_1, \omega_2\}^t$$

The kinetic energy is

$$K = \tfrac{1}{2}m_1\underline{v}^1\cdot\underline{v}^1 + \tfrac{1}{2}I_1\underline{\omega}^1\cdot\underline{\omega}^1 + \tfrac{1}{2}m_2\underline{v}^2\cdot\underline{v}^2 + \tfrac{1}{2}I_2\underline{\omega}^2\cdot\underline{\omega}^2 + \tfrac{1}{2}m_3\underline{v}^3\cdot\underline{v}^3 + \tfrac{1}{2}I_3\underline{\omega}^3\cdot\underline{\omega}^3$$

The equations of motion are obtained directly from Lagrange's equations of the first kind [6],

$$d/dt(\partial K/\partial \dot{q}_i) - \partial K/\partial q_i = Q_i$$

These equations can be written as

$$[M]\ \{\dot{u}\} = \{F\}$$

where

$$M_{11} = m_1 + m_2 + m_3$$

$$M_{12} = (m_2 + m_3)\ell_1\cos\theta_1 + m_3\ell_2(\underline{e}^2_x \cdot \underline{E}_x)$$

$$M_{13} = m_3\ell_2(\underline{e}^2_x \cdot \underline{E}_x)$$

$$M_{21} = M_{12}$$

$$M_{22} = I_1 + I_2 + I_3 + m_2\ell_1^2 + m_3(\ell_1^2 + \ell_2^2 + 2\ell_1\ell_2\cos\theta_2)$$

$$M_{23} = I_2 + I_3 + m_3(\ell_1\ell_2\cos\theta_2 + \ell_2^2)$$

$$M_{31} = M_{13}$$

$$M_{32} = M_{23}$$

$$M_{33} = I_2 + I_3 + m_3\ell_2^2$$

and

$$F_1 = (\underline{f}_1 + \underline{f}_2 + \underline{f}_3)\cdot\underline{E}_x + (m_2 + m_3)\ell_1\sin\theta_1\omega_1^2$$
$$- m_3\ell_2(\underline{e}^2_y \cdot \underline{E}_x)(\omega_1 + \omega_2)^2$$

$$F_2 = [(\underline{g}_1 + \underline{g}_2 + \underline{g}_3) - \ell_1\underline{e}^1_y \times \underline{f}_2 - (\ell_1\underline{e}^1_y + \ell_2\underline{e}^2_y) \times \underline{f}_3]\cdot\underline{E}_z$$
$$+ m_3\ell_1\ell_2\sin\theta_2[(\omega_1 + \omega_2)^2 - \omega_1^2]$$

$$F_3 = [\underline{g}_2 + \underline{g}_3 - \ell_2\underline{e}^2_y \times \underline{f}_3]\cdot\underline{E}_z$$
$$- m_3\ell_1\ell_2[\sin\theta_2\omega_1\omega_2 + \cos\theta_2(\omega_1 + \omega_2)\omega_1]$$

and where $\underline{f}_i$ and $\underline{g}_i$ are the applied forces and moments at the link origins, and $\underline{E}_x$, $\underline{E}_y$, $\underline{E}_z$ are orthogonal unit vectors fixed in the inertial reference frame R.

The accelerations are given by

$$\underline{a}^1 = \dot{v}\underline{E}_x$$

$$\underline{a}^2 = \underline{a}^1 + \ell_1\dot{\omega}_1\underline{e}^1_x + \ell_1\omega_1^2\underline{e}^1_y$$

$$\underline{a}^3 = \underline{a}^2 + \ell_2(\dot{\omega}_1 + \dot{\omega}_2)\underline{e}^1_x + \ell_2(\omega_1 + \omega_2)^2\underline{e}^2_y$$

while the angular accelerations are

$$\underline{R}\dot{\underline{\omega}}^1 = \dot{\omega}_1 \underline{E}_z$$

$$\underline{R}\dot{\underline{\omega}}^2 = (\dot{\omega}_1 + \dot{\omega}_2)\underline{E}_z$$

$$\underline{R}\dot{\underline{\omega}}^3 = \underline{R}\dot{\underline{\omega}}^2$$

The procedures discussed in this paper can be directly applied to give the identical dynamical equations. However, because this formulation has been implemented in a computer program it was of interest to check the generated numerical values. For various initial conditions, the components of the mass matrix, the force vector. and the acceleration vector can be computed and compared. It is sufficient, I believe, to report that the computation of these values with a digital computer using the formulation presented herein is of the same level of accuracy as the computation using the explicit equations and a hand-held calculator.

7. CONCLUSIONS

A methodology has been described that provides for the computer analysis of structures and mechanical systems. This methodology is a natural extension of a finite-element program to include the description and the analysis of mechanical systems. The rigid links in a mechanical system, for example, are processed by the finite-element program as joints with rigid-body mass properties.

Because of the complexity of closed branch-chain mechanical systems, this paper was restricted to the simpler but still complex open branch-chain mechanical systems. The equations of motion for a single kinematic chain are derived in a form that provides for their immediate generalization to an arbitrary branch-chain mechanical system. Finally, a strategy for automatic generation of the system mass matrix and force vector was described. The work presented in this paper has been implemented in a general-purpose finite-element computer program.

Future research is principally being directed at the automatic generation of the system equations for closed branch-chain mechanical systems.

REFERENCES

1. Chace, M.A. and Bayazitoglu, Y.O., "Development and Application of a Generalized d'Alembert Force for Multifreedom Mechanical Systems," Journal of Engineering for Industry, Trans. ASME, Volume 93, Ser. B., No. 1, Feb. 1971, pp. 317-327.

2. Huston, R.L. and Passerello, C.E., "On the Dynamics of Chain Systems--Applications in Manipulator and Human Body Models," ASME Paper No. 74-Wa/Aut.11, 1974.

3. Huston, R.L. and Passerello, C.E., "On Multi-Rigid-Body System Dynamics--Computer Solution for Equations of Motion of Large Mechanical Chains Without Closed Loops," Computers and Structures, Volume 10, June 1979, pp. 439-446.

4. Huston, R.L. and Passerello, C.E., "Multibody Structural Dynamics Including Translation Between the Bodies," Computers and Structures, Volume 12, Nov. 1980, pp. 713-720.

5. Kamman, J.W. and Huston, R.L., "Constrained Multibody System Dynamics - An Automated Approach," Advances and Trends in Structural and Solid Mechanics, Noor, A.K. and Housner, J.M., Editors, 1982, pp. 363-373.

6. Kane, T.R., Dynamics, Holt, Rinehart, and Winston, New York, 1968.

7. Shigley, J.E. and Vicker, J.J., Theory of Machines and Mechanisms, McGraw-Hill, New York, 1980.

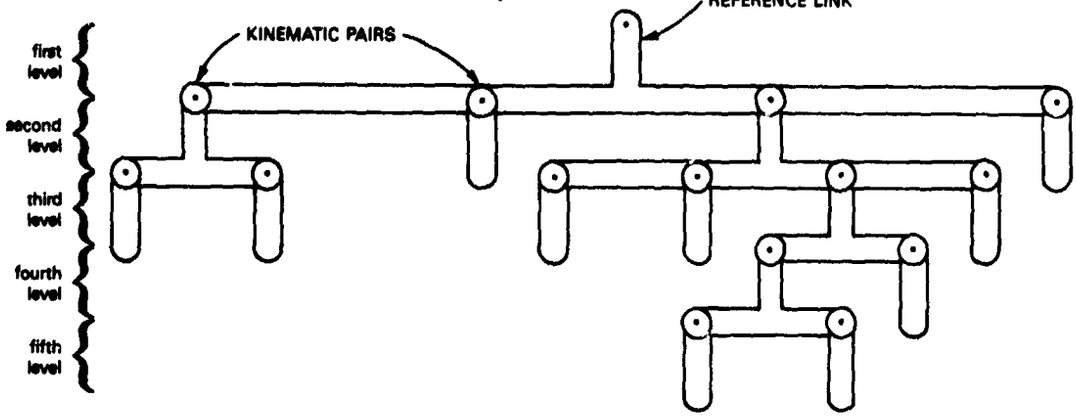

Figure 1.- Hierarchical organization of an open branch-chain mechanical system.

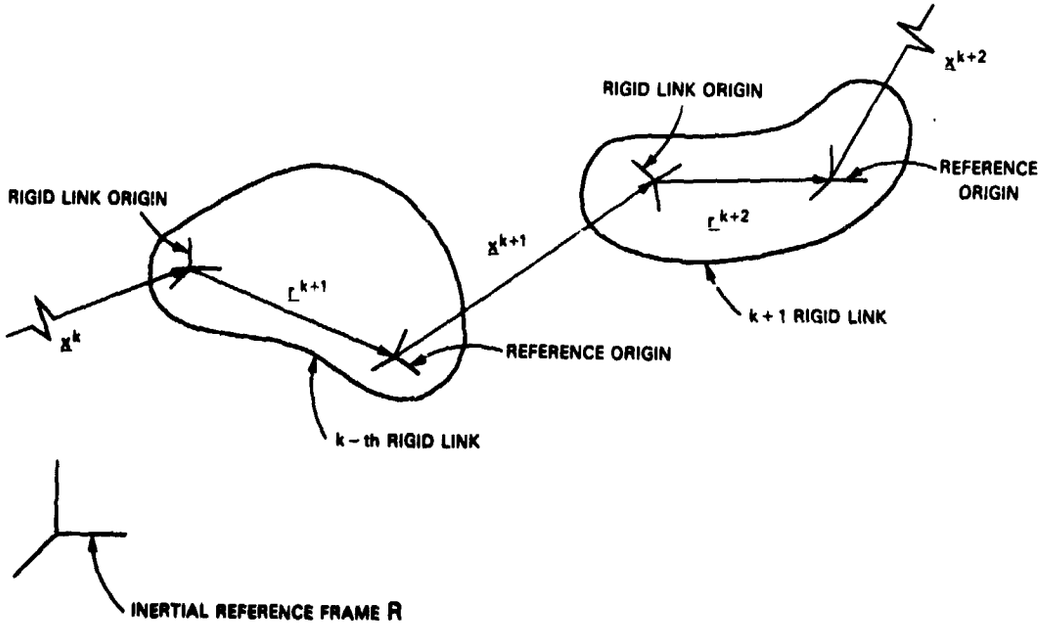

Figure 2.- Two rigid links in a kinematic chain.

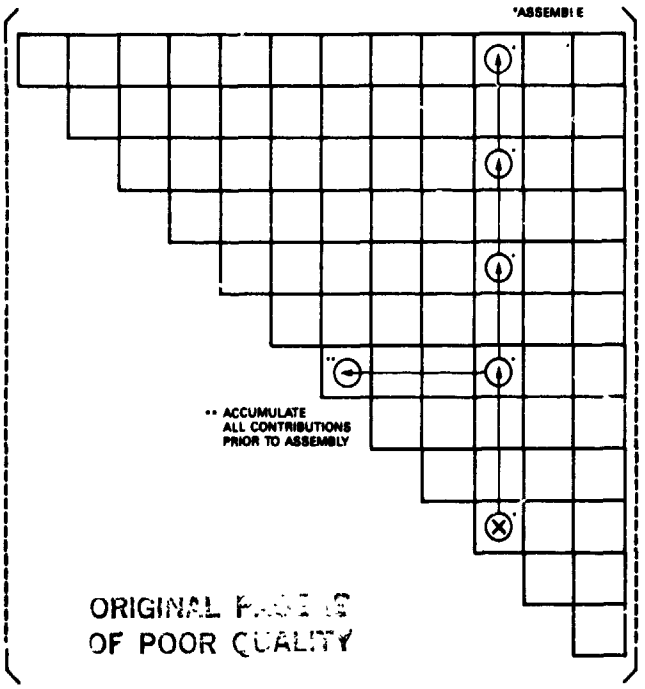

Figure 3.- Assembly of the system mass matrix.

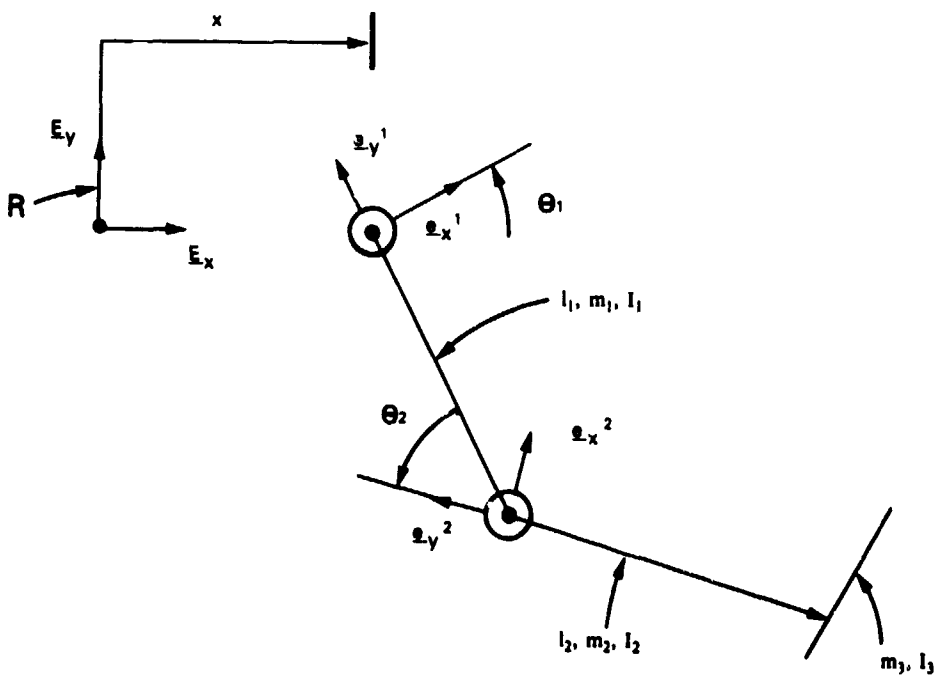

Figure 4.- Translating compound pendulum.